

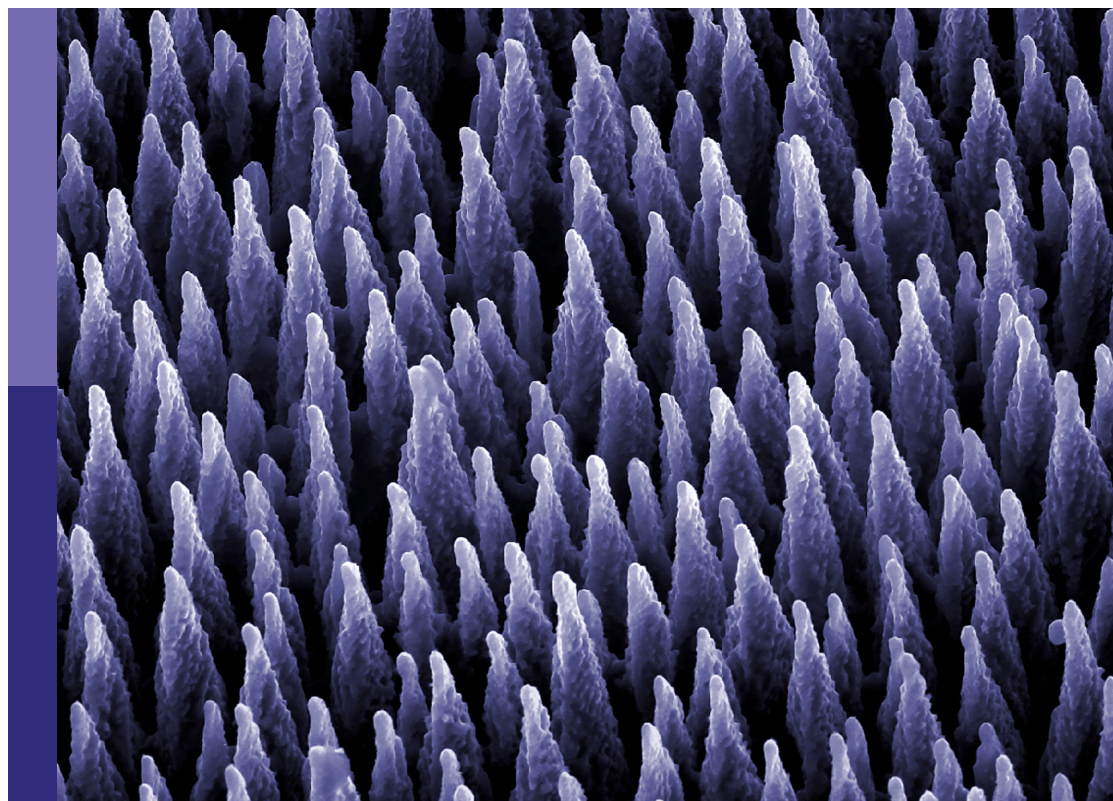
New frontiers in hybrid nanofluids for heat transfer process and applications

Edited by

Taseer Muhammad, Ali Saleh Alshomrani
and Safia Akram

Published in

Frontiers in Materials



FRONTIERS EBOOK COPYRIGHT STATEMENT

The copyright in the text of individual articles in this ebook is the property of their respective authors or their respective institutions or funders. The copyright in graphics and images within each article may be subject to copyright of other parties. In both cases this is subject to a license granted to Frontiers.

The compilation of articles constituting this ebook is the property of Frontiers.

Each article within this ebook, and the ebook itself, are published under the most recent version of the Creative Commons CC-BY licence. The version current at the date of publication of this ebook is CC-BY 4.0. If the CC-BY licence is updated, the licence granted by Frontiers is automatically updated to the new version.

When exercising any right under the CC-BY licence, Frontiers must be attributed as the original publisher of the article or ebook, as applicable.

Authors have the responsibility of ensuring that any graphics or other materials which are the property of others may be included in the CC-BY licence, but this should be checked before relying on the CC-BY licence to reproduce those materials. Any copyright notices relating to those materials must be complied with.

Copyright and source acknowledgement notices may not be removed and must be displayed in any copy, derivative work or partial copy which includes the elements in question.

All copyright, and all rights therein, are protected by national and international copyright laws. The above represents a summary only. For further information please read Frontiers' Conditions for Website Use and Copyright Statement, and the applicable CC-BY licence.

ISSN 1664-8714
ISBN 978-2-8325-2955-3
DOI 10.3389/978-2-8325-2955-3

About Frontiers

Frontiers is more than just an open access publisher of scholarly articles: it is a pioneering approach to the world of academia, radically improving the way scholarly research is managed. The grand vision of Frontiers is a world where all people have an equal opportunity to seek, share and generate knowledge. Frontiers provides immediate and permanent online open access to all its publications, but this alone is not enough to realize our grand goals.

Frontiers journal series

The Frontiers journal series is a multi-tier and interdisciplinary set of open-access, online journals, promising a paradigm shift from the current review, selection and dissemination processes in academic publishing. All Frontiers journals are driven by researchers for researchers; therefore, they constitute a service to the scholarly community. At the same time, the *Frontiers journal series* operates on a revolutionary invention, the tiered publishing system, initially addressing specific communities of scholars, and gradually climbing up to broader public understanding, thus serving the interests of the lay society, too.

Dedication to quality

Each Frontiers article is a landmark of the highest quality, thanks to genuinely collaborative interactions between authors and review editors, who include some of the world's best academicians. Research must be certified by peers before entering a stream of knowledge that may eventually reach the public - and shape society; therefore, Frontiers only applies the most rigorous and unbiased reviews. Frontiers revolutionizes research publishing by freely delivering the most outstanding research, evaluated with no bias from both the academic and social point of view. By applying the most advanced information technologies, Frontiers is catapulting scholarly publishing into a new generation.

What are Frontiers Research Topics?

Frontiers Research Topics are very popular trademarks of the *Frontiers journals series*: they are collections of at least ten articles, all centered on a particular subject. With their unique mix of varied contributions from Original Research to Review Articles, Frontiers Research Topics unify the most influential researchers, the latest key findings and historical advances in a hot research area.

Find out more on how to host your own Frontiers Research Topic or contribute to one as an author by contacting the Frontiers editorial office: frontiersin.org/about/contact

New frontiers in hybrid nanofluids for heat transfer process and applications

Topic editors

Taseer Muhammad — King Khalid University, Saudi Arabia

Ali Saleh Alshomrani — King Abdulaziz University, Saudi Arabia

Safia Akram — National University of Sciences and Technology, Pakistan

Citation

Muhammad, T., Alshomrani, A. S., Akram, S., eds. (2023). *New frontiers in hybrid nanofluids for heat transfer process and applications*. Lausanne: Frontiers Media SA. doi: 10.3389/978-2-8325-2955-3

Table of contents

- 05 **Thermally conductive electro-osmotic propulsive pressure-driven peristaltic streaming flow study with a suspended nanomaterial in a micro-ciliated tube**
Adil Wahid Butt, Noreen Sher Akbar, Rashid Mehmood and Shahid Farooq
- 17 **Energy transport analysis in natural convective flow of water:Ethylene glycol (50:50)-based nanofluid around a spinning down-pointing vertical cone**
Zahoor Iqbal, S. Yashodha, A. K. Abdul Hakeem, Abdulrahman Alsawi, Maryam Ahmed Alyami, El. Sayed Yousef, Ali H. Amin and Sayed M. Eldin
- 26 **Applications of variable thermal properties in Carreau material with ion slip and Hall forces towards cone using a non-Fourier approach via FE-method and mesh-free study**
Umar Nazir, Muhammad Sohail, Kanit Mukdasai, Abha Singh, Reham A. Alahmadi, Ahmed M. Galal and Sayed M. Eldin
- 38 **Numerical analysis of non-Newtonian nanofluids under double-diffusive regimes**
Noreen Sher Akbar and Fouad Othman Mallawi
- 46 **Numerical investigation of fractional Maxwell nano-fluids between two coaxial cylinders via the finite difference approach**
Muhammad Imran Asjad, Muhammad Usman, Taghreed A. Assiri, Arfan Ali and ElSayed M. Tag-ElDin
- 59 **Significance of non-uniform heat source/sink and cattaneo-christov model on hybrid nanofluid flow in a Darcy-forchheimer porous medium between two parallel rotating disks**
Sawan Kumar Rawat, Moh Yaseen, Umair Khan, Manoj Kumar, Sayed M. Eldin, Abeer M. Alotaibi and Ahmed M. Galal
- 74 **Mixed convective eyring-powell ferro magnetic nanofluid flow suspension towards a stretching surface with buoyancy effects through numerical analysis**
Faisal Z. Duraihem, Noreen Sher Akbar and Salman Saleem
- 85 **Effect of Ca doping on the arbitrary canting of magnetic exchange interactions in $\text{La}_{1-x}\text{Ca}_x\text{MnO}_3$ nanoparticles**
Akhtar Ali, Wiqar H. Shah, Akif Safeen, Liaqat Ali, Muhammad Tufail, Zakir Ullah, Kashif Safeen, Sayed M. Eldin, Mohamed R. Ali, Muhammad Sohail and Naveed Imran
- 92 **Effective role of mineral oil and biological nanomaterial on thermal energy influenced by magnetic dipole and nanoparticle shape**
Umar Nazir, Muhammad Sohail, Samaira Naz, Kanit Mukdasai, Manoj Singh, Abha Singh, Chandika Rama Mohan, Sayed M. Eldin and Ahmed M. Galal

- 104 **Effects of Newtonian heating and heat generation on magnetohydrodynamics dusty fluid flow between two parallel plates**
Farhad Ali, Gohar Ali, Arshad Khan, Ilyas Khan, Elsayed Tag Eldin and Matin Ahmad
- 115 **Sb-doped $\text{Ti}_{8.67}\text{Sn}_{1.33-x}\text{Sb}_x\text{Te}_6$ nanoparticles improve power factor and electronic charge transport**
Sabir Khan, Wiqar H. Shah, M. Tufail, Akhtar Ali, Sayed M. Eldin, Naveed Imran and Muhammad Sohail
- 123 **Investigation of bulk magneto-resistance crossovers in iron doped zinc-oxide using spectroscopic techniques**
Liaqat Ali, Wiqar H. Shah, Akhtar Ali, Sayed M. Eldin, Abdullah A. Al-Jaafary, A. Sedky, Javed Mazher, Naveed Imran and Muhammad Sohail
- 136 **Comparative investigation of fractional bioconvection and magnetohydrodynamic flow induced by hybrid nanofluids through a channel**
Ali Raza, Niat Nigar, Umair Khan, Samia Elattar, Sayed M. Eldin and Ahmed M. Abed
- 151 **Analysis of free and forced convections in the flow of radiative viscous fluid with oxytactic microorganisms**
S. Bilal, Asad Ullah, Imtiaz Ali Shah, Muhammad Imran Asjad, Musawa Yahya Almusawa and Sayed M. Eldin



OPEN ACCESS

EDITED BY

Ali Saleh Alshomrani,
King Abdulaziz University, Saudi Arabia

REVIEWED BY

Zahir Shah,
University of Lakki Marwat, Pakistan
Aurang Zaib,
Federal Urdu University of Arts, Sciences
and Technology Islamabad, Pakistan

*CORRESPONDENCE

Noreen Sher Akbar,
noreen.sher@ceme.nust.edu.pk

SPECIALTY SECTION

This article was submitted to Colloidal
Materials and Interfaces,
a section of the journal
Frontiers in Materials

RECEIVED 02 October 2022

ACCEPTED 04 November 2022

PUBLISHED 24 November 2022

CITATION

Butt AW, Akbar NS, Mehmood R and
Farooq S (2022), Thermally conductive
electro-osmotic propulsive pressure-
driven peristaltic streaming flow study
with a suspended nanomaterial in a
micro-ciliated tube.

Front. Mater. 9:1059816.

doi: 10.3389/fmats.2022.1059816

COPYRIGHT

© 2022 Butt, Akbar, Mehmood and
Farooq. This is an open-access article
distributed under the terms of the
[Creative Commons Attribution License](#)
(CC BY). The use, distribution or
reproduction in other forums is
permitted, provided the original
author(s) and the copyright owner(s) are
credited and that the original
publication in this journal is cited, in
accordance with accepted academic
practice. No use, distribution or
reproduction is permitted which does
not comply with these terms.

Thermally conductive electro-osmotic propulsive pressure-driven peristaltic streaming flow study with a suspended nanomaterial in a micro-ciliated tube

Adil Wahid Butt¹, Noreen Sher Akbar^{2*}, Rashid Mehmood³ and
Shahid Farooq¹

¹Department of Mathematics and Statistics, Riphah International University, Rawalpindi, Pakistan,

²DBS&H CEME, National University of Sciences and Technology, Islamabad, Pakistan, ³Department of
Mathematics, Faculty of Natural Sciences, HITEC University, Taxila, Pakistan

This article focuses on the peristaltic flow of carbon nanoparticle-suspended nanofluids under the influence of electroosmosis. The flow is considered inside a vertical tube with ciliated boundary walls. This study holds great importance because it represents the flow inside the esophagus of the human body. Nanoparticles are inserted in blood for diagnosing diseases like cancer and are also useful in angiography, angioplasty, etc. A comparative study is conducted for single-walled carbon nanotubes and multi-walled carbon nanotubes. We used the analytical method to obtain exact solutions of the velocity, temperature, and pressure profiles. The results have been presented graphically. Streamlines are also plotted to visualize the difference with SWCNT and MWCNT. We found that the use of CNT in the base fluid significantly enhances the thermal conductivity and helps increase the velocity of the fluid.

KEYWORDS

electroosmosis, peristalsis, nanofluid, pressure-driven flow, nanomaterial

Introduction

Peristaltic pumping, driven due to contraction or expansion of a distensible tube, is an obvious phenomenon of physiological fluids. Several pertinent examples include digestive tract movement in food transportation, urine transport *via* the bladder, bile flow from the gall bladder, ovum motion in the fallopian tube, blood circulation in vessels, and ciliary movement (Latham, 1966; Fung and Yih, 1968; Shapiro et al., 1969). Several modern day medical, industrial, and technological equipment include dialysis machines, heart-lung machines, and blood pumping devices. Similarly, the noxious food transport mechanisms in nuclear industries all involve the peristaltic transport mechanism. Owing to such fascinating applications, physiological fluid dynamics has been a subject of core interest

for researchers for the past several decades now. Numerous studies have been conducted to explore the peristaltic transport of physiological fluids with various physical characteristics. Mishra and Rao (2003) discussed the peristaltic flow of Newtonian fluids in an asymmetric channel and found out that trapping and reflux regions are directly related to the symmetry of the channel. Reddy et al. (2005) explored the influence of lateral walls on the peristaltic flow by considering the rectangular duct and discussed the effect of the aspect ratio on the pumping characteristics. Ebaid et al. (Elshehawey et al., 2006) considered a similar kind of problem but with the supposition of a porous medium. They concluded that the phase shift between the two walls is strongly effective on transport phenomena, while the axial velocity enhances with the permeability parameter. Nadeem and Akbar (2010) discussed the heat and mass transport in a vertical annulus using the Carreau fluid as a working fluid model and observed smaller trapped boluses for the case of a triangular wave when compared with other waveforms. In another study, Nadeem and Akram (2010) explored the peristaltic phenomenon of the Williamson fluid in an asymmetric channel. Ellahi et al. (2012) discussed the Carreau fluid in a rectangular duct through the porous medium. Their study showed that velocity magnitude increases with an enhancement in the Weissenberg number.

Over the past several years, cilia-driven flows have become a topic of hot research for scientists and engineers. These microscopic hair-like structures which extend from the surface of all mammalian cells, e.g., lungs, kidneys, and respiratory tract, play a critical role in the human physiological system, owing to its visibility in several natural and technological phenomena, microfluidic devices (which uses hair-like structures of artificial cilia), gamete transport in human physiology, respiratory mucus clearance, and embryo development; numerous theoretical studies have been conducted to explore this significant phenomenon. Awais et al. (Awais et al., 2020a; Awais et al., 2020b) have studied the effects of nanoparticles and cilia on the peristaltic motion. Ali et al. (2019) studied the entropy generation of nanofluids in the peristaltic motion. Akbar and Butt (2014) presented the heat transfer analysis due to the metachronal wave of cilia for a viscoelastic fluid. They presented exact solutions for the velocity, temperature, and pressure gradient profiles. A trapping phenomenon along with isotherms was also presented against pertinent parameters. Maqbool et al. (2017) explored the ciliary fluid dynamics in

an inclined tube using the fractional generalized Burgers' fluid model. They observed that relaxation time has a positive impact on the flow region thickness; thus, a greater pressure gradient is desired for the required fluid flow. Bhatti et al. (2017) applied thermal radiation on the MHD particle–fluid suspension induced due to the metachronal wave. Their computed results showed that the fluid parameter augments while the Hartman number suppresses the velocity profile. In another study, Sadaf et al. (2020) scrutinized the cilia-driven flow of a viscoelastic Jeffery fluid within a vertical tube and analyzed that the pumping mechanism is more efficient for the case of the Jeffery fluid than the Newtonian fluid. Farooq et al. (2020) explored the cilia-assisted flow of a magneto-biofluid with chemical reactions using the Darcy–Boussinesq model. Their computed flow rate was extremely close to the flow rate in the ductile efferent and further suggested implementation of their findings in the artificial cilia pumping systems in micro channels. Similarly, the impact of cilia walls on the magneto-fluid peristaltic motion through a porous medium at a moderate Reynolds number has been presented by Abo-Elkhair et al. (2017). The core findings of their study showed a lesser axial velocity without ciliated walls, while a higher pressure gradient in both directions was observed for the case of ciliated channel walls. They also found out that the number of trapped boluses significantly increases without eccentricity of the cilia elliptic path.

Carbon nanotubes (CNTs) are rolled-up graphene sheets having unique thermal, electric, and mechanical properties. In addition, these cylindrical-shaped tubes possess remarkable mechanical tensile strength; these are light in weight and possess good thermal conductivity. Such astonishing properties make them an ideal choice for usage in several biosensors, hydrogen storage cells, transistor batteries, and numerous other electrical shielding applications (Akhtar et al., 2021; Saleem et al., 2021). These nanotubes can be single-walled or multi-walled depending upon the usage of a single layer/multi-layer of carbon atoms. Single- and multi-walled carbon nanotubes are offering promising applications in several modern day industries such as anti-corrosion paints, coatings and thin films, conductive electrodes, engineering plastics, polymers, and many more for the last few decades or so. Meyer et al. (2013) examined the pressure drop characteristics within smooth tubes by utilizing multi-walled carbon nanotubes. Akbar (2015) analyzed the heat transfer in a peristaltic tube using carbon nanotubes and provided the exact analytical expressions for velocity and pressure gradients dependent upon the volume fraction of carbon nanotubes. Hayat et al. (2016) explored the peristaltic flow of a water-based fluid using carbon nanotubes with different thermal conductivity models and reported an increase in the heat transfer rate at the boundaries with a higher volume fraction of carbon nanotubes, while a decline in the velocity profile in the presence of carbon nanotubes was observed. Some more studies on CNTs can be found in the literature (Akbar and Butt, 2014; Khan et al., 2021; Khan et al., 2022; Waini et al., 2022).

TABLE 1 Thermal properties of the base fluid (water) and nanoparticles.

	Fluid phase (water)	Cu	SWCNT	MWCNT
c_p	4,179	385	425	796
ρ	997.1	8,933	2,600	1,600
k	0.613	400	6,600	3,000

TABLE 2 Comparison of the present results with the existing literature.

r	Present work $\varphi = 0$, $U = 0$	Ref (Sadaf et al., 2020)	Ref (Akbar and Butt, 2014) $\lambda_1 = 0$
-1.0	-1.000	-1.000	-1.000
-0.8	0.0815	0.0814	0.0816
-0.6	0.9173	0.9172	0.9174
-0.4	1.5115	1.5114	1.5116
-0.2	1.8668	1.8667	1.8669
0	1.9851	1.9850	1.9852
0.2	1.8668	1.8667	1.8669
0.4	1.5115	1.5114	1.5116
0.6	0.9173	0.9172	0.9174
0.8	0.0815	0.0814	0.0816
1.0	-1.000	-1.000	-1.000

In several areas of biotechnology, numerous micro-channel processes involve chemical separation where the electro-osmotic flow is inevitable due to charge disequilibrium (Nadeem et al., 2015). Some significant applications include tissue culture, cell scaffolding systems, pharmacodynamics, and medical electro-osmotic nanoscale devices (Abbasi and Shehzad, 2021). Tripathi et al. (Abbasi and Shehzad, 2021) inspected the electro-thermal peristaltic transport of nanofluids in a finite micro channel by adopting Chakraborty–Roy nanofluid electro kinetic formulation. Ijaz et al. (Tripathi et al., 2017) computed the influence of electroosmosis on the bio-nanofluid with non-spherical particles in a curved channel. The computed results revealed a rise in heat transfer due to the insertion of blade-shaped particles. Noreen et al. (Ijaz et al., 2018) considered the non-Darcy porous medium to present the heat transfer analysis in the electro-osmotic peristaltic flow and concluded that axial velocity declines with the Darcy number, while the heat transfer rate is significantly influenced with energy dissipation due to Joule heating. Recently, Khan et al. (Noreen and Tripathi, 2019) explored the impact of radiation on the electroosmosis-modulated peristaltic flow inside a tapered channel by using the Prandtl nanofluid and found that isothermal lines enhance with the electro-osmotic parameter.

After a comprehensive review of the existing published literature, it is quite evident that the cilia-driven peristaltic fluid using carbon nanotubes has not been given much attention despite its enormous practical significance. Most of the research on the peristaltic flows has been conducted in the absence of electroosmotic forces. As of authors' knowledge, the thermally conductive nanotube analysis of such fluid models caused by the effects of electroosmosis has not been studied so far. Since this model is studied under the influence of ciliated boundary conditions, the same contributes toward the drug delivery inside the human body.

Problem formulation

Consider an electroosmosis regulated peristaltic fluid flow of an aqueous ionic nanofluid through a vertical micro-ciliated tube of constant radius d . The carbon nanotubes are suspended in the base fluid to prepare the nanofluid. The fluid flow is driven by the combined effect of electroosmosis and peristaltic pumping. Furthermore, it is assumed that ionic species present in the aqueous ionic solution have an equal valence, i.e., the solution is symmetric. These ionic species are set into motion by enforcing an external electric field across the electric double layer carrying the nearby fluid molecules with them. The fluid flow is moving inside a plumb duct under the influence of gravitational force. Peristaltic pumping is generated by the propagation of the sinusoidal waves along the walls of the tube with a constant wave speed c and wavelength λ . The cylindrical coordinate system $(\bar{r}, \bar{z}, \bar{t})$ is found to be more suitable to perform the mathematical formulation of the flow problem in which \bar{r} and \bar{z} represent the radial and axial directions, respectively, and \bar{t} represents time. The deformation in the tube walls is physically shown in Figure 1 and mathematically represented as follows:

The envelopes of the cilia tips can be expressed Figure 2 mathematically as [1, 2]:

$$\bar{R} = \bar{H} = \bar{f}(\bar{Z}, \bar{t}) = a + a\varepsilon \cos\left(\frac{2\pi}{\lambda}(\bar{Z} - c\bar{t})\right), \quad (1a)$$

$$\bar{Z} = \bar{g}(\bar{Z}, \bar{t}) = a + a\varepsilon \alpha \sin\left(\frac{2\pi}{\lambda}(\bar{Z} - c\bar{t})\right), \quad (1b)$$

where a denotes the mean radius of the tube, ε is the non-dimensional measure with respect to the cilia length, and λ and c are the wavelength and wave speed of the metachronal wave, respectively. \bar{Z}_0 is the reference position of the particle, and α is the measure of the eccentricity of the elliptical motion.

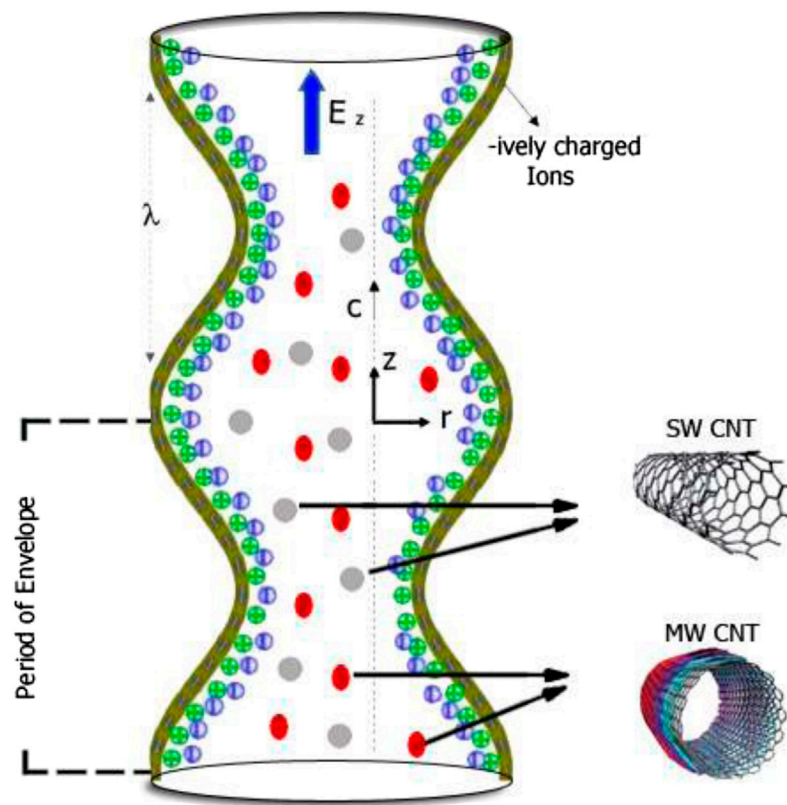


FIGURE 1
Geometry of the problem.

Governing equations

The governing set of equations formulated under the effect of mixed convection, heat source, and electroosmosis is given as follows:

$$\frac{\partial \bar{U}}{\partial \bar{R}} + \frac{\bar{U}}{\bar{R}} + \frac{\partial \bar{W}}{\partial \bar{Z}} = 0, \quad (1)$$

$$\rho_{nf} \left(\frac{\partial \bar{U}}{\partial \bar{t}} + \bar{U} \frac{\partial \bar{U}}{\partial \bar{R}} + \bar{W} \frac{\partial \bar{U}}{\partial \bar{Z}} \right) = -\frac{\partial \bar{P}}{\partial \bar{R}} + \mu_{nf} \left(\frac{\partial^2 \bar{U}}{\partial \bar{R}^2} + \frac{1}{\bar{R}} \frac{\partial \bar{U}}{\partial \bar{R}} - \frac{\bar{U}}{\bar{R}^2} + \frac{\partial^2 \bar{U}}{\partial \bar{Z}^2} \right) + \rho_e E_R, \quad (2)$$

$$\rho_{nf} \left(\frac{\partial \bar{W}}{\partial \bar{t}} + \bar{U} \frac{\partial \bar{W}}{\partial \bar{R}} + \bar{W} \frac{\partial \bar{W}}{\partial \bar{Z}} \right) = -\frac{\partial \bar{P}}{\partial \bar{Z}} + \mu_{nf} \left(\frac{\partial^2 \bar{W}}{\partial \bar{R}^2} + \frac{1}{\bar{R}} \frac{\partial \bar{W}}{\partial \bar{R}} + \frac{\partial^2 \bar{W}}{\partial \bar{Z}^2} \right) + \rho_e E_Z + (\rho\gamma)_{nf} (\bar{T} - T_0), \quad (3)$$

$$(\rho c)_{nf} \left(\frac{\partial \bar{T}}{\partial \bar{t}} + \bar{U} \frac{\partial \bar{T}}{\partial \bar{R}} + \bar{W} \frac{\partial \bar{T}}{\partial \bar{Z}} \right) = k_{nf} \left(\frac{\partial^2 \bar{T}}{\partial \bar{R}^2} + \frac{1}{\bar{R}} \frac{\partial \bar{T}}{\partial \bar{R}} + \frac{\partial^2 \bar{T}}{\partial \bar{Z}^2} \right) + Q_0, \quad (4)$$

in which E_R and E_Z specify the electric body forces in the radial and axial directions, respectively, \bar{U} is the velocity component in the radial direction, \bar{W} is the velocity in the axial direction, \bar{T} is the temperature of the fluid, k_{nf} is the effective thermal conductivity of the nanofluid, Q_0 is the heat source parameter, $(\rho c)_{nf}$ is the specific heat of the nanofluid, ρ_{nf} and μ_{nf} are the effective density and the viscosity of the nanofluid, respectively, $(\rho\gamma)_{nf}$ is the thermal expansion coefficient of the nanofluid, and ρ_e is the electric number density of the electrolyte solution.

If no slip condition is applied, then the velocities of the transporting fluid are just those caused by the cilia tips, which can be given as follows:

$$\bar{W} = \frac{\partial \bar{Z}}{\partial \bar{t}} \bigg|_{z_0} = \frac{\partial \bar{g}}{\partial \bar{t}} + \frac{\partial \bar{g}}{\partial \bar{Z}} \frac{\partial \bar{Z}}{\partial \bar{t}} = \frac{\partial \bar{g}}{\partial \bar{t}} + \frac{\partial \bar{g}}{\partial \bar{Z}} \bar{W}, \quad (5)$$

$$\bar{U} = \frac{\partial \bar{R}}{\partial \bar{t}} \bigg|_{z_0} = \frac{\partial \bar{f}}{\partial \bar{t}} + \frac{\partial \bar{f}}{\partial \bar{Z}} \frac{\partial \bar{Z}}{\partial \bar{t}} = \frac{\partial \bar{f}}{\partial \bar{t}} + \frac{\partial \bar{f}}{\partial \bar{Z}} \bar{W}. \quad (6)$$

Using equations (1) and (2) in equations (5) and (6), we obtain

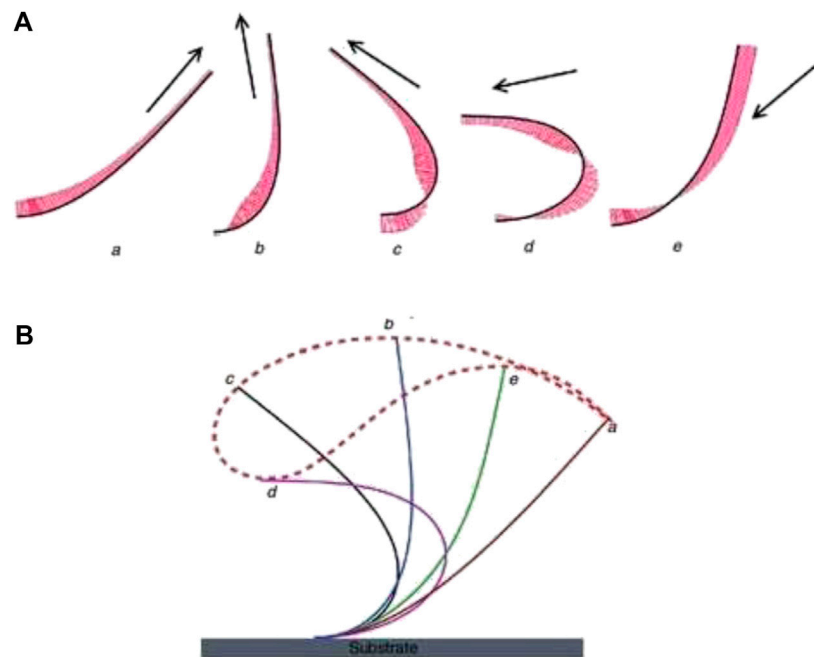


FIGURE 2
Movement of cilia causing fluid transport near the walls.

$$\bar{W} = \frac{-\frac{2\pi}{\lambda}(\epsilon\alpha a c \cos(\frac{2\pi}{\lambda})(\bar{Z} - c\bar{t}))}{1 - \frac{2\pi}{\lambda}(\epsilon\alpha a c \cos(\frac{2\pi}{\lambda})(\bar{Z} - c\bar{t}))} \quad (7)$$

$$\bar{U} = \frac{\frac{2\pi}{\lambda}(\epsilon\alpha c \sin(\frac{2\pi}{\lambda})(\bar{Z} - c\bar{t}))}{1 - \frac{2\pi}{\lambda}(\epsilon\alpha a c \cos(\frac{2\pi}{\lambda})(\bar{Z} - c\bar{t}))} \quad (8)$$

From the general mixture rule, the effective density, specific heat, and thermal expansion coefficient of the Cu–water nanofluid are determined, and the Brinkman's relation and the Maxwell model are employed to specify the viscosity and thermal conductivity of the nanofluid as follows:

$$\rho_{nf} = (1 - \phi)\rho_f + \phi\rho_{CNT}, \quad \mu_{nf} = \frac{\mu_f}{(1 - \phi)^{2.5}}, \quad (9)$$

$$(\rho c_p)_{nf} = (1 - \phi)(\rho c_p)_f + \phi(\rho c_p)_{CNT}, \quad \alpha_{nf} = \frac{k_{nf}}{(\rho c_p)_{nf}}$$

$$(\rho\gamma)_{nf} = (1 - \phi)(\rho\gamma)_f + \phi(\rho\gamma)_{CNT},$$

$$k_{nf} = k_f \left(\frac{(1 - \phi) + \frac{2\phi k_{CNT}}{k_{CNT} - k_f} \log\left(\frac{k_{CNT} + k_f}{2k_f}\right)}{(1 - \phi) + \frac{2\phi k_f}{k_{CNT} - k_f} \log\left(\frac{k_{CNT} + k_f}{2k_f}\right)} \right).$$

Here, ϕ designates the nanoparticle volume fraction, the subscript “ f ” is used to denote the properties of the base fluid, and “ p ” denotes the solid particle properties. The distribution of the electric potential within the fluid medium is described by the Poisson equation as follows:

$$\nabla^2 \bar{\varphi} = \frac{\partial^2 \bar{\varphi}}{\partial \bar{R}^2} + \frac{1}{\bar{r}} \frac{\partial \bar{\varphi}}{\partial \bar{R}} + \frac{\partial^2 \bar{\varphi}}{\partial \bar{Z}^2} = -\frac{\rho_e}{\epsilon_r \epsilon_0}. \quad (10)$$

Here, ϵ_r represents the relative permittivity of the medium, ϵ_0 is the permittivity of the vacuum, and the electric number density in terms of the number density of cations n^+ and the anions n^- is described as follows:

$$\rho_e = e z (n^+ - n^-). \quad (11)$$

Defining the transformation of velocity components and the coordinates from the stationary frame to the wave frame (moving frame of reference), to observe the steady fluid flow, as follows:

$$\bar{z} = \bar{Z} - c\bar{t}, \quad \bar{r} = \bar{R}, \quad \bar{w} = \bar{W} - c, \\ \bar{u} = \bar{U}, \quad \bar{p}(\bar{r}, \bar{z}) = \bar{P}(\bar{R}, \bar{Z}, \bar{t}). \quad (12)$$

The considered flow problem can be simplified by performing the non-dimensional analysis by introducing the following dimensionless parameters:

$$r = \frac{\bar{r}}{\lambda}, \quad z = \frac{\bar{z}}{d}, \quad p = \frac{\bar{p} d^2}{\mu_f c \lambda}, \quad n = \frac{\bar{n}}{n_0}, \quad Re = \frac{\rho_f c d}{\mu_f}, \quad \Psi = \frac{\bar{\Psi}}{c d}, \\ h = \frac{\bar{H}}{d}, \quad Pr = \frac{\mu_f c_p}{k_f}, \quad \delta = \frac{d}{\lambda}, \quad \theta = \frac{\bar{T} - T_0}{T_0}, \quad Gr = \frac{\rho_f g \gamma_f d^2 T_0}{\mu_f c}, \\ U = -\frac{\epsilon_0 \epsilon_r k_f \hat{T}_{avg} E_z}{e z \mu_f c}, \quad \kappa = \sqrt{\frac{2 n_0 e^2 z^2 d^2}{\epsilon_0 \epsilon_r k_f \hat{T}_{avg}}} = \frac{d}{\lambda_d}, \quad \varphi = \frac{e z \bar{\varphi}}{k_f \hat{T}_{avg}}, \\ \beta = \frac{Q_0 d^2}{T_0 k_f}, \quad L = \frac{(\rho\gamma)_{nf}}{(\rho\gamma)_f}. \quad (13)$$

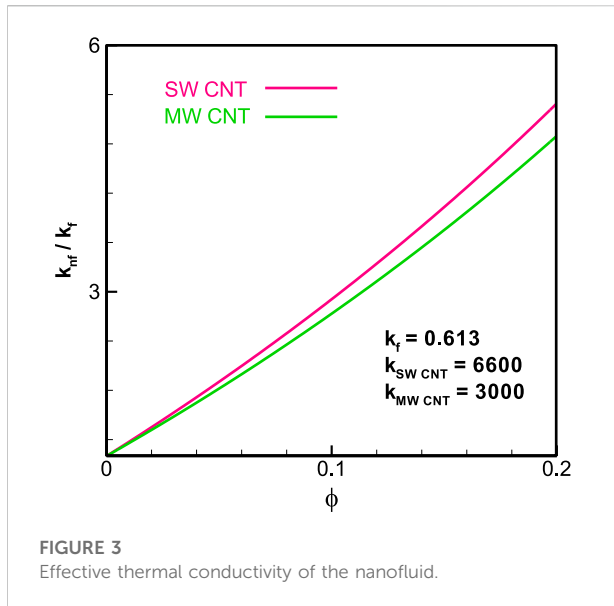


FIGURE 3
Effective thermal conductivity of the nanofluid.

Then, applying the lubrication linearization theory of long wavelength and the low Reynolds number, we are left with the following simplified set of equations:

$$\frac{\partial p}{\partial r} = 0, \quad (14)$$

$$\frac{dp}{dz} = \frac{\mu_{nf}}{\mu_f} \frac{1}{r} \frac{\partial}{\partial r} \left(r \frac{\partial w}{\partial r} \right) + G_r L \theta + U \frac{1}{r} \frac{\partial}{\partial r} \left(r \frac{\partial \varphi}{\partial r} \right), \quad (15)$$

$$\frac{1}{r} \frac{\partial}{\partial r} \left(r \frac{\partial \theta}{\partial r} \right) + \beta \frac{k_f}{k_{nf}} = 0, \quad (16)$$

$$\frac{1}{r} \frac{\partial}{\partial r} \left(r \frac{\partial \varphi}{\partial r} \right) = \kappa^2 \left(\frac{n^- - n^+}{2} \right), \quad (17)$$

where U designates the Helmholtz–Smoluchowski velocity or the electro-osmotic velocity parameter, G_r is the Grashof number, β is the dimensionless heat source parameter, θ is the dimensionless temperature parameter, and κ is the ratio of the characteristic traverse length to the Debye length parameter.

The local ionic distribution of ionic species can be specified by the linearized Boltzmann distribution for low zeta potential which accurately estimates the electric potential established in the fluid medium without increasing the complexity of the flow problem; as for most of the electrolyte solution, the generated electric potential lies in the range less than or equal to 25 mV.

$$n^\pm = e^{\mp \varphi}. \quad (18)$$

Using equation (14) in (13), we get the linearized Poisson–Boltzmann paradigm (Tripathi et al., 2017) as follows:

$$\frac{1}{r} \frac{\partial}{\partial r} \left(r \frac{\partial \varphi}{\partial r} \right) = \kappa^2 \sinh(\varphi), \quad (19)$$

which is further simplified under the Debye–Hückel approximation (Tripathi et al., 2017), i.e., $\sinh(\varphi) \approx \varphi$, as follows:

$$\frac{1}{r} \frac{\partial}{\partial r} \left(r \frac{\partial \varphi}{\partial r} \right) = \kappa^2 \varphi. \quad (20)$$

The dimensionless form of the no-slip boundary conditions for velocity temperature and electric potential enforced along the tube walls is given by the following equations:

$$\varphi = \xi, w = \frac{-2\pi\epsilon\beta_1 \cos(2\pi z)}{1 - 2\pi\epsilon\beta_1}, \theta = 0, \text{ at } r = h = 1 + \epsilon \cos(2\pi z), \quad (21)$$

$$\frac{\partial \varphi}{\partial r} = 0, \frac{\partial w}{\partial r} = 0, \frac{\partial \theta}{\partial r} = 0, \text{ at } r = 0.$$

Solution profiles

An analytical expression for velocity profile, temperature distribution, and electric potential can be obtained by integrating equations (11), (12), and (16) with the help of appropriate boundary conditions. The resulting velocity profile, temperature distribution, and electric potential are given as follows:-

$$w(r, z) = \frac{(h^2 - r^2) \left(G_r L \frac{k_f}{k_{nf}} \beta (3h^2 - r^2) - 16 \frac{dp}{dz} \right) + 64 \left(U \xi - \frac{\mu_{nf}}{\mu_f} \right) - 64 U \xi \frac{I_0(r\kappa)}{I_0(h\kappa)}}{64 \frac{\mu_{nf}}{\mu_f}}, \quad (22)$$

$$\theta(r, z) = \frac{1}{4} \frac{k_f}{k_{nf}} (h^2 - r^2) \beta, \quad (23)$$

$$\varphi = \xi \frac{I_0(r\kappa)}{I_0(h\kappa)}. \quad (24)$$

To find the pressure gradient, we use the flow rate in the moving frame given by the following equation:

$$F = 2\pi \int_0^h r w dr. \quad (25)$$

From Equation 21, the pressure gradient can be obtained in terms of flow rate as follows:

$$\frac{dp}{dz} = \frac{7}{40} G_r L h^2 \frac{k_f}{k_{nf}} \beta + \frac{3F}{h^3} \frac{\mu_{nf}}{\mu_f} + \frac{3\pi U \xi}{h^2 I_0(h\kappa)} [I_1(h\kappa) L_0(h\kappa) - I_0(h\kappa) L_1(h\kappa)], \quad (26)$$

where $I_0(x)$ and $I_1(x)$ are the modified Bessel function of the first kind, defined as follows:

$$I_j(x) = \sum_{i=0}^{\infty} \frac{1}{i! \Gamma(i+j+1)} \left(\frac{x}{2} \right)^{2i+j} \quad (27)$$

and $L_0(x)$, $L_1(x)$ are the modified Struve functions, defined as follows:

$$L_j(x) = \sum_{i=0}^{\infty} \frac{1}{i! \Gamma(\frac{3}{2}+i) \Gamma(\frac{3}{2}+i+j)} \left(\frac{x}{2} \right)^{2i+j+1}. \quad (28)$$

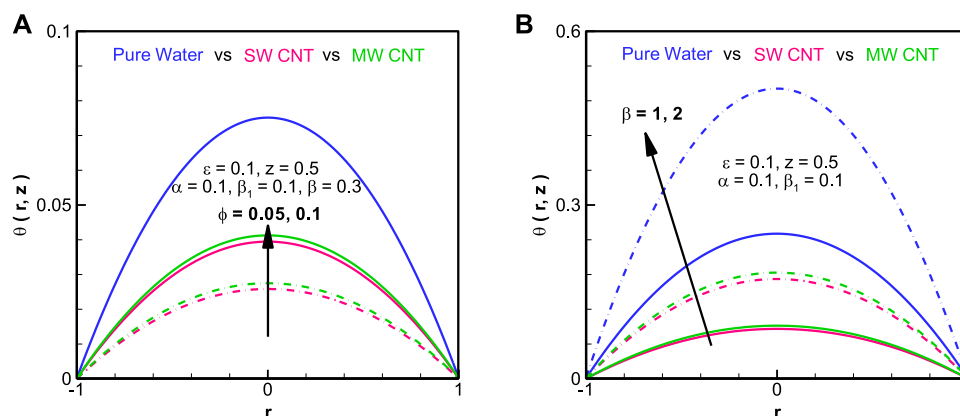


FIGURE 4
Temperature profile of the nanofluid.

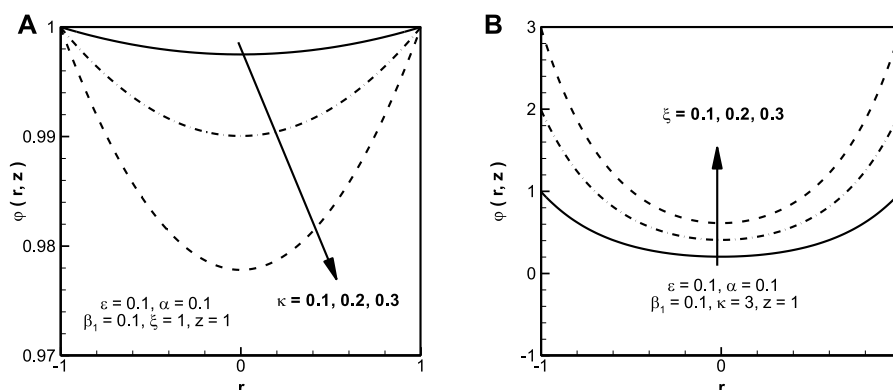


FIGURE 5
Electric potential of the nanofluid.

Using the aforementioned equation (22), we can evaluate the pressure rise ΔP as follows:

$$\Delta P = \int_0^1 \frac{dP}{dz} dz. \quad (29)$$

The exact solutions of all equations have been formulated using Mathematical 11.0.

Results and discussion

We have plotted the graphs for the temperature, electric potential, velocity, and pressure distribution of the given problem. Figure 3, Table 1 tells us about the effective thermal conductivity of the nanofluid while using the single-walled

carbon nanotube (SWCNT) and multi-walled carbon nanotube (MWCNT). We can see that the thermal conductivity enhances in case of MWCNT as compared to the SWCNT. Moreover, the greater the amount of copper in the nanofluid ($\phi > 0$), the more will be the difference in SWCNT and MWCNT. Figure 4 shows the temperature profile of the nanofluid in case of pure water, SWCNT, and MWCNT. Color profiles are utilized in graphs to efficiently differentiate between the different forms of fluids. We can observe that without the addition of copper in the nanofluid (in case of pure water), the temperature is maximum. For SWCNT, the temperature is lower than that of MWCNT. Figure 4A indicates that the addition of copper in the base nanofluid significantly reduces the temperature of the fluid. Figure 4B indicates that if we increase the heat source parameter (β), the temperature increases. In addition, we can see that the temperature

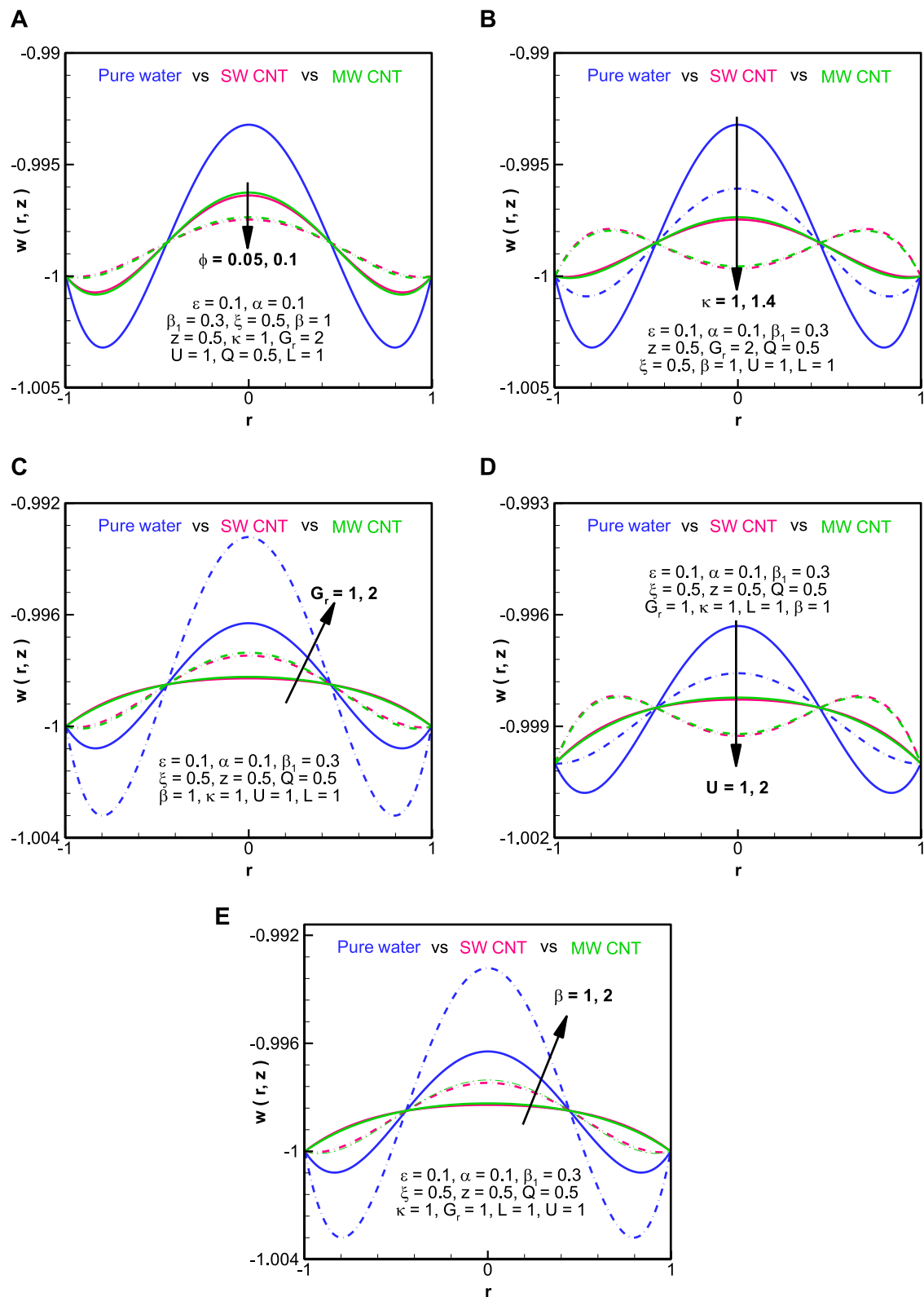


FIGURE 6
Velocity profile of the nanofluid.

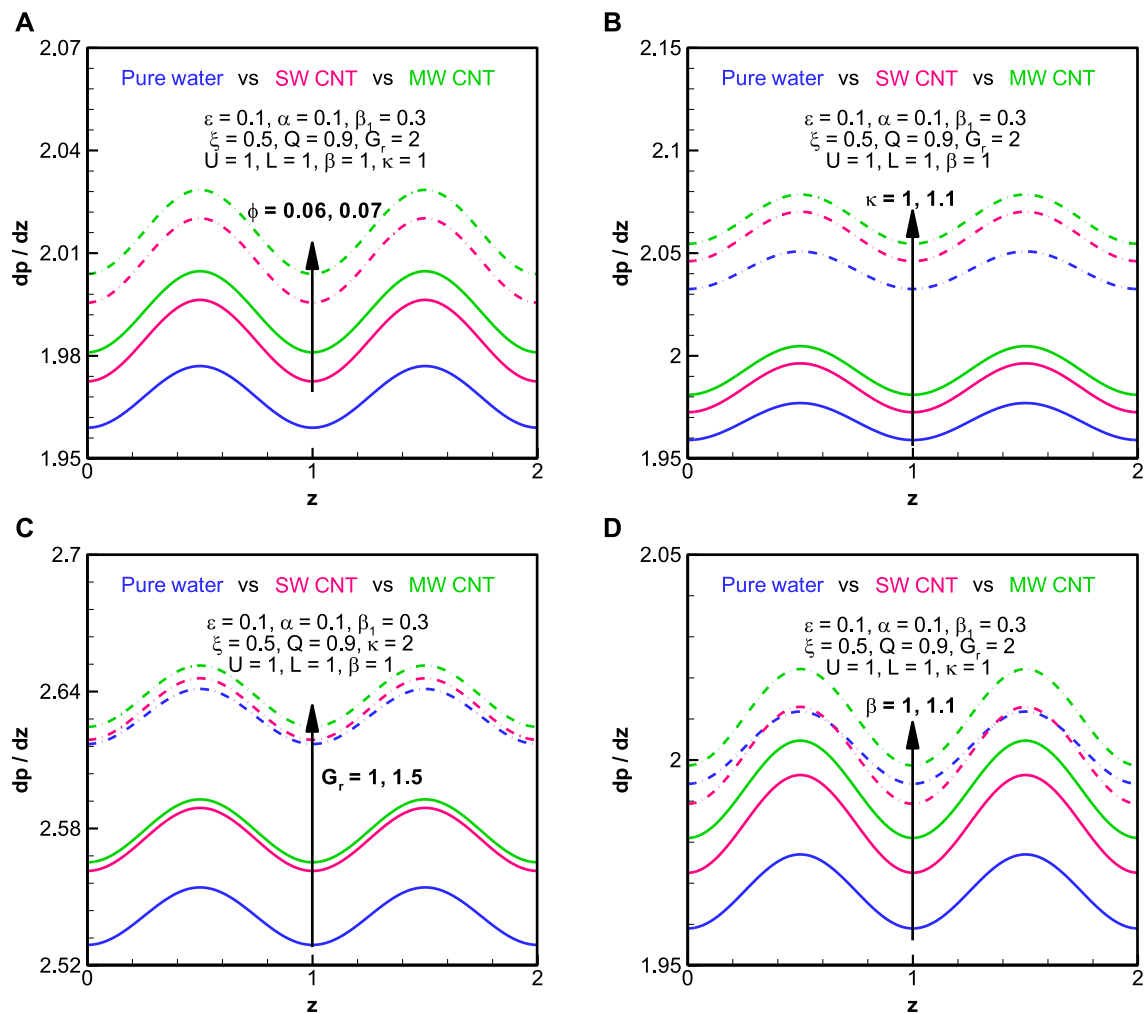


FIGURE 7
Pressure gradient of the nanofluid.

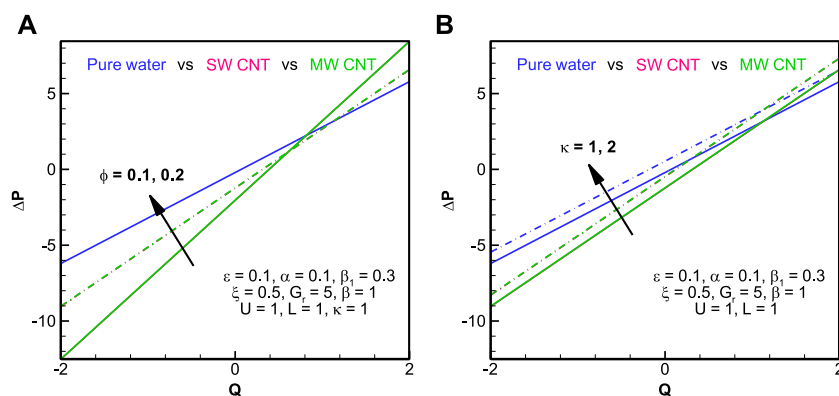
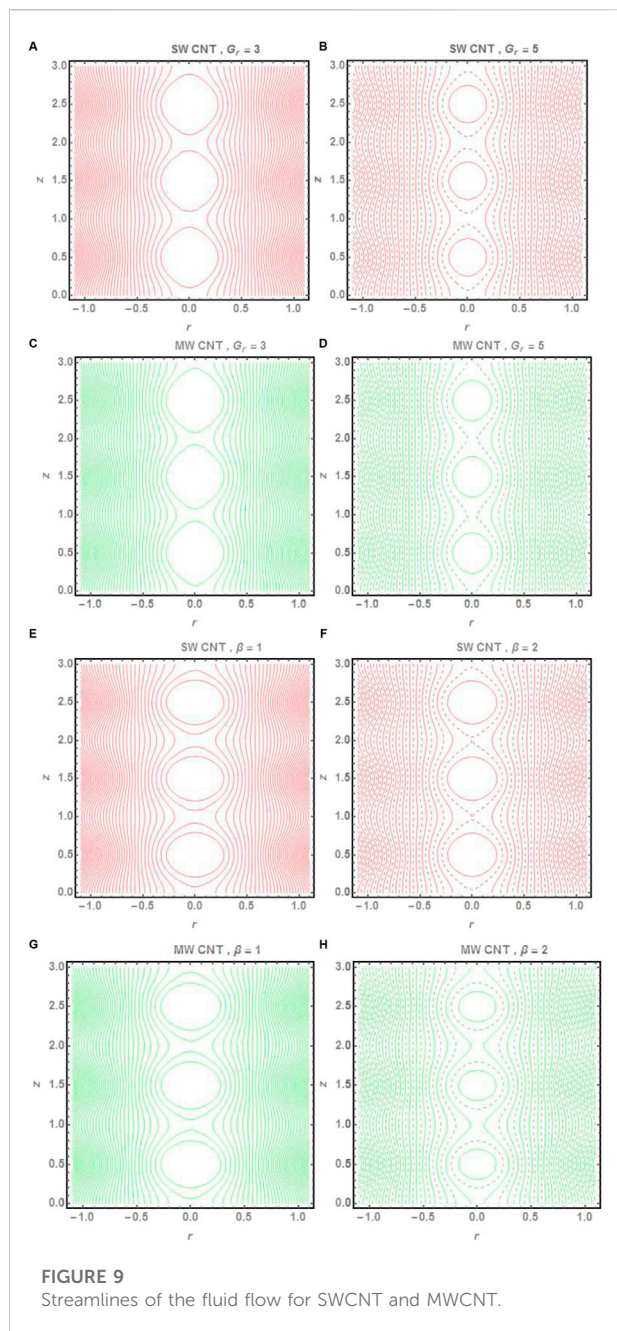


FIGURE 8
Pressure rise of the nanofluid.



increases toward the center of the tube ($r = 0$) and decreases at the boundaries of the tube ($r = 1, -1$).

Figure 5 depicts the electric potential of the nanofluid against the radial distance. Contrary to the temperature profile, the electric potential is minimum at the center of the tube and maximum toward the boundaries of the tube. Furthermore, the electric potential decreases with an increase in the ratio of the characteristic traverse length to the Debye length parameter (κ) and increases with an increase in the zeta potential (ξ). Figure 6 has been plotted to visualize the behavior of the

velocity profile in contrast with the radial distance of the tube. We can see that the velocity profile has a sinusoidal behavior due to the presence of the to and fro motion of cilia. Velocity is minimally differentiated with the use of SWCNT and MWCNT nanofluids. However, at the center of the tube, larger values of the Grashof number (G_r) and the heat source parameter indicate higher values of the velocity, whereas larger values of the nanoparticle volume fraction (ϕ), the ratio of the characteristic traverse length to the Debye length parameter, and the Helmholtz–Smoluchowski velocity indicate a decline in the velocity of the fluid.

Figure 7 shows the graphical profile of the pressure gradient against the axial distance of the fluid. We can see that the pressure gradient of the nanofluids increases with the amount of copper addition in the base fluid. For MWCNT, the pressure gradient remains greater than SWCNT, which remains greater than pure water. The pressure gradient appears to gain volume with the increase in either the ratio of the characteristic traverse length to the Debye length parameter, the Grashof number, or the heat source parameter. Throughout the length of the tube, the behavior of the pressure gradient remains sinusoidal. In Figure 8, we have demonstrated the pressure rise of the nanofluid in contrast with the flow rate parameter (Q). There is a marginal difference in the pressure rise of the nanofluid in case of SWCNT and MWCNT. However, in the peristaltic pumping region ($\Delta P > 0$), the pressure rise is mostly maximum for MWCNT as compared to SWCNT and pure water; opposite behavior can be seen in the augmented pumping region ($\Delta P < 0$). The amount of the nanoparticle volume fraction increases the pressure gradient in the augmented peristaltic region and reduces it in the peristaltic region. Similar behavior is seen in the case of the ratio of the characteristic traverse length to the Debye length parameter.

Streamlines depicting the peristaltic flow of the fluid is represented in Figure 9. Streamlines are plotted both for SWCNT and MWCNT for variation in the values of the Grashof number and the heat absorption parameter. The trapped bolus inside the streamlines depicts the transport of the fluid through the peristaltic movement with the help of the ciliated boundary walls. We can see that with the increase in the values in the Grashof number, the number of trapped boluses increases in the fluid flow and the size of the bolus decreases in both cases of CNTs. However, the trapped bolus appears to be greater in size in the case of MWCNT. A similar pattern and behavior is witnessed when we increase the values of the heat absorption parameter Table 2.

Conclusion

This article focuses on the peristaltic flow of carbon nanoparticle-suspended nanofluids under the influence of electroosmosis. Main findings of the current study are listed as follows.

- 1) It is found that the use of CNT in the base fluid significantly enhances the thermal conductivity and helps increase the velocity of the fluid.
- 2) We can observe that without the addition of copper in the nanofluid (in case of pure water), the temperature is maximum. For SWCNT, the temperature is lower than that of MWCNT.
- 3) We can see that the pressure gradient of the nanofluids increases with the amount of copper addition in the base fluid. For MWCNT, the pressure gradient remains greater than SWCNT.
- 4) There is a marginal difference in the pressure rise of the nanofluid in the case of SWCNT and MWCNT.
- 5) We can see that with the increase in the values in the Grashof number, the number of trapped bolus increases in the fluid flow and the size of the bolus decreases in both cases of CNTs

Data availability statement

The original contributions presented in the study are included in the article/Supplementary Material; further inquiries can be directed to the corresponding author.

References

- Abbasi, F. M., and Shehzad, S. A. (2021). Heat transfer analysis for EMHD peristalsis of ionic-nanofluids via curved channel with Joule dissipation and Hall effects. *J. Biol. Phys.* 23, 1–22.
- Abo-Elkhair, R., Mekheimer, K. S., and Moawad, A. (2017). Cilia walls influence on peristaltically induced motion of magneto-fluid through a porous medium at moderate Reynolds number: Numerical study. *J. Egypt. Math. Soc.* 25, 238–251. doi:10.1016/j.joems.2017.01.001
- Akbar, N. S., and Butt, A. W. (2014). Heat transfer analysis of viscoelastic fluid flow due to metachronal wave of cilia. *Int. J. Biomath.* 7, 1450066. doi:10.1142/s1793524514500661
- Akbar, N. S. (2015). Heat transfer and carbon nano tubes analysis for the peristaltic flow in a diverging tube. *Meccanica* 50, 39–47. doi:10.1007/s11012-014-0067-y
- Akhtar, S., McCash, L. B., Nadeem, S., Saleem, S., and Issakhov, A. (2021). Convective heat transfer for Peristaltic flow of SWCNT inside a sinusoidal elliptic duct. *Sci. Prog.* 104 (2), 003685042110236–17. doi:10.1177/00368504211023683
- Ali, A., Shah, Z., Mumraiz, S., Kumam, P., and Awais, M. (2019). Entropy generation on MHD peristaltic flow of Cu-water nanofluid with slip conditions. *Heat. Trans. Asian. Res.* 48, 4301–4319. doi:10.1002/htj.21593
- Awais, M., Kumam, P., Parveen, N., Ali, A., Shah, Z., and Thounthong, P. (2020). Slip and Hall effects on peristaltic rheology of copper-water nanomaterial through generalized complaint walls with variable viscosity. *Front. Phys.* 7, 249. doi:10.3389/fphy.2019.00249
- Awais, M., Shah, Z., Perveen, N., Ali, A., Kumam, P., Rehman, H., et al. (2020). MHD effects on ciliary-induced peristaltic flow coatings with rheological hybrid nanofluid. *Coatings* 10 (2), 186. doi:10.3390/coatings10020186
- Bhatti, M., Zeeshan, A., and Ellahi, R. (2017). Heat transfer with thermal radiation on MHD particle-fluid suspension induced by metachronal wave. *Pramana - J. Phys.* 89, 48–9. doi:10.1007/s12043-017-1444-6
- Ellahi, R., Riaz, A., Nadeem, S., and Ali, M. (2012). Peristaltic flow of Carreau fluid in a rectangular duct through a porous medium. *Math. problems Eng.* 2012, 1–24. doi:10.1155/2012/329639
- Elshehawey, E., Eldabe, N. T., Elghazy, E., and Ebaid, A. (2006). Peristaltic transport in an asymmetric channel through a porous medium. *Appl. Math. Comput.* 182, 140–150. doi:10.1016/j.amc.2006.03.040
- Farooq, A. A., Shah, Z., Kumam, P., O Alzahrani, E., Shutaywi, M., and Anwar, T. (2020). Darcy-Boussinesq model of cilia-assisted transport of a non-Newtonian magneto-biofluid with chemical reactions. *Appl. Sci.* 10, 1137. doi:10.3390/app10031137
- Fung, Y., and Yih, C. (1968). *Peristaltic transport*. China
- Hayat, T., Ahmed, B., Abbasi, F., and Ahmad, B. (2016). Mixed convective peristaltic flow of carbon nanotubes submerged in water using different thermal conductivity models. *Comput. methods programs Biomed.* 135, 141–150. doi:10.1016/j.cmpb.2016.07.030
- Ijaz, N., Zeeshan, A., and Rehman, S. (2018). Effect of electro-osmosis and mixed convection on nano-bio-fluid with non-spherical particles in a curved channel. *Mech. Industry* 19, 108. doi:10.1051/meca/2017040
- Khan, U., Ishak, A., and Zaib, A. (2021). Hybrid nanofluid flow containing single-wall and multi-wall CNTs induced by a slender stretchable sheet. *Chin. J. Phys.* 74, 350–364. doi:10.1016/j.cjph.2021.10.009
- Khan, U., Zaib, A., Ishak, A., Bakar, S. A., Animasaun, I. L., and Yook, S. J. (2022). Insights into the dynamics of blood conveying gold nanoparticles on a curved surface when suction, thermal radiation, and Lorentz force are significant: The case of Non-Newtonian Williamson fluid. *Math. Comput. Simul.* 193, 250–268. doi:10.1016/j.matcom.2021.10.014
- Latham, T. (1966). "Motion in a peristaltic pump," in *MS thesis* (Cambridge, Mass, USA: MIT-Press).
- Maqbool, K., Mann, A., Siddiqui, A., and Shaheen, S. (2017). Fractional generalized Burgers' fluid flow due to metachronal waves of cilia in an inclined tube. *Adv. Mech. Eng.* 9, 168781401771556–1687814017715565. doi:10.1177/1687814017715565
- Meyer, J. P., McKrell, T., and Grote, K. (2013). The influence of multi-walled carbon nanotubes on single-phase heat transfer and pressure drop characteristics in the transitional flow regime of smooth tubes. *Int. J. Heat Mass Transf.* 58, 597–609. doi:10.1016/j.ijheatmasstransfer.2012.11.074
- Mishra, M., and Rao, A. R. (2003). Peristaltic transport of a Newtonian fluid in an asymmetric channel. *Z. für. Angew. Math. Phys.* 54, 532–550. doi:10.1007/s00033-003-1070-7
- Nadeem, S., and Akbar, N. S. (2010). Effects of heat and mass transfer on peristaltic flow of Carreau fluid in a vertical annulus. *Z. für Naturforsch. A* 65, 781–792. doi:10.1515/zna-2010-1004

Author contributions

AB worked on the solution section and graphs section, NK carried out mathematical modeling, RM worked on the introduction section, and SF carried out the final proof reading and suggested mathematical techniques.

Conflict of interest

The authors declare that the research was conducted in the absence of any commercial or financial relationships that could be construed as a potential conflict of interest.

Publisher's note

All claims expressed in this article are solely those of the authors and do not necessarily represent those of their affiliated organizations, or those of the publisher, the editors, and the reviewers. Any product that may be evaluated in this article, or claim that may be made by its manufacturer, is not guaranteed or endorsed by the publisher.

- Nadeem, S., and Akram, S. (2010). Peristaltic flow of a Williamson fluid in an asymmetric channel. *Commun. Nonlinear Sci. Numer. Simul.* 15, 1705–1716. doi:10.1016/j.cnsns.2009.07.026
- Nadeem, S., Mehmood, R., and Akbar, N. S. (2015). Oblique stagnation point flow of carbon nano tube based fluid over a convective surface. *J. Comput. Theor. Nanosci.* 12, 605–612. doi:10.1166/jctn.2015.3774
- Noreen, S., and Tripathi, D. (2019). Heat transfer analysis on electroosmotic flow via peristaltic pumping in non-Darcy porous medium. *Therm. Sci. Eng. Prog.* 11, 254–262. doi:10.1016/j.tsep.2019.03.015
- Reddy, M. S., Mishra, M., Sreenadh, S., and Rao, A. R. (2005). *Influence of lateral walls on peristaltic flow in a rectangular duct.*
- Sadaf, H., Kiani, A., and Mir, N. A. (2020). Mixed convection analysis of cilia-driven flow of a Jeffrey fluid in a vertical tube. *Can. J. Phys.* 98, 111–118. doi:10.1139/cjp-2018-0753
- Saleem, A., Akhtar, S., Nadeem, S., and Ghalambaz, M. (2021). Microphysical analysis for peristaltic flow of SWCNT and MWCNT carbon nanotubes inside a catheterised artery having thrombus: Irreversibility effects with entropy. *Int. J. Exergy* 34 (3), 301–314. doi:10.1504/ijex.2021.10036473
- Shapiro, A. H., Jaffrin, M. Y., and Weinberg, S. L. (1969). Peristaltic pumping with long wavelengths at low Reynolds number. *J. Fluid Mech.* 37, 799–825. doi:10.1017/s0022112069000899
- Tripathi, D., Sharma, A., and Bég, O. A. (2017). Electrothermal transport of nanofluids via peristaltic pumping in a finite micro-channel: Effects of Joule heating and Helmholtz-Smoluchowski velocity. *Int. J. Heat Mass Transf.* 111, 138–149. doi:10.1016/j.ijheatmasstransfer.2017.03.089
- Waini, I., Khan, U., Zaib, A., Ishak, A., and Pop, I. (2022). Inspection of TiO₂-CoFe₂O₄ nanoparticles on MHD flow toward a shrinking cylinder with radiative heat transfer. *J. Mol. Liq.* 361, 119615. doi:10.1016/j.molliq.2022.119615



OPEN ACCESS

EDITED BY

Safia Akram,
National University of Sciences and
Technology, Pakistan

REVIEWED BY

Aurang Zaib,
Federal Urdu University of Arts, Sciences
and Technology Islamabad, Pakistan
Emad Aly,
Ain Shams University, Egypt

*CORRESPONDENCE

Zahoor Iqbal,
izahoor@math.qau.edu.pk

SPECIALTY SECTION

This article was submitted to Colloidal
Materials and Interfaces,
a section of the journal
Frontiers in Materials

RECEIVED 05 September 2022

ACCEPTED 04 November 2022

PUBLISHED 01 December 2022

CITATION

Iqbal Z, Yashodha S, Hakeem AKA,
Alsawi A, Alyami MA, Yousef ES, Amin AH
and Eldin SM (2022), Energy transport
analysis in natural convective flow of
water: Ethylene glycol (50:50)-based
nanofluid around a spinning down-
pointing vertical cone.
Front. Mater. 9:1037201.
doi: 10.3389/fmats.2022.1037201

COPYRIGHT

© 2022 Iqbal, Yashodha, Hakeem,
Alsawi, Alyami, Yousef, Amin and Eldin.
This is an open-access article
distributed under the terms of the
[Creative Commons Attribution License](https://creativecommons.org/licenses/by/4.0/)
(CC BY). The use, distribution or
reproduction in other forums is
permitted, provided the original
author(s) and the copyright owner(s) are
credited and that the original
publication in this journal is cited, in
accordance with accepted academic
practice. No use, distribution or
reproduction is permitted which does
not comply with these terms.

Energy transport analysis in natural convective flow of water: Ethylene glycol (50:50)-based nanofluid around a spinning down-pointing vertical cone

Zahoor Iqbal^{1*}, S. Yashodha², A. K. Abdul Hakeem²,
Abdulrahman Alsawi³, Maryam Ahmed Alyami⁴,
El. Sayed Yousef^{5,6}, Ali H. Amin^{7,8} and Sayed M. Eldin⁹

¹Department of Mathematics, Quaid-i-Azam University, Islamabad, Pakistan, ²Department of Mathematics, Sri Ramakrishna Mission Vidyalaya College of Arts and Science, Coimbatore, India, ³Department of Physics, College of Science, Qassim University, Buraydah, Saudi Arabia, ⁴Department of Mathematics, Faculty of Sciences, University of Jeddah, Jeddah, Saudi Arabia, ⁵Research Center for Advanced Materials Science (RCAMS), King Khalid University, Abha, Saudi Arabia, ⁶Physics Department, Faculty of Science, King Khalid University, Abha, Saudi Arabia, ⁷Deanship of Scientific Research, Umm Al-Qura University, Makkah, Saudi Arabia, ⁸Zoology Department, Faculty of Science, Mansoura University, Mansoura, Egypt, ⁹Faculty of Engineering and Technology, Future University in Egypt, New Cairo, Egypt

The influence of the magnetic field on $H_2O - C_2H_6O_2$ (50:50)-based nanofluid over a heated and spinning vertical cone is deliberated. Water: ethylene glycol (50:50) mixture-based nanofluid with Al_2O_3 and Fe_3O_4 as nanoparticles exhibits higher thermal conductivity enhancement. Heat transfer analysis for the spinning vertical cone with a prescribed surface temperature was investigated. The influence of magnetic parameter, spin parameter, and nanoparticle volume fraction on tangential velocity profile, spin velocity profile, and thermal profile is analyzed. The results accord strongly with the findings of previous research works in the special cases. Computation shows that as magnetic parameter increases, the thicknesses of hydrodynamic and thermal boundary layers decrease and increase, respectively. The addition of nanoparticles (Al_2O_3 and Fe_3O_4) effectively enhances the skin friction coefficient and Nusselt number.

KEYWORDS

spinning down-pointing vertical cone, water–ethylene glycol, nanofluid, transverse magnetic field, heat transport

Introduction

In this industrialized world, the heat transfer process plays a significant role in upgrading the efficiency of industrial applications. To accomplish this global industrialization, in 1995 Choi devised a new progressive class of heat transfer fluids, known as nanofluids (Choi and Eastman, 1995), in which the characteristics of both

nanoparticles and base fluid become efficient. Heat transfer in nanofluid is more proficient than in common fluids. Preparation of nanofluids is not simply the mixture of solids and liquids but requires beneficial methods, as elaborated in [Xuan and Li \(2000\)](#), which presents the procedure for nanofluid preparation. Choosing the nanoparticle and base fluid wisely leads to excellent results depending on the need, as discussed in [Usri et al. \(2015\)](#). Recent research works have been implemented using a novel category of fluids known as nanofluids, which have brought changes widely, including in the industrial, engineering, and medical fields ([Vishnu Ganesh et al., 2014](#); [Abdul Hakeem et al., 2017](#)). Different geometrical shapes give different results, including cone and wedge ([Anantha Kumar et al. \(2018\)](#)), rotating disk ([Gholinia et al. \(2019\)](#)), and vertical cone geometric shapes ([CemEce, 2005](#); [Raju and Sandeep, 2016](#)). Nanofluids are the best solutions for heat transfer fluids since they have good thermal performance. Therefore, researchers are proposing suitable models. In this regard, three methods are employed for improving thermal performance ([Maleki et al., 2020](#)). To adopt nanofluid applications in daily life, and to increase nanofluid's performance in several applications, nanofluid stability is a critical factor discussed in ([Chakraborty and Kumar Panigrahi, 2020](#)). To enhance heat transfer, comparison among different nanofluids for different parameters has been conducted ([Dinarvand and Pop, 2017](#); [Aghamajidi et al., 2018](#)). Nanofluid applications have been used in multidisciplinary research. There is a broad range of utilizations in the areas of microalgal cultivation, friction reduction, magnetic sealing, reactor-heat exchange, optical and biomedical applications, nanofluid detergent, electronics cooling, and heating buildings ([Vargas-Estrada et al., 2020](#); [Rafiq et al., 2021](#)). With progress in nuclear energy, nanoparticles are also used as coolants in nuclear power plants ([Hamidreza Arab BafraniNoori-kalkhoran et al., 2020](#)), in enhancing oil recovery, nano-refrigerants, and nano-lubricants ([de Carvalho et al., 2020](#); [SahbanAlnarabiji and Husein, 2020](#); [Salari and Seid Mahdi Jafari, 2020](#); [Mallikarjuna et al., 2021](#)), and in turning and grinding processes ([SaswatKhatai et al., 2020](#)). In addition to nanofluid, the flow of hybrid nanofluid across a stretched surface has recently been studied

([Aly and Pop, 2019](#); [Aly and Pop, 2020a](#); [Aly and Ebaid, 2020](#); [Aly and Pop, 2020b](#); [Aly et al., 2021](#); [Ahmad et al., 2022](#); [Aly et al., 2022](#); [Arafat et al., 2022](#); [Reddy et al., 2022](#); [Usafzai et al., 2022](#)).

Using a water-ethylene glycol (50:50) combination as the base fluid and Al_2O_3 and Fe_3O_4 as the nanoparticles, we explored the natural convection flow around a heated vertical spinning cone under the influence of a magnetic field.

The aspect of the present work is listed below.

- Water-ethylene glycol (50:50) mixture is considered a base fluid with $Pr = 29.86$.
- Al_2O_3 and Fe_3O_4 are considered to be non-magnetic and magnetic nanoparticles, respectively, which are in thermal equilibrium with base fluid.
- The geometric cone is used for fluid flow as shown in [Figure 1](#).
- The effect of viscous dissipation, the resistance heating effect of the fluid, and the slip effect are regarded as negligible.

Governing equations and problem formulation

A continuous two-dimensional flow of a combination of $H_2O - C_2H_6O_2$ (50:50) containing Al_2O_3 and Fe_3O_4 nanoparticles was studied, under the influence of a magnetic field. The flow was laminar, and the nanofluid was assumed to be incompressible.

The y^* axis is the dimension normal to the cone's surface, and the x^* axis is the dimension toward the cone's surface. The rotational angle is indicated by θ , and it was assumed that cone spins with a constant angular velocity Ω .

The models that govern the phenomena are given below ([Aghamajidi et al., 2018](#)).

Continuity equation

$$(r^*u^*)_{x^*} + (r^*v^*)_{y^*} = 0 \quad (1)$$

TABLE 1 Thermophysical properties of $H_2O - C_2H_6O_2$ (50:50)-based fluid and Al_2O_3/Fe_3O_4 nanoparticles ([Aghamajidi et al., 2018](#); [Saranya et al., 2018](#); [Saranya et al., 2022](#)).

	$C_p/(J/(kg \cdot K))$	$\rho/(kg/m^3)$	$k/(W/(m \cdot K))$	$\beta/10^{-5}(1/K)$	$\sigma(Sm^{-1})$	Pr
Ethylene glycol and water (50:50) mixture ($H_2O - C_2H_6O_2$) (50:50)	3288	1056	0.425	58	0.00509	29.86
Aluminum oxide (Al_2O_3)	765	3970	40	0.85	$35 \cdot 10^6$	—
Magnetite (Fe_3O_4)	670	5180	9.7	1.3	$2.5 \cdot 10^4$	—

Momentum equation in x direction

$$\rho_{nf} \left((u^*)_{x^*} u^* + (u^*)_{y^*} v^* - \frac{w^{*2}}{x^*} \right) = \mu_{nf} (u^*)_{y^*} + (\rho\beta)_{nf} g \cos \gamma (T - T_0) - \sigma_{nf} B^2 u^* \quad (2)$$

Momentum equation in y direction

$$\rho_{nf} \left((w^*)_{x^*} u^* + (w^*)_{y^*} v^* + \frac{u^* w^*}{x^*} \right) = \mu_{nf} (w^*)_{y^*} - \sigma_{nf} B^2 w^* \quad (3)$$

Energy equation

$$(\rho C_p) (u^* (T)_{x^*} + v^* (T)_{y^*}) = k_{nf} (T)_{y^*} \quad (4)$$

Here, $(r^* u^*)_{x^*}$ denotes the partial derivative of $(r^* u^*)$ with respect to x^* .

The boundary conditions for the above governing equations are given below.

Prescribed surface temperature case:

$$T(x^*, 0) = T_0 + (T_r - T_0) \frac{x^*}{L} \text{ when } y^* = 0 \quad (5)$$

$$u^* = 0, v^* = 0, w^* = r^* \Omega \text{ as } y^* = 0 \quad (6)$$

$$u^* \rightarrow 0, w^* \rightarrow 0, T \rightarrow 0 \text{ as } y^* \rightarrow \infty. \quad (7)$$

γ is considered as half of the vertex angle, and the local radius of the cone is considered as $r = x \sin \gamma$. Dimensional velocity components are denoted by u^* , v^* , and w^* in the x^* , y^* , and θ directions, respectively.

The thermophysical properties are given in Table 1. The nanofluid properties are given by (Saranya et al., 2022)

$$\text{Nanofluid's kinematic viscosity, } \nu_{nf} = \frac{\mu_f}{(1-\phi)^{2.5} [(1-\phi)\rho_f + \phi\rho_s]} \quad (8)$$

$$\text{Nanofluid's density } \rho_{nf} = (1-\phi)\rho_f + \phi\rho_s \quad (9)$$

$$\text{Nanofluid's thermal diffusivity, } \alpha_{nf} = \frac{k_{nf}}{(\rho C_p)_{nf}}, \quad (10)$$

$$\text{Nanofluid's heat capacitance, } (\rho C_p)_{nf} = (1-\phi)(\rho C_p)_f + \phi(\rho C_p)_s, \quad (11)$$

$$\text{Coefficient of thermal expansion, } (\rho\beta)_{nf} = (1-\phi)(\rho\beta)_f + \phi(\rho\beta)_s \quad (12)$$

Nanofluid's thermal conductivity and electrical conductivity are given by

$$\frac{k_{nf}}{k_f} = \frac{(k_s + 2k_f) - 2\phi(k_f - k_s)}{(k_s + 2k_f) + \phi(k_f - k_s)} \text{ and } \frac{\sigma_{nf}}{\sigma_f} = 1 + \frac{3(\sigma - 1)\phi}{(\sigma + 2) - (\sigma - 1)\phi}, \text{ where } \sigma = \frac{\sigma_s}{\sigma_f}, \text{ respectively} \quad (13)$$

Here, ϕ is the solid volume fraction. The subscripts sf, nf, and s denote the fluid, nanofluid, and solid, respectively.

For the current analysis, the following variables are utilized (Aghamajidi et al., 2018):

$$r = \frac{r^*}{L}, x = \frac{x^*}{L}, y = \frac{y^*}{L} Gr^{1/4} \quad (14)$$

$$u = \frac{u^*}{U}, v = \frac{v^*}{U} Gr^{1/4}, w = \frac{w^*}{\Omega L}, \Theta = \frac{T - T_0}{T_r - T_0} \quad (15)$$

where u , v , and w represent the velocity components x direction, y direction, and θ direction, respectively, and Θ is the dimensionless temperature ratio. $r = x \sin \gamma$ is the radius of the cone and the magnetic field strength is $B = B_0 b(x) / (r \sqrt{1 - r'^2})$.

The Prandtl number (Pr), reference velocity (U), and Grashof number (Gr) are defined as

$$Pr = \frac{\nu}{\alpha}, U = [g \cos \gamma \beta L (T_r - T_0)]^{1/2}, Gr = \left(\frac{UL}{\nu} \right)^2 \quad (16)$$

where β is the thermal expansion coefficient, L is the reference length, ν is kinematic viscosity, and α is thermal diffusivity. T_r is any taken reference temperature unequal to the ambient temperature T_0 .

The governing equations from Eq. 1 to Eq. 4 take the following non-dimensional form after substituting the dimensionless variables, as defined in Eqs 14–16:

$$(ru)_x + (rv)_y = 0 \quad (17)$$

$$uu_x + vv_y - \frac{Re^2}{Gr} \frac{r'}{r} w^2 = \frac{1}{[(1-\phi) + \phi(\rho_s/\rho_f)]} \left\{ \frac{1}{(1-\phi)^{2.5}} (u_y)_y + [(1-\phi) + \phi(\rho\beta)_s / (\rho\beta)_f] \Theta - \frac{\sigma_{nf}}{\sigma_f} M \Lambda^2 u \right\} \quad (18)$$

$$uw_x + vw_y + uw \frac{r'}{r} = \frac{1}{(1-\phi + \phi\rho_s/\rho_f)} \left\{ \frac{1}{(1-\phi)^{2.5}} (w_y)_y - \left(\frac{\sigma_{nf}}{\sigma_f} \right) M \Lambda^2 w \right\} \quad (19)$$

$$u\Theta_x + v\Theta_y = \frac{1}{[(1-\phi) + \phi(\rho C_p)_s / (\rho C_p)_f]} \left[\left(\frac{1}{Pr} \frac{K_{nf}}{K_f} \right) (\Theta_y)_y \right] \quad (20)$$

The boundary conditions are given below.

Prescribed surface temperature case:

$$\Theta = x \text{ as } y = 0 \quad (21)$$

$$u = 0, v = 0, w = r \text{ as } y = 0 \quad (22)$$

$$u \rightarrow 0, w \rightarrow 0, \Theta \rightarrow 0 \text{ as } y \rightarrow \infty \quad (23)$$

The rotational Reynolds number, the magnetic field function Λ , and the magnetic parameter are

TABLE 2 Comparison with the results of Ece (2006), Dinarvand (2011), and Aghamajidi et al. (2018) for regular fluid ($\phi = 0$), for the effect of M and ϵ on $F''(0)$ and $-H'(0)$ with prescribed surface temperature, for Prandtl number =1.

ϵ	M	$F''(0)$				$-H'(0)$			
		Ece (2006)	Dinarvand (2011)	Aghamajidi et al. (2018)	Present results	Ece (2006)	Dinarvand (2011)	Aghamajidi et al. (2018)	Present results
0.0	0.0	0.68150	0.68151	0.68151	0.681483	0.63887	0.63887	0.63887	0.638854
	1.0	0.55976	0.55975	0.55976	0.559761	0.55869	0.55867	0.55868	0.558692
	2.0	0.48679	0.48675	0.48678	0.486807	0.50338	0.50341	0.50339	0.503352
0.5	0.0	0.84651	0.84654	0.84651	0.846488	0.67194	0.67196	0.67194	0.671938
	1.0	0.68548	0.68553	0.68549	0.685480	0.58138	0.58142	0.58137	0.581380
	2.0	0.59003	0.59010	0.59003	0.590045	0.51968	0.51963	0.51969	0.519638
1.0	0.0	1.00196	1.00191	1.00195	1.001943	0.70053	0.70056	0.70053	0.700524
	1.0	0.80819	0.80826	0.80820	0.808193	0.60256	0.60250	0.60257	0.602564
	2.0	0.69204	0.69203	0.69205	0.692051	0.53536	0.53543	0.53535	0.535337

$$Re = \frac{\Omega L^2}{\nu_f}, \quad \Lambda = \frac{b(x)}{r\sqrt{1-r'^2}}, \quad M = \frac{\sigma_f B_0^2 L}{U \rho_f}. \quad (24)$$

The function $b(x) = r\sqrt{1-r'^2}$ is the basis of the current analysis, which was conducted in a scenario in which the intensity of the magnetic field applied normal to the surface was uniform along the surface within the boundary layer, such that $\Lambda = 1$:

$$ru = \psi_y, \quad rv = -\psi_x, \quad (25)$$

where ψ is stream function and the boundary layer variables can be presented as

$$\psi(x, y) = x r F(y), \quad w = r G(y), \quad \Theta = x H(y), \quad (26)$$

Applying the boundary layer variables as written in Eq. 26, the non-dimensional governing Eqs 17–20 are converted into the system of Ordinary differential equations (ODEs).

Here $F(y)$, $G(y)$, and $H(y)$ represent the tangential velocity profile, swirl velocity profile, and temperature profile, respectively.

$$A_1 F''' + 2FF'' - F'^2 + \epsilon G^2 - A_2 A_5 M \Lambda^2 F' + A_3 H = 0 \quad (27)$$

$$A_1 G'' + 2FG' - 2GF' - A_2 A_5 M \Lambda^2 G = 0 \quad (28)$$

$$A_4 H'' + \text{Pr} [2FH' - F'H] = 0 \quad (29)$$

where $A_1 = 1/(1-\phi)^{2.5} (1-\phi + \phi(\rho_s/\rho_f))$, $A_2 = 1/(1-\phi + \phi(\rho_s/\rho_f)) A_3 = (1-\phi + \phi(\rho\beta)_s/(\rho\beta)_f)/(1-\phi + \phi(\rho_s/\rho_f))$, $A_4 = (k_{nf}/k_f)/(1-\phi + \phi(\rho C_p)_s/(\rho C_p)_f)$, $A_5 = \sigma_{nf}/\sigma_f = 1 + 3(\sigma - 1)\phi/(\sigma + 2) - (\sigma - 1)\phi$, where $\sigma = \sigma_s/\sigma_f \epsilon = (\text{Resin})^2/\text{Gr}$ is the spin parameter.

The boundary conditions from Eqs 21 to 23 are reduced to

$$F = 0, \quad F' = 0, \quad G = 1, \quad H = 1 \quad \text{as } y = 0 \quad (30)$$

$$F' \rightarrow 0, \quad G \rightarrow 0, \quad H \rightarrow 0 \quad \text{as } y \rightarrow \infty \quad (31)$$

Skin friction coefficient and local Nusselt number

The skin friction coefficient C_f and the local Nusselt number (Nu), have been consequential in the engineering field and are defined as

$$C_f = \frac{2\tau_w}{\rho_f U^2}, \quad \text{Nu} = \frac{Lq_w}{k_f (T_w - T_\infty)} \quad (32)$$

where τ_w is the skin friction and q_w is the surface heat flux, written as

$$\tau_w = \mu_{nf} \left(\frac{\partial u^*}{\partial y^*} \right)_{y^*=0}, \quad q_w = -k_{nf} \left(\frac{\partial T}{\partial y^*} \right)_{y^*=0} \quad (33)$$

Using the non-dimensional transformations, we obtain

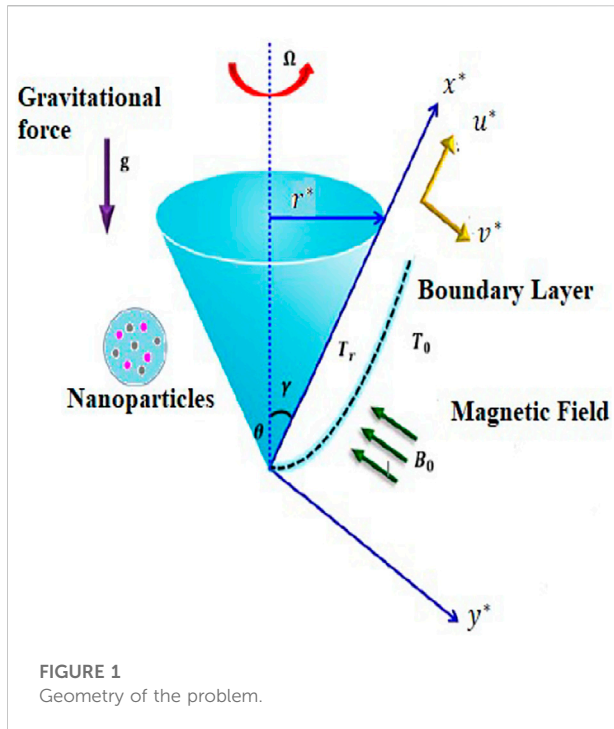
$$C_f \text{Gr}^{1/4} = 2 \left(\frac{\mu_{nf}}{\mu_f} \right) x F''(0), \quad \text{NuGr}^{-1/4} = - \left(\frac{k_{nf}}{k_f} \right) x H'(0) \quad (34)$$

Numerical approach

Eqs 27–29 with boundary conditions (Eqs 30, 31) specify nonlinear ordinary differential equations. By using a fourth-order Runge–Kutta finite difference scheme and shooting approach, this model is solved numerically to examine the effects of M , ϵ , ϕ on $F'(y)$, $G(y)$, $H(y)$, C_f , and Nu.

We represent $F = y_1$, $G = y_4$, $H = y_6$ for our present problem and the important steps of the method as

$$\begin{aligned} y_1' &= y_2 \\ y_2' &= y_3 \\ y_3' &= -1/A_1 [2y_1 y_3 - y_2^2 + \epsilon y_4^2 - A_2 A_5 M \Lambda^2 y_2 + A_3 y_6] \\ y_4' &= y_5 \end{aligned}$$



$$y_5' = -1/A_1 [(2y_1y_5 - 2y_2y_4) - A_2A_5M\Lambda^2y_4]$$

$$y_6' = y_7$$

$$y_7' = -1/A_4 [\text{Pr}(2y_1y_7 - y_2y_6)]$$

To authenticate our work, the outcomes were compared with the results of Ece (2006), Dinarvand (2011), and Aghamajidi et al. (2018), which are shown in Table 2. It is worth mentioning that the present outcomes have excellent compatibility with the solutions obtained by Ece (2006), Dinarvand (2011), and Aghamajidi et al. (2018) for the case $\phi = 0$.

Results and discussion

The effects of spin parameter ϵ , nanoparticle volume fraction ϕ , and magnetic parameter M on tangential velocity profile $F^l(y)$, swirl velocity profile $G(y)$, and temperature profile $H(y)$ for the case of prescribed surface temperature were plotted.

The tangential velocity profile decreases as the range of magnetic parameters increases. This is because a magnetic field creates a drag force, known as the Lorentz force, in an electrically conducting fluid. There is a dip in the velocity profile due to this significant resistive force acting counter to the direction of fluid flow. As a result, as M becomes stronger, the hydrodynamic boundary layer thickness becomes thinner. Fe_3O_4 has higher tangential velocity than Al_2O_3 . In the case of swirl velocity, as the magnetic parameter increases, swirl velocity decreases. Al_2O_3 has higher swirl velocity than Fe_3O_4 , as described in Figure 2

Boundary layer behaviour for the case of prescribed surface temperature

To overcome drag force, the fluid must do some additional work, which is transformed into thermal energy and leads to an increase in the temperature of the fluid. Al_2O_3

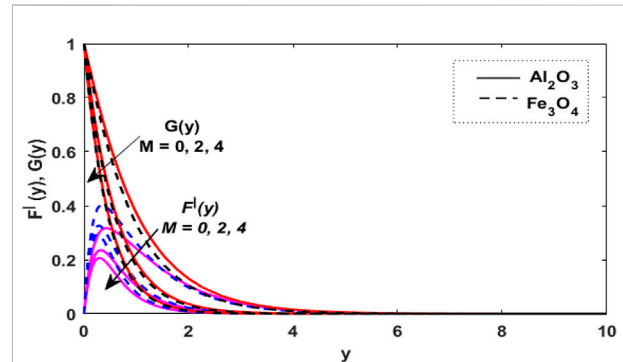


FIGURE 2
Influence of M on $F^l(y)$ and $G(y)$ when $\phi = 0.01$, $\epsilon = 1$, and $\text{Pr} = 29.86$.

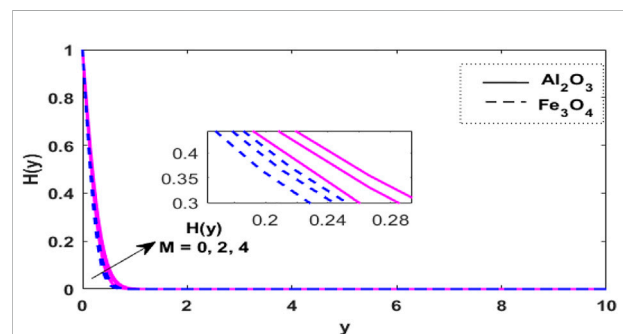


FIGURE 3
Influence of M on $H(y)$ when $\phi = 0.01$, $\epsilon = 1$, and $\text{Pr} = 29.86$.

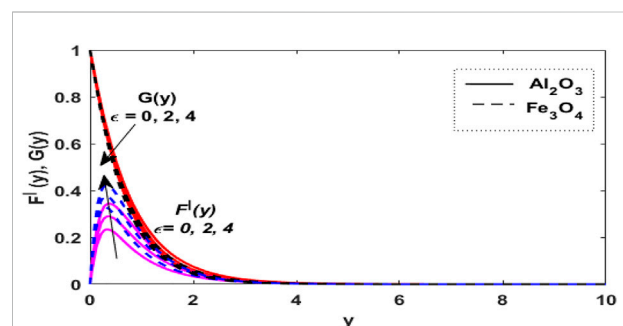


FIGURE 4
Characteristics of ϵ on $F^l(y)$ and $G(y)$, when $\phi = 0.01$, $M = 1$, and $\text{Pr} = 29.86$.

has a higher temperature than Fe_3O_4 . Therefore, as the strength of M increases, the thickness of the thermal boundary value rises, as described in Figure 3. From the physical point of view, as the nanoparticles transfer or dissipate heat, they cause a larger thermal boundary layer thickness and, finally, the intensification in the temperature of the fluid.

As the spin parameter appears in the momentum equation, the effect of spin parameter is more in this equation, and increased values of the spin parameter dynamically promote tangential velocity. Fe_3O_4 has higher tangential velocity than Al_2O_3 . Swirl velocity drops as spin parameter increases near the surface of the cone, as shown in Figure 4.

Temperature is reduced as spin parameter increases. Therefore, there is reduction in the thickness of the thermal boundary layer for varying magnitudes of spin parameter. Fe_3O_4 nanoparticles are compressed more toward the surface than are the Al_2O_3 nanoparticles as the spin parameter rises, as indicated in Figure 5.

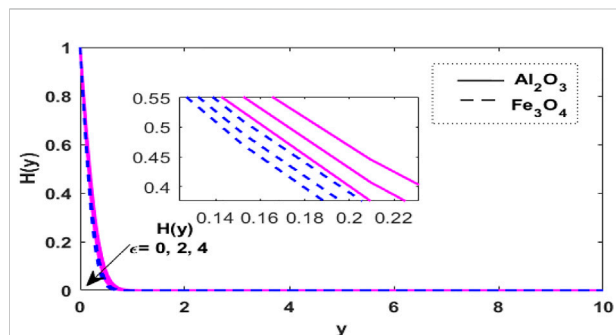


FIGURE 5
Impact of ϵ on $H(y)$, when $\phi = 0.01$, $M = 1$, and $Pr = 29.86$.

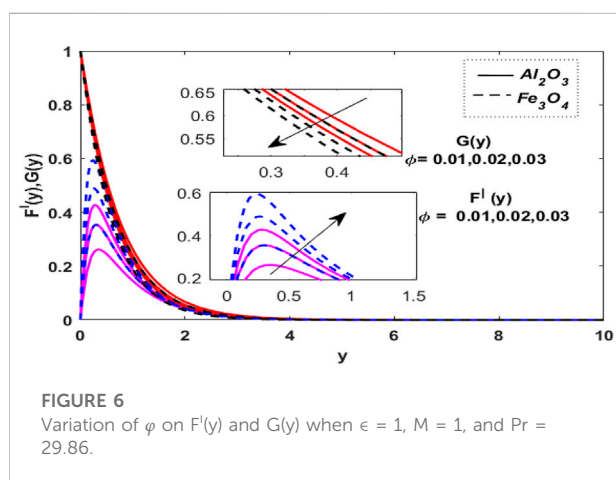


FIGURE 6
Variation of ϕ on $F'(y)$ and $G(y)$ when $\epsilon = 1$, $M = 1$, and $Pr = 29.86$.

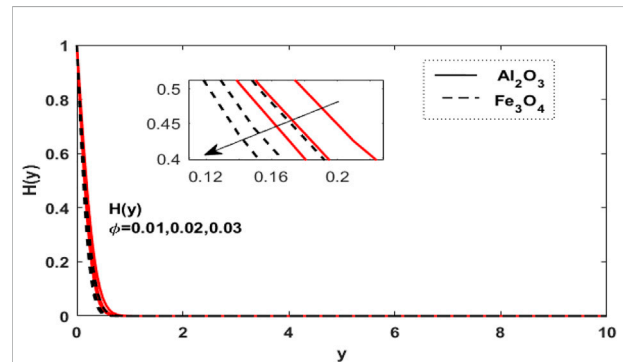


FIGURE 7
Variation of ϕ on $H(y)$ when $\epsilon = 1$, $M = 1$, and $Pr = 29.86$.

The influence of nanoparticle volume fraction on tangential and swirl velocity profile is depicted in Figure 6. As the value of ϕ rises, the tangential velocity of the flow increases. The opposite behavior is examined in the case of swirl velocity profile.

In Figure 7, the influence of the Al_2O_3 and Fe_3O_4 nanoparticle volume fraction for thermal distribution is plotted. Analysis of this plot showed that the temperature distribution builds up by enhancing the volume fraction of Al_2O_3 .

The coefficient of skin friction and Nusselt number

Table 3 shows the variation of skin friction coefficient and nusselt number for different values of solid volume fraction, spin parameter and magnetic parameter. It is found that

TABLE 3 The coefficient of skin friction and Nusselt number.

ϕ	ϵ	M	Pr	$(1/x) C_f Gr^{(1/4)}$		$(1/x) Nu Gr^{-1/4}$	
				Al_2O_3	Fe_3O_4	Al_2O_3	Fe_3O_4
0.01	1	1	29.86	4.1880	6.5685	3.1603	3.6685
0.02				6.6672	10.7914	3.7276	4.3681
0.03				8.9413	14.6327	4.1515	4.8770
0.04				11.1076	18.2739	4.5059	5.2963
0.01	1.0	1	29.86	4.1879	6.5685	3.1603	3.6685
	2.0			3.9995	6.3515	3.0638	3.5858
	3.0			3.8639	6.1865	2.9920	3.5216
	4.0			3.7556	6.0507	2.9334	3.4677
0.01	1	1.0	29.86	4.1879	6.5684	3.1603	3.6685
	2.0			4.5756	6.9253	3.2806	3.7542
	3.0			4.9609	7.2799	3.3921	3.8353
	4.0			5.3430	7.6321	3.4958	3.9125

magnetic nanoparticles have high skin friction and nusselt number values.

Conclusion

The numerical solution was achieved using the fourth-order Runge–Kutta method combined with boundary conditions and shooting methods to the non-dimensional ODEs. The following graph-related points are noteworthy:

- Intensification of the extent of spin parameter dynamically promotes the tangential velocity, and Fe_3O_4 has a higher tangential velocity than Al_2O_3 .
- Higher magnetic parameters decrease the momentum transport of hydrodynamic flow and accelerate thermal transport in the presence of $H_2O - C_2H_6O_2$ (50:50) mixture.
- Higher spin parameter reduces the thermal profile of nanofluid.
- The tangential velocity of Fe_3O_4 is shown to be greater than for the Al_2O_3 nanoparticle.
- It is worth mentioning that the present outcomes are highly compatible with solutions obtained in previous research for the special case.

Data availability statement

The original contributions presented in the study are included in the article/supplementary material; further inquiries can be directed to the corresponding author.

References

- Abdul Hakeem, A. K., Saranya, S., and Ganga, B. (2017). Comparative study on Newtonian/non-Newtonian base fluids with magnetic/non-magnetic nanoparticles over a flat plate with uniform heat flux. *J. Mol. Liq.* 230, 445–452. doi:10.1016/j.molliq.2016.12.087
- Aghamajidi, Mohammad, EftekhariYazdi, Mohammad, Dinarvand, Saeed, and Pop, Ioan (2018). Tiwari-Das nanofluid model for magnetohydrodynamics (MHD) naturalconvective flow of a nanofluid adjacent to a spinning down-pointing vertical cone. *Propuls. Power Res.* 7 (1), 78–90. doi:10.1016/j.jprr.2018.02.002
- Ahmad, N. P., Indumathi, N., Ganga, B., Charles, S., Hakeem, A. K. A., Iqbal, Z., et al. (2022). Forced convection of non-Darcy flow of ethylene glycol conveying copper (II) oxide and titanium dioxide nanoparticles subject to lorentz force on wedges: Non-Newtonian Casson model. *Front. Chem.* 10, 1010591. doi:10.3389/fchem.2022.1010591
- Aly, E. H., and Ebaid, A. (2020). MHD Marangoni boundary layerproblem for hybrid nanofluidswith thermal radiation. *Int. J. Num. Meth. Heat Fluid Flow* 31.
- Aly, E. H., Mahabaleswar, U. S., Anusha, T., Usafzai, W. K., and Pop, I. (2022). Wall jet flow and heat transfer of a hybrid nanofluid subject to suction/injection with thermal radiation. *Therm. Sci. Eng. Prog.* 32 (1), 101294. doi:10.1016/j.tsep.2022.101294
- Aly, E. H., and Pop, I. (2020). Merkin and Needham wall jet problem for hybrid nanofluids withthermal energy. *Eur. J. Mech. - B/Fluids* 83, 195–204. doi:10.1016/j.euromechflu.2020.05.004
- Aly, E. H., and Pop, I. (2020). MHD flow and heat transfer near stagnation point over a stretching/shrinking surface with partial slip and viscous dissipation: Hybrid nanofluid versus nanofluid. *Powder Technol.* 367, 192–205. doi:10.1016/j.powtec.2020.03.030
- Aly, E. H., and Pop, I. (2019). MHD flow and heat transfer over a permeable stretching/shrinking sheet in a hybrid nanofluid with a convective boundary condition. *Int. J. Numer. Methods Heat. Fluid Flow.* 29 (9), 3012–3038. doi:10.1108/hff-12-2018-0794
- Aly, E. H., Rosca, A. V., Rosca, N. C., and Pop, I. (2021). Convective heat transfer of a hybrid nanofluid over a nonlinearly stretching surface with radiation effect. *Mathematics* 9, 2220. doi:10.3390/math9182220
- Anantha Kumar, K., Ramana Reddy, J. V., Sugunamma, V., and Sandeep, N. (2018). Magnetohydrodynamic Cattaneo-Christov flow past a cone and a wedge with variable heat source/sink. *Alexandria Eng. J.* 57, 435–443. doi:10.1016/j.aej.2016.11.013
- Arafat, H., Iqbal, Z., T-Eldin, E., Almohiemn, M., Yassin, M. F., Guedri, K., et al. (2022). Energy transport features of Oldroyd-B nanofluid flow over bidirectional stretching surface subject to Cattaneo-Christov heat and mass fluxes. *Front. Energy Res.* 10, 1361. doi:10.3389/fenrg.2022.985146
- CemEce, Mehmet (2005). Free convection flow about a cone under mixed thermal boundary conditions and a magnetic field. *Appl. Math. Model.* 29, 1121–1134. doi:10.1016/j.apm.2005.02.009
- Chakraborty, Samarshi, and Kumar Panigrahi, Pradipta (2020). Stability of nanofluid: A review. *Appl. Therm. Eng.* 174, 115259. doi:10.1016/j.applthermaleng.2020.115259
- Choi, S. U. S., and Eastman, J. A. (1995). *Enhancing thermal conductivity of fluids with nanoparticles*. ASME International Mechanical Engineering Congress & Exposition, San Francisco, CA, November 12–17, 1995.

Author contributions

All authors listed have made a substantial, direct, and intellectual contribution to the work and approved it for publication.

Acknowledgments

The authors express their appreciation to “The Research Center for Advanced Materials Science (RCAMS)” at King Khalid University, Saudi Arabia, for funding this work under the grant number RCAMS/KKU/002-22. The authors would like to thank the Deanship of Scientific Research at Umm Al-Qura University for supporting this work by Grant Code (22UQU4331100DSR18).

Conflict of interest

The authors declare that the research was conducted in the absence of any commercial or financial relationships that could be construed as a potential conflict of interest.

Publisher’s note

All claims expressed in this article are solely those of the authors and do not necessarily represent those of their affiliated organizations, or those of the publisher, the editors, and the reviewers. Any product that may be evaluated in this article, or claim that may be made by its manufacturer, is not guaranteed or endorsed by the publisher.

- De Carvalho, J. E. S. P., Sotomayor, P. O., Parise, J. A. R., and Florian, P. (2020). Numerical assessment of critical properties of nanofluids: Applications to nanorefrigerants and nanolubricants. *Journal of Molecular Liquids*, 318, doi:10.1016/j.molliq.2020.113938
- Dinarvand, Saeed, and Pop, Ioan (2017). Free-convective flow of copper/water nanofluid about a rotating down-pointing cone using Tiwari-Das nanofluid scheme. *Advanced Powder Technology*, 28, doi:10.1016/j.apt.2016.12.016
- Dinarvand, S. (2011). The laminar free-convection boundary-layer flow about a heated and rotating down-pointing vertical cone in the presence of a transverse magnetic field. *Int. J. Numer. Meth. Fluids* 67 (12), 2141–2156. doi:10.1002/flid.2489
- Ece, M. C. (2006). Free convection flow about a vertical spinning cone under a magnetic field. *Appl. Math. Comput.* 179, 231–242. doi:10.1016/j.amc.2005.11.099
- Gholinia, M., Hosseinzadeh, Kh., Mehrzadi, H., Ganji, D. D., and Ranjbar, A. A. (2019). Investigation of MHD Eyring–Powell fluid flow over a rotating disk under effect of homogeneous–heterogeneous reactions. *Case Stud. Therm. Eng.* 13, 100356. doi:10.1016/j.csite.2018.11.007
- Hamidreza, A. B., Omid, N.-K., Massimiliano, G., Rohollah, A., and Mohammad, M. M. (2020). On the use of boundary conditions and thermophysical properties of nanoparticles for application of nanofluids as coolant in nuclear power plants; a numerical study. *Prog. Nucl. Energy* 126, 103417. doi:10.1016/j.pnucene.2020.103417
- Maleki, Akbar, Elahi, Milad, Mamdouh El Haj AssadAlhuyi Nazari, Mohammad, Mostafa Safdari Shadlooand Nabipour, Narjes (2020). Thermal conductivity modeling of nanofluids with ZnO particles by using approaches based on artificial neural network and MARS. *J. Therm. Anal. Calorim.* 143, 4261–4272. doi:10.1007/s10973-020-09373-9
- Mallikarjuna, K., Santhoshkumar Reddy, Y., Hemachandra Reddy, K., and Sanjeeva Kumar, P. V. (2021). A nanofluids and nanocoatings used for solar energy harvesting and heat transfer applications: A retrospective review analysis. *Mater. Today Proc.* 37, 823–834. doi:10.1016/j.matpr.2020.05.833
- Rafiq, Muhammad, Shafique, Muhammad, Azam, Anam, and Ateeq, Muhammad (2021). Transformer oil-based nanofluid: The application of nanomaterials on thermal, electrical and physicochemical properties of liquid insulation-A review. *Ain Shams Eng. J.* 12, 555–576. doi:10.1016/j.asej.2020.08.010
- Raju, C. S. K., and Sandeep, N. (2016). Heat and mass transfer in MHD non-Newtonian bio-convection flow over a rotating cone/plate with cross diffusion. *J. Mol. Liq.* 215, 115–126. doi:10.1016/j.molliq.2015.12.058
- Reddy, S. C., Asogwa, K. K., Yassen, M. F., AdnanIqbal, Z., M-Eldin, S., et al. (2022). Dynamics of MHD second-grade nanofluid flow with activation energy across a curved stretching surface. *Front. Energy Res.* 10, 1007159. doi:10.3389/fenrg.2022.1007159
- SahbanAlnarabiji, Mohamad, and Husein, Maen M. (2020). Application of bare nanoparticle-based nanofluids in enhanced oil recovery. *Fuel* 267, 117262. doi:10.1016/j.fuel.2020.117262
- Salari, Saeed, and Seid Mahdi Jafari (2020). Application of nanofluids for thermal processing of food products. *Trends Food Sci. Technol.* 97, 100–113. doi:10.1016/j.tifs.2020.01.004
- Saranya, Shekar, Baranyi, László, and Qasem, M. (2022). Al- Free convection flow of hybrid ferrofluid past a heated spinning cone. *Therm. Sci. Eng. Prog.*
- Saranya, S. Ragupathi, P. Ganga, B., Sharma, R. P. and Abdul Hakeem, A. K. (2018). Non-linear radiation effects on magnetic/non-magnetic nanoparticles with different base fluids over a flat plate. *Advanced Powder Technology*, 29, doi:10.1016/j.apt.2018.05.002
- SaswatKhatai, Ramanuj Kumar, Ashok Kumar Sahoo, Panda, Amlana, and Das, Diptikanta (2020). Metal-oxide based nanofluid application in turning and grinding processes: A comprehensive review. *Mater. Today Proc.*
- Usafzai, W. K., Aly, E. H., Alshomrani, A. S., and Ullah, M. Z. (2022). Multiple solutions for nanofluids flow and heat transfer in porous medium with velocity slip and temperature jump. *Int. Commun. Heat Mass Transf.* 131, 105831. doi:10.1016/j.icheatmasstransfer.2021.105831
- Usri, N. A., Azmi, W. H., Rizalman, M., Abdul Hamid, K., and Najafi, G. (2015). Thermal conductivity enhancement of Al₂O₃ nanofluid in ethylene glycol and water mixture, 2015 international conference on alternative energy in developing countries and emerging economies. *Energy Procedia* 79, 397–402. doi:10.1016/j.egypro.2015.11.509
- Vargas-Estrada, Laura, Torres-Arellano, S., Longoria, Adriana, Dulce, M., Arias, Patrick U., and Sebastian, P. J. (2020). Role of nanoparticles on microalgal cultivation: A review. *Fuel* 280, 118598. doi:10.1016/j.fuel.2020.118598
- Vishnu Ganesh, N., Ganga, B., and Abdul Hakeem, A. K. (2014). Lie symmetry group analysis of magnetic field effects on free convective flow of a nanofluid over a semi-infinite stretching sheet. *J. Egypt. Math. Soc.* 22, 304–310. doi:10.1016/j.joems.2013.08.003
- Xuan, Yimin, and Li, Qiang (2000). *Heat transfer enhancement of nanofluids*, school of power EngineeringP. Nanjing: Nanjing University of Science and Technology. people's Republic of China.

Nomenclature

k thermal conductivity, $\text{Wm}^{-1}\text{K}^{-1}$

H dimensionless fluid temperature

G dimensionless swirl velocity

C_p specific heat, $\text{Jkg}^{-1}\text{K}^{-1}$

M magnetic parameter

F dimensionless tangential velocity

g acceleration due to gravity, ms^{-2}

L reference length, m

Nu_x local Nusselt number

C_f skin friction coefficient

B magnetic field intensity, $\text{kgs}^{-2}\text{A}^{-1}$

q_w surface heat flux, Wm^{-2}

r dimensionless radius

T_r reference temperature, K

Gr Grashof number

T_o temperature of the cone surface, K

Pr Prandtl number

u,v,w velocity component in the x,y,z direction respectively

T temperature, K

Re local Reynolds number

y dimensionless coordinate normal to the surface

U reference velocity, ms^{-1}

x dimensionless coordinate measured along the surface

β thermal expansion coefficient, K^{-1}

φ nanoparticle volume fraction

ε spin parameter

τ_w skin friction, Nm^{-2}

γ half of vertex angle

ρ density, kgm^{-3}

ψ dimensionless stream function

Ω angular velocity of the cone

θ angle of rotation

ν kinematic viscosity, m^2s^{-1}

Θ dimensionless temperature ratio

σ electrical conductivity, Sm^{-1}

α thermal diffusivity, m^2s^{-1}

μ dynamic viscosity, $\text{kgm}^{-1}\text{s}^{-1}$



OPEN ACCESS

EDITED BY

Ali Saleh Alshomrani,
King Abdulaziz University, Saudi Arabia

REVIEWED BY

Noreen Akbar,
National University of Sciences and
Technology (NUST), Pakistan
Najeeb Alam Khan,
University of Karachi, Pakistan

*CORRESPONDENCE

Muhammad Sohail,
muhammad_sohail111@yahoo.com
Sayed M. Eldin,
sayed.eldin22@fue.edu.eg

SPECIALTY SECTION

This article was submitted to Colloidal
Materials and Interfaces,
a section of the journal
Frontiers in Materials

RECEIVED 26 September 2022

ACCEPTED 04 November 2022

PUBLISHED 23 December 2022

CITATION

Nazir U, Sohail M, Mukdasai K, Singh A,
Alahmadi RA, Galal AM and Eldin SM
(2022), Applications of variable thermal
properties in Carreau material with ion
slip and Hall forces towards cone using a
non-Fourier approach via FE-method
and mesh-free study.
Front. Mater. 9:1054138.
doi: 10.3389/fmats.2022.1054138

COPYRIGHT

© 2022 Nazir, Sohail, Mukdasai, Singh,
Alahmadi, Galal and Eldin. This is an
open-access article distributed under
the terms of the [Creative Commons
Attribution License \(CC BY\)](https://creativecommons.org/licenses/by/4.0/). The use,
distribution or reproduction in other
forums is permitted, provided the
original author(s) and the copyright
owner(s) are credited and that the
original publication in this journal is
cited, in accordance with accepted
academic practice. No use, distribution
or reproduction is permitted which does
not comply with these terms.

Applications of variable thermal properties in Carreau material with ion slip and Hall forces towards cone using a non-Fourier approach via FE-method and mesh-free study

Umar Nazir¹, Muhammad Sohail^{2*}, Kanit Mukdasai¹,
Abha Singh³, Reham A. Alahmadi⁴, Ahmed M. Galal^{5,6} and
Sayed M. Eldin^{7*}

¹Department of Mathematics, Faculty of Science, Khon Kaen University, Khon Kaen, Thailand,

²Department of Mathematics, Khwaja Fareed University of Engineering and Information Technology,
Rahim Yar Khan, Pakistan, ³Department of Basic Sciences, College of Sciences and Theoretical Studies,
Dammam-branch, Saudi Electronic University, Riyadh, Saudi Arabia, ⁴Department of Basic Sciences,
College of Sciences and Theoretical Studies, Medinah-branch, Saudi Electronic University, Riyadh, Saudi
Arabia, ⁵Mechanical Engineering Department, College of Engineering, Prince Sattam Bin Abdulaziz
University, Wadi addawaser, Saudi Arabia, ⁶Production Engineering and Mechanical Design
Department, Faculty of Engineering, Mansoura University, Mansoura, Egypt, ⁷Center of Research,
Faculty of Engineering, Future University in Egypt New Cairo, New Cairo, Egypt

This research highlights the utilization of two viscosity models to study the involvement of variable properties in heat and momentum transport in a rotating Carreau fluid past over a cone. The rheology of the Carreau material is assessed by the variable dynamic viscosity over the heating cone. The transport of momentum phenomenon is modeled by considering generalized Ohm's law in Carreau liquid and thermal transport is derived by considering variable thermal conductivity, heat flux model. The considered model is derived in the form of nonlinear PDEs with boundary layer analysis. The nonlinear PDEs are converted into coupled ODEs by using approximate transformation and converted equations are solved numerically by finite element methodology. The impact of numerous parameters is displayed graphically, and their behavior is discussed in detail.

KEYWORDS

finite element method, nonlinear ODEs, heat transfer, boundary layer theory, variable properties

Introduction

The features of heat transfer are applicable in several industrial, chemical, and thermal processes. This type of phenomenon is applicable in polymers, gas engineering, cooling process, solar cells, water, thermal process, and oils. Recent work on heat transfer in several rheological fluids should be mentioned. Nazeer et al. (2022) estimated the thermal

aspects of multiphase flow taking into account magnetohydrodynamic and thermal radiation over a stretching frame. Luan et al. (2022) discussed turbulent effects in heat transfer phenomena in an energy transfer mechanism. Imran et al. (2022) discussed enhancement in thermal energy using the concept of several shapes of nanoparticles involving hybrid nanoparticles over a horizontal plate. The characteristics of fluids exhibit a range of rheological behavior. Therefore, it is very complex to study rheological behaviors, taking into account rheological stress (strain relation). The Newtonian model contains only viscosity rheology and its utilization in non-Newtonian contexts provides inaccurate information with respect to mass diffusion, flow, and heat energy. Carreau fluid is type of non-Newtonian fluid. Mathematical model related to Carreau fluid was investigated by Carreau (1972). The stress tensor regarding Carreau fluid is defined as

$$\boldsymbol{\tau} = -p\mathbf{I} + \mu_0 [1 + \Gamma^2 \mathbf{Y}^2]^{n-1/2} \mathbf{A}_1 \quad (1)$$

where $\boldsymbol{\tau}$ is the stress tensor, n is the power law index number, \mathbf{I} is the identity matrix, \mathbf{A}_1 is the Rivlin Ericksen tensor, and \mathbf{Y}^2 is the strain rate tensor. Nazir et al. (2021) discussed the rheology equations of a Carreau liquid using the impacts of ion slip and Hall forces in a rotating cone. They used a numerical approach to find numerical consequences. Sohail et al. (2022) studied three kinds of mass species in Carreau liquid in the presence of activation energy over a stretching plate. Nabwey et al. (2022) investigated the thermal aspects of Carreau nanofluid taking into account the chemical species and bioconvection in a cylinder. Reedy et al. (2022) discussed a model for a Carreau fluid including entropy generation over a heated microchannel. This involved multiple impacts based on thermal radiation and viscous dissipation using no-slip conditions. Imran et al. (2021) estimated the features of a Carreau liquid in energy transfer using magnetic dipoles and radiation containing nanofluids and microorganisms past a wedge, numerically solved with the shooting approach. Song et al. (2022) discussed thermal aspects in Carreau fluid considering nanoparticles in a stretching cylinder using Marangoni boundary conditions (BCs). Farooq et al. (2021) used Cattaneo-Christov theory in energy equations, taking thermal radiation, bioconvection flow, and heat source into account.

Recent investigations have shown that mass diffusion and thermal conductivity during transport mass species and heat cannot increase and remain constant. During changes of thermal energy, viscosity and thermal conductivity are functions of heat energy during the transport of particles. Alhussain and Tassaddiq (2022) proposed a model of variable viscosity in the presence of hybrid nanomaterial in Casson fluid, considering thin film considering magnetic field in

channel. They have utilized analytical approach to simulate numerical consequences. Kumawat et al. (2022) performed numerical results of entropy generation in MHD flow considering variable viscosity in the presence of variable viscosity. Nazir et al. (2020) simulated the numerical study of a Carreau liquid using the concept of variable properties in mass diffusion and heat energy involving non-Fourier's law over a frame using finite element scheme. It was found that the highest heat energy was obtained for variable viscosity than for constant viscosity. Chaurasiya et al. (2022) discussed the influence of variable thermal conductivity taking into account semi-conductor sources using a finite element scheme. Wang et al. (2022) investigated the impacts of tri-hybridized nanofluid taking into account variable properties of fluid in the presence of non-Fourier's law computed by the FE-method. Naseem et al. (2021) discussed the numerical consequences of Soret and Dufour effects involving the role of thermal radiation over a stretching frame, including variable thermal conductivity. Sohail et al. (2021) investigated the performance of entropy generation in a Casson fluid inserting the impact of Lorentz force. They discussed features of variable properties including various effects past a stretching frame. Akbar et al. (2022) performed investigations of unsteady flow in peristaltic transport using variable viscosity (function of temperature) simulating an exact solution approach. Akram et al. (2022a) estimated the thermal features of peristaltic flow involving electroosmotically adding a suspension of nanomaterial in a curved microchannel. Maraj et al. (2022) developed mathematical modeling of rotational MHD flow in the presence of Hall force inserting two types of nanoparticles using slip conditions in a vertical channel. Habib and Akbar (2021) investigated a new to nanofluids using sensitive *Staphylococcus aureus* and *Staphylococcus aureus*. They concluded that drug resistance can be reduced and overcome using drug conjugate and gold nanoparticles. Akram et al. (2021) introduced thermal transfer characterizations inserting hybrid nanofluid (Ag-Au) considering electroosmotic pumping in microchannel. Akram et al. (2022b) analyzed electroosmotic flow based on water-silver nanofluids considering peristalsis flow using two various approaches of nanofluid. Akram et al. (2022c) introduced investigation of electroosmosis in the presence of MHD peristaltic flow containing suspension of SWCNTs nanofluid filled in aqueous media. Multiple aspects of Carreau liquid applied to a magnetic field in a suspension of a nanofluid using slip effects across a slandering surface were studied by Raju et al. (2019). Khan and Sultan (2015) discussed thermal features of Dufour and Soret effects in Eyring-Powell liquid using a porous heated cone. Dawar et al. (2021) investigated flow configurations in Williamson fluid, taking into account non-

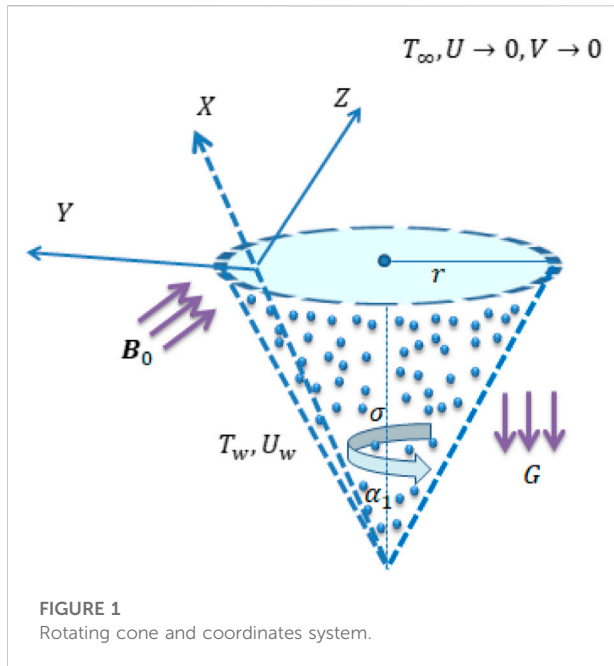


FIGURE 1
Rotating cone and coordinates system.

isosolutal conditions inserting nanofluid over wedge and cone.

The utilization of variable properties to study momentum and thermal transport in Carreau model past over a cone has not been sufficiently thoroughly studied. This contribution covers this question, and the modeled equations are solved numerically *via* finite element approach, and the impact of different involved parameters on velocity and temperature is discussed.

Mathematically development and physical consequences

Three-dimensional thermal features in terms of variable properties in a Carreau liquid in rotating cone are visualized. Two kinds of forces, namely, ion slip and Hall forces, are considered. The rheology of a Carreau liquid in the presence of variable viscosity is imposed into fluidic motion. Heat energy assessed using the non-Fourier approach. Lorentz force is inserted along the z-direction of a heated cone. Additionally, motion associated with particles is generated due to rotational movement of cone with angle Ω . The wall temperature is considered T_w . Thermal conductivity related fluid is considered function of temperature. The rotating cone is captured by Figure 1. Boundary layer approximation (BLA) is utilized to develop model of PDEs. The reduced form of PDEs is given below. Gravitational acceleration acts downward in a cone. Figure 1 predicts the physical behavior of the model (Khan et al., 2014).

Conservation laws (Khan et al., 2014; Malik et al., 2016) are defined as follows:

$$\nabla \cdot \tilde{\mathbf{V}} = 0, \quad (2)$$

$$\rho_{Thmf} \left(\frac{d\tilde{\mathbf{V}}}{dt} \right) = -\nabla p + \nabla \cdot \boldsymbol{\tau} + \mathbf{J} \times \mathbf{B}, \quad (3)$$

$$\nabla \cdot \mathbf{B} = 0, \mu_{Thmf} \mathbf{J} = \nabla \times \mathbf{B}, \nabla \times \mathbf{E} = \frac{\partial \mathbf{B}}{\partial t}, \quad (4)$$

$$\mathbf{J} = \left[\mathbf{E} + \tilde{\mathbf{V}} \times \mathbf{B} \right] \sigma_{Thmf} - (\mathbf{J} \times \mathbf{B}) \frac{B_e}{|\mathbf{B}|} + (\mathbf{J} \times \mathbf{B}) \frac{B_i B_e}{|\mathbf{B}|^2} \times \mathbf{B}, \quad (5)$$

$$(\rho C_p)_{thmf} \left(\frac{dT}{dt} \right) = K_{Thmf} (\nabla^2 T) - \nabla \cdot \mathbf{q} + Q_0 (T - T_\infty). \quad (6)$$

The reduced form of the PD equations (Khan et al., 2014; Malik et al., 2016) is given below:

$$\frac{\partial(XU)}{\partial Y} + \frac{\partial(XV)}{\partial Z} = 0, \quad (7)$$

$$U \frac{\partial U}{\partial X} + W \frac{\partial U}{\partial Z} = \frac{(B_0)^2 \sigma}{\rho [(1 + B_e B_i)^2 + (B_e)^2]} [VB_e - (1 + B_i B_e)U], \\ + \frac{V^2}{X} + G\beta(T - T_\infty) \cos \alpha \\ + \frac{\partial}{\partial z} \left[\left\{ 1 + \Gamma^2 \left(\frac{\partial U}{\partial y} \right)^2 \right\}^{n-1/2} \frac{\partial U}{\partial z} \right], \quad (8)$$

$$U \frac{\partial V}{\partial X} + W \frac{\partial V}{\partial Z} = -\frac{(B_0)^2 \sigma}{\rho [(1 + B_e B_i)^2 + (B_e)^2]} [UB_e + (1 + B_i B_e)V], \\ - \frac{UV}{X} + \frac{\partial}{\partial z} \left[\left\{ 1 + \Gamma^2 \left(\frac{\partial V}{\partial y} \right)^2 \right\}^{n-1/2} \frac{\partial V}{\partial z} \right], \quad (9)$$

$$U \frac{\partial T}{\partial X} + W \frac{\partial T}{\partial Z} = \frac{1}{\rho C_p} \frac{\partial}{\partial Z} \left(K(T) \frac{\partial T}{\partial Z} \right) + \frac{Q_0}{\rho C_p} (T - T_\infty) \\ - \frac{\lambda Q_0}{\rho C_p} \left(U \frac{\partial T}{\partial X} + W \frac{\partial T}{\partial Z} \right) \\ - \lambda \left(U^2 \frac{\partial^2 T}{\partial X^2} + W^2 \frac{\partial^2 T}{\partial Z^2} + 2UW \frac{\partial^2 T}{\partial X \partial Z} \right) \\ - \lambda \left(U \frac{\partial V}{\partial X} + W \frac{\partial V}{\partial Z} \right) \frac{\partial T}{\partial Z} \\ - \lambda \left(U \frac{\partial U}{\partial X} + W \frac{\partial U}{\partial Z} \right) \frac{\partial T}{\partial X}. \quad (10)$$

BCs (boundary conditions) (Malik et al., 2016) are

$$U = 0, V = \Omega X \sin \alpha, T = T_w, U \rightarrow 0, V \rightarrow 0, T \rightarrow T_\infty \quad (11)$$

Viscosity and thermal conductivity (Nazir et al., 2020) are functions of heat energy, as follows:

$$\frac{\mu_\infty}{\mu} = [1 - \gamma(T_\infty - T)], \\ \frac{K(T)}{k_\infty} = \left[1 - \epsilon \left(\frac{T_\infty - T}{T_w - T_\infty} \right) \right] \quad (12)$$

The similarity variables (Malik et al., 2016) of current the analysis are

$$U = -\frac{\Omega X \sin \alpha F'}{2}, V = \Omega X \sin \alpha G, W = (\Omega \nu_f \sin \alpha)^{1/2} F, \\ \Theta = \frac{T - T_\infty}{T_w - T_\infty}, \eta = \left(\frac{\Omega \sin \alpha}{\nu_f} \right)^{1/2} Z \quad (13)$$

Eq. 12 is known as a transformation, and the selection of the transformation is adopted to satisfy the continuity equation. Transformations are used in Eqs. 7–9. The ODEs are derived as

$$\frac{\Theta_\gamma}{\Theta_\gamma - 1} \left\{ 1 + n(WF'')^2 \right\} \left\{ 1 + (WF'')^2 \right\}^{n-3/2} F''' \\ + \frac{\Theta_\gamma}{(\Theta_\gamma - 1)^2} \left\{ 1 + (WF'')^2 \right\}^{n-1/2} F'' \Theta' + \frac{M^2}{(1 + B_e B_i)^2 + (B_e)^2} \quad (14)$$

$$\left[(1 + B_e B_i) F' + 2B_e G \right] + \left(\frac{1}{2} F'^2 - FF'' - 2G^2 - 2\lambda \Theta \right) = 0, \\ \frac{\Theta_\gamma}{\Theta_\gamma - 1} \left\{ 1 + n(WG')^2 \right\} \left\{ 1 + (WG')^2 \right\}^{n-3/2} G'' \\ + \frac{\Theta_\gamma}{(\Theta_\gamma - 1)^2} \left\{ 1 + (WG')^2 \right\}^{n-1/2} G' \Theta' - \frac{M^2}{(1 + B_e B_i)^2 + (B_e)^2} \quad (15)$$

$$\left[(1 + B_e B_i) G - \frac{1}{2} B_e F' \right] + (GF' - F'G') = 0, \\ (1 + \epsilon \Theta) \Theta'' + \epsilon (\Theta')^2 + Pr_\infty F \Theta' + \gamma_1 Pr_\infty \\ \left[F^2 \Theta'' - QF \Theta' + \frac{1}{2} FG' \Theta' \right] + Pr_\infty H_t \Theta = 0. \quad (16)$$

The Prandtl fluid at infinity is delivered as

$$Pr_\infty = (1 + \epsilon \Theta) \left(1 - \frac{\Theta}{\Theta_\gamma} \right) Pr. \quad (17)$$

Substituting Eq. (16) into Eq. (15), we have

$$(1 + \epsilon \Theta) \Theta'' + \epsilon (\Theta')^2 + \gamma_1 (1 + \epsilon \Theta) \left(1 - \frac{\Theta}{\Theta_\gamma} \right) \\ Pr \left[F^2 \Theta'' - QF \Theta' + \frac{1}{2} FG' \Theta' \right] + (1 + \epsilon \Theta) \left(1 - \frac{\Theta}{\Theta_\gamma} \right) Pr F \Theta' \\ + (1 + \epsilon \Theta) \left(1 - \frac{\Theta}{\Theta_\gamma} \right) Pr H_t \Theta = 0. \quad (18)$$

$\theta_\gamma = 1/\gamma(T_w - T_\infty)$ is the fluid viscosity number. The case is known as constant viscosity for $\theta_\gamma \rightarrow \infty$ and case for liquids for $\theta_\gamma = -1$.

Wall stresses (skin friction coefficients) are formulated as

$$Re^{1/2} C_F = \frac{\theta_\gamma}{\theta_\gamma - 1} \left[1 + W^2 (F''(0))^2 \right]^{n-1/2} F''(0) \quad (19)$$

$$Re^{1/2} C_G = \frac{\theta_\gamma}{\theta_\gamma - 1} \left[1 + W^2 (G'(0))^2 \right]^{n-1/2} G'(0) \quad (20)$$

$$Re^{-1/2} Nu = (1 + \epsilon) \Theta'(0) \quad (21)$$

The heat transfer rate in terms of variable thermal conductivity is

Numerical methodology

The formulated ODEs are numerically simulated by a numerical scheme (FEM) [14, 16, and 31]. The description associated with FEM is mentioned below.

Discretization of domain

In this step, the desired ODEs are transformed into numbers of elements (300 elements). Residuals of the current problem are achieved. Eqs. 13–15 are strong forms with boundary conditions. A strong form can be converted into a weak form by collecting all terms on one side and multiplying it by weight functions and integrated it on whole domain. The weighted residuals of the problem implementation due to $F' = S$ are as follows:

$$\int_{\eta_e}^{\eta_{e+1}} w_1 (F' - S) d\eta = 0, \quad (22)$$

$$\int_{\eta_e}^{\eta_{e+1}} w_2 \left[\frac{\Theta_\gamma}{\Theta_\gamma - 1} \left\{ 1 + n(WF'')^2 \right\} \left\{ 1 + (WF'')^2 \right\}^{n-3/2} S'' \right. \\ \left. + \frac{M^2}{(1 + B_e B_i)^2 + (B_e)^2} \left[(1 + B_e B_i) F' + 2B_e G \right] \right. \\ \left. - \left(\frac{1}{2} F'^2 - FF'' - 2G^2 - 2\lambda \Theta \right) \right] d\eta = 0, \quad (23)$$

$$\int_{\eta_e}^{\eta_{e+1}} w_3 \left[\frac{\Theta_\gamma}{\Theta_\gamma - 1} \left\{ 1 + n(WG')^2 \right\} \left\{ 1 + (WG')^2 \right\}^{n-3/2} G'' \right. \\ \left. + \frac{\Theta_\gamma}{(\Theta_\gamma - 1)^2} \left\{ 1 + (WG')^2 \right\}^{n-1/2} G' \Theta' + (GF' - F'G') \right. \\ \left. - \frac{M^2}{(1 + B_e B_i)^2 + (B_e)^2} \left[(1 + B_e B_i) G - \frac{1}{2} B_e F' \right] \right] d\eta = 0, \quad (24)$$

$$\int_{\eta_e}^{\eta_{e+1}} w_4 \left[\frac{\Theta_\gamma}{\Theta_\gamma - 1} \left\{ 1 + n(WF'')^2 \right\} \left\{ 1 + (WF'')^2 \right\}^{n-3/2} S'' \right. \\ \left. + \frac{M^2}{(1 + B_e B_i)^2 + (B_e)^2} \left[(1 + B_e B_i) F' + 2B_e G \right] \right. \\ \left. - \left(\frac{1}{2} F'^2 - FF'' - 2G^2 - 2\lambda \Theta \right) \right] d\eta = 0, \quad (25)$$

Shape functions

Various shape functions are utilized in the current problem. In this approach, however, a linear shape function is implemented to

obtain an approximate solution. Several shape functions are used in FEM. However, the linear type of shape function is utilized in this numerical approach. Shape functions are based on a linear type of polynomial. The values variables (N , F , Θ) are defined as

$$N = \sum_{j=1}^2 (N_j \psi_j), F = \sum_{j=1}^2 (F_j \psi_j), \Theta = \sum_{j=1}^2 (\Theta_j \psi_j). \quad (26)$$

Shape functions are

$$\psi_j = (-1)^{j-1} \frac{\eta - \eta_{j-1}}{\eta_j - \eta_{j-1}}. \quad (27)$$

Developments of stiffness matrices using assemble process

The Galerkin approach is utilized to derive the stiffness matrices. The concept of the assembly process is implemented to find stiffness matrices and global stiffness matrix. The sizes of the boundary vectors, stiffness matrices, and source vectors are

$$K_{ij}^{11} = \int_{\eta_e}^{\eta_{e+1}} \left(\frac{d\psi_j}{d\eta} \psi_i \right) d\eta, K_{ij}^{12} = \int_{\eta_e}^{\eta_{e+1}} (\psi_j \psi_i) d\eta, b_i^1 = 0, K_{ij}^{13} = 0, K_{ij}^{14} = 0, \quad (28)$$

$$K_{ij}^{22} = \int_{\eta_e}^{\eta_{e+1}} \left[\frac{\Theta_j}{\Theta_j - 1} \left\{ 1 + n \left(W \bar{S}' \right)^2 \right\} \left\{ 1 + \left(W \bar{S}' \right)^2 \right\}^{n-3/2} \frac{d\psi_i}{d\eta} \frac{d\psi_j}{d\eta} \right. \\ \left. \frac{\Theta_j}{(\Theta_j - 1)^2} \left\{ 1 + (W F'')^2 \right\}^{n-1/2} \bar{\Theta}' \psi_i \frac{d\psi_j}{d\eta} + \frac{1}{2} \bar{S} \psi_i \psi_j \right. \\ \left. - \bar{F} \psi_i \frac{d\psi_j}{d\eta} + \frac{M^2 (1 + B_e B_i)}{(1 + B_e B_i)^2 + (B_e)^2} \psi_i \psi_j \right] d\eta, b_i^2 = 0, K_{ij}^{21} = 0, \quad (29)$$

$$K_{ij}^{23} = \int_{\eta_e}^{\eta_{e+1}} \left[\frac{M^2 2 B_e}{(1 + B_e B_i)^2 + (B_e)^2} \psi_i \psi_j - 2 \bar{G} \psi_i \psi_j \right] d\eta, K_{ij}^{24} \\ = \int_{\eta_e}^{\eta_{e+1}} [-2 \lambda \bar{G} \psi_i \psi_j] d\eta, \quad (30)$$

$$K_{ij}^{33} = \int_{\eta_e}^{\eta_{e+1}} \left[\frac{\Theta_j}{\Theta_j - 1} \left\{ 1 + n \left(W G' \right)^2 \right\} \left\{ 1 + \left(W G' \right)^2 \right\}^{n-3/2} \frac{d\psi_i}{d\eta} \frac{d\psi_j}{d\eta} \right. \\ \left. \frac{\Theta_j}{(\Theta_j - 1)^2} \left\{ 1 + \left(W G' \right)^2 \right\}^{n-1/2} \bar{\Theta}' \psi_i \frac{d\psi_j}{d\eta} + \bar{G} \psi_i \psi_j + H \psi_i \frac{d\psi_j}{d\eta} \right. \\ \left. - \frac{M^2 (1 + B_e B_i)}{(1 + B_e B_i)^2 + (B_e)^2} \psi_i \psi_j \right] d\eta, \quad (31)$$

$$K_{ij}^{32} = \int_{\eta_e}^{\eta_{e+1}} \left[\frac{M^2 1/2}{(1 + B_e B_i)^2 + (B_e)^2} \psi_i \psi_j \right] d\eta, K_{ij}^{34} = 0, K_{ij}^{31} = 0, b_i^3 = 0, \quad (32)$$

$$K_{ij}^{44} = \int_{\eta_e}^{\eta_{e+1}} \left[\begin{aligned} & - (1 + \epsilon \bar{\Theta}) \frac{d\psi_i}{d\eta} \frac{d\psi_j}{d\eta} + \epsilon \bar{\Theta} \psi_i \frac{d\psi_j}{d\eta} \\ & + (1 + \epsilon \bar{\Theta}) \left(1 - \frac{\bar{\Theta}}{\Theta_j} \right) Pr \left(1 - \frac{\bar{\Theta}}{\Theta_j} \right) \bar{F} \psi_i \frac{d\psi_j}{d\eta} \\ & + (1 + \epsilon \bar{\Theta}) \left(1 - \frac{\bar{\Theta}}{\Theta_j} \right) Pr H_i \psi_i \psi_j \\ & + \gamma_1 (1 + \epsilon \bar{\Theta}) \left(1 - \frac{\bar{\Theta}}{\Theta_j} \right) Pr \left[\frac{d\psi_j}{d\eta} \frac{d\psi_i}{d\eta} - Q \bar{F} \Theta' + \frac{1}{2} \bar{F} G' \psi_i \frac{d\psi_j}{d\eta} \right] \end{aligned} \right] d\eta, \quad (33)$$

$$K_{ij}^{41} = 0, b_i^4 = 0, K_{ij}^{42} = 0, K_{ij}^{43} = 0. \quad (34)$$

Assembly method

The assembly method is used to assemble all elements. The residual is defined as

$$[R] = [M(F^{(r-1)}, S^{(r-1)}, \Theta^{(r-1)}, \phi^{(r-1)})] \begin{bmatrix} F^r \\ G^r \\ S^r \\ \Theta^r \end{bmatrix} = [F]. \quad (35)$$

The convergence of the problem must exist under 10^{-5} , which is delivered as

$$\frac{\left(\sum_{i=1}^N (|\omega^r - \omega^{r-1}|)^2 \right)^{1/2}}{\left(\sum_{i=1}^N |\omega^r| \right)^2} < 10^{-5}. \quad (36)$$

Code development and validation

Code based on FEM is developed on MAPLE. The Galerkin finite element method is used to simulate the problem on MAPLE 18. The FEM code is verified in a published study (Malik et al., 2016), which is recorded in Table 1. The grid-independent analysis is shown in Table 2.

Outcomes and discussion

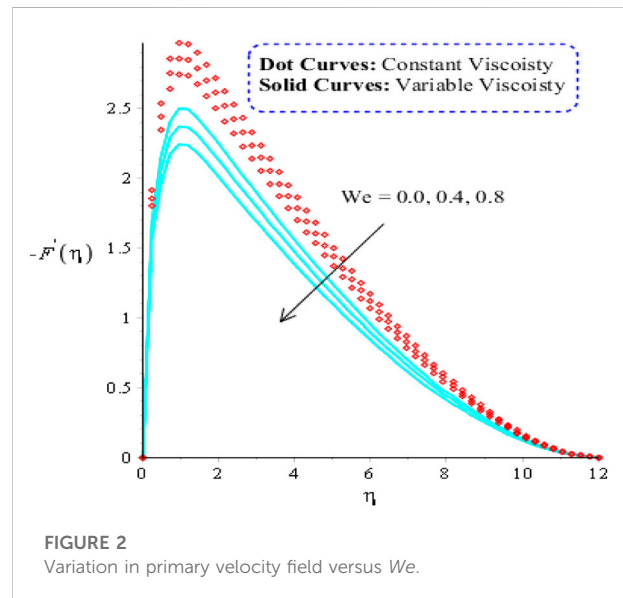
The three-dimensional thermal aspects of a Carreau liquid in the presence of variable viscosity in a rotating cone are developed. Features related to ion slip and Hall theory are added in momentum equations. The concept associated with Cattaneo-Christov model (CCM) is utilized, involving heat generation/heat absorption. Moreover, variable fluidic properties are utilized in terms of variable thermal conductivity and viscosity dependent

TABLE 1 Validation of results in term of shear stresses and Nusselt number when $H_s = 0.0$, $Pr = 0.7$, $Ec = 0.0$, $\beta_e = 0.0$, $\beta_i = 0.0$, and $\beta = 0.2$.

λ	Present work			Malik et al. (2016)		
	$-(Re)^{1/2}C_f$	$-(Re)^{1/2}C_g$	$-(Re)^{-1/2}NU$	$-(Re)^{1/2}C_f$	$-(Re)^{1/2}C_g$	$-(Re)^{-1/2}NU$
0.0	1.0253652070	0.61537912903	0.4294230670	1.0253	0.6153	0.4295
1.0	2.20070023051	0.844695060970	0.6121076213	2.2007	0.8492	0.6121
10	8.5043340330	1.39961520634	1.0098376217	8.5041	1.3990	1.0097

TABLE 2 Grid-independent investigation for $G(\eta_{\max}/2)$, $\Theta(\eta_{\max}/2)$, and $F'(\eta_{\max}/2)$.

e	$F'(\eta_{\max}/2)$	$G(\eta_{\max}/2)$	$\Theta(\eta_{\max}/2)$
20	0.6192543746	0.7775868422	0.02364363915
40	0.3563679813	0.6172517630	0.008213654544
60	0.3472652177	0.6085798291	0.008467428871
80	0.3426854561	0.6042412374	0.008565535885
100	0.3399304701	0.6016370351	0.008615382875
120	0.3380909312	0.5999004990	0.008644849238
140	0.3367764901	0.5986602893	0.008664143487
180	0.3350215280	0.5970053059	0.008687496783
200	0.3344073091	0.5964262953	0.008695060976
220	0.3339043627	0.5959524702	0.008700980450
240	0.5955576215	0.5955576215	0.008705785061
260	0.3331306142	0.5952230675	0.008709730703
280	0.3339886777	0.5951914530	0.004266023555
300	0.3325627516	0.5951883042	0.004215755900

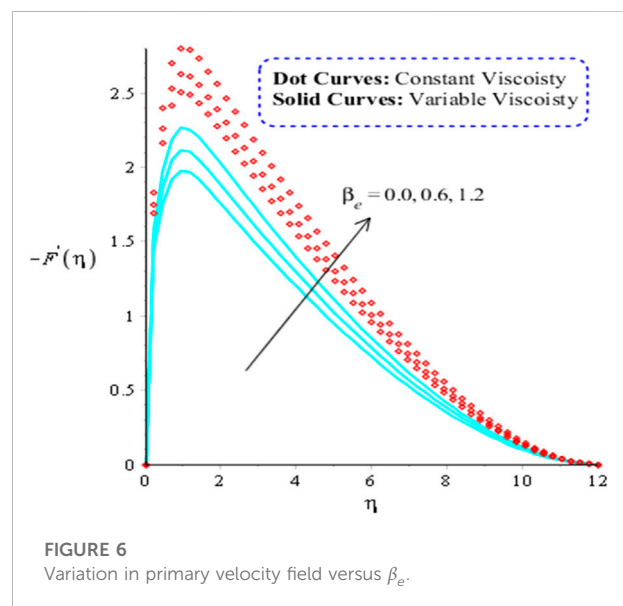
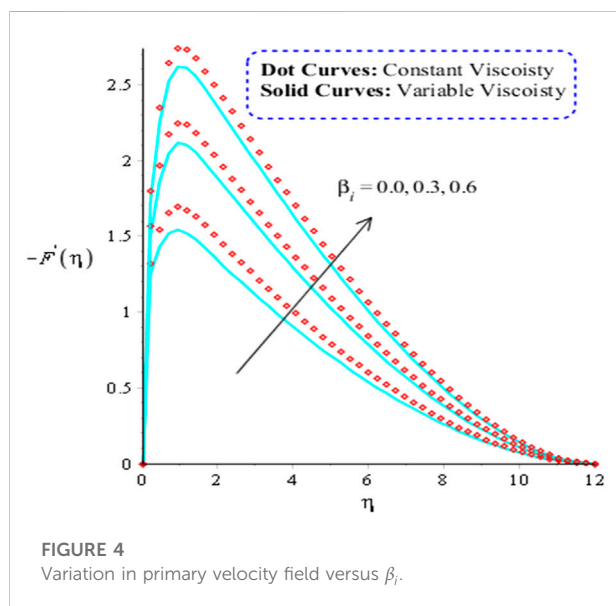
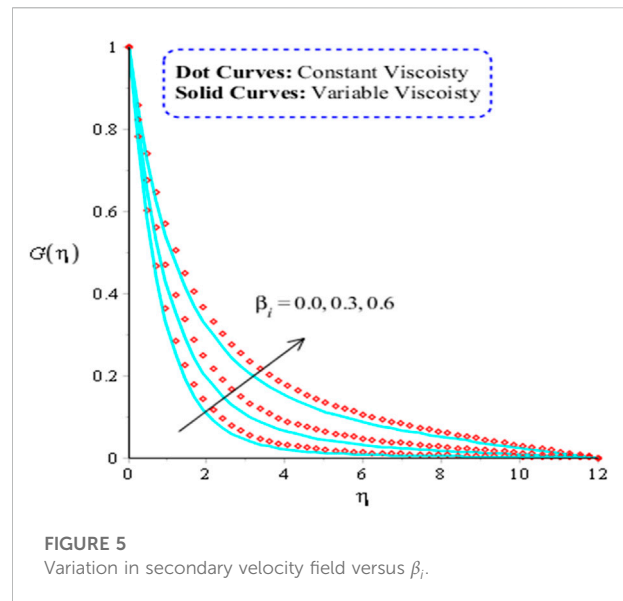
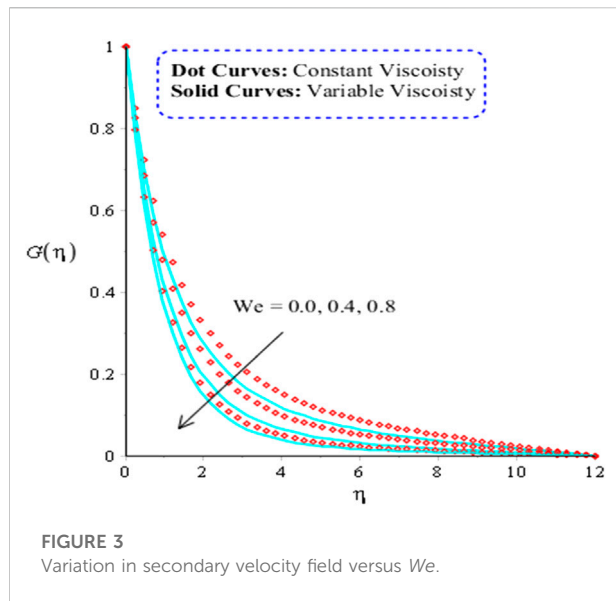
FIGURE 2
Variation in primary velocity field versus We .

heat energy. The developed model is numerically solved using the finite element approach. The graphical results in view of thermal and velocity field are shown below.

Contrast among constant and variable viscosities in velocity field

In this section, Figures 2–9 are plotted reading secondary and primary velocity fields against several parameters. It is noted that dot curves are associated with constant viscosity for $1/\Theta_\gamma = 0$, and solid curves are plotted for representation of variable viscosity for $\Theta_\gamma = -1$. Figures 2, 3 are plotted to notice variation in secondary and $G(\eta)$ velocities against change in We . The flow associated with secondary and primary velocity curves slows down against change in We . The flow for the case of constant viscosity is higher than the flow for variable viscosity. Thickness of the momentum layer is decreased when We is inclined. Physically, We is known as the Weissenberg parameter, and it is defined as the ratio between elastic force and viscous force. From definition point of view, We is

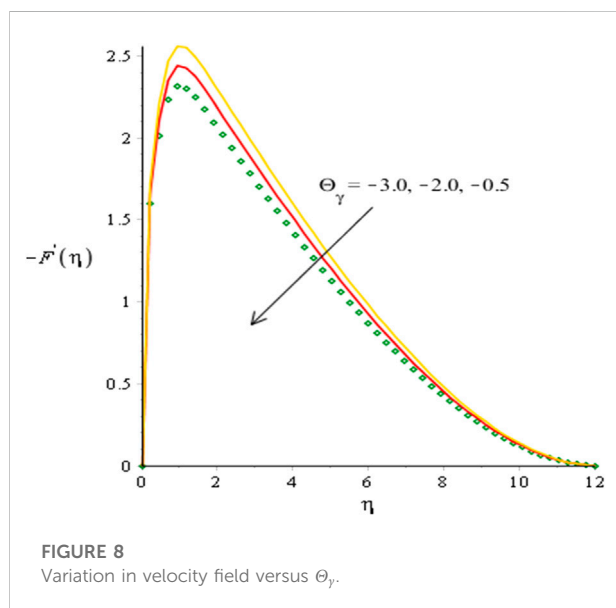
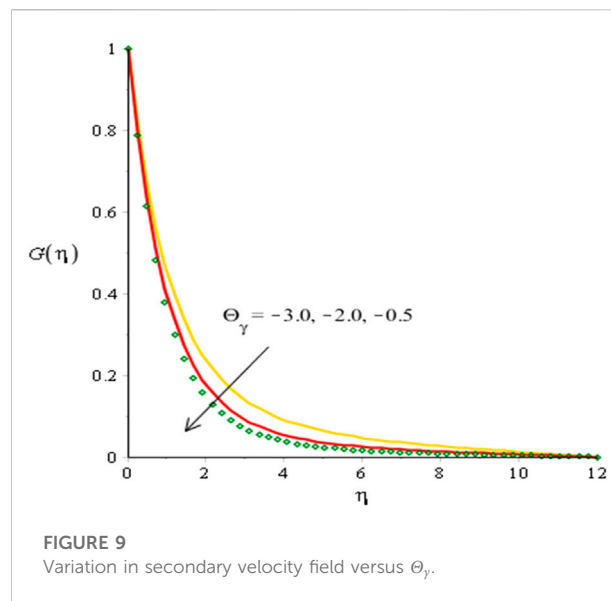
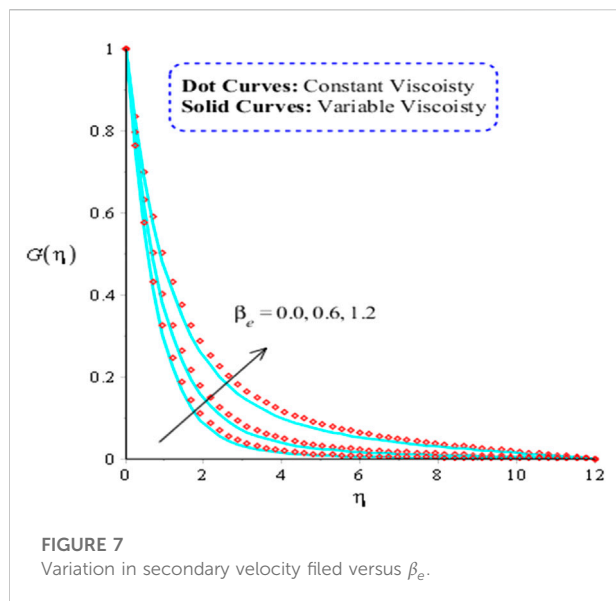
inversely proportional against viscous force. Therefore, the viscosity of fluidic particles is enhanced when We is increased. Figures 4–7 are plotted to determine the visualization of velocities in the presence of ion slip and Hall parameters. For this case, flow of Carreau liquid is enhanced when ion slip and Hall numbers are increased. This is because generalized Ohm's theory is utilized in current analysis. Moreover, the directly proportional relation is predicted among ion slip and Hall parameters. Lorentz force is visualized against implication of B_e and B_i . Therefore, Lorentz force is decreased when B_e and B_i are increased. Lorentz force is produced using a generalized Ohm's law in momentum equations. The production of electron frequency and electron collision (time) is known as B_e . In additionally, the production of ion cyclotron frequency and ion collision time is called B_i . Fluidic velocity is enhanced when collision and frequency among particles are enhanced. The layers of momentum in terms of thickness is an increasing function versus the implication of B_e and B_i . Therefore, significant acceleration is produced among the particles. Thickness regarding MLs (momentum layers) for constant viscosity ($\Theta_\gamma \rightarrow \infty$) is greater than for variable viscosity. The impact of



Θ_γ on velocity fields (primary and secondary directions) is addressed by Figures 8, 9. Θ_γ is defined as $1/\gamma(T_w - T_\infty)$, while Θ_γ has inversely proportional against temperature difference. Temperature differences increase among fluidic particles. Therefore, thickness regarding momentum layers is increased versus change in Θ_γ . Mathematically, Θ_γ has directly proportional relation versus the impact of velocity fields. Therefore, flow declines when Θ_γ also decreases.

Contrast among constant and variable viscosities in temperature field

This subsection contains graphical explanation associated with thermal impacts for two cases (variable viscosity and constant viscosity) against change in heat source, ϵ , Θ_γ , and Pr . These results are shown in Figures 10–13. It is noticed that dot curves are plotted for constant viscosity ($\Theta_\gamma \rightarrow \infty$), and solid curves are

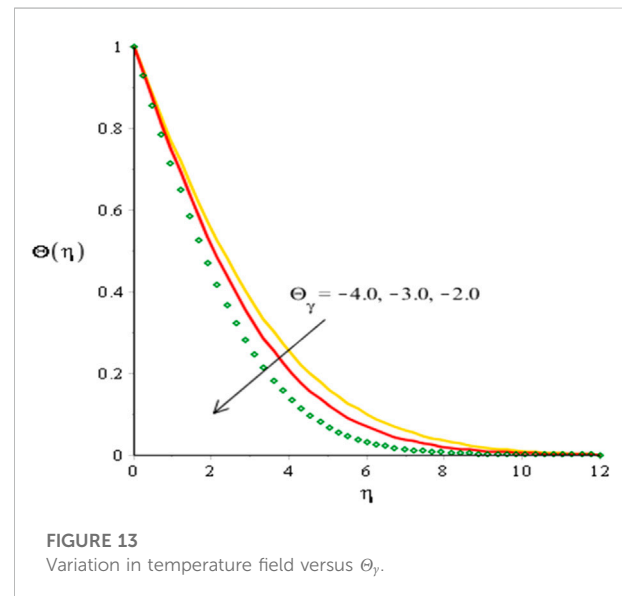
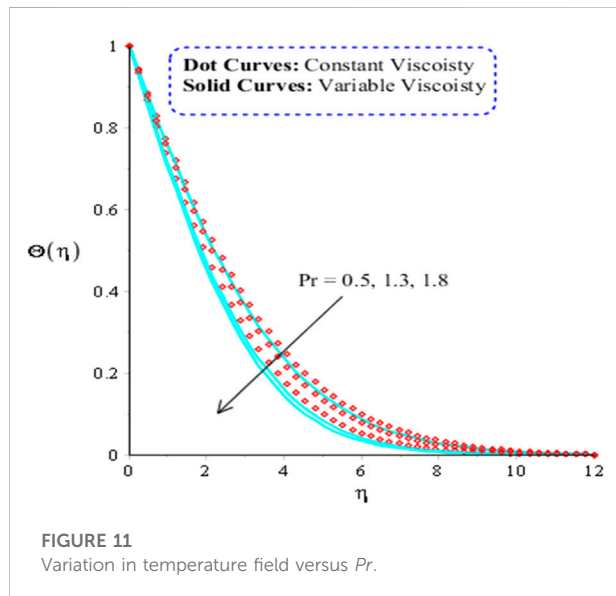
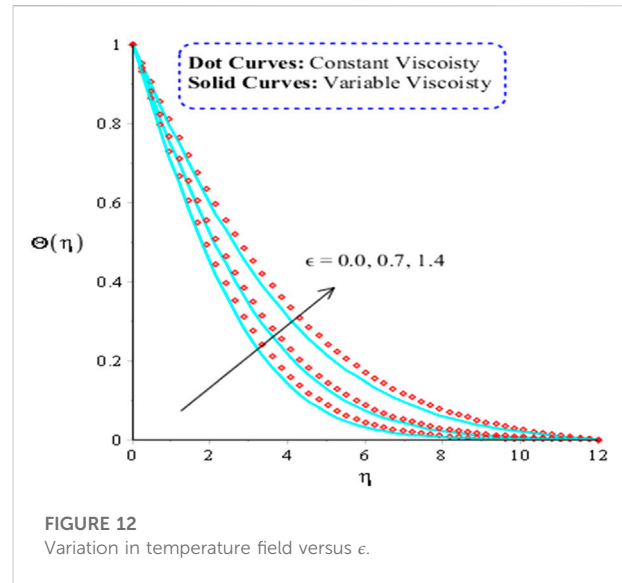
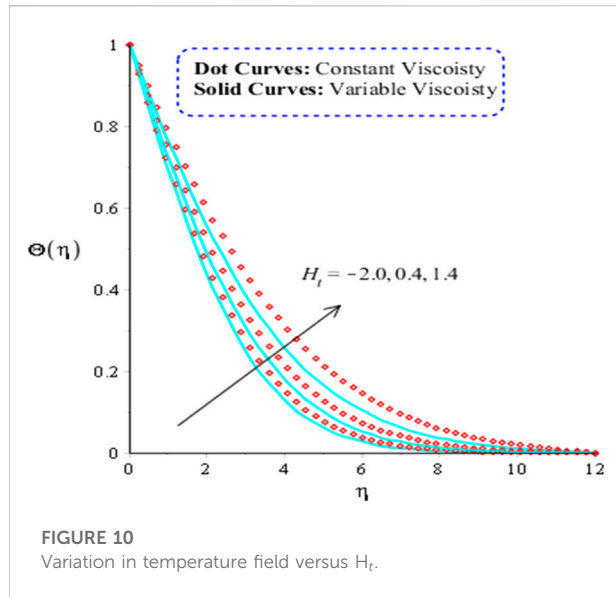


plotted for viscosity (function of temperature). Figure 10 is prepared to determine the impact of H_t on the thermal profile. It is addressed that heat energy is boosted when H_t is increased. Physically, this occurs due to external heat sources on the thermal profile. Hence, extra heat energy can be added using an external heat source. Additionally, heat energy for constant viscosity is greater than heat energy for case of variable viscosity. It can be noted that the behavior of H_t is based on numerical values. For negative values, H_t is called heat absorption while H_t is called heat absorption for positive values. An effect for $H_t > 0$ on temperature performance is greater than effect for $H_t < 0$. Thermal layers thickness can be adjusted through variation in H_t whereas H_t is directly proportional against temperature difference. Therefore, heat energy is

significantly increased when H_t is enhanced. The role of Pr on thermal profile is addressed in Figure 11. Thermal profile decreases against change in Pr . Physically, it refers to division among thermal thickness and momentum thickness. It is observed that inverse proportional relation is experienced between Pr and thermal layers. Consequently, thickness for thermal layers is significantly enhanced when Pr is increased. Therefore, heat energy and TBL (thermal boundary layer) can be controlled using numerical values of Pr . Figure 12 captures the impact of ϵ on thermal profile. Mathematically, a directly proportional relationship can be seen among ϵ and temperature difference. Consequently, heat energy is boosted when ϵ is increased. Figure 13 is based on the relationship between heat energy and Θ_γ . ϵ is dimensionless parameter, which is appeared using concept of non-uniform thermal conductivity. ϵ is appeared in Eq. 11, which has direct proportional relation against temperature dependence (thermal conductivity). Therefore, the temperature difference among particles is increased when ϵ is increased. Physically, temperature increases among particles due to temperature differences. Thermal energy is seen against change in Θ_γ . It can be noted that thermal energy is decreased against decline values of Θ_γ . Mathematically, Θ_γ is termed as $1/\gamma(T_w - T_\infty)$, which is inversely proportional versus temperature difference ($T_w - T_\infty$). Hence, temperature difference is decreased when Θ_γ is increased.

Measurement of shear stresses and temperature gradient

Table 3 demonstrates the impacts of shear stresses and Nusselt numbers against variation in Pr , M , H_t , and Θ_γ . From this table, it can be seen that shear stresses are declined



versus implication of H_t . However, heat transfer rate is reduced when H_t is increased. M is magnetic parameter, which is appeared using concept of Lorentz force. Divergent forces (skin friction coefficients) are decreased versus the implications of the Lorentz force. The Nusselt number (temperature gradient) is enhanced against the implications of higher-impact Lorentz forces. Velocity is increased when the Lorentz force is enhanced. Shear stresses are significantly declined when the Lorentz force is enhanced. These outcomes are presented in Table 3. Additionally, the Prandtl number arguments thermal rate (Nusselt number), and shear stresses are decreased when Pr is enhanced. The division between momentum and thermal layers is represented by Pr .

Therefore, skin friction coefficients are enhanced when Pr is increased.

Prime consequences of performed research

The thermal features of 3D-Carreau model are developed under considerations of ion slip and Hall forces in rotating cone. Variable thermal properties in term of viscosity, mass diffusion, and thermal conductivity are addressed. Chemical species and external heat sources are utilized in the presence of a non-Fourier law. The following are the most important outcomes from this investigation:

TABLE 3 Numerical impacts of shear stresses and temperature gradient versus Pr , M , H_t , and Θ_y .

Change in parameters		$-Re^{1/2}C_F$	$-Re^{1/2}C_G$	$-Re^{-1/2}Nu$
Pr	0.0	0.4438288364	0.2137193533	1.337499994
	0.5	0.4364839833	0.2051746254	1.224569168
	0.7	0.4200424336	0.1966019057	1.066393504
H_t	−1.5	0.3387190600	0.08922203657	1.424510434
	0.2	0.3271335238	0.02858202051	1.397533801
	0.7	0.3111766612	0.01462798772	1.373425184
M	0.0	0.3740169115	0.1282122993	1.370310731
	0.3	0.3840217314	0.1382043278	1.270316816
	0.6	0.3940361885	0.1481804049	1.170335265
Θ_y	−1.5	0.3745150981	0.1274641174	1.370934176
	−1.8	0.3848934552	0.1368848568	1.381406714
	−2.0	0.3951193643	0.1465341738	1.391688290

The computations of the problem become grid independent at 300 elements;
Heat energy diffuses faster into non-Newtonian liquids for temperature-dependent viscosity than for the diffusion of heat energy for constant viscosity;
Motion into fluidic particles is enhanced against higher values of ion slip and Hall currents parameters;
Heat energy is boosted versus higher values of H_t , but heat energy is decreased when the Prandtl number is increased;
An enhancement in thermal energy occurs according to ϵ , utilized in the production of solar energy, cooking, baking, cooling, drying, and heating;
The thermal transfer rate is applicable in metal grinding, wire paintings, glasses melting, chemical products, solar collectors, machine cutting, food processing, electronic components, nuclear reaction, solar systems, glass fiber, and so on.

Data availability statement

The raw data supporting the conclusions of this article will be made available by the authors, without undue reservation.

Author contributions

UN: Conceptualization; Investigation; Software; Validation; Writing—review and editing. MS: Data curation; Writing—original draft; Writing—review and editing

References

Akbar, N. S., Maraj, E. N., Noor, N. F. M., and Habib, M. B. (2022). Exact solutions of an unsteady thermal conductive pressure driven peristaltic transport

Visualization; Methodology. KM: Formal analysis; Funding acquisition; Software. AS: Methodology; Project administration; Resources; Funding acquisition. RA: Project administration; Formal analysis. AG: Visualization; Supervision; Funding acquisition. MS: Software; Validation; Visualization; Supervision; Funding acquisition.

Funding

This work was partially funded by the research center of the Future University in Egypt, 2022.

Conflict of interest

The authors declare that the research was conducted in the absence of any commercial or financial relationships that could be construed as a potential conflict of interest.

Publisher’s note

All claims expressed in this article are solely those of the authors and do not necessarily represent those of their affiliated organizations, or those of the publisher, the editors, and the reviewers. Any product that may be evaluated in this article, or claim that may be made by its manufacturer, is not guaranteed or endorsed by the publisher.

with temperature-dependent nanofluid viscosity. *Case Stud. Therm. Eng.* 35, 102124. doi:10.1016/j.csite.2022.102124

- Akram, J., Akbar, N. S., Alansari, M., and Tripathi, D. (2022). Electroosmotically modulated peristaltic propulsion of TiO₂/10W40 nanofluid in curved microchannel. *Int. Commun. Heat Mass Transf.* 136, 106208. doi:10.1016/j.icheatmasstransfer.2022.106208
- Akram, J., Akbar, N. S., and Tripathi, D. (2021). A theoretical investigation on the heat transfer ability of water-based hybrid (Ag–Au) nanofluids and Ag nanofluids flow driven by electroosmotic pumping through a microchannel. *Arab. J. Sci. Eng.* 46 (3), 2911–2927. doi:10.1007/s13369-020-05265-0
- Akram, J., Akbar, N. S., and Tripathi, D. (2022). Analysis of electroosmotic flow of silver-water nanofluid regulated by peristalsis using two different approaches for nanofluid. *J. Comput. Sci.* 62, 101696. doi:10.1016/j.jocs.2022.101696
- Akram, J., Akbar, N. S., and Tripathi, D. (2022). Electroosmosis augmented MHD peristaltic transport of SWCNTs suspension in aqueous media. *J. Therm. Anal. Calorim.* 147 (3), 2509–2526. doi:10.1007/s10973-021-10562-3
- Alhussain, Z. A., and Tassaddiq, A. (2022). Thin film blood based Casson hybrid nanofluid flow with variable viscosity. *Arab. J. Sci. Eng.* 47 (1), 1087–1094. doi:10.1007/s13369-021-06067-8
- Carreau, P. J. (1972). Rheological equations from molecular network theories. *Trans. Soc. Rheology* 16 (1), 99–127. doi:10.1122/1.549276
- Chaurasiya, V., Chaudhary, R. K., Awad, M. M., and Singh, J. (2022). A numerical study of a moving boundary problem with variable thermal conductivity and temperature-dependent moving PCM under periodic boundary condition. *Eur. Phys. J. Plus* 137 (6), 714. doi:10.1140/epjp/s13360-022-02927-w
- Dawar, A., Shah, Z., Tassaddiq, A., Kumam, P., Islam, S., and Khan, W. (2021). A convective flow of Williamson nanofluid through cone and wedge with non-isothermal and non-isosolutal conditions: A revised buongiorno model. *Case Stud. Therm. Eng.* 24, 100869. doi:10.1016/j.csite.2021.100869
- Farooq, U., Waqas, H., Khan, M. I., Khan, S. U., Chu, Y. M., and Kadry, S. (2021). Thermally radioactive bioconvection flow of Carreau nanofluid with modified Cattaneo-Christov expressions and exponential space-based heat source. *Alexandria Eng. J.* 60 (3), 3073–3086. doi:10.1016/j.aej.2021.01.050
- Habib, M. B., and Akbar, N. S. (2021). New trends of nanofluids to combat *Staphylococcus aureus* in clinical isolates. *J. Therm. Anal. Calorim.* 143 (3), 1893–1899. doi:10.1007/s10973-020-09502-4
- Imran, M., Farooq, U., Muhammad, T., Khan, S. U., and Waqas, H. (2021). Bioconvection transport of Carreau nanofluid with magnetic dipole and nonlinear thermal radiation. *Case Stud. Therm. Eng.* 26, 101129. doi:10.1016/j.csite.2021.101129
- Imran, M., Yasmin, S., Waqas, H., Khan, S. A., Muhammad, T., Alshammari, N., et al. (2022). Computational analysis of nanoparticle shapes on hybrid nanofluid flow due to flat horizontal plate via solar collector. *Nanomaterials* 12 (4), 663. doi:10.3390/nano12040663
- Khan, N. A., Aziz, S., and Khan, N. A. (2014). Numerical simulation for the unsteady MHD flow and heat transfer of couple stress fluid over a rotating disk. *PLoS One* 9 (5), e95423. doi:10.1371/journal.pone.0095423
- Khan, N. A., and Sultan, F. (2015). On the double diffusive convection flow of Eyring-Powell fluid due to cone through a porous medium with Soret and Dufour effects. *AIP Adv.* 5 (5), 057140. doi:10.1063/1.4921488
- Kumawat, C., Sharma, B. K., Al-Mdallal, Q. M., and Rahimi-Gorji, M. (2022). Entropy generation for MHD two phase blood flow through a curved permeable artery having variable viscosity with heat and mass transfer. *Int. Commun. Heat Mass Transf.* 133, 105954. doi:10.1016/j.icheatmasstransfer.2022.105954
- Luan, X. D., Xu, Y. P., Ayed, H., and Selim, M. M. (2022). Heat transfer treatment of nanomaterial with considering turbulator effects. *Int. Commun. Heat Mass Transf.* 131, 105787. doi:10.1016/j.icheatmasstransfer.2021.105787
- Malik, M. Y., Jamil, H., Salahuddin, T., Bilal, S., Rehman, K. U., and Mustafa, Z. (2016). Mixed convection dissipative viscous fluid flow over a rotating cone by way of variable viscosity and thermal conductivity. *Results Phys.* 6, 1126–1135. doi:10.1016/j.rinp.2016.11.027
- Maraj, E. N., Zehra, I., and SherAkbar, N. (2022). Rotatory flow of MHD (MoS₂-SiO₂)/H₂O hybrid nanofluid in a vertical channel owing to velocity slip and thermal periodic conditions. *Colloids Surfaces A Physicochem. Eng. Aspects* 639, 128383. doi:10.1016/j.colsurfa.2022.128383
- Nabwey, H. A., Alshber, S. I., Rashad, A. M., and Mahdy, A. E. N. (2022). Influence of bioconvection and chemical reaction on magneto-Carreau nanofluid flow through an inclined cylinder. *Mathematics* 10 (3), 504. doi:10.3390/math10030504
- Naseem, T., Nazir, U., El-Zahar, E. R., Algelany, A. M., and Sohail, M. (2021). Numerical computation of Dufour and Soret effects on radiated material on a porous stretching surface with temperature-dependent thermal conductivity. *Fluids* 6 (6), 196. doi:10.3390/fluids6060196
- Nazeer, M., Saleem, S., Hussain, F., Zia, Z., Khalid, K., and Feroz, N. (2022). Heat transmission in a magnetohydrodynamic multiphase flow induced by metachronal propulsion through porous media with thermal radiation. *Proc. Institution Mech. Eng. Part E J. Process Mech. Eng.*, 095440892210752. doi:10.1177/09544089221075299
- Nazir, U., Saleem, S., Nawaz, M., Sadiq, M. A., and Alderremy, A. A. (2020). Study of transport phenomenon in Carreau fluid using Cattaneo-Christov heat flux model with temperature dependent diffusion coefficients. *Phys. A Stat. Mech. its Appl.* 554, 123921. doi:10.1016/j.physa.2019.123921
- Nazir, U., Sohail, M., Selim, M. M., Alrabaiah, H., and Kumam, P. (2021). Finite element simulations of hybrid nano-Carreau Yasuda fluid with hall and ion slip forces over rotating heated porous cone. *Sci. Rep.* 11 (1), 19604–19615. doi:10.1038/s41598-021-09116-z
- Raju, C. S. K., Hoque, M. M., Khan, N. A., Islam, M., and Kumar, S. (2019). Multiple slip effects on magnetic-Carreau fluid in a suspension of gyrotactic microorganisms over a slendering sheet. *Proc. Institution Mech. Eng. Part E J. Process Mech. Eng.* 233 (2), 254–266. doi:10.1177/0954408918776723
- Reedy, S., Srihari, P., Ali, F., and Naikoti, K. (2022). Numerical analysis of Carreau fluid flow over a vertical porous microchannel with entropy generation. *Partial Differ. Equations Appl. Math.* 5, 100304. doi:10.1016/j.padiff.2022.100304
- Sohail, M., Chu, Y. M., El-Zahar, E. R., Nazir, U., and Naseem, T. (2021). Contribution of joule heating and viscous dissipation on three dimensional flow of Casson model comprising temperature dependent conductance utilizing shooting method. *Phys. Scr.* 96 (8), 085208. doi:10.1088/1402-4896/ac00e5
- Sohail, M., Nazir, U., El-Zahar, E. R., Alrabaiah, H., Kumam, P., Mousa, A. A. A., et al. (2022). A study of triple-mass diffusion species and energy transfer in Carreau-Yasuda material influenced by activation energy and heat source. *Sci. Rep.* 12 (1), 10219–10317. doi:10.1038/s41598-022-13890-y
- Song, Y. Q., Waqas, H., Al-Khaled, K., Farooq, U., Gouadria, S., Imran, M., et al. (2022). Aspects of thermal diffusivity and melting phenomenon in Carreau nanofluid flow confined by nonlinear stretching cylinder with convective Marangoni boundary constraints. *Math. Comput. Simul.* 195, 138–150. doi:10.1016/j.matcom.2022.01.001
- Wang, F., Nazir, U., Sohail, M., El-Zahar, E. R., Park, C., and Thounthong, P. (2022). A Galerkin strategy for tri-hybridized mixture in ethylene glycol comprising variable diffusion and thermal conductivity using non-Fourier's theory. *Nanotechnol. Rev.* 11 (1), 834–845. doi:10.1515/ntrev-2022-0050

Nomenclature

Z, Y, X space coordinates

B_0 magnitude of magnetic field

B_e Hall parameter

G gravitational acceleration

T_∞ ambient temperature

n power law index number

λ mixed convection number

C_p specific heat capacitance

Ω angular velocity

μ fluidic viscosity

$\gamma F, \Theta$ dimensionless velocity and temperature

W Weissenberg number

Pr Prandtl number

H_t heat source parameter

Sc_∞ Schmidt number at infinity

Re Reynolds number

Nu Nusselt number

PDEs partial differential equations

w_2, w_1, w_3 weight functions

ψ_j shape function

\tilde{V} fluid velocity vector

∇ gradient operator

τ Cauchy stress tensor

B magnetic induction

V, W, U velocity components

σ electrical conductivity

B_i ion slip number

T fluid temperature

β coefficient of thermal expansion

Γ time relaxation number

ρ fluid density

K thermal conductivity

T_w wall temperature

μ_∞ ambient viscosity

ϵ very small number

Θ_γ fluidic viscosity

M magnetic parameter

Pr_∞ Prandtl number at infinity

Sc Schmidt number

γ_1 thermal relaxation number

C_f skin friction coefficient

ODEs ordinary differential equations

FEM finite element method

η independent variable

η_e, η_{e+1} stiffness elements

E electrical field vector

d/dt material derivative

J vector current density

Q heat flux vector



OPEN ACCESS

EDITED BY

Taseer Muhammad,
King Khalid University, Saudi Arabia

REVIEWED BY

Liaquat Ali Lund,
Sindh Agriculture University, Pakistan
Aurang Zaib,
Federal Urdu University of Arts, Sciences
and Technology Islamabad, Pakistan

*CORRESPONDENCE

Noreen Sher Akbar,
✉ noreensher1@gmail.com

SPECIALTY SECTION

This article was submitted to Colloidal
Materials and Interfaces,
a section of the journal
Frontiers in Materials

RECEIVED 24 October 2022

ACCEPTED 06 December 2022

PUBLISHED 04 January 2023

CITATION

Sher Akbar N and Mallawi FO (2023),
Numerical analysis of non-Newtonian
nanofluids under double-
diffusive regimes.
Front. Mater. 9:1078467.
doi: 10.3389/fmats.2022.1078467

COPYRIGHT

© 2023 Sher Akbar and Mallawi. This is
an open-access article distributed
under the terms of the [Creative
Commons Attribution License \(CC BY\)](#).
The use, distribution or reproduction in
other forums is permitted, provided the
original author(s) and the copyright
owner(s) are credited and that the
original publication in this journal is
cited, in accordance with accepted
academic practice. No use, distribution
or reproduction is permitted which does
not comply with these terms.

Numerical analysis of non-Newtonian nanofluids under double-diffusive regimes

Noreen Sher Akbar^{1*} and Fouad Othman Mallawi²

¹DBS&H, College of Electrical and Mechanical Engineering (CEME), National University of Sciences and Technology, Islamabad, Pakistan, ²Mathematical Modeling and Applied Computation (MMAC) Research Group, Department of Mathematics, King Abdulaziz University, Jeddah, Saudi Arabia

In the present study, the slip velocity of a non-Newtonian fluid flowing above a continuously stretching surface with double-diffusive nanofluid is examined at prespecified values of surface temperature, while also accounting for salt concentration. An initial set of partial differential equations, along with the boundary conditions, are first cast into a dimensionless form; subsequently, the comparison variables are invoked to reduce the partial differential equations to ordinary differential equations; and finally, the reduced ordinary differential equations are solved numerically via the shooting method. Values for dimensionless velocity, temperature, salt concentration distribution, local Nusselt number, and Sherwood number are calculated numerically and presented visually in a set of graphs. A extensive parametric study is conducted to probe the effects of adjusting various parameters in the cases of both assisting and opposing flow.

KEYWORDS

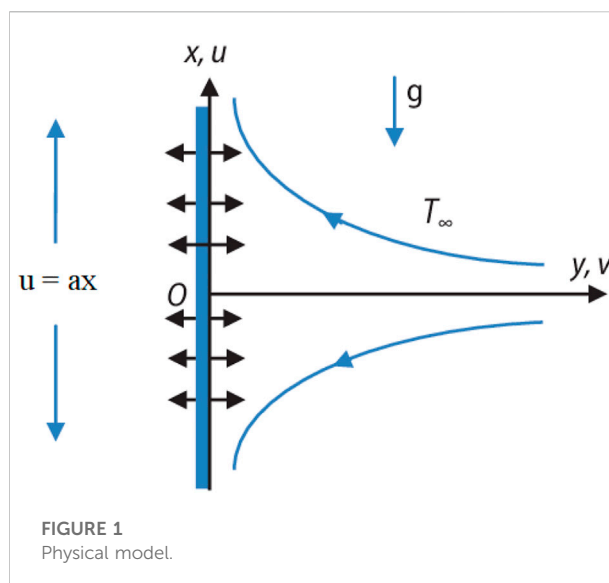
oldroyd-B fluid, double-diffusive nanofluid, stretching sheet, numerical solution, slip effects

Introduction

Non-Newtonian fluids moving over a porous, continuously stretching sheet, especially in the presence of slip, have generally garnered extensive attention owing to their numerous applications in engineering processes for both micro- and macro-scale apparatuses (Kim et al., 2002; Johnson et al., 2008). In manufacturing, it has been generally recognized that non-Newtonian fluids are more suitable than Newtonian fluids, perhaps due to their wide range of applications in fluid mechanics. Examples of such fluids include shampoo, paints, clay coatings and suspensions, grease, cosmetic products, blood, and body fluids, among many others (Jang and Lee, 2000; Iverson and Garimella, 2008). As we know, biological fluids are characteristically non-Newtonian. A detailed non-Newtonian fluid analysis with different (Ellahi, 2009; Ellahi and Afzal, 2009; Ellahi and Riaz, 2010; Nadeem et al., 2013a; Sher Akbar et al., 2013a).

A nanofluid is a fluid containing nanometer-sized particles, called nanoparticles. For more than half a century, nanofluids have been developed and used in anticancer drug targeting; see (Folkman and Long, 1964) and (Xiao et al., 2018). Beyond the pharmaceutical industry, nanofluids have a major set of applications in the study of

processes involving heat generation, including space heating, power generation, transportation, and manufacturing. The presence of nanoparticles may lead to significant modification of the thermodynamic properties of the base fluid. Thus, nanoparticles enable tailoring of important properties of their base fluids. Accounts of the development of various nanofluids and investigations of their thermal conductivity can be found in (Choi et al., 1995; Xuan and Li, 2000; Choi et al., 2001). Choi (Choi et al., 1995), in this context, discusses the role of low thermal conductivity and is of the opinion that this limits the development of energy-efficient heat transfer fluids, which have become a key requirement in many industrial applications. Choi (Choi et al., 1995) proposes that it may be possible to design a new class of heat transfer fluids by omitting the metallic nanoparticles contained in conventional heat transfer fluids. In (Xuan and Li, 2000), a theoretical model is proposed to promote the transmission of heat laterally with dispersion of solid particles. Discussion of the shapes, sizes, and volume fraction of nanoparticles can also be found in (Xuan and Li, 2000). Masuda et al. (Masuda et al., 1993) propose the modification of the thermal conductivity and viscidness of liquids by means of scattering of ultra-fine particles. Furthermore, deliberations on nanofluid coolants for progressive nuclear power plants are presented by Buongiorno and Hu (Buongiorno and Hu, 1920). Analyses of heat transfer in relation to nanofluids are provided by Xuan and Roetzel (Xuan and Roetzel, 2000). Recently, boundary-layer flow and heat transfer in a viscous fluid comprising metallic nanoparticles over a non-linearly stretching sheet have been examined by Hamad and Ferdows (Hamad and Ferdows, 2012). They discuss multiple dissimilar types of nanoparticles and propose that the behavior of the fluid flow varies with the type of nanoparticles. The Oldroyd-B model is well known for elucidating the behavior of polymeric fluids in terms of retardation time, relaxation time, and viscosity. A significant study on Oldroyd-B fluids can be found in (Lozinski and Owens, 2003), wherein Lozinski and Owens offer a numerical scheme for energy estimates for the stresses of an Oldroyd-B fluid and suggest that conventional schemes may lead to a violation of energy evaluation. It is clear from this overview that work on Oldroyd-B fluids and nanofluids is very limited. Nadeem et al. (Nadeem et al., 2013b) measure two-dimensional steady incompressible Oldroyd-B nanofluid flow past a stretching sheet. According to these authors, the various Oldroyd-B parameters exert conflicting effects on behavior in terms of velocity, temperature, and mass fraction function. Recently, the effects of heat on an Oldroyd-B nanofluid flowing over a bidirectional stretching sheet have been examined in (Azeem Khan et al., 2014). More recently still, Sandeep et al. (Sandeep et al., 2015) have conducted a comparative study examining heat and mass transfer in non-Newtonian nanofluids flowing over a stretching sheet. According to (Sandeep et al., 2015), the heat and mass transfer rate is higher in Oldroyd-B nanofluids than in



Jeffery and Maxwell nanofluids. New publications in the literature on nanofluids include (Noreen et al., 2013; Sher Akbar et al., 2013b; Zaib et al., 2019; Khan et al., 2021a; Khan et al., 2021b).

In the current study, we consider Oldroyd-B double-diffusive nanofluid flow over a stretching sheet at prespecified values for surface temperature and salt concentration. The partial differential equations governing this system, along with the boundary conditions, are reduced to ordinary differential equations using similarity transformation; subsequently, these reduced ordinary differential equations are solved numerically using the shooting method. A complete parametric study is presented to explore the effects of the relevant parameters on both assisting and opposing flow both explicitly and in physical terms.

Mathematical development

We consider the two-dimensional, laminar boundary layer flow of an Oldroyd-B nanofluid over a continuously stretching surface at a prespecified surface temperature in the presence of a particular salt concentration. It is assumed in solving the problem that the Oldroyd-B non-Newtonian nanofluid is incompressible. The governing equations for velocity under slip-flow boundary conditions at the walls are considered to capture the relevant physical processes. The model used for the fluid incorporates the effects of double diffusion. The positive y -coordinate is measured normal to the sheet, while the x -coordinate is taken transverse to it. The corresponding velocity components in the x and y directions are u and v , respectively. The physical model for the flow geometry is shown in Figure 1.

We now make the standard boundary layer approximation, based on a scale analysis, and write the governing equations:

$$\frac{\partial u}{\partial x} + \frac{\partial v}{\partial y} = 0, \quad (1)$$

$$u \frac{\partial u}{\partial x} + v \frac{\partial v}{\partial y} + \Lambda_1 \left(u^2 \frac{\partial^2 u}{\partial x^2} + v^2 \frac{\partial^2 u}{\partial y^2} + 2uv \frac{\partial^2 u}{\partial x \partial y} \right) = v \frac{\partial^2 u}{\partial y^2} + \Lambda_2 \left(u \frac{\partial^3 u}{\partial x \partial y^2} + v \frac{\partial^3 u}{\partial y^3} - \frac{\partial u}{\partial x} \frac{\partial^2 u}{\partial y^2} - \frac{\partial u}{\partial y} \frac{\partial^2 u}{\partial x^2} \right) + [-g(\rho_p - \rho)(\phi - \phi_\infty) + (1 - \phi_\infty)\rho(g\beta_T(T - T_\infty) + g\beta_C(C - C_\infty))] \quad (2)$$

$$\left(u \frac{\partial T}{\partial x} + v \frac{\partial T}{\partial y} \right) = \alpha \frac{\partial^2 T}{\partial y^2} + \tau \left[D_B \frac{\partial T}{\partial y} \frac{\partial \phi}{\partial y} + \left(\frac{D_T}{T_\infty} \right) \left(\frac{\partial T}{\partial y} \right)^2 \right] + D_{TC} \frac{\partial^2 C}{\partial y^2}, \quad (3)$$

$$\left(u \frac{\partial C}{\partial x} + v \frac{\partial C}{\partial y} \right) = D_S \frac{\partial^2 C}{\partial y^2} + D_{CT} \frac{\partial^2 T}{\partial y^2}, \quad (4)$$

$$\left(u \frac{\partial \phi}{\partial x} + v \frac{\partial \phi}{\partial y} \right) = D_B \frac{\partial^2 \phi}{\partial y^2} + \left(\frac{D_T}{T_\infty} \right) \frac{\partial^2 T}{\partial y^2}. \quad (5)$$

$$u = u_w(x) = ax, v = 0, T = T_w, C = C_w, \phi = \phi_w, \text{ at } y = 0 \quad (6a)$$

$$u \rightarrow 0, v \rightarrow 0, T \rightarrow T_\infty, C \rightarrow C_\infty, \phi \rightarrow \phi_\infty, \text{ as } y \rightarrow \infty, \quad (6b)$$

where $\alpha = \frac{k}{(\rho c)_p}$, $\tau = \frac{(\rho c)_p}{(\rho c)_f}$.

The similarity transformations for this problem can be written as:

$$u = ax f'(\eta) v = -\sqrt{(av)} f(\eta), \eta = \sqrt{\left(\frac{a}{v}\right)}, \theta(\eta) = \frac{T - T_\infty}{T_w - T_\infty}, \gamma(\eta) = \frac{C - C_\infty}{C_w - C_\infty}, \xi(\eta) = \frac{\phi - \phi_\infty}{\phi_w - \phi_\infty}, \quad (7)$$

$$f''' - (f')^2 + f f'' - \beta_1 (f^2 f'' - 2 f f' f'') - \beta_2 (f f''' - (f'')^2) + G_r (\theta + N_c \gamma - N_r \xi) = 0, \quad (8)$$

$$\theta'' + \text{Pr} f \theta' + N_b \theta' \xi' + N_t \theta'^2 + N_d \xi'' = 0, \quad (9)$$

$$\gamma'' + \text{Pr} L_e f \gamma' + L_d \text{Pr} \theta'' = 0, \quad (10)$$

$$\xi'' + \text{Pr} L_n f \xi' + \frac{N_t}{N_b} \theta'' = 0, \quad (11)$$

$$f(0) = 0, f'(0) = 1 + \beta f''(0), \theta(0) = 1, \gamma(0) = 1, N_b \xi'(0) + N_t \theta'(0) = 0, f'(\infty) = 0, \theta(\infty) = 0, \gamma(\infty) = 0, \xi(\infty) = 0, \quad (12)$$

where

$$R_{ax} = \frac{u_w(x)x}{\nu}, G_T = \frac{(1 - \phi_\infty)\rho_f g \beta_T (T_w - T_\infty)}{\nu^2}, G_r = \frac{G_T}{R_{ax}^2}, \beta = \frac{N_1 \nu R_{ax}^4}{L}, N_c = \frac{B_r}{G_r} = \frac{B_C}{G_T} = \frac{\beta_C (C_w - C_\infty)}{\beta_T (T_w - T_\infty)}, \text{Pr} = \frac{\nu}{\alpha}, N_d = \frac{D_{TC} (C_w - C_\infty)}{\alpha \Delta T}, L_e = \frac{\alpha}{D_B}, N_t = \frac{\tau D_T (T_w - T_\infty)}{\nu T_\infty}, N_b = \frac{\tau D_B (\phi_w - \phi_\infty)}{\nu}, L_d = \frac{\Delta T D_{TC}}{\Delta C D_S}, L_n = \frac{\alpha}{D_B}, N_\gamma = \frac{(\rho_p - \rho_{f\infty}) \Delta \phi}{(\rho_p - \rho_{f\infty}) \beta \Delta T (1 - \phi_\infty)}. \quad (13)$$

in which R_{ax} is the local Reynolds number, $\beta = \frac{N_1 \nu R_{ax}^4}{L}$, G_T is the local thermal Grashof number, G_r is the local Grashof number, β is the slip parameter, N_c is the ratio of the buoyancy forces B_r to the local Grashof number, Pr is the effective Prandtl number, N_d is the modified Dufour parameter, L_e is the Lewis number, N_t is the thermophoresis parameter, N_b is the Brownian motion parameter, L_d is the Dufour Lewis number, L_n is the nanofluid Lewis number, and N_γ is the nanofluid buoyancy ratio.

Expressions for the local Nusselt number and the local Sherwood number are defined as:

$$Nu = \frac{x q_w}{\alpha (T_w - T_\infty)}, Sh = \frac{x q_m}{\alpha (C_w - C_\infty)}, \quad (14)$$

$$q_w = -\alpha \left(\frac{\partial T}{\partial y} \right), q_m = -\alpha \left(\frac{\partial C}{\partial y} \right). \quad (15)$$

$$\text{Re}_x^{-1/2} Nu_x = -\theta'(0), \text{Re}_x^{-1/2} Sh_x = -\gamma'(0). \quad (16)$$

Discussion

The initial differential equations, along with the appropriate boundary conditions, were solved using the shooting method. The effects of various relevant parameters on double-diffusive absorption can also be examined for the Oldroyd-B fluid. A range of graphs are presented below for comparison of the properties of assisting and opposing flow. Figures 2A–C illustrates the effects on local Grashof number of variation in Deborah number (as a relaxation parameter) and nanofluid buoyancy ratio. It is realistic that, in the case of both assisting and opposing flow, the velocity profile decreases with an increase in local Grashof number. The rise in the local Grashof number shows that the buoyancy effects supersede those of the viscous forces. Deborah number is associated with the nature of the fluid material: low Deborah number values indicate that the fluid will act like a Newtonian fluid, and higher values correspond to non-Newtonian fluid behavior. Figure 2B illustrates that the velocity profile decreases with an increase in Deborah number, while Figure 2C illustrates that the velocity profile decreases with an increase in the nanofluid buoyancy ratio. Figures 2A–C illustrate that whether an assisting or opposing flow regime is in operation does not affect the behavior of the velocity profile.

The plots in Figures 3A–C present the effects of local Grashof number, Deborah number, and nanofluid buoyancy ratio on temperature profile for assisting and opposing flow regimes. The temperature profile decreases with an increase in local Grashof number, while it increases with an increase in Deborah number and nanofluid buoyancy ratio. Once again, it can be observed that the temperature profile behaves similarly for the assisting and opposing flow regimes. The thickness of the thermal boundary layer decreases with an increase in local Grashof number, while it increases with an increase in Deborah number and nanofluid buoyancy ratio.

The plots in Figures 4A–C are presented to examine the effects of Dufour number and Lewis number on the salt concentration

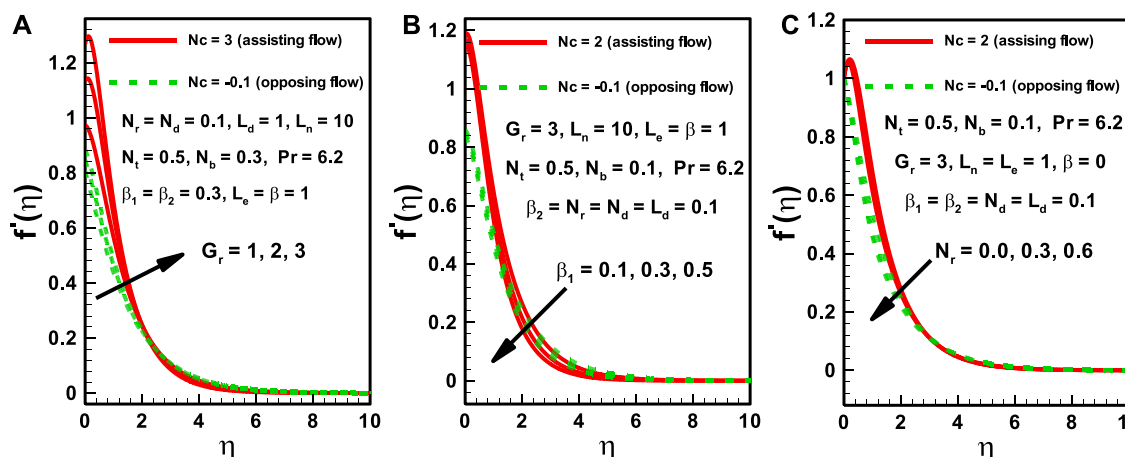


FIGURE 2
Effects of various parameters on dimensionless velocity for both assisting and opposing flows.

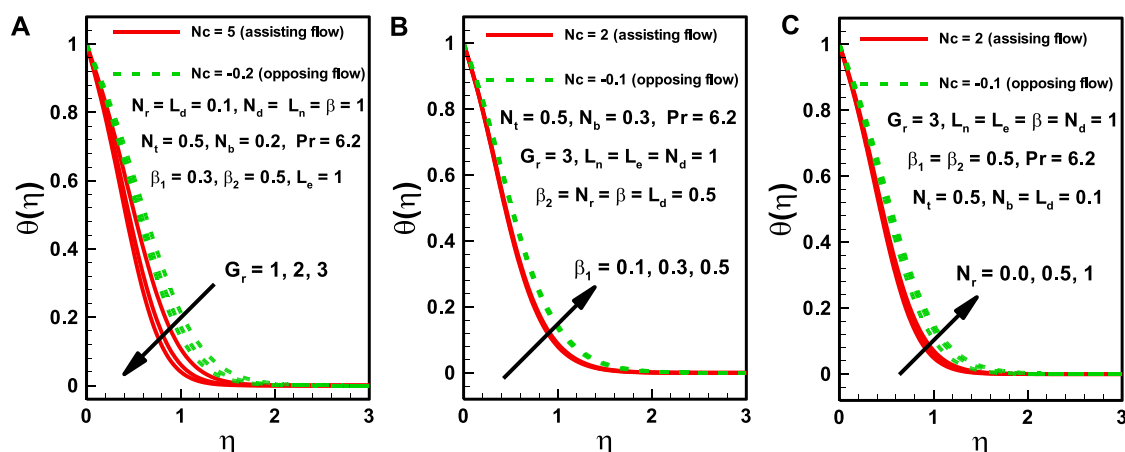


FIGURE 3
Effects of various parameters on dimensionless temperature for both assisting and opposing flows.

profile for assisting and opposing flow regimes. The salt concentration profile appears to increase with an increase in the Dufour Lewis number, while it decreases with an increase in the modified Dufour number and Lewis number. The Dufour number reflects the energy flux in a fluid flow due to the concentration gradient. The behavior of salt concentration against various parameters is not affected by whether an assisting or opposing flow regime is in operation. The Lewis number measures the ratio of thermal diffusivity to mass diffusivity. A Lewis number greater than one indicates that thermal diffusivity is higher than the mass diffusivity. The gradient of the salt concentration profile becomes less steep at a Lewis number of 5, which means that the variation in salt concentration is lower for higher Lewis numbers.

In Figures 5A–C, three important parameters (the thermophoresis parameter, Brownian motion parameter, and nanofluid Lewis number) are considered in order to determine their effects on the rescaled nanoparticle volume fraction. It can be observed that the rescaled nanoparticle volume fraction increases with an increase in thermophoresis and in the Brownian parameter, but this cannot be generalized throughout the boundary layer. The effect near the wall is in the opposite direction to the effect that is visible near the free stream region. This effect occurs due to the heated surface, which significantly affects the motion of particles near it. The increase in nanofluid Lewis number causes a decrease in nanoparticle concentration near the free stream region, while the concentration increases near the heated surface.

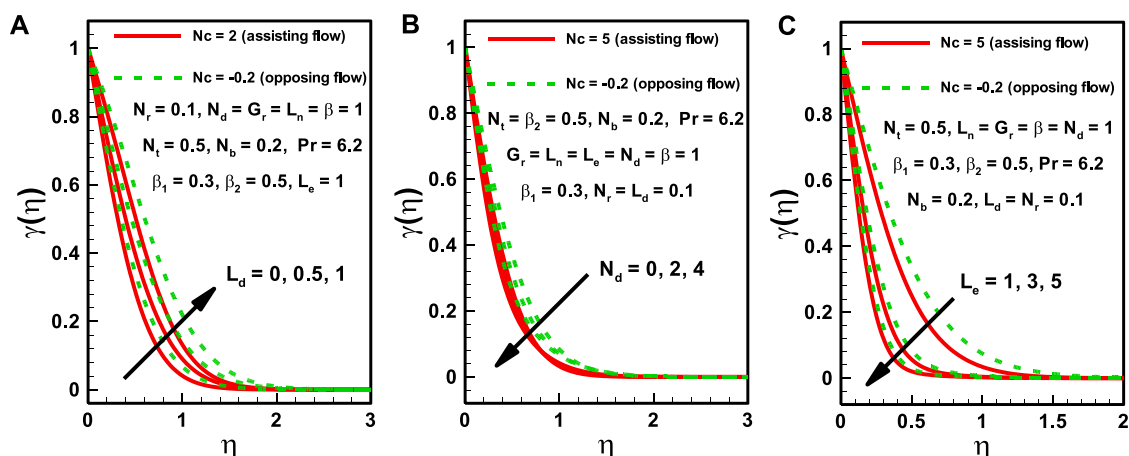


FIGURE 4
Effects of various parameters on dimensionless salt concentration distribution for both assisting and opposing flows.

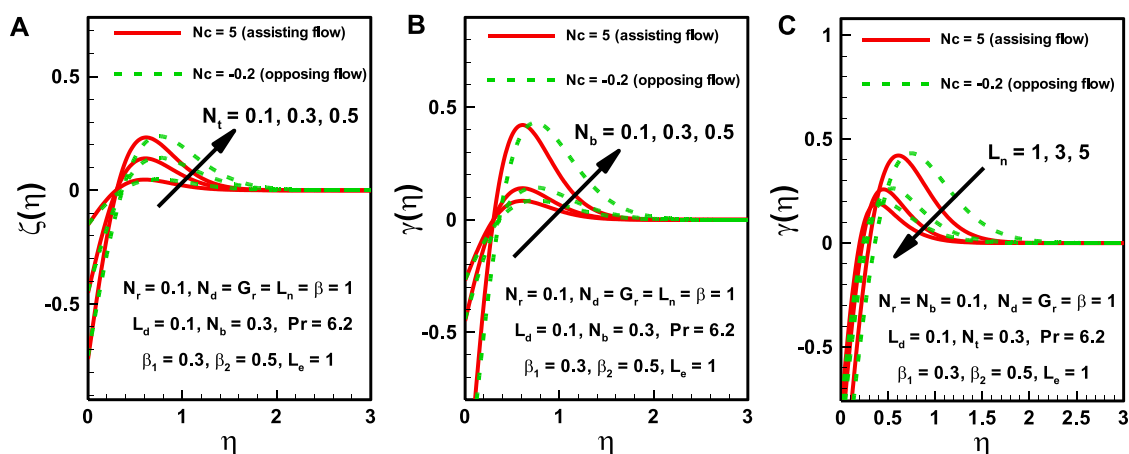


FIGURE 5
Effects of nanofluid parameters on rescaled nanoparticle volume fraction distribution for both assisting and opposing flows.

Heat transfer is an important phenomenon for nanofluid flow and is significantly affected by the heat transfer parameters involved in the equations presented above. In [Figures 6A–C](#), we plot Nusselt number against only six of the relevant parameters. Nusselt number decreases as the slip velocity parameter increases, while it increases as the local Grashof number increases, and it is also higher for the assisting flow regime in comparison to the opposing flow regime. [Figure 6B](#) illustrates the effect of Dufour number on the heat transfer profile. It can be observed that Nusselt number responds in opposing directions to a rise in the relaxation and retardation parameters. Specifically, it increases as the retardation parameter increases, while it decreases as the relaxation parameter increases. [Figure 6C](#)

illustrates the effect on Nusselt number of variation in the thermophoresis parameter and Dufour Lewis number. The heat transfer rate decreases as the thermophoresis parameter increases, and it increases as Dufour Lewis number increases. Once again, it can be observed that the assisting flow regime produces a higher Nusselt number in comparison to the opposing flow regime.

Sherwood number is plotted against various parameters in [Figures 7A–C](#). It can be observed that, generally, the Sherwood number is higher for the assisting flow regime in comparison to the opposing flow regime. [Figure 7A](#) illustrates the effects of the relaxation and slip velocity parameters on Sherwood number. It can be observed that Sherwood number decreases as the slip velocity

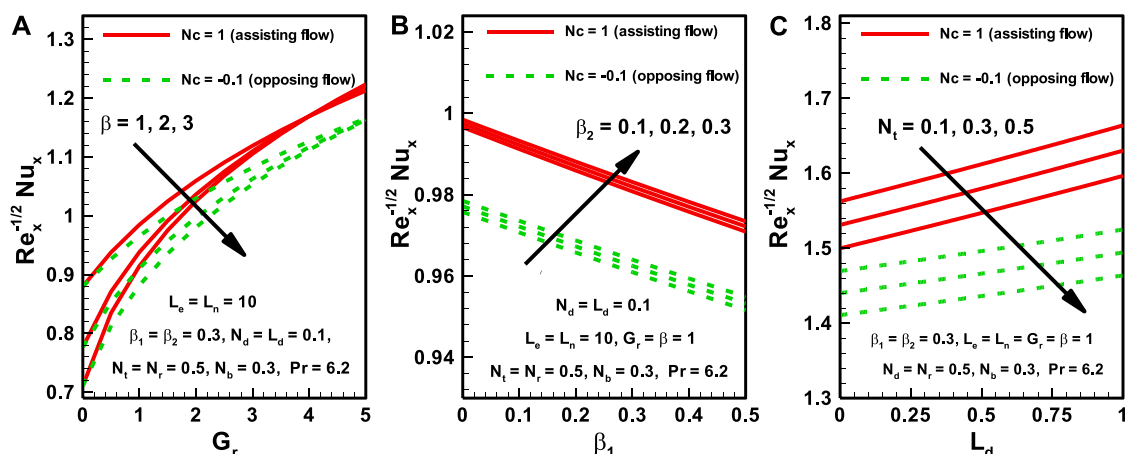


FIGURE 6
Variation in Nusselt number with variation in the values of several parameters for both assisting and opposing flows.

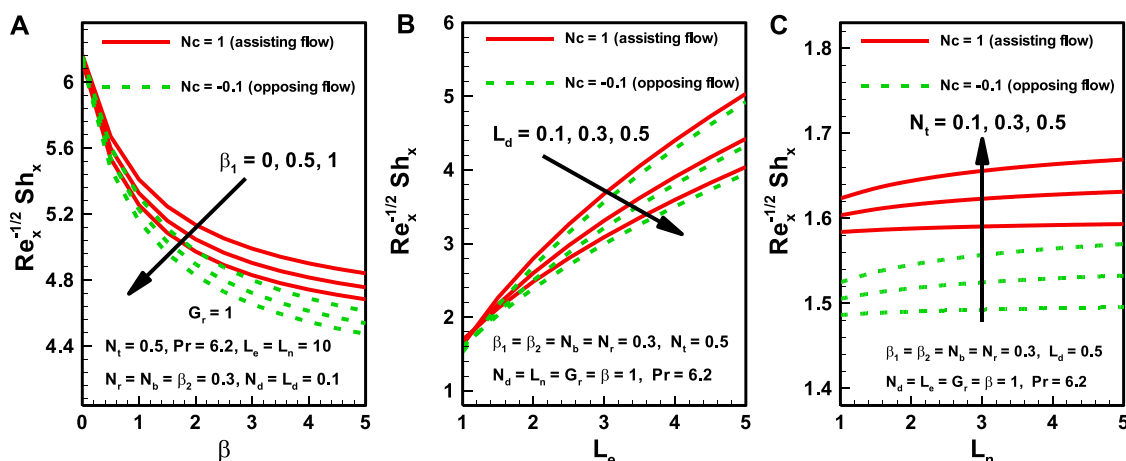


FIGURE 7
Variation in Sherwood number with variation in the values of several parameters for both assisting and opposing flows.

parameter and relaxation parameter increase. Figure 7B shows that Sherwood number decreases as the Dufour Lewis parameter increases, and increases against the Lewis number. The last figure shows that Sherwood number increases with an increase in the thermophoresis parameter and nanofluid Lewis number.

Conclusion

The present study considers the effects of slip velocity on the double-diffusive flow of an Oldroyd-B fluid in the case of assisting and opposing flow regimes. Diffusion of

nanoparticles is considered, along with salt concentration, and separate concentration equations are considered for each of these parameters. The governing partial differential equations, along with the boundary conditions, are reduced to ordinary differential equations using similarity transformation; subsequently, the reduced ordinary differential equations are solved numerically using the shooting method. The following important conclusions can be drawn from the above analysis.

1. Whether an assisting or opposing flow regime is in operation exerts a strong effect on the temperature, velocity, and concentration profiles.

2. The profiles for Nusselt number and Sherwood number cover higher values for the assisting flow regime in comparison to the opposing flow regime.
3. Nusselt number values increase against the retardation parameter and decrease with increasing values of the relaxation parameter.
4. The Nusselt and Sherwood numbers decrease with increasing values of the slip velocity parameter.
5. The presence of nanoparticles and the salt concentration significantly affect the heat transfer characteristics of an ordinary non-Newtonian Oldroyd-B fluid.

Data availability statement

The original contributions presented in the study are included in the article/supplementary material, further inquiries can be directed to the corresponding author.

Author contributions

All authors listed have made a substantial, direct, and intellectual contribution to the work and approved it for publication.

References

- Azeem Khan, W., Khan, M., and Malik, R. (2014). Three-dimensional flow of an Oldroyd-B nanofluid towards stretching surface with heat generation/absorption. *PLOS ONE* 9 (8), e105107. doi:10.1371/journal.pone.0105107
- Buongiorno, J., and Hu, W. (1920). "Nanofluid coolants for advanced nuclear power plants," in Proceedings of ICAPP '05. Seoul. Paper no. 5705.
- Choi, S. (1995). "Enhancing thermal conductivity of fluids with nanoparticle," in *Developments and applications of non-Newtonian flows*. Editors D. A. Siginer and H. P. Wang (Argonne: ASME MD), 231, 99–105. and FED vol. 66.
- Choi, S. U. S., Zhang, Z. G., Yu, W., Lockwood, F. E., and Grulke, E. A. (2001). Anomalous thermal conductivity enhancement in nanotube suspensions. *Appl. Phys. Lett.* 79 (14), 2252–2254. doi:10.1063/1.1408272
- Ellahi, R., and Afzal, S. (2009). Effects of variable viscosity in a third grade fluid with porous medium: An analytic solution. *Commun. Nonlinear Sci. Numer. Simulat.* 14, 2056–2072. doi:10.1016/j.cnsns.2008.05.006
- Ellahi, R. (2009). Effects of the slip boundary condition on non-Newtonian flows in a channel. *Commun. Nonlinear Sci. Numer. Simulat.* 14, 1377–1384. doi:10.1016/j.cnsns.2008.04.002
- Ellahi, R., and Riaz, A. (2010). Analytical solutions for MHD flow in a third-grade fluid with variable viscosity. *Math. Comput. Model.* 52, 1783–1793. doi:10.1016/j.mcm.2010.07.005
- Folkman, J., and Long, D. M. (1964). The use of silicone rubber as a carrier for prolonged drug therapy. *J. Surg. Res.* 4 (3), 139–142. doi:10.1016/s0022-4804(64)80040-8
- Hamad, M. A. A., and Ferdows, M. (2012). Similarity solutions to viscous flow and heat transfer of nanofluid over nonlinearly stretching sheet. *Appl. Math. Mech. Engl. Ed.* 33 (33), 923–930. doi:10.1007/s10483-012-1595-7
- Iverson, B. D., and Garimella, S. V. (2008). Recent advances in microscale pumping technologies: A review and evaluation. *Microfluid. Nanofluidics* 5 (2), 145–174. doi:10.1007/s10404-008-0266-8
- Jang, J., and Lee, S. S. (2000). Theoretical and experimental study of MHD (magnetohydrodynamic) micropump. *Sensors Actuators A Phys.* 80 (1), 84–89. doi:10.1016/s0924-4247(99)00302-7

Acknowledgments

The Deanship of Scientific Research (DSR) at King Abdulaziz University (KAU), Jeddah, Saudi Arabia has funded this project under Grant No. RG-11-130-43.

Conflict of interest

The authors declare that the research was conducted in the absence of any commercial or financial relationships that could be construed as a potential conflict of interest.

Publisher's note

All claims expressed in this article are solely those of the authors and do not necessarily represent those of their affiliated organizations, or those of the publisher, the editors and the reviewers. Any product that may be evaluated in this article, or claim that may be made by its manufacturer, is not guaranteed or endorsed by the publisher.

- Johnson, R. D., Gavalas, V. G., Daunert, S., and Bachas, L. G. (2008). Microfluidic ion-sensing devices. *Anal. Chim. Acta* 613 (1), 20–30. doi:10.1016/j.aca.2008.02.041
- Khan, U., Zaib, A., Abu Bakar, S., and Ishak, A. (2021). Stagnation-point flow of a hybrid nanofluid over a non-isothermal stretching/shrinking sheet with characteristics of inertial and microstructure. *Case Stud. Therm. Eng.* 26, 101150. doi:10.1016/j.csite.2021.101150
- Khan, U., Zaib, A., and Ishak, A. (2021). Magnetic field effect on sisko fluid flow containing gold nanoparticles through a porous curved surface in the presence of radiation and partial slip. *Mathematics* 9 (9), 921. doi:10.3390/math9090921
- Kim, J. H., and Yoon, J. Y. (2002). "Protein adsorption on polymer particles," in *Encyclopedia of surface and colloidal science*. Editor T. A. Hubbard (New York: Marcel Dekker), 4373–4381.
- Lozinski, A., and Owens, R. G. (2003). An energy estimate for the Oldroyd B model: Theory and applications. *J. Newt. Fluid Mech.* 112 (2–3), 161–176. doi:10.1016/s0377-0257(03)00096-x
- Masuda, H., Ebata, A., Teramae, K., and Hishinuma, N. (1993). Alteration of thermal conductivity and viscosity of liquid by dispersing ultra-fine particles. *Netsu Bussei* 7, 227–233. doi:10.2963/jjtp.7.227
- Sher Akbar, N., Nadeem, S., Haq, R. U., and Khan, Z. H. (2013a). Numerical solutions of Magnetohydrodynamic boundary layer flow of tangent hyperbolic fluid towards a stretching sheet. *Indian J. Phys.* 87 (11), 1121–1124. doi:10.1007/s12648-013-0339-8
- Nadeem, S., Ul Haq, R., and Khan, Z. H. (2013). MHD three-dimensional Casson fluid flow past a porous linearly stretching sheet. *Alexandria Eng. J.* 52, 577–582. doi:10.1016/j.aej.2013.08.005
- Nadeem, S., Ul Haq, R., Sher Akbar, N., Lee, C., and Khan, Z. H. (2013). Numerical study of boundary layer flow and heat transfer of Oldroyd-B nanofluid towards a stretching sheet. *PLoS ONE* 8 (8), e69811. doi:10.1371/journal.pone.0069811
- Noreen, S. A., Nadeem, S., Haq, R. U., and Khan, Z. H. (2013). Radiation effects on MHD stagnation point flow of nano fluid towards a stretching surface with convective boundary condition. *Chin. J. Aeronautics* 26 (6), 1389–1397. doi:10.1016/j.cja.2013.10.008

Sandeep, N., Rushi Kumar, B., and Jagadeesh Kumar, M. S. (2015). A comparative study of convective heat and mass transfer in non-Newtonian nanofluid flow past a permeable stretching sheet. *J. Mol. Liq.* 212, 585–591. 585-591ISSN 0167-7322. doi:10.1016/j.molliq.2015.10.010

Sher Akbar, N., Nadeem, S., Lee, C., Khan, Z. H., and Ul Haq, R. (2013b). Numerical study of Williamson nano fluid flow in an asymmetric channel. *Results Phys.* 3, 161–166. doi:10.1016/j.rinp.2013.08.005

Xiao, H., Yan, L., Dempsey, E. M., Song, W., Qi, R., Li, W., et al. (2018). Recent progress in polymer-based platinum drug delivery systems. *Prog. Polym. Sci.* 87, 70–106. doi:10.1016/j.progpolymsci.2018.07.004

Xuan, Y., and Li, Q. (2000). Heat transfer enhancement of nanofluids. *Int. J. Heat Fluid Flow* 21 (1), 58–64. doi:10.1016/s0142-727x(99)00067-3

Xuan, Y., and Roetzel, W. (2000). Conceptions for heat transfer correlation of nanofluids. *Int. J. Heat. Mass Transf.* 43, 3701–3707. doi:10.1016/s0017-9310(99)00369-5

Zaib, A., Khan, U., Khan, I., and Asiful, H. (2019). Numerical investigation of aligned magnetic flow comprising nanoliquid over a radial stretchable surface with cattaneo–christov heat flux with entropy generation. *Symmetry* 11 (12), 1520. doi:10.3390/sym11121520



OPEN ACCESS

EDITED BY
Safia Akram,
National University of Sciences and
Technology, Pakistan

REVIEWED BY
A. M. Rashad,
Aswan University, Egypt
Ndolane Sene,
Cheikh Anta Diop University, Senegal

*CORRESPONDENCE
Muhammad Imran Asjad,
✉ Imran.asjad@umt.edu.pk

[†]These authors have contributed equally to
this work

SPECIALTY SECTION
This article was submitted to Colloidal
Materials and Interfaces,
a section of the journal
Frontiers in Materials

RECEIVED 22 September 2022
ACCEPTED 21 December 2022
PUBLISHED 10 January 2023

CITATION
Asjad MI, Usman M, Assiri TA, Ali A and
Tag-ELDin EM (2023), Numerical
investigation of fractional Maxwell nano-
fluids between two coaxial cylinders via
the finite difference approach.
Front. Mater. 9:1050767.
doi: 10.3389/fmats.2022.1050767

COPYRIGHT
© 2023 Asjad, Usman, Assiri, Ali and Tag-
ELDin. This is an open-access article
distributed under the terms of the [Creative
Commons Attribution License \(CC BY\)](#).
The use, distribution or reproduction in
other forums is permitted, provided the
original author(s) and the copyright
owner(s) are credited and that the original
publication in this journal is cited, in
accordance with accepted academic
practice. No use, distribution or
reproduction is permitted which does not
comply with these terms.

Numerical investigation of fractional Maxwell nano-fluids between two coaxial cylinders via the finite difference approach

Muhammad Imran Asjad^{1*†}, Muhammad Usman^{2,3†},
Taghreed A. Assiri^{4†}, Arfan Ali^{1†} and ElSayed M. Tag-ELDin^{5†}

¹Department of Mathematics, School of Sciences, University of Management and Technology, Lahore, Pakistan, ²School of Mathematical Science, Jiangsu University, Zhenjiang, China, ³Department of Mathematics, National University of Modern Languages (NUML), Islamabad, Pakistan, ⁴Department of Mathematics, Faculty of Science, Umm Al-Qura University, Makkah, Saudi Arabia, ⁵Faculty of Engineering and Technology, Future University in Egypt, New Cairo, Egypt

This study deals with numerical solution of momentum and heat transfer of fractional ordered Maxwell fluids within a coaxial cylinder. It is well known that the complex dynamics of flow regime can be well-described by the fractional approach. In this paper, a fractional differentiation operator D_t^α of Caputo was applied for fractional modeling of magneto-hydro-dynamic (MHD) fluid. A set of appropriate transformations was applied to make the governing equations dimensionless. The finite differences were calculated by the discretization of momentum profile $u(r, t)$ and heat profile $T(r, t)$. The results obtained for $u(r, t)$ and $T(r, t)$ were plotted against different physical parameters, such as Prandtl number Pr , the square of Hartmann number H_a , thermal Grashof number Gr , thermal radiation parameter Nr , and heat source/sink parameter Q_0 . The results were verified by comparing data from the proposed method with MAPLE built-in command results. Subjecting the system to a strong magnetic field led to increasing $T(r, t)$ and decreasing $u(r, t)$. It was found that increasing Gr and Pr increased the velocity and temperature profiles. Addition of Cu nanoparticles to a base fluid of H_2O enhanced its heat transfer capability. Also, increasing the angular frequency of inner cylinder velocity resulted in a high velocity profile of fractional Maxwell nano-fluids within a coaxial region (cylinder).

KEYWORDS

fractional calculus, Maxwell fluids, cylindrical coordinate, nano-fluids, thermal radiations

Introduction

The viscoelastic flow of Maxwell fluids within a circular cylinder requires more attention in many areas, such as the chemical, food, and petroleum industries. Nguyen et al. (1983), Nieckele and Patankar (1985), Hayase et al. (1992), Haldar (1998), and Chung (1999) have studied viscoelastic flow between two concentric cylinders. Dependent flow of second-grade fluid in cylindrical geometry has been investigated by Ting (1963). In a similar trend, Maxwell fluids have been examined in a cylindrical coordinate system (Srivastava, 1966). Also, Waters and King (1971) studied Oldroyd-B fluid focused in a cylindrical domain. All results were analytically driven. Considerable work has been carried out by Fetecau et al. in investigating one-dimensional viscoelastic flow between circular regions under different conditions, such as a rotating axis. In Fetecau et al. (2008), an exact solution of Oldroyd-B fluid was examined. A solution was offered as the sum of steady-state and transient-state solution. M Jamil et al., studied helical flow Maxwell fluids by using the analytical approach of

Hankel transformation (Jamil and Fetecau, 2010). Wood investigated an exact solution of Oldroyd-B fluids in a straight pipe of circular cross sections (Wood, 2001). However, the study of coaxial cylindrical geometry of an oscillating inner cylinder has been infrequent. An important geometry and motion problem is that of cylindrical geometry. Finite or infinite lengths of annular geometry play vital roles in fluid dynamics. Cylindrical flow has various applications in different fields of the food industry, medicine, chemistry, bio-engineering, and oil exploitation (Hartnett and Kostic, 1989).

In research already discussed, a classical approach of constitutive relations for Maxwell fluids had been applied for mathematical modeling. Recently, the fractional approach of constitutive equations of viscoelastic fluid has been the focus of researchers as the fractional approach can provide a better interpretation of viscoelastic fluids than the classical integer-order derivative approach (Bagley and Torvik, 1983; Friedrich, 1991; Haitao and Mingyu, 2009; Magin, 2010; Ming et al., 2016; Sun et al., 2018).

Fractional calculus has been a hot topic among researchers in the recent era of basic science as it provides a new direction in describing dynamics such as time relaxation, time retardation, viscoelastic behavior, and flow regime. Fractional-order (non-integer) partial differential equations (PDEs) are well-suited to address the physical phenomena related to transportation of heat and mass as well. The fractional mathematical model was initially one of classical integer order, which has been modified by replacing integer-order with non-integer order (Sheikh et al., 2017; Saqib et al., 2018; Saqib et al., 2020). For the purpose fractional differentiation, some operators that have been used include Riemann, Riemann–Liouville, Caputo, Caputo–Fabrizio, and Anatangna Beleanu fractional operators (Shah et al., 2018a; Shah et al., 2018b). Using Laplace and Hankel transformation, the analytical solution of a generalized Maxwell model was solved by Mahmood et al. (2009). Subsequently, exact solutions of fractional Maxwell fluids were investigated using Laplace and Hankel transformation (Fetecau et al., 2010; Fetecau et al., 2011).

For the last few decades, nanotechnology has been a research focus due to its broad range of applications, including those in solar energy, weapons, vehicles, and electronics, stemming from strong thermal properties. Nano-fluids are prepared by mixing up nano-sized (1 nm–100 nm) particles in base fluids (water, blood, engine oil, kerosene oil, etc.). The idea of nano-fluids was first developed by Choi and Eastman (1995), and considerable work has since been by carried out by Tiwari and Das on the effectiveness of different shapes and sizes of nanoparticles in a flow regime (Tiwari and Das, 2007). Using Laplace Transform, a study of a nano-fluid model has been done, while considering the flow passing through an accelerating infinite vertical plate situated in porous medium. Activation energy of Maxwell nano-fluids and binary chemical reaction of carbon nanotubes (CNTs) have been investigated using Runge–Kutta on MAPLE (Subbarayudu et al., 2019). Non-Newtonian nano-fluids have been examined numerically by Rashad et al. (2013) using finite difference methods (FDMs). In Rashad and Nabwey (2019), FDM was applied to investigate the gyrotactic mixed bioconvection flow of a nano-fluid passing through a circular region.

Considering the literature discussed previously, research gaps exist. These include the following:

- Lack of study of the problems involving non-linearity and cylindrical geometry.

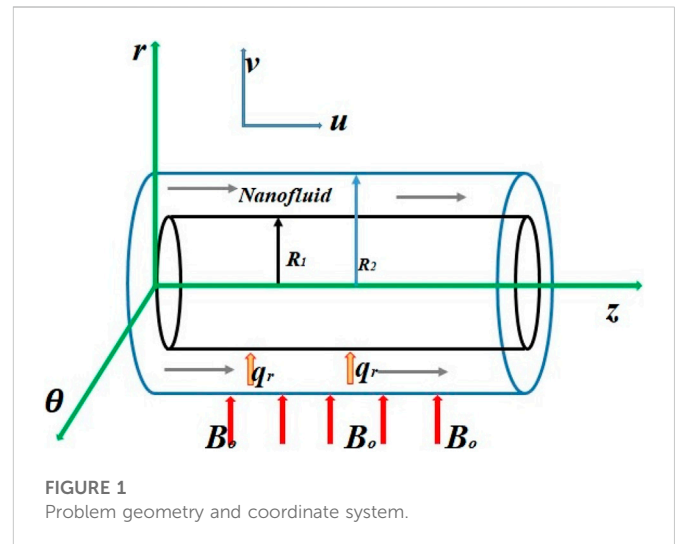


FIGURE 1
Problem geometry and coordinate system.

- Assumptions made to simplify systems governing equations to obtain analytical solutions.
- Application of analytical techniques to calculate results.

In order to address these gaps, we focused on unsteady flow fractional Maxwell nano-fluids between coaxial cylinders. Flow through an annular region was assumed due to oscillation of the inner cylinder under the effects of thermal radiation and strong magnetic field. Due to its flexibility and efficiency in addressing problems with initial and boundary conditions, the Caputo time fractional operator was used as the mathematical model. Cylindrical geometry is complex to solve numerically, therefore, the numerical approach of the finite difference method was applied to obtain the results. We compared the results obtained using the built-in command in MAPLE with those obtained using our model.

Mathematical formulation

Suppose that an incompressible, unsteady, and one-dimensional flow of viscoelastic nano-fluid is at rest at time $t = 0$ within the annular region of two infinite coaxial cylinders having radii R_1 and R_2 such that $R_1 < R_2$. The inner cylinder oscillates with angular velocity ω along z -direction, whereas the outer cylinder remains stationary. These cylinders are subjected to the strong magnetic field B_0 and thermal radiation. With the passage of time, the fractional Maxwell nano-fluid moves with velocity $V(r, \theta, z, t) = u(r, t)$. The flow diagram of the physical problem is given in Figure 1, as referenced in Fetecau et al. (2011).

The following assumptions were made for the aforementioned problem.

- The flow is one-dimensional, unsteady, and incompressible.
- Body forces are considered.
- Viscous dissipation and pressure gradients are neglected.
- Fluid is magnetic-hydro-dynamic (MHD), but induced magnetic field is ignored.
- Thermal radiation is applied.

Then, the equation of continuity in cylindrical form (Zhang et al., 2019) is as follows:

$$\frac{1}{r} \frac{\partial [ru(r, t)]}{\partial r} = 0. \quad (1)$$

The stress tensor for fractional Maxwell nano-fluid (Anwar et al., 2020) is as follows:

$$\mathbf{T} = -p\mathbf{I} + \mathbf{S} \quad (2)$$

and

$$\mathbf{S} + \lambda \frac{\delta \mathbf{S}}{\delta t} = \mu \mathbf{A}_1, \quad (3)$$

in which $-p\mathbf{I}$ is the intermediate spherical stress tensor of order 3×3 . \mathbf{S} is the extra stress tensor, which is defined by Eq. 3, and $\frac{\delta \mathbf{S}}{\delta t}$ is further expressed as (Salah, 2013)

$$\frac{\delta \mathbf{S}}{\delta t} = \frac{D\mathbf{S}}{Dt} - \mathbf{L}\mathbf{S} - \mathbf{S}\mathbf{L}^t. \quad (4)$$

Also, \mathbf{A}_1 is first Rivline Ericksen tensor (Salah, 2013):

$$\mathbf{A}_1 = \mathbf{L} + \mathbf{L}^t. \quad (5)$$

In the expression, $\mathbf{L} = \nabla \mathbf{V}$ is the velocity gradient and superscript t is transpose notation.

Accounting for significant body forces and the strong magnetic field (neglecting induced magnetic field) to which the cylinders are subjected, then the Navier Stokes equation in cylindrical form (Zhao et al., 2022) is as follows:

$$\rho_{nf} \frac{\partial \mathbf{u}(r, t)}{\partial t} = -\frac{\partial p}{\partial z} + \frac{\mathbf{S}(r, t)}{r} + \frac{\partial \mathbf{S}(r, t)}{\partial r} + g(\rho\beta_T)_{nf}(T - T_0) + (\mathbf{J} \times \mathbf{B})_r. \quad (6)$$

With rotational symmetry $\frac{\partial p}{\partial \theta} = 0$ and ignoring pressure gradient, then $\frac{\partial p}{\partial z} = 0$ (Awan et al., 2020) is as follows:

$$\rho_{nf} \frac{\partial \mathbf{u}(r, t)}{\partial t} = \frac{\mathbf{S}(r, t)}{r} + \frac{\partial \mathbf{S}(r, t)}{\partial r} + g(\rho\beta_T)_{nf}(T - T_0) + (\mathbf{J} \times \mathbf{B})_r. \quad (7)$$

In the aforementioned expression, $\mathbf{S}(r, t)$ is the extra stress tensor and its non-zero component based on the aforementioned assumptions is $S_{rz}(r, t)$. The balance of the aforementioned equation in the absence of the both pressure gradient and viscous dissipation in the flow direction leads to $S_{rr} = S_{\theta\theta} = S_{zz} = S_{r\theta} = S_{\theta z} = 0$, and the constitutive equation for fractional Maxwell nano-fluid is then defined as follows (Jamil and Fetecau, 2010):

$$(1 + \lambda_1^\alpha D_t^\alpha) S_{rz}(r, t) = \mu_{nf} \frac{u(r, t)}{\partial r}. \quad (8)$$

Also,

$$(\mathbf{J} \times \mathbf{B})_r = -(\sigma_{nf} B_0^2 u(r, t), 0, 0). \quad (9)$$

Taking into the account that $\mathbf{B} = B_0 + b_0$, where B_0 is applied and b_0 is the induced magnetic field, respectively, Eq. 7 then takes the form

$$\rho_{nf} \frac{\partial u(r, t)}{\partial t} = \frac{\mathbf{S}(r, t)}{r} + \frac{\partial \mathbf{S}(r, t)}{\partial r} + g(\rho\beta_T)_{nf}(T - T_0) + (\mathbf{J} \times \mathbf{B})_r. \quad (10)$$

Multiplying both sides of the aforementioned equation by $(1 + \lambda_1^\alpha D_t^\alpha)$ and using Eqs 8, 9 in Eq. 10:

$$\begin{aligned} \rho_{nf} (1 + \lambda_1^\alpha D_t^\alpha) \frac{\partial u(r, t)}{\partial t} &= (1 + \lambda_1^\alpha D_t^\alpha) \frac{S_{rz}(r, t)}{r} + (1 + \lambda_1^\alpha D_t^\alpha) \frac{\partial S_{rz}(r, t)}{\partial r} \\ &\quad + g(\rho\beta_T)_{nf} (1 + \lambda_1^\alpha D_t^\alpha) (T - T_0) \\ &\quad - \sigma_{nf} B_0^2 (1 + \lambda_1^\alpha D_t^\alpha) u(r, t). \end{aligned} \quad (11)$$

In this expression, λ_1^α is the time relaxation and D_t^α is the Caputo fractional derivative as defined by (Asjad et al., 2017):

$$D_t^\alpha u(r, t) = \frac{1}{\Gamma(1 - \alpha)} \int_0^t (t - \tau)^{-\alpha} \frac{\partial u(r, \tau)}{\partial \tau} d\tau. \quad (12)$$

In Askey and Roy (2010), $\Gamma(\cdot)$ is the gamma function and may be expressed as follows:

$$\Gamma(x) = \int_0^\infty \eta^{x-1} e^{-\eta} d\eta, \quad x \in \mathbb{C}, \quad \Re(x) > 0, \quad (13)$$

$$\begin{aligned} \rho_{nf} (1 + \lambda_1^\alpha D_t^\alpha) \frac{\partial u(r, t)}{\partial t} &= \mu_{nf} \frac{1}{r} \frac{u(r, t)}{\partial r} + \mu_{nf} \frac{\partial^2 u(r, t)}{\partial r^2} \\ &\quad + g(\rho\beta_T)_{nf} (1 + \lambda_1^\alpha D_t^\alpha) (T - T_0) \\ &\quad - \sigma_{nf} B_0^2 (1 + \lambda_1^\alpha D_t^\alpha) u(r, t). \end{aligned} \quad (14)$$

By following a similar trend for heat transfer analysis, the governing equation for temperature profile is expressed as (Khan and Mustafa, 2018)

$$(\rho C_p)_{nf} \frac{\partial T}{\partial t} = K_{nf} \left(\frac{1}{r} \frac{\partial T}{\partial r} + \frac{\partial^2 T}{\partial r^2} \right) - \nabla \cdot \mathbf{q}_r + Q(T - T_0). \quad (15)$$

In the aforementioned expression, ρ is viscosity, C_p is the specific heat, T is temperature, T_0 is ambient temperature at time $t = 0$, K_{nf} is the thermal conductivity, Q is the heat absorption/source, and \mathbf{q}_r is radiative heat flux of the fractional Maxwell nano-fluid, where \mathbf{q}_r is defined by (Rosseland, 2013)

$$\mathbf{q}_r = -\left(\frac{4}{3k^*}\right) \nabla e_b, \quad (16)$$

where k^* is the mean absorption coefficient and e_b denotes the black body emissive power of the mathematical form $e_b = \sigma^* T^4$, with $\sigma^* = 5.7 \times 10^{-8} \text{ W/m}^2 \text{ K}^4$ as the Stefan-Boltzmann constant (Khan and Mustafa, 2018). Then, Eq. 16 can be written as follows:

$$\mathbf{q}_r = -\left(\frac{4}{3k^*}\right) \frac{\partial T^4}{\partial r}. \quad (17)$$

Using Taylor series expansion, approximation of T^4 has been made near T_0 ; therefore, with $T^4 = 4T_0^3 T - 3T_0^4$ and neglecting higher power (Taitel and Hartnett, 1968),

$$\mathbf{q}_r = -\frac{16\sigma^* T_0^3}{3k^*} \frac{\partial T}{\partial r}. \quad (18)$$

Eq. 17 takes the following form;

Then, multiplying both sides of Eq. 15 by $(1 + \lambda_2^\beta D_t^\beta)$,

$$\begin{aligned} (\rho C_p)_{nf} (1 + \lambda_2^\beta D_t^\beta) \frac{\partial T}{\partial t} &= K_{nf} (1 + \lambda_2^\beta D_t^\beta) \left(\frac{1}{r} \frac{\partial T}{\partial r} + \frac{\partial^2 T}{\partial r^2} \right) - \nabla \cdot \mathbf{q}_r \\ &\quad + Q(1 + \lambda_2^\beta D_t^\beta) (T - T_0). \end{aligned} \quad (19)$$

Using Eq. 18, the resulting expression is as follows:

$$(\rho C_p)_{nf} (1 + \lambda_2^\beta D_t^\beta) \frac{\partial T}{\partial t} = K_{nf} \frac{1}{r} (1 + \lambda_2^\beta D_t^\beta) \frac{\partial T}{\partial r} + K_{nf} \left[1 + \frac{16\sigma^* T_0^3}{3k^* K_{nf}} \right] \times (1 + \lambda_2^\beta D_t^\beta) \frac{\partial^2 T}{\partial r^2} + Q(1 + \lambda_2^\beta D_t^\beta) (T - T_0). \quad (20)$$

The proposed initial and boundary conditions for momentum and heat of this physical phenomenon are given as follows:

$$u(r, 0) = \frac{\partial u(r, 0)}{\partial t} = 0, \quad R_1 \leq r \leq R_2, \quad (21)$$

$$u(R_1, t) = E(1 - \cos \omega t), \quad u(R_2, t) = 0, \quad t > 0. \quad (22)$$

For temperature,

$$T(r, 0) = T_0, \quad \frac{\partial T(r, 0)}{\partial t} = 0, \quad R_1 \leq r \leq R_2, \quad (23)$$

$$T(R_1, t) = T_0, \quad \frac{\partial T(R_2, t)}{\partial r} = 0, \quad \text{for } t > 0. \quad (24)$$

Under the aforementioned initial and boundary conditions, ω is the frequency of inner cylinder velocity and R_1, R_2 are radii of the inner and outer cylinders such that $R_2 > R_1$, and E is the maximum velocity term.

Introducing the transformation for proposed geometry in Eqs 14, 20,

$$x^* = \frac{x}{R_2}, \quad r^* = \frac{r}{R_2}, \quad u^* = u \frac{R_2}{v_f}, \quad t^* = t \frac{v_f}{R_2^2}, \quad \lambda_1^* = \lambda_1 \frac{v_f}{R_2^2}, \quad \lambda_2^* = \lambda_2 \frac{v_f}{R_2^2}, \\ T^* = \frac{T - T_0}{T_0}, \quad \omega^* = \omega \frac{R_2^2}{v_f},$$

and with the usage of thermo-physical properties of nanoparticles,

$$\left. \begin{aligned} \frac{\rho_{nf}}{\rho_f} = a_1 &= \left[(1 - \phi) + \phi \frac{\rho_s}{\rho_f} \right], \quad \frac{(\rho \beta_\theta)_{nf}}{(\rho \beta_\theta)_f} = a_2 = \left[(1 - \phi) + \phi \left(\frac{(\rho \beta_T)_s}{(\rho \beta_T)_f} \right) \right], \\ \frac{\mu_{nf}}{\mu_f} = a_3 &= \frac{1}{(1 - \phi)^{2.5}}, \quad \frac{(\rho C_p)_{nf}}{(\rho C_p)_f} = a_4 = \left[(1 - \phi) + \phi \left(\frac{(\rho C_p)_s}{(\rho C_p)_f} \right) \right], \\ \frac{k_{nf}}{k_f} = a_5 &= \frac{k_s + 2k_f - 2\phi(k_f - k_s)}{k_s + 2k_f + \phi(k_f - k_s)}, \quad \frac{(\sigma)_{nf}}{(\sigma)_f} = a_6 = 1 + \frac{3 \left(\frac{\sigma_s}{\sigma_f} - 1 \right) \phi}{\left(\frac{\sigma_s}{\sigma_f} - 2 \right) - \left(\frac{\sigma_s}{\sigma_f} - 1 \right) \phi} \end{aligned} \right\} \quad (25)$$

The non-dimensional form of velocity profile along a circular cylinder is as follows:

$$(1 + \lambda_1^\alpha D_t^\alpha) \frac{\partial u^*}{\partial t^*} = b_1 \left[\frac{\partial^2 u^*}{\partial r^{*2}} + \frac{1}{r^*} \frac{\partial u^*}{\partial r^*} \right] - b_2 H_a^2 (1 + \lambda_1^\alpha D_t^\alpha) u^* + b_3 Gr (1 + \lambda_1^\alpha D_t^\alpha) T^*. \quad (26)$$

The heat equation takes the following dimensionless form:

$$(1 + \lambda_2^\beta D_t^\beta) \frac{\partial T^*}{\partial t^*} = \frac{b_1}{r^* Pr} (1 + \lambda_2^\beta D_t^\beta) \frac{\partial T^*}{\partial r^*} + \frac{b_1}{Pr} [1 + N_r] (1 + \lambda_2^\beta D_t^\beta) \frac{\partial^2 T_0}{\partial r^{*2}} + \frac{Q_0}{a_4} (1 + \lambda_2^\beta D_t^\beta) T^*. \quad (27)$$

The dimensionless initial and boundary conditions are as follows:

$$u^*(r, 0) = 0, \quad \frac{\partial u^*(r, 0)}{\partial r} = 0, \quad R_1 \leq r \leq R_2, \quad (28)$$

$$u^*(r, t) = E^* [1 - \cos \omega^* t^*], \quad u^*(R_2, t) = 0, \quad t > 0. \quad (29)$$

For temperature profile,

$$T^*(r, 0) = 0, \quad \frac{\partial T^*(r, 0)}{\partial t^*} = 0, \quad R_1 \leq r \leq R_2, \quad (30)$$

$$T^*(R_2, t) = 0, \quad t > 0. \quad (31)$$

The dimensionless velocity and temperature profiles of the problem are given, and after eliminating (*) representation, for the sake of simplicity, is as follows:

$$(1 + \lambda_1^\alpha D_t^\alpha) \frac{\partial u}{\partial t} = b_1 \left[\frac{\partial^2 u(r, t)}{\partial r^2} + \frac{1}{r} \frac{\partial u(r, t)}{\partial r} \right] - b_2 H_a^2 (1 + \lambda_1^\alpha D_t^\alpha) u(r, t) + b_3 Gr (1 + \lambda_1^\alpha D_t^\alpha) T(r, t) \quad (32)$$

and

$$(1 + \lambda_2^\beta D_t^\beta) \frac{\partial T}{\partial t} = \frac{b_4}{r \cdot Pr} (1 + \lambda_2^\beta D_t^\beta) \frac{\partial T}{\partial r} + b_4 \frac{1 + N_r}{Pr} (1 + \lambda_2^\beta D_t^\beta) \frac{\partial^2 T}{\partial r^2} + \frac{Q_0}{a_4} (1 + \lambda_2^\beta D_t^\beta) T. \quad (33)$$

Also, initial and boundary conditions are as follows:

$$u(r, 0) = 0, \quad \frac{\partial u(r, 0)}{\partial r} = 0, \quad R_1 \leq r \leq R_2, \quad (34)$$

$$u(r, t) = E[1 - \cos \omega t], \quad u(R_2, t) = 0, \quad t > 0. \quad (35)$$

For temperature profile,

$$T(r, 0) = 0, \quad \frac{\partial T(r, 0)}{\partial t} = 0, \quad R_1 \leq r \leq R_2, \quad (36)$$

$$T(R_2, t) = 0, \quad t > 0, \quad (37)$$

where

$$b_1 = \frac{a_3}{a_1}, \quad b_2 = \frac{a_6}{a_1}, \quad b_3 = \frac{a_2}{a_1}, \quad b_4 = \frac{a_5}{a_4}, \quad H_a^2 = \frac{\sigma_f B_0^2 R_2^2}{\mu_f}, \\ Gr = \frac{g(\beta_T)_f T_0 R_2^3}{\nu_f^2}, \quad Pr = \frac{\mu_f (C_p)_f}{K_f}, \quad N_r = \frac{16\sigma^* T_0^3}{3a_5 k^* K_f}, \quad Q_0 = \frac{QR_2^2}{\mu_f (C_p)_f}.$$

The dimensionless governing equations for velocity and temperature profiles in Eqs 32, 33 and non-dimensional initial and boundary conditions in Eqs 34–37 express the physical phenomenon of flow of fractional Maxwell nano-fluid within a coaxial cylinder under the influence of magnetic field and heat source/sink, in which b_1, b_2, b_3 , and b_4 are constants and ratios of thermo-physical properties of nanoparticle and base fluid, and where H_a^2, Gr, Pr, N_r , and Q_0 are the square of Hartmann number, and the Grashof number, Prandtl number, thermal radiation parameter, and constant of heat source/sink, respectively. Table 1 contains the numerical values of nanoparticles and different base fluids at room temperature (25 C°) (Usman et al., 2018).

Skin friction and Nusselt number

The significant physical quantities of skin friction and local Nusselt number for prescribed geometry are described as follows (Khan and Mustafa, 2018):

$$C_f = \frac{\mu_{nf}}{\rho u_0^2} \left(\frac{\partial u}{\partial r} \right)_{r=R_2}. \quad (38)$$

TABLE 1 Contains the numerical values of nanoparticles and different base fluids at room temperature 25° presented in (Usman et al., 2018).

Material	$\rho (kgm^{-3})$	$C_p (J Kg^{-1}K^{-1})$	$k (Wm^{-1}K^{-1})$	$\beta \times 10^{-5} (K^{-1})$	$\sigma (\Omega m)^{-1}$
Water	997	4197	0.613	21	.05
Copper	8933	385	400	1.67	5.96×10^7
Alumina	3970	765	40	0.85	2.6×10^6

The instantaneous Nusselt number near the wall for a cylindrical region is given as follows (Zhao et al., 2022):

$$Nu = -k_{nf} \left(1 + \frac{16\sigma^* T_0^3}{3k^* K_{nf}} \right) \left(\frac{\partial T}{\partial y} \right)_{r=R_2}. \quad (39)$$

After applying the fractional Maxwell operator to both sides of Eqs 38, 39, we have

$$C_f (1 + \lambda_1^\alpha D_t^\alpha) = \frac{\mu_{nf}}{\rho u_0^2} \left(\frac{\partial u}{\partial r} \right)_{r=R_2} \quad (40)$$

and

$$Nu(1 + \lambda_2^\beta D_t^\beta) = -k_{nf} \left(1 + \frac{16\sigma^* T_0^3}{3k^* K_{nf}} \right) \left(\frac{\partial T}{\partial y} \right)_{r=R_2}. \quad (41)$$

Using transformations and the thermo-physical properties of nano-fluids expressed in Eq. 25,

$$\left(C_f + \lambda_1^\alpha \frac{\partial C_f}{\partial t^\alpha} \right) = \frac{a_3}{Re^2} \left(\frac{\partial u^*}{\partial r^*} \right)_{r=R_2}. \quad (42)$$

The dimensionless expression for the Nusselt number is obtained (after ignoring the star notation) as follows:

$$\left(Nu + \lambda_1^\alpha \frac{\partial Nu}{\partial t^\alpha} \right) = -a_5 k_f (1 + Nr) \left(\frac{\partial T}{\partial y} \right)_{r=R_2} \quad (43)$$

in which a_3, a_5 are constants, and Nr, Re are the thermal radiation parameter and the Reynold number, respectively, and defined as follows:

$$Nr = \frac{16\sigma^* T_0^3}{3k^* K_f}, \quad Re = \frac{u_0^2 R_2^2}{\nu_f^2}.$$

Numerical procedure

The numerical technique of the finite difference method is a strong and accurate tool used for solving the partial difference equation, even of non-linear order. The proposed model is a non-linear coupled model of PDEs that express the momentum and temperature equations. The discretization of governing equations are expressed as. It is well-known that the discretization of ${}_0^C D_t^\alpha u, {}_0^C D_t^{1+\alpha} u$ for $0 < \alpha \leq 1, u_t$ and u_{rr} is defined as follows (Liu et al., 2004):

$${}_0^C D_{t_{j+1}}^\alpha u(r_i, t_{j+1}) = \frac{\Delta t^{-\alpha}}{\Gamma(2-\alpha)} [u_i^{j+1} - u_i^j] + \frac{\Delta t^{-\alpha}}{\Gamma(2-\alpha)} \sum_{l=1}^j (u_i^{j-l+1} - u_i^{j-l}) b_l^\alpha, \quad (44)$$

$${}_0^C D_{t_{j+1}}^{1+\alpha} u(r_i, t_{j+1}) = \frac{\Delta t^{-(1+\alpha)}}{\Gamma(2-\alpha)} [u_i^{j+1} - 2u_i^j + u_i^{j-1}] + \frac{\Delta t^{-(1+\alpha)}}{\Gamma(2-\alpha)} \times \sum_{l=1}^j (u_i^{j-l+1} - 2u_i^{j-l} + u_i^{j-l-1}) b_l^\alpha, \quad (45)$$

$$\frac{\partial}{\partial t} u(r_i, t_{j+1}) \Big|_{t=t_{j+1}} = \frac{1}{\Delta t} [u_i^{j+1} - u_i^j], \quad (46)$$

$$\frac{\partial^2}{\partial r^2} u(r_{i+1}, t_j) \Big|_{r=r_{i+1}} = \frac{1}{\Delta r^2} [u_{i+1}^{j+1} - 2u_i^{j+1} + u_{i-1}^{j+1}]. \quad (47)$$

In Eq. 44, $b_l^\alpha = (l+1)^{1-\alpha} - l^{1-\alpha}$, $l = 1, 2, 3, \dots, j$. Rectilinear grids are pondered for the numerical solution, with grid spacing $\Delta t > 0, \Delta r > 0$, where $\Delta r = (R_2 - R_1)/M, \Delta t = T/N$ with $\Delta r, \Delta t$ from \mathbb{Z}^+ . Points (r_i, t_j) in $\Omega = [0, T] \times [0, L]$ are defined as $r_i = i\Delta r$ and $t_j = j\Delta t$. Considering the aforementioned assumptions, the discussed model of Eqs 32, 33 at (i, j) is defined as follows:

$$\begin{aligned} & \frac{1}{\Delta t} (u_i^{j+1} - u_i^j) \\ & + \frac{\lambda_1^\alpha \Delta r t^{1-\alpha}}{\Gamma(2-\alpha)} \left(u_i^{j+1} - 2u_i^j + u_i^{j-1} + \sum_{l=1}^j (u_i^{j-l+1} - 2u_i^{j-l} + u_i^{j-l-1}) b_l^\alpha \right) \\ & = b_1 \left(\frac{u_{i+1}^{j+1} - 2u_i^{j+1} + u_{i-1}^{j+1}}{\Delta r^2} + \frac{1}{2i\Delta r^2} (u_{i+1}^{j+1} - u_{i-1}^{j+1}) \right) \\ & + b_2 Gr \left(T_i^{j+1} + \frac{\lambda_1^\alpha \Delta r t^{1-\alpha}}{\Gamma(2-\alpha)} (T_i^{j+1} - T_i^j + \sum_{l=1}^j (T_i^{j-l+1} - T_i^{j-l}) b_l^\alpha) \right) \\ & - b_3 Ha^2 \left(u_i^{j+1} + \frac{\lambda_1^\alpha \Delta r t^{1-\alpha}}{\Gamma(2-\alpha)} \left(u_i^{j+1} - u_i^j + \sum_{l=1}^j (u_i^{j-l+1} - u_i^{j-l}) b_l^\alpha \right) \right), \\ & \frac{1}{\Delta r t} (T_i^{j+1} - T_i^j) \\ & + \frac{\lambda_2^\beta \Delta r t^{1-\alpha}}{\Gamma(2-\alpha)} \left(T_i^{j+1} - 2T_i^j + T_i^{j-1} + \sum_{l=1}^j (T_i^{j-l+1} - 2T_i^{j-l} + T_i^{j-l-1}) b_l^\alpha \right) \\ & = \frac{b_4}{2Pr i \Delta r^2} \left(T_{i+1}^{j+1} - T_{i-1}^{j+1} + \frac{\lambda_2^\beta \Delta r t^{1-\alpha}}{\Gamma(2-\alpha)} \left(T_{i+1}^{j+1} - T_{i+1}^j + \sum_{l=1}^j (T_{i+1}^{j-l+1} - T_{i+1}^{j-l}) b_l^\alpha \right. \right. \\ & \quad \left. \left. - T_{i-1}^{j+1} + T_{i-1}^j - \sum_{l=1}^j (T_{i-1}^{j-l+1} - T_{i-1}^{j-l}) b_l^\alpha \right) \right) \\ & + \frac{b_4 (1 + Nr)}{\Delta r^2 Pr} \left(T_{i+1}^{j+1} - 2T_i^{j+1} + T_{i-1}^{j+1} + \frac{\lambda_2^\beta \Delta r t^{1-\alpha}}{\Gamma(2-\alpha)} \right. \\ & \quad \times \left(T_{i+1}^{j+1} - T_{i+1}^j + \sum_{l=1}^j (T_{i+1}^{j-l+1} - T_{i+1}^{j-l}) b_l^\alpha - 2T_i^{j+1} \right. \\ & \quad \left. \left. + 2T_i^j - 2 \sum_{l=1}^j (T_i^{j-l+1} - T_i^{j-l}) b_l^\alpha + T_{i-1}^{j+1} - T_{i-1}^j \right. \right. \\ & \quad \left. \left. + \sum_{l=1}^j (T_{i-1}^{j-l+1} - T_{i-1}^{j-l}) b_l^\alpha \right) \right) \end{aligned}$$

$$\begin{aligned}
& + \frac{Q_0}{a_4} \left(T_i^{j+1} + \frac{\lambda_2^\beta \Delta t^{-\alpha}}{\Gamma(2-\alpha)} \left(T_i^{j+1} - T_i^j + \sum_{l=1}^j (T_i^{j-l+1} - T_i^{j-l}) b_l^\alpha \right) \right) \\
& + \frac{Q_0}{a_4} \left(T_i^{j+1} + \frac{\lambda_2^\beta t^{-\alpha}}{\Gamma(2-\alpha)} \left(T_i^{j+1} - T_i^j + \sum_{l=1}^j (T_i^{j-l+1} - T_i^{j-l}) b_l^\alpha \right) \right) \\
& \left(-\frac{b_1}{\Delta r^2} + \frac{b_1}{2i\Delta r^2} \right) u_{i-1}^{j+1} \\
& + \left(\frac{1}{\Delta t} + \lambda_1^\alpha \frac{\Delta t^{-1-\alpha}}{\Gamma(2-\alpha)} + \frac{2b_1}{\Delta r^2} + b_3 Ha^2 + b_3 Ha^2 \lambda_1^\alpha \frac{t^{-\alpha}}{\Gamma(2-\alpha)} \right) u_i^{j+1} \\
& + \left(-\frac{b_1}{\Delta r^2} - \frac{b_1}{2i\Delta r^2} \right) u_{i+1}^{j+1} + \left(-b_2 Gr - b_2 Gr \lambda_1^\alpha \frac{t^{-\alpha}}{\Gamma(2-\alpha)} \right) T_i^{j+1} \\
& = \lambda_1^\alpha \frac{t^{-1-\alpha}}{\Gamma(2-\alpha)} u_i^{j-1} \\
& + \left(\frac{1}{\Delta t} + 2\lambda_1^\alpha \frac{\Delta t^{-1-\alpha}}{\Gamma(2-\alpha)} - b_3 Ha^2 \lambda_1^\alpha \frac{t^{-\alpha}}{\Gamma(2-\alpha)} \right) u_i^j - b_2 Gr \lambda_1^\alpha \frac{\Delta t^{-\alpha}}{\Gamma(2-\alpha)} T_i^j \\
& + f_{i,j}^1 + f_{i,j}^2 + f_{i,j}^3 \\
& \left(\frac{b_4}{2Pr i \Delta r^2} + \frac{b_4}{2Pr i \Delta r^2} \frac{\lambda_2^\beta \Delta t^{-\alpha}}{\Gamma(2-\alpha)} - \frac{b_4(1+Nr)}{\Delta r^2 Pr} - \frac{b_4(1+Nr)}{\Delta r^2 Pr} \frac{\lambda_2^\beta \Delta t^{-\alpha}}{\Gamma(2-\alpha)} \right) T_{i-1}^{j+1} \\
& + \left(\frac{1}{\Delta t} + \lambda_2^\beta \frac{\Delta t^{-1-\alpha}}{\Gamma(2-\alpha)} + 2\frac{b_4(1+Nr)}{\Delta r^2 Pr} + 2\frac{b_4(1+Nr)}{\Delta r^2 Pr} \frac{\lambda_2^\beta \Delta t^{-\alpha}}{\Gamma(2-\alpha)} - \frac{Q_0}{a_4} - \frac{Q_0}{a_4} \frac{\lambda_2^\beta \Delta t^{-\alpha}}{\Gamma(2-\alpha)} \right) T_i^{j+1} \\
& + \left(-\frac{b_4}{2Pr i \Delta r^2} - \frac{b_4}{2Pr i \Delta r^2} \frac{\lambda_2^\beta \Delta t^{-\alpha}}{\Gamma(2-\alpha)} - \frac{b_4(1+Nr)}{\Delta r^2 Pr} - \frac{b_4(1+Nr)}{\Delta r^2 Pr} \frac{\lambda_2^\beta \Delta t^{-\alpha}}{\Gamma(2-\alpha)} \right) T_{i+1}^{j+1} \\
& = \left(\frac{\lambda_2^\beta \Delta t^{-1-\alpha}}{\Gamma(2-\alpha)} + \frac{b_4}{2Pr i \Delta r^2} \frac{\lambda_2^\beta \Delta t^{-\alpha}}{\Gamma(2-\alpha)} - \frac{b_4(1+Nr)}{\Delta r^2 Pr} \frac{\lambda_2^\beta \Delta t^{-\alpha}}{\Gamma(2-\alpha)} \right) T_{i-1}^j \\
& + \left(\frac{1}{\Delta t} + 2\frac{\lambda_2^\beta \Delta t^{-1-\alpha}}{\Gamma(2-\alpha)} + 2\frac{b_4(1+Nr)}{\Delta r^2 Pr} \frac{\lambda_2^\beta \Delta t^{-\alpha}}{\Gamma(2-\alpha)} - \frac{Q_0}{a_4} \frac{\lambda_2^\beta \Delta t^{-\alpha}}{\Gamma(2-\alpha)} \right) T_i^j \\
& + \left(-\frac{b_4}{2Pr i \Delta r^2} \frac{\lambda_2^\beta \Delta t^{-\alpha}}{\Gamma(2-\alpha)} - \frac{b_4(1+Nr)}{\Delta r^2 Pr} \frac{\lambda_2^\beta \Delta t^{-\alpha}}{\Gamma(2-\alpha)} \right) T_{i+1}^j + g_{i,j}^1 + g_{i,j}^2 + g_{i,j}^3 \\
& + g_{i,j}^4 + g_{i,j}^5 + g_{i,j}^6 + g_{i,j}^7 \\
& f_{i,j}^1 = -\lambda_1^\alpha \frac{\Delta t^{-1-\alpha}}{\Gamma(2-\alpha)} \sum_{l=1}^j (u_i^{j-l+1} - 2u_i^{j-l} + u_i^{j-l-1}) b_l^\alpha, f_{i,j}^2 \\
& = b_2 Gr \frac{\lambda_1^\alpha \Delta t^{-\alpha}}{\Gamma(2-\alpha)} \sum_{l=1}^j (T_i^{j-l+1} - T_i^{j-l}) b_l^\alpha, \\
& f_{i,j}^3 = -b_3 Ha^2 \lambda_1^\alpha \frac{\Delta t^{-\alpha}}{\Gamma(2-\alpha)} \sum_{l=1}^j (u_i^{j-l+1} - u_i^{j-l}) b_l^\alpha, \\
& g_{i,j}^1 = \frac{\lambda_2^\beta \Delta t^{-1-\alpha}}{\Gamma(2-\alpha)} \sum_{l=1}^j (T_i^{j-l+1} - 2T_i^{j-l} + T_i^{j-l-1}) b_l^\alpha, g_{i,j}^2 \\
& = \frac{b_4}{2Pr i \Delta r^2} \frac{\lambda_2^\beta \Delta t^{-\alpha}}{\Gamma(2-\alpha)} \sum_{l=1}^j (T_{i+1}^{j-l+1} - T_{i+1}^{j-l}) b_l^\alpha, \\
& g_{i,j}^3 = \frac{b_4}{2Pr i \Delta r^2} \frac{\lambda_2^\beta \Delta t^{-\alpha}}{\Gamma(2-\alpha)} \sum_{l=1}^j (T_{i-1}^{j-l+1} - T_{i-1}^{j-l}) b_l^\alpha, g_{i,j}^4 \\
& = \frac{b_4(1+Nr)}{\Delta r^2 Pr} \frac{\lambda_2^\beta \Delta t^{-\alpha}}{\Gamma(2-\alpha)} \\
& \quad \times \sum_{l=1}^j (T_{i+1}^{j-l+1} - T_{i+1}^{j-l}) b_l^\alpha, g_{i,j}^5 \\
& = -2\frac{b_4(1+Nr)}{\Delta r^2 Pr} \frac{\lambda_2^\beta \Delta t^{-\alpha}}{\Gamma(2-\alpha)} \sum_{l=1}^j (T_i^{j-l+1} - T_i^{j-l}) b_l^\alpha,
\end{aligned}$$

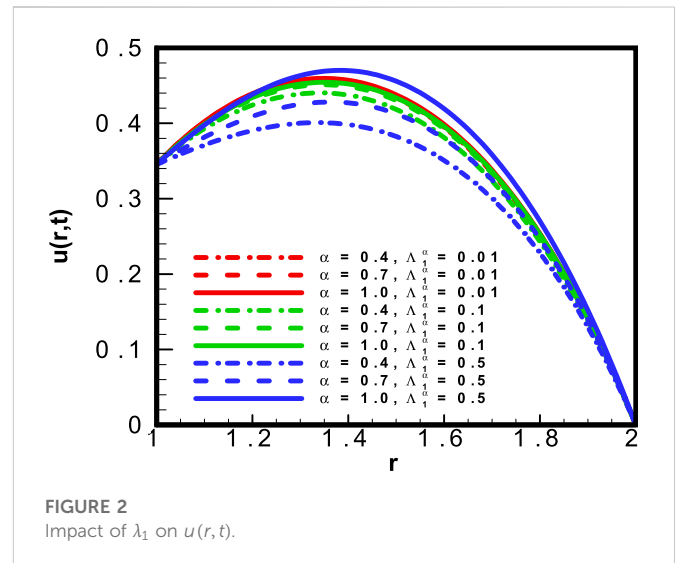


FIGURE 2
Impact of λ_1 on $u(r, t)$.

$$\begin{aligned}
g_{i,j}^6 &= \frac{b_4(1+Nr)}{\Delta r^2 Pr} \frac{\lambda_2^\beta \Delta t^{-\alpha}}{\Gamma(2-\alpha)} \sum_{l=1}^j (T_{i-1}^{j-l+1} - T_{i-1}^{j-l}) b_l^\alpha, g_{i,j}^7 \\
&= \frac{Q_0}{a_4} \frac{\lambda_2^\beta \Delta t^{-\alpha}}{\Gamma(2-\alpha)} \sum_{l=1}^j (T_i^{j-l+1} - T_i^{j-l}) b_l^\alpha.
\end{aligned}$$

For $j = 1, 2, 3, \dots, N-1$, $i = 1, 2, 3, \dots, N-1$, with the following initial and boundary conditions,

$$\begin{aligned}
u_0^0 &= 0, u_i^1 = u_i^{-1}, T_i^0 = 0, T_i^1 = T_i^{-1}, \text{ for } i = 0, 1, 2, 3, \dots, M, \\
u_0^j &= E_M(1 - \cos w \Delta t), u_M^j = 0, T_0^j = 1, T_M^j = 0, \text{ for } j \\
&= 1, 2, 3, \dots, N-1.
\end{aligned}$$

Results and discussion

We have developed a fractional model of Maxwell nano-fluids under the effects of magnetic field, thermal radiation, and heat source/sink. The physical properties of nano-fluids were utilized to model the physical phenomenon. The focus of the problem was the cylindrical coordinate system in which coaxial geometry was assumed to formulate the problem. Using the Caputo fractional order operator in the model, the finite difference scheme was applied to obtain numerical results using mathematical software MAPLE. In this section, we report our results and discuss the plots and comparison, of important physical properties such as Ha , Pr , Nr , Gr , ϕ , α , β , Re , and Q_0 , demonstrating the square of the Hartmann number (magnetic field parameter), non-dimensional Prandlt number, thermal radiation parameter, non-dimensional Grashof number, volumetric fraction of nanoparticle, non-integral-order parameters, non-dimensional Reynolds number, and heat source/sink parameter. The trends of the aforementioned parameters were observed for momentum and temperature profiles of the system in the annular region. The results were obtained by developing MAPLE code and then used to produce graphical plots.

The results were obtained through discretization of the governing equations (Eqs 32, 33), with initial and boundary conditions expressed

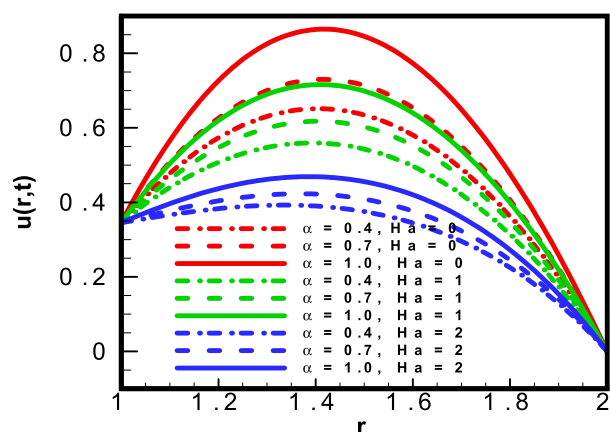


FIGURE 3
Impact of Ha on $u(r,t)$.

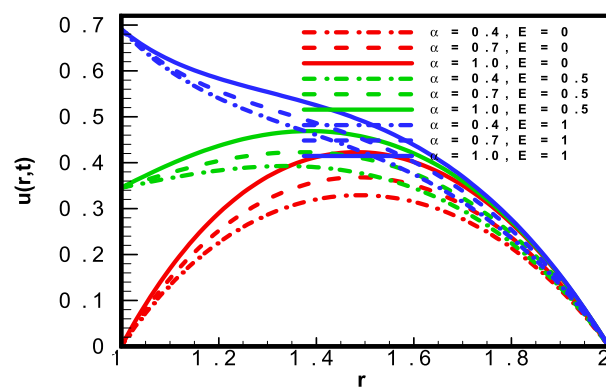


FIGURE 6
Impact of E on $u(r,t)$.

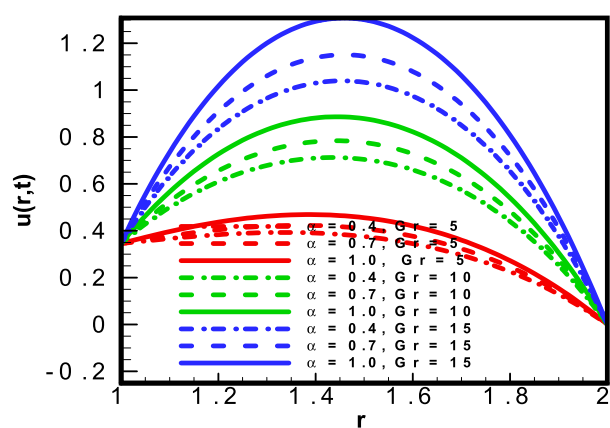


FIGURE 4
Impact of Gr on $u(r,t)$.

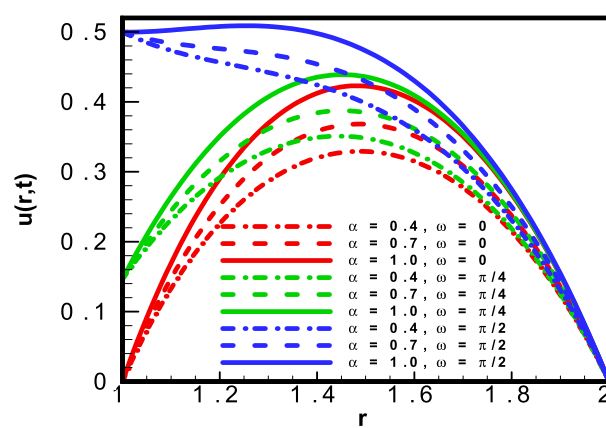


FIGURE 7
Impact of ω on $u(r,t)$.

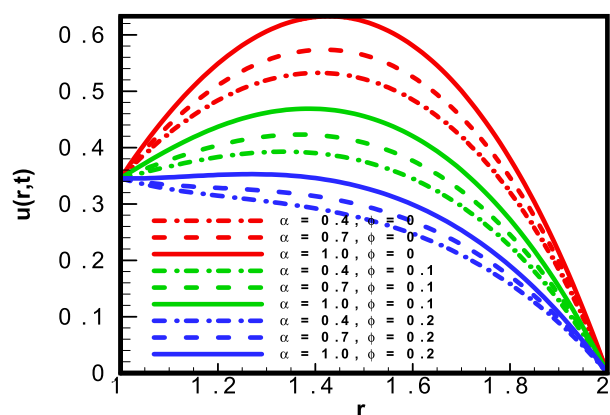


FIGURE 5
Impact of ϕ on $u(r,t)$.

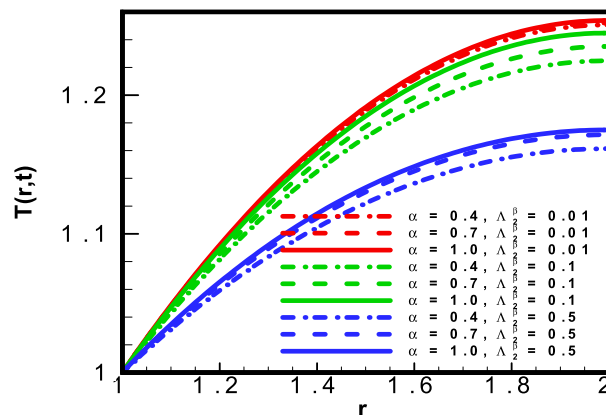
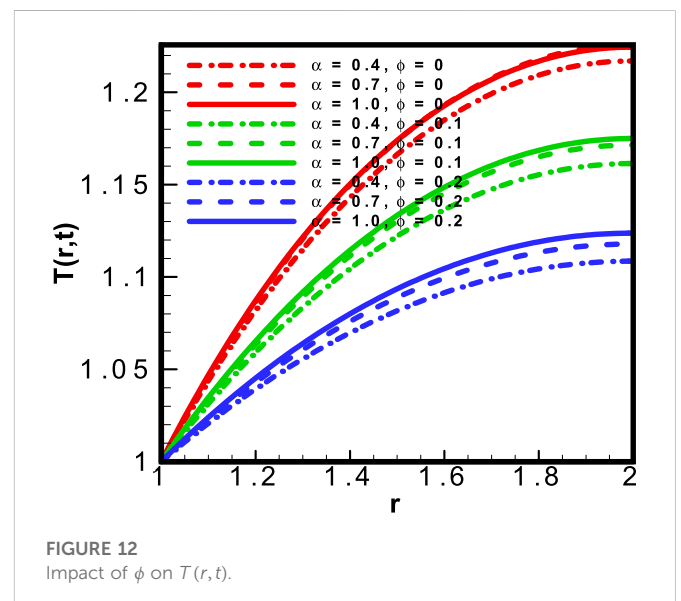
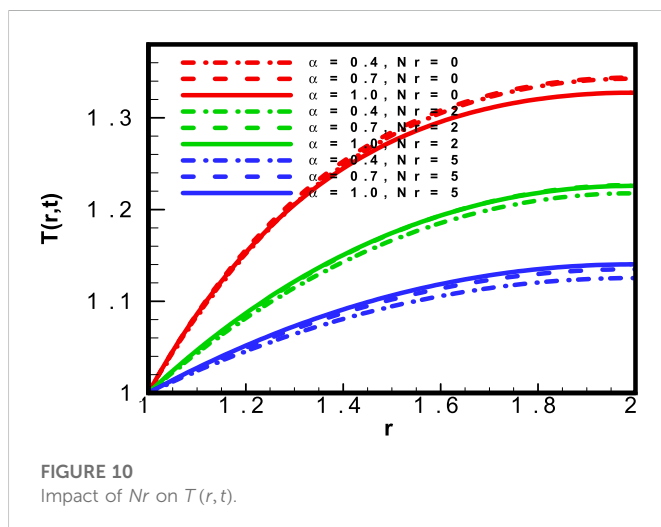
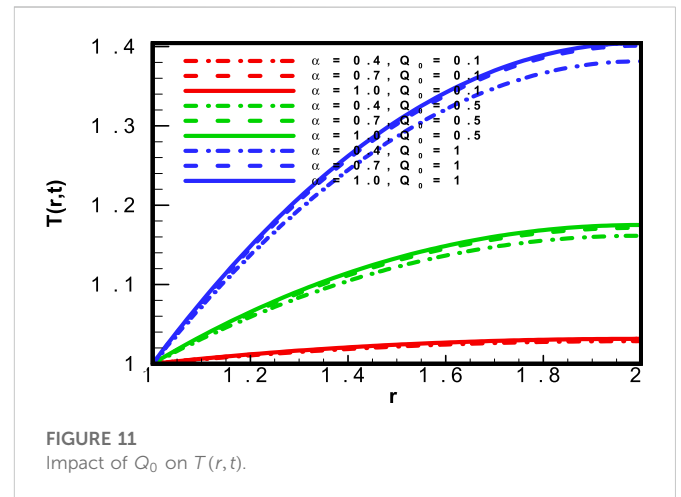
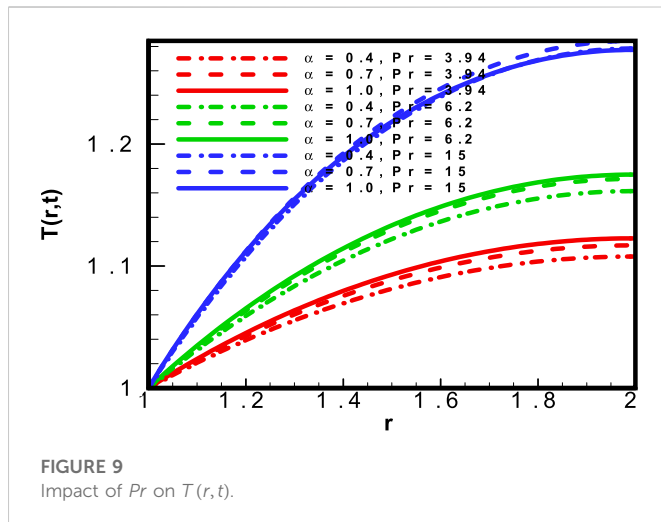


FIGURE 8
Impact of λ_2^β on $T(r,t)$.



in Eqs 34–37. The graphical results for the velocity profile $u(r,t)$ and temperature profile $T(r,t)$ were plotted against H_a , Pr , Nr , Gr , ϕ ,

α , β , Re , and Q_0 . For validation, results obtained using our model were compared with those from the built-in model using MAPLE.

Figure 2 shows the results obtained for velocity profile $u(r,t)$ with respect to the time relaxation parameter λ_1 for a range of values ($\lambda_1 = 0.01, 0.1, 0.5$), with varying fractional-order parameters ($\alpha = 0.4, 0.7, 1.0$). The data demonstrate that an increase in the time relaxation parameter led to a direct increase in the velocity profile. Time relaxation is a material's characteristic capacity to be relaxed for a certain period of time. With the passage of time, fluid flow becomes laminar and internal resistance decreases, which increases the velocity profile of the fractional Maxwell nano-fluid within an annular region of a coaxial cylinder.

In Figure 3, the results for velocity profile $u(r,t)$ are plotted against the magnetic field parameter H_a (the square of the Hartmann number) for a range of values ($H_a = 0, 1, 2$), with a range of fractional-order parametric values ($\alpha = 0.4, 0.7, 1.0$). The plots

demonstrate that by increasing the value of the magnetic field parameter, the velocity profile $u(r,t)$ is reduced. The increased value of H_a gives rise to Lorentz force that increases the intermolecular force and the internal resistance between fluid particles. Consequently, a reducing trend in the velocity profile $u(r,t)$ is apparent; the value is high near the boundary of the inner cylinder, and the velocity profile $u(r,t)$ gains its maximum at the mid-point between the inner and outer cylinder.

The plot for velocity $u(r,t)$ against the Grashof number Gr is presented in Figure 4 for a range of values ($Gr = 5, 10, 15$). Since the Grashof number is the ratio of two different forces related to the fluid properties of buoyancy and viscosity, an increase in Gr is observed when viscous forces decrease. Therefore, the value of Gr increases only when there is a reduction in viscous force and, consequently, the velocity profile $u(r,t)$ within the cylindrical region increases and gains its maximum value at the middle of the two radii due to decreasing viscous behavior of the MHD fractional Maxwell nano-fluid.

TABLE 2 Variation in the skin friction coefficient with respect to varying physical parameters and α .

λ_1^α	Ha	Gr	E	ω	ϕ	Fractional-order parameter α		
						$\alpha = 0.4$	$\alpha = 0.7$	$\alpha = 1$
0.01	2	5	0.5	$\frac{2\pi}{5}$	0.1	0.8405	0.8549	0.8601
0.1						0.7195	0.7787	0.7985
0.5						0.3636	0.5046	0.7305
0.6	0	5	0.5	$\frac{2\pi}{5}$	0.1	1.9487	2.3667	3.1888
	1					1.3938	1.7032	2.2985
	2					0.2851	0.4390	0.7026
0.6	2	5	0.5	$\frac{2\pi}{5}$	0.1	0.2851	0.4390	0.7026
		10				2.2954	2.6536	3.2204
		15				4.3056	4.8682	5.7381
0.6	2	5	0	$\frac{2\pi}{5}$	0.1	2.0102	2.2146	2.5177
			0.5			0.2851	0.4390	0.7026
			1			-1.4400	-1.3365	1.1124
0.6	2	5	0.5	0	0.1	2.0102	2.2146	2.5177
				$\frac{\pi}{4}$		1.2650	1.4424	1.7212
				$\frac{\pi}{2}$		-0.4406	-0.2910	-0.0203
0.6	2	5	0.5	$\frac{2\pi}{5}$	0	0.9085	1.0617	1.2837
					0.1	0.2851	0.4390	0.7026
					0.2	-0.4288	-0.2938	-0.0387

TABLE 3 Variation in the local Nusselt number with respect to varying physical parameters and α .

λ_2^β	Pr	Nr	Q_0	Fractional-order parameter		
				$\beta = 0.4$	$\beta = 0.7$	$\beta = 1$
0.01	6.2	3.5	0.5	0.6694	0.6733	0.6777
0.1				0.6041	0.6319	0.6581
0.5				0.4392	0.4706	0.4883
0.5	3.94	3.5	0.5	0.2904	0.3163	0.3351
	6.2			0.4392	0.4706	0.4883
	15			0.8221	0.8597	0.8666
0.5	6.2	0	0.5	0.5322	0.6899	0.9403
		2		0.3525	0.5085	0.7693
		5		0.2416	0.3932	0.6572
0.5	6.2	3.5	0.1	0.1192	0.2563	0.5016
			0.5	0.2851	0.4390	0.7026
			1	0.5495	0.7263	1.0104

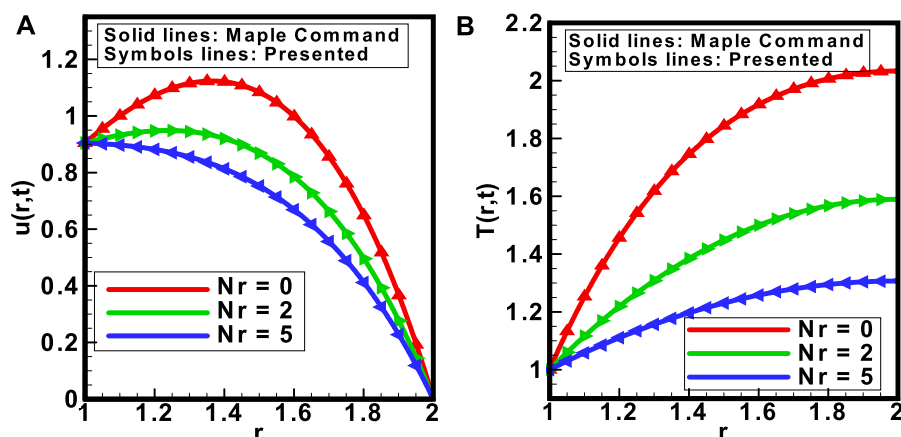


FIGURE 13

Comparison between the MAPLE built-in command results and results obtained from the model for (A) velocity and (B) temperature profiles in respect to the variation in Nr .

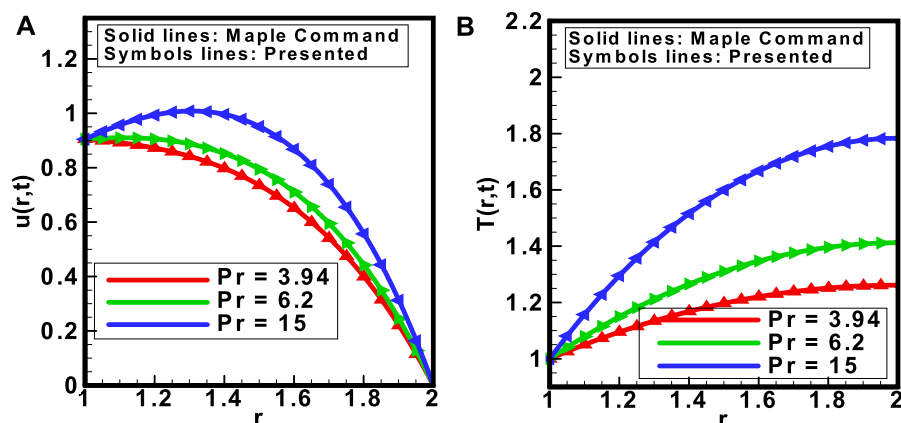


FIGURE 14

Comparison between the MAPLE built-in command results and results obtained from the model for (A) velocity and (B) temperature profiles in respect to the variation in Pr .

Figure 5 depicts the results for the most important physical parameter: the volumetric fraction ϕ of nanoparticles in base fluid. The addition of nanoparticles to base fluid reduces the velocity profile $u(r,t)$ within the coaxial cylinder. Therefore, the results were plotted for a range of values ($\phi = 0, 0.1, 0.2$), considering different values of the fractional-order parameter α . Addition of nanoparticles to base fluid increases intermolecular forces and collision of molecules increase, thereby decreasing the velocity profile $u(r,t)$.

Figure 6 is a graphical representation of the maximum velocity term E , indicating that velocity reaches its maximum value of E near the boundary of the inner cylinder; on the other hand, it is at its lowest degree at the boundary of the outer cylinder. This graph indicates that, for the lowest value of r and maximum of value of E , $u(r,t)$ increases in value.

The term ω is the frequency of inner cylinder velocity, and Figure 7 depicts the graphical results for a range of values, such as ($\omega = 0, \pi/4, \pi/2$). For the interval $[0, \pi/4]$, due to the cosine function,

increasing the value of ω results in an increased velocity profile $u(r,t)$. The reverse trend occurred for the closed interval $[\pi/4, \pi/2]$.

The impact of the time relaxation parameter λ_2^β on temperature profile $T(r,t)$ is plotted in Figure 8. The range of values for λ_2^β ($\lambda_2^\beta = 0.01, 0.1, 0.5$) was assessed for impact on $T(r,t)$. It was noted that increasing the value of λ_2^β reduced the temperature. This effect is based on the characteristics of the material and the time in which the system relaxes under specific conditions. Therefore, as collision between particles in a fluid decreases, the heat transfer process of system is reduced. The graph shows that the temperature profile attained its high value near the wall of the outer cylinder for different fractional parametric values of β .

The impact of the Prandtl number (Pr) on heat transfer capability of a coupled non-linear fractional model is illustrated in Figure 9 for a range of values ($Pr = 3.94, 6.2, 15$). Pr is the basic fluid property used to calculate heat transfer capability. It is the ratio of kinematic viscosity to thermal diffusivity. Pr is inversely related to thermal diffusivity,

which is directly related to heat capability. Increasing heat capacity increases the thermal diffusivity of a material. Therefore, increasing Pr increases the temperature profile $T(r, t)$ of the system.

In Figure 10, the temperature profile $T(r, t)$ of the fractional Maxwell nano-fluid is quantified for a range of thermal radiation parameters ($Nr = 0, 2, 5$). It has been observed that an increase in the thermal radiation parameter Nr increases the heat transfer capability of a system for a specific range of fractional-order parameters ($\alpha = 0.4, 0.7, 1.0$), thereby reducing the temperature profile of the system, which is very low near the inner cylinder surface.

Figure 11 describes the conduct of the heat profile $T(r, t)$ for the flow of fractional Maxwell nano-fluid within a coaxial cylinder under the effects of the heat source/sink parameter Q_0 . Subjecting the system to a heat source directly affected the heat capability, with the temperature profile $T(r, t)$ increasing with increasing heat source/sink values ($Q_0 = 0.1, 0.5, 1.0$) and achieving its maximum value at the outer boundary of the cylinders. Within the cylindrical region, the temperature profile attained its minimum value near the boundary of the inner cylinder and gained its maximum value near the boundary of outer cylinder.

The addition of nanoparticles to base fluids enhances entropy generation, and there is reduced loss of useful energy. This expected result was obtained over a range of values of volumetric fraction of nanoparticles ($\phi = 0, 0.1, 0.2$) and is depicted in Figure 12. Heat transfer was reduced by the addition of nanoparticles to base fluids.

The important physical quantities of skin friction (C_f) and local Nusselt number (Nu) have been quantified against different physical parameters mentioned in the previous sections. The results are arranged in Table 2 and Table 3 respectively.

Table 2 shows an ascending trend in C_f for increasing values of fractional-order parameter $\alpha = 0.4, 0.7, 1.0$ and varying $\lambda_1^\alpha, Ha, Gr, E, \omega$, and ϕ .

Similar behavior of Nu was observed, as shown in Table 3, in that increasing values of fractional-order parameter $\beta = 0.4, 0.7, 1.0$ resulted in increased Nu for different values of λ_2^β, Pr, Nr , and Q_0 .

Validation of scheme

This section of the study focused on validation of the proposed scheme. The graphical results were obtained by using mathematical software MAPLE. Figures 13A, B depict the effectiveness and accuracy of the proposed scheme for the velocity profile $u(r, t)$ and temperature profile $T(r, t)$ against an important physical parameter, the thermal radiation parameter Nr . MAPLE built-in command results and results obtained *via* our model were compared.

Figures 14A, B illustrate the comparison between results obtained using the built-in command in MAPLE and results obtained using the proposed scheme. The investigation assessed the velocity profile $u(r, t)$ and temperature profile $T(r, t)$ with respect to the non-dimensional Prandtl number Pr .

Conclusion

In this study, we numerically investigated the MHD flow of fractional Maxwell nano-fluid and heat transfer. The flow was measured within a cylindrical coordinate system in which coaxial geometry was considered. Thermal radiation was applied across

the circular region. Water (H_2O) was adopted as the base fluid, whereas Cu was considered in preparation of the nano-fluid. The problem was modeled fractionally using the Caputo time fractional differentiation operator. For discretization, the finite difference method was applied to the governing equations for the velocity and temperature profiles. The results were organized graphically using MAPLE mathematical software. For validation, the results obtained *via* the proposed scheme *versus* the built-in analysis *via* MAPLE were compared. Some of our key findings are as follows:

- By increasing the angular frequency of inner cylinder velocity, the velocity profile of fractional Maxwell nano-fluids is increased.
- The addition of Cu nanoparticles to a base fluid of water enhances its heat transfer capability.
- Subjecting the system to a strong magnetic field increases heat transfer and lowers the velocity profile of the system.
- The thermal radiation parameter Nr has a direct impact on the temperature profile $T(r, t)$ of fractional Maxwell nano-fluids.
- The non-dimensional parameters Pr, Gr are directly related to the temperature and velocity profiles, respectively.
- The finite difference scheme is a strong technique that can be used to solve fractional-order mathematical models.
- The result validation section shows that the scheme applied is strong and effective for the proposed problem in cylindrical geometry.
- These findings lead further toward the numerical investigation of fractional Maxwell bio-nano fluids within blood arteries.

Data availability statement

The original contributions presented in the study are included in the article/Supplementary material; further inquiries can be directed to the corresponding author.

Author contributions

Conceptualization, MIA; methodology, MU; validation, ATA; investigation, MIA; writ draft preparation, AA and MU; write and editing, TEM; visualization, MU and AA; supervision, MIA; project administration, ATA; funding acquisition, TEM. All authors have read and agreed to the published version of the manuscript.

Acknowledgments

The authors are grateful to HEC Pakistan for facilitating this research under research project No 15911 (NRPU).

Conflict of interest

The authors declare that the research was conducted in the absence of any commercial or financial relationships that could be construed as a potential conflict of interest.

Publisher's note

All claims expressed in this article are solely those of the authors and do not necessarily represent those of their affiliated

organizations, or those of the publisher, the editors, and the reviewers. Any product that may be evaluated in this article, or claim that may be made by its manufacturer, is not guaranteed or endorsed by the publisher.

References

- Aleem, M., Asjad, M. I., Shaheen, A., and Khan, I. (2020). MHD Influence on different water based nanofluids (TiO₂, Al₂O₃, CuO) in porous medium with chemical reaction and Newtonian heating. *Chaos, Solit. Fractals* 130, 109437. doi:10.1016/j.chaos.2019.109437
- Anwar, T., Kumam, P., Khan, I., and Watthayu, W. (2020). Heat transfer enhancement in unsteady MHD natural convective flow of CNTs Oldroyd-B nanofluid under ramped wall velocity and ramped wall temperature. *Entropy* 22 (4), 401. doi:10.3390/e22040401
- Asjad, M. I., Shah, N. A., Aleem, M., and Khan, I. (2017). Heat transfer analysis of fractional second-grade fluid subject to Newtonian heating with caputo and caputo-fabrizio fractional derivatives: A comparison. *Eur. Phys. J. plus* 132 (8), 340–358. doi:10.1140/epjp/i2017-11606-6
- Askey, R. A., and Roy, R., Gamma function. Available at: https://en.wikipedia.org/wiki/Gamma_function, 2010.
- Awan, A. U., Imran, M., Athar, M., Kamran, M., et al. (2020). Exact analytical solutions for a longitudinal flow of a fractional Maxwell fluid between two coaxial cylinders. *Punjab Univ. J. Math.* 45 (1).
- Bagley, R. L., and Torvik, P. (1983). A theoretical basis for the application of fractional calculus to viscoelasticity. *J. Rheology* 27 (3), 201–210. doi:10.1122/1.549724
- Choi, S. U., and Eastman, J. A. (1995). "Enhancing thermal conductivity of fluids with nanoparticles," in Conference: 1995 International mechanical engineering congress and exhibition, Argonne, IL (United States) (Lemont, IL: Argonne National Lab.ANL).
- Chung, J. (1999). Numerical investigation on the bifurcative natural convection in a horizontal concentric annulus. *Numer. Heat. Transf. Part A Appl.* 36 (3), 291–307. doi:10.1080/104077899274778
- Fetecau, C., Hayat, T., and Fetecau, C. (2008). Starting solutions for oscillating motions of Oldroyd-B fluids in cylindrical domains. *J. Newt. fluid Mech.* 153 (2–3), 191–201. doi:10.1016/j.jnnfm.2008.02.005
- Fetecau, C., Mahmood, A., and Jamil, M. (2010). Exact solutions for the flow of a viscoelastic fluid induced by a circular cylinder subject to a time dependent shear stress. *Commun. Nonlinear Sci. Numer. Simul.* 15 (12), 3931–3938. doi:10.1016/j.cnsns.2010.01.012
- Fetecau, C., Retracted, A. R. T. I. C. L. E., Jamil, M., and Mahmood, A. (2011). Retracted article: Flow of fractional Maxwell fluid between coaxial cylinders. *Archive Appl. Mech.* 81 (8), 1153–1163. doi:10.1007/s00419-011-0536-x
- Friedrich, C. (1991). Relaxation and retardation functions of the Maxwell model with fractional derivatives. *Rheol. Acta* 30 (2), 151–158. doi:10.1007/bf01134604
- Haitao, Q., and Mingyu, X. (2009). Some unsteady unidirectional flows of a generalized Oldroyd-B fluid with fractional derivative. *Appl. Math. Model.* 33 (11), 4184–4191. doi:10.1016/j.apm.2009.03.002
- Haldar, S. (1998). Combined convection in developing flow through a horizontal concentric annulus. *Numer. Heat. Transf. Part A Appl.* 34 (6), 673–685. doi:10.1080/10407789808914009
- Hartnett, J. P., and Kostic, M. (1989). Heat transfer to Newtonian and non-Newtonian fluids in rectangular ducts. *Adv. heat Transf.* 19, 247–356. Elsevier. doi:10.1016/S0065-2717(08)70214-4
- Hayase, T., Humphrey, J., and Greif, R. (1992). Numerical calculation of convective heat transfer between rotating coaxial cylinders with periodically embedded cavities. *J. Heat. Transf.* 114 (3), 589–597. doi:10.1115/1.2911322
- Jamil, M., and Fetecau, C. (2010). Helical flows of Maxwell fluid between coaxial cylinders with given shear stresses on the boundary. *Nonlinear Anal. Real World Appl.* 11 (5), 4302–4311. doi:10.1016/j.nonrwa.2010.05.016
- Khan, J. A., and Mustafa, M. (2018). A numerical analysis for non-linear radiation in MHD flow around a cylindrical surface with chemically reactive species. *Results Phys.* 8, 963–970. doi:10.1016/j.rinp.2017.12.067
- Liu, F., Anh, V., and Turner, I. (2004). Numerical solution of the space fractional Fokker–Planck equation. *J. Comput. Appl. Math.* 166 (1), 209–219. doi:10.1016/j.cam.2003.09.028
- Magin, R. L. (2010). Fractional calculus models of complex dynamics in biological tissues. *Comput. Math. Appl.* 59 (5), 1586–1593. doi:10.1016/j.camwa.2009.08.039
- Mahmood, A., Parveen, S., Ara, A., and Khan, N. (2009). Exact analytic solutions for the unsteady flow of a non-Newtonian fluid between two cylinders with fractional derivative model. *Commun. Nonlinear Sci. Numer. Simul.* 14 (8), 3309–3319. doi:10.1016/j.cnsns.2009.01.017
- Ming, C., Liu, F., Zheng, L., Turner, I., and Anh, V. (2016). Analytical solutions of multi-term time fractional differential equations and application to unsteady flows of generalized viscoelastic fluid. *Comput. Math. Appl.* 72 (9), 2084–2097. doi:10.1016/j.camwa.2016.08.012
- Nguyen, T. H., Vasseur, P., Robillard, L., and Chandra Shekar, B. (1983). Combined free and forced convection of water between horizontal concentric cylinders. *J. Heat. Transf.* 105 (3), 498–504. doi:10.1115/1.3245613
- Nieckele, A., and Patankar, S. (1985). Laminar mixed convection in a concentric annulus with horizontal axis. *J. Heat. Transf.* 107 (4), 902–909. doi:10.1115/1.3247519
- Rashad, A., Chamkha, A. J., and Abdou, M. (2013). Mixed convection flow of non-Newtonian fluid from vertical surface saturated in a porous medium filled with a nanofluid. *J. Appl. Fluid Mech.* 6 (2), 301–309.
- Rashad, A., and Nabwey, H. A. (2019). Gyrotactic mixed bioconvection flow of a nanofluid past a circular cylinder with convective boundary condition. *J. Taiwan Inst. Chem. Eng.* 99, 9–17. doi:10.1016/j.jtice.2019.02.035
- Rosseland, S. (2013). *Astrophysik: Auf atomtheoretischer Grundlage*, 11. Berlin, Germany: Springer-Verlag.
- Salah, F., (2013). MHD accelerated flow of Maxwell fluid in a porous medium and rotating frame. *Int. Sch. Res. Notices*.
- Saqib, M., Ali, F., Khan, I., Sheikh, N. A., Jan, S. A. A., and Samiulhaq (2018). Exact solutions for free convection flow of generalized jeffrey fluid: A caputo-fabrizio fractional model. *Alexandria Eng. J.* 57 (3), 1849–1858. doi:10.1016/j.aej.2017.03.017
- Saqib, M., Hanif, H., Abdeljawad, T., Khan, I., Shafie, S., and Sooppy Nisar, K. (2020). Heat transfer in mhd flow of Maxwell fluid via fractional cattaneo-friedrich model: A finite difference approach. *Comput. Mat. Contin.* 65 (3), 1959–1973. doi:10.32604/cmc.2020.011339
- Shah, N. A., Elnaqeeb, T., Animasaun, I. L., and Mahsud, Y. (2018). Insight into the natural convection flow through a vertical cylinder using caputo time-fractional derivatives. *Int. J. Appl. Comput. Math.* 4 (3), 80–18. doi:10.1007/s40819-018-0512-z
- Shah, N., Hajizadeh, A., Zeb, M., Ahmad, S., and Mahsud, Y. (2018). Effect of magnetic field on double convection flow of viscous fluid over a moving vertical plate with constant temperature and general concentration by using new trend of fractional derivative. *Open J. Math. Sci.* 2 (1), 253–265. doi:10.30538/oms2018.0033
- Sheikh, N. A., Ali, F., Saqib, M., Khan, I., Jan, S. A. A., Alshomrani, A. S., et al. (2017). Comparison and analysis of the Atangana–Baleanu and Caputo–Fabrizio fractional derivatives for generalized Casson fluid model with heat generation and chemical reaction. *Results Phys.* 7, 789–800. doi:10.1016/j.rinp.2017.01.025
- Srivastava, P. (1966). Non-steady helical flow of a visco-elastic liquid (Nonsteady helical flow of viscoelastic liquid contained in circular cylinder, noting occurrence of oscillations in fluid decaying exponentially with time). *Arch. Mech. Stosow.* 18 (2), 145–150.
- Subbarayudu, K., Suneetha, S., Bala Anki Reddy, P., and Rashad, A. M. (2019). Framing the activation energy and binary chemical reaction on CNT's with Cattaneo–Christov heat diffusion on Maxwell nanofluid in the presence of nonlinear thermal radiation. *Arabian J. Sci. Eng.* 44 (12), 10313–10325. doi:10.1007/s13369-019-04173-2
- Sun, H., Zhang, Y., Wei, S., Zhu, J., and Chen, W. (2018). A space fractional constitutive equation model for non-Newtonian fluid flow. *Commun. Nonlinear Sci. Numer. Simul.* 62, 409–417. doi:10.1016/j.cnsns.2018.02.007
- Taitel, Y., and Hartnett, J. (1968). Application of Rosseland approximation and solution based on series expansion of the emission power to radiation problems. *AIAA J.* 6 (1), 80–89. doi:10.2514/3.4444
- Ting, T. W. (1963). Certain non-steady flows of second-order fluids. *Archive Ration. Mech. Analysis* 14 (1), 1–26. doi:10.1007/bf00250690
- Tiwari, R. K., and Das, M. K. (2007). Heat transfer augmentation in a two-sided lid-driven differentially heated square cavity utilizing nanofluids. *Int. J. heat Mass Transf.* 50 (9–10), 2002–2018. doi:10.1016/j.ijheatmasstransfer.2006.09.034
- Usman, M., Hamid, M., Zubair, T., Ul Haq, R., and Wang, W. (2018). Cu-ALO/Water hybrid nanofluid through a permeable surface in the presence of nonlinear radiation and variable thermal conductivity via LSM. *Int. J. Heat Mass Transf.* 126, 1347–1356. doi:10.1016/j.ijheatmasstransfer.2018.06.005
- Waters, N., and King, M. (1971). The unsteady flow of an elastico-viscous liquid in a straight pipe of circular cross section. *J. Phys. D Appl. Phys.* 4 (2), 304–211. doi:10.1088/0022-3727/4/2/304
- Wood, W. (2001). Transient viscoelastic helical flows in pipes of circular and annular cross-section. *J. Newt. fluid Mech.* 100 (1–3), 115–126. doi:10.1016/s0377-0257(01)00130-6
- Zhang, Y., Jiang, J., and Bai, Y. (2019). MHD flow and heat transfer analysis of fractional Oldroyd-B nanofluid between two coaxial cylinders. *Comput. Math. Appl.* 78 (10), 3408–3421. doi:10.1016/j.camwa.2019.05.013
- Zhao, Q., Mao, B., Bai, X., Chen, C., and Wang, Z. (2022). Heat transfer suppression mechanism of magnetogasdynamic flow in a circular tube subjected to transverse magnetic field regulation. *Int. Commun. Heat Mass Transf.* 134, 105990. doi:10.1016/j.icheatmasstransfer.2022.105990

Nomenclature

velocity $u(r, t)$ (m/s)

temperature $T(r, t)$ (K)

density of nano-fluid ρ_{nf} (kg/m^3)

dynamic viscosity of nano-fluid μ_{nf} (kg/ms)

thermal conductivity of nano-fluid K_{nf} (W/mK)

volumetric thermal expansion coefficient β_θ (K^{-1})

gravitational acceleration g (m/s^2)

heat capacity of nanoparticles $(C_p)_{nf}$

electrical conductivity of nanoparticles σ_{nf} (S/m)

kinematic viscosity of nanoparticles ν_{nf} (m^2/s)

volume fraction of nanoparticles ϕ

radius of the inner cylinder R_1

radius of the outer cylinder R_2



OPEN ACCESS

EDITED BY

Safia Akram,
National University of Sciences and
Technology, Pakistan

REVIEWED BY

Mustafa Turkyilmazoglu,
Hacettepe University, Türkiye
Zeeshan Asghar,
Prince Sultan University, Saudi Arabia

*CORRESPONDENCE

Umair Khan,
✉ Umairkhan@iba-suk.edu.pk

SPECIALTY SECTION

This article was submitted to
Colloidal Materials and Interfaces,
a section of the journal
Frontiers in Materials

RECEIVED 13 November 2022

ACCEPTED 29 December 2022

PUBLISHED 12 January 2023

CITATION

Rawat SK, Yaseen M, Khan U, Kumar M,
Eldin SM, Alotaibi AM and Galal AM (2023),
Significance of non-uniform heat source/
sink and cattaneo-christov model on
hybrid nanofluid flow in a Darcy-
forchheimer porous medium between two
parallel rotating disks.
Front. Mater. 9:1097057.
doi: 10.3389/fmats.2022.1097057

COPYRIGHT

© 2023 Rawat, Yaseen, Khan, Kumar, Eldin,
Alotaibi and Galal. This is an open-access
article distributed under the terms of the
[Creative Commons Attribution License](https://creativecommons.org/licenses/by/4.0/)
(CC BY). The use, distribution or
reproduction in other forums is permitted,
provided the original author(s) and the
copyright owner(s) are credited and that
the original publication in this journal is
cited, in accordance with accepted
academic practice. No use, distribution or
reproduction is permitted which does not
comply with these terms.

Significance of non-uniform heat source/sink and cattaneo-christov model on hybrid nanofluid flow in a Darcy-forchheimer porous medium between two parallel rotating disks

Sawan Kumar Rawat¹, Moh Yaseen², Umair Khan^{3,4*}, Manoj Kumar⁵,
Sayed M. Eldin⁶, Abeer M. Alotaibi⁷ and Ahmed M. Galal^{8,9}

¹Department of Mathematics, Graphic Era Deemed to be University, Dehradun, Uttarakhand, India, ²Department of Applied Science, Meerut Institute of Engineering and Technology, Meerut, Uttar Pradesh, India, ³Department of Mathematical Sciences, Faculty of Science and Technology, Universiti Kebangsaan Malaysia (UKM), Bangi, Selangor, Malaysia, ⁴Department of Mathematics and Social Sciences, Sukkur IBA University, Sukkur, Sindh, Pakistan, ⁵Department of Mathematics, Statistics and Computer Science, G. B. Pant University of Agriculture and Technology, Pantnagar, Uttarakhand, India, ⁶Center of Research, Faculty of Engineering, Future University in Egypt, New Cairo, Egypt, ⁷Department of Mathematics, Faculty of Science, University of Tabuk, Tabuk, Saudi Arabia, ⁸Department of Mechanical Engineering, College of Engineering in Wadi Alldawasir, Prince Sattam bin Abdulaziz University, Al-Kharj, Saudi Arabia, ⁹Production Engineering and Mechanical Design Department, Faculty of Engineering, Mansoura University, Mansoura, Egypt

The suspension of nanoparticles in fluid influences several properties of the resulting fluid. Many production and manufacturing applications need knowledge of the heat transference mechanism in nanofluids. The current paper concerns the influence of non-uniform heat source/sink on (MoS₂-Go/water flow) hybrid nanofluid flow and (Go/water flow) nanofluid flow in a Darcy-Forchheimer porous medium between two parallel and infinite spinning disks in the occurrence of radiation. The Cattaneo-Christov model is utilized to analyze heat and mass transmission. The Cattaneo-Christov model introduces the time lag factors in the process of heat and mass transmission, known as the thermal relaxation parameter and solutal relaxation parameter, respectively. The governing equations are numerically solved employing the "bvp4c function in MATLAB." The effect of the primary relevant parameters on the velocity, temperature, nanoparticle concentration, and is graphically depicted. Finally, a table is drawn to show the relationships of various critical factors on the Nusselt number, and Sherwood number. Results reveal that an increase in the thermal relaxation parameter reduces the heat transmission rate at both the upper and lower plate. Furthermore, an increase in the nanoparticle's volume fraction causes enhancement in thermal conduction, which increases the heat transmission rate at the upper disk. The results of this study will be helpful to many transportation processes, architectural design systems, enhanced oil recovery systems, medical fields that utilize nanofluids, and so on.

KEYWORDS

rotating disks, hybrid nanofluid, cattaneo-christov model, Darcy-forchheimer porous medium, non-uniform heat source/sink

1 Introduction

To address today's escalating energy demands, the variety of industries has risen exponentially. Optimizing heating performance is an essential alternative for improving cooling and heating efficiency in nuclear and chemical reactors, electronic equipment, and so on. To extract the most out of these applications, scientists and researchers are very much concerned about boosting heating efficiency. [Turkylmazoglu \(2022a\)](#) studied the influence of a horizontal uniform magnetic field in the flow instigated by a rotating disk. In another study, [Turkylmazoglu \(2022b\)](#) investigated the influence of heat source/sink in the convective flow of fluids due to a vertical flat surface/cone immersed in porous media. [Ali et al. \(2019a\)](#) utilized the Bingham and Carreau models to investigate the complex rheology of slime. [Asghar et al. \(2020a\)](#) utilized the couple stress fluid model to study the movement of microorganisms in two-dimensional channel. [Ali et al. \(2019b\)](#) investigated the optimum speed of microorganisms through Carreau fluid models with under magnetic and porous effects. [Javid et al. \(2019\)](#) studied and gave the numerical solution of magnetically induced flow of fluid confined inside two curled peristaltic walls. [Asghar et al. \(2020b\)](#) studied the non-Newtonian fluid flow confined within a complex wavy walls of a 2-dimensional channel using Taylor's swimming sheet model. [Asghar et al. \(2022a\)](#) studied the non-Newtonian Couple stress fluid in 2-dimensional inclined channel with magnetic and electrical field. Some other remarkable studies on applications of fluid models on bio-medical fields can be referred from Refs. ([Asghar et al., 2020c](#); [Asghar et al., 2022d](#); [Asghar et al., 2022b](#); [Asghar et al., 2022c](#); [Asghar et al., 2023](#); [Wu et al., 2020](#); [Shah et al., 2022](#)). Two decades-long, exploration of nanofluids ([Choi, 1995](#)) has confirmed that they have superior heat transmission potential. The varied characteristics of nanoparticles (NPs) may be adjusted by modifying their size (diameter), substance (metallic oxides, non-metallic, metallic, etc.), and nanoparticle dispersion in the working fluid. Keeping in mind the properties, [Rahman et al. \(2022\)](#) studied the influence of suction and magnetic field on several water-based nanofluids over a decelerating rotating disk. They studied the different water-based nanofluids (NFs) with copper oxide, copper, alumina, silver, and titania. The primary issue with single nanoparticle NFs is that they have either better rheological characteristics or superior thermal networks. Mono nanoparticles lack all of the desirable characteristics needed for some applications. The features of nanofluids may be improved by adjusting the nanoparticle volume fraction; however, this has a limitation as the difficulty arises in the trade-off due rise in viscosity. This is a constraint, which may be overcome by combining more than one variety of NPs in the working fluid. Later, the researcher's developed hybrid nanofluids (HNFs) that optimize the exclusive features of many varieties of nanoparticles.

Many studies have used hybrid nanofluid combinations of metallic and non-metal oxide nanoparticles to maximize thermal performance and nanoparticle stability. The development of nanoclusters increases the relative viscosity of HNFs, and HNFs have superior thermal conductivity than solitary nanoparticle nanofluids and base fluids ([Ranga Babu et al., 2017](#)). [Ranga Babu et al. \(2017\)](#) also marked out that metal nanoparticles make a nanolayer atop metallic oxide nanoparticles, and it

produces a thermal interfacial layer between weak boundaries of the working fluid and hybrid NPs, resulting in significant thermal conductivity augmentation. [Devi and Devi \(2016\)](#) studied the significance of Newtonian heating in HNF flow over a three-dimensional stretched surface. They analyzed the comparative behavior of Cu–Al₂O₃/water and Cu/water. They concluded that HNF has a higher heat transmission rate (HTR) compared to NF. [Waqas et al. \(2021\)](#) also explained and gave the solution to a HNF flow problem over a rotating disk with non-linear radiation. They studied the model with water as a base fluid and SWCNT–TiO₂ and MWCNT–CoFe₂O₄ NPs. [Khan et al. \(2020c\)](#) expounded on the HNF flow over a thick moving surface instigated by mixed convection. They modeled the flow with water as a main fluid and SiO₂ and MoS₂ NPs. [Masood et al. \(2021\)](#) discussed the significance of a HNF flow over a stretched surface near a stagnation point. They studied the problem with heat generation/absorption and water as a working fluid with polystyrene and titanium oxide NPs. [Alrabaiah et al. \(2022\)](#) inspected the HNF flow inside a conical slit of a cone and a disk. They modeled the flow with water and magnesium oxide, and silver NPs. [Yaseen et al. \(2022c\)](#) expounded on the significance of the magnetic field on HNF flow and NF flow between two parallel plates. They studied the flow problem with MoS₂–SiO₂/H₂O–C₂H₆O₂ for HNF flow and MoS₂/H₂O for NF flow. [Qureshi et al. \(2021\)](#) investigated the HNF flow between two moving co-axial orthogonal disks. They considered the flow problem with water as a main fluid and titania and copper NPs and studied the significance of the magnetic field. [Rashid et al. \(2021\)](#) inspected the HNF flow over a cylinder in motion. They considered the flow problem with water as a main fluid and Titania and silver NPs. [Khan et al. \(2022\)](#) explicated the significance of suction in a HNF flow between two parallel plates. They considered the flow problem with water as a base fluid and carbon nanotubes and Fe₃O₄ NPs.

Technological advancements have considerably enhanced human interaction with fundamental tasks such as heating and cooling food and materials, transportation, and manufacturing. The heat alteration process in equipment or applications intended to suit social requirements is a key aspect typically seen in the aforementioned activities. This has been a significant issue for manufacturers over the decades, particularly recently, in improving the thermal control of various maneuvers in the electronic sector, power systems, thermal sector, and medicinal bids. For a long period, the Fourier law ([Fourier, 1822](#)) was used to analyze the heat transmission attributes. Years later, Cattaneo ([Cattaneo, 1948](#)) altered the Fourier law by including a parameter related to the time lag in the traditional Fourier law, which states that the heat transfer mechanism permits heat to be carried at a restricted pace through the transmission of heat waves. Later, Christov ([Christov, 2009](#)) used thermal relaxation time and the upper convective derivative of Oldroyd to overcome the limitation of the Cattaneo rule and arrive at a material invariant formulation. The developments by Cattaneo ([Cattaneo, 1948](#)) and Christov ([Christov, 2009](#)) have led the way for researchers to study the HTR with a time lag factor and it is called the Cattaneo-Christov heat flux model (CCM). Very recently, [Turkylmazoglu \(2021\)](#) provided an analytical explanation of the application of CCM in cooling and its role in enhancing the HTR from surfaces. In recent times; [Khan et al. \(2020b\)](#) explicated the consequence of the thermal stratification and CCM in the water-based

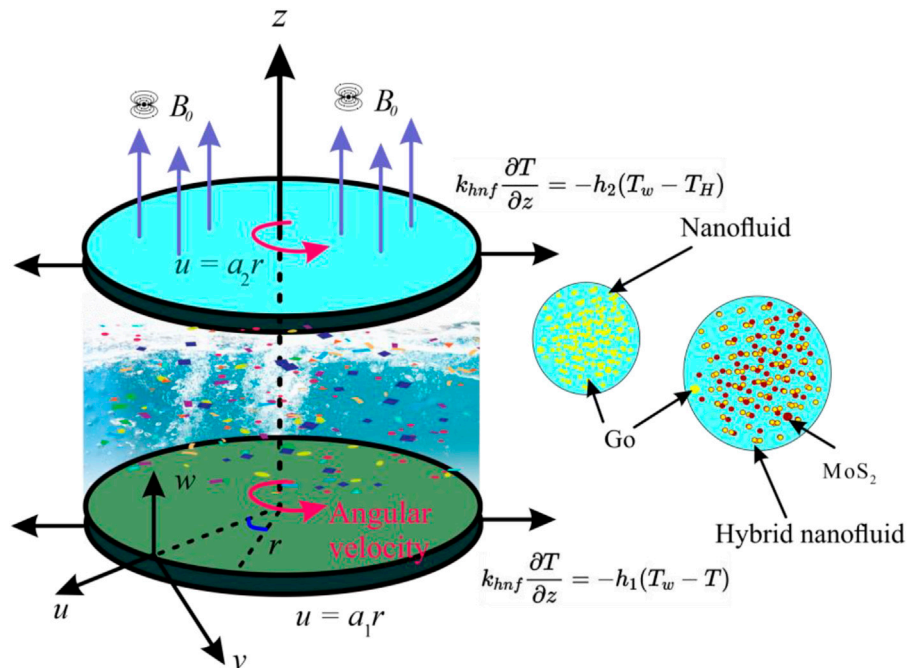


FIGURE 1
Physical Model.

NF flow over a surface having an exponential stretching rate. They analyzed the behavior of NF with three diverse NPs, namely, copper, Titania, and alumina; Yaseen et al. (2022a) studied the difference in HTR of MoS_2 /Kerosene oil and MoS_2 - SiO_2 /Kerosene oil flow between two spinning disks with CCM. They concluded that at the lower disk, the HTR of the hybrid nanofluid transcends the HTR of the nanofluid. (Ashraf and Ghehsareh (2021) explored the significance of CCM in the flow of Casson fluid past a heated surface; Kumar et al. (2021) studied the flow of water-based NF with carbon nanotubes (multi and single-walled) between two spinning disks in a porous medium with CCM. Bai et al. (2022) derived the analytical solution of an Oldroyd-B nanofluid flow problem through a vibrating tensile plate with CCM. Naz et al. (2022) also discussed the analytical solution of a Carreau nanoliquid flow problem over a rotating and stretchable disk with CCM. Some more interesting research on CCM can be found in Refs. (Irfan et al., 2018; Garia et al., 2021; Khan et al., 2021; Madhukesh et al., 2021).

According to the preceding discussion, it can be inferred that only a few studies are published to study the significance of HNF between two spinning disks. Authors have developed a model to analyze the HNF flow (MoS_2 -Go/water flow) and NF flow (Go/water flow) between two parallel and infinite spinning disks. Furthermore, as a novelty, the significance of non-uniform heat source/sink, CCM, thermal radiation, magnetic field, and Darcy-Forchheimer porous medium are also studied. This research paper also aims to analyze the HTR and mass transmission rate (MTR) of HNF flow (MoS_2 -Go/water flow) and NF flow (Go/water flow) at both disks. The numerical solution is sought via the bvp4c solver in MATLAB. As per the author's information, such a comparative analysis of the HNF flow (MoS_2 -Go/water) and NF flow (Go/water) between two parallel and infinite spinning disks has never been reported before and the results are new and novel.

2 Flow model and governing equations

2.1 Assumptions of the problem

Consider the three-dimensional incompressible, steady, and axisymmetric flow of the HNF (MoS_2 -Go/water) and NF (Go/water) between the two spinning infinite disks placed along parallel lines (see Figure 1). The notation (r, θ, z) has been used for the cylindrical coordinate system (see Figure 1). The flow is exposed to a magnetic field B_0 in the z -direction. As a novelty, to develop the model, the Darcy-Forchheimer law is used for porous medium. In addition, the non-uniform heat source/sink, Cattaneo-Christov double diffusion model, and thermal radiation is used to investigate HTR and MTR. Moreover, the last term in the energy equation (Eq. 5) denotes the non-uniform heat source/sink term (q''') and it is explained later. The lower disk and upper disk are placed at $z = 0$ and $z = H$ (see Eq. 7). In the boundary conditions, a_1 and a_2 denote the shrinkage rates of the lower and upper disks in the radial direction, respectively. Furthermore, b_1 and b_2 are taken as the angular velocities of the lower and upper disks, respectively. The outer surfaces of the disks are assumed to be convectively heated by hot liquids having temperatures T_w (lower disk) and T_H (upper disk), with h_1 (lower disk) and h_2 (upper disk) as their heat transfer coefficients. In addition, C_w and C_H denote the NPs concentration at the lower and upper disks, respectively.

Based on the aforesaid points, the flow equations are (see Bhattacharyya et al., 2020; Mabood et al., 2021; Yaseen et al., 2022a):

Continuity equation:

$$\frac{\partial u}{\partial r} + \frac{\partial w}{\partial z} + \frac{u}{r} = 0 \quad (1)$$

Momentum equations:

$$\rho_{hmf} \left(u \frac{\partial u}{\partial r} + w \frac{\partial u}{\partial z} - \frac{v^2}{r} \right) = -\frac{\partial p}{\partial r} + \mu_{hmf} \left(\frac{\partial^2 u}{\partial r^2} + \frac{\partial^2 u}{\partial z^2} + \frac{1}{r} \frac{\partial u}{\partial r} - \frac{u}{r^2} \right) - \sigma_{hmf} B_0^2 u - \frac{\mu_{hmf}}{k_{fn}} u - \frac{\rho_{hmf} F}{\sqrt{k_{fn}}} u^2 \quad (2)$$

$$\rho_{hmf} \left(u \frac{\partial v}{\partial r} + w \frac{\partial v}{\partial z} + \frac{uv}{r} \right) = \mu_{hmf} \left(\frac{\partial^2 v}{\partial r^2} + \frac{\partial^2 v}{\partial z^2} + \frac{1}{r} \frac{\partial v}{\partial r} - \frac{v}{r^2} \right) - \sigma_{hmf} B_0^2 v - \frac{\mu_{hmf}}{k_{fn}} v - \frac{\rho_{hmf} F}{\sqrt{k_{fn}}} v^2 \quad (3)$$

$$\rho_{hmf} \left(w \frac{\partial w}{\partial z} + u \frac{\partial w}{\partial r} \right) = -\frac{\partial p}{\partial z} + \mu_{hmf} \left(\frac{\partial^2 w}{\partial r^2} + \frac{1}{r} \frac{\partial w}{\partial r} + \frac{\partial^2 w}{\partial z^2} \right) \quad (4)$$

Energy equation:

$$u \frac{\partial T}{\partial r} + w \frac{\partial T}{\partial z} + \gamma_t \left(\frac{\partial T}{\partial r} \left(w \frac{\partial u}{\partial z} + u \frac{\partial w}{\partial r} \right) + \frac{\partial T}{\partial z} \left(w \frac{\partial w}{\partial z} + u \frac{\partial w}{\partial r} \right) + 2uw \frac{\partial^2 T}{\partial z \partial r} + u^2 \frac{\partial^2 T}{\partial r^2} + w^2 \frac{\partial^2 T}{\partial z^2} \right) = \frac{1}{(\rho C_p)_{hmf}} \left(k_{hmf} + \frac{16\sigma^* T_H^3}{3k^*} \right) \left(\frac{\partial^2 T}{\partial r^2} + \frac{\partial^2 T}{\partial z^2} + \frac{1}{r} \frac{\partial T}{\partial r} \right) + \frac{q''' }{(\rho C_p)_{hmf}} \quad (5)$$

Concentration equation:

$$u \frac{\partial C}{\partial r} + w \frac{\partial C}{\partial z} + \gamma_c \left(\frac{\partial C}{\partial r} \left(w \frac{\partial u}{\partial z} + u \frac{\partial w}{\partial r} \right) + \frac{\partial C}{\partial z} \left(w \frac{\partial w}{\partial z} + u \frac{\partial w}{\partial r} \right) + 2uw \frac{\partial^2 C}{\partial z \partial r} + u^2 \frac{\partial^2 C}{\partial r^2} + w^2 \frac{\partial^2 C}{\partial z^2} \right) = D \left[\frac{1}{r} \frac{\partial C}{\partial r} + \frac{\partial^2 C}{\partial r^2} + \frac{\partial^2 C}{\partial z^2} \right] \quad (6)$$

with Boundary conditions (BCs):

$$\left. \begin{aligned} u = a_1 r, v = b_1 r, w = 0, k_{hmf} \frac{\partial T}{\partial z} = -h_1 (T_w - T), C = C_w \text{ at } z = 0 \\ u = a_2 r, v = b_2 r, w = 0, k_{hmf} \frac{\partial T}{\partial z} = -h_2 (T - T_H), C = C_H \text{ at } z = H \end{aligned} \right\} \quad (7)$$

where “(u, v, w) are the velocity components along with (r, θ , z) directions,” respectively, “C is nanoparticles concentration,” “T is temperature,” “p is pressure,” “k* is the mean absorption coefficient,” “ σ^* is the Stefan-Boltzmann constant,” “F is the Forchheimer coefficient and k_{fn} is the porous medium permeability,” respectively, “D is diffusion coefficient,” “ γ_t is the thermal relaxation time,” and “ γ_c is the solutal relaxation time.” Furthermore, “k is thermal conductivity, μ is dynamic viscosity, C_p is heat capacity, ρ is density, σ is electrical conductivity.” Moreover, subscript *hmf* is for hybrid nanofluid, *nf* is for nanofluid, and *f*, *bf* is for fluid. In addition, the last term in the energy Eq. 5 i.e., q''' denotes the significance of “non-uniform heat source/sink” and it is demarcated as follows (Yaseen et al., 2022b):

$$q''' = \frac{k_{hmf} u_w (T_w - T_H)}{r v_{hmf}} \left\{ A^* \frac{df}{d\xi} + B^* \theta \right\} \quad (8)$$

where $u_w = b_1 r$ and the heat source/sink corresponding to space coefficients and corresponding to temperature dependence are signified by constants A^* and B^* , respectively. As a result, the heat

TABLE 1 Thermo-physical properties of water, MoS₂ and Go nanoparticles (Khan et al., 2020d).

	ρ (Kg/m ³)	C_p (J/KgK)	k (W/mK)	σ ($\Omega \cdot m$) ⁻¹
Water	997.1	4,179	.613	.05
Go	1800	717	5,000	6.30×10^7
MoS ₂	5,060	397.746	904.4	2.09×10^4

source phenomena is characterized by $A^* > 0$ and $B^* > 0$, whereas the heat sink phenomena is characterized by $A^* < 0$ and $B^* < 0$.

2.2 Properties of hybrid nanofluid and nanofluid

This study describes the analysis of HNF and NF. The thermal characteristics of HNF and NF are influenced by the base fluid (water) and NPs; as well as by the volume fraction of MoS₂ and Go NPs, as shown in Table 1 (Khan et al., 2020d). The Shape of MoS₂ and Go NPs is taken as spherical. In this paper, the volume fraction of Go NPs and MoS₂ NPs is denoted by ϕ_1 and ϕ_2 , respectively. Furthermore, s_1 is used for Go NPs, and s_2 is used for MoS₂ NPs. The MoS₂ belongs to the transition metal class and Go belongs to the oxide class. The combination of MoS₂ and Go NPs is taken because metal nanoparticles make a nanolayer atop oxide nanoparticles, and it produces a thermal interfacial layer between weak boundaries of the working fluid and hybrid NPs, resulting in thermal conductivity augmentation.

2.2.1 Thermophysical correlations of Go/water nanofluid

The thermophysical correlations of the NF model used are as follows (Rawat and Kumar, 2020):

$$\frac{\mu_{nf}}{\mu_f} = \frac{1}{(1 - \phi_1)^{2.5}}, \rho_{nf} = (1 - \phi_1)\rho_f + \phi_1\rho_{s1}, \frac{k_{nf}}{k_f} = \frac{[k_{s1} + 2k_f - 2\phi_1(k_f - k_{s1})]}{[k_{s1} + 2k_f + \phi_1(k_f - k_{s1})]} \quad (9)$$

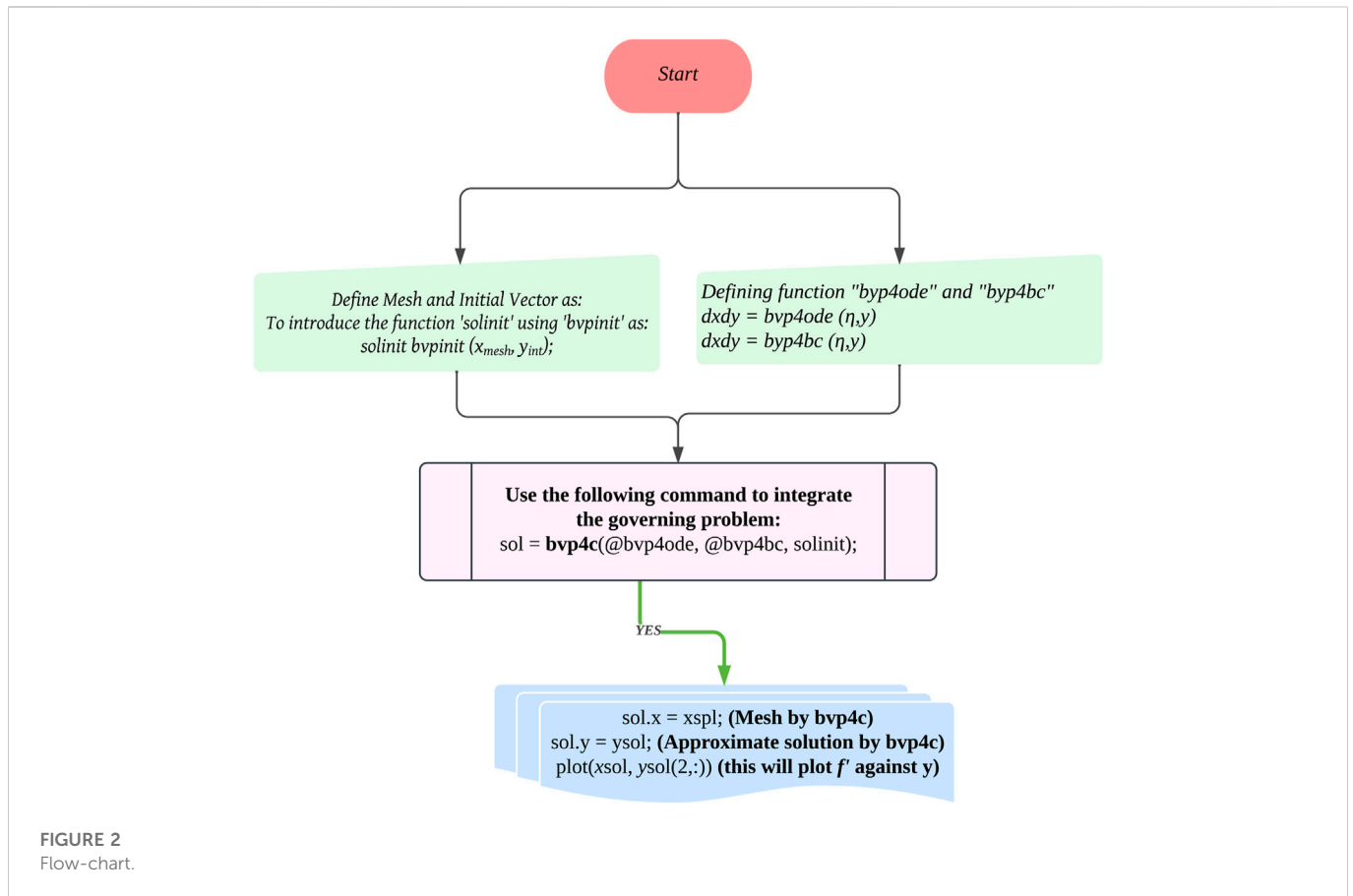
$$\frac{\sigma_{nf}}{\sigma_f} = 1 + \frac{3(\sigma - 1)\phi_1}{2 + \sigma - (\sigma - 1)\phi_1} \text{ where } \sigma = \sigma_{s1} / \sigma_f, (\rho C_p)_{nf} = (1 - \phi_1)(\rho C_p)_f + \phi_1(\rho C_p)_{s1} \quad (10)$$

2.2.2 Thermophysical correlations of MoS₂-Go/water hybrid nanofluid

The thermophysical correlations of the HNF model used are as follows (Khan et al., 2020c):

$$\rho_{hmf} = (1 - \phi_2) [(1 - \phi_1)\rho_f + \phi_1\rho_{s1}] + \phi_2\rho_{s2}, \frac{\mu_{hmf}}{\mu_f} = \frac{1}{(1 - \phi_1)^{2.5} (1 - \phi_2)^{2.5}} \quad (11)$$

$$\frac{k_{hmf}}{k_{bf}} = \frac{[k_{s2} + 2k_{bf} - 2\phi_2(k_{bf} - k_{s2})]}{[k_{s2} + 2k_{bf} + \phi_2(k_{bf} - k_{s2})]} \text{ where } \frac{k_{bf}}{k_f} = \frac{[k_{s1} + 2k_f - 2\phi_1(k_f - k_{s1})]}{[k_{s1} + 2k_f + \phi_1(k_f - k_{s1})]} \quad (12)$$



$$\frac{\sigma_{hmf}}{\sigma_{bf}} = \left[\frac{\sigma_{s2} + 2\sigma_{bf} - 2\varphi_2(\sigma_{bf} - \sigma_{s2})}{\sigma_{s2} + 2\sigma_{bf} + \varphi_2(\sigma_{bf} - \sigma_{s2})} \right] \text{ where } \frac{\sigma_{bf}}{\sigma_f} = \left[\frac{\sigma_{s1} + 2\sigma_f - 2\varphi_1(\sigma_f - \sigma_{s1})}{\sigma_{s1} + 2\sigma_f + \varphi_1(\sigma_f - \sigma_{s1})} \right] \quad (13)$$

$$(\rho C_p)_{hmf} = (1 - \varphi_2) \left[(1 - \varphi_1)(\rho C_p)_f + \varphi_1(\rho C_p)_{s1} \right] + \varphi_2(\rho C_p)_{s2} \quad (14)$$

$$P' + 4 \frac{\omega_2}{\omega_1} Re f f' + 2 f'' = 0 \quad (18)$$

$$(\omega_5 + R_d - \omega_4 Pr Re \tau_E f^2) \theta'' + \frac{Re \omega_5 \omega_2}{\omega_1} \{A^* f' + B^* \theta\} + \omega_4 Pr Re (2 f \theta' - \tau_E (f f' \theta')) = 0 \quad (19)$$

$$\phi'' = Re \tau_c Sc (f f' \phi' + f^2 \phi'') - 2 Re Sc f \phi' \quad (20)$$

The BCs are obtained as follows:

$$\left. \begin{aligned} f(\eta) = 0, f'(\eta) = k_1, g(\eta) = 1, \theta'(\eta) = -\frac{\gamma_1}{\omega_5} (1 - \theta(\eta)), P(\eta) = 0, \phi(\eta) = 1 \text{ at } \eta = 0 \\ f(\eta) = 0, f'(\eta) = k_2, g(\eta) = \Omega, \theta'(\eta) = -\frac{\gamma_2}{\omega_5} \theta(\eta), \phi(\eta) = 0 \text{ at } \eta = 1 \end{aligned} \right\} \quad (21)$$

2.3 Similarity transformations

The transformations listed below are utilized to transform the governing equations (Yaseen et al., 2022a):

$$\begin{aligned} u &= r b_1 f'(\eta), v = r b_1 g(\eta), w = -2 H b_1 f(\eta), P \\ &= b_1 \rho_{hmf} v_{hmf} \left[P(\eta) + \frac{r^2 \varepsilon}{2 H^2} \right], \xi = \frac{z}{H}, \theta = \frac{T - T_H}{T_w - T_H}, \phi = \frac{C - C_H}{C_w - C_H} \end{aligned} \quad (15)$$

Eq. 1 is satisfied, and Eqs 2, 3, 4, 5, 6, 7 reduce to

$$Re \frac{\omega_2}{\omega_1} \left(f'^2 - 2 f f'' - g^2 + \frac{\omega_3}{\omega_2} M f' + F^* f'^2 \right) + Re \lambda f' = -\varepsilon + f''' \quad (16)$$

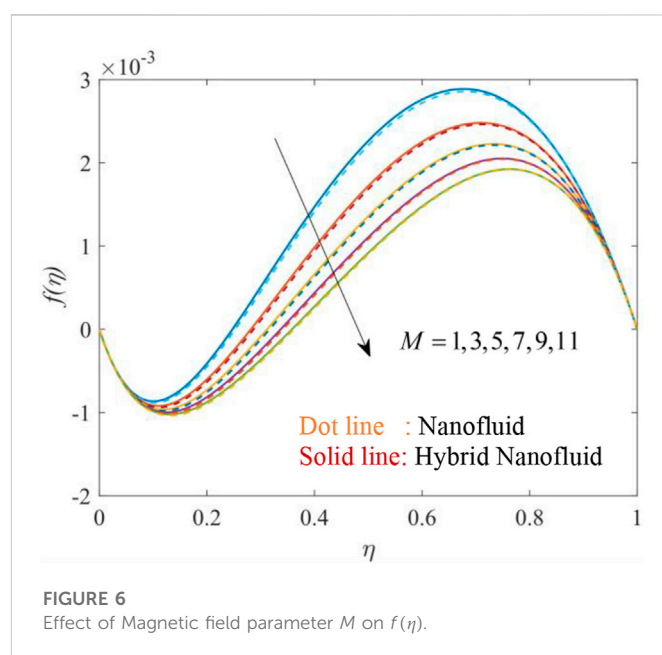
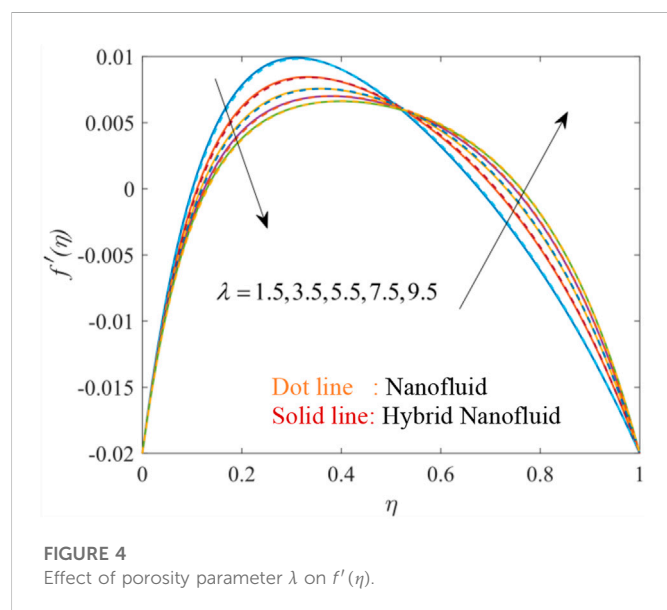
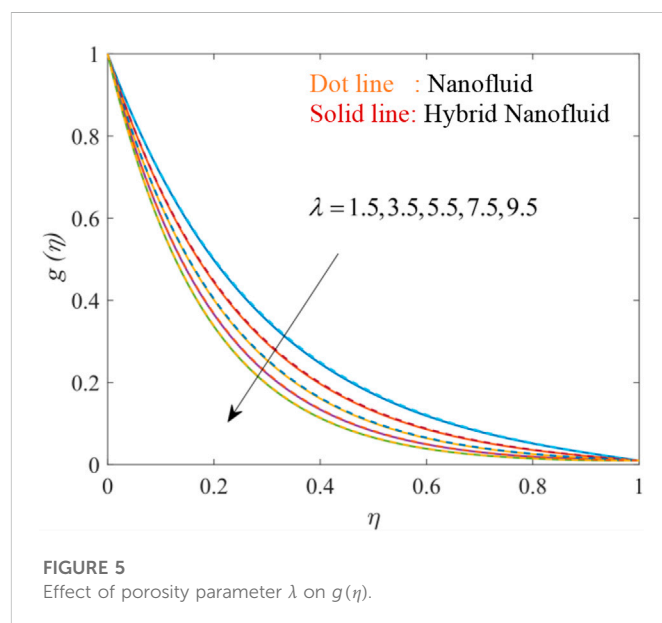
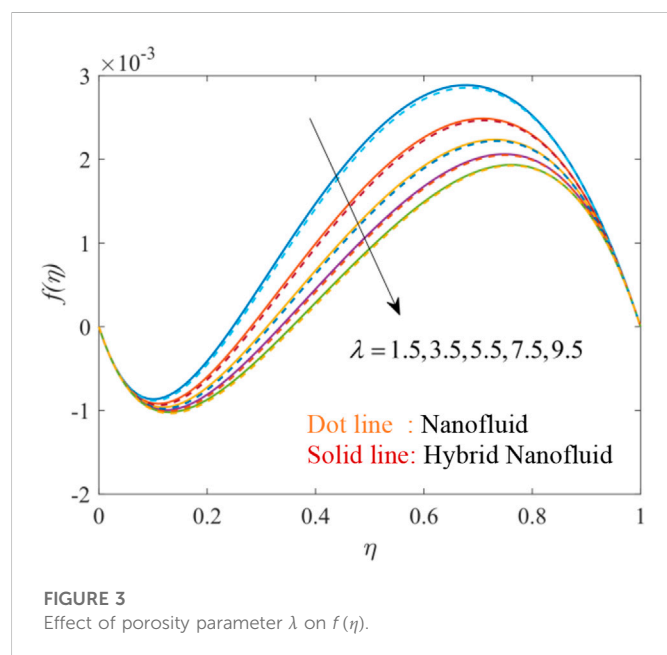
$$g'' - Re \lambda g = Re \frac{\omega_2}{\omega_1} \left(\frac{\omega_3}{\omega_2} g M + g F^* - 2 (g' f - f' g) \right) \quad (17)$$

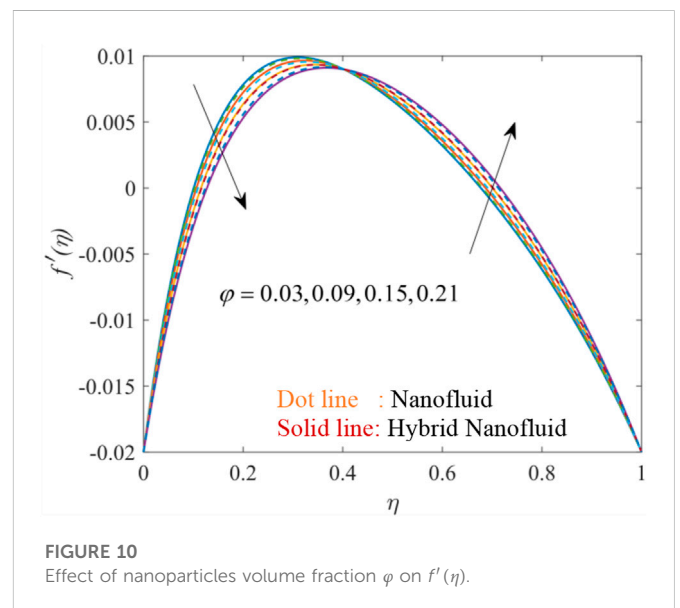
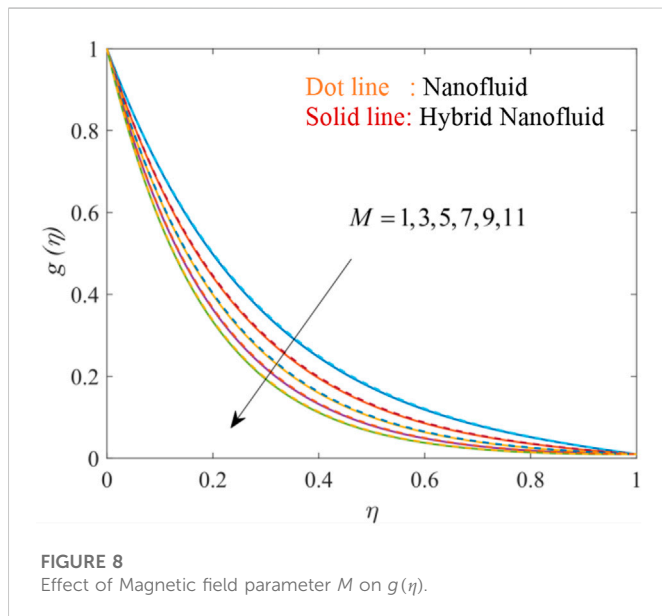
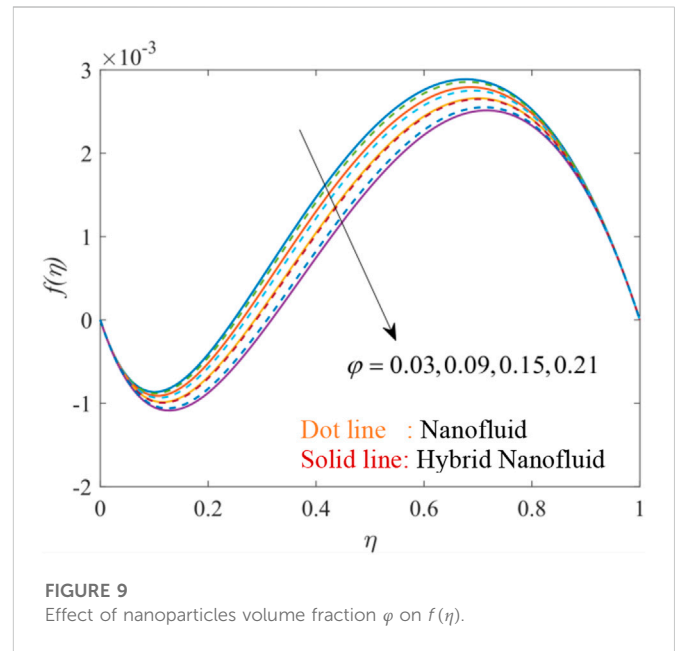
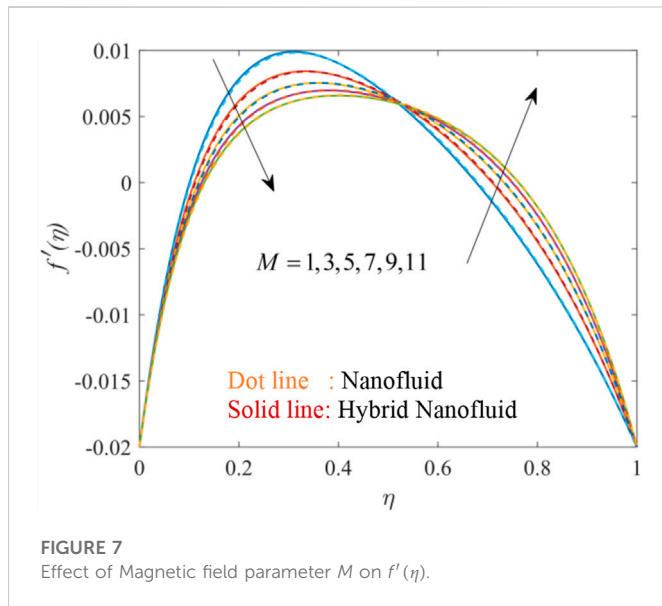
In the aforementioned equations, “ $Re (= \frac{b_1 H^2}{\nu_f})$ ” represents Reynold number, “ $F^* (= \frac{Fr}{\sqrt{k_{fn}}})$ ” represents the inertial coefficient, “ $Pr (= \frac{\nu_f}{\alpha_f})$ ” is the Prandtl number, “ $\lambda (= \frac{\nu_f}{b_1 k_{fn}})$ ” is the porosity parameter, “ $M (= \frac{\sigma_f B_0^2}{\rho_f b_1})$ ” represents the magnetic field parameter, “ A^* and “ B^* ” represents heat source/sink parameters, “ $R_d (= \frac{16 \sigma^* T_H^3}{3 k_f k^*})$ ” represents thermal radiation parameter, “ $\tau_E (= 4 \gamma_t b_1)$ ” represents the thermal relaxation parameter, “ $\tau_c (= 4 \gamma_c b_1)$ ” represents the solutal relaxation parameter, “ $k_1 (= \frac{a_1}{b_1})$ ” and “ $k_2 (= \frac{a_2}{b_1})$ ” represent shrinking parameters, “ $\Omega (= \frac{b_2}{b_1})$ ” is the rotation parameter, “ $\gamma_1 (= \frac{H h_1}{k_f})$ ” and “ $\gamma_2 (= \frac{H h_2}{k_f})$ ” are Biot numbers, “ $Sc (= \frac{\nu_f}{D})$ ” represents Schmidt number and “ $\omega_1 = \frac{\mu_f}{\mu_{hmf}}, \omega_2 = \frac{\rho_{hmf}}{\rho_f}, \omega_3 = \frac{\sigma_{hmf}}{\sigma_f}, \omega_4 = \frac{(\rho C_p)_{hmf}}{(\rho C_p)_f}, \omega_5 = \frac{k_{hmf}}{k_f}$ are constants”.

Eq. 16 is then differentiated w.r.t η for the elimination of ε (pressure variable), and we get:

TABLE 2 The comparison of the values $f''(0)$ and $g'(0)$ for the various value of Ω and the rest parameters are, $Pr = 6.2$, $\phi_1 = \phi_2 = M = F^* = \lambda = r = k_1 = k_2 = \gamma_1 = \gamma_2 = 0$.

Ω	$f''(0)$ (Khan et al., 2018)	$f''(0)$ [present]	$-g'(0)$ (Khan et al., 2018)	$-g'(0)$ [present]
-1	.06666314	.06666303	2.0009522	2.00095213
-0.8	.08394207	.08394201	1.8025885	1.80258846
-0.3	.10395088	.10395088	1.3044236	1.30442355
0	.09997221	.09997221	1.0042776	1.00427756
0.5	.06663419	.06663416	.5026135	.50261344





$$\omega_1 (f^{iv} - \lambda \text{Re} f'') + \omega_2 \text{Re} \left(2f f''' + 2g g' - M \frac{\omega_3}{\omega_2} f'' - 2f' f'' F^* \right) = 0 \quad (22)$$

Eqs 16–21 define the ε (pressure variable) as follows:

$$\varepsilon = f'''(0) - \text{Re} \frac{\omega_2}{\omega_1} \left(f'(0)^2 - 2f''(0)f(0) - g(0)^2 + F^* f'(0)^2 + \frac{\omega_3}{\omega_2} M f'(0) \right) - \lambda \text{Re} f'(0) \quad (23)$$

To solve Eqn. (18) for P , use integration from 0 to η and obtain the following form:

$$P = -2 \left\{ (f' - f'(0)) + \frac{\omega_2}{\omega_1} \text{Re} (f)^2 \right\} = 0 \quad (24)$$

3 Engineering parameters

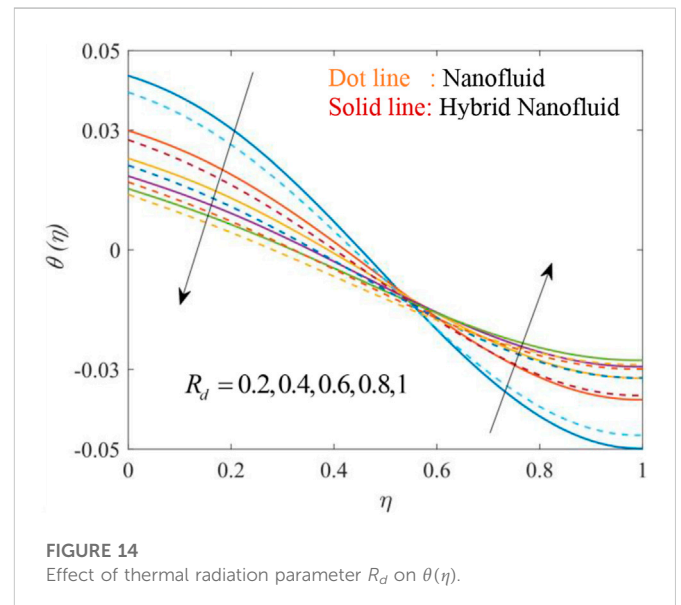
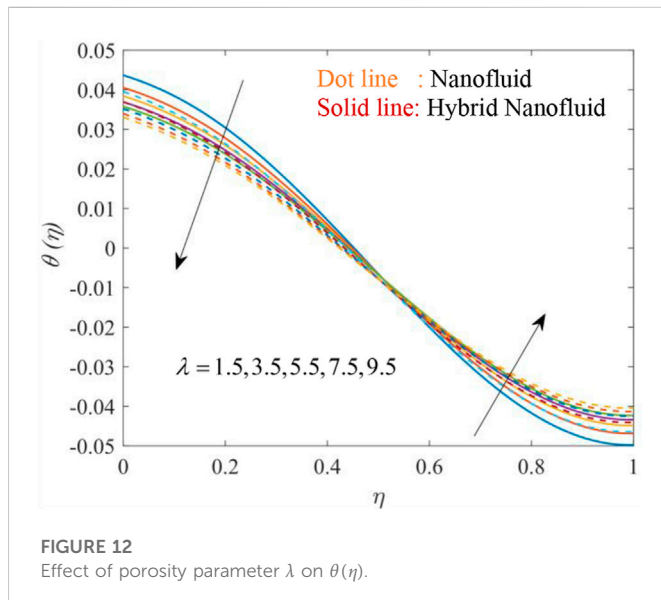
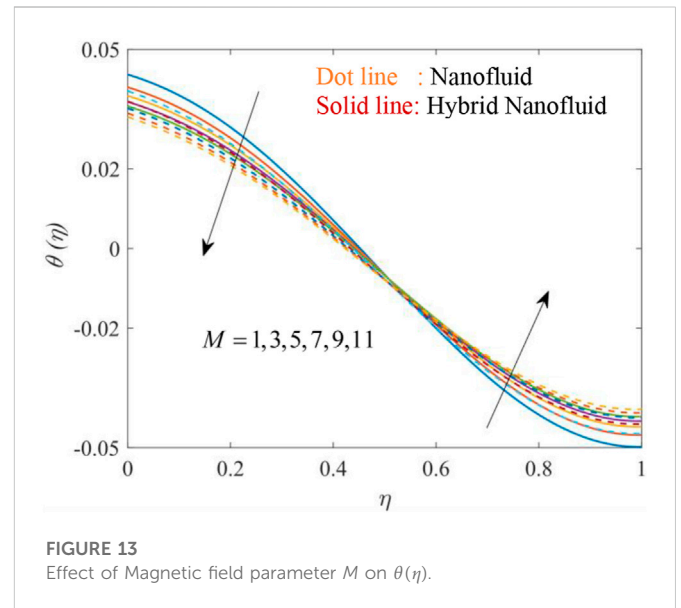
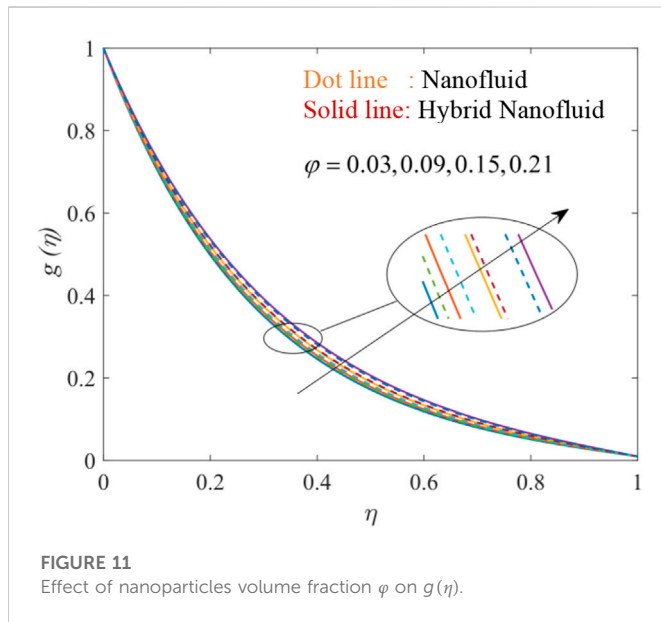
3.1 Nusselt numbers

The Nusselt numbers at the lower disk (Nu_{r0}) and upper disk (Nu_{r1}) are (Mabood et al., 2021) and (Yaseen et al., 2022a):

$$Nu_{r0} = -(\omega_4 + R_d) \theta'(0) \text{ and } Nu_{r1} = -(\omega_4 + R_d) \theta'(1) \quad (24a)$$

3.2 Sherwood numbers

The Sherwood numbers at the lower disk (Sh_{r0}) and upper disk (Sh_{r1}) are defined as (Khan et al., 2020a):



$$Sh_{r0} = -\phi'(0) \text{ and } Sh_{r1} = -\phi'(1) \quad (25)$$

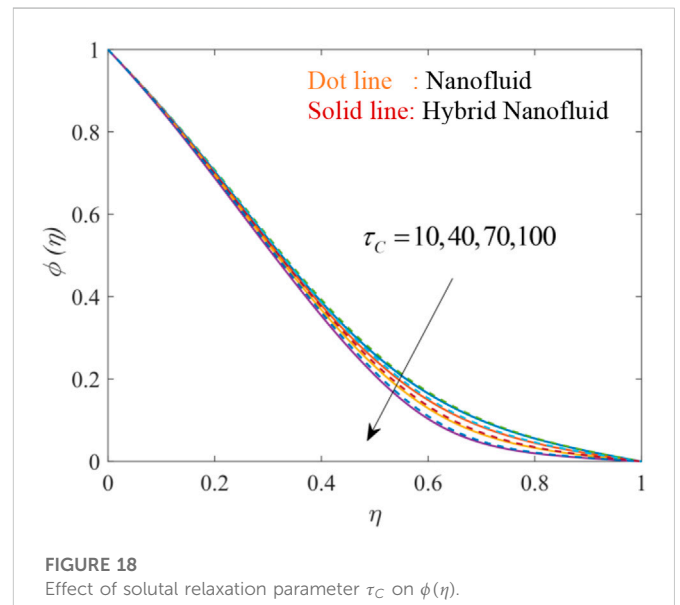
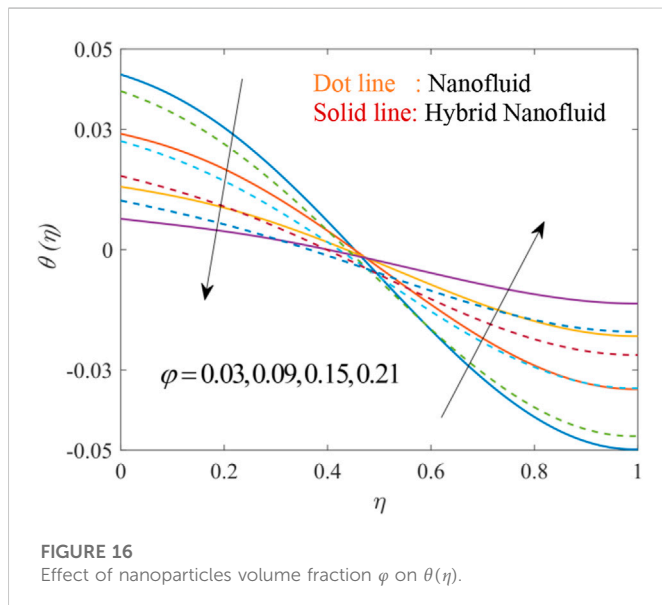
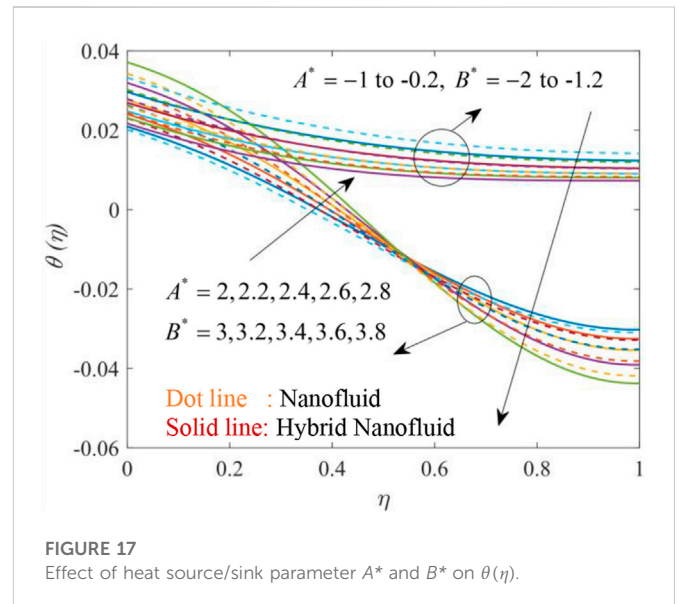
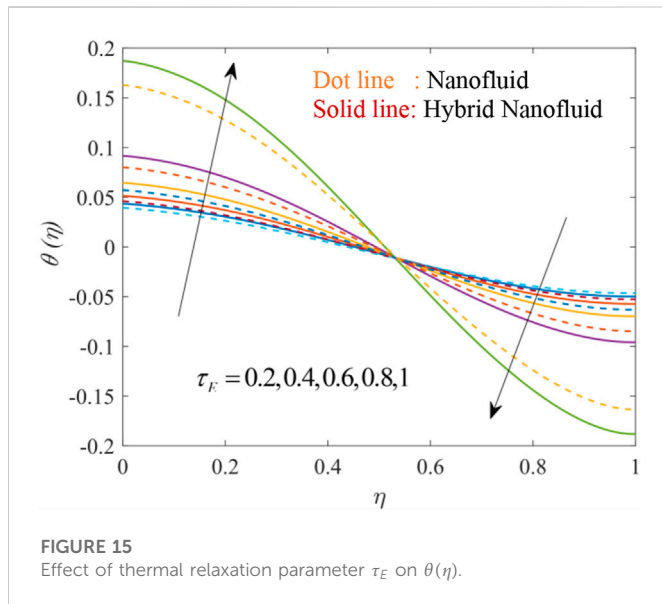
$$\begin{aligned} & "y_1 = f, y_2 = f', y_3 = f'', y_4 = f''', y_5 = g, y_6 = g', y_7 = \theta, y_8 = \theta', y_9 \\ & = \phi, y_{10} = \phi'" \end{aligned} \quad (26)$$

4 Methodology of numerical approach

This section focuses on the methodology used for deducing solutions as well as code validation. The equations are at first modeled as PDEs and later, converted into ODEs *via* similarity variables. The numerical solution of the Eqs 16, 17, 18, 19, 20 along with BCs (21) is deduced with the “bvp4c function” (a built-in package in MATLAB), the more specific details of the bvp4c function can be referred from the Shampine et al. (2003). The “bvp4c function” uses a finite difference scheme together with a precision of fourth order with the help of the “3-stage Lobatto IIIA formula”. To deduce the solution of the model, the ODEs obtained after similarity transformation are reduced into first-order ODEs by the following substitution:

Utilizing the new variables, the Eqs 16, 17, 18, 19, 20 are reduced to first-order ODEs and the following MATLAB syntax is used:

$$\begin{pmatrix} yy_1 \\ yy_2 \\ yy_3 \\ yy_4 \end{pmatrix} = \begin{pmatrix} Re \frac{\omega_2}{\omega_1} \left(-2y_1 y_4 - 2y_5 y_6 + \frac{\omega_3}{\omega_2} M y_3 + 2F^* y_2 y_3 \right) + \lambda Re y_3; \\ Re \frac{\omega_2}{\omega_1} \left(-2y_1 y_4 - 2y_5 y_6 + \frac{\omega_3}{\omega_2} M y_3 + 2F^* y_2 y_3 \right); \\ Re \frac{\omega_5 \omega_2}{\omega_1} \left(A_1 y_2 + B_1 y_7 \right) + \omega_4 Pr Re \left(2y_1 y_8 - \tau_E y_1 y_2 y_8 \right); \\ \frac{\omega_4 + R_d - \omega_3 \tau_E Pr Re y_1^2}{1 - Re \tau_c Sc y_1^2}; \end{pmatrix} \quad (27)$$



The above system Eq. 27 is subjected to the following BCs at the lower disk ($\eta = 0$) and upper disk ($\eta = 1$):

$$\left. \begin{aligned} y_1 = 0, y_2 = k_1, y_5 = 1, y_8 = -\frac{\gamma_1}{\omega_5}(1 - y_7), y_9 = 1 \text{ at } \eta = 0 \\ y_1 = 0, y_2 = k_2, y_5 = \Omega, y_8 = -\frac{\gamma_2}{\omega_5}y_7, y_9 = 0 \text{ at } \eta = 1 \end{aligned} \right\} \quad (28)$$

From new variables in Eq. 26 and BCs Eq. 28, it is seen that the following conditions at the ($\eta = 0$) and ($\eta = 1$) are missing:

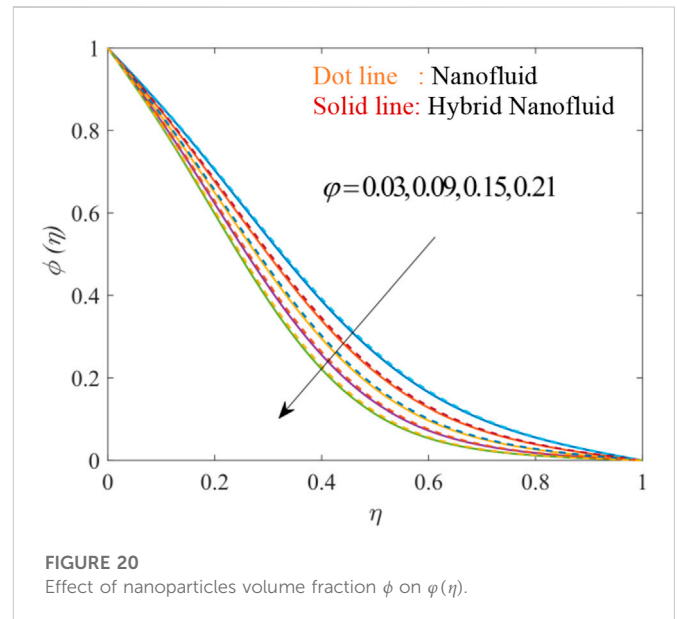
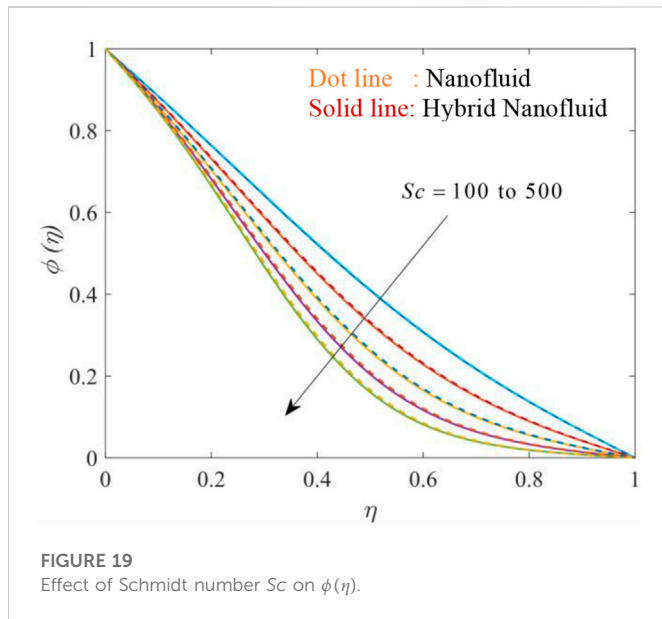
$$y_3(0), y_3(1), y_4(0), y_4(1), y_6(0), y_6(1), y_7(0), y_7(1), y_{10}(0), \text{ and } y_{10}(1) \quad (29)$$

Furthermore, the values of missing conditions are guessed to initiate the process of finding the solution and other parameters present in the Eqs 27, 28 are set to find the desired solution. The

process of iteration is repeated and the solution is accepted only when the conditions in Eq. 28 are satisfied. The process of finding the solution is shown *via* a flow chart in Figure 2. To validate the model and the code used to find the numerical solution, an assessment in Table 2 is outlined with the published computations of (Khan et al., 2018) study as a limiting case to validate the numerical code utilized to solve the current model. The comparative results are quite consistent, ensuring that the current conclusions are valid.

5 Results and discussion

This section focuses on the numerical outcomes and graphical and tabular results are interpreted physically. Authors have used



the following general values in the numerical computations: $Pr = 6.2$, $M = 1$, $Re = 2.2$, $Sc = 300$, $F^* = 3$, $\lambda = 1.5$, $R_d = .2$, $\tau_E = 1$, $\tau_C = 10$, $A^* = 3$, $B^* = 3$, $\Omega = 0.01$, $\gamma_1 = .05$, $\gamma_2 = 0.1$, $-k_1 = -k_2 = .02$, and $\phi_1 = \phi_2 = .03$. The analysis is performed for the porosity parameter ($1.5 \leq \lambda \leq 9.5$), magnetic field parameter ($1 \leq M \leq 11$), nanoparticles volume fraction ($.03 \leq \phi \leq .21$), thermal radiation parameter ($.2 \leq R_d \leq 1$), thermal relaxation parameter ($.2 \leq \tau_E \leq 161$), heat source/sink parameters ($-1 \leq A^* \leq 3$, $-2 \leq B^* \leq 4$), solutal relaxation parameter ($10 \leq \tau_c \leq 100$), and Schmidt number ($100 \leq Sc \leq 500$). The influence of the primary relevant factors on the velocity, temperature, and nanoparticle concentration is graphically depicted. Finally, a Table is drawn to show the relationships of various critical factors on the Nusselt and Sherwood number. The results are shown for both HNF (MoS₂-Go/water flow) and NF (Go/water flow) and in the figures, solid lines are drawn for HNF and dot lines are drawn for NF.

5.1 Velocity distribution

Figures 3, 4, 5, 6, 7, 8, 9, 10, 11 show the fluctuation of dimensionless velocity against the similarity variable while altering distinct flow-regulating parameters one at a time while leaving others unchanged. Figures 3, 4, 5 depict the influence of porosity parameter λ on axial velocity distribution $f(\eta)$, radial velocity distribution $f'(\eta)$, and tangential velocity distribution $g(\eta)$, respectively. Within the core areas of the boundary layer region (BLR), there is a noticeable decrease in the axial velocity distribution $f(\eta)$ and tangential velocity distribution $g(\eta)$ with growing values of λ . The radial velocity shows transitioning nature in BLR and the transition point lies near $\eta \sim 0.5$. $f'(\eta)$ rises near the lower disk and behavior changes near the upper disk w.r.t to growing values of λ . Physically, the porosity parameter is linked to the friction force. Resistance increases with a rise in the porosity parameter, and therefore the velocity falls. Figures 6, 7, 8 elucidate the effectiveness of magnetic parameter M on $f(\eta)$, $f'(\eta)$ and $g(\eta)$. The increasing magnitude of

parameter M is responsible for the decrease in velocity $f(\eta)$ and $g(\eta)$. The radial velocity $f'(\eta)$ shows transitioning nature in BLR w.r.t parameter M . The decrease in the velocity $f(\eta)$ and $g(\eta)$ is related to the generation of Lorentz force. The presence of magnetic force generates the Lorentz force opposite to the flow direction, hence it opposes the motion, and hence velocity decreases.

Figures 9, 10, 11 elucidate the effectiveness of volume fraction on velocity distribution. On increasing the volume fraction of each nanoparticle Go (ϕ_1), and MoS₂ (ϕ_2) in equal quantity (ϕ), the axial velocity $f(\eta)$ decreases and tangential velocity $g(\eta)$ increases, whereas radial velocity $f'(\eta)$ shows transitioning nature in BLR, i.e., it first decreases and then increases. The increasing nanoparticles volume fraction in the base fluid causes the hindrance for the motion in the axial direction, hence the velocity $f(\eta)$ decreases. On contrary, the tangential velocity $g(\eta)$ increases, because the addition of nanoparticles causes the outward movement of fluid. In Figures 3, 4, 5, 6, 7, 8, 9, 10, 11, the authors have presented a comparison in velocity profiles of HNF (MoS₂-Go/water flow) and NF (Go/water flow). HNF is seen to have the higher axial velocity $f(\eta)$ and NF has the higher tangential velocity $g(\eta)$. Near the lower disk, HNF has a higher radial velocity, but as fluid approaches the upper disk, NF has a higher radial velocity.

5.2 Temperature distribution

Figures 12, 13, 14, 15, 16, 17 show the fluctuation of dimensionless temperature $\theta(\eta)$ against the similarity variable while altering distinct flow-regulating parameters one at a time while leaving others unchanged. Figures 12, 13, 14 depict the influence of porosity parameter λ , magnetic parameter M , and radiation parameter R_d on the temperature profile. It is observed that with an increment in the aforesaid parameters, the temperature $\theta(\eta)$ shows transitioning nature in BLR. The temperature $\theta(\eta)$ falls near the lower disk and rises near the upper disk. The effect of resistance forces due to the porosity parameter and the effect of generated Lorentz force due to the magnetic field is significant near

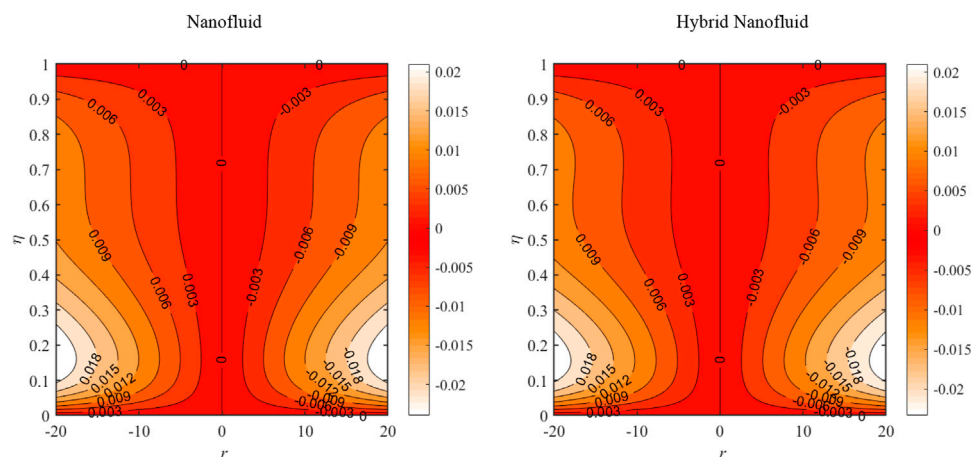


FIGURE 21
Streamlines for Nanofluid and Hybrid nanofluid.

TABLE 3 Numerical values of the heat transfer coefficient and Sherwood number when $Pr = 6.2$.

A^*	B^*	R_d	τ_E	τ_C	Sc	ϕ_1	ϕ_2	Hybrid nanofluid				Nanofluid			
								Lower disk		Upper disk		Lower disk		Upper disk	
								Nu_{r0}	Sh_{r0}	Nu_{r1}	Sh_{r1}	Nu_{r0}	Sh_{r0}	Nu_{r1}	Sh_{r1}
-1	-2	0.2	1	10	300	.03	.03	.057107		.000849		.057708		.000970	
-0.6	-1.6							.056925		.001055		.057502		.001219	
-0.2	-1.2							.056643		.001438		.057182		.001672	
2	3							.057153		-.00352		.057958		-.00365	
2.4	3.4							.056760		-.00413		.057598		-.00416	
2.8	3.8							.056207		-.00510		.057123		-.00495	
3	4	0.2						.056731	1.362876	-.00421	.2360413	.056977	1.362876	-.00519	.2360413
		0.6						.073872		-.00424		.075884		-.00489	
		1						.090865		-.00484		.094490		-.00551	
		0.2	41					.055367		-.00667		.056418		-.00622	
			81					.054603		-.00814		.055761		-.00745	
			161					.047451		-.02197		.049522		-.01933	
			1	40					1.372419		.1824050		1.349601		.1897056
				100					1.409904		.0722179		1.383349		.0796101
				10	100				1.149931		.6515081		1.142216		.6562210
					200				1.272361		.4019200		1.257269		.4086483
					500				1.455823		.0718406		1.424433		.0758839
					300	.09	.09	.054332	1.301495	-.00389	.256299	.056149	1.272015	-.00399	.266096
						.15	.15	.053425	1.211009	-.00234	.288401	.0555	1.202725	-.00297	.291286
						.21	.21	.052689	1.107517	-.00143	.329396	.054883	1.134009	-.00227	.31828

the upper disk, which opposes the motion of the flow and increases friction. As a result, the temperature rises near the upper disk with increasing porosity parameter λ and magnetic parameter M . Figure depicts that augmenting parameter R_d causes the temperature to decrease first, then after a transition point, it increases. This means that near the upper disk, the heat carried by radiation supplies energy to the particles, increasing their kinetic energy and velocity, and causing an increase in the temperature.

Figure 15 depicts that an increase in the thermal relaxation parameter τ_E lead the temperature $\theta(\eta)$ to rise near the lower disk but for the same, the temperature falls near the upper disk. The non-zero thermal relaxation parameter τ_E denotes time lag during heat transfer. For the zero value of τ_E , the heat transfer is governed by Fourier's law. The results depict that near the lower disk the more time lag in heat transfer implies higher temperature but the same condition near the upper disk relates to the lower temperature. Figure 16 elucidates the effectiveness of volume fraction on temperature $\theta(\eta)$. On increasing the volume fraction of each nanoparticle Go (ϕ_1), and MoS₂ (ϕ_2) in equal quantity (ϕ), the temperature falls near the lower disk and surges near the upper one. The rise in the temperature near the upper disk can be attributed to the enhancement in the thermal conduction of the HNF or NF due to an increase in the nanoparticles in the base fluid. Figure 17 depicts that for the case of heat source ($A^* > 0$, $B^* > 0$), the temperature $\theta(\eta)$ shows transitioning nature in BLR. Temperature first increases then decreases for increasing A^* and B^* ($A^* > 0$, $B^* > 0$). Whereas, for the case of the heat sink ($A^* < 0$, $B^* < 0$), the temperature increases for increasing magnitude of heat sink parameters. In Figures 12, 13, 14, 15, 16, 17, the authors have presented a comparison of temperature profiles of HNF (MoS₂-Go/water flow) and NF (Go/water flow). Near the lower disk, HNF has a higher thermal profile $\theta(\eta)$, but as fluid approaches the upper disk, NF has a higher thermal profile $\theta(\eta)$.

5.3 Nanoparticle concentration distribution

Figures 18, 19, 20 show the fluctuation of dimensionless concentration of nanoparticles against the similarity variable while altering distinct flow regulating parameters one at a time while leaving others unchanged. Figures 18, 19 depict the influence of the solutal relaxation parameter τ_C and Schmidt number Sc on the concentration $\phi(\eta)$. Figure 18 depicts that increasing values of the solutal relaxation parameter τ_C leads concentration to fall. The non-zero values of the solutal relaxation parameter τ_C denote the presence of time lag during mass transfer. The increasing time lag during mass transfer has an adverse effect on concentration. The increasing time lag during mass transfer leads to a fall in the concentration profile. Figure 19 depicts that increasing values of Sc cause concentration to fall. The concentration decreases as Sc increases. The Schmidt number is an important parameter to consider as it physically connects the depths of the hydrodynamic layer and the mass transfer boundary layer. The momentum diffusion of particles in fluid increases as the strength of the Schmidt number increases in fluid flow. As a result, concentration falls. Figure 20 depicts that on increasing the volume fraction of each nanoparticle Go (ϕ_1), and MoS₂ (ϕ_2) in equal quantity (ϕ), the concentration falls. The reason for this behavior can be attributed to the fact the mixing of more nanoparticles causes the HNF or NF to be more viscous and flow is resisted, hence the concentration of NPs falls. In Figures 18, 19, 20, the authors have presented a comparison in

concentration profiles of HNF (MoS₂-Go/water flow) and NF (Go/water flow). It is seen that NF has a higher concentration profile $\phi(\eta)$ as compared to HNF.

5.4 Streamlines and engineering parameters

Figure 21 visualizes the streamlines pattern of HNF (MoS₂-Go/water flow) and NF (Go/water flow). The streamlines represent the movement of the suspended particles in the stream and which are driven by it. The direction of velocity at each point in the streamline is given by the tangent at that location. The denser streamlines indicate that the fluid velocity is greater than when it is open out. The HNF is seen to have slightly less dense streamlines in the present case which means more nanoparticles cause fluid to be more viscous and flow is resisted.

Table 3 elucidates the effectiveness of pertinent parameters on the Nusselt and Sherwood number. Nusselt number corresponds to the heat transmission rate (HTR) and the Sherwood number corresponds to the mass transmission rate (MTR) in the BLR at both disks. At the higher magnitude of the heat sink parameter, the HTR rises for HNF and NF at the lower disk but contrary behavior is seen at the upper disk. Whereas, the HTR decreases for HNF and NF at both the upper and lower disk. At the higher values of radiation parameter R_d , HTR increases at the lower disk and decreases at the upper disk. An increase in the volume fraction of each nanoparticle Go (ϕ_1), and MoS₂ (ϕ_2) in equal quantity (ϕ) enhances the thermal conductivity of the THNF due to an increase in the nanoparticles in the base fluid. The rising thermal conductivity enhances the MTR and HTR at the upper disk. It is also observed that at the higher values of the thermal relaxation parameter τ_E , HTR reduces at both disks. The non-zero values of the thermal relaxation parameter τ_E denote the time lag during heat transfer. Thus on augmenting τ_E , HTR at both disks reduces. Moreover, on increasing the magnitude of the Schmidt number Sc and solutal relaxation parameter τ_C , the MTR reduces at upper disks, whereas, on increasing the magnitude of the same parameters, the MTR rises at the lower disk.

6 Conclusion

The current problem concerns the influence of a non-uniform heat source/sink in the flow of a HNF (MoS₂-Go/water flow) and NF (Go/water flow) between two parallel and infinite spinning disks with the Cattaneo-Christov model in a porous medium in the presence of the magnetic field, and radiation. The numerical solution is deduced by employing the "bvp4c" function in MATLAB. Some vital conclusions are listed below.

- Radial velocity shows decreasing behavior near the lower disk and increasing behavior near the upper disk for increasing values of porosity parameter, magnetic parameter, and nanoparticles volume fraction.
- The heat transmission and mass transmission rate is higher at the lower disk.
- A higher magnitude of the heat sink parameter causes the rate of heat transmission to rise at the lower disk.
- The increase in nanoparticle volume fraction causes an enhancement in the rate of heat transmission at the upper

disk and the time lag during heat transfer is negatively correlated with the heat transmission rate at both disks.

- The combination of heat sink parameter and thermal relaxation parameter can be used to modulate the heat transmission rate at the surface.

6.1 Future scope of research

The present study discuss the flow of nanofluid and hybrid nanofluid without the nanoparticle aggregation effect. The study can be extended with proper modeling of fluid flow by utilization of validated thermophysical correlations for nanoparticle aggregation effect.

Data availability statement

The raw data supporting the conclusion of this article will be made available by the authors, without undue reservation.

Author contributions

SR and MY: Conceptualization, methodology, software, formal analysis, writing—original draft. MK and SE: Writing—original draft, data curation, investigation, visualization, validation. UK: Conceptualization, writing—original draft, writing—review and editing, supervision, resources. AA: Validation, investigation, writing—review and editing, formal analysis. AG: Writing—review

References

- Ali, N., Asghar, Z., Sajid, M., and Anwar Bég, O. (2019b). Biological interactions between Carreau fluid and microswimmers in a complex wavy canal with MHD effects. *Journal of the Brazilian Society of Mechanical Sciences and Engineering*. 41, 446–513. doi:10.1007/S40430-019-1953-Y
- Ali, N., Asghar, Z., Sajid, M., and Abbas, F. (2019a). A hybrid numerical study of bacteria gliding on a shear rate-dependent slime. *Physica A: Statistical Mechanics and its Applications*. 535, 122435. doi:10.1016/J.PHYSA.2019.122435
- Alrabaiah, H., Bilal, M., Khan, M. A., Muhammad, T., and Legas, E. Y. (2022). Parametric estimation of gyrotactic microorganism hybrid nanofluid flow between the conical gap of spinning disk-cone apparatus. *Scientific Reports*. 12, 59–14. doi:10.1038/s41598-021-03077-2
- Asghar, Z., Ali, N., Javid, K., Waqas, M., Dogonchi, A. S., and Khan, W. A. (2020a). Bio-inspired propulsion of micro-swimmers within a passive cervix filled with couple stress mucus. *The Computer Methods and Programs in Biomedicine*. 189, 105313. doi:10.1016/j.cmpb.2020.105313
- Asghar, Z., Ali, N., Waqas, M., and Javed, M. A. (2020b). An implicit finite difference analysis of magnetic swimmers propelling through non-Newtonian liquid in a complex wavy channel. *Computers and Mathematics with Applications*. 79, 2189–2202. doi:10.1016/J.CAMWA.2019.10.025
- Asghar, Z., Ali, N., Waqas, M., Nazeer, M., and Khan, W. A. (2020c). Locomotion of an efficient biomechanical sperm through viscoelastic medium. *Biomechanics and Modeling in Mechanobiology*. 19, 2271–2284. doi:10.1007/S10237-020-01338-Z
- Asghar, Z., Saeed Khan, M. W., Gondal, M. A., and Ghaffari, A. (2022a). Channel flow of non-Newtonian fluid due to peristalsis under external electric and magnetic field. *Proceedings of the Institution of Mechanical Engineers, Part E*. 236, 2670–2678. doi:10.1177/095544089221097693
- Asghar, Z., Shah, R. A., and Ali, N. (2022b). A computational approach to model gliding motion of an organism on a sticky slime layer over a solid substrate. *Biomechanics and Modeling in Mechanobiology*. 21, 1441–1455. doi:10.1007/S10237-022-01600-6
- Asghar, Z., Shah, R. A., Pasha, A. A., Rahman, M. M., and Khan, M. W. S. (2022c). Controlling kinetics of self-propelled rod-like swimmers near multi sinusoidal substrate. *Computers in Biology and Medicine*. 151, 106250. doi:10.1016/J.COMPBIOMED.2022.106250
- Asghar, Z., Shatanawi, W., Shah, R. A., and Gondal, M. A. (2023). Impact of viscoelastic ooze slime on complex wavy gliders near a solid boundary. *Chinese Journal of Physics*. 81, 26–36. doi:10.1016/J.CJPH.2022.10.013
- and editing, data curation, validation, resources. Also, co-authors are thankful to NA for his very less contribution in the introduction part of the original paper. After, revision we have remove his name because of his permission due to his contribution was negligible. Further, he is not able to give us feedback and assisted us in the revised manuscript.
- This work was partially funded by the research center of the Future University in Egypt 2022. Also, this study is supported via funding from Prince Sattam bin Abdulaziz University project number (PSAU/2023/R/1444).
- The authors declare that the research was conducted in the absence of any commercial or financial relationships that could be construed as a potential conflict of interest.
- All claims expressed in this article are solely those of the authors and do not necessarily represent those of their affiliated organizations, or those of the publisher, the editors and the reviewers. Any product that may be evaluated in this article, or claim that may be made by its manufacturer, is not guaranteed or endorsed by the publisher.

Funding

Conflict of interest

Publisher's note

- Irfan, M., Khan, M., and Khan, W. A. (2018). Interaction between chemical species and generalized Fourier's law on 3D flow of Carreau fluid with variable thermal conductivity and heat sink/source: A numerical approach. *Results in Physics*. 10, 107–117. doi:10.1016/j.rinp.2018.04.036
- Javid, K., Ali, N., and Asghar, Z. (2019). Rheological and magnetic effects on a fluid flow in a curved channel with different peristaltic wave profiles. *Journal of the Brazilian Society of Mechanical Sciences and Engineering*. 41, 483–514. doi:10.1007/S40430-019-1993-3
- Khan, M. I., Qayyum, S., Chu, Y. M., Khan, N. B., Kadry, S., Mackolil, J., et al. (2021). Transportation of Marangoni convection and irregular heat source in entropy optimized dissipative flow. *International Communications in Heat and Mass Transfer*. 120, 105031–105110. doi:10.1016/j.icheatmasstransfer.2020.105031
- Khan, M. I., Qayyum, S., Hayat, T., and Alsaedi, A. (2018). Entropy generation minimization and statistical declaration with probable error for skin friction coefficient and Nusselt number. *Chinese Journal of Physics*. 56, 1525–1546. doi:10.1016/j.cjph.2018.06.023
- Khan, M. S., Mei, S., ShabnamAli Shah, N., Chung, J. D., Khan, A., et al. (2022). Steady squeezing flow of magnetohydrodynamics hybrid nanofluid flow comprising carbon nanotube-ferrous oxide/water with suction/injection effect. *Nanomaterials* 12, 660. doi:10.3390/nano12040660
- Khan, N. S., Shah, Q., Bhaumik, A., Kumam, P., Thounthong, P., and Amiri, I. (2020a). Entropy generation in bioconvection nanofluid flow between two stretchable rotating disks. *Scientific Reports*. 10, 4448–4526. doi:10.1038/s41598-020-61172-2
- Khan, U., Ahmad, S., Hayyat, A., Khan, I., Sooppy Nisar, K., and Baleanu, D. (2020b). On the cattaneo-christov heat flux model and OHAM analysis for three different types of nanofluids. *Applied Sciences*. 10, 886. doi:10.3390/app10030886
- Khan, U., Shafiq, A., Zaib, A., and Baleanu, D. (2020c). Hybrid nanofluid on mixed convective radiative flow from an irregular variably thick moving surface with convex and concave effects. *Case Studies in Thermal Engineering*. 21, 100660. doi:10.1016/j.csite.2020.100660
- Khan, U., Zaib, A., Sheikholsami, M., Wakif, A., and Baleanu, D. (2020d). Mixed convective radiative flow through a slender revolution bodies containing molybdenum-disulfide graphene oxide along with generalized hybrid nanoparticles in porous media. *Crystal (Basel)* 10, 771–818. doi:10.3390/cryst10090771
- Kumar, B., Seth, G. S., Singh, M. K., and Chamkha, A. J. (2021). Carbon nanotubes (CNTs)-based flow between two spinning discs with porous medium, Cattaneo–Christov (non-Fourier) model and convective thermal condition. *Journal of Thermal Analysis and Calorimetry*. 146, 241–252. doi:10.1007/s10973-020-09952-w
- Mabood, F., Berrehal, H., Yusuf, T. A., and Khan, W. A. (2021). Carbon nanotubes-water between stretchable rotating disks with convective boundary conditions: Darcy-forchheimer scheme. *International Journal of Ambient Energy*. 43, 3981–3994. doi:10.1080/01430750.2021.1874527
- Madhukesh, J. K., Naveen Kumar, R., Punith Gowda, R. J., Prasannakumara, B. C., Ramesh, G. K., Ijaz Khan, M., et al. (2021). Numerical simulation of aa7072-aa7075/water-based hybrid nanofluid flow over a curved stretching sheet with Newtonian heating: A non-fourier heat flux model approach. *Journal of Molecular Liquids*. 335, 116103. doi:10.1016/j.molliq.2021.116103
- Masood, S., Farooq, M., and Anjum, A. (2021). Influence of heat generation/absorption and stagnation point on polystyrene-TiO₂/H₂O hybrid nanofluid flow. *Scientific Reports*. 11, 22381. doi:10.1038/s41598-021-01747-9
- Naz, R., Raza, R., Zafra, Y., and Javed, M. (2022). Scrutiny of Carreau nanoliquid over rotating disk with radiation impacts and the Cattaneo–Christov flux theory. *Waves Random Complex Media*, 1–16. doi:10.1080/17455030.2022.2128231
- Qureshi, M. Z. A., Bilal, S., Malik, M. Y., Raza, Q., Sherif, E. S. M., and Li, Y. M. (2021). Dispersion of metallic/ceramic matrix nanocomposite material through porous surfaces in magnetized hybrid nanofluids flow with shape and size effects. *Scientific Reports*. 11, 12271–12319. doi:10.1038/s41598-021-91152-z
- Rahman, M., Sharif, F., Turkyilmazoglu, M., and Siddiqui, M. S. (2022). Unsteady three-dimensional magnetohydrodynamics flow of nanofluids over a decelerated rotating disk with uniform suction. *Pramana* 96, 170–179. doi:10.1007/S12043-022-02404-0
- Ranga Babu, J. A., Kumar, K. K., and Srinivasa Rao, S. (2017). *State-of-art review on hybrid nanofluids*. Pergamon.
- Rashid, U., Liang, H., Ahmad, H., Abbas, M., Iqbal, A., and Hamed, Y. S. (2021). Study of (Ag and TiO₂)/water nanoparticles shape effect on heat transfer and hybrid nanofluid flow toward stretching shrinking horizontal cylinder. *Results in Physics*. 21, 103812. doi:10.1016/j.rinp.2020.103812
- Rawat, S. K., and Kumar, M. (2020). Cattaneo–christov heat flux model in flow of copper water nanofluid through a stretching/shrinking sheet on stagnation point in presence of heat generation/absorption and activation energy. *International Journal of Applied and Computational Mathematics*. 6, 112. doi:10.1007/s40819-020-00865-8
- Shah, R. A., Asghar, Z., and Ali, N. (2022). Mathematical modeling related to bacterial gliding mechanism at low Reynolds number with Ellis Slime. *The European Physical Journal Plus*. 137, 600–612. doi:10.1140/EPJP/S13360-022-02796-3
- Shampine, L. F., Gladwell, I., and Thompson, S. (2003). *Solving ODEs with MATLAB*. Cambridge, United States: Cambridge University Press.
- Turkyilmazoglu, M. (2022a). Flow and heat over a rotating disk subject to a uniform horizontal magnetic field. *Zeitschrift fur Naturforschung - Section A Journal of Physical Sciences*. 77, 329–337. doi:10.1515/zna-2021-0350
- Turkyilmazoglu, M. (2021). Heat transfer enhancement feature of the non-fourier cattaneo-christov heat flux model. *Journal of Heat Transfer*. 143, 094501. doi:10.1115/1.4051671
- Turkyilmazoglu, M. (2022b). Multiple exact solutions of free convection flows in saturated porous media with variable heat flux. *Journal of Porous Media*. 25, 53–63. doi:10.1615/JPORMEDIA.2022041870
- Waqas, H., Farooq, U., Naseem, R., Hussain, S., and Alghamdi, M. (2021). Impact of MHD radiative flow of hybrid nanofluid over a rotating disk. *Case Studies in Thermal Engineering*. 26, 101015. doi:10.1016/j.csite.2021.101015
- Wu, A., Abbas, S. Z., Asghar, Z., Sun, H., Waqas, M., and Khan, W. A. (2020). A shear-rate-dependent flow generated via magnetically controlled metachronal motion of artificial cilia. *Biomechanics and Modeling in Mechanobiology*. 19, 1713–1724. doi:10.1007/S10237-020-01301-Y
- Yaseen, M., Rawat, S. K., and Kumar, M. (2022a). Cattaneo–Christov heat flux model in Darcy–Forchheimer radiative flow of MoS₂–SiO₂/kerosene oil between two parallel rotating disks. *Journal of Thermal Analysis and Calorimetry*. 147, 10865–10887. doi:10.1007/s10973-022-11248-0
- Yaseen, M., Rawat, S. K., and Kumar, M. (2022b). Hybrid nanofluid (MoS₂–SiO₂/water) flow with viscous dissipation and Ohmic heating on an irregular variably thick convex/concave-shaped sheet in a porous medium. *Heat transfer*. 51, 789–817. doi:10.1002/htj.22330
- Yaseen, M., Rawat, S. K., Shafiq, A., Kumar, M., and Nonlaopon, K. (2022c). Analysis of heat transfer of mono and hybrid nanofluid flow between two parallel plates in a Darcy porous medium with thermal radiation and heat generation/absorption. *Symmetry* 14, 1943. doi:10.3390/sym14091943

Nomenclature

Alphabetical Symbols

A^* , B^* Heat source/sink parameter
 a_1 shrinkage rate of the lower disk
 a_2 shrinkage rate of the upper disk
 b_1 angular velocity of the lower disk
 b_2 angular velocity of the upper disk
 B_o Magnetic field strength
 C Nanoparticles concentration
 C_w Nanoparticles concentration at lower disk
 C_H Nanoparticles concentration at the upper disk
 C_p Heat capacity
 D Diffusion coefficient
 F Forchheimer coefficient
 F^* inertial coefficient
 f Axial velocity
 f' Radial velocity
 h_1 heat transfer coefficient of hot liquid at lower plate
 h_2 heat transfer coefficients of hot liquid at the upper plate
 H Distance between disks
 g Tangential velocity
 k Thermal conductivity
 k^* Mean absorption coefficient
 k_{fh} Permeability of the porous medium
 k_1 , k_2 Shrinking parameters
 M Magnetic field parameter
 Nu_{ro} , Nu_{r1} Nusselt numbers
 p Pressure
 Pr Prandtl number
 (q''') Non-uniform heat source/sink term
 R_d Radiation parameter
 Re Reynolds number
 Sh_{ro} , Sh_{r1} Sherwood numbers
 Sc Schmidt number
 T Temperature
 T_w Temperature of hot liquid at lower disk
 T_H Temperature of hot liquid at lower disk
 (u, v, w) Components of velocity
 (r, θ, z) cylindrical coordinate system

Greek Symbols

Ω Rotation parameter
 λ Porosity parameter
 γ_t Thermal relaxation time
 γ_c Solutal relaxation time
 γ_1 , γ_2 Biot numbers
 τ_E thermal relaxation parameter
 τ_c solutal relaxation parameter
 ϕ Dimensionless concentration
 ϕ_1 Volume fraction of Go nanoparticles
 ϕ_2 Volume fraction of MoS_2 nanoparticles
 Θ Dimensionless temperature
 μ Dynamic viscosity
 ε Pressure variable
 ρ Density
 σ^* Stefan–Boltzmann constant
 σ Electrical conductivity
 ξ Similarity variable
 ω_i ($i = 1 - 5$) Constant

Subscripts

bf , f Base fluid
 nf Nanofluid
 hnf Hybrid nanofluid

Superscripts

' Derivative w. r. to η

Abbreviations

NPs Nanoparticles
NFs Nanofluids
HNFs Hybrid Nanofluids
HTR Heat transmission rate
CCM Cattaneo-Christov model
MTR Mass transmission rate
BLR Boundary layer region
MoS₂ Molybdenum disulfide
Go Graphene oxide



OPEN ACCESS

EDITED BY

Ali Saleh Alshomrani,
King Abdulaziz University, Saudi Arabia

REVIEWED BY

Aurang Zaib,
Sciences and Technology Islamabad,
Pakistan
Mustafa Turkyilmazoglu,
Hacettepe University, Türkiye

*CORRESPONDENCE

Noreen Sher Akbar,
✉ noreen.sher@ceme.nust.edu.pk

SPECIALTY SECTION

This article was submitted to Colloidal
Materials and Interfaces,
a section of the journal
Frontiers in Materials

RECEIVED 28 November 2022

ACCEPTED 05 January 2023

PUBLISHED 23 January 2023

CITATION

Duraihem FZ, Sher Akbar N and Saleem S
(2023), Mixed convective eyring-powell
ferro magnetic nanofluid flow suspension
towards a stretching surface with
buoyancy effects through
numerical analysis.
Front. Mater. 10:1109755.
doi: 10.3389/fmats.2023.1109755

COPYRIGHT

© 2023 Duraihem, Sher Akbar and Saleem.
This is an open-access article distributed
under the terms of the [Creative Commons
Attribution License \(CC BY\)](#). The use,
distribution or reproduction in other
forums is permitted, provided the original
author(s) and the copyright owner(s) are
credited and that the original publication in
this journal is cited, in accordance with
accepted academic practice. No use,
distribution or reproduction is permitted
which does not comply with these terms.

Mixed convective eyring-powell ferro magnetic nanofluid flow suspension towards a stretching surface with buoyancy effects through numerical analysis

Faisal Z. Duraihem¹, Noreen Sher Akbar^{2*} and Salman Saleem³

¹Department of Mathematics, College of Science, King Saud University, Riyadh, Saudi Arabia, ²DBS and H, CEME, National University of Sciences and Technology, Islamabad, Pakistan, ³Department of Mathematics, College of Science, King Khalid University, Abha, Saudi Arabia

This article examines the impact of buoyancy on the magnetic Eyring-Powell nanofluid flow toward a stretching surface. Coupled similarity equations are created from the governing flow equations. For the particular instance of pure fluid flow, the numerically computed self-similar results are matched with the available literature and found to be in acceptable harmony. The shooting approach was used to arrive at numerical computations to the constitutive ordinary differential equations. The impacts of different fluid flow parameters, nano concentration parameters and heat transfer, are shown graphically for both aiding and opposing flows. It has been discovered that for both aiding and opposing problems, the skin friction is less affected by the buoyant force brought on by temperature differences. Under buoyancy, the rate of heat transfer increments for aiding flow problem while it declines for opposing flow.

KEYWORDS

double diffusion, magnetic field, natural convection, eyring-powell model, nanofluids, stretching sheet

1 Introduction

Water, oil, and other common fluids have relatively low thermal conductivities. As a result, heat transport analysis *via* these common fluids has been difficult for many years. The concept of raising the solid volume percentage in a fluid-solid mixture to increase thermal conductivity was initially proposed by Maxwell (Maxwell, 1873). These combinations contained particles of dimensions of millimeters and micrometers. Even though these fluids have improved thermal performance, they are nevertheless prone to a number of difficulties such as abrasion, clogging, and pressure loss. According to Choi (Choi et al., 1995), a nanofluid is a type of fluid that has a tiny concentration of nanoparticles (about 100 nm) dispersed in the base fluid. Such nanoparticles' thermal performance is dramatically altered by dispersion in common fluids. The study of magneto-hydrodynamic flow is crucial since it is used in various technical phenomena, such as the production of electrical energy and geo-physics. The MHD impact on a free convection heat transport was modeled by Sparrow et al. (Sparrow and Cess, 1961). They discovered that the presence of a magnetic field has a major impact on free convection. In a stretched surface with fixed given velocity and temperature, Chen and Strobel (Chen and Strobel, 1980) investigated the buoyancy effect in a

laminar boundary layer. The magnetic field impact flow model of a Newtonian fluid for stretching wall due to unvarying temperature was taken into consideration by Chakrabarti and Gupta (Chakrabarti and Gupta, 1979). The unsteady flow case of a non-Newtonian fluid above a revolving disc was investigated by Attia (Attia, 2014). View more recent literature by visiting Refs. (Xu et al., 2007; Buongiorno, 2010; Vajravelu et al., 2011; Ibrahim and Shanker, 2012; Aly and Vajravelu, 2014; Akbar et al., 2015; Khan et al., 2021; Khan et al., 2022; Waini et al., 2022).

When performing a heat transfer analysis on a steady MHD boundary layer extent, Mukhopadhyay (Mukhopadhyay, 2013) noticed that the expanse of the skin friction parameter rises in the extant of a magnetic impact, which results in a decrease in velocity. Stretching surfaces have recently come under the attention of many researchers due to their widespread use in engineering processes. Nadeem et al. (Nadeem et al., 2014) used numerical evaluation to interpret the MHD boundary layer extent of a nanoparticle-saturated Maxwell non-Newtonian fluid past a stretched surface. The heat transfer with radiation impacts, chemical reactions of n th order and viscous effects, Makinde (Makinde, 2011) looked into the modeling of heat and mass flux for a non-Newtonian Boussinesq fluid over a vertically held porous sheet. Ibrahim and Makinde (Ibrahim and Makinde, 2013) had investigated the issue of boundary layer extent and heat transmission caused by a nano-fluids across a vertical surface with double stratification. When analyzing the transport equations, Brownian movement, thermo-phoresis, solutal layer and thermal layer characteristics were all taken into account. Akbar et al. (Akbar et al., 2014) had used a homogeneous model to discuss the stagnation-point flow problem for carbon nanotubes flow over a stretching surface using base flow as water with slip and convective constraints. The constitutive boundary layer modeling of nanofluid is streamlined *via* similarity transformations. Through Refs. (Ebaid et al., 2013; Ellahi et al., 2015; Ibrahim and Makinde, 2015; Sheikholsami et al., 2015; Anuar et al., 2020; Turkiymazoglu, 2020; Wahid et al., 2020; Rostami et al., 2021; Turkiymazoglu, 2021), more recent research material can be reviewed.

The influence of buoyancy on the MHD flow problem of Eyring Prandtl nanofluid toward a stretching wall has been investigated in this work. Coupled similarity equations are created from the governing flow equations. For the particular instance of pure fluid flow, the numerically evaluated self-similar results are matched with the accessible literature and established to be in good harmony. The impacts of different fluid flow, heat flux, and nano particles concentration parameters are shown graphically for each aiding and adhesive flows. It has been discovered that for each aiding and opposite flow problems, the skin friction is less affected by the buoyant force brought on by temperature differences. Under buoyancy, the rate of heat flux rises for aiding flow and decreases for opposite flow. The results from the base fluid's limiting case comparison are in good accord with those from the literature. Although the aforementioned studies point to the fact that the Eyring-Powell model has been extensively studied in different flow configurations with the consideration of a number of different geometries. The prime motivation here is to discuss the non-Newtonian Eyring-Powell fluid model with buoyancy

and nanofluid effects. Therefore, the objective is to solve the momentum, thermal and concentration equations and attempt to find numerical solutions representing the flow, temperature and concentration fields. The rheology of the Eyring-Powell fluid as associated to the Newtonian fluid is mined from the exact average velocity expression.

2 Mathematical model

According to (Akbar et al., 2015), the constitutive modelling for the Eyring-Powell fluid non-Newtonian model is provided as.

$$\bar{S} = \mu \nabla \bar{V} + \frac{1}{\beta_1} \sinh^{-1} \left(\frac{1}{c} \nabla \bar{V} \right) \quad (1)$$

$$\sinh^{-1} \left(\frac{1}{c} \nabla \bar{V} \right) \approx \frac{1}{c} \nabla \bar{V} - \frac{1}{6} \left(\frac{1}{c} \nabla \bar{V} \right)^3, \left| \frac{1}{c} \nabla \bar{V} \right| \approx 1. \quad (2)$$

3 Mathematical formulation

We talk about a constant, two-dimensional flow over a wall that coincides with the flow's confinement plane of an incompressible, non-Newtonian, Eyring-Powell fluid. The linear stretching is what causes the flow (see Figure 1).

Following the application of boundary layer approximations, the constitutive equations for the Eyring-Powell nanofluid model with buoyancy effects can be defined as follows.

$$\frac{\partial u}{\partial x} + \frac{\partial v}{\partial y} = 0, \quad (3)$$

$$u \frac{\partial u}{\partial x} + v \frac{\partial u}{\partial y} = \left(\nu + \frac{1}{\rho \beta_1 c} \right) \frac{\partial^2 u}{\partial y^2} - \frac{1}{2 \rho \beta_1 c^3} \left(\frac{\partial u}{\partial y} \right)^2 \left(\frac{\partial^2 u}{\partial y^2} \right) - \frac{\sigma B^2}{\rho} u \pm (1 - \varphi_\infty) \frac{1}{\rho} \rho_{f\infty} [g \beta_T (T - T_\infty) + g \beta_C (C - C_\infty)], \quad (4)$$

$$\left(u \frac{\partial T}{\partial x} + v \frac{\partial T}{\partial y} \right) = \alpha \frac{\partial^2 T}{\partial y^2} + \tau \left[D_B \frac{\partial T}{\partial y} \frac{\partial C}{\partial y} + \left(\frac{D_T}{T_\infty} \right) \left(\frac{\partial T}{\partial y} \right)^2 \right], \quad (5)$$

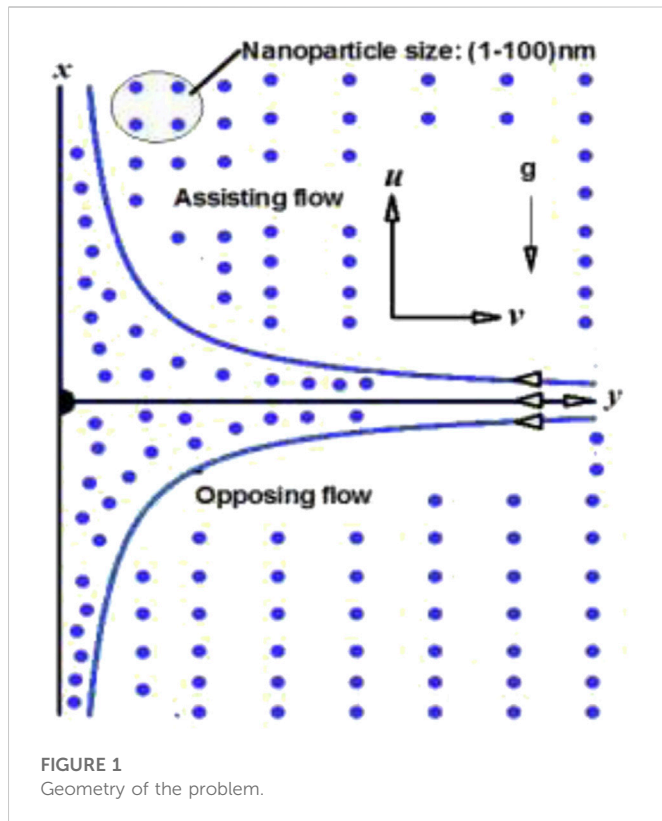
$$\left(u \frac{\partial C}{\partial x} + v \frac{\partial C}{\partial y} \right) = D_B \frac{\partial^2 C}{\partial y^2} + \left(\frac{D_T}{T_\infty} \right) \frac{\partial^2 T}{\partial y^2}, \quad (6)$$

The final term in Eq. 2's right-hand side denotes the effect of the thermal buoyancy effect on the flow profile, having "+" and "-" notations denotes, respectively, the buoyancy-assist and the opposing flow areas.

By using cross-differentiation, we can take p out of Eqs 4, 5. For this issue, the similarity transformations can be expressed as

$$u = ax f'(\eta), v = -\sqrt{(a\nu)} f(\eta), \eta = \sqrt{\left(\frac{a}{\nu}\right)} y, \theta(\eta) = \frac{T - T_\infty}{T_w - T_\infty}, \varphi(\eta) = \frac{C - C_\infty}{C_w - C_\infty}, \quad (7)$$

The following ordinary (similarity) differential equations are produced using the similarity transformation 7).



$$(1 + \gamma)f''' - (f')^2 + ff'' - \gamma\beta f''(f'')^2 - M^2 f' \pm G_r(\theta + N_c\varphi) = 0, \quad (8)$$

$$\frac{1}{Pr}\theta'' + f\theta' + N_b\phi'\theta' + N_t\theta'^2 = 0, \quad (9)$$

$$\varphi'' + L_e f\varphi' + \frac{N_t}{N_b}\theta'' = 0, \quad (10)$$

depending on the boundary constraints

$$\begin{aligned} f(0) = 0, f'(0) = 1, \theta(0) = 1, \varphi(0) = 1, \\ f' \rightarrow 0, \theta \rightarrow 0, \varphi \rightarrow 0, \text{ as } \eta \rightarrow \infty \end{aligned} \quad (11)$$

primes indicate differentiation with relation to η

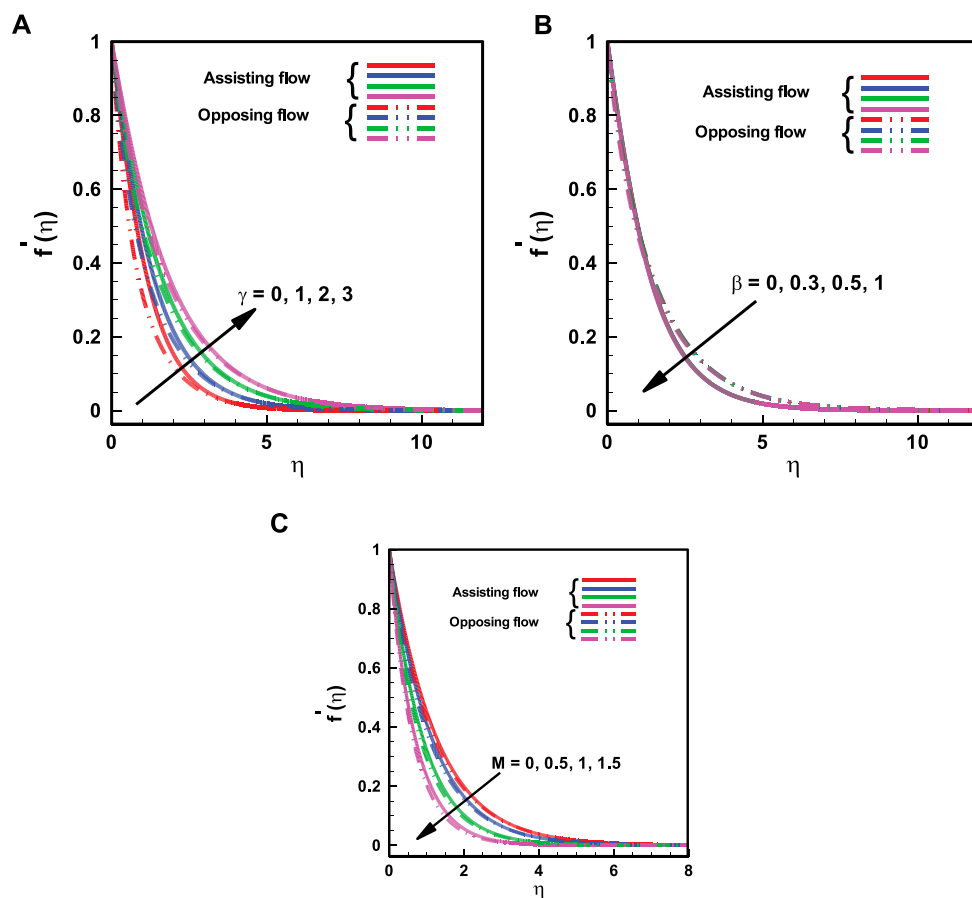
$$M^2 = \frac{\sigma B_0^2}{\rho a}, R_{ax} = \frac{u_w(x)x}{\nu}, G_T = \frac{(1 - \varphi_\infty)\rho_f g \alpha^3 \beta_T (T_w - T_\infty)}{\nu^2},$$

$$G_r = \frac{G_T}{R_{ax}^2}, B_C = \frac{(1 - \varphi_\infty)(\rho_f g \alpha^3 \beta_C (C_w - C_\infty))}{\nu^2}, B_r = \frac{B_C}{R_{ax}^2},$$

$$N_c = \frac{B_r}{G_r} = \frac{B_C}{G_T} = \frac{\beta_C (C_w - C_\infty)}{\beta_T (T_w - T_\infty)}, Pr = \frac{\nu}{\alpha}, N_b = \frac{\tau D_B (\varphi_w - \varphi_\infty)}{\nu},$$

$$L_e = \frac{\alpha}{D_s}, \gamma = \frac{1}{\mu\beta_1 c}, N_t = \frac{\tau D_T (T_w - T_\infty)}{\nu T_\infty}, \beta = \frac{(ax)^3}{2x\nu c^2}, \alpha = \frac{k}{(\rho c)_p},$$

$$\tau = \frac{(\rho c)_p}{(\rho c)_f} \quad (12)$$



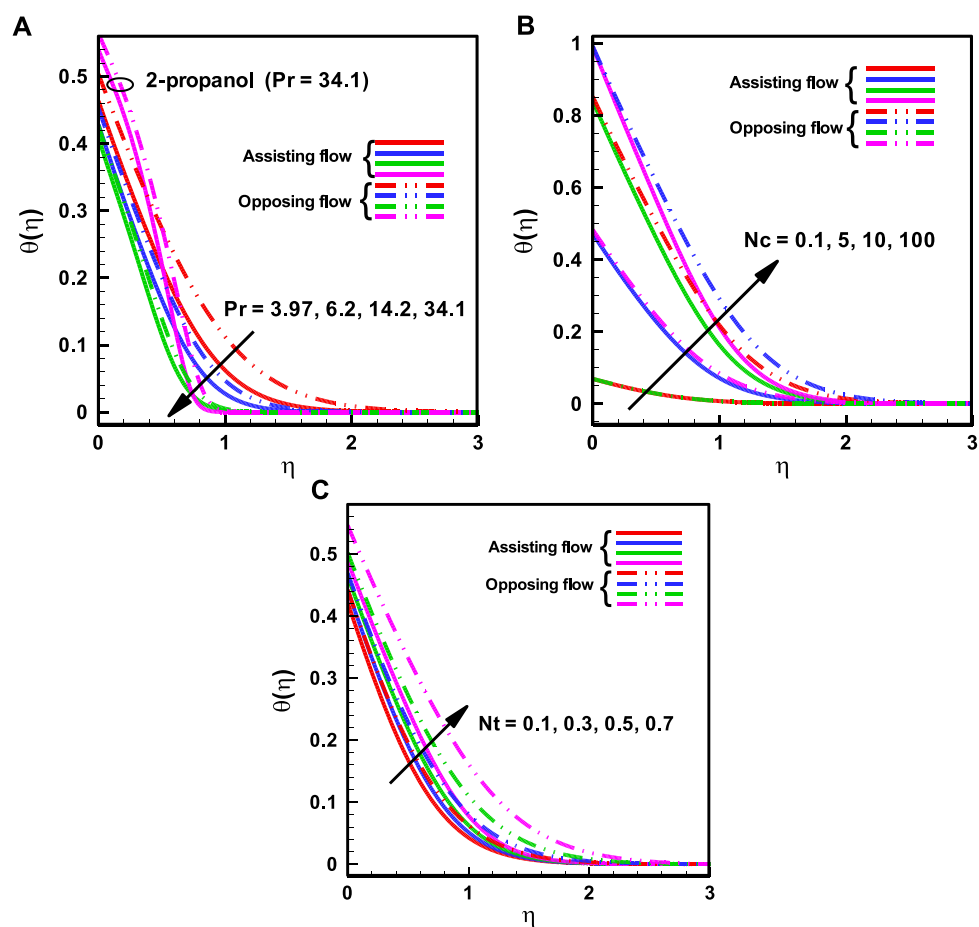


FIGURE 3

Variation of Temperature Profile for (A) Pr , (B) The ratio of buoyancy forces on the rescaled nanoparticle volume fraction N_c (C) The thermophoresis parameter N_t .

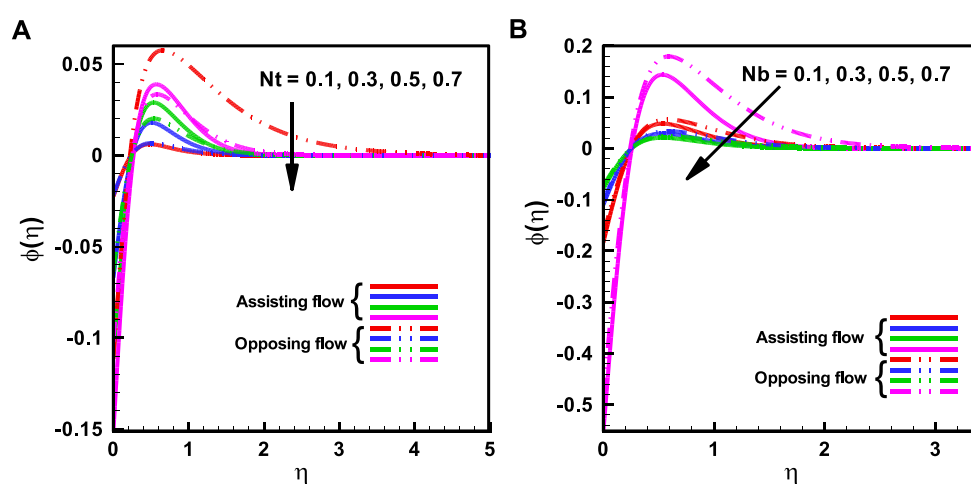


FIGURE 4

Variation of nanoparticles fraction profile (A). The Thermo-Phoresis Parameter N_t . (B) The Brownian Motion Parameter N_b .

Expressions for the Sherwood Number, Nusselt Number, and the Skin friction are considered by:

$$C_f = \frac{\tau_w}{\rho u_w^2}, Nu = \frac{xq_w}{\alpha(T_w - T_\infty)}, Sh = \frac{xq_m}{\alpha(C_w - C_\infty)},$$

$$\tau_w = \left(1 + \frac{1}{\beta_1 c}\right) \frac{\partial u}{\partial y} - \frac{1}{6\beta_1 c^3} \left(\frac{\partial u}{\partial y}\right)^3, q_w = -\alpha \left(\frac{\partial T}{\partial y}\right),$$

$$q_m = -\alpha \left(\frac{\partial C}{\partial y}\right), \sqrt{Re_c} f = \left[(1 + \gamma) f'' - \frac{\beta \gamma}{3} (f'')^3 \right]_{\eta=0},$$

$$Re_x^{-\frac{1}{2}} Nu_x = -\theta'(0), Re_x^{-\frac{1}{2}} Sh_x = -\gamma'(0) \quad (13)$$

constraints in Eq (11). The (BVP) Boundary value Problem was first converted into an initial value problem (IVP), and the far field boundary condition was given an appropriate finite value, such as, say i.e., $\eta \rightarrow \infty$, say η_∞ , the values for $f''(0)$, $\theta'(0)$ and $\phi'(0)$ are required to solve the IVP, although they are not provided before the computation. The Fourth Order Runge-Kutta technique is used to find a numerical result using the initial guess values of $f''(0)$, $\theta'(0)$ and $\phi'(0)$. We compared the estimated values of $f'(\eta)$, $\theta(\eta)$ and $\phi'(\eta)$ at the away from surface boundary condition $\eta_\infty (= 20)$ with the given boundary conditions $f'(\eta_\infty), \theta(\eta_\infty), \gamma(\eta_\infty), \zeta(\eta_\infty) \rightarrow 0$, respectively, and then corrected the values of $f''(0)$, $\theta'(0)$ and $\phi'(0)$ using the Secant technique for proper and good solution approach. The step-size is set at $\Delta\eta = 0.01$, and the 5th decimal place accuracy serves as the convergence criteria.

4 Numerical method

The shooting approach was used to arrive at numerical computations to the constitutive Ordinary Differential Eqs 8–10 with the boundary

5 Results and discussion

The Eyring-Powell nanofluid numerical solutions for stretching sheets are shown here with graphs that show the

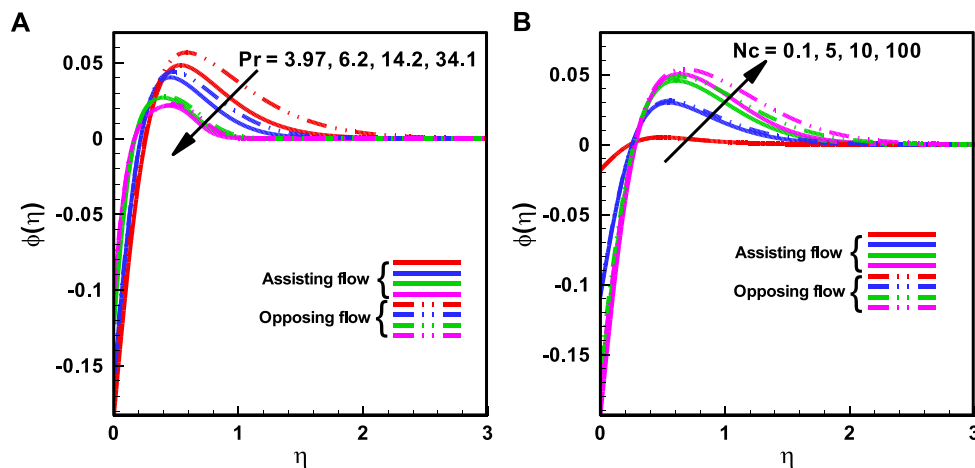


FIGURE 5

Variation of nanoparticles fraction profile for (A) Prandtl number Pr (B) The ratio of buoyancy forces on the rescaled nanoparticle volume fraction Nc .

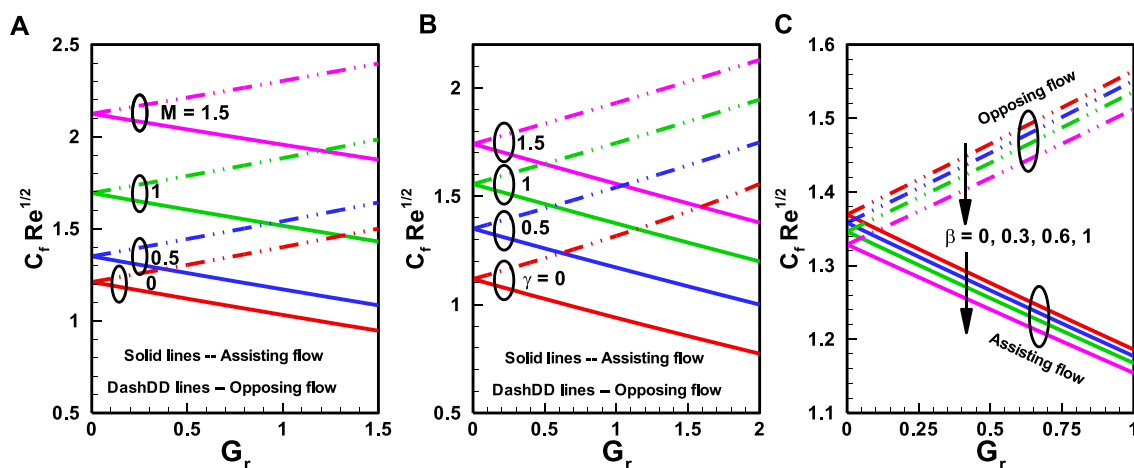


FIGURE 6

Variation of Coefficient for Skin friction (A) Hartmann number M , (B) Eyring-Powell fluid parameter γ and (C) Eyring-Powell fluid parameter β .

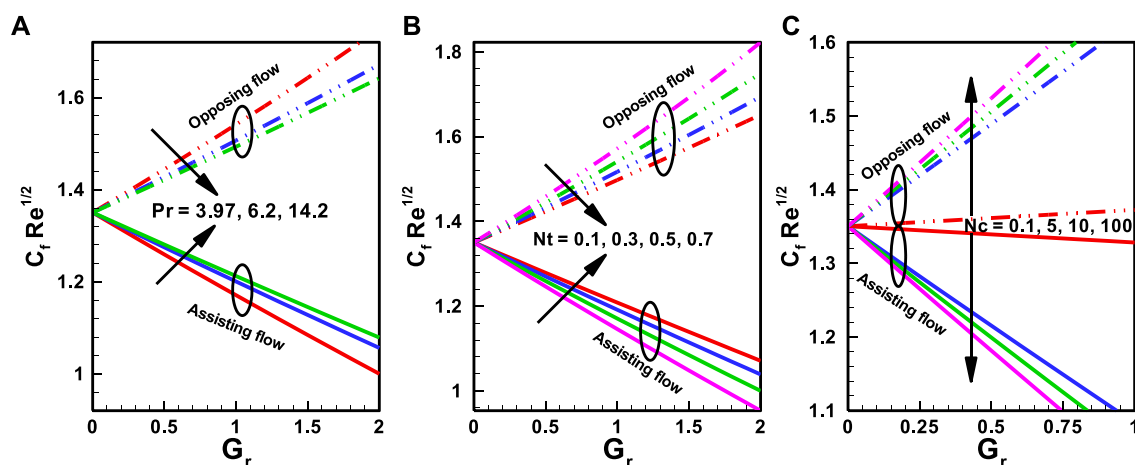


FIGURE 7

Variation of Coefficient for Skin friction (A) Prandtl number Pr , (B) The thermophoresis parameter N_t (C) The ratio of buoyancy forces on the rescaled nanoparticle volume fraction N_c .

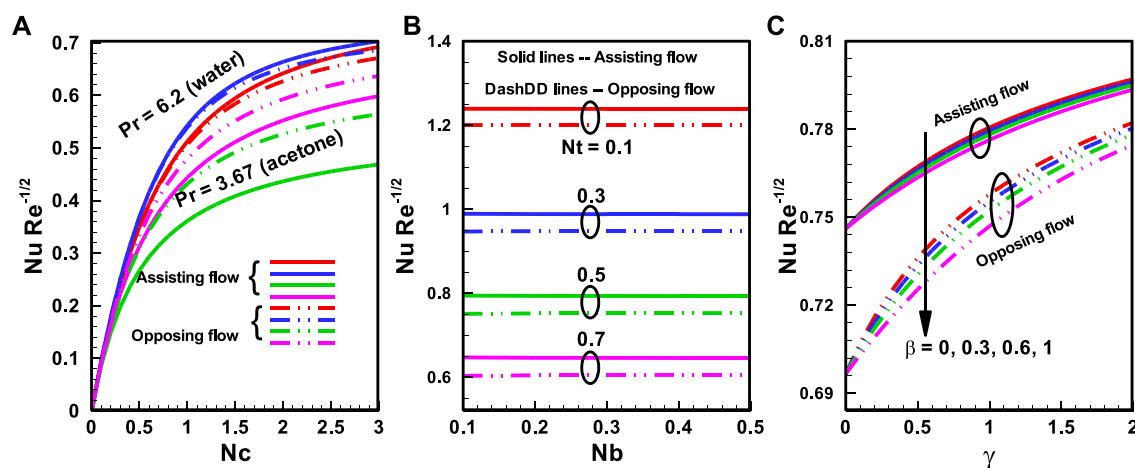


FIGURE 8

Alteration of Nu for (A) Pr (B) N_t (C) β .

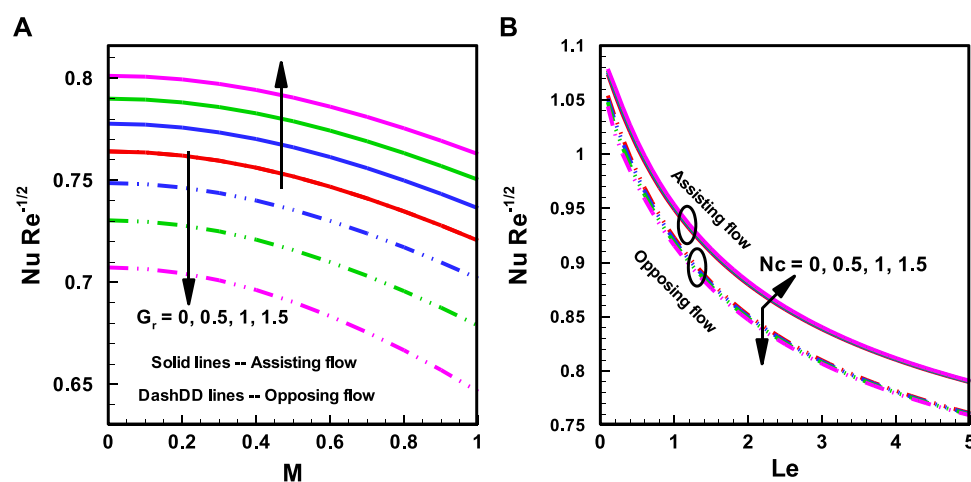


FIGURE 9

Nusselt number for (A) buoyancy influence via Temperature Difference G_r , (B) The ratio of Buoyancy forces on the rescaled concentration of nano-particles N_c .

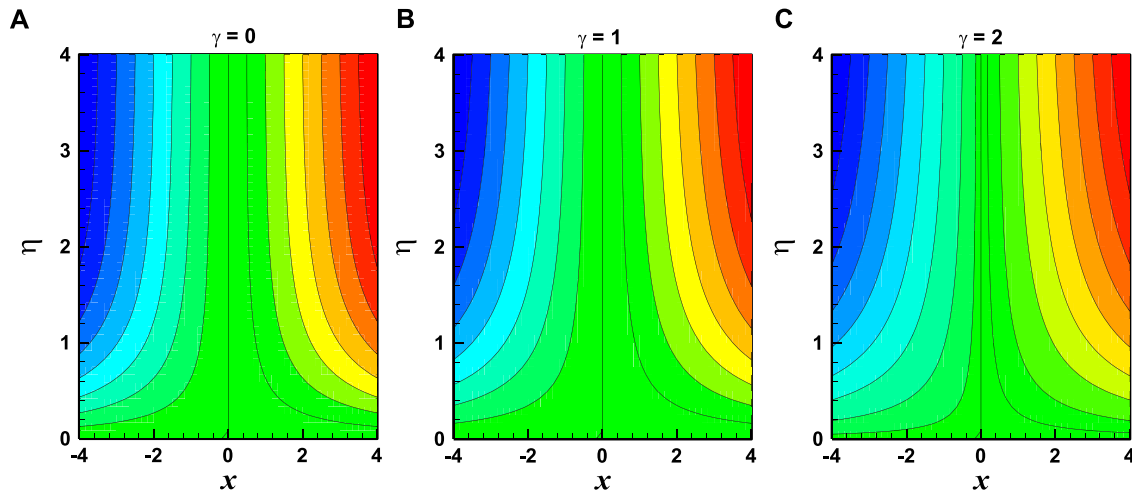


FIGURE 10

Variation of streamlines for $Nb = 0.3, Nt = 0.5, Le = 1, Pr = 3.97, \beta = 0.3, Nc = 0.5, Gr = 0.5, M = 0.5$.

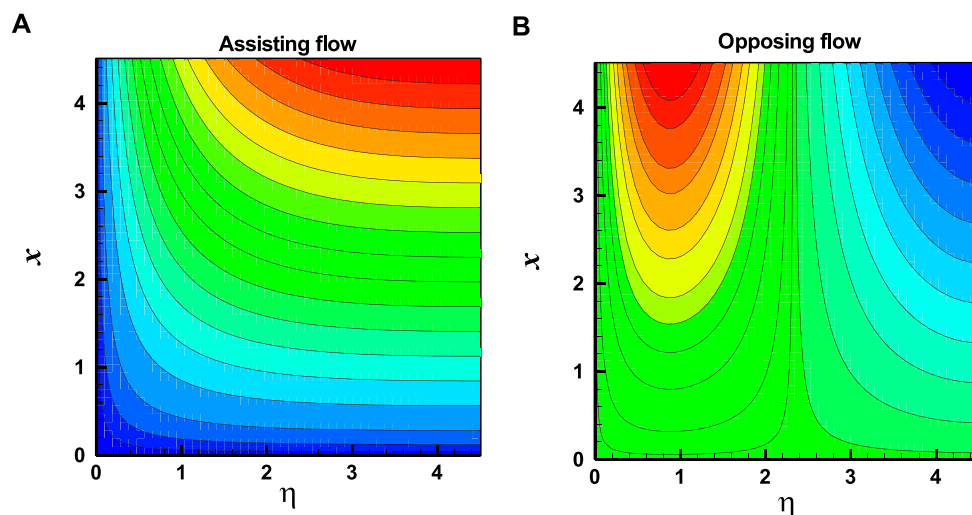


FIGURE 11

Variation of streamlines for assisting and opposing flow with $Nb = 0.3, Nt = 0.5, Le = 1, Pr = 3.97, \beta = \gamma = 0.3, Nc = 0.5, Gr = 0.5, M = 0.5$.

buoyancy effects. Figs (2a) to (2c) are generated to show how different fluid parameters affect the velocity profile. These graphs show how the buoyant force caused by the temperature differential Gr and γ , β have an impact on the dimensionless velocity. The impact of γ , β on the velocity profile are shown in Fig. 2(a). With an uplift in γ , β , the velocity profile and boundary layer extent both rises. Figure 2B illustrates how the Eyring-Powell fluid parameter affects the velocity profile and the flow profile is reduced. But as the value of β grows, the extent of the boundary layer increases. The influence of Hartmann number M on flow is shown in Figure 2C. Figures show that as Hartmann number M is raised, velocity profile declines but boundary layer thickness rises. Additionally, it has been found that the flow profile behaviour for the Eyring-Powell fluid parameters is the same for both helpful and opposing flows.

In Figures 3A–C, the influence of the flow parameters on the dimensionless heat flux is explored. Both helpful and opposing flows are covered by Figures 3A–C. The thermal boundary layer thickness is generally increased by Prandtl number, the ratio of buoyancy forces on the rescaled nano-particles volume fraction, and the thermophoresis parameter, whereas temperature profile increases with an increase in the ratio of buoyancy forces on the rescaled nanoparticle concentration and the thermophoresis parameter and decreases with an uplift in Pr . In each scenario, it is discovered that opposing flows have thicker thermal boundary layers.

Figures 4A, and Figure 5B) illustrate how the N_c is affected by N_b ; N_t ; Pr , and the ratio of buoyancy influences. The N_t ; N_b parameter; Pr all reduce the rescaled nanoparticle volume percentage for each favourable and opposite flows, as illustrated in Figures 4A, 5B). However, the volume fraction of rescaled nanoparticles tends to

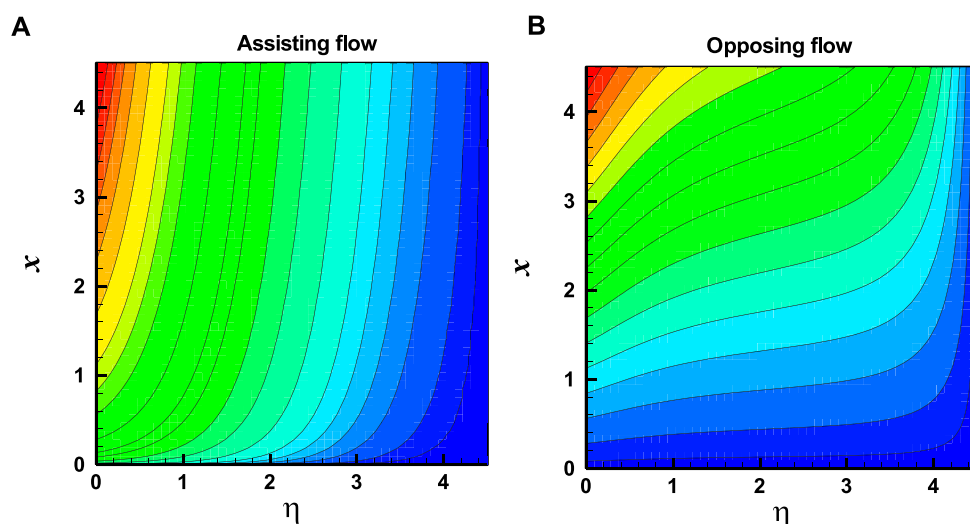


FIGURE 12

Variation of Isotherms for assisting and opposing flow with $Nb = 0.3$, $Nt = 0.5$, $Le = 1$, $Pr = 3.97$, $\beta = \gamma = 0.3$, $Nc = 0.5$, $Gr = 0.5$, $M = 0.5$.

TABLE 1 Comparison of coefficient of skin friction with [*] for $Gr = 0$.

n	M	Akbar et al. (Akbar et al., 2015)			Present results		
		$\beta=\gamma=0$	$\beta=\gamma=0.3$	$\beta=\gamma=0.5$	$\beta=\gamma=0$	$\beta=\gamma=0.3$	$\beta=\gamma=0.5$
0	0	1	1	1	1	1	1
0.1	0	0.94868	0.94248	0.93826	0.94868	0.94248	0.93826
0.2	0	0.89442	0.88023	0.87026	0.89443	0.88023	.87026
0.3	0.5	1.09544	0.98804	0.96001			
0.3	1	1.26491	1.13454	1.09616		1.13454	1.09616
0.3	1.5	1.41421	1.26193	1.21235			
$C_f Re^{1/2}$							

TABLE 2 Coefficient of skin friction for helping and obstructing flow.

Assisting case flow					Opposing case flow			
Gr	$\gamma = 0$		$\gamma = 0.5$		$\gamma = 0$		$\gamma = 0.5$	
	$M = 0$	$M = 0.5$	$M = 0$	$M = 0.5$	$M = 0$	$M = 0.5$	$M = 0$	$M = 0.5$
0	1.00000	1.11803	1.21089	1.35032	1.00000	1.11803	1.21089	1.35032
0.2	0.96331	1.08092	1.17437	1.31361	1.03742	1.15593	1.24783	1.38748
0.4	0.92730	1.04452	1.13826	1.27733	1.07564	1.19470	1.28524	1.42512
0.6	0.89191	1.00878	1.10254	1.24145	1.11475	1.23443	1.32313	1.46329
0.8	0.85709	0.97365	1.06718	1.20595	1.15485	1.27526	1.36154	1.50201
1	0.82280	0.93909	1.03216	1.17081	1.19606	1.31733	1.40051	1.54134

grow when the buoyancy forces ratio increases see Figure 5B. In contrast to aiding flow, the fraction of nanoparticles is higher in opposing flow.

As seen in the Figures 6A–C, the N_u rises with the Hartmann number M and the Eyring-Powell fluid parameters but falls with an increment in the latter. The N_t ; P_r both have an impact on the skin friction coefficient; Figures 7A, B illustrates how skin friction coefficient increases for aiding flow but diminishes for opposite flow when Prandtl number and thermophoresis parameter increase. The graph in Figure 7C demonstrates that the skin friction coefficient uplifts for opposing flow but lowers for assisting flow depending on the buoyancy forces on the rescaled nanoparticle volume fraction N_c . Additionally, it can be seen that for all flow parameters, the skin friction coefficient is larger in the case of opposing flow than aiding flow.

In Figures 8A, and Figure 9B, both for aiding and opposing flows, the influences of various factors on N_u are shown. In every instance; N_u for aiding flows is shown to have a high magnitude. The local Nusselt number for both assisting and opposing flows increases with an uplift in P_r , whereas a decrease in the thermophoresis parameter N_t and the Eyring-Powell fluid parameter causes a decrease in the local Nusselt number for each favourable and opposite flows, as displayed in Figures 8A–C. The local N_u is increased for assisting flow and decreased for opposing flow due to the buoyancy force caused by temperature differential G_r and the ratio of buoyancy forces on the rescaled nanoparticle volume fraction N_c (see Figures 9A, B).

Streamlines and isotherms have been displayed in the Figure 10, and Figure 12) to aid in understanding the fluid flow behaviour. The streamlines will be close to the sheet's axis when we increase the Eyring-Powell fluid parameter, as shown in Figure 10. In contrast to the aiding flow, opposing flow streams are being confined and moving toward the sheet's axis. When compared to streamlines, isotherm outcomes are, however, the opposite. In contrast to the opposing flow, isotherms lines for aiding flows are contained and moving in the direction of the sheet's axis, as seen in the Figure 11, and Figure 12. Table 1 compares the results of the current study to the body of prior research. The skin friction coefficient's numerical values are provided in Table 2.

6 Conclusion

The influence of buoyancy forces on a magnetic Eyring-Powell nano-fluid flow over a vertical stretching wall is numerically analysed. The linear stretching case is considered for this incompressible non-Newtonian Eyring-Powell fluid flow problem. The major outcomes of this work are presented as follows.

- The extent of the boundary layer and the velocity profile each rise with an uplift in the Eyring-Powell fluid

parameter. The boundary layer becomes thicker as the value of β rises.

- The Eyring-Powell flow characteristics and velocity profile behavior is the same for both favorable and adverse flows.
- The P_r often uplifts the thermal boundary layer extent. When the buoyancy pressures on the rescaled nanoparticle concentration and the thermophoresis parameter are increased, the heat flux profile rises, whereas when the P_r is raised, the profile falls. We find that the thermal boundary layers of opposing flows are thicker in each case.
- It is clear that for all flow values, opposing flow has a higher skin friction coefficient than helping flow.
- When we increase the Eyring-Powell fluid parameter, the streamlines will be near to the axis of the sheet. Opposing flow streams are constrained and travelling in the direction of the sheet's axis in contrast to the assisting flow. However, the results of isotherms are the opposite of streamlines. Isotherms lines for assisting flows are contained and travelling in the direction of the sheet's axis, in contrast to the opposing flow.

Data availability statement

The original contributions presented in the study are included in the article/supplementary material, further inquiries can be directed to the corresponding author.

Author contributions

FD model the problem NS Done the writeup of the manuscript and done solution methodology SS Write introduction and prepared graphs All three authors done the proof reading.

Conflict of interest

The authors declare that the research was conducted in the absence of any commercial or financial relationships that could be construed as a potential conflict of interest.

Publisher's note

All claims expressed in this article are solely those of the authors and do not necessarily represent those of their affiliated organizations, or those of the publisher, the editors and the reviewers. Any product that may be evaluated in this article, or claim that may be made by its manufacturer, is not guaranteed or endorsed by the publisher.

References

- Akbar, N. S., Ebaid, A., and Khan, Z. H. (2015). Numerical analysis of magnetic field effects on Eyring-Powell fluid flow towards a stretching sheet. *J. Magnetism Magnetic Mater.* 382, 355–358. doi:10.1016/j.jmmm.2015.01.088
- Akbar, N. S., Nadeem, S., and Hayat Khan, Z. (2014). The combined effects of slip and convective boundary conditions on stagnation-point flow of CNT suspended nanofluid over a stretching sheet. *J. Mol. Liq.* 196, 21–25. doi:10.1016/j.molliq.2014.03.006

- Aly, E. H., and Vajravelu, K. (2014). Exact and numerical solutions of MHD nano boundary-layer flows over stretching surfaces in a porous medium. *Appl. Math. Comput.* 232, 191–204. doi:10.1016/j.amc.2013.12.147
- Anuar, N. S., Bachok, N., Turkyilmazoglu, M., MdArifina, N., and Rosali, H. (2020). Analytical and stability analysis of MHD flow past a nonlinearly deforming vertical surface in Carbon Nanotubes. *Alexandria Eng. J.* 59, 497–507. doi:10.1016/j.aej.2020.01.024
- Attia, H. A. (2014). Unsteady flow of a non-Newtonian fluid above a rotating disk with heat transfer. *Int. J. Heat Mass Transf.* 46 (14), 2695–2700. doi:10.1016/s0017-9310(03)00029-2
- Buongiorno, J. (2010). Convective transport in nanofluids. *J. Heat Transf. Am. Soc. Mech. Eng.* 128 (3), 240–250. doi:10.1115/1.2150834
- Chakrabarti, A., and Gupta, A. S. (1979). Hydromagnetic flow and heat transfer over a stretching sheet. *Quart. Appl. Math.* 37, 73–78. doi:10.1090/qam/99636
- Chen, T. S., and Strobel, F. A. (1980). Buoyancy effects in boundary layer adjacent to a continuous, moving horizontal flat plate. *Trans. ASME J. Heat. Transf.* 102, 170–172. doi:10.1115/1.3244232
- Choi, S. U. S. (1995). “Enhancing thermal conductivity of fluids with nanoparticles,” in *Developments and applications of non-Newtonian flows*. Editors D. A. Siginer and H. P. Wang (New York: ASME), 66, 99–105.
- Ebaid, A., El-arabawy, H. A., and Nader, Y. (2013). New exact solutions for boundary-layer flow of a nanofluid past a stretching sheet. *Int. J. Diff. Eq.* 10 (11), 2591–2594. doi:10.1166/jctn.2013.3253
- Ellahi, R., Hassan, M., and Zeeshan, A. (2015). Shape effects of nanosize particles in Cu–H₂O nanofluid on entropy generation. *Int. J. Heat Mass Transf.* 81, 449–456. doi:10.1016/j.ijheatmasstransfer.2014.10.041
- Ibrahim, W., and Makinde, O. D. (2015). Double-diffusive in mixed convection and MHD stagnation point flow of nanofluid over a stretching sheet. *J. Nanofluids* 4, 28–37. doi:10.1166/jon.2015.1129
- Ibrahim, W., and Makinde, O. D. (2013). The effect of double stratification on boundary-layer flow and heat transfer of nanofluid over a vertical plate. *Comput. Fluids* 86, 433–441. doi:10.1016/j.compfluid.2013.07.029
- Ibrahim, W., and Shanker, B. (2012). Unsteady MHD boundary-layer flow and heat transfer due to stretching sheet in the presence of heat source or sink. *Comput. Fluids* 70, 21–28. doi:10.1016/j.compfluid.2012.08.019
- Khan, U., Zaib, A., Ishak, A., Bakar, S. A., Animasaun, I. L., Yook, S. J., et al. (2022). Insights into the dynamics of blood conveying gold nanoparticles on a curved surface when suction, thermal radiation, and Lorentz force are significant: The case of Non-Newtonian Williamson fluid. *case Newt. Williamson fluid Math. Comput. Simul.* 193, 250–268. doi:10.1016/j.matcom.2021.10.014
- Khan, U., Ishak, A., and Zaib, A. (2021). Simulation of MHD CuO–water nanofluid flow and convective heat transfer considering Lorentz forces. *Chin. J. Phys.* 74, 350–364.
- Makinde, O. D. (2011). Mhd mixed-convection interaction with thermal radiation and nth order chemical reaction past A vertical porous plate embedded in A porous medium. *Chem. Eng. Commun.* 198 (4), 590–608. doi:10.1080/00986445.2010.500151
- Maxwell, J. C. (1873). *Electricity and magnetism*. Oxford: Clarendon Press.
- Mukhopadhyay, S. (2013). MHD boundary layer flow and heat transfer over an exponentially stretching sheet embedded in a thermally stratified medium. *Alexandria Eng. J.* 52, 259–265. doi:10.1016/j.aej.2013.02.003
- Nadeem, S., Ul Haq, R., and Khan, Z. H. (2014). Numerical study of MHD boundary layer flow of a Maxwell fluid past a stretching sheet in the presence of nanoparticles. *J. Taiwan Inst. Chem. Eng.* 45 (1), 121–126. doi:10.1016/j.jtice.2013.04.006
- Rostami, S., Ellahi, R., Oztop, H. F., and Goldanlou, A. S. (2021). A study on the effect of magnetic field and the sinusoidal boundary condition on free convective heat transfer of non-Newtonian power-law fluid in a square enclosure with two constant-temperature obstacles using lattice Boltzmann method. *J. Therm. Analysis Calorim.* 144 (6), 2557–2573. doi:10.1007/s10973-020-10202-2
- Sheikholeslami, M., Ganji, D. D., Younus Javed, M., and Ellahi, R. (2015). Effect of thermal radiation on magnetohydrodynamics nanofluid flow and heat transfer by means of two phase model. *J. Magnetism Magnetic Mater.* 374, 36–43. doi:10.1016/j.jmmm.2014.08.021
- Sparrow, E. M., and Cess, R. D. (1961). The effect of a magnetic field on free convection heat transfer. *Int. J. Heat. Mass Tran.* 3 (4), 267–274. doi:10.1016/0017-9310(61)90042-4
- Turkyilmazoglu, M. (2020). Eyring-Powell fluid flow through a circular pipe and heat transfer: Full solutions. *Int. J. Numer. Methods Heat Fluid Flow* 30, 4765–4774. doi:10.1108/hff-12-2019-0925
- Turkyilmazoglu, M. (2021). Stagnation-point flow and heat transfer over stretchable plates and cylinders with an oncoming flow: Exact solutions. *Chem. Eng. Sci.* 238, 116596. doi:10.1016/j.ces.2021.116596
- Vajravelu, K., Prasad, K. V., Lee, J., Lee, C., Pop, I., and Gorder, R. A. V. (2011). Convective heat transfer in the flow of viscous Ag-water and Cu-water nanofluids over a stretching surface. *Int. J. Therm. Sci.* 50, 843–851. doi:10.1016/j.ijthermalsci.2011.01.008
- Wahid, N. S., Turkyilmazoglu, M., Hafidzuddin, M. E. H., Abd Rahmin, N. A., Wahid, N. S., Arifin, N. M., et al. (2020). MHD hybrid Cu-Al₂O₃/water nanofluid flow with thermal radiation and partial slip past a permeable stretching surface: Analytical solution. *J. Nano Res.* 64, 75–91. doi:10.4028/www.scientific.net/jnanor.64.75
- Waini, I., Khan, U., Zaib, A., Ishak, A., and Pop, I. (2022). Inspection of TiO₂-CoFe₂O₄ nanoparticles on MHD flow toward a shrinking cylinder with radiative heat transfer. *J. Mol. Liq.* 361, 119615. doi:10.1016/j.molliq.2022.119615
- Xu, H., Liao, S. J., and Pop, I. (2007). Series solutions of unsteady three-dimensional MHD flow and heat transfer in the boundary layer over an impulsively stretching plate. *Eur. J. Mech. - B/Fluids* 26, 15–27. doi:10.1016/j.euromechflu.2005.12.003

Nomenclature

(x, y) coordinate axes

L_e lewis number

γ, β eyring-powell fluid parameters

α thermal diffusivity

$\bar{\tau}$ extra stress tensor

Γ time-dependent material constant

f' dimensionless velocity

C concentration

ρ density of nanofluid

β_T thermal expansion coefficient

τ effective heat capacity of the nanoparticle ratio to heat capacity of the fluid

M hartmann number

N_b brownian motion parameter

N_c the ratio of buoyancy forces

G_r buoyancy force owing to the temperature distribution

B_c solutal grashoff number

(u, v) velocity field

P_r prandtl number

C concentration within the boundary layer

C_∞ free stream concentration

μ_∞ infinite shear rate viscosity

μ_0 zero shear rate viscosity

T fluid temperature within the boundary layer

T_∞ free stream temperature

g acceleration due to gravity

β_C coefficient of nanoparticle volumetric expansion

D_B brownian diffusion coefficient

D_T thermophoretic diffusion coefficient

N_t thermophoresis parameter

B_r ratio between the buoyancy force due to concentration difference

G_T thermal grashoff number

R_{ax} local reynolds number



OPEN ACCESS

EDITED BY

Ali Saleh Alshomrani,
King Abdulaziz University, Saudi Arabia

REVIEWED BY

Ahmed ElGendy,
The University of Texas at El Paso,
United States
S. D. Kaushik,
UGC-DAE Consortium for Scientific
Research Mumbai Centre, India

*CORRESPONDENCE

Akhtar Ali,
✉ akhtarhitec@gmail.com
Akif Safeen,
✉ akifsafeen@upr.edu.pk
Sayed M. Eldin,
✉ sayed.eldin22@fue.edu.eg

SPECIALTY SECTION

This article was submitted to Colloidal
Materials and Interfaces,
a section of the journal
Frontiers in Materials

RECEIVED 06 December 2022

ACCEPTED 16 January 2023

PUBLISHED 30 January 2023

CITATION

Ali A, Shah WH, Safeen A, Ali L, Tufail M,
Ullah Z, Safeen K, Eldin SM, R. Ali M,
Sohail M and Imran N (2023), Effect of Ca
doping on the arbitrary canting of
magnetic exchange interactions in
 $\text{La}_{1-x}\text{Ca}_x\text{MnO}_3$ nanoparticles.
Front. Mater. 10:1117793.
doi: 10.3389/fmats.2023.1117793

COPYRIGHT

© 2023 Ali, Shah, Safeen, Ali, Tufail, Ullah,
Safeen, Eldin, R. Ali, Sohail and Imran. This
is an open-access article distributed under
the terms of the [Creative Commons
Attribution License \(CC BY\)](#). The use,
distribution or reproduction in other
forums is permitted, provided the original
author(s) and the copyright owner(s) are
credited and that the original publication in
this journal is cited, in accordance with
accepted academic practice. No use,
distribution or reproduction is permitted
which does not comply with these terms.

Effect of Ca doping on the arbitrary canting of magnetic exchange interactions in $\text{La}_{1-x}\text{Ca}_x\text{MnO}_3$ nanoparticles

Akhtar Ali^{1*}, Wiqar H. Shah¹, Akif Safeen^{2*}, Liaqat Ali¹,
Muhammad Tufail¹, Zakir Ullah¹, Kashif Safeen³, Sayed M. Eldin^{4*},
Mohamed R. Ali⁵, Muhammad Sohail⁶ and Naveed Imran⁷

¹Department of Physics, Faculty of Basic and Applied Sciences, International Islamic University, Islamabad, Pakistan, ²Department of Physics, University of Poonch Rawalakot, Rawalakot, Azad Jammu and Kashmir, Pakistan, ³Department of Physics, Abdul Wali Khan University Mardan, Mardan, Pakistan, ⁴Center of Research, Faculty of Engineering, Future University in Egypt, New Cairo, Egypt, ⁵Faculty of Engineering and Technology, Future University, New Cairo, Egypt, ⁶Department of Mathematics, Khwaja Fareed University of Engineering and Information Technology, Rahim Yar Khan, Pakistan, ⁷HITEC Schools and Colleges, HIT Taxila, Taxila, Pakistan

$\text{La}_{1-x}\text{Ca}_x\text{MnO}_3$ nanoparticles ($x = 0.1, 0.2, 0.3$) (LCMO NPs) were synthesized using the coprecipitation method. The prepared samples were investigated using x-ray diffraction (XRD), which confirmed the single-phase structure. The nanoparticle's crystallite size was determined using Debye–Scherrer's formula. Scanning electron microscopy showed that the size of the nanoparticles was between 33 nm and 55 nm. Energy-dispersive x-ray spectroscopy (EDX) was used to determine the elemental composition of samples. The four-probe method was used to measure the temperature-dependent electrical resistivity. Magnetic properties, such as hysteresis loop, magnetoresistance, and magnetization *versus* temperature, were measured using a vibrating sample magnetometer. The study of magnetization *versus* applied magnetic field $M(H)$ showed that, at 77 K, all the loops exhibit ferromagnetism. DC magnetization *versus* temperature at a 70-Oe-applied field for all samples showed a paramagnetic-ferromagnetic phase transition. A decrease in Curie temperature T_C after increasing the concentration of x was observed. The real and imaginary parts of temperature-dependent ac magnetic susceptibility were measured and revealed a transition from the ferromagnetic to the paramagnetic phase at a particular temperature T_C , with DC magnetization behavior.

KEYWORDS

nanomaterials, magnetic nanoparticles, Curie temperature, exchange interactions, magnetoresistance

1 Introduction

Hole-doped perovskite manganites $\text{R}_{1-x}\text{A}_x\text{MnO}_3$, where rare earth ion is indicated by R and divalent ions, such as Pb, Ca, Sr, or Ba, are represented by A, have drawn great technological and scientific interest for many decades. The potential properties that these materials can possess include a metal-insulator transition (T_{MI}) colossal magneto-resistance (CMR) effect, electronic phase transition, orbital ordering, charge ordering (T_{CO}), and a giant magnetic entropy effect (Dagotto et al., 2001; Gor'kov and Kresin, 2004; Mormooidae, 2009). The physical properties of $\text{La}_{1-x}\text{Ca}_x\text{MnO}_3$ synthesized by various methods have recently been studied. The structural, magneto-transport, and electrical properties of $\text{La}_{1-x}\text{Ca}_x\text{MnO}_3$ prepared using the sol-gel combustion method have been examined (Channagoudra et al., 2020). XRD for LCMO

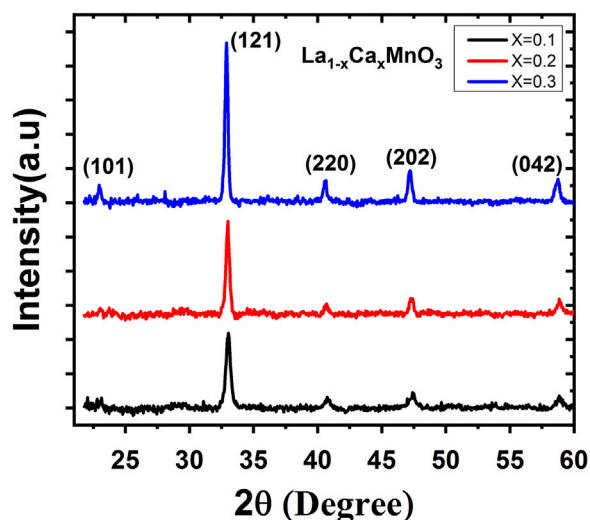


FIGURE 1
XRD pattern of $\text{La}_{1-x}\text{Ca}_x\text{MnO}_3$ nanoparticles, where $x = 0.1, 0.2$, or 0.3 .

($x = 0.375$ and 0.625) confirmed the single-phase orthorhombic perovskite structure. The low magnetoresistance in $x = 0.625$ is observed due to charge order (CO). In the absence of a magnetic field, the metal-insulator (MI) was observed for sample $x = 0.375$ at 172 K. A significant decrease in resistivity was observed after the application of a magnetic field. Additionally, it has been shown that the size of the nanoparticles is directly dependent on the annealing temperature (Xia et al., 2017b). The LCMO samples were synthesized and annealed at 600°C, 650°C, and 700°C for 5 h in the absence of an applied magnetic field to study temperature-dependent resistivity. Metal-insulator transition at 266 K, 267 K, and 248 K was observed. Additionally, the same transitions have been found for two systems, LCMO-PAS (plasma activated sintering) and LCMO-HP (hot pressing), at a zero and 3T magnetic field at a temperature below 50 K; an upturn in resistivity shows an insulating behavior (Li et al., 2018b).

Temperature dependence on resistivity has also been reported for $\text{La}_{1-x}\text{Sr}_x\text{MnO}_3$ in the temperature range of 5–300 K with $x = 0.1, 0.2$,

and 0.3 at zero external magnetic field. An increase in T_p between $x = 0.1$ and $x = 0.3$ and a decrease in resistivity with increasing Sr concentration was observed (Van Cuong and Kim, 2009). The temperature dependence of ac susceptibility of LCMO and LCSMO showed a transition from a ferromagnetic to a paramagnetic state at 206 K and 277 K, respectively (Tank et al., 2015). Interesting results regarding ac susceptibility were obtained by a study of Fe-doped $\text{La}_{0.65}\text{Ca}_{0.35}\text{Mn}_{1-x}\text{Fe}_x\text{O}_3$ (Shah and Hasanain, 2010). Fe substitution gradually changed from a metallic ferromagnetic insulator to a ferromagnetic insulator at $T_c = 270\text{ K} - 79\text{ K}$. The increment in Fe concentration resulted in increased dissipation and disorder at low temperatures. The use of a DC field of 550 Oe resulted in a large decrease in susceptibility. The peaks of out-of-phase susceptibility broaden with increasing Fe concentration (Tola et al., 2017). M_s increases while H_c decreases with particle size. The larger H_c values at $D < 40\text{ nm}$ are caused by a magnetic dead layer. A broad phase transition has been shown for $D \leq 40\text{ nm}$, whereas transition is sharp for $D > 40\text{ nm}$. T_c increases initially then decreases slightly with increasing D above 40 nm (Xia et al., 2017b). This decrease in T_c with increasing annealing temperature or particle size is recognized as the decline of the double exchange interaction, as the bandwidth and mobility of the e_g electron decreases. This occurs because of the rise in Mn-O bond length and the reduction in the Mn-O-Mn bond angle. A branching in the MFC (T) and MZFC (T) curve, showing a glass-like behavior, has been found for a wide range of temperatures. An M-H study showed that the values of M_s and M_r are greater for samples annealed at 650°C than those annealed at 600°C and 700°C.

The structural, magnetic, and electronic properties of these materials are strongly dependent on doping level. Therefore, in this study, we report on the effect of Ca doping on the transport and magnetic properties of $\text{La}_{1-x}\text{Ca}_x\text{MnO}_3$ nanoparticles with $x = 0.1, 0.2$, or 0.3 . Different methods are used to synthesize these materials, such as a solid state reaction, the sol gel process, the molten salt route, and the glycerin-assisted combustion technique (Lu et al., 2007; Gubin, 2009; Prasad and Singh, 2011; Li et al., 2018a). However, these methods cause energy loss and environmental issues as they need expensive and toxic reagents and therefore cannot be used at a large scale (Gadani et al., 2017). In this study, we use the facile coprecipitation method, which has a simple operating procedure, is inexpensive, and can possibly create pure and homogeneous material that is environmental friendly.

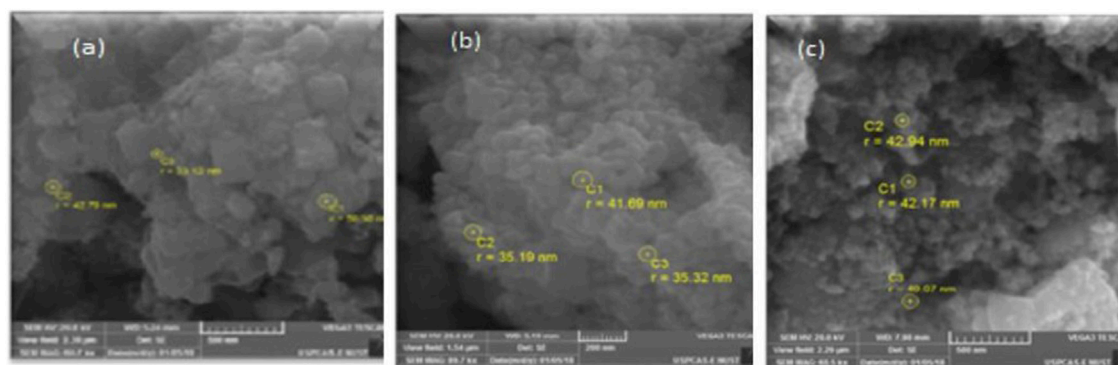


FIGURE 2
(A–C) SEM micrographs of $\text{La}_{1-x}\text{Ca}_x\text{MnO}_3$ ($x = 0.1, 0.2$, or 0.3).

2 Experimental techniques

LCMO nanoparticles were prepared using $\text{Mn}(\text{NO}_3)_2 \cdot 4\text{H}_2\text{O}$, $\text{CaCl}_2 \cdot 2\text{H}_2\text{O}$, and $\text{La}(\text{NO}_3)_3 \cdot 6\text{H}_2\text{O}$ as precursors purchased from Sigma-Aldrich with 99.99% purity. The desired stoichiometric amounts of these precursors were dissolved in deionized water, while NaOH was used as a precipitant. The first solution was continuously stirred at 80°C for 2 h to ensure homogeneity and the completion of the reaction. To maintain pH at 8.5, NaOH was added drop wise. The precipitate was filtered and cooled to room temperature. The powder was dispersed with ultrasonic waves in ethanol for 15 min to prepare mono-disperse LCMO nanoparticles and was then centrifuged and washed with distilled water. It was then dried in an oven for 1 h at 100°C. At 450°C, the dried samples were annealed in a furnace for 8 h. The same procedure was used for all samples.

We performed XRD (XPRT-3 Malvern Panalytical diffractometer system) using Cu K_α radiation with a wavelength of 1.54 Å over the angular range of $20^\circ \leq 2\theta \leq 70^\circ$ by step scanning results at a step size of 0.02 at a counting time of 3 s per step. Scanning electron microscopy (SEM-VEGA 3 TESKAN) was used to reveal the shape morphologies of all LCMO NPs. An EDX (SEM-VEGA 3 TESKAN) attached to the SEM was used to study the elemental composition and phase purity of the LCMO NPs. $M(H)$ behavior of $\text{La}_{1-x}\text{Ca}_x\text{MnO}_3$ ($x = 0.1, 0.2, 0.3$) was determined at a temperature of 77 K by applying a magnetic field at a strength of 10 kOe using a VSM. Magnetization *versus* temperature $M(T)$ was examined at a field of 70 Oe using field-cooled (FC) and zero-field-cooled (ZFC) protocols. A self-made ac probe with a commercial lock-in amplifier and split secondary (astatically wound) was used to study the ac susceptibility of all LCMO samples in the range $f = 573 \text{ Hz}$, $H_{ac} = 10 \text{ Oe}$, and $0 < H_{dc} < 550 \text{ Oe}$. A home-based solenoid magnet was used to orient the dc magnetic field in the same direction as the ac field. A commercial liquid nitrogen variable temperature cryostat was used to measure resistivity. We determined electrical resistance using air-drying conducting silver paste with the help of a standard four probe technique. A calibrated thermocouple Rh-Fe at a temperature range of 77 K–300 K was used to measure sample temperature. The accuracy of the temperature reading had a margin of error of 0.05 K. A digital voltmeter was used to determine voltage across the sample, and a constant current of 100 μA to 1 mA was provided.

3 Results and discussion

3.1 Structural analysis

The XRD patterns of the samples $\text{La}_{1-x}\text{Ca}_x\text{MnO}_3$ ($x = 0.1, 0.2, 0.3$) are shown in Figure 1. After fitting to the space group Pbnm and JCPDS No 89-0662, all the peaks matched the standard orthorhombic structure of perovskite manganite nanoparticles [6]. At diffraction angles $2\theta = 22.50^\circ, 32.85^\circ, 40.45^\circ, 48.30^\circ$, and 58.75° , the peaks were indexed to (101), (121), (220), (202), and (042) planes. No additional and unidentified peaks were found, revealing that impurities were not present in the samples. It shows that the system is structurally single phase. The range of crystallite sizes was 25–32 nm using Debye–Scherrer's formula ($D = 0.9\lambda/\beta\cos\theta$) (Safeen et al., 2022a; Safeen et al., 2022b), where “D” represents the crystallite size, “ λ ” is the wavelength of the x-ray, “ θ ” is the Bragg

diffraction angle, and “ β ” is the full width at the half maximum (FWHM) of the diffraction peak (Asghar et al., 2020).

3.2 Morphological studies

SEM images for $\text{La}_{1-x}\text{Ca}_x\text{MnO}_3$ ($x = 0.1, 0.2$, or 0.3) are featured in Figures 2A–C, which shows agglomerative particles that were, on average, 33–46 nm in size with a cage-like surface morphology. The samples were bulky and porous as gas was released in large amounts during heat treatment and sonication. The samples overall have a sphere-shaped cage-surface morphology.

3.3 Energy dispersive X-ray (EDX) spectroscopy

EDX spectra for $\text{La}_{1-x}\text{Ca}_x\text{MnO}_3$ ($x = 0.1, 0.2$, or 0.3) is shown in Figures 3A–C, which shows the presence of La, Mn, O, and Ca peaks, confirming elemental compositional and phase purity. No extra peaks related to impurities can be observed. The atomic percentage of La, Ca, Mn, and O obtained from EDX spectra are in close agreement with the initial values used during synthesis. Elemental percentages of samples are shown in Table 1.

3.4 $M(H)$ loops

The field-dependent magnetization $M(H)$ behavior of $\text{La}_{1-x}\text{Ca}_x\text{MnO}_3$ ($x = 0.1, 0.2$, and 0.3) at 77 K is shown in Figure 4, which shows that coercivity increases from $x = 0.1$ to $x = 0.3$. All the $M(H)$ loops showed ferromagnetic behavior, as confirmed by the $M(T)$ study. The enhanced coercivity could be attributed to single domain to multidomain magnetic behavior and randomly oriented equiaxial cubic magneto-crystalline anisotropy due to larger grain size (Chinnasamy et al., 2003). Additionally, the saturation magnetization increased with the concentration of x due to random canting of the grain surface spin occurring from the competition between ferromagnetic (FM) and anti-ferromagnetic (AFM) exchange interactions close to the surface. The M_r/M_s ratio was initially constant but decreased with doping concentration. Atoms have several domains of huge size, so magnetization reversal is gained by domain wall motion, thus coercivity is small. Magnetization reversal remains uniform for the single domain. For instance, it is necessary to respond with this field when the size of the spherical particle is larger for the identical spin rotation. Hence, initially, the energy wall for magnetization rotation increases with increasing particle size within a range of particle sizes. Therefore, coercivity increases because of the increase in particle size (Chinnasamy et al., 2003; Shah et al., 2012). The values of different parameters, such as M_s , M_r/M_s , M_r and H_c , obtained from the magnetic measurement of the synthesized nanoparticles are shown in Table 2.

3.5 Temperature-dependent DC magnetization

The temperature-dependent magnetization $M(T)$ for three samples at a magnetic field of 70 Oe is shown in Figure 5.

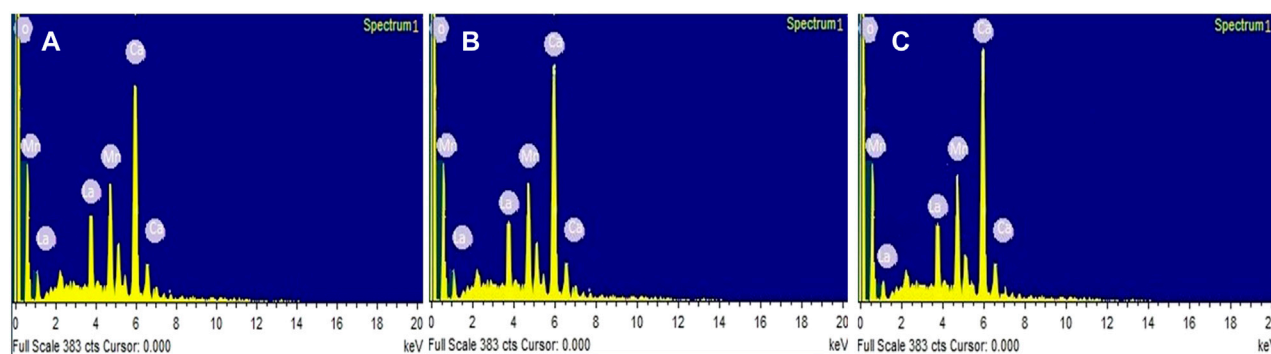


FIGURE 3
(A–C) EDX spectra of $\text{La}_{1-x}\text{Ca}_x\text{MnO}_3$ ($x = 0.1, 0.2$, or 0.3).

TABLE 1 Elemental composition of $\text{La}_{1-x}\text{Ca}_x\text{MnO}_3$ ($x = 0.1, 0.2$, and 0.3).

Samples	O (%)	La (%)	Ca (%)	Mn (%)	Total
$\text{La}_{0.9}\text{Ca}_{0.1}\text{MnO}_3$	47.41	35.61	13.64	3.34	100
$\text{La}_{0.8}\text{Ca}_{0.2}\text{MnO}_3$	46.32	33.55	16.53	3.60	100
$\text{La}_{0.7}\text{Ca}_{0.3}\text{MnO}_3$	43.34	32.45	20.15	4.06	100

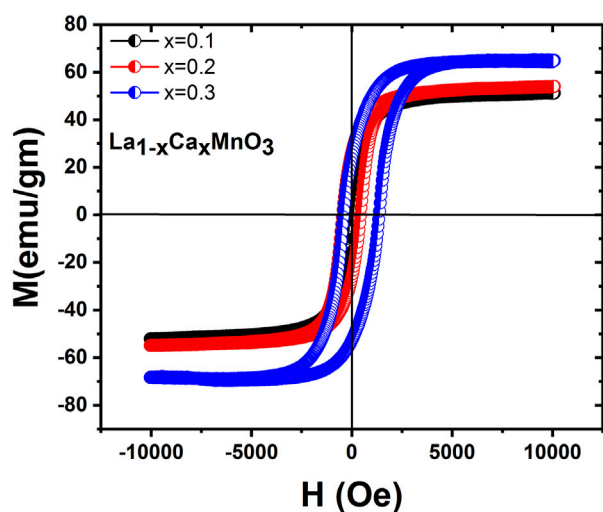


FIGURE 4
Field dependence of magnetization for $\text{La}_{1-x}\text{Ca}_x\text{MnO}_3$ samples at Ca concentrations of $x = 0.1, 0.2$, and 0.3 .

TABLE 2 Saturation-magnetization (M_s), remanent/saturation-magnetization (M_r/M_s), remanent magnetization (M_r), and coercive-field (H_c) of $\text{La}_{1-x}\text{Ca}_x\text{MnO}_3$ ($x = 0.1, 0.2$, and 0.3).

Samples	M_s (emu/gm)	M_r/M_s	M_r (emu/gm)	H_c (Oe)
$\text{La}_{0.9}\text{Ca}_{0.1}\text{MnO}_3$	51.55	0.28	14.34	79.53
$\text{La}_{0.8}\text{Ca}_{0.2}\text{MnO}_3$	54.28	0.287	15.57	208.9
$\text{La}_{0.7}\text{Ca}_{0.3}\text{MnO}_3$	66.50	0.195	12.97	172.58

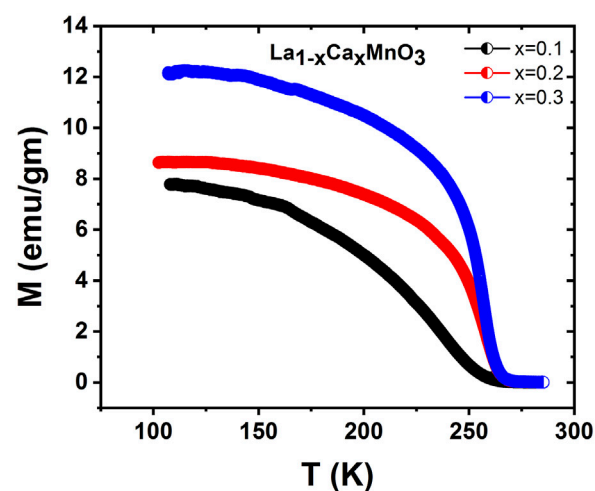


FIGURE 5
Magnetization as a function of temperature for $\text{La}_{1-x}\text{Ca}_x\text{MnO}_3$ ($x = 0.1, 0.2$, and 0.3).

Paramagnetic (PM) to ferromagnetic (FM) transition was observed due to cooling at a particular temperature of the material. The Curie temperatures T_c (the temperature representing the peak of $-dM/dT$ in the M vs T curve) were 258 K, 255 K, and 250 K for $x = 0.1, 0.2$, and 0.3 , respectively. The fall in T_c was caused by a decline in double exchange due to a reduction in mobility electrons and bandwidth. This reduction is up on rise in bond-length and decline in bond-angle of Mn-O-Mn (Shah, 2011).

Examination of $M(T)$ behavior of $\text{La}_{1-x}\text{Ca}_x\text{MnO}_3$ ($x = 0.2$ and 0.3) at a field of 70 Oe for FC and ZFC conditions to determine the behavior of magnetic spin freezing is shown in Figure 6. A split in the magnetization field cooled *versus* temperature and magnetization zero field cooled *versus* temperature curves over a wide temperature range. Upon cooling, the magnetic moment increased for all samples up to the lowest temperature for FC curves. A phase transition from paramagnetic to ferromagnetic was observed, but ZFC was different from FC, in which magnetic moments decreased as the temperature fell. We observed a huge difference in magnetization at lower temperatures between FC and ZFC curves. The dissimilarity between ZFC and FC magnetization was due to the significant spin

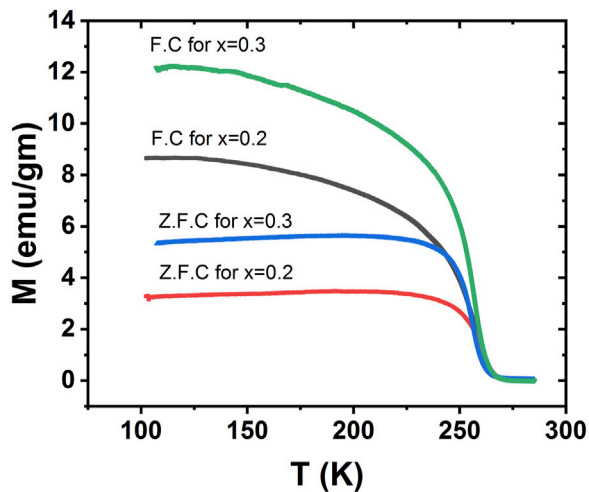


FIGURE 6
FC and ZFC DC magnetization as a function of temperature for $\text{La}_{1-x}\text{Ca}_x\text{MnO}_3$, where $x = 0.2$ and 0.3 .

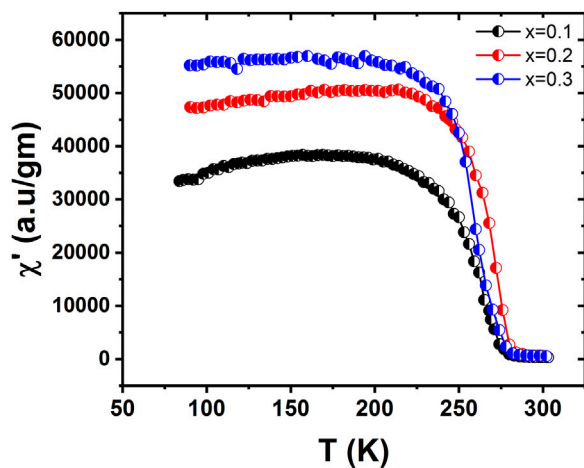


FIGURE 7
Variation of the in-phase of ac susceptibility as a function of temperature for $\text{La}_{1-x}\text{Ca}_x\text{MnO}_3$, where $x = 0.1, 0.2$, or 0.3 .

disorder and competing interaction between different phases (Hasanain et al., 2004). For FC curves, the maximum values of magnetization were 8.47 emu/gm and 12.16 emu/gm for $x = 0.2$ and 0.3 , respectively, while for ZFC curves, these values were 3.49 emu/gm and 5.49 emu/gm, respectively. As the temperature increased this difference minimized, and finally both curves merged. Such a behavior can be explained by the fact that when temperature is low the magnetic moment becomes frozen so that there is no order state in the long range. As a result of this spin disorder, strong competition occurred among ferromagnetic double-exchange (DE) and anti-ferromagnetic super-exchange (SE) so that a specific spin could obtain contradictory information, such as how to align with its neighbors due to exchange energy (Xia et al., 2017a). It may not be feasible to choose an assured spin configuration for the system to be

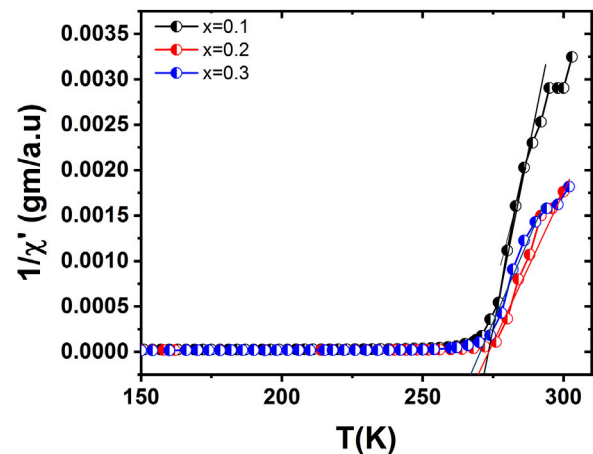


FIGURE 8
ac susceptibility versus temperature for $\text{La}_{1-x}\text{Ca}_x\text{MnO}_3$ ($x = 0.1, 0.2$, and 0.3) showing different paramagnetic Curie temperatures.

able to minimize its energy. This decrease of the magnetic moment is due to frustration. Between 240 K and 258 K, there is a delay in the increase in the magnetic moment during transition. The super exchange and strong double exchange magnetic interaction between Mn^{4+} and Mn^{3+} ions reduces the increase due to low temperature. As a result, there is competition between two phases and a spin-glass-like phase occurs due to the generation of some degree of frustration resulting from such a FM and AFM interaction. When the metallic-like conduct disappears, distinctive glass-like behavior is observed with small ions (Shah, 2011).

3.6 ac susceptibility measurement

There are two phases in which ac susceptibility measurements of the samples can be taken, namely, the in-phase and out-of-phase behavior as a function of temperature. Figure 7 shows the in-phase part of ac susceptibility. A sharp increase was observed at approximately 275 K, peaking at approximately 250 K. After the peak, there was a steady fall of ferromagnetic ac susceptibilities, with a sharp decline starting at approximately 100 K. A phase transition from the paramagnetic to the ferromagnetic phase occurred for all the samples in the transition region. Figure 7 shows that as Ca content increases, susceptibilities and sharpness in the transition region systematically decrease. Additionally, a decrease from the peak to the smallest value was observed. An increase of Ca concentration results in dissipation and spin disorder at low temperatures (Shah and Safeen, 2012). The presence of Ca results in a distortion not found in the XRD pattern. There is a possibility that an AFM arrangement is favored by local distortion catalyzed by Ca ions. Ferromagnetic clusters are found in the paramagnetic phase region. These ferromagnetic clusters increase in volume so that there is a complete ferromagnetic transition. However, in the clustering region, a continuous fluctuation occurs at high temperatures (Shah and Hasanain, 2010).

The behavior of the imaginary part of ac susceptibility is quite dissimilar from the real part as it sharply decreases at high T_c . The values of T_c for three samples ($x = 0.1, 0.2$, and 0.3) were 272.01 K,

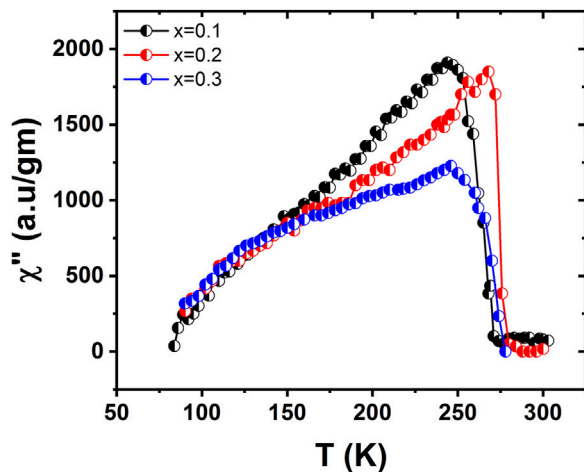


FIGURE 9
Variation of the out-of-phase part of ac susceptibility as a function of temperature for $\text{La}_{1-x}\text{Ca}_x\text{MnO}_3$ ($x = 0.1, 0.2$, and 0.3) showing T_c at different temperatures.

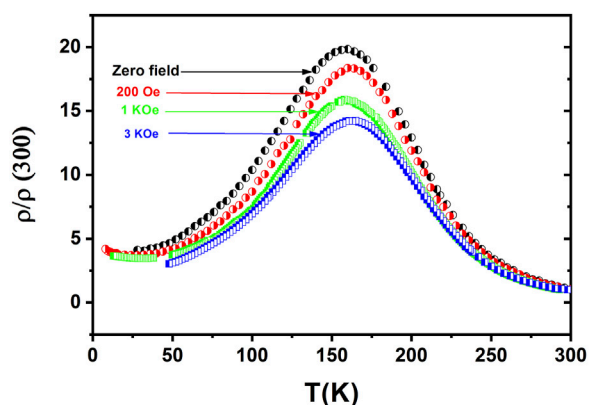


FIGURE 10
Temperature-dependent resistivity curves under different magnitudes of the magnetic field of $\text{La}_{0.8}\text{Ca}_{0.2}\text{MnO}_3$ for $x = 0.2$.

271.20 K, and 265.87 K, respectively, as shown in Figure 8. The out-of-phase part of susceptibility occurs because of spin direction and/or fluctuation losses. At phase transition, these losses become large. Within the low temperature region, the generation of losses is dependent on the merger of small clusters to form the major clusters. The fluctuation in the magnetization is proportional to the loss components for a system that is going through a magnetic transition, as described by the fluctuation dissipation theorem (Karoblis et al., 2020). The dynamical changes occurring in the critical region are related to the lost components. The development of dynamical correlation of the spin occurs due to energy losses that appear in the behavior. The variation of the out-of-phase part of ac susceptibility is shown in Figure 9. The peaks in the out-of-phase part of susceptibility occur near the T_c , where $M(T)$ shows no specific

structure except for the decrease of the variations in magnetization. The losses continue growing to a point at which the magnetization starts to rise sharply. This occurs during the persistent fast growth of small clusters in this range. These small clusters decrease in number at lower temperatures (Supplementary Material S1).

3.7 Resistivity measurements

To study the thermal fluctuation mechanism, the four-probe method was employed to determine the temperature-dependent electrical resistivity of $\text{La}_{0.8}\text{Ca}_{0.2}\text{MnO}_3$ nanoparticles. Figure 10 shows the effect of the applied magnetic field on resistivity in different temperature ranges. The values of resistivity were $1.4 \Omega\text{-cm}$ with the cooling protocol and $1.5 \Omega\text{-cm}$ with heating. This result shows that the transition temperature for the cooling curve rose as the magnetic field increased from 0 to 3 KOe. Additionally, resistivity decreased upon application of the magnetic field, as the microstructure of the large-range grain domain was parallel to the applied field. When the magnetic field was increased, the large-range magnetic array was increased, resulting in a decrease in resistivity. A rapid change in metal-to-insulator transition peak temperature (T_p) was observed. At room temperature, the sample was a semiconductor and had a temperature above the peak, i.e., at $T_p = 170 \text{ K}$ it exhibited metallic behavior. This alteration is related to magnetic ordering. The double-exchange mechanism defines the co-occurrence of FM and metallic behavior. At the highest value of Hund's exchange energy, the conductivity maximizes. Thus, ferromagnetism is associated with metal-like behavior. T_p is rather different for heating and cooling curves (Hao et al., 2013). T_p is low compared to normal. This drop of T_p is caused by the decrease of oxygen (Van Cuong and Kim, 2009). Identical and smaller particles have unlike stoichiometric oxygen. The deduction of oxygen reduces Mn^{4+} to Mn^{3+} . It preserves the electrical neutrality of the assemblage. The elimination of the oxygen bond stops the conduction pathways for e_g electrons. For the large range, the insulating part is further enhanced in the high-temperature range. With the rise in temperature, these defects decrease resistivity, resulting in an insulating appearance.

4 Conclusion

In conclusion, coprecipitation is a facile method for preparing LCMO nanoparticles. The XRD results show that prepared samples are pure in phase, and doping has no effect on the space group Pbnm. Particle size, identified by SEM, confirmed the nanocrystalline structure of the LCMO system. The hysteresis study revealed an increase in saturation magnetization with the increase of Ca because of arbitrary canting of the grain surface spin occurring near the surface of the competition between FM and AFM exchange interactions. A bifurcation in the magnetization FC and magnetization ZFC versus temperature curves over a wide range of temperatures was observed. The addition of Ca increased spin disorder, resulting in a decrease in the in-phase part of susceptibilities. The out-of-phase part of susceptibility occurred

due to the losses that were proportional to the fluctuation in the magnetization of a system. Resistivity measurements showed that the sample is a semiconductor at room temperature and becomes metallic above the peak transition temperature. Additionally, resistivity decreased as a function of the applied field. The investigated system may be used in magnetoresistance and other related applications.

Data availability statement

The raw data supporting the conclusion of this article will be made available by the authors, without undue reservation.

Author contributions

Conceptualization (AA, WS, and AS); Formal analysis (KS, MT, ZU, LA, SE, and NI); Investigation (MS, MR, and AA); Methodology (AA and WS); Project administration (WS); Supervision (WS); Writing—original draft (AA, WS, SE, and NI); Writing—review and editing (SE, AA, WS, KS, MT, ZU, LA, and AS).

References

- Asghar, G., Asri, S., Khushro, S. N., Tariq, G. H., Awan, M., Irshad, M., et al. (2020). Enhanced magnetic properties of barium hexaferrite. *J. Elec Materi* 49, 4318–4323. doi:10.1007/s11664-020-08125-7
- Channagoudra, G., Saw, A. K., and Dayal, V. (2020). Low temperature spin polarized tunnelling magneto-resistance in La_{1-x}CaxMnO₃ (x=0.375 and 0.625) nanoparticles. *Emergent Mat.* 3, 45–49. doi:10.1007/s42247-019-00067-z
- Chinnasamy, C., Jeyadevan, B., Shinoda, K., Tohji, K., Djayaprawira, D., Takahashi, M., et al. (2003). Unusually high coercivity and critical single-domain size of nearly monodispersed CoFe₂O₄ nanoparticles. *Appl. Phys. Lett.* 83, 2862–2864. doi:10.1063/1.1616655
- Cuong, P., and Kim, D. H. (2009). Effect of strontium doping level on electrical transport and magnetic properties of La_{1-x}SrxMnO₃ perovskite nanoparticles. *J. Phys. Conf. Ser.* 187, 012090. doi:10.1088/1742-6596/187/1/012090
- Dagotto, E., Hotta, T., and Moreo, A. (2001). Colossal magnetoresistant materials: The key role of phase separation. *Phys. Rep.* 344, 1–153. doi:10.1016/s0370-1573(00)00121-6
- Gadani, K., Keshvani, M., Dhruv, D., Boricha, H., Rathod, K., Prajapati, P., et al. (2017). Low field magnetoelectric and magnetotransport properties of sol-gel grown nanostructured LaMnO₃ manganites. *J. Alloys Compd.* 719, 47–57. doi:10.1016/j.jallcom.2017.05.165
- Gor'kov, L. P., and Kresin, V. Z. (2004). Mixed-valence manganites: Fundamentals and main properties. *Phys. Rep.* 400, 149–208. doi:10.1016/j.physrep.2004.08.003
- Gubin, S. P. (2009). *Magnetic nanoparticles*. John Wiley & Sons.
- Hao, F., Jing, D., Xiao-Peng, H., Fang-Yi, C., and Jun, C. (2013). Sol-gel synthesis of perovskite La_{1-x}CaxMnO₃ (x= 0 similar to 0.4) nanoparticles for electrocatalytic oxygen reduction. *Chin. J. Inorg. Chem.* 29, 1617–1625.
- Hasanain, S., Shah, W. H., Mumtaz, A., Nadeem, M., and Akhtar, M. (2004). Re-entrant spin freezing behavior in La_{0.85}Ca_{0.15}Mn_{0.95}Fe_{0.05}O₃ manganite. *J. magnetism magnetic Mater.* 271, 79–87. doi:10.1016/j.jmmm.2003.09.020
- Karoblis, D., Mazeika, K., Baltrunas, D., Lukowiak, A., Strek, W., Zarkov, A., et al. (2020). Novel synthetic approach to the preparation of single-phase BixLa_{1-x}MnO₃+δ solid solutions. *J. Sol-Gel Sci. Technol.* 93, 650–656. doi:10.1007/s10971-019-05098-w
- Li, S., Wang, C., Liu, H., Li, L., Shen, Q., Hu, M., et al. (2018a). Effect of sintering temperature on structural, magnetic and electrical transport properties of La_{0.67}Ca_{0.33}MnO₃ ceramics prepared by Plasma Activated Sintering. *Mater. Res. Bull.* 99, 73–78. doi:10.1016/j.materresbull.2017.10.049
- Li, S., Wang, C., Zhou, D., Liu, H., Li, L., Shen, Q., et al. (2018b). Preparation of dense La_{0.67}Ca_{0.33}MnO₃ ceramics by plasma activated sintering and hot-pressing. *Ceram. Int.* 44, 550–555. doi:10.1016/j.ceramint.2017.09.210
- Lu, A. H., Salabas, E. E. L., and Schüth, F. (2007). Magnetic nanoparticles: Synthesis, protection, functionalization, and application. *Angew. Chem. Int. Ed.* 46, 1222–1244. doi:10.1002/anie.200602866
- Mormoopidae (2009). “Leaf-nosed bat,” in *Encyclopædia britannica* (Britannica).
- Prasad, R., and Singh, P. (2011). Applications and preparation methods of copper chromite catalysts: A review. *Bull. Chem. React. Eng. Catal.* 6, 63–113. doi:10.9767/bcrec.6.2.829.63-113
- Safeen, A., Safeen, K., Shafique, M., Iqbal, Y., Ahmed, N., Rauf Khan, M. a. R., et al. (2022a). The effect of Mn and Co dual-doping on the structural, optical, dielectric and magnetic properties of ZnO nanostructures. *RSC Adv.* 12, 11923–11932. doi:10.1039/d2ra01798a
- Safeen, A., Safeen, K., Ullah, R., ZulfqarShah, W. H., Shah, Q., Zaman, K., et al. (2022b). Enhancing the physical properties and photocatalytic activity of TiO₂ nanoparticles via cobalt doping. *RSC Adv.* 12, 15767–15774. doi:10.1039/d2ra01948e
- Shah, W. H. (2011). Dynamic response in Fe-doped La_{0.65}Ca_{0.35}Mn_{1-x}Fe_xO₃: Rare-Earth manganites. *J. Mat. Res.* 26, 2599–2603. doi:10.1557/jmr.2011.228
- Shah, W. H., and Hasanain, S. (2010). Ac susceptibility studies in Fe doped La_{0.65}Ca_{0.35}Mn_{1-x}Fe_xO₃: Rare Earth manganites. *J. Appl. Phys.* 108, 113907. doi:10.1063/1.3517113
- Shah, W. H., and Safeen, A. (2012). Effects of frequency on AC conductivity and magnetoresistance in doped La_{0.65}Ca_{0.35}MnO₃ manganites. *J. Elec Materi* 41, 2243–2249. doi:10.1007/s11664-012-2092-8
- Shah, W. H., Safeen, K., and Rehman, G. (2012). Effects of divalent alkaline Earth ions on the magnetic and transport features of La_{0.65}A_{0.35}Mn_{0.95}Fe_{0.05}O₃ (A = Ca, Sr, Pb, Ba) compounds. *Curr. Appl. Phys.* 12, 742–747. doi:10.1016/j.cap.2011.10.015
- Tank, T. M., Bodhayee, A., Mukovskii, Y. M., and Sanyal, S. (2015). “Electrical-transport, magnetoresistance and magnetic properties of La_{0.7}Ca_{0.3}MnO₃ and La_{0.7}Ca_{0.24}Sr_{0.06}MnO₃ single crystals,” in *AIP conference proceedings* (AIP Publishing LLC), 100027.
- Tola, P., Kim, H., Kim, D., Phan, T., Rhyee, J., Shon, W., et al. (2017). Tunable magnetic properties and magnetocaloric effect of off-stoichiometric LaMnO₃ nanoparticles. *J. Phys. Chem. Solids* 111, 219–228. doi:10.1016/j.jpcs.2017.07.022
- Xia, W., Li, L., Wu, H., Xue, P., and Zhu, X. (2017a). Molten salt route of La 1-x Ca x MnO 3 nanoparticles: Microstructural characterization, magnetic and electrical transport properties. *Mater. Charact.* 131, 128–134. doi:10.1016/j.matchar.2017.07.002
- Xia, W., Li, L., Wu, H., Xue, P., and Zhu, X. (2017b). Structural, morphological, and magnetic properties of sol-gel derived La_{0.7}Ca_{0.3}MnO₃ manganite nanoparticles. *Ceram. Int.* 43, 3274–3283. doi:10.1016/j.ceramint.2016.11.160

Conflict of interest

NI was employed by the company Heavy Industries Taxila.

The remaining authors declare that the research was conducted in the absence of any commercial or financial relationships that could be construed as a potential conflict of interest.

Publisher's note

All claims expressed in this article are solely those of the authors and do not necessarily represent those of their affiliated organizations, or those of the publisher, the editors and the reviewers. Any product that may be evaluated in this article, or claim that may be made by its manufacturer, is not guaranteed or endorsed by the publisher.

Supplementary material

The Supplementary Material for this article can be found online at: <https://www.frontiersin.org/articles/10.3389/fmats.2023.1117793/full#supplementary-material>



OPEN ACCESS

EDITED BY

Ali Saleh Alshomrani,
King Abdulaziz University, Saudi Arabia

REVIEWED BY

Noreen Akbar,
National University of Sciences and
Technology (NUST), Pakistan
Aurang Zaib,
Federal Urdu University of Arts, Sciences
and Technology Islamabad, Pakistan

*CORRESPONDENCE

Muhammad Sohail,
✉ muhammad_sohail111@yahoo.com
Sayed M. Eldin,
✉ sayed.eldin22@fue.edu.eg

SPECIALTY SECTION

This article was submitted to Colloidal
Materials and Interfaces,
a section of the journal
Frontiers in Materials

RECEIVED 25 November 2022

ACCEPTED 12 January 2023

PUBLISHED 03 February 2023

CITATION

Nazir U, Sohail M, Naz S, Mukdasai K,
Singh M, Singh A, Mohan CR, Eldin SM and
Galal AM (2023), Effective role of mineral
oil and biological nanomaterial on thermal
energy influenced by magnetic dipole and
nanoparticle shape.
Front. Mater. 10:1107661.
doi: 10.3389/fmats.2023.1107661

COPYRIGHT

© 2023 Nazir, Sohail, Naz, Mukdasai, Singh,
Singh, Mohan, Eldin and Galal. This is an
open-access article distributed under the
terms of the [Creative Commons
Attribution License \(CC BY\)](#). The use,
distribution or reproduction in other
forums is permitted, provided the original
author(s) and the copyright owner(s) are
credited and that the original publication in
this journal is cited, in accordance with
accepted academic practice. No use,
distribution or reproduction is permitted
which does not comply with these terms.

Effective role of mineral oil and biological nanomaterial on thermal energy influenced by magnetic dipole and nanoparticle shape

Umar Nazir¹, Muhammad Sohail^{2*}, Samaira Naz³, Kanit Mukdasai¹,
Manoj Singh⁴, Abha Singh⁵, Chandika Rama Mohan⁶,
Sayed M. Eldin^{7*} and Ahmed M. Galal^{8,9}

¹Department of Mathematics, Faculty of Science, Khon Kaen University, Khon Kaen, Thailand, ²Institute of Mathematics, Khwaja Fareed University of Engineering and Information Technology, Rahim Yar Khan, Pakistan, ³Department of Mathematics, Government College University Faisalabad, Faisalabad, Pakistan, ⁴Department of Mathematics, Faculty of Science, Jazan University, Jazan, Saudi Arabia, ⁵Department of Basic Sciences, College of Sciences and Theoretical Studies, Dammam-Branch, Saudi Electronic University, Riyadh, Saudi Arabia, ⁶Clinical Nutrition Department Applied Medical Science College Jazan University, Jazan, Saudi Arabia, ⁷Center of Research, Faculty of Engineering, Future University in Egypt, New Cairo, Egypt, ⁸Mechanical Engineering Department, College of Engineering, Prince Sattam Bin Abdulaziz University, Al-Kharj, Saudi Arabia, ⁹Production Engineering and Mechanical Design Department, Faculty of Engineering, Mansoura University, Mansoura, Egypt

This study of synovial fluid was conducted by considering two different nanofluid models over a two-dimensional stretched surface using nanoparticles of different shapes. We obtained remarkable results regarding the impact of nanoparticles on thermal performance. Through this study, we assessed heat and mass transfer and the involvement of magnetic dipole of chemically reactive species in two-dimensional steady incompressible flow. Heat generation was incorporated in the energy equation and a first-order chemical reaction was involved in the mass transport phenomenon. The concept of boundary layer was adopted to derive the physical problem in Cartesian coordinates, with results in the form of coupled partial differential equations (PDEs). The derived PDEs were highly non-linear, and exact solutions were not possible. Therefore, the PDEs were converted into non-linear ordinary differential equations (ODEs) using appropriate similarity transformation and then solved numerically via the finite element method. The impact of numerous emerging parameters on the solutions are displayed graphically, and the physical significance is discussed. An increment in Sc , K_c , and γ decelerated the solute field, while the concentration gradient increased with enhancement in Sc . Maximum acceleration in velocity for model-I was produced compared to acceleration in the velocity field for model-II.

KEYWORDS

nanomaterial shape, biological fluid, heat source, nanoparticles, magnetic dipole, thermo-phoretic particle, flat plate

1 Introduction

In laboratories worldwide, researchers are investigating a wide range of possible applications for nanofluids. These applications include mineral oils, water, solar energy, and microelectronics. It is possible that using chemotherapy in conjunction with nanoparticles will result in the death of cancer cells. The operation of the thermal extrusion mechanism is not due to the presence of low-energy reservoirs but rather to the process by which nanoparticles are produced. Thermo-physical

properties of nano-liquids, such as thermal infusibility and thermal conductivity, are among the most advanced in the industry, which could benefit various industries. It is possible to use nanomaterials in multiple applications, such as cooling of engines, processing of pharmaceuticals, operation of fuel cells, and function of residential cooling systems. Large-capacity cooling systems are now feasible thanks to the energy-saving characteristics of nano-liquids. A nano liquid-based smart material has the potential to regulate the flow of heat and act as a heat valve. In addition to these applications, there are potential uses of nano-liquids in geothermal energy production and fuel production for nuclear reactors. Both the minimum quantity cooling lubrication (MQCL) and the MQCG nanofluid technologies benefit the environment due to their reduced reliance on oil and grease. They not only cool and lubricate but also eliminate the need for cutting fluids. Choi and Eastman (1995) developed the concept of nanofluids. Nanofluids are characterized by nanoparticles suspended in liquids. The behavior of a nano-liquid can be significantly altered depending on the temperature and viscosity of the fluid's boundary layer. Khan et al. (2021a) discussed the role of gold nanoparticles in Sisko fluid under the impacts of thermal radiation and Lorentz force using slip conditions toward a curved surface. Khan et al. (2021b) derived mono and hybrid nanomaterials in motion at the stagnation point utilizing characteristics of the microstructure of moveable frames *via* non-isothermal condition. Khan et al. (2022a) studied various impacts of stagnation point characteristics in thermal and mass diffusion fields under the role of magnetic fields containing graphene oxide and water nanoparticles on the surface. Khan et al. (2022b) have driven multiple features of AA7075 and AA7072 nanoparticles within heat transfer on a cylinder utilizing slip conditions. Akbar et al. (2022) described the heat transfer mechanism of unsteady peristaltic liquid, including variable thermal properties, *via* the exact solution approach. Akram et al. (2022a) modeled the flow of peristaltic propulsion in the motion of TiO₂/10W40 nanoparticles using mechanisms of electro-osmotic in a curved microchannel. Maraj et al. (2017) estimated the consequences of Lorentz force and thermal deposition in a vertical channel filled with carbon nanotubule (CNT) nanoparticles. Akram et al. (2022b) modeled a flow problem based on peristaltic transport that involved adding a mixture of nanoparticles considering Lorentz force in aqueous media. Shafee et al. (2021) developed a non-equilibrium theory that sheds light on how the shape factor, Lorentz force, and radiation term influence heat transfer and behavior in nanomaterials. Akbar et al. (2019) analyzed features of ethylene glycol in thermal transfer when inserting suspensions of different shaped nanoparticles in a vertical channel. Habib and Akbar (2021) investigated the use of dispersed nanoparticles to combat *Staphylococcus aureus* in clinical isolates.

When electrokinetic Jeffrey fluid and peristalsis are combined, a phenomenon known as the Soret–Dufour cross-diffusion effect occurs. When scientists are trying to figure out how streamlines move, they frequently consider the “trapping theory” as one of the possible explanations. Peristalsis is defined as a wave-like movement of fluids through a channel, which happens naturally in the body. The production of heat is caused by the passage of a chemically reactive liquid through a porous medium with the assistance of a semi-infinite vertical permeable plate, which also contributes to the movement of the liquid. Hall currents and a liquid called Jeffrey liquid have been studied by Babu et al. (2020). Ali et al. (2020) researched how heat and thermal energy moved through the stretching cylinder in Jeffrey fluids. During an experiment conducted by Aleem and Alex, there was a consistent flow of Jeffrey fluid between two hot plates. The existence of a strong magnetic field piqued their

interest in this subject matter. According to Saif et al. (2020), the mechanisms that control the flow of magnetic hydrodynamic (MHD) fluid and heat transfer are governed by the curvature of the stretching surface. Research conducted by Gireesha et al. (2020) looked at the three-dimensional flow of radiating Jeffrey liquids on a stretched surface. According to Manjunatha et al. (2020), the effects of heat and solutes on peristaltic flow of Jeffrey fluid are not uniformly distributed throughout the system. This plan defies logic in every way. Sinha et al. (2020) investigated the effects of thermal radiation and Hall current on a nanofluid. Use of a thermal tube that vibrated and emitted moving ultrasound waves was required for that method. The effect of a specific variable electrical field on the flow of Jeffrey fluid is illustrated in Haroun (2020). As part of their experiment, they observed the non-steady and hydromagnetic flow using a flat plate and a magnetic field to observe the flow of the electrical conductor but incompressible fluid. In a porous Darcy-type medium, a third-grade nano-liquid that is optically dense and electrically conductive transfers heat to a porous surface *via* a Lie symmetry mechanism. This surface is located in the middle of the medium. This nano-liquid has a high density when measured in light and electricity. Maraj et al. (2022) discussed the results of rotational flow in a channel filled with hybrid nanoparticles under the impact of Lorentz forces using slip conditions. Akram et al. (2021) estimated theoretical results of thermal transfer with a mixture of hybrid nanoparticles and base fluid (water) in microchannels *via* electroosmotic pumping.

Bioconvection makes the growth process easier for bacteria and algae suspended in water. Microorganisms make the process of bioconvection possible. Microbes capable of bioconvection rise to the surface because they are 5–10 percent denser than water. They are referred to as “bioconvective” because of this characteristic. The action of these microorganisms causes the primary fluid to become thicker as a side effect. Examples of bioconvection can be observed in a wide variety of organic applications and microsystems, pharmaceuticals, biopolymers, environmentally friendly applications, developments in the utilization of cost-effective energy sources, microbial advanced oil recovery, biosensors and biotechnology, and continuous numerical display. One industry that uses bioconvection is the continuous numerical display (CND) industry. In their analysis, they examined MHD flow of nanofluids in the vicinity of a stretching surface, taking both velocity slip and viscous dissipation into account; in their research on the ferromagnetic materials of general Newtonian fluids, Khan et al. used bioconvection species that were chemically and paraboloid reactive. For example, Shehzad et al. (2020) have demonstrated that fluid can flow through spinning discs, analogous to the way water flows through tubes. Khan et al. (2020) proposed the hypothesis that gyrotactic microorganisms move around in nano-liquids that have thixotropic viscosity. According to Veera Krishna (2020), a magnetic field is generated when a steady convective magnetohydrodynamic flow of a viscous nanofluid is combined with a permeable porous surface that expands exponentially. As a consequence of the interaction of these two variables, the magnetic field will exhibit some movement. The Carreau–Yasuda nanofluid flow was the result of combining the findings of Hassan et al. (Waqas et al., 2020) on second-order velocity slip and moving microorganisms. Akram et al. (2022c) analyzed electroosmotic flow based on peristalsis flow of silver–water nanomaterials by implementing two approaches. Research conducted by Hosseinzadeh et al. (2020) focused on second-grade convective nanofluid flows. A square cavity that was open on all sides was used to investigate how an oxytactic microbe moved throughout the space. The Boussinesq–Darcy approximation was utilized for both the flow of

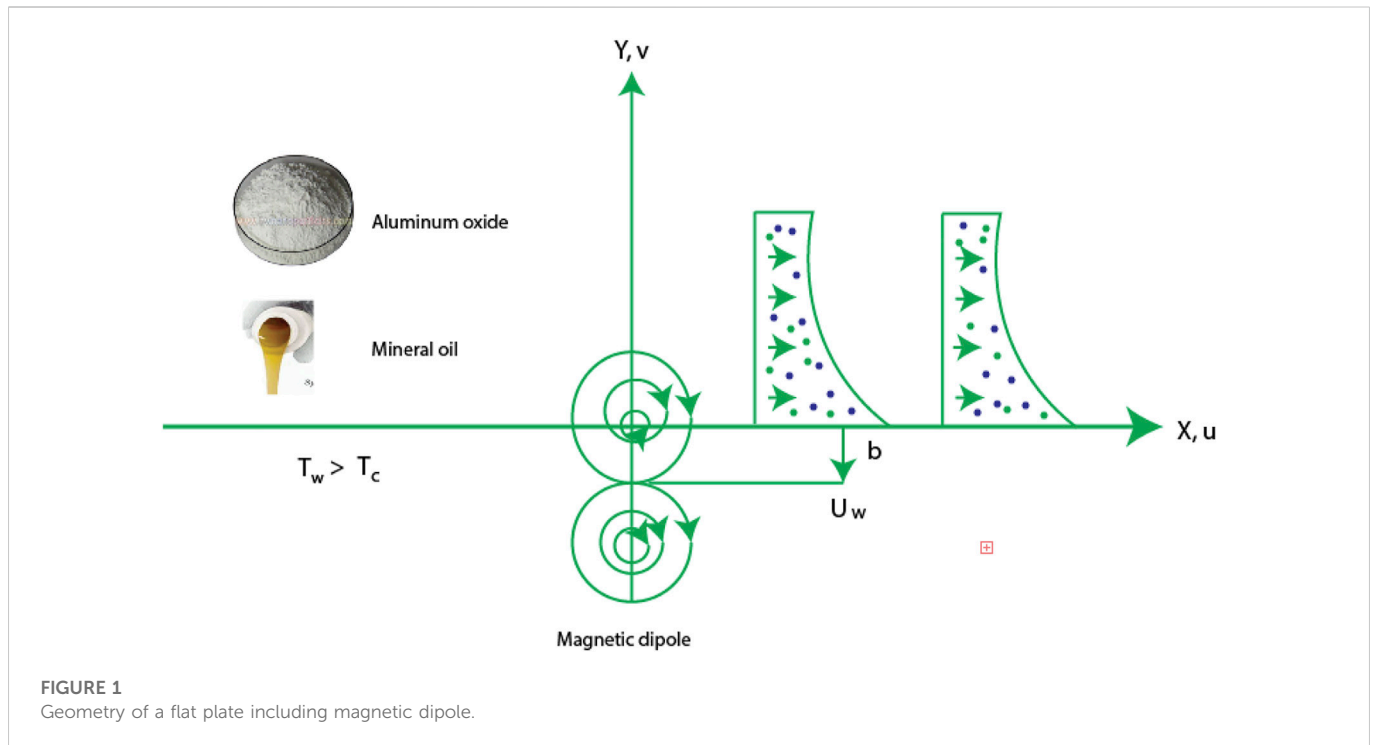


TABLE 1 Thermal properties associated with nanoparticles in base liquid (Hanif and Shafie, 2022; Wang et al., 2022).

	ρ	K	C_p	σ	μ
Al_2O_3	3,970	40		765	35×10^6
Mineral oil	861	0.157	1860	$0.33 \cdot 10^{-9}$	0.01335

heat and bioconvection. Activation energy and gyrotactic microorganisms are being used to study nanofluid rheology throughout porous media. A horizontal porous expansion sheet can influence the flow of a fluid infested with gyrotactic microorganisms in a manner comparable to that of a magnetohydrodynamic model for students using the third-grade model (Madhukesh et al., 2022).

Rostami et al. (2022) studied the hydro-thermal analysis. Moreover, the studies reported by, Hosseinzadeh et al. (2021a); Hosseinzadeh et al. (2021b); Sohail et al. (2022a); Sohail et al. (2022b); Hou et al. (2022) are prepared to notice the comportment of numerous involved parameters on momentum and thermal transport. There are no studies in the existing literature that involve synovial fluid and consider the two different nanofluid models over a two-dimensional stretched surface through use of different shaped nanoparticles. In the current study, the modeled problem is solved numerically, and the results are displayed through tables and graphs.

2 Model characteristics and mathematical analysis

The following assumptions were made:

- SF (synovial fluid) is considered over a 2D surface;
- Several shapes (cylinder, brick, sphere, and platelet) of nanoparticles are addressed;

- Magnetic dipole is considered;
- Correlations based on nanoparticles are assumed;
- Heat source is taken out;
- Chemical species and thermo-phoretic properties are addressed;
- Base fluid is taken as mineral oil;
- Figure 1 represents the geometry of the model.

Two models of viscosity (Salmi et al., 2022) are defined as

$$\mu(C, N) = e^{bC} \mu_0 (\gamma^2 |N|^2 + \epsilon)^n \text{ for model - I.} \quad (1)$$

$$\mu(C, N) = \mu_0 (\gamma^2 |N|^2 + \epsilon)^{n(c)} \text{ for model - II.} \quad (2)$$

Here, Eqs 1, 2 are known as model-I and model II, respectively. Governing equations (Salmi et al., 2022; Wang et al., 2022) are derived utilizing conservation laws. PDEs in view of SF implicating magnetic dipole are

$$u_x + v_y = 0, \quad (3)$$

Two models regarding momentum equations are obtained using Eqs (1) and (2). Momentum equation for model-I is

$$\rho_{Nf} (uu_x + vv_y) = -P_x + M\mu_{Nf} H_x + 2\mu_{Nf} \left[u_{yy} + 3\gamma^2 (u_y)^2 u_{yy} + \alpha^* u_{yy} \phi + \alpha^* u_y \phi_y \right] + \alpha^* \gamma^2 (u_y)^3 \phi_y + 3\alpha^* \gamma^2 \phi (u_y)^2 u_{yy} \quad (4)$$

The momentum equation for model-II is

TABLE 2 Shapes of nanoparticles associated with size (Naseem et al., 2021).

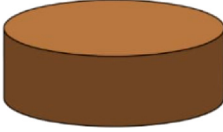

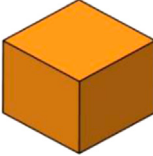
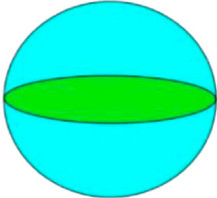
Shape of nanoparticles	M	A_1	A_2
 Platelet	5.72	37.1	612.6
 Cylinder	4.82	13.5	904.4
 Brick	3.72	1.9	471.4
 Sphere	3.0	2.5	6.5

TABLE 3 Grid size analysis in terms of velocity, concentration, and temperature fields simulated by 300 elements when $\alpha = 2.0$, $n = 0.5$, $Re = 2.0$, $\gamma = 3.0$, $\beta = 1.3$, $\Lambda = 0.3$, $Pr = 5.0$, $\epsilon = 0.1$, $H_t = 2.0$, $Sc = 0.4$, $\lambda = 0.4$, $K_c = -1.5$, $\chi = 0.3$, $\tau = 0.3$, and $We = 0.7$.

e	$F'(\frac{\eta_\infty}{2})$	$\theta(\frac{\eta_\infty}{2})$	$\phi(\frac{\eta_\infty}{2})$
30	0.5333,333,270	0.1754,080,591	0.3094,245,544
60	0.5166,666,704	0.1648,496,296	0.2950,440,665
90	0.5111,110,865	0.1614,464,769	0.2903,546,386
120	0.5083,333,305	0.1597,661,853	0.2880,288,454
150	0.5066,666,515	0.1587,644,986	0.2866,390,692
180	0.5055,555,689	0.1580,996,219	0.2857,156,200
210	0.5047,636,551	0.1576,259,302	0.2850,569,932
240	0.5041,665,982	0.1572,718,391	0.2845,632,498
270	0.5037,037,880	0.1569,962,944	0.2841,804,318
300	0.5033,309,189	0.1567,760,666	0.2838,742,789

$$\rho_{Nf}(uu_x + vv_y) = -P_x + M\mu_{Nf}H_x + 2\mu_{Nf}\left[u_{yy} - \frac{\alpha^*\gamma^2}{2}(u_y)^3\phi_y - \frac{3\alpha^*\gamma^2}{2}\phi(u_y)^2u_{yy}\right], \quad (5)$$

$$(uT_x + vT_y) + \frac{1}{(\rho C_p)_{Nf}}(uH_x + vH_y)\mu_{Nf}TM_T = \frac{K_{Nf}}{(\rho C_p)_{Nf}}T_{yy} - \frac{Q_0}{(\rho C_p)_{Nf}}(T - T_\infty), \quad (6)$$

The mass diffusion equation (Madhukesh et al., 2022) is defined as

$$uC_x + vC_y = DT_{yy} + \left((C - C_\infty)k_{yf}\frac{T_w - T_\infty}{T_s}\right)_y - K(C - C_\infty). \quad (7)$$

Developing boundary conditions (Wang et al., 2022) are

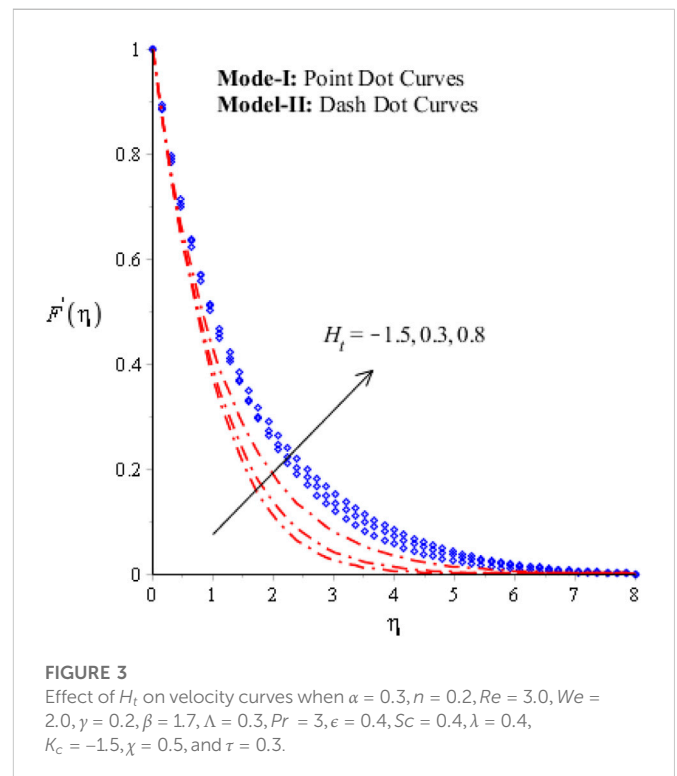
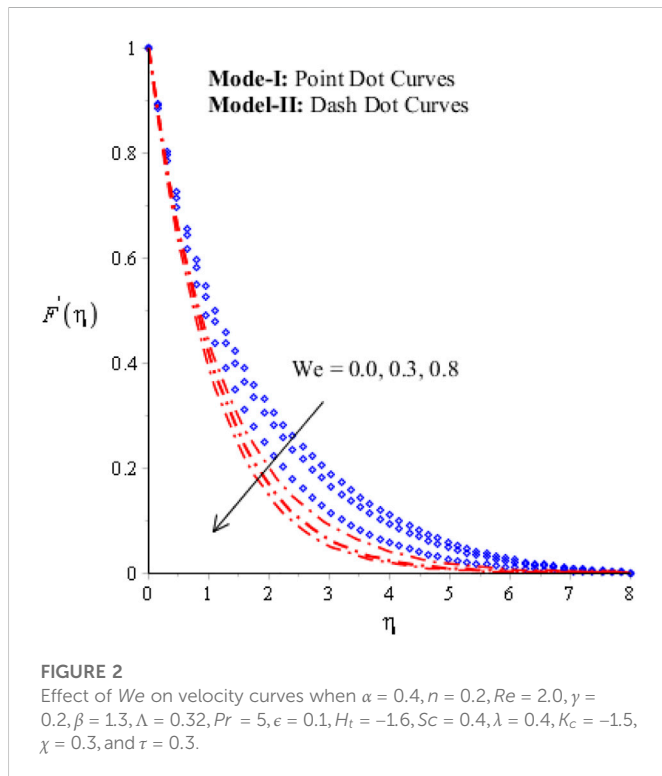
$$C = C_w, v = 0, u = U_w = aX, T = T_w: y = 0, \\ T \rightarrow T_\infty = T_c, u \rightarrow u_e, C \rightarrow C_\infty: y \rightarrow \infty. \quad (8)$$

The magnetic field via magnetic dipole (Wang et al., 2022) is

$$\beta_1 = \frac{\delta}{2\pi} \left(\frac{X}{X^2 + (Y + d)^2} \right). \quad (9)$$

TABLE 4 Validation results for Nusselt number based on published data (Muhammad and Nadeem, 2017) when $H_t = 0, \beta = \epsilon = 0 = \Lambda = 0, \chi = 0, \lambda = 0, \alpha = 0.3, n = 0.2, Re = 3.0, We = 2.0, Sc = 0.4, K_c = -1.5$, and $\tau = 0.3$.

Pr	Present results	Muhammad and Nadeem (2017)
0.72	0.8086,330,926	0.808,641
1.0	1.0005,315,382	1.000000
3.0	1.9232,636,052	1.923,690
4.0	2.0031,160,400	2.003170



Components of magnetic dipole (Wang et al., 2022) are

$$H_X = -\frac{\partial \delta}{\partial X} = \frac{\delta}{2\pi} \left(\frac{X^2 - (Y+d)^2}{\{X^2 + (Y+d)^2\}^2} \right), \quad (10)$$

$$H_Y = -\frac{\partial \delta}{\partial Y} = \frac{\delta}{2\pi} \left(\frac{2X(Y+d)}{\{X^2 + (Y+d)^2\}^2} \right). \quad (11)$$

The magnitude of magnetic dipole (Wang et al., 2022) is

$$H = \left(\left(\frac{\partial \delta}{\partial Y} \right)^2 + \left(\frac{\partial \delta}{\partial X} \right)^2 \right)^{1/2}, \quad (12)$$

$$\frac{\partial H}{\partial Y} = -\frac{\delta}{2\pi} \left[-\frac{2}{(Y+d)^3} + \frac{4X^2}{(Y+d)^5} \right], \frac{\partial H}{\partial X} = -\frac{\delta}{2\pi} \left[-\frac{2X}{(Y+d)^4} \right], \quad (13)$$

Similarity variables (Gul et al., 2020; Wang et al., 2022) are defined as

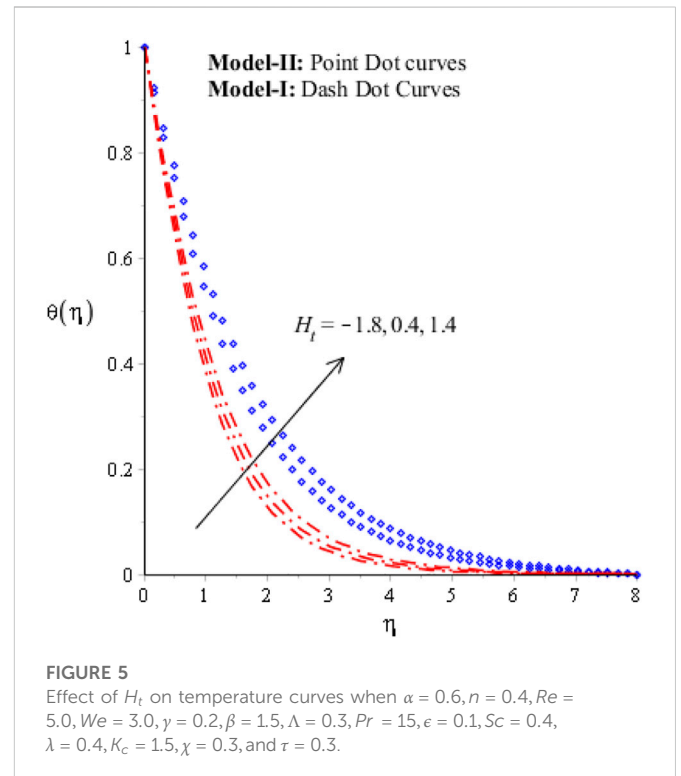
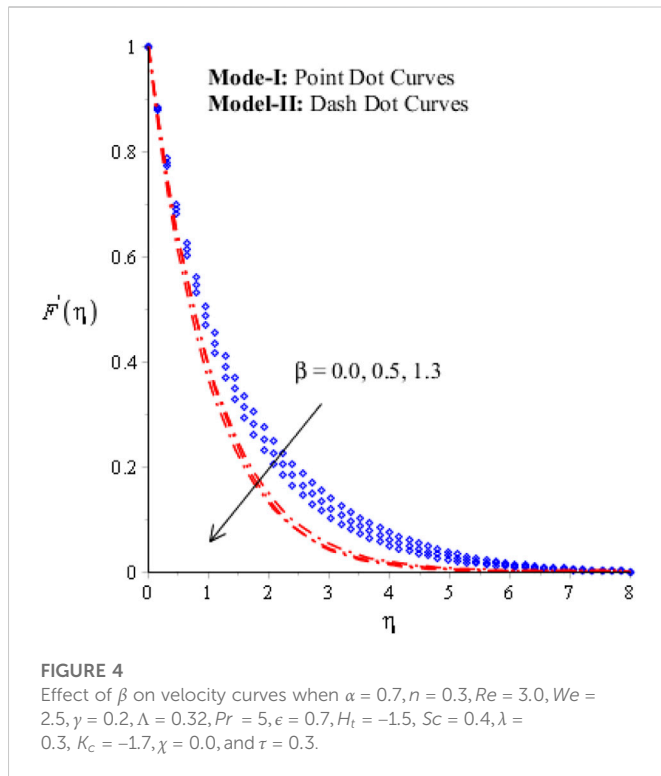
$$u = \alpha X F', v = -(a\nu_f)^{1/2} F, \theta = \frac{T_c - T}{T_c - T_w}, \eta = X \left(\frac{a\rho_f}{\mu_f} \right)^{1/2}, \phi = \frac{C_\infty - C}{C_\infty - C_w}. \quad (14)$$

Dimensionless representations of ODEs (Gul et al., 2020; Salmi et al., 2022; Wang et al., 2022) are

$$2 \left[(1 + \alpha\phi + nReWe^2 F'^2 + 3nReWe^2 F'^2 \phi) F''' \right] + 2n\alpha\gamma^2 F'' \phi + 2n\gamma^2 F'' \phi, \\ + 2nReWe^2 F'^3 \phi' - \frac{\nu_{Nf}}{\nu_f} \left[F' F' + F F'' - \frac{\theta 2\beta}{(\eta + \Lambda)^4} \right] = 0, \quad (15)$$

$$2 \left[(1 - 3\alpha ReWe^2 F'^2 \phi) F''' \right] - \alpha ReWe^2 F'^3 \phi' \\ - \frac{\nu_{Nf}}{\nu_f} \left[F' F' + F F'' - \frac{\theta 2\beta}{(\eta + \Lambda)^4} \right] = 0, \quad (16)$$

$$\theta'' + \frac{(\rho C_p)_{Nf} k_f}{(\rho C_p)_f k_{Nf}} Pr (F\theta' - 2F'\theta) + \frac{(\rho C_p)_{Nf} k_f}{(\rho C_p)_f k_{Nf}} \frac{\lambda 2\beta f (\theta - \epsilon)}{(\eta + \Lambda)^3} \\ + \frac{k_f}{k_{Nf}} Pr H_t \theta = 0, \quad (17)$$



$$(1 - \chi)^{2.5} \phi'' + ScF\phi' + \frac{\lambda 2\beta f(\phi - \epsilon)}{(\eta + \Lambda)^3} - \tau Sc\theta''\phi + \theta'\phi' + K_c Sc\phi = 0. \quad (18)$$

Correlations based on nanoparticles were captured as indicated as follows. The nanoparticle properties are listed in Table 1 and Table 2 contains information about nanoparticle shapes (Naseem et al., 2021).

$$K_{Nf} = \frac{-2\chi(-K_s + K_f) + 2K_f + K_s}{2\chi(-K_s + K_f) + 2K_f + K_s}, \mu_{Nf} = \frac{\mu_f}{(1 - \chi)^{2.5}}, \rho_{Nf} = \rho_f \left(1 - \chi + \chi \frac{\rho_s}{\rho_f} \right), \quad (19)$$

$$D_{Nf} = D_f (1 - \chi)^{2.5}, (\rho C_p)_{Nf} = \left(-\chi + 1 + \frac{(\rho C_p)_s}{(\rho C_p)_f} \chi \right) (\rho C_p)_f, \quad (20)$$

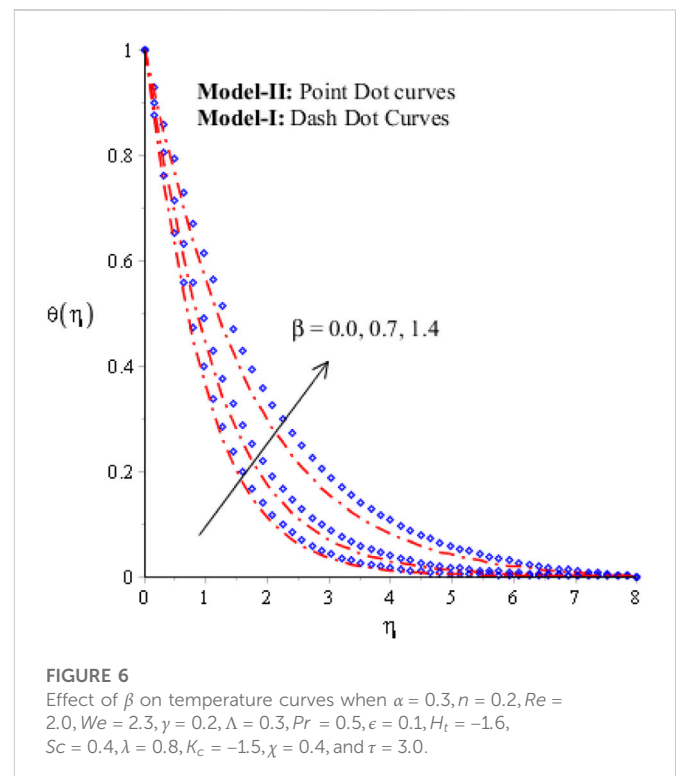
$$\frac{K_{Nf}}{K_f} = \frac{K_s + (m - 1)K_f + (m - 1)(K_s - K_f)\chi}{K_s + (m - 1)K_f + (K_s - K_f)\chi}. \quad (21)$$

Boundary conditions (BCs) are

$$F(\eta) = 0, \theta(\eta) = 1, \phi(\eta) = 1, F'(\eta) = 1: \eta = 0, F'(\eta) \rightarrow 0, \theta(\eta) \rightarrow 0, \phi(\eta) \rightarrow 0: \eta \rightarrow \infty. \quad (22)$$

Parameters are defined as

$$Re = \frac{\alpha x^2}{\nu_f}, We = \alpha \gamma^2, \beta = \frac{\delta}{2\pi} \frac{\mu_0 k (T_c - T_w) \rho_f}{(\mu_f)^2}, H_t = \frac{Q_0}{(C_p)_f a}, Pr = \frac{\mu C_p}{k}, K_c, Sc = \frac{\nu_f}{D_f}, \Lambda = \left(\frac{a(\mu_f)^2}{\rho_f k (T_c - T_w)} \right)^{1/2}, \tau = \frac{k_f (T_w - T_\infty)}{T_s}, \epsilon = \frac{T_\infty}{T_c - T_\infty}, K_c = \frac{K_c}{a}, \alpha = \alpha^* (C - C_\infty).$$



Surface forces for model-I and model-II (Salmi et al., 2022) were delivered as

$$Re^{1/2} C_f = \frac{1}{(1 - \chi)^{2.5}} [(1 + \alpha \phi(0) F'') + RenWe^2 (1 + \alpha \phi(0)) F'''(0)^3], \quad (23)$$

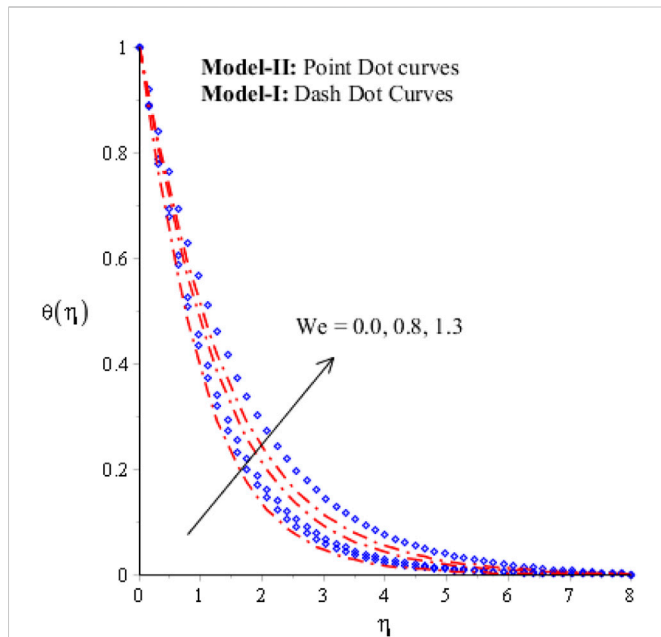


FIGURE 7

Effect of We on temperature curves when $\alpha = 0.4, n = 0.3, Re = 3.0, \gamma = 0.5, \beta = 1.3, \Lambda = 0.32, Pr = 5, \epsilon = 0.7, H_t = -1.6, Sc = 0.4, \lambda = 0.4, K_c = -1.7, \chi = 0.3$, and $\tau = 0.3$.

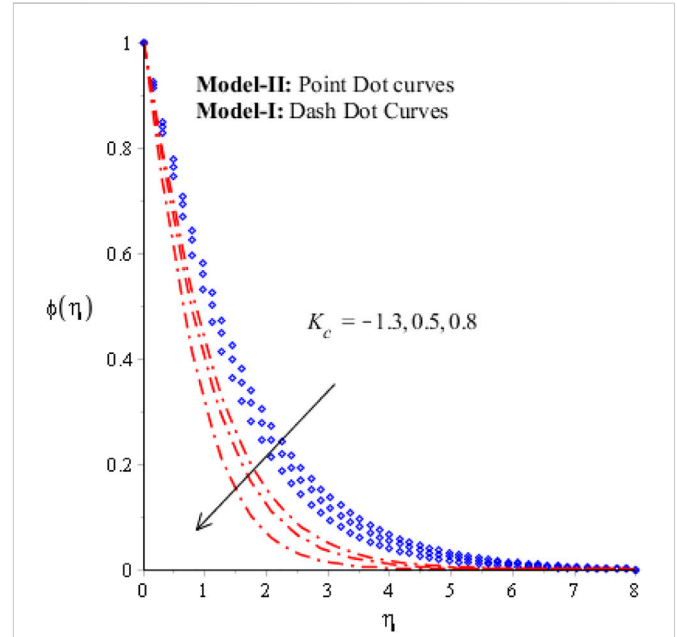


FIGURE 9

Effect of K_c on concentration curves when $\alpha = 2.0, n = 0.3, Re = 2.0, We = 5.0, \gamma = 0.4, \beta = 1.3, \Lambda = 0.2, Pr = 5, \epsilon = 0.8, H_t = -2.0, Sc = 0.4, \lambda = 0.3, \chi = 0.35$, and $\tau = 0.8$.

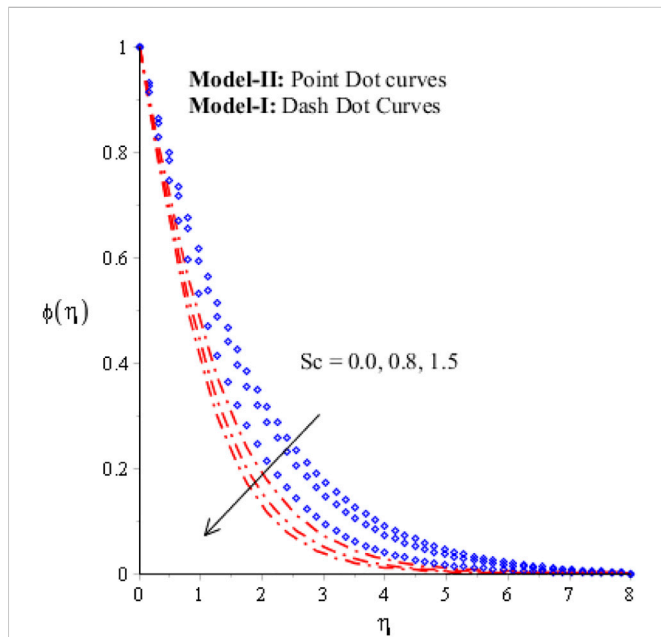


FIGURE 8

Effect of Sc on concentration curves when $\alpha = 0.4, n = 0.2, Re = 3.0, We = 2.5, \gamma = 0.2, \beta = 1.3, \Lambda = 0.3, Pr = 5, \epsilon = 0.01, H_t = -1.6, \lambda = 0.4, \gamma = 0.4, K_c = -1.5, \chi = 0.3$, and $\tau = 0.5$.

$$Re^{\frac{1}{2}} Cf = \frac{1}{(1-\chi)^{2.5}} \left[F''(0) + \frac{\alpha}{2} We^2 Re F'''(0)^3 \right]. \quad (24)$$

Temperature and concentration gradients for biological fluid (Salmi et al., 2022) are

$$Re^{-1/2} NU = -\frac{K_{Nf}}{K_f} \theta'(0), \quad Re^{-\frac{1}{2}} Sh = \frac{1}{(1-\chi)^{2.5}} \phi'(0). \quad (25)$$

3 Finite element analysis

The finite element method (FEM) was utilized to simulate numerical solution of ODE-associated BCs. Steps for explanation of the FEM are listed as follows.

Step-I: In step-I, the desired domain of the problem was discretized into a number of elements. Weak form was achieved using the concept of weighted residual. Shape functions based on linear-type polynomial were derived as follows.

The variables N, F, θ , and ϕ are defined as

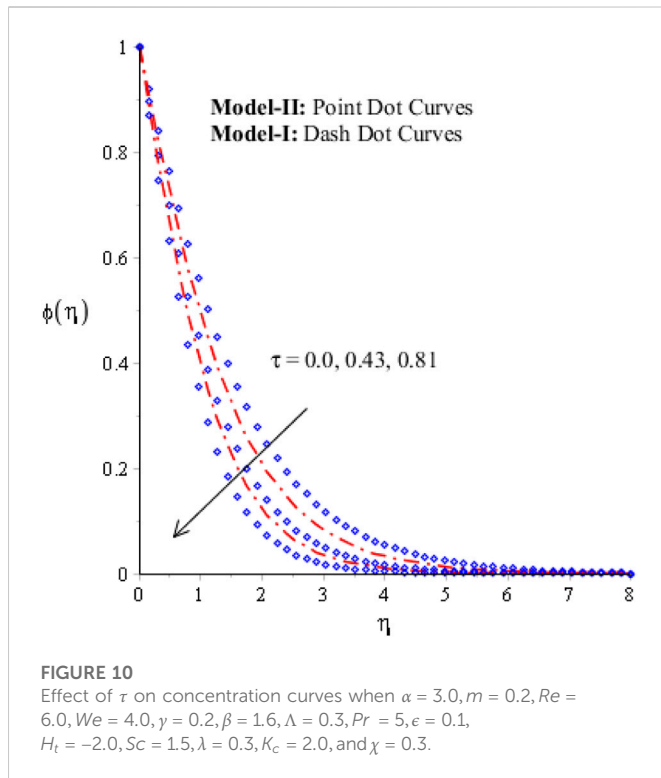
$$N = \sum_{j=1}^2 (N_j \psi_j), F = \sum_{j=1}^2 (F_j \psi_j), \theta = \sum_{j=1}^2 (\theta_j \psi_j), \phi = \sum_{j=1}^2 (\phi_j \psi_j). \quad (26)$$

The shape function is

$$\psi_j = (-1)^{j-1} \frac{\eta - \eta_{j-1}}{\eta_j - \eta_{j-1}}. \quad (27)$$

Step-II: Stiffness elements were calculated over each element based on the breakdown of the problem domain. Moreover, a global stiffness matrix was achieved. The Picard approach was implemented to differentiate linear systems from non-linear systems. The residual view is defined as

$$[R] = [M(F^{(r-1)}, N^{(r-1)}, \theta^{(r-1)}, \phi^{(r-1)})] \begin{bmatrix} F^r \\ \theta^r \\ \phi^r \end{bmatrix} = [F]. \quad (28)$$



$$\frac{\left(\sum_{i=1}^N (|\omega^r - \omega^{r-1}|)^2\right)^{\frac{1}{2}}}{\left(\sum_{i=1}^N |\omega^r|^2\right)^{\frac{1}{2}}} < 10^{-8}. \quad (29)$$

Step-III: In this step, the system of linear equations is

$$M(F, N, \theta, \phi) \begin{bmatrix} F \\ \theta \\ \phi \end{bmatrix} = [F]. \quad (30)$$

Step-IV: Maple 18 was used to develop code regarding the FEM. The computational domain was taken as $[0, 8]$ and grid size study is

shown in Table 3. Validation of a present problem already published (Muhammad and Nadeem, 2017) is shown in Table 4.

4 Explanations regarding graphical outcomes

This study describes the development of a 2D model associated with mass diffusion and thermal energy in two viscosity models. Shape effects based on cylinder, platelet, brick, and sphere were assessed in mineral oil. Chemical reaction and heat generation/absorption were also investigated. It is important to note that magnetic dipoles were taken out in this research project. Such considerations were used to generate a complex model, and the complex model was solved by implementing a finite element approach. Detailed outcomes based on graphical outcomes associated flow, mass diffusion, and thermal energy are discussed below.

4.1 Comparative impacts of viscosity models via flow distribution

The impacts of magnetic dipole number, heat source parameter, Weissenberg number, and Reynolds number on flow distribution were observed using model-I and model-II. These graphical outcomes are shown in Figures 2–4. Figure 2 demonstrates the distribution of We on flow distribution via two viscosity models. Flow is gradually slowed down versus variation in We . This decreasing impact is produced because of the concept of Weissenberg number. This concept involves the ratio between viscous and elastic forces. Here, We is a dimensionless number that is modeled using the concept of synovial fluid in the current model. In physics, division of elastic forces by viscous forces is called the Weissenberg number. An inverse proportional relation between We and a viscous force has been studied. Therefore, flow is reduced. Thickness associated with momentum layers is based on distribution in We . Viscous force is

TABLE 5 Numerical behavior of We, H_t, β , and Sc on flow gradient, concentration gradient, and temperature gradient when $\alpha = 0.4, n = 0.2, Re = 2.0, \gamma = 0.2, \Lambda = 0.32, Pr = 5, \epsilon = 0.1, \lambda = 0.4, \gamma = 0.4, K_c = -1.5, \chi = 0.3$, and $\tau = 0.3$.

Distribution in parameters		$-Re^{\frac{1}{2}} Cf$	$-Re^{-1/2} NU$	$-Re^{-1/2} Sh$
We	0.0	0.1273,748,635	1.196,172,066	0.2713,624,327
	0.6	0.2925,411,043	1.197,164,591	0.2713,245,446
	1.2	0.3592,454,952	1.197,715,853	0.2712,971,370
	-1.6	0.3572,115,843	0.8443,226,354	0.3274,391,887
H_t	0.4	0.3308,657,546	0.4674,461,360	0.2870,622,052
	0.8	0.3212,466,514	0.3573,940,886	0.2222,874,817
	0.0	0.3606,600,647	0.3746,374,058	0.2895,486,000
β	0.8	0.3617,286,068	0.2049,585,284	0.2387,259,550
	1.2	0.3637,933,627	0.1341,445,446	0.2179,434,740
	0.0	0.3535,361,988	0.3429,470,506	0.3490,419,026
Sc	0.6	0.3423,512,080	0.3426,948,032	0.4440,915,206
	1.4	0.3257,942,182	0.3423,634,404	0.5894,510,546

enhanced among momentum layers. Consequently, change in viscosity of motion can be determined by change in We . Flow for $We = 0$ is greater than flow for $We \neq 0$. Furthermore, thickness *via* momentum layers for model-I is greater than thickness *via* momentum layers for model-II. Figure 3 is plotted to measure the impact of H_t on flow distribution based on two viscosity models (model-II and model-I). It has been suggested that fluid particles absorb more heat energy when a heat source is applied. Two types of impacts are addressed when H_t is applied. One is heat generation *via* positive values and the other is heat absorption *via* negative values. This kind of impact occurs due to an external heat source. The flow produced using model-I is higher than the flow produced using model-II. Mathematically, H_t is proportional to the difference in temperature. Hence, heat variation is based on distribution in H_t . Velocity field is also based on distribution of heat energy. Motion of particles on the surface is enhanced when variation in heat is increased. Momentum thickness for $H_t < 0$ is greater than momentum thickness for $H_t > 0$. Thickness of thermal layers is an inclined function *versus* heat source number. Moreover, flow for the case of model-I is greater than that for model-II. Different effects of magnetic dipole on flow behavior are associated with various shapes (Figure 4). From Figure 4, it is estimated that flow of nanoparticles declines with higher magnetic dipole number. β is a dimensionless number. The occurrence of β is due to a magnetic dipole at the wall (of the surface). A retardation force is visualized using the concept of magnetic dipole. Due to magnetic dipole, frictional force is also generated among layers (momentum) and flow slows due to frictional force. Furthermore, thickness (for momentum layers) is decreased when the strength of magnetic dipole is magnified. Velocity field for $\beta = 0$ is greater than velocity field for $\beta \neq 0$.

4.2 Comparative effects of viscosity models *via* thermal distribution

Figures 5–7 are plotted to estimate the effects of heat source number, Prandtl number, and magnetic dipole number on temperature profile. These figures indicate measurement of thermal distribution *via* model-I and model-II, which account for the impacts of nanoparticle shape. Figure 5 illustrates visualization of H_t on thermal field. Heat energy related to fluidic particles was improved using a heat source (external). Layers based on thermal boundary were enhanced against distribution in H_t . Hence, thermal energy can be adjusted using higher values of H_t . Mathematically, H_t appeared in the energy equation. From the energy equation, H_t has a proportional relation to temperature variation. Temperature is increased when H_t is distributed because of the direct proportional relation of $(T - T_\infty)$; H_t . Figure 5 shows two types of heat characterization. The mechanism of heat generation is based on $H_t > 0$, and the mechanism of heat absorption is based on $H_t < 0$. The thermal thickness (for thermal layers) for $H_t < 0$ is less than the thermal thickness for $H_t > 0$. In addition, thermal performance is boosted significantly in the case of model-I compared to the thermal energy in model-II. Figure 6 demonstrates the role of magnetic dipole (β) in thermal variation, showing that a magnetic dipole enhances heat energy in nanoparticles. Thermal layers have a tendency to absorb more heat energy when a magnetic dipole is

implemented. Mathematically, direct proportional relation between a magnetic dipole and temperature field has been visualized using the dimensionless energy equation. Consequently, an increase in β results in enhancement in the thermal field. Dimensionless parameter (β) brings enhancement in thickness of thermal layers. Furthermore, width of thermal layers for $\beta = 0$ is greater than width for $\beta > 0$. Hence, temperature of nanoparticles increased with an increase in magnetic dipole. Figure 7 predicts the impact of We on energy transfer. The thermal profile was inclined against implication of We . The formulation of We was modeled using tensor of synovial fluid in momentum equations. From a physics point of view, division between elastic force and viscous force is the Weissenberg number. By increasing the impact of We , the viscosity of particles is magnified when We is magnified. The width and thickness associated with thermal layers are magnified utilizing large values of We . Moreover, thickness of thermal layers for $We = 0$ is less than thickness of thermal layers for $We > 0$.

4.3 Comparative impacts of viscosity models *via* concentration distribution

Figures 8–10 show estimation of various important impacts of parameters on thermal energy that occurred in two viscosity models that account for impacts of nanoparticle shape. We demonstrate impacts of Sc , chemical reaction, and thermophoretic particle number on mass diffusion. The influence of Sc on concentration profile *via* two viscosity models is shown in Figure 8. Physically, diffusion into chemical species slowly declined when Sc was increased. The effects of Sc are modeled in the concentration equation. A division between viscous diffusion (rate) and mass diffusion (rate) is termed the Schmidt number. From this, Sc has an inverse proportional relation to mass species. Due to the inverse relation between Sc and mass diffusion, diffusion in mass species slows down. Furthermore, thickness *via* mass diffusion layers for $Sc = 0$ is higher than thickness *via* mass diffusion layers for $Sc \neq 0$. Mass diffusion in model-I is faster than mass diffusion in model-II. Figure 9 demonstrates the influence of chemical reaction number on concentration profile *via* two models of viscosity. In Figure 10, two types of chemical reactions are shown based on destructive chemical species and constructive chemical species in mass diffusion. In Figure 9, K_c is a dimensionless number that is utilized to assess chemical reaction toward a solute field. $K_c > 0$ is termed a destructive chemical (reaction), whereas the generative chemical (reaction) is dependent on $K_c < 0$, and $K_c = 0$ indicates that no chemical reaction has occurred. An enhancement in solute field occurs for the generative mechanism, but a decrease is observed on the solute field for destructive reaction (mechanism). Diffusion into chemical species slows down when chemical reaction into particles occurs. Furthermore, the amount of mass diffusion in model-II is less than the amount of mass diffusion in model-I. The thickness of concentration layers reduced with greater influence of chemical reaction number. Figure 10 demonstrates the effects of τ (thermophoretic parameter) on solute field *via* two viscosity models. Figure 10 indicates that the solute field decreases with enhancement in τ . Physically, this reduction happens because concentration decreases due to increased movement of particles.

4.4 Visualizations of mass diffusion rate, skin friction coefficient, and heat energy rate against different parameters

Impacts of We , H_t , β , and Sc on mass diffusion rate, Nusselt number, and shear stress are shown in Table 5. Shear stress was reduced with greater influence of heat source number, but rates of mass diffusion and heat energy were enhanced with greater influence of H_t . Maximum amount of shear stress increases relative to distribution in magnetic dipole, and temperature and concentration gradients are reduced relative to the impact of magnetic dipole. Schmidt number increases mass diffusion rate. These outcomes are recorded in Table 5.

5 Conclusion

The numerical scheme, namely, finite element algorithm, has been applied successfully for the solution of heat and mass transportation in bio-fluids, implicating magnetic dipole in the effects of shape factors and nanoparticles. Important outcomes of the current study are:

- Velocity field increases relative to change in magnetic dipole and heat sink, but velocity field decreases with enhancement in We ;
- The production for temperature field and mass diffusion for model-II is higher than that for mass diffusion and temperature field for model-I;
- Temperature gradient declines with enhancement in heat sink, magnetic dipole, and Weissenberg number, but opposite treatment was investigated in temperature field;
- An increment in Sc , K_c , and τ decelerates solute field, while concentration gradient increases with enhancement in Sc ;

References

- Akbar, N. S., Iqbal, Z., Ahmad, B., and Maraj, E. N. (2019). Mechanistic investigation for shape factor analysis of SiO₂/MoS₂-ethylene glycol inside a vertical channel influenced by oscillatory temperature gradient. *Can. J. Phys.* 97 (9), 950–958. doi:10.1139/cjp-2018-0717
- Akbar, N. S., Maraj, E. N., Noor, N. F. M., and Habib, M. B. (2022). Exact solutions of an unsteady thermal conductive pressure driven peristaltic transport with temperature-dependent nanofluid viscosity. *Case Stud. Therm. Eng.* 35, 102124. doi:10.1016/j.csite.2022.102124
- Akram, J., Akbar, N. S., Alansari, M., and Tripathi, D. (2022). Electroosmotically modulated peristaltic propulsion of TiO₂/10W40 nanofluid in curved microchannel. *Int. Commun. Heat Mass Transf.* 136, 106208. doi:10.1016/j.icheatmasstransfer.2022.106208
- Akram, J., Akbar, N. S., and Tripathi, D. (2021). A theoretical investigation on the heat transfer ability of water-based hybrid (Ag–Au) nanofluids and Ag nanofluids flow driven by electroosmotic pumping through a microchannel. *Arabian J. Sci. Eng.* 46 (3), 2911–2927. doi:10.1007/s13369-020-05265-0
- Akram, J., Akbar, N. S., and Tripathi, D. (2022). Analysis of electroosmotic flow of silver-water nanofluid regulated by peristalsis using two different approaches for nanofluid. *J. Comput. Sci.* 62, 101696. doi:10.1016/j.jocs.2022.101696
- Akram, J., Akbar, N. S., and Tripathi, D. (2022). Electroosmosis augmented MHD peristaltic transport of SWCNTs suspension in aqueous media. *J. Therm. Analysis Calorim.* 147 (3), 2509–2526. doi:10.1007/s10973-021-10562-3
- Ali, U., Rehman, K. U., and Malik, M. Y. (2020). Thermal energy statistics for jeffery fluid flow regime: A generalized fourier's law outcomes. *Phys. A Stat. Mech. its Appl.* 542, 123428. doi:10.1016/j.physa.2019.123428
- Babu, D. D., Venkateswarlu, S., and Keshava Reddy, E. (2020). Multivariate Jeffrey fluid flow past a vertical plate through porous medium. *J. Appl. Comput. Mech.* 6 (3), 605–616.
- Choi, S. U., and Eastman, J. A. (1995). *Enhancing thermal conductivity of fluids with nanoparticles* (No. ANL/MSD/CP-84938; CONF-951135-29). Lemont, Illinois: Argonne National Lab. ANL.
- Gireesha, B. J., Umeshaiah, M., Prasannakumara, B. C., Shashikumar, N. S., and Archana, M. (2020). Impact of nonlinear thermal radiation on magnetohydrodynamic three dimensional boundary layer flow of Jeffrey nanofluid over a nonlinearly permeable stretching sheet. *Phys. A Stat. Mech. its Appl.* 549, 124051. doi:10.1016/j.physa.2019.124051
- Gul, T., Khan, A., Bilal, M., Alreshidi, N. A., Mukhtar, S., Shah, Z., et al. (2020). Magnetic dipole impact on the hybrid nanofluid flow over an extending surface. *Sci. Rep.* 10 (1), 8474–8513. doi:10.1038/s41598-020-65298-1
- Habib, M. B., and Akbar, N. S. (2021). New trends of nanofluids to combat *Staphylococcus aureus* in clinical isolates. *J. Therm. Analysis Calorim.* 143 (3), 1893–1899. doi:10.1007/s10973-020-09502-4
- Hanif, H., and Shafie, S. (2022). Interaction of multi-walled carbon nanotubes in mineral oil based Maxwell nanofluid. *Sci. Rep.* 12 (1), 4712–4716. doi:10.1038/s41598-022-07958-y
- Haroun, M. H. (2020). On electrohydrodynamic flow of Jeffrey fluid through a heating vibrating cylindrical tube with moving endoscope. *Archive Appl. Mech.* 90 (6), 1305–1315. doi:10.1007/s00419-020-01665-8
- Hosseinzadeh, K., Asadi, A., Mogharrebi, A. R., Ermia Azari, M., and Ganji, D. D. (2021a). Investigation of mixture fluid suspended by hybrid nanoparticles over vertical cylinder by considering shape factor effect. *J. Therm. Analysis Calorim.* 143 (2), 1081–1095. doi:10.1007/s10973-020-09347-x
- Hosseinzadeh, K., Moghaddam, M. E., Asadi, A., Mogharrebi, A. R., Jafari, B., Hasani, M. R., et al. (2021b). Effect of two different fins (longitudinal-tree like) and

- Maximum acceleration in velocity for model-I was greater than acceleration in velocity field for model-II.

Data availability statement

The raw data supporting the conclusions of this article will be made available by the authors, without undue reservation.

Author contributions

All authors listed have made a substantial, direct, and intellectual contribution to the work and approved it for publication.

Acknowledgments

This study is supported via funding from Prince Sattam bin Abdulaziz University project number (PSAU/2023/R/1444).

Conflict of interest

The authors declare that the research was conducted in the absence of any commercial or financial relationships that could be construed as a potential conflict of interest.

Publisher's note

All claims expressed in this article are solely those of the authors and do not necessarily represent those of their affiliated organizations, or those of the publisher, the editors, and the reviewers. Any product that may be evaluated in this article, or claim that may be made by its manufacturer, is not guaranteed or endorsed by the publisher.

hybrid nano-particles (MoS₂-TiO₂) on solidification process in triplex latent heat thermal energy storage system. *Alexandria Eng. J.* 60 (1), 1967–1979. doi:10.1016/j.aej.2020.12.001

Hosseinzadeh, K., Roghani, S., Mogharrebi, A. R., Asadi, A., Waqas, M., and Ganji, D. D. (2020). Investigation of cross-fluid flow containing motile gyrotactic microorganisms and nanoparticles over a three-dimensional cylinder. *Alexandria Eng. J.* 59 (5), 3297–3307. doi:10.1016/j.aej.2020.04.037

Hou, E., Jabbar, N., Nazir, U., Sohail, M., Javed, M. B., Shah, N. A., et al. (2022). Significant mechanism of Lorentz force in energy transfer phenomena involving viscous dissipation via numerical strategy.

Khan, M. I., Haq, F., Khan, S. A., Hayat, T., and Khan, M. I. (2020). Development of thixotropic nanomaterial in fluid flow with gyrotactic microorganisms, activation energy, mixed convection. *Comput. methods programs Biomed.* 187, 105186. doi:10.1016/j.cmpb.2019.105186

Khan, U., Zaib, A., Bakar, S. A., and Ishak, A. (2021). Stagnation-point flow of a hybrid nanofluid over a non-isothermal stretching/shrinking sheet with characteristics of inertial and microstructure. *Case Stud. Therm. Eng.* 26, 101150. doi:10.1016/j.csite.2021.101150

Khan, U., Zaib, A., Ishak, A., Eldin, S. M., Alotaibi, A. M., Raizah, Z., et al. (2022). Features of hybridized AA7072 and AA7075 alloys nanomaterials with melting heat transfer past a movable cylinder with Thompson and Troian slip effect. *Arabian J. Chem.* 16, 104503. doi:10.1016/j.arabjc.2022.104503

Khan, U., Zaib, A., and Ishak, A. (2021). Magnetic field effect on Sisko fluid flow containing gold nanoparticles through a porous curved surface in the presence of radiation and partial slip. *Mathematics* 9 (9), 921. doi:10.3390/math9090921

Khan, U., Zaib, A., Ishak, A., Waini, I., Pop, I., Elattar, S., et al. (2022). Stagnation point flow of a water-based graphene-oxide over a stretching/shrinking sheet under an induced magnetic field with homogeneous-heterogeneous chemical reaction. *J. Magnetism Magnetic Mater.* 565, 170287. doi:10.1016/j.jmmm.2022.170287

Madhukesh, J. K., Varun Kumar, R. S., Punith Gowda, R. J., Prasannakumara, B. C., and Shehzad, S. A. (2022). Thermophoretic particle deposition and heat generation analysis of Newtonian nanofluid flow through magnetized Riga plate. *Heat. Transf.* 51 (4), 3082–3098. doi:10.1002/htj.22438

Manjunatha, G., Rajashekhar, C., Vaidya, H., Prasad, K. V., Makinde, O. D., and Viharika, J. U. (2020). Impact of variable transport properties and slip effects on MHD Jeffrey fluid flow through channel. *Arabian J. Sci. Eng.* 45 (1), 417–428. doi:10.1007/s13369-019-04266-y

Maraj, E. N., Akbar, N. S., Iqbal, Z., and Azhar, E. (2017). Framing the MHD mixed convective performance of CNTs in rotating vertical channel inspired by thermal deposition: Closed form solutions. *J. Mol. Liq.* 233, 334–343. doi:10.1016/j.molliq.2017.03.041

Maraj, E. N., Zehra, I., and SherAkbar, N. (2022). Rotatory flow of MHD (MoS₂-SiO₂)/H₂O hybrid nanofluid in a vertical channel owing to velocity slip and thermal periodic conditions. *Colloids Surfaces A Physicochem. Eng. Aspects* 639, 128383. doi:10.1016/j.colsurfa.2022.128383

Muhammad, N., and Nadeem, S. (2017). Ferrite nanoparticles Ni-Zn Fe₂O₄, Mn-Zn Fe₂O₄ and Fe₂O₄ in the flow of ferromagnetic nanofluid. *Eur. Phys. J. Plus* 132 (9), 377–412. doi:10.1140/epjp/i2017-11650-2

Naseem, T., Nazir, U., Sohail, M., Alrabaiah, H., Sherif, E. S. M., and Park, C. (2021). Numerical exploration of thermal transport in water-based nanoparticles: A computational strategy. *Case Stud. Therm. Eng.* 27, 101334. doi:10.1016/j.csite.2021.101334

Rostami, A. K., Hosseinzadeh, K., and Ganji, D. D. (2022). Hydrothermal analysis of ethylene glycol nanofluid in a porous enclosure with complex snowflake shaped inner wall. *Waves Random Complex Media* 32 (1), 1–18. doi:10.1080/17455030.2020.1758358

Saif, R. S., Muhammad, T., Sadia, H., and Ellahi, R. (2020). Hydromagnetic flow of Jeffrey nanofluid due to a curved stretching surface. *Phys. A Stat. Mech. its Appl.* 551, 124060. doi:10.1016/j.physa.2019.124060

Salmi, A., Madkhali, H. A., Arif, U., Alharbi, S. O., and Malik, M. Y. (2022). Thermal bio-convective transport in biological fluid using two viscosity models. *Case Stud. Therm. Eng.* 34, 101924. doi:10.1016/j.csite.2022.101924

Shafee, A., Rezaeianjouybari, B., and Tlili, I. (2021). Treatment of nanofluid within porous media using non-equilibrium approach. *J. Therm. Analysis Calorim.* 144 (4), 1571–1583. doi:10.1007/s10973-020-09587-x

Shehzad, S. A., Reddy, M. G., Rauf, A., and Abbas, Z. (2020). Bioconvection of Maxwell nanofluid under the influence of double diffusive Cattaneo–Christov theories over isolated rotating disk. *Phys. Scr.* 95 (4), 045207. doi:10.1088/1402-4896/ab5ca7

Sinha, V. K., Kumar, B., Seth, G. S., and Nandkeolyar, R. (2020). Features of Jeffrey fluid flow with Hall current: A spectral simulation. *Pramana* 94 (1), 64–68. doi:10.1007/s12043-020-1940-y

Sohail, M., El-Zahar, E. R., Mousa, A. A. A., Nazir, U., Althobaiti, S., Althobaiti, A., et al. (2022a). Finite element analysis for ternary hybrid nanoparticles on thermal enhancement in pseudo-plastic liquid through porous stretching sheet. *Sci. Rep.* 12 (1), 9219–9313. doi:10.1038/s41598-022-12857-3

Sohail, M., Nazir, U., El-Zahar, E. R., Alrabaiah, H., Kumam, P., Mousa, A. A. A., et al. (2022b). A study of triple-mass diffusion species and energy transfer in Carreau–Yasuda material influenced by activation energy and heat source. *Sci. Rep.* 12 (1), 10219–10317. doi:10.1038/s41598-022-13890-y

Veera Krishna, M. (2020). Heat transport on steady MHD flow of copper and alumina nanofluids past a stretching porous surface. *Heat. Transf.* 49 (3), 1374–1385. doi:10.1002/htj.21667

Wang, F., Sohail, M., Nazir, U., El-Zahar, E. R., Park, C., and Jabbar, N. (2022). An implication of magnetic dipole in Carreau Yasuda liquid influenced by engine oil using ternary hybrid nanomaterial. *Nanotechnol. Rev.* 11 (1), 1620–1632. doi:10.1515/ntrev-2022-0100

Waqas, H., Khan, S. U., Bhatti, M. M., and Imran, M. (2020). Significance of bioconvection in chemical reactive flow of magnetized Carreau–Yasuda nanofluid with thermal radiation and second-order slip. *J. Therm. Analysis Calorim.* 140 (3), 1293–1306. doi:10.1007/s10973-020-09462-9

Nomenclature

v, u Velocity components (ms^{-1})

ρ Density (Kgm^{-3})

H Magnetic field (tesla)

μ_0 Dynamic viscosity at zero ($Kgm^{-1}s^{-1}$)

n Power-law index number

α Concentration-dependent viscosity number

C_p Specific heat capacity ($JKg^{-1}K$)

Q_0 Heat generation

C_∞ Ambient concentration (s^{-1})

PDEs Partial differential equations

U_w Wall velocity (ms^{-1})

δ Region of a magnetic dipole

θ Dimensionless temperature

Re Reynolds number

ν Kinematic viscosity (m^2s^{-1})

H_t Heat source parameter

Sc Schmidt number

ϵ Material parameter

Sh Schmidt number

ψ_j Stream function

N Deformation tensor

T_c Highest temperature rather than wall temperature

τ Thermophoretic parameter

T_s Reference temperature (K)

N_f Nanofluid

Y, X Space coordinates (m)

P Pressure (Nm^{-2})

M Magnetization number

μ Viscosity ($Kgm^{-1}s^{-1}$)

γ Material parameter

ϕ Concentration

T Fluidic temperature (K)

T_∞ Ambient temperature (K)

K Thermal conductivity (Wm^{-1})

C Concentration (s^{-1})

T_w Wall temperature (K)

β Hydrodynamic interaction number

F Dimensionless velocity

η Independent variable

we Weissenberg number

Pr Prandtl number

K_c Chemical reaction number

NU Nusselt number

ODEs Ordinary differential equations

FEM Finite element method

b, ϵ Material parameters

D Mass diffusion (m^2s^{-1})

χ Volume fraction of nanoparticles

k_{ν_f} Thermophoretic constant

ODEs Ordinary differential equations



OPEN ACCESS

EDITED BY

Safia Akram,
National University of Sciences and
Technology, Pakistan

REVIEWED BY

Animasaun I. L.,
Federal University of Technology, Nigeria
Mustafa Turkiymazoglu,
Hacettepe University, Türkiye

*CORRESPONDENCE

Farhad Ali,
✉ farhadali@cusit.edu.pk
Arshad Khan,
✉ arshadkhan@aup.edu.pk

SPECIALTY SECTION

This article was submitted to Colloidal
Materials and Interfaces,
a section of the journal
Frontiers in Materials

RECEIVED 10 December 2022

ACCEPTED 11 January 2023

PUBLISHED 07 February 2023

CITATION

Ali F, Ali G, Khan A, Khan I, Eldin ET and
Ahmad M (2023), Effects of Newtonian
heating and heat generation on
magnetohydrodynamics dusty fluid flow
between two parallel plates.
Front. Mater. 10:1120963.
doi: 10.3389/fmats.2023.1120963

COPYRIGHT

© 2023 Ali, Ali, Khan, Khan, Eldin and
Ahmad. This is an open-access article
distributed under the terms of the [Creative
Commons Attribution License \(CC BY\)](#).
The use, distribution or reproduction in
other forums is permitted, provided the
original author(s) and the copyright
owner(s) are credited and that the original
publication in this journal is cited, in
accordance with accepted academic
practice. No use, distribution or
reproduction is permitted which does not
comply with these terms.

Effects of Newtonian heating and heat generation on magnetohydrodynamics dusty fluid flow between two parallel plates

Farhad Ali^{1*}, Gohar Ali¹, Arshad Khan^{2*}, Ilyas Khan³,
Elsayed Tag Eldin⁴ and Matin Ahmad¹

¹Department of Mathematics, City University of Science and Information Technology, Peshawar, Pakistan, ²Institute of Computer Sciences and Information Technology, The University of Agriculture, Peshawar, Pakistan, ³Department of Mathematics, College of Science Al-Zulfi, Majmaah University, Al-Majmaah, Saudi Arabia, ⁴Faculty of Engineering and Technology, Future University in Egypt, New Cairo, Egypt

Dusty fluids are utilized to minimize heat in systems like gas-freezing systems and nuclear-powered reactors, among other places. The present study aims to investigate the effect of Newtonian heating on dusty fluid flow. Between two parallel plates, the two-phase MHD fluctuating flow of the dusty fluid is considered. The dust particles inside the fluid are thought to be spherical and uniformly distributed. The generation and absorption of heat were also taken into consideration. The motion of the fluid is due to the motion of the right plate with free stream velocity $U(t)$. Partial differential equations are utilized to represent the flow regime. The Poincare-Light Hill Technique is used to find exact solutions. The impact of parameters on the temperature and velocity profiles are shown graphically. Skin friction and rate of heat transfer, two essential fluid parameters for engineers, are also evaluated in tabular form. The velocity of the fluid is shown to decrease with increasing magnetic field. The Newtonian heating phenomena has an effect on the plate's heating.

KEYWORDS

Newtonian heating condition (NHC), dust particles, casson fluid, lighthill perturbation technique, heat transfer, heat generation

1 Introduction

Fluid is a material that constantly deforms (flows) when shear (tangential) stress is applied. Water, honey, oil, and air are a few examples of fluids. In the universe, there are numerous fluids. Non-Newtonian fluids and Newtonian fluids are two types of fluids based on their rheologies. Engineering procedures, industry (thermal power plants, nuclear power plants, refrigerators, air conditioners, and so on), and medical science all use these fluids. Many physical phenomena are not properly described by Newtonian viscous fluids. Non-Newtonian fluids are essential in a wide range of engineering operations, industrial processes, and biological applications. There are several types of non-Newtonian fluids. Non-Newtonian fluids include differential type fluids, rate type fluids, and viscoelastic fluids. Casson fluid and other differential viscoelastic fluids are frequently employed in everyday life. According to the Casson Fluid Definition a fluid that shear-thins to zero viscosity has a yield stress below which no flow occurs and zero viscosity at an infinite rate of shear (Rundora, 2021). The study of viscoelastic Casson fluids cannot be adequately handled by a single governing equation due to their complicated rheology (Makinde, 2009). Some of the Casson fluid's applications include coal in water, synthetic petroleum products, China clay, paints, biological products fluid, jelly, and fibrinogen

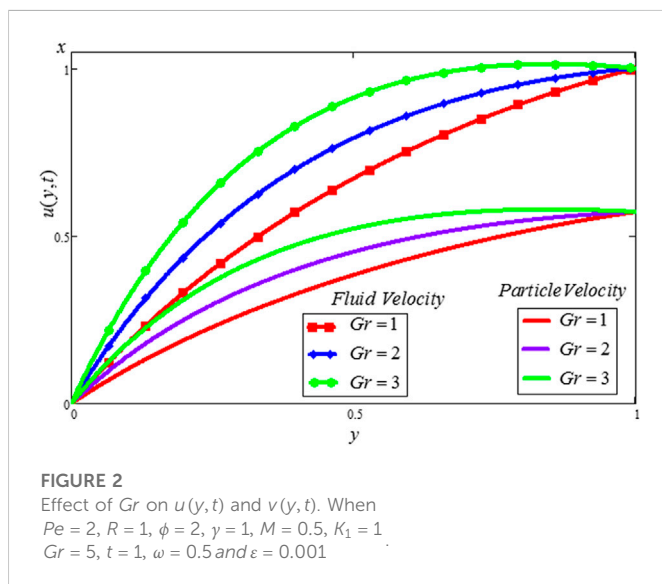
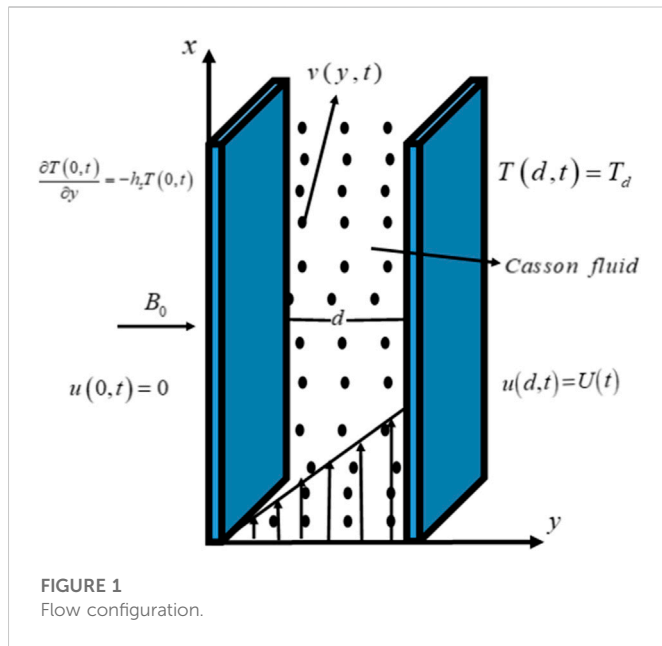
(Pramanik, 2014). The Casson first presented the Casson fluid model in “1959” (Casson, 1959). Oka (1971) was the first to investigate Casson fluids in tubes. According to Mukhopadhyay (2013), thermal radiation over the stretched surface has an impact on the unstable Casson viscoelastic fluid flow. In a curved sheet that is stretching exponentially with MHD, Kumar et al. (2020) scrutinized the influence of radiation of heat on a viscoelastic Casson fluid. By Gangadha et al. (2021), a dual solution analysis for MHD Casson fluid and Newtonian heating travelling through a decreasing sheet was presented. Reddy et al. investigated the effect of radiant heat on the MHD viscous dissipation of a Casson fluid flow across an oscillation parallel plate in their work described in Reddy et al. (2018). Rafiq et al. (2020) examine the influence of variable viscosity on the asymmetric flow of a non-Newtonian fluid driven *via* an expanding/constricting conduit with porous walls. The flow of a non-Newtonian (Casson) fluid between parallel discs travelling in opposite directions on a plane is being investigated (Abbas et al., 2020). Jyothi et al. (2021a) proposed the Casson fluid, which is driven between parallel plates and acts as a heat source or sink as well as a thermophoretic particle deposition. Ramesh et al. (2022) investigated the relationship between the transportation of aluminium alloy particles over parallel plates and chemical reaction and activation energy. Madhukesh et al. (2021) gained scientific insight into heat and mass transfer in a Riga plate with thermophoresis and brownian atomic diffusion in a Casson hybrid flow of nanofluid. Jyothi et al. (2021b) scrutinized the effect of Stefan blowing on Casson nanofluid flow and heat transmission through a moving thin needle. Furthermore, several scholars investigate the relationships between Casson fluid flow, heat transmission, and Newton’s equation of cooling (Obalalu et al., 2020; Obalalu, 2021).

According to Newton’s rule of cooling (or heating), the heat loss rate of a body is directly proportional to the temperature differential between the system and its surroundings (Hussain et al., 2018). In forced air or pushed fluid cooling (or heating), when fluid properties do not considerably fluctuate with temperature, Newton’s Law of heating (or cooling) is obeyed. However, buoyancy-driven convection, where flow velocity grows with temperature difference, only roughly follows this law. Finally, Newton’s law of cooling (or heating) only holds for very small temperature differences when heat is transmitted by thermal radiation. When modeling MHD two-phase fluctuation flows between parallel plates, ramped wall temperatures or constant surface heat flux assumptions and constant surface temperature are commonly used (O’Sullivan, 1990; Khalid et al., 2015; Ali et al., 2019a; Das et al., 2021; Krishna et al., 2021). Further from that, the assumptions above fail in a variety of real-world situations where heat transport is inversely proportional to surface temperature and the Newtonian heating condition (NHC) is required. It was Merkin (1994) who was the first to explore four forms of temperature distributions on walls, one of which being NHC. Newtonian heating conditions are used in heat exchangers, the oil industry, solar radiation, and conjugated heat transfer around fins. The impacts of NHC, magnetic field, chemical reaction and heat generation on viscoelastic Casson fluid free convection flow among the vertical plates are reported by Khan et al. (2019). Hussanan et al. (2017a) investigated the impact of Newtonian heating on viscoelastic Casson fluid flow between oscillating vertical plates. Hussanan et al. (2017b) investigated the viscoelastic Casson fluid flow (CFF) with heat transfer and Newtonian heating between porous materials. Loganathan et al. (2021) investigated the viscoelastic CFF over a cylinder with NHC and heat absorption effects. Hussanan et al. (2016) investigated the effects

of NHC and magnetic field on the CFF of a two-dimensional travelling through a stretched sheet. Manjula and Sekhar (2021) investigated how heat transport and thermal expansion affect the CFF of a vertical surface with NHC.

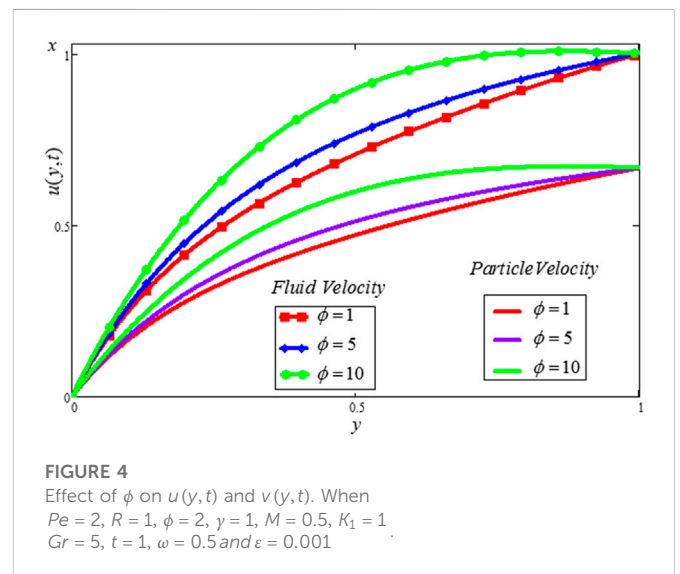
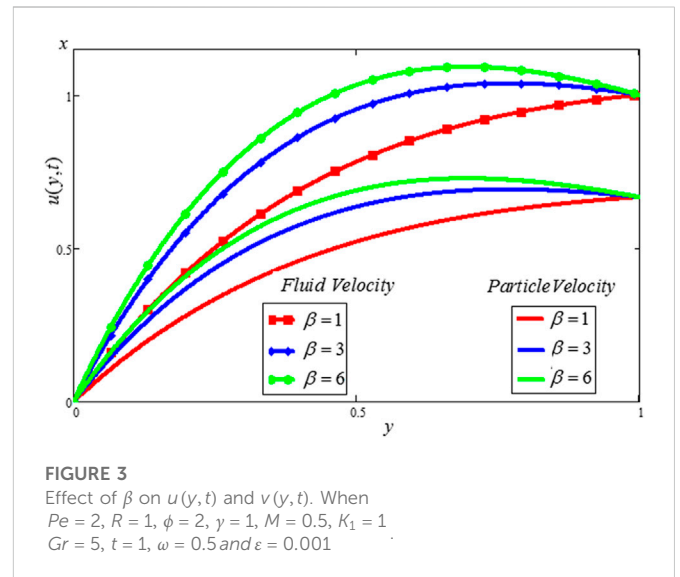
Magnetohydrodynamics is the analysis of the magnet properties and performance of electrically conducting fluids. Liquid metals, salt water, plasmas, and electrolytes are examples of magnetofluids. MHD flow with free convection has a wide range of applications in fluid engineering issues such as flow metres, blood flow, gas cooling system heat transfer improvement, MHD generators, and accelerators (Ali et al., 2020). In the existence of a chemical reaction, Afkuzzaman et al. (2018) reported heat transfer and free convective flow across an upright plate with MHD. Dusty fluid in an annulus with hydrodynamic velocity behavior was studied by Jha and Gambo (2022). A magnetic field was found to impact Couette flow. It was found that viscosity, heat transfer, and thermal conductivity had a significant effect on the movement of dusty fluids with MHD. Using thermal radiation and MHD, Mabood et al. (2016) examined and analysed the influence of melting heat transfer on Casson fluid flow in a porous media over a moving surface. Sayed-Ahmed et al. (2011) explore the effect of a time-dependent pressure gradient and heat transfer in unsteady Casson fluid flow with MHD. Newtonian heating (or cooling) and thermal radiation, according to (Jalil et al., 2017), can influence MHD flow with an induced magnetic field. Gireesha et al. (2012) investigated the effects of heat transfer, magnetic field, and viscous dissipation on MHD dusty flow using a stretched sheet. Upadhyaya et al. investigated the radiative MHD flow of suspended Casson fluid within a conical gap (Upadhyaya et al., 2022). Raju et al. (2021) demonstrated MHD radiated flow in a thermal convective condition using Casson fluid. Hamid et al. (2021) investigate Casson fluid MHD flow with Hall current and homogeneous-heterogeneous interactions. Ali et al. (2019b), Hussain et al. (2021) explore the thermal and magnetic impacts of a bi-viscosity fluid contained in a triangular chamber using finite element analysis. The heat and flow across a revolving disc that is being affected by a constant horizontal magnetic field are investigated by Turkylmazoglu (2022). Furthermore, several scholars investigate the MHD flow, dusty fluid with analytical solution (Anuar et al., 2020; Wahid et al., 2020).

Dusty fluid flow occurs when a fluid (liquid or gas) has a solid particle distribution (Ezzat et al., 2010). For example, in fluidization problems, dusty air motion the motion and the process of chemical reactions by which raindrops are formed by the coalescence of particles. Dusty fluid flow (multiphase flow) is used in powder technology, nuclear reactor cooling, paint spray, solid fuel rock nozzle performance, dust collecting, and guidance systems (Chanson, 2004). Archimedes of Syracuse invented multi stage flow when he proposed the Principle of Buoyant force, which evolved into the well-known Archimedes principle, which is used in multiphase flow modelling (Khan et al., 2022). The most common type of multiphase flow is two-phase flow (Miwa and Hibiki, 2022). While remaining interested in two-phase flows, several scientists worked on the dusty flow model for a variety of flow configurations and physical situations. Despite the system of quadratic solutions’ challenges, nothing effort has been made to improve a perfect approach. Saffman (1962) was the first to do study on dusty fluid flow laminar. The importance of partial slip caused by lateral velocity and viscous dissipation is investigated using numerical solutions to the partial differential equations are reported by Koriko et al. (2021). The



Casson dusty nanofluid: The role of the magnetic field, the non-Fourier heat flow model are discussed by [Rehman et al. \(2022\)](#).

In the above-mentioned literature, the researchers examined non-Newtonian, incompressible, electrically conducting dusty fluids that have been moving with free convection and MHD. Following the Light-Hill technique, no study has been published to our knowledge that combines the fluids energy equation with the dust particles energy equation for a viscoelastic Casson dusty fluid using the fluids energy equation and the dust particles energy equation. Using a distinct equation of heat for the dust particles, this study investigates the impact of NHC on the two-phase MHD fluctuation flow of Casson fluid and dust particles between two vertical plates with suspended electrically conducting particles. The scientific findings of the current study also show that Casson dusty fluid is a very complicated phenomena with a wide range of engineering and product-making



uses, such as the usage of Casson dusty fluids in nuclear reactors and gas cooling systems to reduce system temperature. Consequently, the goal of the current work is to ascertain how Newtonian heating affects Casson dusty fluid flow. Additionally, using a graphical representation, this study investigates the impact of various physical characteristics on the Casson dusty fluid flow.

2 Mathematical formulation

Take electrically conducting, the incompressible, unidirectional, unsteady, two-phase fluctuating flow of MHD Casson fluid with dust particles between two vertical plates. A transverse magnetic field is applied to the flow. The motion of the fluid is due to the motion of the right plate with free stream velocity $U(t)$, while the left plate is static as shown in [Figure 1](#). The left plate is taken heated with the Newtonian heating condition, while T_d is the temperature of the right plate, and T_p is the particle temperature. Heat generation is only considered in

the fluid and not for the particle energy equation. Furthermore, the influence of the particle concentration parameter and the particle energy equation are taken into account. The mass concentration equation for both the fluid and particle is not considered.

The velocity and temperature fields are shown below (Ali et al., 2020):

$$\vec{V} = (u(y, t), 0, 0) \quad (1)$$

$$T = T(y, t) \quad (2)$$

The Casson fluid's constitutive equations are (Ali et al., 2020).

$$\nabla \cdot \mathbf{V} = 0 \quad (3)$$

$$\rho \frac{d\mathbf{V}}{dt} = \mathbf{s} + \rho \cdot \mathbf{b} + \text{div}(\boldsymbol{\tau}_{ij}) \quad (4)$$

By using Maxwell law, generalized ohm's law and Boussinesqs approximation, the body and surface forces in Eq. 4 becomes (Ali et al., 2020).

$$\rho \cdot \mathbf{b} = \rho g \beta_T (T - T_d) + \mathbf{J} \times \mathbf{B} = g \rho \beta_T (T - T_d) - \sigma B_0^2 \mathbf{u}(y, t) \quad (5)$$

$$\mathbf{s} = -K_0 N_0 (\mathbf{u}(y, t) - \mathbf{v}(y, t)) \quad (6)$$

The rheological equation for unsteady Casson fluid flow is established and derived by Casson (1959) and is denoted by Rehman et al. (2022).

$$\tau_{ij} = \begin{cases} \left(\mu_e + \frac{p_y}{\sqrt{2\pi_1}} \right) 2e_{ij}, & \pi_1 > \pi_e \\ \left(\mu_e + \frac{p_y}{\sqrt{2\pi_e}} \right) 2e_{ij}, & \pi_1 < \pi_e \end{cases} \quad (7)$$

$$\mathbf{e}_{ij} = -p\mathbf{I} + \mu \mathbf{A}_1 \quad (8)$$

$$\text{div}(\boldsymbol{\tau}_{ij}) = \left(\mu_e + \frac{p_y}{\sqrt{2\pi_1}} \right) \frac{\partial^2 \mathbf{u}}{\partial y^2} \quad (9)$$

Equation 4 may be stated in component form using Eqs 5–9 and Eq. 1 as (Ali et al., 2020).

$$\frac{\partial u(y, t)}{\partial t} = v \left(1 + \frac{1}{\beta} \right) \frac{\partial^2 u(y, t)}{\partial y^2} + \frac{K_0 N_0}{\rho} (v(y, t) - u(y, t)) - \frac{\sigma B_0^2 u}{\rho} + \beta_T g (T - T_d) \quad (10)$$

$$\frac{\partial v(y, t)}{\partial t} = \frac{K_0}{m} (u(y, t) - v(y, t)) \quad (11)$$

$$\frac{\partial T(y, t)}{\partial t} = \left(\frac{k}{\rho c_p} \right) \frac{\partial^2 T(y, t)}{\partial y^2} - \left(\frac{\rho_p c_s}{\rho c_p \gamma_T} \right) (T_p(y, t) - T(y, t)) - \left(\frac{Q_0}{\rho c_p} \right) \times (T(y, t) - T_d(y, t)) \quad (12)$$

$$\gamma_T \cdot \frac{\partial T_p(y, t)}{\partial t} = (T(y, t) - T_d(y, t)) \quad (13)$$

The physical conditions are as follows (Khan et al., 2019).

$$\left. \begin{aligned} u(0, t) &= 0 \\ u(d, t) &= U(t) \\ \frac{\partial T(0, t)}{\partial y} &= -h_s T(0, t) \\ T(d, t) &= T_d \end{aligned} \right\} \quad (14)$$

Where, $U(t) = u_0 (1 + \frac{\varepsilon}{2} (e^{i\omega t} + e^{-i\omega t}))$.

Assume you obtained the result to Eq. 11 through PLHT (Nayfeh, 2008).

$$v(y, t) = e^{i\omega t} v_0(y) \quad (15)$$

from Eq. 15, the solution is obtained.

$$v(y, t) = K_0 \left(\frac{u(y, t)}{K_0 + mi\omega} \right) \quad (16)$$

Equation 10 in view of Eq. 16 becomes.

$$\frac{\partial u(y, t)}{\partial t} = \left(1 + \frac{1}{\beta} \right) v \frac{\partial^2 u(y, t)}{\partial y^2} + \frac{K_0 N_0}{\rho} \left\{ \left(\frac{K_0}{mi\omega + K_0} \right) - 1 \right\} u(y, t) - \frac{\sigma B_0^2 u(y, t)}{\rho} + g \beta_T (T(y, t) - T_d(y, t)) \quad (17)$$

The following dimensionless variables are used in the process of non-depersonalization;

$$y^* = yh_s, u^* = \frac{u}{u_0}, t^* = v h_s^2 t, \theta^* = \frac{T - T_d}{T_d}, \theta_p^* = \frac{T_p - T_d}{T_d} \quad (18)$$

Using Eq. 18, Eqs 12, 13, 17 become;

$$\frac{\partial u}{\partial t} = \beta_1 \frac{\partial^2 u}{\partial y^2} - (M + K_1 - K_2)u + Gr\theta \quad (19)$$

$$\frac{\partial \theta(y, t)}{\partial t} = -\phi \theta(y, t) + \frac{1}{Pe} \left(\frac{\partial^2 \theta(y, t)}{\partial y^2} + R(\theta_p(y, t) - \theta(y, t)) \right) \quad (20)$$

$$\frac{\partial \theta_p(y, t)}{\partial t} = (\theta(y, t) - \theta_p(y, t)) \quad (21)$$

The dimensionless criteria are as follows (the (*) sign has been removed for clarity):

$$\left. \begin{aligned} u(0, t) &= 0 \\ u(1, t) &= 1 + \varepsilon \left(\frac{e^{i\omega t} + e^{-i\omega t}}{2} \right) \\ \frac{\partial \theta(0, t)}{\partial y} &= (-1 - \theta(0, t)) \\ \theta(1, t) &= 0 \end{aligned} \right\} \quad (22)$$

The dimensionless quantities are;

$$M = \frac{\sigma B_0^2}{\rho v h_s^2}, Gr = \frac{g \beta_T T_\infty}{u_0 v h_s^2}, K_2 = \frac{K_0^2 N_0}{\rho v h_s^2 (mi\omega + K_0)}, K_1 = \frac{K_0 N_0}{\rho v h_s^2}, Pe = \frac{v \rho c_p}{k}$$

$$\beta_1 = 1 + \frac{1}{\beta}, \gamma = \frac{1}{v h_s^2 \gamma_T}, R = \frac{\rho_p c_s}{k h_s^2 \gamma_T}, \phi = \frac{Q_0}{v h_s^2 \rho c_p}$$

Assume you derived the solution to Eq. 21 using the PLHT (Nayfeh, 2008).

$$\theta_p(y, t) = \theta_{p0}(y) e^{i\omega t} \quad (23)$$

Results in:

$$\theta_p(y, t) = \gamma \left(\frac{1}{\gamma + i\omega} \right) \theta(y, t) \quad (24)$$

Equation 20 in observation of Eq. 24 converts;

$$\frac{\partial \theta(y, t)}{\partial t} = P e^{-1} \frac{\partial^2 \theta(y, t)}{\partial y^2} + \frac{R}{Pe} \left(\left(\frac{\gamma}{i\omega + \gamma} \right) - 1 \right) \theta(y, t) - \phi \theta(y, t) \quad (25)$$

3 Solution of the energy equation

To solve Eq. 25, the following periodic solution is assumed (Nayfeh, 2008):

$$\theta(y, t) = \theta_0(y) + \theta_1(y)e^{i\omega t} \quad (26)$$

Now by using Eq. 26 in Eq. 25, and then using the corresponding conditions from Eq. 22, the following solutions is achieved:

$$\theta(y, t) = \frac{\sinh(\sqrt{m_0} - y\sqrt{m_0})}{\sqrt{m_0} \cosh(\sqrt{m_0}) - \sinh(\sqrt{m_0})} \quad (27)$$

Equation 17 in view of Eq. 27 becomes;

$$\begin{aligned} \frac{\partial u(y, t)}{\partial t} = \beta_1 \frac{\partial^2 u(y, t)}{\partial y^2} - (M + K_1 - K_2)u(y, t) \\ + Gr \left\{ \frac{\sinh(\sqrt{m_0} - y\sqrt{m_0})}{\sqrt{m_0} \cosh(\sqrt{m_0}) - \sinh(\sqrt{m_0})} \right\} \end{aligned} \quad (28)$$

4 Solution of the velocity profile

To solve Eq. 28, the following periodic solution is assumed (Comstock, 1972) and (Nayfeh, 2008).

$$u(y, t) = \psi_0(y) + \frac{\varepsilon}{2} (\psi_1(y)e^{i\omega t} + \psi_2(y)e^{-i\omega t}) + O(\varepsilon^2) \quad (29)$$

$$\left. \begin{aligned} \psi_0(0) &= 0, & \psi_0(1) &= 1 \\ \psi_1(0) &= 0, & \psi_1(1) &= 1 \\ \psi_2(0) &= 0, & \psi_2(1) &= 1 \end{aligned} \right\} \quad (30)$$

Now obtain the following values $\psi_0(y)$, $\psi_1(y)$, and $\psi_2(y)$ by putting Eq. 29 into Eq. 28;

$$\left. \begin{aligned} \psi_0(y) &= \left(\frac{(1 + H \cosh(\sqrt{A_1})).\sinh(y\sqrt{A_1})}{\sinh(\sqrt{A_1})} \right) - H \cosh(y\sqrt{A_1}) \\ &\quad + Gr \cdot A_1 \left\{ \frac{\sinh(\sqrt{m_0} - y\sqrt{m_0})}{\sqrt{m_0} \cosh(\sqrt{m_0}) - \sinh(\sqrt{m_0})} \right\} \\ \psi_1(y) &= \frac{\sinh(y\sqrt{m_2})}{\sinh(\sqrt{m_2})} \\ \psi_2(y) &= \frac{\sinh(y\sqrt{m_3})}{\sinh(\sqrt{m_3})} \end{aligned} \right\} \quad (31)$$

Where,

$$\begin{aligned} m_0 &= \frac{Ri\omega + Pe\phi(i\omega + \gamma)}{i\omega + \gamma}, A = M + K_1 - K_2, A_1 = \frac{A}{\beta_1} \\ H &= \frac{A_1 \cdot Gr \cdot \sinh(\sqrt{m_0})}{\sqrt{m_0} \cosh(\sqrt{m_0}) - \sinh(\sqrt{m_0})}, m_2 = \frac{A + i\omega}{\beta_1}, m_3 = \frac{A - i\omega}{\beta_1} \\ H_1 &= \frac{A \cdot Gr \cdot \sinh(\sqrt{m_0})}{\sqrt{m_0} \cosh(\sqrt{m_0}) - \sinh(\sqrt{m_0})} \\ A &= M + K_1 - K_2, m_4 = A + i\omega, m_5 = A - i\omega \end{aligned}$$

In last putting the values $\psi_0(y)$, $\psi_1(y)$, and $\psi_2(y)$ into Eq. 29, becomes:

$$\begin{aligned} u(y, t) = -H \cosh(\sqrt{A_1} \cdot y) + \left(\frac{1 + H \cosh(\sqrt{A_1})}{\sinh(\sqrt{A_1})} \right) \cdot \sinh(\sqrt{A_1} \cdot y) + A_1 \cdot Gr \left\{ \frac{\sinh(\sqrt{m_0} - y\sqrt{m_0})}{\sqrt{m_0} \cosh(\sqrt{m_0}) - \sinh(\sqrt{m_0})} \right\} \\ + \frac{\varepsilon}{2} \left(\frac{\sinh(y\sqrt{m_2})}{\sinh(\sqrt{m_2})} \right) e^{i\omega t} + \frac{\varepsilon}{2} \left(\frac{\sinh(y\sqrt{m_3})}{\sinh(\sqrt{m_3})} \right) e^{-i\omega t} \end{aligned} \quad (32)$$

It is worth noting that the obtained general solution that is Eq. 32 satisfies all the imposed physical boundary conditions.

5 Limiting case; Flow of Newtonian viscous fluid

New use of the Casson parameter $\beta \rightarrow \infty$, we get the dimensionless form by putting $\beta_1 = 1$ it into Eq. 19.

$$\frac{\partial u}{\partial t} = \frac{\partial^2 u}{\partial y^2} - (M + K_1 - K_2)u + Gr\theta \quad (33)$$

$$\frac{\partial u}{\partial t} = \frac{\partial^2 u}{\partial y^2} - A \cdot u + Gr \cdot \theta \quad (34)$$

To solve Eq. 34, the following periodic solution is (Comstock, 1972; Nayfeh, 2008)

$$u(y, t) = \psi_{01}(y) + \frac{\varepsilon}{2} (\psi_{12}(y)e^{i\omega t} + \psi_{23}(y)e^{-i\omega t}) \quad (35)$$

$$\left. \begin{aligned} \psi_{01}(0) &= 0, & \psi_{01}(1) &= 1 \\ \psi_{12}(0) &= 0, & \psi_{12}(1) &= 1 \\ \psi_{23}(0) &= 0, & \psi_{23}(1) &= 1 \end{aligned} \right\} \quad (36)$$

New obtain the following values $\psi_{01}(y)$, $\psi_{12}(y)$, and $\psi_{23}(y)$ by putting Eqs 35, 36 into Eq. 34;

$$\left. \begin{aligned} \psi_{01}(y) &= -H_1 \cosh(y\sqrt{A}) + \left(\frac{(1 + H_1 \cosh(\sqrt{A})).\sinh(y\sqrt{A})}{\sinh(\sqrt{A})} \right) \\ &\quad + Gr \cdot A \left\{ \frac{\sinh(\sqrt{m_0} - y\sqrt{m_0})}{\sqrt{m_0} \cosh(\sqrt{m_0}) - \sinh(\sqrt{m_0})} \right\} \\ \psi_{12}(y) &= \frac{\sinh(y\sqrt{m_4})}{\sinh(\sqrt{m_4})} \\ \psi_{23}(y) &= \frac{\sinh(y\sqrt{m_5})}{\sinh(\sqrt{m_5})} \end{aligned} \right\} \quad (37)$$

In last putting the values $\psi_{01}(y)$, $\psi_{12}(y)$, and $\psi_{23}(y)$ into Eq. 35, become;

$$u(y, t) = \left\{ \begin{aligned} &-H_1 \cosh(y\sqrt{A}) + \left(\frac{(1 + H_1 \cosh(\sqrt{A})).\sinh(y\sqrt{A})}{\sinh(\sqrt{A})} \right) \\ &+ Gr \cdot A \left\{ \frac{\sinh(\sqrt{m_0} - y\sqrt{m_0})}{\sqrt{m_0} \cosh(\sqrt{m_0}) - \sinh(\sqrt{m_0})} \right\} \\ &+ \frac{\varepsilon}{2} \left(\frac{\sinh(y\sqrt{m_4})}{\sinh(\sqrt{m_4})} \right) e^{i\omega t} + \frac{\varepsilon}{2} \left(\frac{\sinh(y\sqrt{m_5})}{\sinh(\sqrt{m_5})} \right) e^{-i\omega t} \end{aligned} \right\} \quad (38)$$

The results obtained in Eq. 38 are the same as those obtained by Khan et al. (2022). As a result, this validates the validity of the current research.

6 Skin friction and nusselt number

Casson fluid shear stress can be defined as (Nayfeh, 2008),

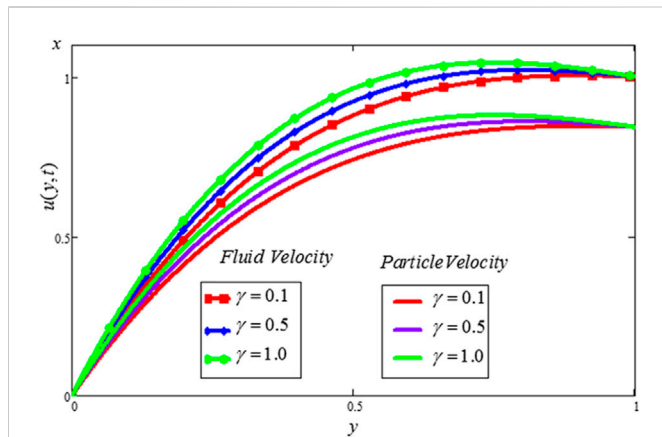


FIGURE 5

Effect of γ on $u(y,t)$ and $v(y,t)$. When $Pe = 2$, $R = 1$, $Gr = 5$, $\phi = 1$, $M = 0.5$, $K_1 = 1$, $\beta = 0.5$, $t = 1$, $\omega = 0.5$ and $\varepsilon = 0.001$.

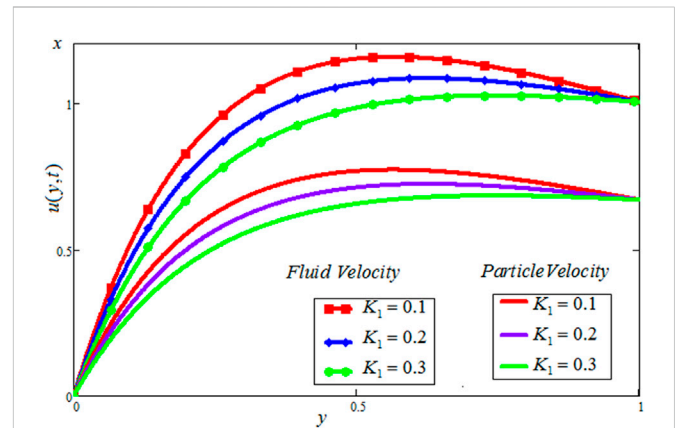


FIGURE 8

Effect of K_1 on $u(y,t)$ and $v(y,t)$. When $Pe = 2$, $M = 0.5$, $Gr = 5$, $\phi = 2$, $\gamma = 1$, $K_1 = 1$, $\beta = 0.5$, $t = 1$, $\omega = 0.5$ and $\varepsilon = 0.001$.

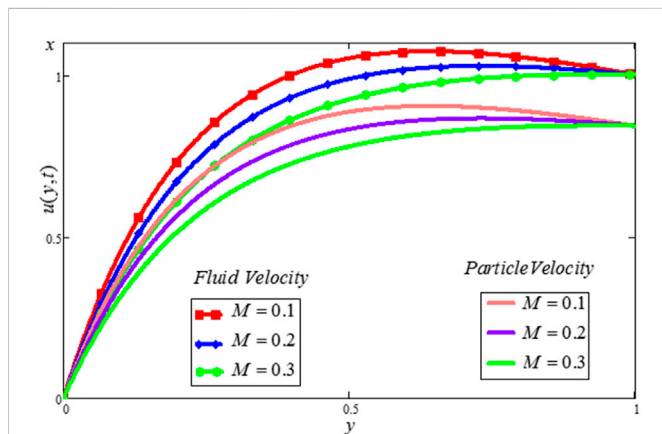


FIGURE 6

Effect of M on $u(y,t)$ and $v(y,t)$. When $Pe = 2$, $R = 1$, $Gr = 5$, $\phi = 2$, $\gamma = 1$, $K_1 = 1$, $\beta = 0.5$, $t = 1$, $\omega = 0.5$ and $\varepsilon = 0.001$.

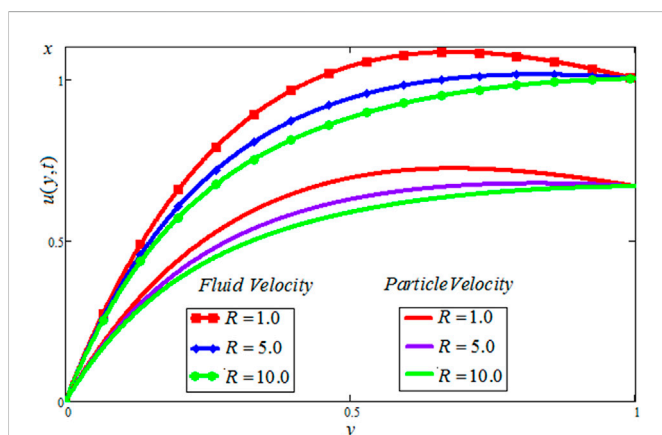


FIGURE 7

Effect of R on $u(y,t)$ and $v(y,t)$. When $Pe = 2$, $M = 0.5$, $Gr = 5$, $\phi = 2$, $\gamma = 1$, $K_1 = 1$, $\beta = 0.5$, $t = 1$, $\omega = 0.5$ and $\varepsilon = 0.001$.

$$\tau = \mu \left(1 + \frac{1}{\beta} \right) \frac{\partial u(y,t)}{\partial y} \quad (39)$$

By using a dimensionless variable from Eq. 10 and ignore the (*) sign;

$$Cf = \beta_1 \left. \frac{\partial u(y,t)}{\partial y} \right|_{y=0} = \beta_1 \left\{ \left(\sqrt{A_1} \right) \left(\frac{1 + H \cosh(\sqrt{A_1})}{\sinh(\sqrt{A_1})} \right) - A_1 Gr \left(\frac{\sqrt{m_0} \cosh(\sqrt{m_0})}{\sqrt{m_0} \cosh(\sqrt{m_0}) - \sinh(\sqrt{m_0})} \right) \right. \\ \left. + \frac{1}{2} \left(\frac{\varepsilon \sqrt{m_2}}{\sinh(\sqrt{m_2})} e^{i\omega t} + \frac{\varepsilon \sqrt{m_3}}{\sinh(\sqrt{m_3})} e^{-i\omega t} \right) \right\} \quad (40)$$

The heat transfer rate is (Saffman, 1962)

$$Nu = \left. \frac{\partial \theta(y,t)}{\partial y} \right|_{y=0} = \sqrt{m_0} \left(\frac{\cosh(\sqrt{m_0})}{\sqrt{m_0} \cosh(\sqrt{m_0}) - \sinh(\sqrt{m_0})} \right) \quad (41)$$

7 Physical interpretations and graphical results

The Casson dusty fluid velocity distribution, particle velocity, skin friction, and heat transfer rate are covered in this section, along with the influence of different dimensionless variables on these parameters. The velocity distribution of the Casson fluid, the velocity distribution of the dust particles, and the temperature profile are all affected by different physical characteristics, as shown in Figures 2–11. Tables 1, 2 discuss the Nu , and Cf , respectively.

Graphical representations of the Gr behavior of both the velocities are shown in Figure 2. The buoyancy-to-viscous force ratio is denoted by Gr . Increasing Gr , rises buoyancy forces and reduces viscous forces which causes both velocities enhanced. The β has an important impact on both the velocity profiles shown in Figure 3. The greater the β , the thinner the boundary layer becomes, which slows decrease both the velocities profiles. Figure 4 demonstrates the outcome of ϕ on both the velocities profiles. It is clear from these graphs that both the velocities profiles increase. This is true because the thermal forces strengthen as

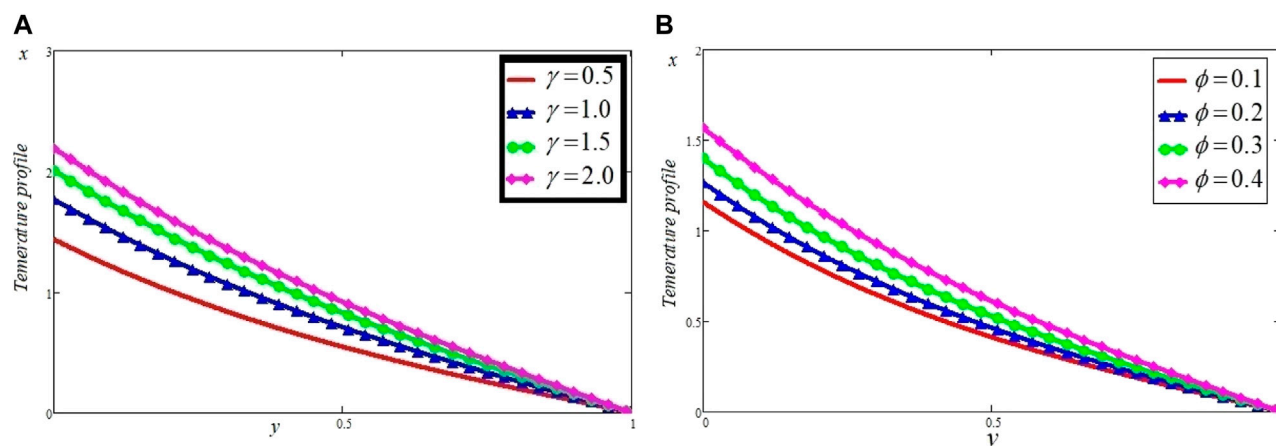


FIGURE 9
Effect of γ and ϕ on $\theta(y, t)$. When $Pe = 2$, $R = 3$, $\phi = 2$, and $\gamma = 2$.

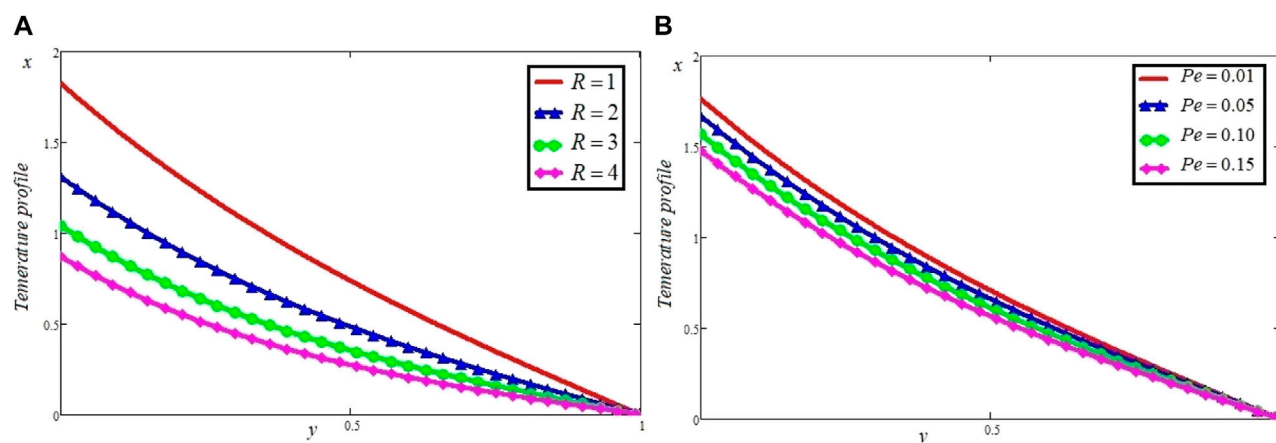


FIGURE 10
Effect of R and Pe on $\theta(y, t)$. When $Pe = 2$, $R = 3$, $\phi = 2$, and $\gamma = 2$.

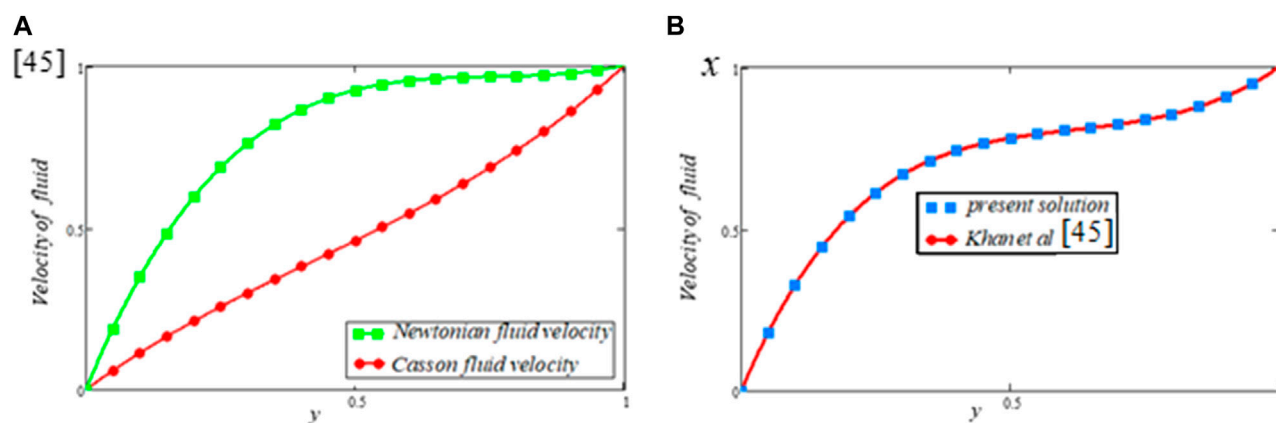


FIGURE 11
Comparison of the present study with (Wahid et al., 2020).

TABLE 1 Influence of different parameters on Nu .

Pe	R	ϕ	γ	Nu
3	3	2	2	1.39598
6	3	2	2	1.62532
3	4	2	2	1.61159
3	3	3	2	1.36354
3	3	2	4	1.26256

TABLE 2 Effect of different parameters on skin friction.

t	Pe	R	ϕ	γ	M	β	K_1	Gr	ω	ε	Cf
1.0	1	1	2	1	4	1	1	2	0.5	0.001	0.45109
1.0	1.1	1	2	1	4	1	1	2	0.5	0.001	0.54129
1.0	1	1.5	2	1	4	1	1	2	0.5	0.001	0.51518
1.0	1	1	3	1	4	1	1	2	0.5	0.001	1.01256
1.0	1	1	2	2	4	1	1	2	0.5	0.001	0.24493
1.0	1	1	2	1	5.0	1	1	2	0.5	0.001	2.00198
1.0	1	1	2	1	4	2.0	1	2	0.5	0.001	0.37355
1.0	1	1	2	1	4	1	2.0	2	0.5	0.001	0.38903
1.0	1	1	2	1	4	1	1	4.0	0.5	0.001	2.60591

heat generation increases, which cause an increment in both the velocities. The increasing values of temperature time relaxation parameter, enhance both the velocities profiles. More physically, this compartment is that γ has inverse relation with dynamic viscosity. As the values of rise, the dynamic viscosity reduces, causing both velocities to increase, as seen in Figure 5. Figure 6 depicts the influence of the magnetic parameter M on the velocity's profiles for both the velocities profiles. This is due to the fact that Lorentz forces become stronger as M increases which act as resistive forces, and therefore retard the flow. Figure 7 displays the influence of R on the both velocities profiles. The increasing the particle concentration parameter causes extra collisions in the dusty phase, which increase the internal resistive forces, and thus increase both the velocities profiles. The effect of K_1 on both velocities is shown from Figure 8. The figure makes it obvious that both velocities decrease as the values of K_1 rise. This performance is truthful, as by Stocks drag formula ($K_1 = 6\pi\mu$), it is clear that increasing K_1 viscous forces increase which resist the flow and consequently decrease the both velocities. The increasing values of temperature time relaxation parameter, enhance temperature profile. The physics is that, the temperature time relaxation parameter γ is inverse relation to viscous force, when increases the temperature time relaxation parameter, and reduces viscous forces which causes both velocities enhanced. Figure 9A shows that when the values of γ increase, the dynamic viscosity drops and the temperature profile rises as a

result. The increasing values of, enhance $\theta(y, t)$. The physics behind this behavior is that ϕ has direct relation with heat generation. When the values of heat generation parameter ϕ increase the heat generation increases that consequently increase $\theta(y, t)$ as shown in Figure 9B. The impact of R on $\theta(y, t)$ is sketched in Figure 10A. By rising the values of R , the $\theta(y, t)$ is decreased. The physics behind this behavior is that the particle concentration parameter R has inverse relation conductivity of thermal. The fluid's conductivity of thermal decreases as the values R rise, which lowers the temperature distribution. The effect of Pe on $\theta(y, t)$ is sketched in Figure 10B. By rising the values of Pe the $\theta(y, t)$ is decreased. The physics behind this behavior is that Pe has the inverse relation thermal conductivity. When the values of Pe increase the thermal conductivity of the fluid decrease therefore, decrease $\theta(y, t)$; Figure 11A compres Newtonian fluid velocity to viscoelastic Casson fluid velocity. It can be noticed that the viscoelastic Casson fluid has an extremely low velocity than the Newtonian fluid. The greater the Casson parameter β , the thinner the boundary layer becomes, which slow retard Casson fluid velocity. The value of $\beta \rightarrow \infty$ then $\frac{1}{\beta} = 0$ has been used for Newtonian fluid. Just for comparison, the Newtonian fluid velocity is much larger than the Casson fluid velocity in this case. Finally; Figure 11B depicted the correlation between the current solutions and (Wahid et al., 2020). Our current solution is reduced to (Wahid et al., 2020) solution by taking $\beta_1 = 1$ into account.

Table 1; Table 2 plot the effect of various parameters on Nu and Cf . Table 1 shows the variation Nu with rising values of Pe and R . The Pe and R illustrates a direct relation with the Nu that is by increasing Pe and R an enhances in Nu , while the ϕ and γ depicts an inverse relation with the Nu that is by increasing ϕ and γ a decrease in Nu . It can be seen that raising M , Pe , R , γ and ϕ enhances the numerical value of Cf , whereas increasing Gr , and β decreases the numerical value of Cf because these parameters decrease viscous forces, which reduces the Cf .

8 Conclusion

The unsteady MHD flow of an incompressible Casson fluid with dust particles between two parallel plates is analytically investigated when the effects of Newtonian heating are taken into consideration. Using the Lighthill perturbation technique, the perturb solutions for both velocities (fluid and dust) are obtained. Similarly, solutions to the Casson dusty fluid and particle energy equations are obtained separately. To define the impact of β and M on the Casson fluid motion, some numerical and graphical results are reported in the Figures 2–11 for various values of physical parameters. The main outcomes are:

- The effect of M , R and Gr on the $u(y, t)$, and $v(y, t)$ studied in detail.
- The dusty fluid and particle velocities are declining function for M , because of the Lorentz force, the magnetic parameter retards fluid motion.
- The Casson parameter β increases then both velocities are enhanced, which also increases the Cf .

- Both the velocities (fluid and dust particle velocities) and temperature profile are enhanced when the temperature relaxation time parameter is increased.
- The temperature relaxation time parameter should be increased to manage the rate of heat transfer in fluid.
- The Newtonian heating phenomenon affects the heating on the plate.

Data availability statement

The raw data supporting the conclusion of this article will be made available by the authors, without undue reservation.

Author contributions

FA conceptualization, formulation, supervision, GA Analysis, and writing draft, AK: Calculations and results, IK software, writing the

draft, supervision, ETE: supervision, conceptualization, funding, MA data analysis, revision.

Conflict of interest

The authors declare that the research was conducted in the absence of any commercial or financial relationships that could be construed as a potential conflict of interest.

Publisher's note

All claims expressed in this article are solely those of the authors and do not necessarily represent those of their affiliated organizations, or those of the publisher, the editors and the reviewers. Any product that may be evaluated in this article, or claim that may be made by its manufacturer, is not guaranteed or endorsed by the publisher.

References

- Abbas, Z., Jafar, M. A., and Hasnain, J. (2020). Analysis of asymptotic solutions for non-Newtonian fluid flow between two parallel discs with dissimilar in-plane motion. *European Journal of Mechanics-B/Fluids* 84, 129–138. doi:10.1016/j.euromechflu.2020.06.002
- Afikuzzaman, M., Biswas, R., Mondal, M., and Ahmmed, S. (2018). MHD free convection and heat transfer flow through a vertical porous plate in the presence of chemical reaction. *Frontiers in Heat and Mass Transfer (FHMT)* 11 (1), 1–23. doi:10.5098/hmt.11.13
- Ali, F., Bilal, M., Gohar, M., Khan, I., Sheikh, N. A., and Nisar, K. S. (2020). A report on fluctuating free convection flow of heat absorbing viscoelastic dusty fluid past in a horizontal channel with MHD effect. *Scientific Reports* 10 (1), 8523–8615. doi:10.1038/s41598-020-65252-1
- Ali, F., Bilal, M., Sheikh, N. A., Khan, I., and Nisar, K. S. (2019). Two-phase fluctuating flow of dusty viscoelastic fluid between non-conducting rigid plates with heat transfer. *IEEE Access* 7, 123299–123306. doi:10.1109/access.2019.2933529
- Ali, N., Nazeer, M., Javed, T., and Razzaq, M. (2019). Finite element analysis of bi-viscosity fluid enclosed in a triangular cavity under thermal and magnetic effects. *The European Physical Journal Plus* 134 (1), 2–20. doi:10.1140/epjp/i2019-12448-x
- Anuar, N. S., Bachok, N., Turkyilmazoglu, M., Arifin, N. M., and Rosali, H. (2020). Analytical and stability analysis of MHD flow past a nonlinearly deforming vertical surface in Carbon Nanotubes. *Alexandria Engineering Journal* 59 (1), 497–507. doi:10.1016/j.aej.2020.01.024
- Casson, N. (1959). "A flow equation for pigment-oil suspensions of the printing in ink type." in *Rheology of disperse Systems*, Editor C. C. Mill (Oxford: Pergamon Press), 84–104. doi:10.4236/wjm.2018.810030
- Chanson, H. (2004). *Hydraulics of open channel flow*. Amsterdam, Netherlands: Elsevier.
- Comstock, C. (1972). The Poincaré-Lighthill perturbation technique and its generalizations. *SIAM Review* 14 (3), 433–446. doi:10.1137/1014069
- Das, S., Banu, A. S., and Jana, R. N. (2021). Delineating impacts of non-uniform wall temperature and concentration on time-dependent radiation-convection of Casson fluid under magnetic field and chemical reaction. *World Journal of Engineering* 18, 780–795. doi:10.1108/wje-11-2020-0607
- Ezzat, M. A., El-Bary, A. A., and Morsey, M. M. (2010). Space approach to the hydro-magnetic flow of a dusty fluid through a porous medium. *Computers and Mathematics with Applications* 59 (8), 2868–2879. doi:10.1016/j.camwa.2010.02.004
- Gangadhar, K., Kannan, T., Jayalakshmi, P., and Sakthivel, G. (2021). Dual solutions for MHD Casson fluid over a shrinking sheet with Newtonian heating. *International Journal of Ambient Energy* 42 (3), 331–339. doi:10.1080/01430750.2018.1550018
- Gireesha, B. J., Ramesh, G. K., and Bagewadi, C. S. (2012). Heat transfer in MHD flow of a dusty fluid over a stretching sheet with viscous dissipation. *Advances in Applied Science Research* 3 (4), 2392–2401.
- Hamid, A., Naveen Kumar, R., Punith Gowda, R. J., Varun Kumar, R. S., Khan, S. U., Ijaz Khan, M., et al. (2021). Effect of Hall current and homogenous-heterogeneous reactions on MHD flow of GO-MoS₂/water (H₂O)-ethylene glycol (C₂H₆O₂) hybrid nanofluid past a vertical stretching surface. *Waves in Random and Complex Media* 3 (1), 1–18.
- Hussain, F., Nazeer, M., Altanji, M., Saleem, A., and Ghafar, M. M. (2021). Thermal analysis of Casson rheological fluid with gold nanoparticles under the impact of gravitational and magnetic forces. *Case Studies in Thermal Engineering* 28, 101433. doi:10.1016/j.csite.2021.101433
- Hussain, S. M., Jain, J., Seth, G. S., and Rashidi, M. M. (2018). Effect of thermal radiation on magneto-nanofluids free convective flow over an accelerated moving ramped temperature plate. *Scientia Iranica* 25 (3), 1243–1257.
- Hussanan, A., Salleh, M. Z., and Khan, I. (2016). Effects of Newtonian heating and inclined magnetic field on two dimensional flow of a casson fluid over a stretching sheet. 5th World Conference on Applied Sciences, Engineering & Technology, HCMUT, Vietnam. 251–255.
- Hussanan, A., Salleh, M. Z., Khan, I., and Tahar, R. M. (2017a). Heat transfer in magnetohydrodynamic flow of a Casson fluid with porous medium and Newtonian heating. *Journal of nanofluids* 6 (4), 784–793. doi:10.1166/jon.2017.1359
- Hussanan, A., Salleh, M. Z., Khan, I., and Tahar, R. M. (2017b). Heat transfer in magnetohydrodynamic flow of a Casson fluid with porous medium and Newtonian heating. *Journal of Nanofluids* 6 (4), 784–793. doi:10.1166/jon.2017.1359
- Jalil, M., Asghar, S., and Yasmeen, S. (2017). An exact solution of MHD boundary layer flow of dusty fluid over a stretching surface. *Mathematical Problems in Engineering* 2017, 5. 2307469doi:10.1155/2017/2307469
- Jha, B. K., and Gambo, D. (2022). Hydrodynamic behaviour of velocity of applied magnetic field on unsteady MHD Couette flow of dusty fluid in an annulus. *The European Physical Journal Plus* 137 (1), 67–20. doi:10.1140/epjp/s13360-021-02284-0
- Jyothi, A. M., Kumar, R. N., Gowda, R. P., and Prasannakumara, B. C. (2021). Significance of Stefan blowing effect on flow and heat transfer of Casson nanofluid over a moving thin needle. *Communications in Theoretical Physics* 73 (9), 095005. doi:10.1088/1572-9494/ac0a65
- Jyothi, A. M., Varun Kumar, R. S., Madhukesh, J. K., Prasannakumara, B. C., and Ramesh, G. K. (2021). Squeezing flow of Casson hybrid nanofluid between parallel plates with a heat source or sink and thermophoretic particle deposition. *Heat Transfer* 50 (7), 7139–7156. doi:10.1002/htj.22221
- Khalid, A., Khan, I., Khan, A., and Shafie, S. (2015). Unsteady MHD free convection flow of Casson fluid past over an oscillating vertical plate embedded in a porous medium. *Engineering Science and Technology, An International Journal* 18 (3), 309–317. doi:10.1016/j.jestech.2014.12.006
- Khan, D., Ali, G., Kumam, P., and ur Rahman, A. (2022). A scientific outcome of wall shear stress on dusty viscoelastic fluid along heat absorbing in an inclined channel. *Case Studies in Thermal Engineering* 30, 101764–101771. doi:10.1016/j.csite.2022.101764
- Khan, D., Khan, A., Khan, I., Ali, F., ul Karim, F., and Tili, I. (2019). Effects of relative magnetic field, chemical reaction, heat generation and Newtonian heating on convection flow of Casson fluid over a moving vertical plate embedded in a porous medium. *Scientific Reports* 9 (1), 400–418. doi:10.1038/s41598-018-36243-0
- Koriko, O. K., Adegbie, K. S., Shah, N. A., Animasaun, I. L., and Olotu, M. A. (2021). Numerical solutions of the partial differential equations for investigating the significance of partial slip due to lateral velocity and viscous dissipation: The case of blood-gold carreau nanofluid and dusty fluid. *Numerical Methods for Partial Differential Equations* 2021, 1–29. doi:10.1002/num.22754
- Krishna, M. V., Ahamad, N. A., and Chamkha, A. J. (2021). Hall and ion slip impacts on unsteady MHD convective rotating flow of heat generating/absorbing second grade fluid. *Alexandria Engineering Journal* 60 (1), 845–858. doi:10.1016/j.aej.2020.10.013

- Kumar, K. A., Sugunamma, V., and Sandeep, N. (2020). Effect of thermal radiation on MHD Casson fluid flow over an exponentially stretching curved sheet. *Journal of Thermal Analysis and Calorimetry* 140 (5), 2377–2385. doi:10.1007/s10973-019-08977-0
- Loganathan, K., Sivakumar, M., Mohanraj, M., and Sakthivel, P. (2021). Thermally radiative casson fluid flow over a cylinder with Newtonian heating and heat generation/absorption. *Journal of Physics: Conference Series*, 1964 (2), 022001. doi:10.1088/1742-6596/1964/2/022001
- Mabood, F., Abdel-Rahman, R. G., and Lorenzini, G. (2016). Effect of melting heat transfer and thermal radiation on Casson fluid flow in porous medium over moving surface with magnetohydrodynamics. *Journal of Engineering Thermophysics* 25 (4), 536–547. doi:10.1134/s1810232816040111
- Madhukesh, J. K., Alhadhrami, A., Naveen Kumar, R., Punith Gowda, R. J., Prasannakumara, B. C., and Varun Kumar, R. S. (2021). Physical insights into the heat and mass transfer in Casson hybrid nanofluid flow induced by a Riga plate with thermophoretic particle deposition. *Proceedings of the Institution of Mechanical Engineers, Part E: Journal of Process Mechanical Engineering* 3 (2), 1–19.
- Makinde, O. D. (2009). On thermal stability of a reactive third-grade fluid in a channel with convective cooling the walls. *Applied Mathematics and Computation* 213 (1), 170–176. doi:10.1016/j.amc.2009.03.003
- Manjula, V., and Sekhar, K. C. (2021). Heat and mass transfer analysis of MHD Casson fluid flow over a permeable vertical surface with thermal radiation and Newtonian heating AIP Conference Proceedings. *AIP Publishing LLC* 2375 (1), 030010. doi:10.1063/5.0066543
- Merkin, J. H. (1994). Natural-convection boundary-layer flow on a vertical surface with Newtonian heating. *Int. J. Heat Fluid Flow* 15 (5), 392–398. doi:10.1016/0142-727x(94)90053-1
- Miwa, S., and Hibiki, T. (2022). Inverted annular two-phase flow in multiphase flow systems. *International Journal of Heat and Mass Transfer* 18 (6), 122340–122354. doi:10.1016/j.ijheatmasstransfer.2021.122340
- Mukhopadhyay, S. (2013). Effects of thermal radiation on Casson fluid flow and heat transfer over an unsteady stretching surface subjected to suction/blowing. *Chinese Physics B* 22 (11), 114702–114714. doi:10.1088/1674-1056/22/11/114702
- Nayfeh, A. H. (2008). *Perturbation methods*. Hoboken, NJ, USA: John Wiley & Sons.
- Obalalu, A. M. (2021). Heat and mass transfer in an unsteady squeezed Casson fluid flow with novel thermophysical properties: Analytical and numerical solution. *Heat Transfer* 50 (8), 7988–8011. doi:10.1002/htj.22263
- Obalalu, A. M., Wahaab, F. A., and Adebayo, L. L. (2020). Heat transfer in an unsteady vertical porous channel with injection/suction in the presence of heat generation. *Journal of Taibah University for Science* 14 (1), 541–548. doi:10.1080/16583655.2020.1748844
- Oka, S. (1971). An approach to a unified theory of the flow behavior of time-independent non-Newtonian suspensions. *Japanese Journal of Applied Physics* 10 (3), 287–298. doi:10.1143/jjap.10.287
- O'Sullivan, C. T. (1990). Newton's law of cooling—a critical assessment. *American Journal of Physics* 58 (10), 956–960. doi:10.1119/1.16309
- Pramanik, S. (2014). Casson fluid flow and heat transfer past an exponentially porous stretching surface in presence of thermal radiation. *Ain Shams Engineering Journal* 5 (1), 205–212. doi:10.1016/j.asej.2013.05.003
- Rafiq, S., Abbas, Z., Sheikh, M., and Hasnain, J. (2020). Effects of variable viscosity on asymmetric flow of non-Newtonian fluid driven through an expanding/contracting channel containing porous walls. *Arabian Journal for Science and Engineering* 45 (11), 9471–9480. doi:10.1007/s13369-020-04798-8
- Raju, C. S. K., Upadhyay, S. M., and Seth, D. (2021). Thermal convective conditions on MHD radiated flow with suspended hybrid nanoparticles. *Microsystem Technologies* 27 (5), 1933–1942. doi:10.1007/s00542-020-04971-x
- Ramesh, G. K., Madhukesh, J. K., Prasannakumara, B. C., and Roopa, G. S. (2022). Significance of aluminium alloys particle flow through a parallel plates with activation energy and chemical reaction. *Journal of Thermal Analysis and Calorimetry* 147 (12), 6971–6981. doi:10.1007/s10973-021-10981-2
- Reddy, G. J., Raju, R. S., and Rao, J. A. (2018). Influence of viscous dissipation on unsteady MHD natural convective flow of Casson fluid over an oscillating vertical plate via FEM. *Ain Shams Engineering Journal* 9 (4), 1907–1915. doi:10.1016/j.asej.2016.10.012
- Rehman, S. U., Fatima, N., Ali, B., Imran, M., Ali, L., Shah, N. A., et al. (2022). The Casson dusty nanofluid: Significance of Darcy–forchheimer law, magnetic field, and non-Fourier heat flux model subject to stretch surface. *Mathematics* 10 (16), 2877. doi:10.3390/math10162877
- Rundora, L. (2021). Unsteady magnetohydrodynamic mixed convective flow of a reactive casson fluid in a vertical channel filled with a porous medium, *Defect and Diffusion Forum*. 408, 33–49. doi:10.4028/www.scientific.net/DDF.408.33
- Saffman, P. G. (1962). On the stability of laminar flow of a dusty gas. *Journal of Fluid Mechanics* 13 (1), 120–128. doi:10.1017/s0022112062000555
- Sayed-Ahmed, M. E., Attia, H. A., and Ewis, K. M. (2011). Time dependent pressure gradient effect on unsteady mhd Couette flow and heat transfer of a Casson fluid. *Engineering* 3 (1), 38–49. doi:10.4236/eng.2011.31005
- Turkylmazoglu, M. (2022). Flow and heat over a rotating disk subject to a uniform horizontal magnetic field. *Zeitschrift für Naturforschung A* 77 (4), 329–337. doi:10.1515/zna-2021-0350
- Upadhyay, S. M., Raju, C. S. K., Vajravelu, K., Sathy, S., and Farooq, U. (2022). Significance of radiative magnetohydrodynamic flow of suspended PEG based ZrO₂ and MgO₂ within a conical gap. *Waves in Random and Complex Media* 8 (2), 4575–4599.
- Wahid, N. S., Arifin, N. M., Turkylmazoglu, M., Hafidzuddin, M. E. H., and Abd Rahmin, N. A. (2020). MHD hybrid Cu-Al₂O₃/water nanofluid flow with thermal radiation and partial slip past a permeable stretching surface: Analytical solution, *Journal of Nano Research*, 64, 75–91. doi:10.4028/www.scientific.net/JNanoR.64.75

Glossary

h_s Heat transfer coefficient (m^{-1})

B_0 Applied Magnetic Field ($N.s/C.m$)

K_0 Stock's Resistance Coefficient

K_1 Dusty fluid parameter

K_2 Dusty fluid parameter

N_0 Number Density of the Dust Particles

P_p Density of the dust particle (kg/m^3)

T_d Ambient Temperature K

c_p Specific heat capacity of fluid ($J \cdot kg^{-1} \cdot K^{-1}$)

\vec{s} Surface forces N

u_0 Constant Velocity (m/s)

β_T Coefficient of Thermal Expansion

γ_T Temperature relaxation time

c_s Specific heat capacity of the dust particle

R Particle concentration parameter

T_∞ Ambient temperature K

ϕ Heat absorption coefficient

Cf Skin friction.

Gr Grashof Number

M Non-dimensional Magnetic Parameter

Nu Nusslet number

P Pressure ($kg \cdot m^{-1} s^{-2}$)

Pe Pectlet Number

T Temperature of the Fluid K

d is the distance between parallel plates(m)

g Gravitational Acceleration (ms^{-2})

k Thermal Conductivity of the Fluid (W/mK).

m Mass of particles (kg)

t Time (s)

$u(y, t)$ Velocity of the base fluid (m/s)

$v(y, t)$ Velocity of the particle (m/s)

β Casson fluid parameter

θ Dimensionless Temperature of the fluid

μ Dynamic Viscosity ($kg \cdot m^{-1} s^{-1}$)

ρ Fluid Density (kg/m^3)

$\rho \vec{b}$ Body Forces

σ Electrical Conductivity (S/m)

ν Kinematic Viscosity (kg/m^3).



OPEN ACCESS

EDITED BY
Safia Akram,
National University of Sciences and
Technology, Pakistan

REVIEWED BY
Liaquat Ali Lund,
Sindh Agriculture University, Pakistan
Yun Zheng,
Jiangnan University, China

*CORRESPONDENCE
M. Tufail,
✉ tufail.phdphy61@iiu.edu.pk
Wiqar H. Shah,
✉ wiqar.hussain@iiu.edu.pk
Muhammad Sohail,
✉ muhammad.sohail@kfueit.edu.pk

SPECIALTY SECTION

This article was submitted to Colloidal
Materials and Interfaces,
a section of the journal
Frontiers in Materials

RECEIVED 25 November 2022

ACCEPTED 18 January 2023

PUBLISHED 08 February 2023

CITATION

Khan S, Shah WH, Tufail M, Ali A, Eldin SM,
Imran N and Sohail M (2023), Sb-doped
 $\text{Ti}_{8.67}\text{Sn}_{1.33-x}\text{Sb}_x\text{Te}_6$ nanoparticles
improve power factor and electronic
charge transport.
Front. Mater. 10:1108048.
doi: 10.3389/fmats.2023.1108048

COPYRIGHT

© 2023 Khan, Shah, Tufail, Ali, Eldin, Imran
and Sohail. This is an open-access article
distributed under the terms of the [Creative
Commons Attribution License \(CC BY\)](#).
The use, distribution or reproduction in
other forums is permitted, provided the
original author(s) and the copyright
owner(s) are credited and that the original
publication in this journal is cited, in
accordance with accepted academic
practice. No use, distribution or
reproduction is permitted which does not
comply with these terms.

Sb-doped $\text{Ti}_{8.67}\text{Sn}_{1.33-x}\text{Sb}_x\text{Te}_6$ nanoparticles improve power factor and electronic charge transport

Sabir Khan¹, Wiqar H. Shah^{1*}, M. Tufail^{1*}, Akhtar Ali¹, Sayed M. Eldin²,
Naveed Imran^{3,4} and Muhammad Sohail^{5*}

¹Department of Physics, Faculty of Basic and Applied Sciences, International Islamic University, Islamabad, Pakistan, ²Center of Research, Faculty of Engineering, Future University in Egypt New Cairo, New Cairo, Egypt, ³HITEC School and Colleges, HIT Taxila Cant, Islamabad, Pakistan, ⁴Institute of Space Technology, Islamabad, Pakistan, ⁵Khwaja Fareed University of Engineering and Information Technology, Rahim Yar Khan, Pakistan

Thallium telluride $\text{Ti}_{8.67}\text{Sn}_{1.33-x}\text{Sb}_x\text{Te}_6$ nano compound doped with different concentration ratios of Sb ($x = 0.63, 0.65, 0.66, 0.68, 0.70$, or 0.72) was prepared using solid-state techniques, and the compound was heated up to 550 K in vacuum silica tubes. The structure of the nano system was studied using XRD and EDX. It was confirmed that, without any other impurities, the nano system had a single-phase tetragonal crystal structure. The measured Seebeck coefficient (S) of all nano compounds showed that S increased with increase in temperature from 300 to 550 K. S was positive at all temperatures, showing characteristics of a p-type semiconductor. The complex behaviour of S in an Sb-doped nano system showed that at low temperature (room temperature), S first decreased with an increase in Sb concentration up to $x = 0.65$ and then increased with an increase in the Sb dopant up to $x = 0.72$. Similarly, electrical conductivity (σ) decreased with an increase in temperature, and the power factor showed complex behaviour relative to Sb concentration. The power factor observed for $\text{Ti}_{8.67}\text{Sn}_{1.33-x}\text{Sb}_x\text{Te}_6$ nano compound increased with an increase in temperature, within a temperature range of 300–550 K. Tellurides are semiconductors of very narrow band-gap, with component elements in common oxidation states, according to (Ti^{+9}) (Sb^{3+}) (Te^{2-})⁶. The phase range was also assessed, and results demonstrated that different Sb dopant ratios were associated with differences in properties (e.g., electrical, thermal, and Seebeck effect) and hence variation in power factor. These results indicate a route through which the thermoelectric characteristics of $\text{Ti}_{8.67}\text{Sn}_{1.33-x}\text{Sb}_x\text{Te}_6$ -based nano materials were harnessed for the development of thermoelectric and electronic applications.

KEYWORDS

Sb-doped thermoelectric materials, Seebeck coefficient, thermoelectric materials, electrical conductivity, power factor

1 Introduction

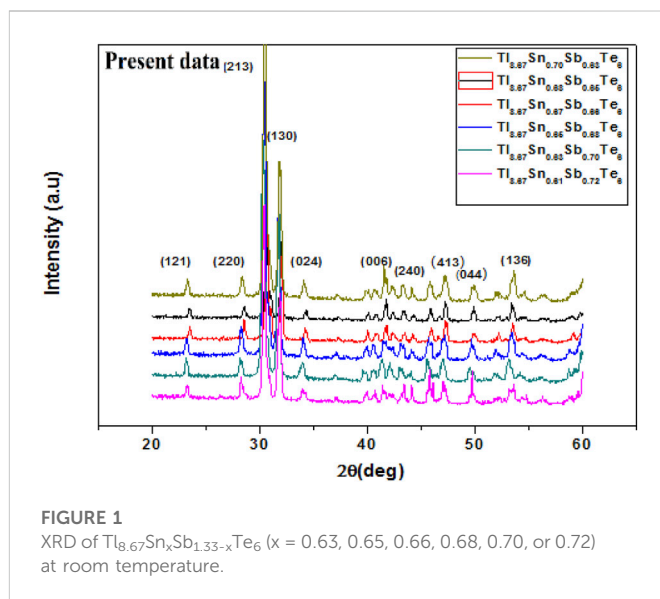
Green energy and its sources are of great interest due to environmental issues. It provides a way to overcome the energy crises and minimize the use of fossil fuel (Adam et al., 2017; Liu et al., 2018; Rahman et al., 2019), as well as improve the efficiency of existing thermoelectric (TE) materials; therefore, it is important to find new TE materials (Luu and Vaqueiro, 2015; Chen et al., 2016; Ouyang et al., 2018). Scientists and researchers of the current era are taking great interest in TE materials as they are among the best green energy sources, particularly at the

nano size, as demonstrated by the chalcogenide nano system of rare Earth elements, which has a high Seebeck coefficient, moderate thermal conductivity, and high electrical conductivity. The bulk of the nano material $\text{Tl}_9\text{Te}_{10}$ was prepared using ball milling and hot-pressing techniques along with doped lead. The thermal and electrical properties were studied by Yu et al. (2010a), who showed that the figure of merit (ZT) was 1.30 at 299.99°C. The Seebeck coefficient (S) estimated at 400°C was slightly higher than Na nano particle dopants. The temperature at which a nano system ($\text{Tl}_{0.020}\text{Pb}_{0.98}\text{Te}$) has a high ZT and high TE property was calculated to be 500°C. Pb-doped ($\text{Bi}_{0.2}\text{Sb}_{0.8-x}\text{Pb}_x$) $_2\text{Te}_3$ nano compound was synthesized using the hot pressing sintering and quenching technique established by Lin et al. (2016), and assessment of TE characteristics demonstrated that ZT was enhanced with doping. In order to improve and synthesise new TE material (Khan et al., 2018), nano compounds with different Sb concentration ratios ≥ 1 were synthesised using a solid-state reaction technique, and the nano particles of the compound were prepared from the ingot using ball milling. It was confirmed that the structure of the compound was tetragonal, with a space group (I4/mcm) and no impurities. P-type behaviour was reported due to doping of thallium telluride with Sb. TE properties, including electrical properties, S, and ZT increased and, therefore, the power factor increased. It was also noted that the semiconduction behaviour of the compound gradually became electrical in nature, while the structure of the compound remained unchanged. The thermal properties of synthesized thallium antimony telluride were carefully studied by Kurosaki et al. (2004), with watchful measurement of thallium and tellurium nano materials. Powder made up of these nano materials was mixed, and pellets were formed by condensing the particles for 6 h in a closed quartz holder K and heated below Argon gas in a 674 K mp climate. The TE power (S) and the electrical resistivity (ρ) were measured over the temperature range of 300 K–800 K. The estimation of TE power at $3.93 \times 10^{20}\text{C}$ was measured and found to be basically identical in position of strength for TE properties, while TlSbTe_6 showed positive behaviour in the range of perfect temperature. The compound showed comparatively low thermal conductivity, and the power factor at 400 K was greater, with a value of 0.9. This effect was due to the combination of TE materials. According to an in-depth study by Zhang and Zhao (2015), the thermal and electrical properties of nano materials, such as TE materials, have resulted in revolutionary changes since the last century, by providing another approach through which researchers can generate new methods of power generation. Due to high electrical and thermal properties, thallium tellurides were synthesized with lanthanides by Guo and Kleinke (2015). At the first stage, Tl_9CeTe_6 had a unit cell volume with a wavelength in the range of 1,033 Å. The electrical and thermal conductivity increases from La to Tb, while the thermoelectric power decreases from La to Tb in the lanthanide series. Although both Tl_9GdTe_6 and Tl_9SmTe_6 are exceptional, Tl_9GdTe_6 has more significant TE power. In the lanthanide series, Tl_9LaTe_6 has the most elevated figure of merit. Increasing the ratio of La (0.9, 0.95, 1.00, 1.05, and 1.10) causes improved unit cell volume, hence a decrease in thermal conductivity and an increase in thermal power. At 600 K, the ZT value for Tl_9LaTe_6 is 0.57. The research of Kim and Ha (2013) showed isolation of alumina nanoparticles with bismuth–antimony–tellurium lattice ($\text{Al}_2\text{O}_3/\text{BST}$) using the framing ball milling technique. At 323 K, the value of ZT increased. The study of Sankar et al. (2012) showed that, in the application of TE materials, thermal and

electrical properties play key roles. They worked on compounds of ternary chalcogenides of thallium such as TlGdY_2 (Y = Te or Se), wherein Tl_{96} achieved α - Na_2 structure, with isostructure demonstrated by TlSbY_2 (space group R_3m), and Tl_9Te_6 was isostructural through Tl_{96} (space group $I4/cm$). The wide band p -type semiconductor was discovered to have low/lower electrical conductivity and a high Seebeck coefficient of TlGdSe_2 . Telluride TlGdTe_2 had low thermal conductivity (K) of 0.5 W/mK and possessed a semiconductor at 298 K (ambient temperature). Tl_9Te_6 displayed a relatively small amount of high thermal conductivity at 298 K (room temperature). The impurity of TlBiTe polycrystalline was synthesized by using hot squeezing techniques; the thermoelectric properties were then evaluated at temperatures ranging from 293 K (room temperature) to 700 K by (Yamanaka et al. (2003), confirming that the Seebeck effect was increased across the full temperature range. These data demonstrated that the material acted like a p (hole)-type semiconductor. The electrical resistivity was 12 times higher than the TE materials. The highest assessed ZT was 0.86 at 590 K. Sn at different ratios served as the dopant for ($\text{Bi}_{0.25}\text{Sb}_{0.75}$) $_{2-x}\text{Sn}_x\text{Te}_3$ nano compounds, where ($x = 0, 0.005, 0.01, 0.05, 0.1, \text{ or } 0.2$) in experiments by Cai et al. (2016) using hot energy ball mill and spark plasma techniques to study TE properties. With the help of SEM and TEM, it was confirmed that ($\text{Bi}_{0.25}\text{Sb}_{0.75}$) $_{2-x}\text{Sn}_x\text{Te}_3$ nanostructure was inhomogeneous and of encrusted structure. The elevated value of ZT was 1.30 at 338 K when the doping value of $x = 0.1$. The thermal and electrical properties of tellurium telluride ($\text{Tl}_{8.67}\text{Pb}_x\text{Sb}_{1.33-x}\text{Te}_6$) with doping of Pb were studied by Shah et al. (2016) with different concentration ratios ($x = 0.61, 0.63, 0.65, 0.67, 0.68, \text{ or } 0.70$). The samples were synthesized by a solid-state reaction in an air-free silica tube. The crystal structure was examined by XRD and EDX. It was observed that all the compounds were phase pure. The S values for these compounds increased with the increase in temperature from 295 K to 550 K, which showed that S was positive for the entire temperature range; from these data, it was clear that the compound was a semiconductor with p -type behaviour. At room temperature, it showed complex behaviour after doping with Pb; with increased doping, the Seebeck effect decreased. The electrical conductivity and power factor also showed complex behaviour related to Pb concentration. The power factor over the entire temperature range, from 290 K to 550 K, for $\text{Tl}_{8.67}\text{Pb}_x\text{Sb}_{1.33-x}\text{Te}_6$ compounds also increased. As tellurides are semiconductors of small band-gap, a state of normal oxidation was also shown by (Tl^+) $_9$ (Sb^{3+}) (Te^{2-}) $_6$. The doping with Pb showed effects on its thermal and electrical properties. The increased concentration of Pb resulted in the increase in hole which led to higher scattering of electrons and reduced S value. The TE characteristics of the quaternary/quadruplet telluride series $\text{Tl}_{10-x-y}\text{Sn}_x\text{Bi}_y\text{Te}_6$ were introduced by Kuropatwa et al. (2014), with thermal conductivity (κ), thermo power (S), and electrical conductivity (σ). Tl fixations have three divers, which are 8.33, 8.67, and 9 for each formula unit, and there are different Sn concentrations, each with a Bi ratio to resemble the characteristic for each Tl focus. They also found that the crystal structures supported their calculations and observations. The realistic value of ZT was calculated to be 0.6 at 525 K and 575 K for $\text{Tl}_{8.67}\text{Sn}_{0.50}\text{Bi}_{0.83}\text{Te}_6$ and $\text{Tl}_{8.33}\text{Sn}_{1.12}\text{Bi}_{0.55}\text{Te}_6$, respectively. It was suggested by Chen et al. (2010) that semiconductors of nanostructured thermo materials are becoming a new source of energy in thermo electrical nano materials and may change the proficiency of novel energy sources by keeping the high value of electrical conductivity to

allow measurement of the De Broglie wavelength in a way that is similar to the practicality of the TE nanostructure crystal. They showed that there is another easy technique, which involves self-assembly of nano particles of Sb_2Te_3 by a controlled dimension of particles in a vapour-free crystal transport. With this technique, the sample Sb_2Te_3 showed an improved Seebeck coefficient at same concentration and that the thermal conductivity was less than the bulk of Sb_2Te_3 . It was confirmed by Yu et al. (2010b) that doping of thallium to lead telluride expanded the ZT value due to expansion of the Seebeck coefficient, while the thermal conductivity was unchanged despite improvement of resonant state around the Fermi level ($E_{\text{gap}/2}$). Still, the technology is monotonous due to moderate cooling for the development of crystal, higher time waste, hot squeezing, and post-smashing. The value of ZT (1.3) at 373 K was examined with a grain size of $3\text{--}7 \times 10^{-6}\text{ m}$ by using the ball milling technique with concentrations of thallium, tellurium, and elemental lead nano powder and the hot squeezing technique. In the two I-V bands, which were considered by Min et al. (2016), one was kept under continuous temperature gradient and the other was used to obtain continuous thermal information. Solvable information on this special type of procedure was obtained. The investigators developed a new method that enabled sorting of both I-V bands for acquiring natural results by using impedance techniques and then estimated the TE module results. In our previous paper (Khan et al., 2022), Sn was doped to $\text{Tl}_{8.67}\text{Sb}_{1.33-x}\text{Sn}_x\text{Te}_6$ at different concentration ratios using a solid-state reaction technique. XRD and EDX were used to confirm that the compound was of single phase tetragonal structure without any impurities. The TE properties, including Seebeck effect, electrical conductivity, and ZT, increased. With associated doping concentrations of Sn, the power factor increased with increased temperature (300 K–500 K). Similar studies have been carried out by other groups (Ouyang et al., 2018; Tufail et al., 2021; Xia et al., 2023), but the main differences are in approach to enhancement of TE properties using different techniques.

In this research, $\text{Tl}_{8.67}\text{Sn}_{1.33-x}\text{Sb}_x\text{Te}_6$ was doped with Sb and the resulting electrical properties were studied using crystal structure data obtained through XRD and EDX; pellet morphology was studied using SEM. The electrical and thermal properties of the nano compound changed relative to Sb doping. This research focused on the Seebeck coefficient and electrical conductivity because both have significant effects on electrical properties. Four probes were used to evaluate electrical conductivity (σ), and the power factor was calculated based on the Seebeck



coefficient. It was noted that increased temperature also increased the Seebeck coefficient.

2 Experimental details

$\text{Tl}_{8.67}\text{Sn}_{1.33-x}\text{Sb}_x\text{Te}_6$ was doped with Sb and synthesised using the solid-state reaction technique and different concentrations ($x = 0.63, 0.65, 0.66, 0.68, 0.70$, or 0.72) in air-free silica tubes and sealed in the presence of oxygen to reduce moisture. Ultra-high purity materials ($\geq 99.999\%$; Sigma-Aldrich) were used to synthesise the nano materials in powder form in silica tubes in the presence of argon gas, which was heated to a temperature of 650 K for at least 24 h, at a rate of 1K/min. To avoid imperfections, such as dislocation, quenching, and deformation of crystal, the sample was cooled down at a very slow rate. The sample was kept at 27°C for at least 12 h for uniformity. The Seebeck coefficient (S) of each sample in the formed pellet, each at dimensions of $5 \times 1 \times 1\text{ mm}^3$, was measured. Unfortunately, there was no change in the Seebeck coefficient on weakly biases tenure when the sample was in open air. For measurement of electrical conductivity, the four-probe method was used to assay each pellet in the rectangular form.

TABLE 1 Crystallite size (D in nm), lattice constant, and volume (\AA^3) of the unit cell.

Sample	Crystallite size $D''(\text{nm})$	$D \ni$ spacing (\AA)		Volume (\AA^3) ³
		$a = b$	c	
$\text{Tl}_{8.67}\text{Sn}_{0.61}\text{Sb}_{0.72}\text{Te}_6$	26.89	8.81	13.005	1,005.50
$\text{Tl}_{8.67}\text{Sn}_{0.63}\text{Sb}_{0.70}\text{Te}_6$	27.93	8.83	13.075	1,022.90
$\text{Tl}_{8.67}\text{Sn}_{0.65}\text{Sb}_{0.68}\text{Te}_6$	29.04	8.89	13.00	1,012.44
$\text{Tl}_{8.67}\text{Sn}_{0.67}\text{Sb}_{0.66}\text{Te}_6$	30.91	8.91	13.001	1,009.086
$\text{Tl}_{8.67}\text{Sn}_{0.68}\text{Sb}_{0.65}\text{Te}_6$	32.48	8.92	13.062	1,022.67
$\text{Tl}_{8.67}\text{Sn}_{0.70}\text{Sb}_{0.63}\text{Te}_6$	34.43	8.94	13.096	1,039.22

It is just to prominent the values.

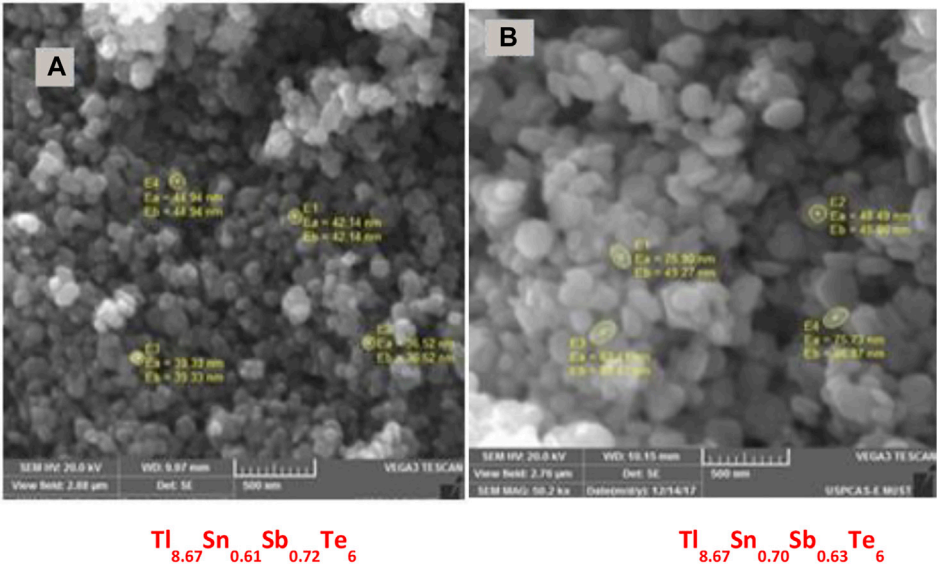


FIGURE 2
SEM image of the nano compound $\text{Tl}_{8.67}\text{Sn}_{1.33-x}\text{Sb}_x\text{Te}_6$. (A) $\text{Tl}_{8.67}\text{Sn}_{0.61}\text{Sb}_{0.72}\text{Te}_6$ and (B) $\text{Tl}_{8.67}\text{Sn}_{0.70}\text{Sb}_{0.63}\text{Te}_6$.

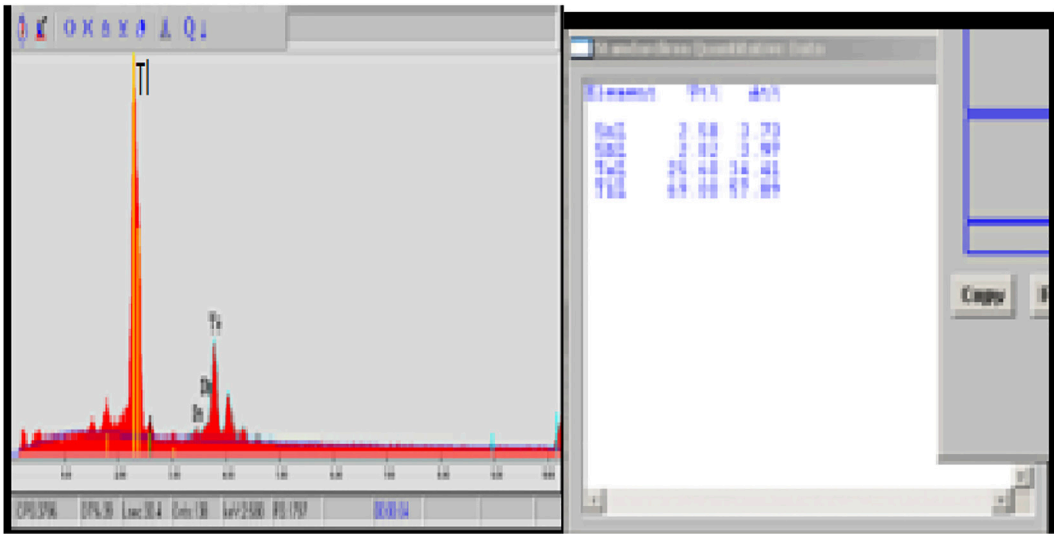


FIGURE 3
EDX data for $\text{Tl}_{8.67}\text{Sn}_{0.67}\text{Sb}_{0.66}\text{Te}_6$ at room temperature for the confirmation of stoichiometric ratios from elemental analysis.

TABLE 2 Weight% and atomic% of the elements in the compound $\text{Tl}_{8.67}\text{Sn}_{0.67}\text{Sb}_{0.66}\text{Te}_6$.

Sample	Weight%	Atomic%
Tl	69	57.89
Sn	2.58	3.73
Sb	2.82	3.97
Te	25.60	34.41
	100%	100%

3 Results and discussion

3.1 X-ray diffraction analysis

The following XRD figure shows $\text{Tl}_{8.67}\text{Sn}_{1.33-x}\text{Sb}_x\text{Te}_6$ doped with Sb at different ratios (0.63, 0.65, 0.68, 0.70, or 0.72). The highest peak value was observed at an angle of 31.8° . It was also confirmed by XRD that $\text{Tl}_9\text{Sb}_1\text{Te}_6$ has a single-phase tetragonal structure, as shown in Figure 1. Data from the published literature have shown that the values for lattice constant at 27°C are $a = .866\text{ nm}$ and $c = 1.305$. The crystal structure of the sample was obtained using an experimental

TABLE 3 Electrical conductivity (σ S (m⁻¹))(S=Siemens) of $\text{Ti}_{8.67}\text{Sn}_{1.33-x}\text{Sb}_x\text{Te}_6$ ($x = 0.63, 0.65, 0.66, 0.68, 0.70$, or 0.72) of thermoelectric properties at the temperatures 300, 400, and 500 K.

Sample	Electrical conductivity σ S(m) ⁻¹ * 10 ² at 300 K	Electrical conductivity σ S(m) ⁻¹ * 10 ² at 400 K	Electrical conductivity σ S(m) ⁻¹ * 10 ² at 500 K
$\text{Ti}_{8.67}\text{Sn}_{0.70}\text{Sb}_{0.63}\text{Te}_6$	776	495	4.12
$\text{Ti}_{8.67}\text{Sn}_{0.68}\text{Sb}_{0.65}\text{Te}_6$	831	545	462
$\text{Ti}_{8.67}\text{Sn}_{0.67}\text{Sb}_{0.66}\text{Te}_6$	507	315	285
$\text{Ti}_{8.67}\text{Sn}_{0.65}\text{Sb}_{0.68}\text{Te}_6$	1,231	945	862
$\text{Ti}_{8.67}\text{Sn}_{0.63}\text{Sb}_{0.70}\text{Te}_6$	1,327	1,045	962
$\text{Ti}_{8.67}\text{Sn}_{0.61}\text{Sb}_{0.72}\text{Te}_6$	1,616	1,295	1,212

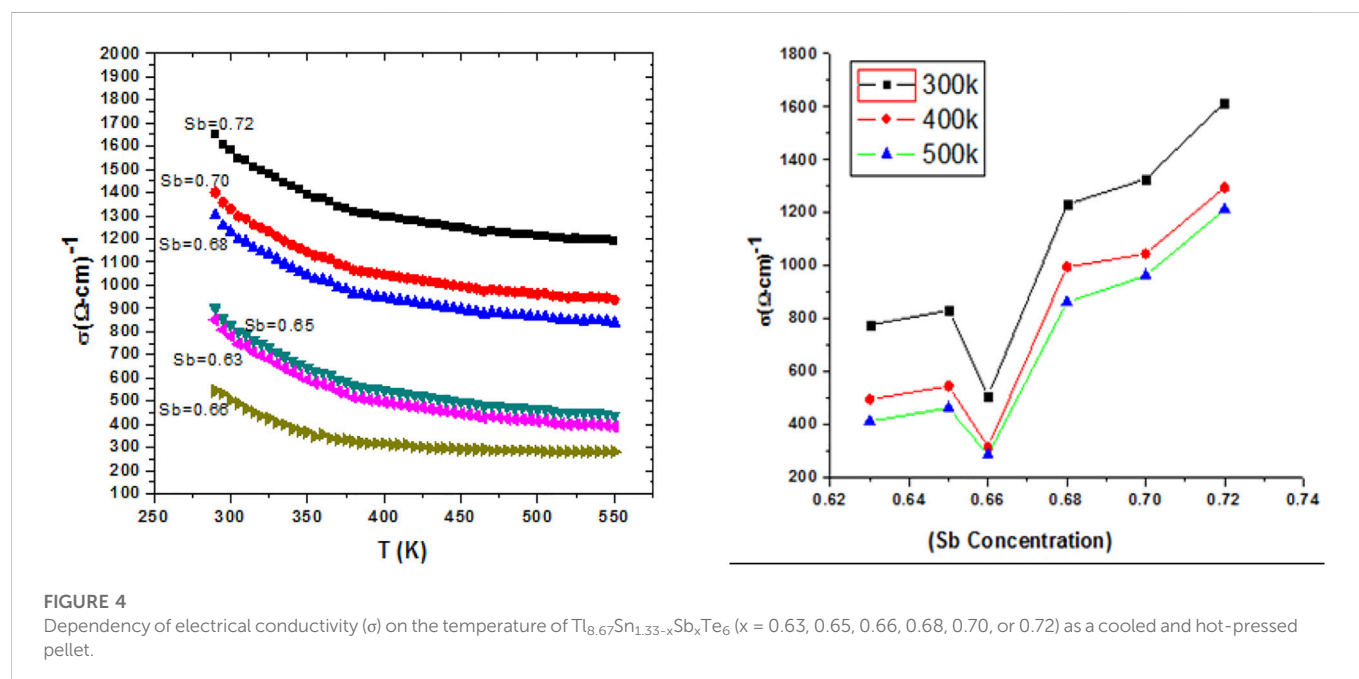


FIGURE 4

Dependency of electrical conductivity (σ) on the temperature of $\text{Ti}_{8.67}\text{Sn}_{1.33-x}\text{Sb}_x\text{Te}_6$ ($x = 0.63, 0.65, 0.66, 0.68, 0.70$, or 0.72) as a cooled and hot-pressed pellet.

formula (Sankar et al., 2012) and simulation with binary tellurium telluride ($\text{Ti}_{10}\text{Te}_6$) compared with reference data (Pradel et al., 1982; Skomedal et al., 2014). Considering the entire topology, Miller indices, position of grain size, interatomic distance, etc., can also be calculated (Glusker and Trueblood, 2010), as shown in Table 1.

An Intel diffractometer with CuK α radiation was used for XRD. The peaks of the graph show the concentration of Sb in the nano compound $\text{Ti}_{8.67}\text{Sn}_{1.33-x}\text{Sb}_x\text{Te}_6$.

3.1.2 Scanning electron microscopy

For structural and chemical analyses, SEM was used. To achieve better and more accurate results, samples were in solid form, as well as sized to fit in the niche shown in Figure 2. For electrical conductivity, the samples were shielded with thin metal to allow better results in measurement of S ; mostly carbon is the best option a compound like. $\text{Ti}_{8.67}\text{Sn}_{1.33-x}\text{Sb}_x\text{Te}_6$ was doped with Sb, and due to concentration of Sb, the insignificant grain size paved a path of bulky scattering to the electron. The thermo power of the chalcogenide system was slightly improved; thermo power increased with decreased grain size of the

compound to the micro and nano levels (Kuropatwa et al., 2011). These findings have already been illustrated in the literature on the SbTe nano compound.

3.1.3 Energy dispersive X-ray analysis (EDX)

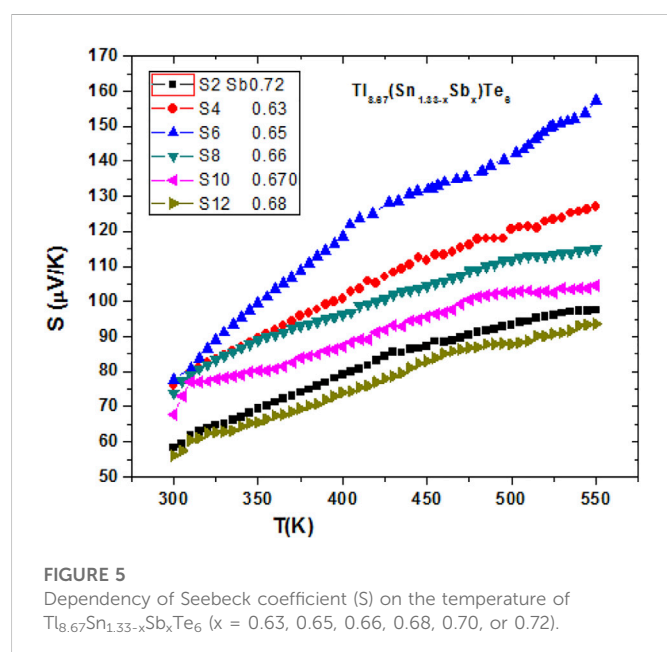
The percentage ratio of each element in the compound can be found by using EDX analysis. In the compound, the atomic percentage of each element was assessed: Ti (57.89%), Sb (3.97%), Sn (3.73%), and Te (34.41%). The maximum percentage of Ti was 57.89%. Figure 3 shows the concentration of each element. The weight percentages and atomic percentages are also given in Table 2.

3.2 Electrical conductivity

The electrical conductivity and temperature were plotted against each other and show the inverse behaviour for all samples; increased temperature led to a decreased conductivity (σ) and *vice versa*, due to the charge carriers being scattered from phonons of the material.

TABLE 4 Seebeck coefficient S ($\mu\text{V/K}$) of $\text{Ti}_{8.67}\text{Sn}_{1.33-x}\text{Sb}_x\text{Te}_6$ ($x = 0.63, 0.65, 0.66, 0.68, 0.70$, or 0.72) at 300, 400, and 550 K.

Sample	Seebeck coefficient S ($\mu\text{V/K}$) at 300 K	Seebeck coefficient S ($\mu\text{V/K}$) at 400 K	Seebeck coefficient S ($\mu\text{V/K}$) at 550 K
$\text{Ti}_{8.67}\text{Sn}_{0.70}\text{Sb}_{0.63}\text{Te}_6$	75.89	100.78	126.84
$\text{Ti}_{8.67}\text{Sn}_{0.68}\text{Sb}_{0.65}\text{Te}_6$	77.64	118.68	157.29
$\text{Ti}_{8.67}\text{Sn}_{0.67}\text{Sb}_{0.66}\text{Te}_6$	74.00	96.11	113.05
$\text{Ti}_{8.67}\text{Sn}_{0.65}\text{Sb}_{0.68}\text{Te}_6$	56.03	74.12	92.08
$\text{Ti}_{8.67}\text{Sn}_{0.63}\text{Sb}_{0.70}\text{Te}_6$	67.79	87.16	103.57
$\text{Ti}_{8.67}\text{Sn}_{0.61}\text{Sb}_{0.72}\text{Te}_6$	58.00	79.18	97.54



Our focus in this research on electrical conductivity was on Sb doping of the compound at different concentrations ($0.63 \leq x \leq 0.72$) and at various temperature ranges. Results are provided in Table 3. It was noticed that, at the concentration of Sb = 0.66, the electrical conductivity did not increase due to a change in the band gap. The power factor with doping at different concentrations of Sb improved with increased temperature. The concept of discussion given previously is that the semiconductor material is prone to degeneration. Figure 4 shows the change in electrical conductivity (σ) related to the doping concentration ratio of Sb.

3.3 Seebeck coefficient

In this research work, it was observed that the Seebeck coefficient of the p-type compound/sample $\text{Ti}_{10-x}\text{Sn}_x\text{Te}_6$ increased with rise in temperature and also with doping of Sb at different ratios. It can be seen from the Table 4 that, at $x = 0.65$, the Seebeck coefficient (S) was maximum, $S = 77.65$ and 157.36 , at temperatures of 300 K and 550 K, respectively, whereas the minimum value for $x = 0.68$ was 56.04 at 300 K and increased to 93.04 at 550 K. Similarly when the concentration of Sb

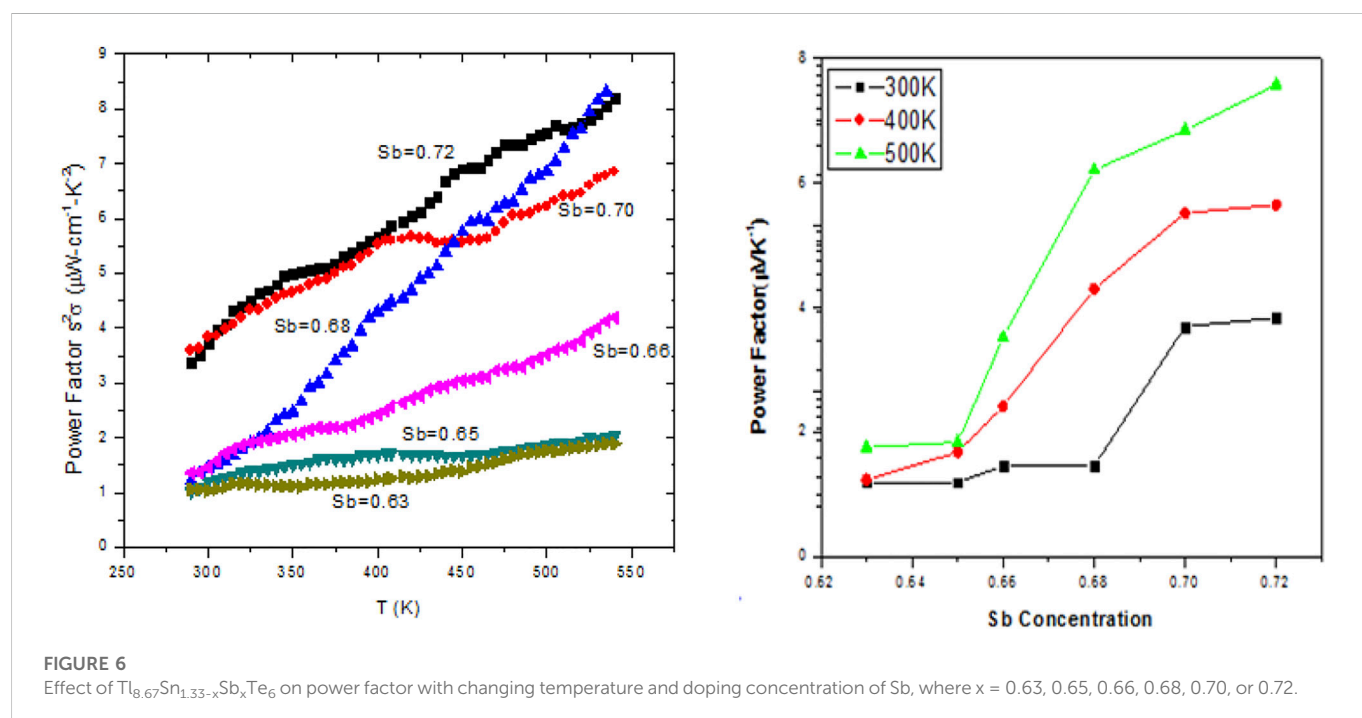


TABLE 5 Variation of power factor at room temperature, 300 K, 400 K, and 550 K.

Sample	Power factor at 300 K	Power factor at 400 K	Power factor at 550 K
Tl _{8.67} Sn _{0.70} Sb _{0.63} Te ₆	1.2	1.24	1.76
Tl _{8.67} Sn _{0.68} Sb _{0.65} Te ₆	1.2	1.68	1.84
Tl _{8.67} Sn _{0.67} Sb _{0.66} Te ₆	1.46	2.42	3.52
Tl _{8.67} Sn _{0.65} Sb _{0.68} Te ₆	1.46	4.3	6.21
Tl _{8.67} Sn _{0.63} Sb _{0.70} Te ₆	3.7	5.52	6.85
Tl _{8.67} Sn _{0.61} Sb _{0.72} Te ₆	3.84	5.65	7.58

was 0.63 or 0.72, the Seebeck coefficients varied from 73.87 to 127.00, respectively, at temperatures of 300K–550 K, as indicated in Figure 5.

3.4 Power factor

The power factor is the product of the square of the Seebeck coefficient and the electrical conductivity ($S^2\sigma$); therefore, a change in either variable will result in a change in the power factor. All the observed values of the compound are plotted in the following Figure 6, which shows changes in the power factor. The compound Tl_{8.67}Sn_{0.61}Sb_{0.72}Te showed its highest values of 7.58 $\mu\text{W}/\text{cm}^1\text{K}^2$ and 3.84 $\mu\text{W}/\text{cm}^1\text{K}^2$ at temperatures 500 K and 300 K, respectively. The lowest power factor values of Tl_{8.67}Sn_{0.70}Sb_{0.63}Te were also recorded: 1.76 $\mu\text{W}/\text{cm}^1\text{K}^2$ and 1.20 $\mu\text{W}/\text{cm}^1\text{K}^2$ at temperatures 500 K and 300 K, respectively. The values of the power factor of all compounds at different temperatures and various doping concentrations are given in Table 5.

4 Conclusion

- Tl_{8.67}Sn_{1.33-x}Sb_xTe₆ nanoparticles doped with Sb at different concentration ratios were synthesised using solid-state reaction techniques.
- XRD analysis confirmed that the sample was single-phase with space group equal to Tl₅Te₃.
- The observed Seebeck coefficient over the entire range showed that the Seebeck coefficient increased with increased concentration of Sb doping, as well as increased temperature, and *vice versa*.
- The Seebeck coefficient decreased with high Sb concentration ratio, indicating conduction through holes in the samples; carrier density increased with increased concentration of Sb other than $x = 0.65$. Therefore, the thermo power also increased due to enhanced electron scattering in the system. Additionally, the power factor increase was likely due to effects at the micro to nano levels, which have been observed in many other studies on SbTe.

References

- Adam, A. M., Lilov, E., and Petkov, P. (2017). Optical and thermoelectric properties of nano-particles based Bi₂ (Te_{1-x}Se_x)₃ thin films. *Super Lattices Microstruct.* 101, 609–624. doi:10.1016/j.spmi.2016.09.034
- Cai, Z., Guo, L., Xu, X., Yan, Y., Peng, K., Wang, G., et al. (2016). Effect of Sn doping in (Bi_{0.25}Sb_{0.75})_{2-x}Sn_xTe₃ ($0 \leq x \leq 0.1$) on thermoelectric performance. *J. Electron. Mater.* 45 (3), 1441–1446. doi:10.1007/s11664-015-4061-5

- Our data indicate that various dopants enhance the TE properties of samples that can be used as TE generators.

Data availability statement

The original contributions presented in the study are included in the article/supplementary material, further inquiries can be directed to the corresponding authors.

Author contributions

The contributions of authors are listed as follows: i) NI, SK, WS, and MT developed the model; ii) AA, SE, and MS handled the resulting expression and plotted the graphs; iii) NI, SK, WS, and MT helped in the literature survey; iv) AA, SE, MS, and MT updated the Introduction section; v) SK, WS, MT, and SE prepared the Results and discussion section; vi) SK, WS, MT, and AA improved the Results and discussion section; vii) NI, SK, WS, MT, and AA updated the Conclusion section in the final stage of submission.

Conflict of interest

The authors declare that the research was conducted in the absence of any commercial or financial relationships that could be construed as a potential conflict of interest.

Publisher's note

All claims expressed in this article are solely those of the authors and do not necessarily represent those of their affiliated organizations, or those of the publisher, the editors, and the reviewers. Any product that may be evaluated in this article, or claim that may be made by its manufacturer, is not guaranteed or endorsed by the publisher.

- Chen, J., Sun, T., Sim, D., Peng, H., Wang, H., Fan, S., et al. (2010). Sb₂Te₃ nanoparticles with enhanced Seebeck coefficient and low thermal conductivity. *Chem. Mater.* 22 (10), 3086–3092. doi:10.1021/cm9038297

- Chen, W., Pöhls, J.-H., Hautier, G., Broberg, D., Bajaj, S., Aydemir, U., et al. (2016). Understanding thermoelectric properties from high-throughput calculations: Trends, insights, and comparisons with experiment. *J. Mat. Chem.* 4, 4414–4426. doi:10.1039/c5tc04339e

- Glusker, J. P., and Trueblood, K. N. (2010). *Crystal structure analysis: a primer*, 14. Oxford University Press.
- Guo, Q., and Kleinke, H. (2015). Thermoelectric properties of hot-pressed Tl_9LnTe_6 (Ln = La, Ce, Pr, Nd, Sm, Gd, Tb) and $\text{Tl}_{10-x}\text{La}_x\text{Te}_6$ ($0.90 \leq x \leq 1.05$). *J. Alloys Compd.* 630, 37–42. doi:10.1016/j.jallcom.2015.01.025
- Khan, W. M., Shah, W. H., Khan, S., Shah, S., Syed, W. A., Safeen, A., et al. (2018). Enhanced of thermoelectric properties and effects of Sb doping on the electrical properties of $\text{Tl}_{10-x}\text{Sb}_x\text{Te}_6$ nano-particles. *Int. J. Heat Technol.* 36, 602–606. doi:10.18280/ijht.360224
- Khan, S., Shah, W. H., Tufail, M., Syed, W. A., and Khan, W. M. (2022). Effects of Sn dopant on power factor of $\text{Tl}_{8.67}\text{Sb}_{1.33-x}\text{Sn}_x\text{Te}_6$ nanoparticles. *Chalcogenide Lett.* 19, 45–54. doi:10.15251/cl.2022.191.45
- Kim, K. T., and Ha, G. H. (2013). Fabrication and enhanced thermoelectric properties of alumina nanoparticle-dispersed Bi 0.5 Sb 1.5 Te 3 matrix composites. *J. Nanomater.* 8, 2013. doi:10.1155/2013/821657
- Kuropatwa, B. A., Assoud, A., and Kleinke, H. (2011). Abdel jalil Assoud, and Holger Kleinke. "Phase range and physical Properties of the thallium tin tellurides $\text{Tl}_{10-x}\text{Sn}_x\text{Te}_6$ ($x \leq 2.2$). *J. Alloys Compd. Can.* 509 (24), 6768–6772. doi:10.1016/j.jallcom.2011.03.182
- Kuropatwa, B. A., Guo, Q., Assoud, A., and Kleinke, H. (2014). Optimization of the telluride $\text{Tl}_{10-x-y}\text{Sn}_x\text{Bi}_y\text{Te}_6$ for the Ther-moelectric energy conversion. *Z. Anorg. Allg. Chem.* 640 (5), 774–780. doi:10.1002/zaac.201300577
- Kurosaki, K., Uneda, H., Muta, H., and Yamanaka, S. (2004). Thermoelectric properties of thallium antimony telluride. *J. Alloys Compd. Jpn.* 376 (1), 43–48. doi:10.1016/j.jallcom.2004.01.018
- Lin, C.-C., Ginting, D., Lydia, R., Lee, M. H., and Rhyee, J. S. (2016). Thermoelectric properties and extremely low lattice thermal conductivity in p-type Bismuth Tellurides by Pb-doping and PbTe precipitation. *J. Alloys Compd.* 671, 538–544. doi:10.1016/j.jallcom.2016.02.123
- Liu, S., Sun, N., Sucharitakul, S., and Gao, X. P. A. (2018). Nanostructured SnSe: Synthesis, doping, and thermoelectric properties. *J. Appl. Phys.* 123, 115109. doi:10.1063/1.5018860
- Luu, S. D., and Vaqueiro, P. (2015). Synthesis, characterisation and thermoelectric properties of the oxytelluride $\text{Bi}_2\text{O}_2\text{Te}$. *J. Solid State Chem.* 226, 219–223. doi:10.1016/j.jssc.2015.02.026
- Min, G., Singh, T., Garcia-Canadas, J., and &Ellor, R. (2016). Evaluation of thermoelectric generators by i–v curves. *J. Electron. Mater.* 45 (3), 1700–1704. doi:10.1007/s11664-015-4180-z
- Ouyang, T., Jiang, E., Tang, C., Li, J., He, C., and Zhong, J. (2018). Thermal and thermoelectric properties of monolayer indium tri phosphide (InP_3): A first-principles study. *J. Mat. Chem. A* 6, 21532–21541. doi:10.1039/c8ta07012a
- Pradel, A., Tedenac, J. C., Coquillat, D., and Brun, G. (1982). Proprieties of thermoelectric ques de Tl_9BiTe_6 . *Rev. Chim. Miner.* 19, 43–48.
- Rahman, J. U., Nam, W. H., Du, N. V., Rahman, G., Rahman, A. U., Shin, W. H., et al. (2019). Oxygen vacancy revived phonon-glass electron-crystal in SrTiO_3 . *J. Eur. Ceram. Soc.* 39, 358–365. doi:10.1016/j.jeurceramsoc.2018.09.036
- Sankar, C. R., Bangarigadu- Sanasy, S., and Kleinke, H. (2012). Thermoelectric properties Of TlGdQ 2 (Q = Se, Te) and Tl 9 GdTe 6. *J. Electron. Mater.* 41 (6), 1662–1666. doi:10.1007/s11664-011-1846-z
- Shah, W. H., Khan, A., and Syed, W. A. (2016). Effects of Pb doping on the thermoelectric properties of $\text{Tl}_{8.67}\text{Pb}_{1.33-x}\text{Te}_6$ materials. Xiv preprint arXiv:1610.00849.
- Skomedal, G., Kristiansen, N. R., Engvoll, M., and Middleton, H. (2014). Methods for enhancing the thermal durability of high- Temperature thermoelectric materials. *J. Electron. Mater.* Nor. 43 (6), 1946–1951. doi:10.1007/s11664-013-2917-0
- Tufail, M., U Rahman, A., Gul, B., Akram, W., Ullah, H., Iqbal, M. W., et al. (2021). Effect of Pb doping on electronic and thermoelectric properties of thallium antimony telluride ($\text{Tl}_{8.33}\text{Sb}_{1.67-x}\text{Pb}_x\text{Te}_6$) nano-compound: A combined experimental and theoretical investigations. *Phys. Condens. B* 608, 412789. doi:10.1016/j.physb.2020.412789
- Xia, M., Record, M. C., and Boulet, P. (2023). Investigation of PbSnTeSe high-entropy thermoelectric alloy: A dft approach. *A DFT Approach Mater.* 16, 235. doi:10.3390/ma16010235
- Yamanaka, S., Kosuga, A., and Kurosaki, K. (2003). Thermoelectric properties of Tl_9BiTe_6 . *J. Alloys Compd.* 352 (1–2), 275–278. doi:10.1016/s0925-8388(02)01114-3
- Yu, B., Zhang, Q., Wang, H., Wang, X., Wang, H., Wang, D., et al. (2010). Thermoelectric property studies on thallium-doped lead telluride prepared by ball milling and hot pressing. *J. Appl. Phys. U. S. A.* 108, 016104. doi:10.1063/1.3452323
- Yu, B., Zhang, Q., Wang, H., Wang, X., Wang, H., Wang, D., et al. (2010). Thermoelectric property studies on thallium-doped lead telluride prepared by ball milling and hot pressing. *J. Appl. Phys.* 108, 016104. doi:10.1063/1.3452323
- Zhang, X., and Zhao, L. D. (2015). Thermoelectric materials: Energy conversion between heat and electricity. *J. Materiomics* 1 (2), 92–105. doi:10.1016/j.jmat.2015.01.001



OPEN ACCESS

EDITED BY
Safia Akram,
National University of Sciences and
Technology, Pakistan

REVIEWED BY
Salman Saleem,
King Khalid University, Saudi Arabia
S. D. Kaushik,
UGC-DAE Consortium for Scientific
Research, Mumbai Centre, India

*CORRESPONDENCE
Liaquat Ali,
✉ liaquatphy17@gmail.com
Wiqar H. Shah,
✉ wiqar.hussain@iiu.edu.pk

SPECIALTY SECTION
This article was submitted
to Colloidal Materials and Interfaces,
a section of the journal
Frontiers in Materials

RECEIVED 30 November 2022
ACCEPTED 24 January 2023
PUBLISHED 09 February 2023

CITATION
Ali L, Shah WH, Ali A, Eldin SM,
Al-Jaafary AA, Sedky A, Mazher J, Imran N
and Sohail M (2023), Investigation of bulk
magneto-resistance crossovers in iron
doped zinc-oxide using
spectroscopic techniques.
Front. Mater. 10:1112798.
doi: 10.3389/fmats.2023.1112798

COPYRIGHT
© 2023 Ali, Shah, Ali, Eldin, Al-Jaafary,
Sedky, Mazher, Imran and Sohail. This is an
open-access article distributed under the
terms of the [Creative Commons
Attribution License \(CC BY\)](https://creativecommons.org/licenses/by/4.0/). The use,
distribution or reproduction in other
forums is permitted, provided the original
author(s) and the copyright owner(s) are
credited and that the original publication in
this journal is cited, in accordance with
accepted academic practice. No use,
distribution or reproduction is permitted
which does not comply with these terms.

Investigation of bulk magneto-resistance crossovers in iron doped zinc-oxide using spectroscopic techniques

Liaquat Ali^{1*}, Wiqar H. Shah^{1*}, Akhtar Ali¹, Sayed M. Eldin²,
Abdullah A. Al-Jaafary³, A. Sedky⁴, Javed Mazher³, Naveed Imran^{5,6}
and Muhammad Sohail⁷

¹Physics Department, Faculty of Basic and Applied Sciences, International Islamic University, Islamabad, Pakistan, ²Center of Research, Faculty of Engineering, Future University in Egypt, New Cairo, Egypt, ³Physics Department, College of Science, King Faisal University, Al-Ahsa, Saudi Arabia, ⁴Physics Department, Faculty of Science, Assiut University, Assiut, Egypt, ⁵HITEC Colleges, HIT Taxila Cantt, Islamabad, Pakistan, ⁶Institute of Space Technology, Islamabad, Pakistan, ⁷Institute of Mathematics, Khwaja Fareed University of Engineering and Information Technology, Rahim YarKhan, Pakistan

Pellets of Pure and Fe-doped dilute magnetic semiconducting (DMS) samples are studied for bulk magneto-resistance (BMR) at room temperature and at low-temperatures ~100K. Raman-, photoluminescence- and X-ray photoelectron-spectroscopic techniques are used to determine chemical and electronic structures of the samples. A broadband intense yellow-green-orange luminescence is observed in Fe-doped ZnO samples and emission red-shifts are investigated. Electrical transport is studied with and without applied magnetic field up to 9T and thermal activation and hopping modes of conduction is discussed in light of nature of Fe substitution in the host lattice. Several decremental- to incremental-BMR crossovers are obtained corresponding to experimental variables of Fe concentration $0.025 \leq x \leq 0.1$, temperature and applied magnetic field. Several possible modes of magneto-transport are discussed to further elucidate the origin of the as-found BMR crossovers in our samples. Positive BMR in pure- and highly doped ($x \geq 0.1$) ZnO is found to originate from F-centers and thermal fluctuations, respectively. However, modestly doped ($x \leq 0.05$) ZnO exhibit thermally activated conduction and magnetic polaron mediated negative BMR.

KEYWORDS

magnetoresistance, zinc-oxide, Raman, luminescence, x-ray spectroscopy (EDXS)

1 Introduction

When bulk granular composites are exposed to a magnetic field, their electrical resistance changes, this phenomenon, known as BMR ($\Delta\rho/\rho_0$), has been linked to separate spin and itinerant charge carriers' spin-dependent dispersion from localized moment's bands (Jansson et al., 2014). Typically, along the samples' longitudinal resistance (ρ_{xx}), BMR is observed and the electrical magneto transport is assessed by maintaining a parallel voltage and current probe arrangement (Hsu et al., 2008). According to research, the BMR has both positive and negative elements that are caused by roving particles with different conductivities and motilities, as well as two-band spin splitting from spin dispersed itinerants with localized magnetic moments (Hsu et al., 2008; Chattopadhyay et al., 2013). The fluctuation in the relative intensities of the competing itinerant spin scattering processes is connected to the BMR transitions from negative to positive (Gacic et al., 2007; Balamurugan, 2012; Jansson

et al., 2014; Can et al., 2016; Sapkota et al., 2016). The strength of spin scattering processes in doped magnetic oxides is affected by the amount of doping, the type of manipulated element, the type of doping, its solubility in the host-lattice, the concentrations of defects, the temperature, the applied magnetic field, the orbital overlap of the dopant, and the and the state-specific spin density (SDOS) (Wang et al., 2015a; Wang et al., 2015b; Lorite et al., 2015; Lv et al., 2015; Montes-Valenzuela et al., 2015; Lee et al., 2016; Mukherjee et al., 2017). Zinc-oxide is well known among metal-oxides for having a very high intrinsic n-type charge carrier density and for being sensitive to its defect and lattice structure related donor states like native oxygen vacancy, interstitial hydrogen impurity states and intermediate ZnO (Shi et al., 2005). It has a 3.3 eV optical energy gap and is a wurtzite (hexagonal) structured material. However, oxygen vacancies (V_o), which are double donor states in ZnO host-lattice and are responsible for n-type carriers, are usually suggested to be the source of ZnO's impurity band. As a result, by varying the V_o concentration, the carriers may be successfully modified (Wang and Tanaka, 2009). ZnO is being utilized to manufacture solar cells, trace gas sensors, conductive glasses, and self-cleaning surfaces. It functions as a photon harvester. A little quantity of transition metal (TM) ions, such as Ni, Co., Fe, Mn, and others, doped in the ZnO host lattice effectively alters the semiconductor's lattice configuration and induces magnetic (Borges et al., 2011). This is owing to the existence of an unpaired electron in the dopant -Fe's partly filled d-electron states ($4s^2 3d^6$). The restricted, unpaired d-electrons hybridize with the host ZnO's wandering sp-electrons to generate magnetically coupled electrons that participate in exchange interactions, resulting in SDOS between the host charge transporters. Commonly referred to as solid solutions of TM doped semiconductors to be DMS materials since n-type semiconductors also exhibit magnetic ordering. DMS oxides are useful in numerous opto - electronic devices, including as diodes with optical spin, spin driven random access memory, spin field effect transistors, and light emitting devices (LED), thanks to their functional properties. DMS oxides also have greater magnetic moments and high Curie temperatures, which are essential characteristics for the perfect spintronics material (Han et al., 2002). Additionally, it is possible to further customize the electrical structure, optical band gap, and as well as kind of magnetism in DMS systems by modifying the doped ZnO's particle size and TM atom concentration (Liu and Guyot-Sionnest, 2015; Quan et al., 2016). The multifunctional quantum dots made of ZnO, a transparent, non-toxic, affordable, and biocompatible nanomaterial, have recently attracted a lot of attention for their potential use in cutting-edge processes such as targeted drug delivery using magnetic fields, magnetic tagging, magnetic resonance imaging, and protein-macromolecule separation. (Lorenz et al., 2016). A uniform solid solution of Fe doped may be created using a variety of wet-chemical and sol-gel, including solid-state processes (Ariyakkani et al., 2017), bottom up co-precipitation (Fabbiyola et al., 2016; Pazhanivelu et al., 2016), common solid state reaction (Sedky and KotbMahfouz, 2013), hydrothermal (Mihalache et al., 2017), and others. To achieve repeatable DMS characteristics, a faultless solid solution must be generated in which the host-lattice and substitutional dopant ions encounter the optimal magnetic coupling environment. In this sense, achieving a homogeneous local dopant profile has been very successful for solid state reaction techniques (Das et al., 2015). In

the cationic sub-lattice of ZnO, the Fe^{2+} ion (~ 0.078 nm) typically replaces Zn^{2+} (~ 0.074 nm) at lower dopant concentrations, forming a $Zn_{1-x}Fe_xO$ solid solution of mixed alloy (Salem et al., 2016) (Sedky and KotbMahfouz, 2013). Though, trivalent iron inclusion is more likely at higher dopant concentrations, leading to a reduced solubility of the Fe^{3+} ion (~ 0.055 nm). This is because the ZnO cationic-lattice, which is primarily made up of Zn^{2+} ions, has a larger radius difference, $r_{Zn}/r_{Fe} \sim 1.35$. The formation of a secondary oxide phase of iron with flaws and structural distortions is therefore envisaged at higher dopant concentrations. Additionally, it has been demonstrated that substitutional iron is in the F_{2+3} + oxidation state coexist in chemical evaluations of DMS samples where Fe-doping levels are greater than 2 wt% (Lin et al., 2010; Saikia et al., 2016). A stronger ferromagnetic ordering has also been noticed (Beltrán et al., 2015) (Liu et al., 2011) depending on the creation of imperfections and secondary phases, like as $ZnFe_3O_4$ associated to a state where Fe^{3+} oxidations are additionally present. However, it has also been discovered that higher Fe concentrations cause a decrease in ZnO's electronic conductivity (Sedky et al., 2009). Therefore, replacing Zn^{2+} in the cationic lattice of ZnO with a non-magnetic ad-atom such as Cu, Al, etc. through doping could increase the number of carriers accessible in the interaction of the exchange. However non-magnetic atoms have also been proved to be beneficial in the production of secondary phases, which weakens the conductivity-related BMR enhancement in transport experiments (Liu et al., 2011). Dilute magnetic semiconducting oxides have recently been the subject of extensive research to better understand any anomalies in spin-based transport. These studies can be roughly categorized into four fundamental spin transport mechanisms (Jansson et al., 2014; Wang et al., 2015a; Sapkota et al., 2016). Two concurrent spintronic processes, thermally stimulated transport has revealed pd-electron spin exchange and ferromagnetic ordering, which, depending on the number of carriers and the degree of magnetic ion doping, can be explained by a two band spin split model. (Jansson et al., 2014; Sapkota et al., 2016). Second, a monotonous increase in positive-BMR across un-doped metal oxides can be attributed reduced overlapping between neighboring donor states and wave function shrinkage caused by the magnetic field dependence of itinerants surrounding donor vacancies (Jansson et al., 2014). Finally, BMR resulting from a donor-bound magnetic polaronic effect in which ferromagnetic spin alignment and energy minimization occur as a result of electrons coupled to donor sites (F-centers) interacting with nearby magnetic dopants' spins. As a result, the energy barrier that the creation of polarons establishes for hopping electrons causes the sample's resistivity to rise. The forced realignment of magnetic dopants in the direction of the field, however, causes the net polaronic effect to decrease in the presence of an external magnetic field. As a result, the dopants' spin interactions with the F-centers are considerably diminished, which causes a rise in hopping-conduction and negative magnetoresistance (Ahmed et al., 2012). Finally, thermally oscillating magnetic dopant atoms are another explanation for BMR in the intermediate temperature range. In these atoms, the resonance between the hopping sites and the thermal variations of localizes magnetic moments allows for increased hopping conduction (Petukhov and Foygel, 2000). However, because to a declining resonance mode producing a positive BMR, it is anticipated that the hopping resistivity will rise under an external magnetic field. Due to these competing processes,

DMS oxides may simultaneously contain two or more processes (Peters et al., 2010; Wang et al., 2015a; Wang et al., 2015b; Montes-Valenzuela et al., 2015; Venkatesh et al., 2016). BMR of metal-oxides has often been attributed at increasing carrier concentrations (nc), to the spin-exchange mechanism between itinerant sp-hybridized host-carriers and confined d-shell electrons of TM dopants (Wang et al., 2015a). To fully understand how BMR in ZnO came about and whether or not several spintronic processes might coexist, all-inclusive experimental approaches are required, especially at room temperature given the multiple complexities involved in DMS based magneto-transport. We describe spectroscopic and transport studies on various samples of Fe doped ZnO in this research. With regard to the TM dopant concentration in DMS oxides, we are attempting to examine spectroscopic changes and magnetization in this case.

2 Experimental techniques

To manufacture a set of Zn_{1-x}Fe_xO micro-particulates, a typical solid state reaction approach is utilised, in which FeO₃ precursor in normal powder form (usually in micrometer range) (Aldrich, 99.999% purity, 200 nm) is added to ZnO micro particles and ground at Fe²⁺ with various concentrations value of 2.5%, 5%, 10%, 30%, and 50%. The powder is calcined at 1,000 °C for 12 h to complete the reaction, and then it is quenched to 25 °C. Sintering of 4-ton pressed pellets (1-cm dia. and 2-mm thick) of re-ground DMS powders takes 10 h at 1,100 °C. The pellets of powder are marked A-E based on their Fe concentration 'x' 0 (A), 2.5% (B), 5% (C), 10% (D), 30% (E), and 50% (F). In the presence of a magnetic field, temperature against resistance (−9 up to 9 T) In a physical property testing tool (Quantum Design, Evercool2/ETO), the resistance of the pellets is assessed in relation to their temperature and magnetic field in the temperature range of (100–350 K). Silver-epoxy resin (Epo-tek, H20E), which is thermally and electrically conductive down to 1 K, was used to electrically contact the pellets. A laser scanning microscope is used to examine the surface morphology of DMS pellets (Carl Zeiss, LSM800-Mat.).

XPS data is collected utilising an Omicron ESCA-II system with Mg-K radiation at 1,253.6 eV in a single channel detection mode. Prior to collecting data, samples A-E are dried in an extremely high vacuum for 12 h at 10–10 mbar. The bands have undergone painstaking calibration with respect to the adventitious-C1s binding energy value of 284.8 eV. The XPS data are obtained using an energy step of 0.05 eV and a dwell duration of 0.2 s at 50W X-ray power. The Casa-XPS programme is then used to evaluate high resolution XPS spectra after de-convoluting the spectra in relation to different components. In order to match each spectrum to its associated Gaussian bands, an iterative least-squares approach is used. Using a confocal Horiba (Labram-Evolution) spectrometer with a 100 m hole-aperture, micro Raman spectra of DMS samples are obtained. At 50% numerical density, a 300 W near infrared (NIR) diode laser (with 785 nm notch filter) is used. The stimulated Raman signal is collected ultra-low frequency geometry (ULF), using 50 long working distance-NIR objective lenses. The spatial and spectral resolutions of the spectrometer are maintained at 2 cm^{−1} and 1.1 m, respectively. Using an excitation source of a (325 nm) UV He-Cd laser, A Horiba (Labram) spectrometer is also used to acquire confocal photoluminescence (PL) spectra. With a silicon detector, the PL signals are tracked using a confocal hole-aperture of 100 m, which yields a PL spot size of 1.1 m.

3 Results and discussions

Temperature dependence of BMR, which results from differences in electronic mobility and conductivity seen in distinct modes of magneto-transport, is depicted in Figure 1 for pellets A-to-D with respect to a fixed 9 T magnetic field and a 100–350 K temperature range. The positive BMR development creates a spike that is triggered by more cooling, which is followed at 210 K by a high BMR of 8.5% and shows a delayed BMR degrading in proportion to cooling. There is no substantial change in the BMR value with greater cooling below 150 K. Although the BMR value of pure ZnO is higher, this is only true for a small range of temperatures (150 K–230 K), which is not technically significant for spintronic devices at room temperature. Interestingly, magnetic ordering changes can be blamed for the higher BMR values found in the pure sample. Which are frequently generated by lattice disorder, structural distortions, or oxygen vacancies. Emphasis should be placed on O vacancies or other defect sites, can serve as donor polarons as well (F-centers), preferentially trapping itinerants of comparable spin and enhancing conduction and a net localized magnetic moment. In reality, it has been demonstrated that applying an external magnetic field decreases itinerant exchange interaction due to F-centers being singularly aligned, especially at lower carrier concentrations, producing a positive BMR peak (Ovhal et al., 2017) and (Ariyakkani et al., 2017). Therefore, the induction of the spin-split band in pure ZnO may be caused by F-centers (Beltrán et al., 2015). The iron doped ZnO samples B and C, on the other hand, exhibit a negative magneto-resistance behaviour around RT. Sample C had a maximum negative BMR of ~3.7% at ~290 K and a steady negative BMR of 1% across the temperature range. A considerable BMR value of 1.5% is detected even at ambient temperature and decays to ~0.5% at ~340 K, indicating that magnetic ordering persists even at high temperatures in the absence of any signs of abrupt demagnetization or rising Curie temperature. In Ni doped dilute magnetic semiconductors, carrier ordering and spin polarisation have previously been shown to occur above room temperature (Montes-Valenzuela et al., 2015). The observed room temperature BMR in DMS semiconductors can be attributed to a variety of factors, including the presence of free metal in the form of nanoclusters, related binary phases of iron (II, I) oxides (Fe₂O₃, FeO) or ferrite (Fe₃O₄), and more (Ahmed et al., 2012). Nonetheless, the BMR's crossover with respect to Fe-doped, from being positive at $x \approx 0$ and higher $x \approx 10\%$ to being negative in samples with 2.5% Fe > 10%, reveals that BMR is not just barely emerging from the impurity stage, but is instead produced from iron ions replacement in the Zn ion sub lattice of ZnO. Curiously, sample B also exhibits a temperature-dependent crossover in BMR values, a BMR crossover from 0.15% up to −0.5% is found during sample cooling in a magnetic field, as shown by the magnified BMR-curve (red-dotted-line) connected to the figure's right-abcissa. Furthermore, The sample B BMR curve reveals that, up to 350 K, a sizable proportion of negative BMR consistently persists above room temperature. The BMR of sample B, on the other hand, becomes positive at ~225 K and reaches a maximum at ~190 K. The BMR trend of sample D, on the other hand, appears to be comparable to that of the pure sample, with a significant temperature shift of the BMR peak and an early BMR onset omitted. The iron doped sample has a positive BMR of 13.2% throughout a wide range temperature range start at 300 K and reaching a maximum BMR at 240 K. Furthermore, by lowering the temperature to 190 K, BMR steadily decays to less than 4% of its value at 240 K. Therefore, In

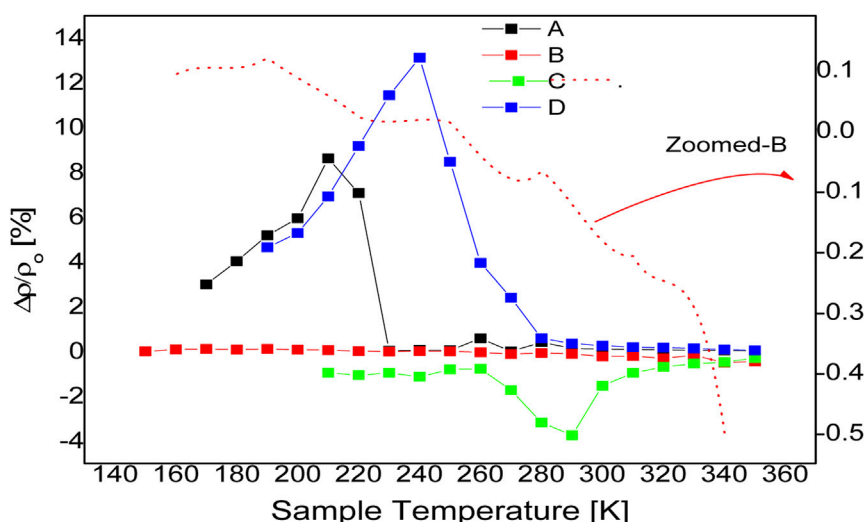


FIGURE 1

Temperature-dependent magnetoresistance studies were conducted for samples (A), a pure ZnO pellet, (B), (C), and (D), which, respectively, might include 2.5%, 5%, and 10% Fe in ZnO, applying resistance measurements during zero-field cooling (zfc) and 9 T-field cooling.

terms of Fe content, a BMR crossover can be easily identified, and samples with Fe concentrations more than 10% often exhibit positive BMR. In conclusion, based solely on BMR data, the real processes of magnetic ordering in both pure and Fe-doped ZnO are unclear and require further investigation by full flaw analysis utilizing structural, optical and compositional probes.

For samples A to E, respectively, the ($1\mu\text{m} \times 1\mu\text{m}$) pictures in Figure 2(i-iv) depict the surface morphology of $\text{Fe}_x\text{Zn}_{1-x}\text{O}$ pellets analyzed by laser scanning microscopy. Figure 2 depicts hexagonally faceted large-grained ZnO structures 1). ZnO grains with sizes ranging from 1–3 μm are produced, suggesting that the sample has been fully sintered. Furthermore, the oxide particles are arranged in a compact morphology with closely packed grain boundaries. Figure 2 depicts the effects of Fe doping on surface morphology. 2 to 4; Maybe a little Fe-doping a higher density of grain boundaries, and less faceted grain development. Samples E ($\sim 0.3\mu\text{m}$), D ($\sim 0.4\mu\text{m}$), and B ($\sim 0.7\mu\text{m}$) exhibit a consistent decrease in particle size. The decrease in grain growth and orientation produced by Fe doping has generally been attributed to an increase in native-defects in the host lattice such as dislocations, point defects, and so on. Though, the surface morphology of the Fe-doped sample is still characterized by a uniformly distributed tight grain packing, while inter-granular interactions appear to diminish significantly as Fe doping levels increase.

TM-doped DMS systems underwent micro Raman scattering tests to look for any alloying related structural changes at various doping doses, alterations to the wurtzite structure of ZnO, produced stresses with Fe-ions substitution in the Zn-ions sub-lattice, and unique phonon bands linked to impurities (Lang et al., 2010; Kaur et al., 2014; Das et al., 2015). Furthermore, Cationic and anionic vacancies in the host-interstitial lattice's ions can be identified using the Raman technique (Fan et al., 2011). Group theory has revealed that the vibrational mode $2\text{E}_2+\text{E}_1+\text{A}_1+2\text{B}_1$ make up the wurtzite structure of ZnO (Space Group. $\text{C}_6\text{v}/\text{P}_6\text{mc}$), which approximate, respectively, the polar, non-polar (high/low), and silent Raman modes. (Bundermann et al., 2003). To fully understand the nature of Fe doping in ZnO, a wide range of Raman spectra (200–1,200 cm^{-1}) are

obtained for various samples A-F. As the order of Fe content rises, the Raman lines change in Figure 3. Because Fe^{3+} has a smaller radius than Zn^{2+} , structural distortions in the doped $\text{Zn}_x\text{Fe}_{1-x}\text{O}$ alloy are unavoidable due to poorer solubility. As a result, at higher doping levels, The Zn sub-lattice can support interstitial Fe^{3+} ions. Raman peaks can be seen in the ZnO Raman spectra at 208,331,381,434,539,581, and 658 cm^{-1} , which are entirely compatible with previously reported vibrational modes for ZnO; A_1TO , E_2H , E_1TO , $\text{E}_1\text{LO}/\text{A}_1\text{LO}$, 2 ($\text{E}_2\text{H}-\text{E}_2\text{L}$), and $2\text{E}_2\text{L}$ modes are among the others (Das et al., 2015; Pazhanivelu et al., 2016). Most doped and pure ZnO spectra have a high intensity Raman peak at 436 cm^{-1} . A high frequency non-polar vibrational mode (E_2H) is typically responsible for the peak, which is routinely employed to build wurtzite structure in ZnO binaries (Ruan et al., 2012). Fe-doped in the ZnO sub lattice clearly suppresses the reported E_2H vibrational mode, Its peak intensity declines as the Zn/Fe ratio is reduced. Furthermore, with greater $\text{Fe} > 10\%$, a wide E_2H mode is still active at low intensity, E_2H mode indicating the ZnO structure is still in wurtzite form. Furthermore, Due to the crystal's E_2H mode's sensitivity to the motion of lighter oxygen-ions, broadening of the E_2H mode at high frequency and low intensity may indicate a possible decline of ZnO crystal structure. Higher doping levels seem likely to result in the Fe atom acquiring interstitial locations in the cationic sub-lattice of ZnO (Silambarasan et al., 2015). Thus, extra stresses and deformations in the host-wurtzite structural lattice are anticipated. Furthermore, the low frequency and broadening of mode $2\text{E}_2\text{L}$ peak is seen to fade substantially more quickly even at $\text{Fe} > 2.5\%$ in response to the aforementioned disorder. Because of a direct Fe^{2+} replacement in the Zn sub-lattice, the $2\text{E}_2\text{L}$ seems to be considerably more susceptible to heavier zinc-ion motion. Furthermore, the presence of a second order multi-phonon mode2 ($\text{E}_2\text{H}-\text{E}_2\text{L}$) in sample A shows high-quality ZnO, While in doped samples, the mode vanishes. For $\text{Fe} > 10\%$, a new dopant-related Raman mode appears at 646 cm^{-1} . Bundermann et al. identified the extra mode as a characteristic mode for Fe that may be utilized to calculate the amount of Fe inclusion in the ZnO host-lattice (Bundermann et al., 2003). The unique Fe-mode,

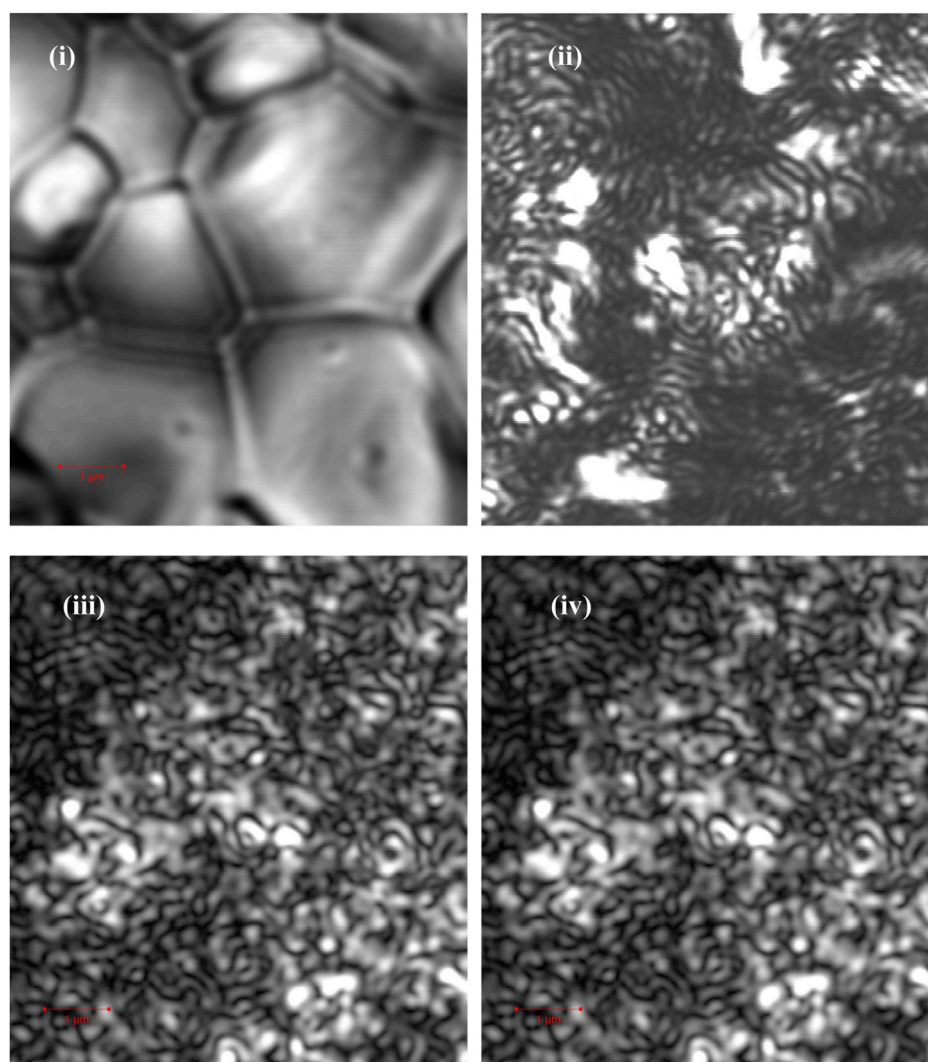


FIGURE 2

Laser confocal scanning microscopy was used to obtain the surface morphology of samples A 1), B 2), D 3), and E 4). The red bar in the graphic corresponds to a length of 1 μm , and each image has the same size.

however, might be related to the presence of either the ferrite Fe_3O_4 phase or only to the activation of distinctive defect sites in the host-lattice of ZnO (Silambarasan et al., 2015). A doping-related shift in the E1TO mode, located at 539 cm^{-1} , in addition to the usual wurtzite-structural changes discernible from E2H mode behavior, is also observed in the Raman-data in Figure 3. Even if the mode is barely noticeable in samples A and B, sample C with 5% Fe-doping exhibits dramatically increased peak amplification, further more doping lowers the peak, indicating the possibility of changes in the atomic vibrational mode caused by doping. The competitive character of Froehlich contacts and deformation potential driven suppression of Raman modes have been linked to the weak nature of E1TO mode in highly crystalline pure ZnO (Ruan et al., 2012). However, in sample C the causing the strong E1TO mode in the presence of Fe dopant ions, crystal-symmetry is disrupted and the competitive effect of the contacts is diminished. Additionally, the mode disappears once more in samples D, E, and F with rising Fe-doping concentrations $>10\%$, indicating a significant disorder, and the

mode ultimately disappears, much as the E2H mode. The shift in E1TO mode has also been attributed by Silambarasan et al. (2015), to a significant number of oxygen-related faults.

Figure 4 displays the photoluminescence (PL) spectra for all samples (A to F) at room temperature, in highly pure ZnO frequently exhibits a narrow Ultra Violet-blue PL emission band that has been determined to be the result of a near band-edge (NBE) radiative mechanism. Charge carriers being photo-excited from the valance band to the conduction band, generating an exciton (e-h pair), and then radiatively recombining electrons and holes are two possible explanations for the near band-edge NBE emission. Bulk ZnO's observed UV energy band-gap is 3.3 eV. This has a perfect correspondence with sample A at 377 nm NBE peak location (Cerneș et al., 2017). In samples with weak doping, the kind of NBE emission and its location, Fe 10%, C, and D samples matches the un-doped ZnO NBE peak exactly. For larger amount Fe contents $>10\%$, E and F samples, there is a red-shift found, which is demonstrated by a shifted NBE signal position at 390 nm and a

FIGURE 4
Global photoluminescence spectra recorded at 325 nm excitation wave-length for samples (A-F) containing different percentages of iron (0% to 50%) in ZnO. Abscissa-break in PL-intensity elucidates intense and broad luminescence in green-orange band. Vertical arrow and inset figure shows the positions near band edge luminescence from the assorted samples. 4: Global photoluminescence spectra recorded at 325 nm excitation wave-length for les (A-F) containing different percentages of iron (0%–50%) in ZnO. Abscissa-break in PL-intensity elucidates intense and broad luminescence in green-orange band. Vertical arrow and t figure shows the positions near band edge luminescence from the assorted ples.

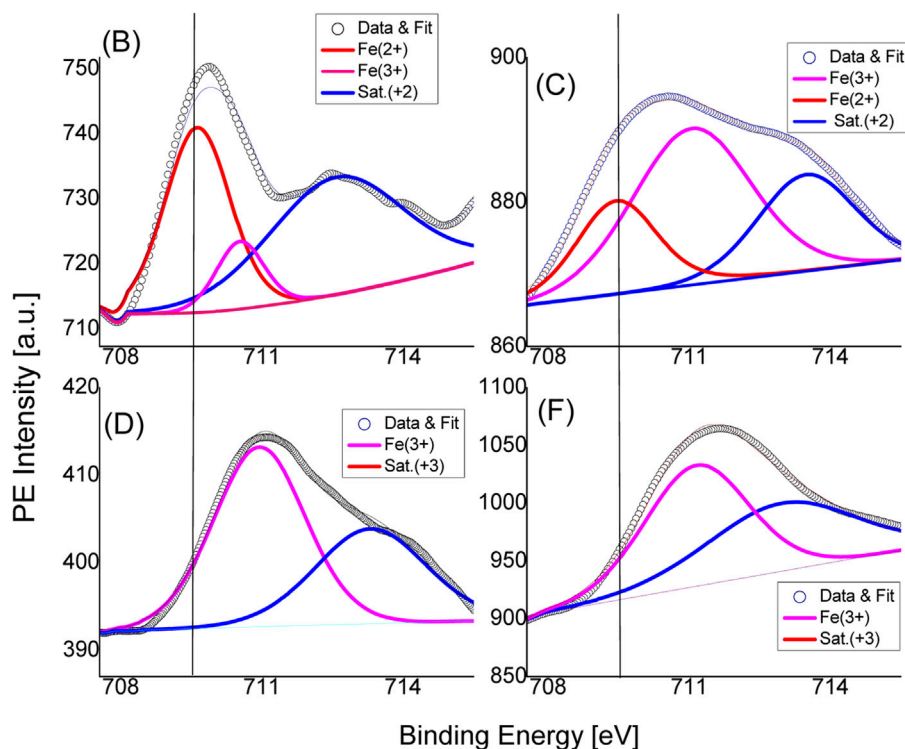


FIGURE 5

Results from X-ray photoelectron spectroscopy for iron-2p electrons, along with their corresponding satellite structures, demonstrate binding energy fluctuations for Fe^{2+} and Fe^{3+} oxidation states in a variety of Fe-doped substrates (B–F).

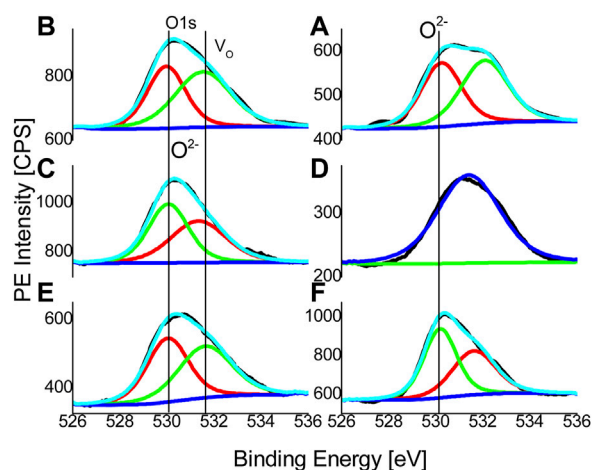


FIGURE 6

The XPS spectra for oxygen-1s electrons are displayed together with a Gaussian component that has been fitted for oxygen vacancies and the anionic sub-lattice of ZnO, respectively. Metal-oxide and oxygen vacancy states, respectively, are indicated by the vertical lines at ~530 and ~532 eV (A–F).

respectively. It is clear that the higher intensity binding energy peak (red) that overlaps the reference line signifies a greater incorporation of the Fe^{2+} ion as well as the replacement of Zn atoms by Fe in the cationic sub-lattice of ZnO. The diminished presence of Fe^{3+} in the

host-lattice is associated with the latter peak (magenta), which is of lower intensity. Overall, hetero-valent chemical states, including mixed Fe^{2+} and Fe^{3+} states, are used to incorporate Fe into the ZnO host-lattice. Furthermore, no Gaussian component is seen near 706 eV, ruling out the possibility of free metal clusters in the samples. Similarly to sample B, sample C exhibits two distinct oxidation states that are connected to binding energies of 709.5 eV (Fe^{2+}) and 710.9 eV (Fe^{3+}). However, the $\text{Fe}^{2+}/\text{Fe}^{3+}$ intensity ratio noticeably decreases to 0.5 from 1.8 ($\text{Fe} = 2.5\%$) when the Fe-content is increased to 5%, demonstrating that low Fe doping promotes Fe^{2+} ion substitution in the host lattice. Sample D, and sample F completely lacks the Fe^{2+} oxidation state, it is clear that Fe inclusion in the ZnO host has changed from Fe^{2+} to Fe^{3+} . All samples show the shake-up satellite structures as well as Fe-2p binding energies. In $\text{Zn}_{1-x}\text{Fe}_x\text{O}$ systems, satellite peaks at the Fe-2p binding energy have frequently been seen. These peaks result from a limited likelihood of Fe-ion photoelectron excitation to their spin-excited triplet states at energies of a few eV (Biesinger et al., 2011).

All (A–E) $\text{Zn}_{1-x}\text{Fe}_x\text{O}$ samples between 713 and 714 eV have satellite structures, which are normally isolated from the ground state, verifies the Fe ions' magnetic properties even more because they are incorporated into the host-lattice (Biesinger et al., 2011). Typically, the satellite structures are shifted from the ground state and observed in between 713 and 714 eV for all $\text{Zn}_{1-x}\text{Fe}_x\text{O}$ samples and their presence further corroborate the magnetic nature of as-incorporated Fe ions in host-lattice.

Figure 6 displays XPS data for O-1s binding-energies together with a reference line, it depicts the position of the observed O-1s (O^{2-})

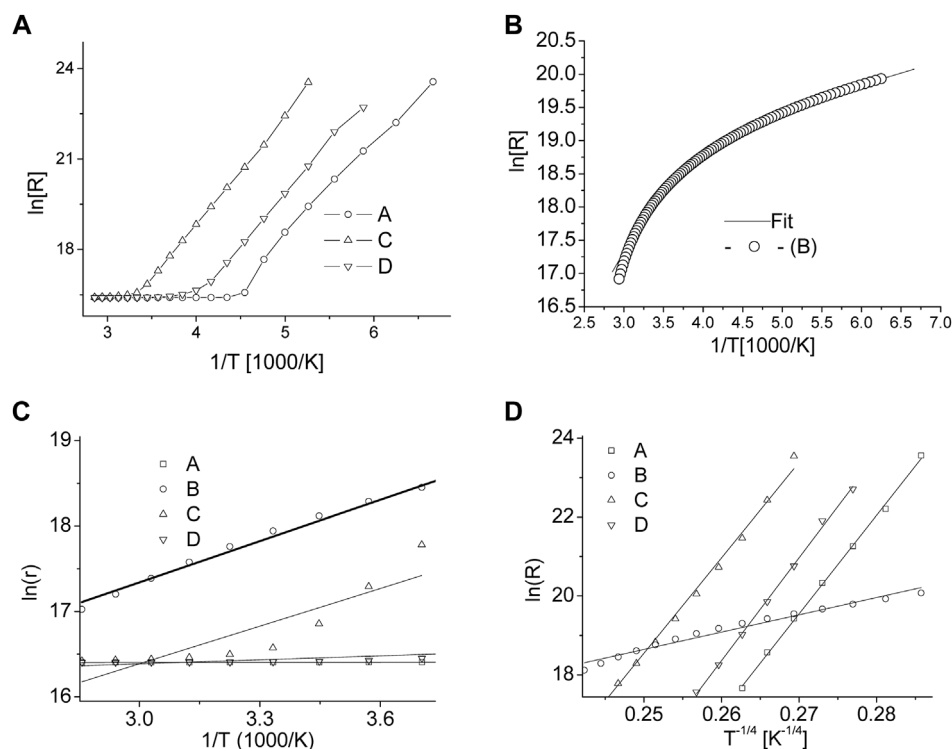


FIGURE 7

(A) Distinctive two-slope logarithmic-dependence of resistivity with sample cooling indicates an early thermally activated conduction which is followed by hopping mode of conduction at lower temperatures. (B) Experimental data and TA mode of conduction fitting for sample-B shows a singular conduction process. (C) Fitting of the temperature experimental data ($T \geq 250$ K) with phonon assisted TA mode of conduction also explained in the text. (D) Fitting of the low temperature experimental data ($T \leq 250$ K) with variable range hopping conduction model as described in the text.

binding energy of 530 eV for metal-oxides is reported (Nohira et al., 2002). Though, as asymmetrical single peaks, O-1s peaks are found, however from their de-convolutions, which are represented by the red and green colour components of Figure 6, at least two distinct broad and overlapping Gaussian components can be seen (A to F). The first part, which is connected to the oxygen sub lattice, is detected with a little doping-related change of ± 0.1 eV at a fixed location of ~ 530 eV. The constituent is the O^{2-} (1 s) binding energy that results from oxygen atoms strategically positioned within hexagonal ZnO's anionic sub lattice. Usually, the component represents a complete nearest-neighbor (NN) (Zn^{2+} or Fe^{2+}) cationic-coordination of oxygen. Obviously, it is discovered that the second overlapping Gaussian at ~ 532.1 eV is more sensitive to compositional changes, which show up in doped samples as both intensity changes and energy position shifts (B to F). Additional, The presence of native oxygen vacancies (V_o) in the oxygen sub-lattice can be attributed to the second Gaussian component. in which the NN cationic-coordination remains incomplete (Lin et al., 2010). Moreover, intensity of the V_o peak in sample B, C, E and F are found to be smaller than the oxygen peak indicative of a general trend of Fe-doping decreasing the percentage of oxygen vacancies. Extraordinarily, the form and position of the binding energy in sample D are relatively similar to those of un doped ZnO. Additionally, the anionic oxygen sub-lattice in sample D appears to have a tiny positive charge because of the abundance of V_o states, which are also known to function as donor states (Lin et al., 2010). Non-convoluting single oxygen peaks, as depicted in Figure 6D, also exhibit the additional charge on oxygen

sub-lattice conversely, Fe^{3+} ions' occupancy of interstitial sites in the cationic sub-lattice and their promotion of oxygen interstitial defects in the anionic sub-lattice can also be used to explain sample D extraordinary results. In distinction, the Zn-2p binding-energies, which are also included in an additional Supplementary Figure S1, The divalent Zn-2p ($_{3/2}$) peak location remains fairly consistent around $\sim 1,022$ eV for all un-doped and Fe doped samples, and there appears to be no change in the Zn^{2+} oxidation state.

Temperature dependence of resistance (R) of ~ 2 mm thick pellets is shown in Figure 7 (a) for samples A, C and D and in Figure 7 (b) for sample-B. Apparently, all the oxide samples are marked by high resistance with strong temperature dependence, since the n_c is strongly dependent on thermal excitation in a typical oxide semiconductor. Especially, samples B and C have unusually higher resistance even at higher $k_B T$ values. However, it can be seen from the two slope nature of Figure 7A that all samples, except sample-B, exhibit two distinct regimes of conduction; a relative low R-range (200–350 K) and high R-range (< 200 K). The onset of high resistance regime, which is indeed the hopping mode of conduction, is found at 221, 298 and 250 K for samples A, C and D, respectively. The conduction regimes are usually assigned to a thermally activated (TA) conduction $\rho_T = \rho_0 \exp(\Delta E/k_B T)$ at higher temperatures and a variable range hopping (VRH) conduction $\rho_T = \rho_0 \exp(T_c/T)^{1/4}$ at lower temperatures, respectively. The ΔE is activation energy of electrons and T_c is characteristic temperature. Using above transport relations, theoretical fits of TA- and VRH-conduction modes to experimental data are shown in Figure 7C and

Figure 7D, respectively. It can be seen that for samples A, B and D, entirely overlapping theoretical fits are obtained to experimental data, also shown in Figures 7B, C. Thus, a dominant mode of conduction at higher temperatures is found to be thermal-activation in samples A, B and D. Unexpectedly, sample C shows a variation from the usual conduction mode and exhibits thermal activation only during initially stages of cooling and quickly switchover to the VRH conduction. The switchover happens at above room temperature ~ 305 K, which is also evident from early hopping conduction onset for sample-C and that is also evident from a poor TA fit (C) of Figure 7C. The early onset of hopping in sample C can be attributed to a higher contribution of TA mode in the conduction process along with the smaller conductivity. Calculated values of activation energies obtained by using the theoretical fittings are 3, 126, 139 and 13.5 meV for A, B, C and D, respectively. During the TA conduction, higher thermal activation energy ~ 0.13 eV in samples B and C points toward a greater role of thermally excited phonons in conduction process and enhanced electron-phonon coupling, which is also observed in the TM doped systems (Schrettle et al., 2012). Accordingly, the thermal activation contributes to free carrier density *via* release of electrons from shallow donor states of ZnO's electronic band-structure. Thus, we can see that there is a continuous decrease in resistivity with increasing $k_B T$ in all samples owing to high density of shallow donor states and continuous supply of electrons to conduction band. ZnO surfaces are also known for absorption of H related shallow donors incorporating in the lattice *via* various diffusion processes from ambience (Qiu et al., 2008). However, in spite of higher value of activation energy ~ 0.13 eV for sample C, the hopping conduction also seems to start at higher temperatures ~ 290 K indicative of a possible mixing of the two conduction modes. It is important to recall from the as-described Raman results that sharp phonon modes are observed at lower Fe content in sample C, thus, the high ΔE may be due to polar phonon E_1 mode's re-appearance owing to Fe^{2+} substitution and their contribution to thermal activation. It is also quite possible that the reappearing modes exhibit more electron-phonon coupling and energy transfer, which is responsible for the higher activation energy in the samples B and C. Similarly, we can explain the decrease in the activation energy in sample D by the disappearance of coupled phonon modes as also evident from the Raman results along with increase in the lattice disorder.

The VRH model of conduction, as shown in Figure 7 (d), has a good fitness to samples A, C and D at lower temperatures indicating the electronic hopping at lower carrier density. The VRH indicates the freezing of various phonon modes and depopulating the thermally activated carrier states. Quite remarkably, the phonon mediated conduction in sample B remains a dominant conduction mode even at low temperatures < 200 K and exhibits a relatively lower resistance. A complete absence of hopping mode in the sample can be explained by using the character of Fe-substitution in ZnO host-lattice. During initial stages of $Zn_{1-x}Fe_xO$ formation, any Zn-interstitial neutral atoms present in the cationic sub-lattice is ionized to Zn^+ or Zn^{++} by releasing free electrons available for conduction (Sedky et al., 2009). Moreover, the Fe^{2+} substitution remains dominant for $Fe < 5\%$ and any Fe^{3+} substitution would release extra electrons by Fe^{3+} to Fe^{2+} conversion *via* a native oxygen formation process; $Fe_2O_3 \rightarrow O_2 + Fe^{Zn-O} + e + O^{O-Zn}$ (Sedky et al., 2009). Thus, the rise in carrier density seems to be responsible for the stronger TA mode in sample B in comparison to sample A. Similarly, the above mentioned processes of carrier

generation can also be ascribed to the shared conduction mode of sample C. On the other hand, at higher doping levels ($Fe > 10\%$) the iron attains a stable trivalent configuration and prefers interstitial positions in cationic sub-lattice releasing a positive hole i.e., acting as an electron acceptor; $Fe_2O_3 \rightarrow O_2 + Fe^* + P$. Thus, an overall decrease of the carrier density is related to the strong VRH mode in sample D.

As shown in Figures 8A–D for samples (A–D), respectively, at 320 K, 250 K, and 200 K different temperature shows the magnetic field dependency on % BMR, $(\rho_{(H)} - \rho_0) \times 100/\rho_0$. As can be seen, the BMR value increases sharply with applied magnetic field (0 to ± 9 T) for both un-doped and Fe-doped samples to rise sharply. Depending on the nature and hybridization mechanism of the transferred electrons and the TM dopant's d-orbital electrons, the BMR behaviour differs greatly depending on the amount of iron, sample temperature and applied magnetic field limitations. Even at temperatures greater than room temperature (320 K), samples still retain a tiny BMR of 0.4%, which indicates a higher level of magnetic ordering and peripatetic coupling. BMR rises substantially in all samples when the temperature is lowered by 250 K, the BMR increases sharply for all samples, reaching a maximum of 20%, 1%, 7% and 7.5% at 9 T for sample A–D. Unexpectedly, for sample B, the applied field oscillates and the BMR is still only 1%. The field-induced switch from positive to negative BMR is typically brought about by a weakening of the DBMP effect, which results from spontaneous spin alignment between the F-centre and the dopant atoms. This reduces electron scattering. In fact, because of the aforementioned spintronic process, the pd-hybridized itinerants exhibit more spin dispersion at zero field conditions. The spin alignment of close neighbors is reduced by the external magnetic field, which also reduces the spin dispersion of itinerants and total resistance (Mukherjee et al., 2017). In Fe (=10%) doped ZnO, cross-over of the spin alignment is particularly evident; at 250 K, sample C's BMR is negative by -7% . The BMR for sample D is still positive by 7.5% and rises sharply with respect to magnetic field at 0.5 T and 250 K. In samples C and D, the abrupt BMR jump at lower magnetic fields reveals spin dependent transport and stronger magnetic order. All of the samples' BMR inclinations at 200 K are comparable to those at 250 K, although the absolute BMR falls with temperature, possibly because of a drop in itinerants. As a result, both local magnetic moment-itinerant interactions and thermally triggered conduction are necessary for the BMR process to occur in the sample. Negative-BMR does not exhibit crossover-type behaviour for sample C and continues to be linearly relational to applied magnetic field strength. Furthermore, samples (B and C) with negative BMR have greater thermal activation energies 0.13 eV, which suggests that phonons and carrier concentrations may have had a larger impact on the spontaneous spin alignment between the F-center and dopant atoms. A probable magnetic saturation at higher field values is also indicated by the two separate BMR rules that are seen in sample D with regard to the applied field. BMR is observed to increase abruptly and highly depend on magnetic field at lower fields up to 2 T, whereas it increases gradually at higher fields from 2 T to 9 T. The BMR saturation does in fact display a magnetic ordering saturation due to the sample's low dopant content ($Fe = 10\%$). But on the other side, the un-doped ZnO result in Figure 8A shows a positive BMR reliance that is almost monotone on applied magnetic field pointing towards a continuous magnetic ordering among the defect related F-centers, it could be the outcome of an abundance of vacancies and donor states in the pure oxide. It could be the outcome of an abundance of vacancies and donor

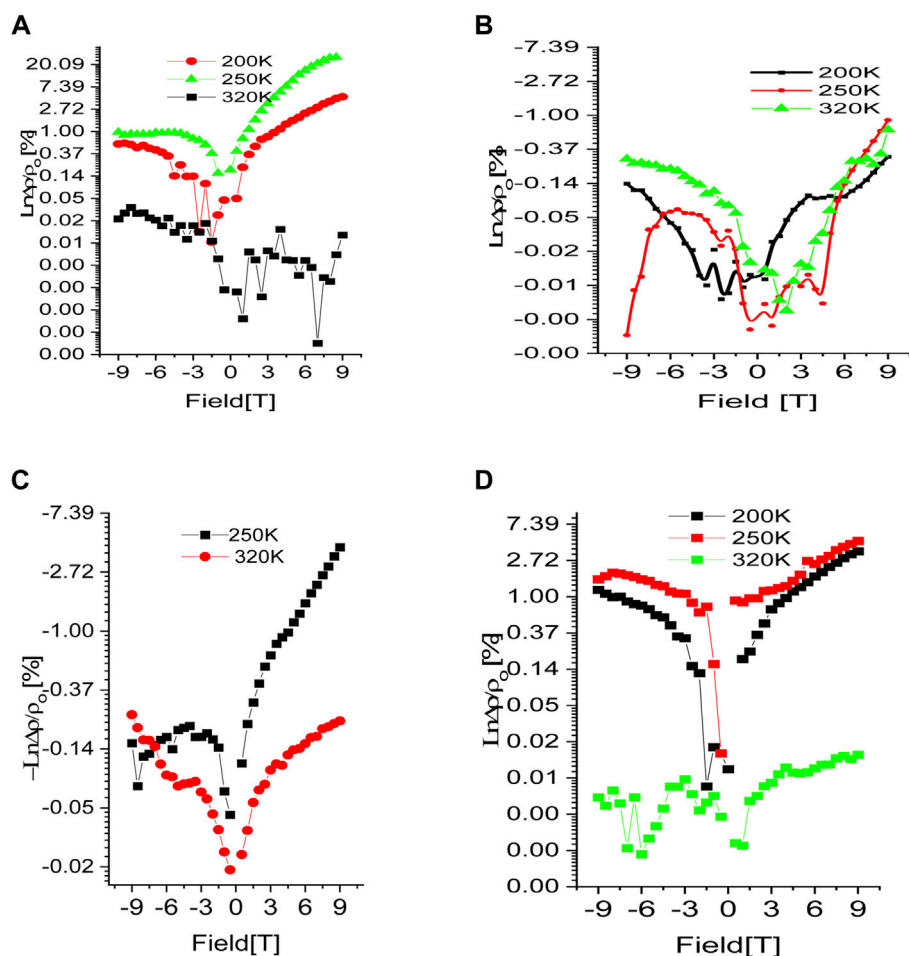


FIGURE 8

Magnetic field dependence of MR in samples (A–D). Noticeably, samples (A, D) show positive MR while samples (B, C) show negative MR.

states in the pure oxide. The R and T plots are displayed in supplemental [Supplementary Figure S2](#) to further clarify the negative and positive temperature dependence of resistance of pure ZnO and Fe-doped samples under field cooling (FC) and zero field cooling (ZFC) in the absence and presence of a 9 T magnetic field. In the temperature range of 340 K–280 K, the zoomed inset of [Supplementary Figure S2](#) (b) clearly shows an increase in negative resistance for sample B. Because of the low concentration of TM dopant and the lack of effective F-centers, B sample with Fe 5% exhibits lower MR values. Additionally, at all temperature [Supplementary Figure S2](#) (a) and (c) show positive and negative BMR, respectively.

To analyses our findings, we used a Khosla-MR Fisher's mode to better understand the peculiar behavior of BMR in respect to doping levels in our samples (B and C). The model predicts that a complete magneto-transport equation be expressed as where decremental- and incremental-BMR are, respectively, represented by the two terms (Hamieh et al., 2015; Lorite et al., 2015; Modepalli et al., 2016; Mukherjee et al., 2017). While, Higher conductivity and greater differential two-band spin split mobility are represented by the incremental fitting parameters (c and d), respectively, while localised moment-itinerant spin scattering and a fourth-order total spin exchange integral are represented by the decremental fitting

parameters (a and b), respectively (Modepalli et al., 2016). The experimental BMR data for samples B and C that have been fitted using the model equation are displayed in [Figure 9](#). [Table 1](#) provides a summary of the fitting parameter values that were obtained. Due to the bulk oxide pellets' normally high resistance, which is in the range of several hundred mega-ohms when they are manufactured, All of the samples have a negligible or zero value for the parameter c. The stronger DBMP (vacancy-donor ordering) effect of the samples leads to the maximum value of negative the maximum negative BMR value of -4% when a magnetic field is applied, which is shown in [Figure 1](#) by the large negative BMR peak located between 290 and 250 K temperature range, as shown by the greater values of parameter a, more than any other parameter by at least two orders, particularly at intermediate temperature 250 K. Therefore, the negative value of BMR can be explained by the reduced localized moment itinerant scattering that takes place when a magnetic field is supplied when conduction is in the optimistic mode. Indeed, the larger thermal activation energies are contributing significantly to the phonon mediation's function in the DBMP production in B and C samples. Considering that sample C 305 K, which is also depicted in [Figure 7](#), has the greatest VRH onset temperature is important at this point (a). In both the higher and lower temperature ranges, the parameter's strength is shown to diminish. Due to their higher

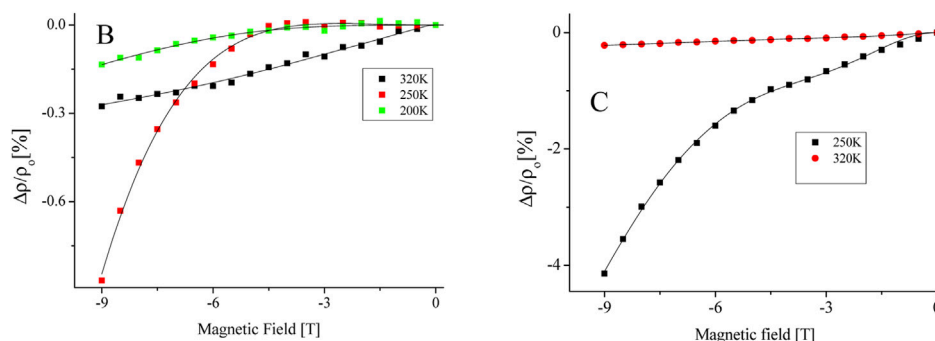


FIGURE 9

Khosla and Fisher model equation selectively (-9T-0T) fitted on experimental data of magnetic field dependence of MR for samples (B, C), which are showing negative MR values.

TABLE 1 Table shows parametric values obtained by data fitting using Khosla and Fischer model of magneto-transport and experimental results of magnetoresistance variation in between -9 to 9T magnetic fields. Typical definitions of the fitting parameters a, b, c and d are described in the text.

(T)	Sample B ($x = 0.025$)			Sample C ($x = 0.05$)	
	320K	250K	200K	320K	250K
a	$1.0 \times 10^{-3} \pm 2.1 \times 10^{-4}$	$1.9 \pm 9.0 \times 10^{-1}$	$5.9 \times 10^{-3} \pm 2.0 \times 10^{-4}$	$1.8 \times 10^{-3} \pm 6.1 \times 10^{-4}$	$2.1 \times 10^{-1} \pm 2.0 \times 10^{-3}$
b	$3.0 \times 10^{-5} \pm 1.0 \times 10^{-5}$	6.0×10^{-6}	1.4×10^{-5}	$1.3 \times 10^{-5} \pm 1 \times 10^{-5}$	$2.4 \times 10^{-5} \pm 1.6 \times 10^{-6}$
c	0	0	0	0	0
d	1.2×10^{-4}	4.8×10^{-6}	1.2×10^{-5}	$9.6 \times 10^{-5} \pm 1.7 \times 10^{-5}$	$1.5 \times 10^{-5} \pm 8.1 \times 10^{-7}$

resistivity and lower carrier concentration, samples B and C have lower values for the parameters c and d, which further suggests that any function performed in negative BMR by the Magneto-transport in the two-band spin split mode is quite poor. Based on the aforementioned analysis, it is possible to conclude that Lightly doped (Fe10%) ZnO's reported negative BMR can be largely ascribed to the donor and vacancy ordering gradually deteriorating with the application of an external magnetic field (DBMP effect). However, the high positive BMR in both pure ZnO and substantially Fe-doped (Fe>10%) ZnO is caused by increased spin scattering of itinerants and field-induced magnetic ordering of either F-centers or Fe atoms with a stronger magnetic field. Our spectroscopic findings for samples with lower Fe concentrations (10%), increased wurtzite character, arousal of a specific phonon mode connected to iron, fine PL spectra line, and lower Fe³⁺/Fe²⁺ ratio, Some of the primary reasons contributing to negative BMR *via* F-center- magnetic dopant coupling - DBMP effect are reduced percentages of O-vacancy resulting in fewer F-centers. While un-doped ZnO devoid of magnetic dopants exhibits positive-BMR. Similar to this, samples with high Fe contents (>10%) show positive BMR. Apart from the lack of unique phonon modes, larger Fe³⁺ ion presence, lower TA energy, and higher oxygen vacancy states, the heavily Fe-doped ZnO also exhibits these spectroscopic characteristics. At lower Fe doping levels, it is discovered that the electron-transport is dominated by the spin dispersion of the itinerants from localised moments, such as F-centers, magnetic dopant, or DBMP. Negative BMR crossover in Fe-doped ZnO is also caused by spin scattered itinerants.

4 Conclusion

Several spectroscopic factors are discussed in the manuscript in relation to as-observed positive and negative BMR. The oxygen vacancy, multivalent Fe nature, novel phonon modes, PL emission lines are found to play important role in positive and negative BMR.

- Various compositional alterations the development of structural, luminous, compositional, all Samples of Fe-doped zinc oxide produced by a common solid state reaction technique are examined for their magneto-resistance characteristics.
- A high positive BMR of 14% is observed in samples with a lot of oxygen vacancies.
- A reduced density of oxygen vacancies is observed in ZnO with lower doping levels (Fe10%).
- Negative BMR's occurrence, having a significant negative BMR of 4%, is observed to be improved by reducing doping.
- Thermally activated and variable range hopping at low- and high-resistivity, respectively, are two regimes of temperature-dependent electrical conduction that were identified.
- Hopping high resistivity doped samples will display conduction onsets at higher temperatures. The particular Raman pattern indicates a lattice distortion in the wurtzite structure of the ZnO at first, followed by phonon softening and wurtzite disintegration at Fe > 30%. Raman spectra show an additional Fe-related phonon mode at 530 cm⁻¹, which diminishes at higher doping levels (Fe > 10%).

- As-prepared samples always have the distinctive NBE emission peak of ZnO in their PL spectra. However, by raising the Fe content, the peak is redshifted. In addition to the NBE, all samples show a strong mid-gap luminescence.
- The band in pure ZnO is attributed to the existence of big oxygen-vacancy states.
- The broad band is connected to a larger fraction of Fe interstitials at higher Fe concentrations. Chemical states of multivalent iron

Moreover, several mechanisms of as-found BMRs and their crossovers are discussed.

Data availability statement

The original contributions presented in the study are included in the article/[Supplementary Material](#), further inquiries can be directed to the corresponding authors.

Author contributions

NI, MS, LA, WS, AA, SE, AA-J, AS, and JM contributed in initial design and modeling of problem. LA, WS, AA, and SE contributed for graphical analysis of the current study by plotting new graphs, AA-J,

AS, and JM also re-confirmed/verify the mathematical modeling and computation. NI, MS, LA, WS, and AA also contributed in revising Abstract, Introduction, results and discussion and conclusion.

Conflict of interest

The authors declare that the research was conducted in the absence of any commercial or financial relationships that could be construed as a potential conflict of interest.

Publisher's note

All claims expressed in this article are solely those of the authors and do not necessarily represent those of their affiliated organizations, or those of the publisher, the editors and the reviewers. Any product that may be evaluated in this article, or claim that may be made by its manufacturer, is not guaranteed or endorsed by the publisher.

Supplementary material

The Supplementary Material for this article can be found online at: <https://www.frontiersin.org/articles/10.3389/fmats.2023.1112798/full#supplementary-material>

References

- Ahmed, F., Kumar, S., Arshi, N., Anwar, M. S., and Koo, B. H. (2012). Morphological evolution between nanorods to nanosheets and room temperature ferromagnetism of Fe-doped ZnO nanostructures. *CrystEngComm* 14, 4016–4026. doi:10.1039/c2ce25227a
- Ariyakkani, P., Suganya, L., and Sundaresan, B. (2017). Investigation of the structural, optical and magnetic properties of Fe doped ZnO thin films coated on glass by sol-gel spin coating method. *J. Alloys Compd.* 695, 3467–3475.
- Balamurugan, S. (2012). Syntheses and magnetic-properties of Zn-diluted Sr-based perovskite cobalt oxides, $\text{Sr}_{1-x}\text{Zn}_x\text{CoO}_3$; $0.05 \leq x \leq 0.3$. *J. Supercond. Nov. magnetism* 25, 1603–1609. doi:10.1007/s10948-012-1488-2
- Beltrán, J. J., Barrero, C. A., and Punnoose, A. (2015). Understanding the role of iron in the magnetism of Fe doped ZnO nanoparticles. *Phys. Chem. Chem. Phys.* 17, 15284–15296. doi:10.1039/c5cp01408e
- Biesinger, M. C., Payne, B. P., Grosvenor, A. P., Lau, L. W. M., Gerson, A. R., and Smart, R. S. C. (2011). Resolving surface chemical states in XPS analysis of first row transition metals, oxides and hydroxides: Cr, Mn, Fe, Co and Ni. *Appl. Surf. Sci.* 257, 2717–2730. doi:10.1016/j.apsusc.2010.10.051
- Borges, R. P., Ribeiro, B., Costa, A. R. G., Silva, C., da Silva, R. C., Evans, G., et al. (2011). Magnetic and transport properties of transition-metal implanted ZnO single crystals. *Eur. Phys. J. B-Condensed Matter Complex Syst.* 79, 185–195. doi:10.1140/epjb/e2010-10512-3
- Bundesmann, C., Ashkenov, N., Schubert, M., Spemann, D., Butz, T., Kaidashev, E. M., et al. (2003). Raman scattering in ZnO thin films doped with Fe, Sb, Al, Ga, and Li. *Appl. Phys. Lett.* 83, 1974–1976. doi:10.1063/1.1609251
- Can, M. M., Shawuti, S., Firat, T., and Shah, S. I. (2016). Experimentally tailoring sd and p interactions in spin polarization via post deposition annealing conditions. *J. Alloys Compd.* 660, 423–432. doi:10.1016/j.jallcom.2015.11.063
- Cerne, M., Mihalache, V., Secu, E. C., Trusca, R., Bercu, V., and Diamandescu, L. (2017). Structural, morphological, ferromagnetic and photoluminescence properties of Fe-doped ZnO, prepared by hydrothermal route. *Superlatt. Microstruc.* 104, 362–373.
- Chattopadhyay, S., Panda, J., and Nath, T. K. (2013). Enhanced temperature dependent junction magnetoresistance in $\text{LaO}_{0.7}\text{Sr}_{0.3}\text{MnO}_3/\text{Zn}(\text{Fe}, \text{Al})\text{O}$ carrier induced dilute magnetic semiconductor junctions. *J. Appl. Phys.* 113, 194501. doi:10.1063/1.4805052
- Das, J., Mishra, D. K., Srinivasu, V. V., Sahu, D. R., and Roul, B. K. (2015). Photoluminescence and Raman studies for the confirmation of oxygen vacancies to induce ferromagnetism in Fe doped Mn₂ZnO compound. *J. Magn. Mater.* 382, 111–116.
- Fabbiyola, S., Kennedy, L. J., Ratnaji, T., Vijaya, J. J., Aruldoss, U., and Bououdina, M. (2016). Effect of Fe-doping on the structural, optical and magnetic properties of ZnO nanostructures synthesised by co-precipitation method. *Ceramics Inter.* 42 (1), 1588–1596.
- Fan, D., Zhang, R., and Wang, X. (2011). Effect of phosphorus incorporation on the morphology and optical properties of ZnO nanorods. *Mater. Res. Bull.* 46 (4), 596–600.
- Gacic, M., Jakob, G., Herbort, C., Adrian, H., Tietze, T., Brück, S., et al. (2007). Magnetism of Co-doped ZnO thin films. *Phys. Rev. B* 75, 205206. doi:10.1103/physrevb.75.205206
- Hamieh, M., Jedrecy, N., Hebert, C., Demaille, D., and Perriere, J. (2015). Ferromagnetism and magnetoresistance of nanocomposite ZnO-Co thin films. *Phys. Rev. B* 92, 155302. doi:10.1103/physrevb.92.155302
- Han, S. J., Song, J. W., Yang, C.-H., Park, S. H., Park, J.-H., Jeong, Y. H., et al. (2002). A key to room-temperature ferromagnetism in Fe-doped ZnO: Cu. *Appl. Phys. Lett.* 81, 4212–4214. doi:10.1063/1.1525885
- Hsu, C. Y., Huang, J.-C. A., Chen, S. F., Liu, C. P., Sun, S. J., and Tzeng, Y. (2008). Tunable magnetic order of Co nanoparticles and magnetotransport in Co/ZnO nanocomposites. *Appl. Phys. Lett.* 93, 072506. doi:10.1063/1.2959081
- Jansson, F., Wiemer, M., Nenashev, A. V., Petznick, S., Klar, P. J., Hetterich, M., et al. (2014). Large positive magnetoresistance effects in the dilute magnetic semiconductor (Zn, Mn) Se in the regime of electron hopping. *J. Appl. Phys.* 116, 083710. doi:10.1063/1.4894236
- Jaquez, M., Yu, K. M., Ting, M., Hettick, M., Sanchez-Royo, J. F., Welna, M., et al. (2015). Growth and characterization of ZnO_{1-x}Sx highly mismatched alloys over the entire composition. *J. Appl. Phys.* 118, 215702. doi:10.1063/1.4936551
- Kaur, J., Kotnala, R. K., Gupta, V., and Verma, K. C. (2014). Anionic polymerization in Co and Fe doped ZnO: Nanorods, magnetism and photoactivity. *Curr. Appl. Phys.* 14 (5), 749–756.
- Kumar, S., Tiwari, N., Jha, S. N., Chatterjee, S., Bhattacharyya, D., Sahoo, N. K., et al. (2015). Insight into the origin of ferromagnetism in Fe-doped ZnO diluted magnetic semiconductor nanocrystals: An EXFAS study of local structure. *RSC Adv.* 5, 94658–94669. doi:10.1039/c5ra12828e
- Lang, J., Han, Q., Li, C., Yang, J., Li, X., Yang, L., et al. (2010). Effect of Mn doping on the microstructures and photoluminescence properties of CBD derived ZnO nanorods. *Appl. Surf. Sci.* 256 (11), 3365–3368.
- Lee, S., Park, J. H., Kim, W.-K., Dal Park, H., Lee, B. C., Moriyoshi, C., et al. (2016). Control of magneto-transport characteristics of Co-doped ZnO by electron beam irradiation. *RSC Adv.* 6 (47), 41067–41073.

- Lin, F., Jiang, D., and Ma, X. (2010). The influence of annealing on the magnetism of Fe-doped ZnO prepared by mechanical alloying. *Physica B: Condensed Matter*. 405 (6), 1466–1469.
- Liu, H., and Guyot-Sionnest, P. (2015). Magnetoresistance of manganese-doped colloidal quantum dot films. *J. Phys. Chem. C* 119, 14797–14804. doi:10.1021/acs.jpcc.5b01964
- Liu, H., Yang, J., Hua, Z., Liu, Y., Yang, L., Zhang, Y., et al. (2011). Cu-doping effect on structure and magnetic properties of Fe-doped ZnO powders. *Mater. Chem. Phys.* 125 (3), 656–659.
- Lorenz, M., Rao, M. R., Venkatesan, T., Fortunato, E., Barquinha, P., Branquinho, R., et al. (2016). The 2016 oxide electronic materials and oxide interfaces roadmap. *Appl. Phys.* 49 (43), 433001.
- Lorite, I., Zandalazini, C., Esquinazi, P., Spemann, D., Friedländer, S., Pöpl, A., et al. (2015). Study of the negative magneto-resistance of single proton-implanted lithium-doped ZnO microwires. *J. Phys.: Condensed Matter*. 27 (25), 256002.
- Ly, M., Wang, H., Xu, Y., Yu, G., Zhang, H., Lin, T., et al. (2015). Long phase coherence length and anisotropic magnetoresistance in MgZnO thin film. *J. Appl. Phys.* 117, 155304. doi:10.1063/1.4918541
- Mihalache, V., Cernea, M., and Pasuk, I. (2017). Relationship between ferromagnetism and, structure and morphology in un-doped ZnO and Fe-doped ZnO powders prepared by hydrothermal route. *Curr. Appl. Phys.* 17 (8), 1127–1135.
- Modepalli, V., Jin, M.-J., Park, J., Jo, J., Kim, J. H., Baik, J. M., et al. (2016). Gate-tunable spin exchange interactions and inversion of magnetoresistance in single ferromagnetic ZnO nanowires. *ACS Nano* 10, 4618–4626. doi:10.1021/acsnano.6b00921
- Montes-Valenzuela, I., Romero-Paredes, G., Vázquez-Agustín, M. A., Baca-Arroyo, R., and Peña-Sierra, R. (2015). Synthesis and characterization of nanostructured magnetoresistive Ni doped ZnO films. *Mater. Sci. Semicon. Process.* 37, 185–189.
- Mukherjee, J., Mannam, R., and Rao, M. S. R. (2017). Variable range hopping crossover and magnetotransport in PLD grown Sb doped ZnO thin film. *Semicond. Sci. Technol.* 32, 045008. doi:10.1088/1361-6641/aa5fcc
- Nohira, H., Tsai, W., Besling, W., Young, E., Petry, J., Conard, T., et al. (2002). Characterization of ALCVD-Al 2 O 3 and ZnO 2 layer using X-ray photoelectron spectroscopy. *J. non-crystalline solids* 303, 83–87. doi:10.1016/s0022-3093(02)00970-5
- Ovhal, M. M., Kumar, A. S., Khullar, P., Kumar, M., and Abhyankar, A. C. (2017). Photoluminescence quenching and enhanced spin relaxation in Fe doped ZnO nanoparticles. *Mater. Chem. Phys.* 195, 58–66.
- Pazhanivelu, V., Selvadurai, A. P. B., Kannan, R., and Murugaraj, R. (2016). Room temperature ferromagnetism in 1st group elements codoped ZnO-Fe nanoparticles by co-precipitation method. *Physica B: Condensed Matter*. 487, 102–108.
- Peters, J. A., Parashar, N. D., Rangaraju, N., and Wessels, B. W. (2010). Magnetotransport properties of InMnSb magnetic semiconductor thin films. *Phys. Rev. B* 82, 205207. doi:10.1103/physrevb.82.205207
- Petukhov, A. G., and Foygel, M. (2000). Bound magnetic polaron hopping and giant magnetoresistance in magnetic semiconductors and nanostructures. *Phys. Rev. B* 62, 520–531. doi:10.1103/physrevb.62.520
- Qiu, H., Meyer, B., Wang, Y., and Wöll, C. (2008). Ionization energies of shallow donor states in ZnO created by reversible formation and depletion of H interstitials. *Phys. Rev. Lett.* 101, 236401. doi:10.1103/physrevlett.101.236401
- Quan, Z., Liu, X., Song, Z., and Xu, X. (2016). Magnetism and magnetoresistance from different origins in Co/ZnO-Al granular films. *Physica B: Condensed Matter*. 502, 16–20.
- Ruan, H. B., Fang, L., Qin, G. P., Wu, F., Yang, T. Y., Li, W. J., et al. (2012). Raman scattering and electrical properties of Zn1-xMnxO films. *J. Alloys Comp.* 531, 77–81.
- Saikia, D., Raland, R. D., and Borah, J. P. (2016). Influence of Fe doping on the structural, optical and magnetic properties of ZnS diluted magnetic semiconductor. *Physica E: Low-Dimen. Sys. Nanostruc.* 83, 56–63.
- Salem, M., Akir, S., Ghrif, T., Daoudi, K., and Gaidi, M. (2016). Fe-doping effect on the photoelectrochemical properties enhancement of ZnO films. *J. Alloys Comp.* 685, 107–113.
- Sapkota, K. R., Chen, W., Maloney, F. S., Poudyal, U., and Wang, W. (2016). Magnetoresistance manipulation and sign reversal in Mn-doped ZnO nanowires. *Sci. Rep.* 6, 35036. doi:10.1038/srep35036
- Schrettle, F., Kant, C., Lunkenheimer, P., Mayr, F., Deisenhofer, J., and Loidl, A. (2012). Wüstite: Electric, thermodynamic and optical properties of FeO. *Eur. Phys. J. B-Condensed Matter Complex Syst.* 85, 164–212. doi:10.1140/epjb/e2012-30201-5
- Sedky, A., Al-Sawalha, A., and Yassin, A. M. (2009). Enhancement of electrical conductivity by Al-doped ZnO ceramic varistors. *Phys. B Condens. Matter* 404, 3519–3524. doi:10.1016/j.physb.2009.05.054
- Sedky, A., and Kotb, H. M. (2013). Possible two non-linear regions in the I-V characteristics of ZnO varistors. *Curr. Appl. Phys.* 13 (9), 2117–2122.
- Shi, G. A., Stavola, M., Pearton, S. J., Thieme, M., Lavrov, E. V., and Weber, J. (2005). Hydrogen local modes and shallow donors in ZnO. *Phys. Rev. B* 72, 195211. doi:10.1103/physrevb.72.195211
- Silambarasan, M., Saravanan, S., and Soga, T. (2015). Effect of Fe-doping on the structural, morphological and optical properties of ZnO nanoparticles synthesized by solution combustion process. *Physica E: Low-dimensional. Sys. Nanostruc.* 71, 109–116.
- Venkatesh, S., Baras, A., Lee, J.-S., and Roqan, I. S. (2016). The magnetic ordering in high magnetoresistance Mn-doped ZnO thin films. *AIP Adv.* 6, 035019. doi:10.1063/1.4944954
- Wang, X. L., Shao, Q., Zhuravlyova, A., He, M., Yi, Y., Lortz, R., et al. (2015). Giant negative magnetoresistance in manganese-substituted zinc oxide. *Sci. Rep.* 5, 9221. doi:10.1038/srep09221
- Wang, Y., Luo, X., Tseng, L.-T., Ao, Z., Li, T., Xing, G., et al. (2015). Ferromagnetism and crossover of positive magnetoresistance to negative magnetoresistance in Na-Doped ZnO. *Chem. Mater.* 27, 1285–1291. doi:10.1021/cm504261q
- Wang, Z. J., and Tanaka, I. (2009). Conduction-band structures of wurtzite ZnO solid solutions by first principles calculations. *Mater. Trans.* 50, 1067–1070. doi:10.2320/matertrans.mc200816



OPEN ACCESS

EDITED BY

Ali Saleh Alshomrani,
King Abdulaziz University, Saudi Arabia

REVIEWED BY

Mustafa Turkyilmazoglu,
Hacettepe University, Türkiye
Prasannakumara B. C.,
Davangere University, India

*CORRESPONDENCE

Umair Khan,
✉ umairkhan@iba-suk.edu.pk

SPECIALTY SECTION

This article was submitted to Colloidal
Materials and Interfaces,
a section of the journal
Frontiers in Materials

RECEIVED 13 January 2023

ACCEPTED 24 January 2023

PUBLISHED 16 February 2023

CITATION

Raza A, Nigar N, Khan U, Elattar S,
Eldin SM and Abed AM (2023),
Comparative investigation of fractional
bioconvection and
magnetohydrodynamic flow induced by
hybrid nanofluids through a channel.
Front. Mater. 10:1143612.
doi: 10.3389/fmats.2023.1143612

COPYRIGHT

© 2023 Raza, Nigar, Khan, Elattar, Eldin
and Abed. This is an open-access article
distributed under the terms of the
[Creative Commons Attribution License](#)
(CC BY). The use, distribution or
reproduction in other forums is
permitted, provided the original author(s)
and the copyright owner(s) are credited
and that the original publication in this
journal is cited, in accordance with
accepted academic practice. No use,
distribution or reproduction is permitted
which does not comply with these terms.

Comparative investigation of fractional bioconvection and magnetohydrodynamic flow induced by hybrid nanofluids through a channel

Ali Raza^{1,2}, Niat Nigar², Umair Khan^{3,4*}, Samia Elattar⁵,
Sayed M. Eldin⁶ and Ahmed M. Abed^{7,8}

¹Department of Mathematics, University of Engineering and Technology, Lahore, Pakistan, ²Department of Mathematics, Minhah University, Lahore, Pakistan, ³Department of Mathematical Sciences, Faculty of Science and Technology, Universiti Kebangsaan Malaysia, Selangor, Malaysia, ⁴Department of Mathematics and Social Sciences, Sukkur IBA University, Sukkur, Sindh Pakistan, ⁵Department of Industrial & Systems Engineering, College of Engineering, Princess Nourah bint Abdulrahman University, Riyadh, Saudi Arabia, ⁶Center of Research, Faculty of Engineering, Future University in Egypt, New Cairo, Egypt, ⁷Department of Industrial Engineering, College of Engineering, Prince Sattam Bin Abdulaziz University, Alkharj, Saudi Arabia, ⁸Industrial Engineering Department, Faculty of Engineering, Zagazig University, Zagazig, Egypt

The functional effects of medications, such as those that slow down and calm the body, have been investigated for the polarized diffusion coefficient based on the subsequent increase through magnetism. This study examines generalized Mittag–Lefer kernel-based fractional derivatives in MHD Brinkman-type fluids under bioconvection that contain hybrid titanium dioxide (TiO₂) and silver (Ag) nanoparticles with water (H₂O) and sodium alginate (NaC₆H₇O₆) as the base fluids. Atangana–Baleanu (AB) and Caputo–Fabrizio (CF) fractional derivatives, which are two contemporary definitions of fractional-order derivatives with a memory effect, were used to explore the modified fractional model utilizing the Laplace transformation and certain numerical algorithms. The impacts of restrictions on various nanoparticles were investigated and graphically displayed. We observed that the volumetric fraction improvement controls the fluid velocity by slowing it down. The water-based hybrid nanofluid has a greater influence on the temperature and momentum fields than the sodium alginate-based hybrid nanofluid due to the physical characteristics of the explored nanoparticles and base fluids. Additionally, the memory effect causes a higher substantial value for the AB-fractional derivative of the velocity profile than the CF-fractional derivative.

KEYWORDS

hybrid nanofluid, parallel plates, Mittag–Leffler function, magnetohydrodynamics, AB and CF derivatives

Abbreviations: W , fluid velocity (m/s); t , times (s); g , gravity acceleration (m/s^2); k_{nf} , thermal conductivity of the nanofluid ($\frac{W}{mK}$); C_f , skin friction ($-$); ρ_{nf} , nanofluid density ($\frac{kg}{m^3}$); U_0 , characteristic velocity (ms^{-1}); θ , angle of magnetic inclination ($-$); Gm , mass Grashof number ($-$); μ_{nf} , dynamic viscosity ($\frac{kg}{ms}$); Pr_{eff} , Prandtl number ($-$); T_w , wall temperature, (K); Gr , heat Grashof number ($-$); T_a , ambient temperature (K); α, β , fractional parameters ($-$); Sc , Schmidt number ($-$); M , magnetic field ($-$); D , thermal diffusion coefficient ($-$); $(\rho C_p)_{nf}$, heat capacitance of the nanofluid ($-$); B_o , magnetic field strength (Kg/s^2); C_p , specific heat at constant pressure (J/kgK); β_T , thermal expansion coefficient ($1/k$); σ , electrical conductivity ($-$); Nu , Nusselt number ($-$); Sh , Sherwood number ($-$).

1 Introduction

Channel flow has been applied in various industrial fields including chemical reactors in pharmacological manufacturing and thermal exchangers in energy plants. Although various natural phenomena and Newtonian actions in equal stages may be named two-phase movements, there are many related applications where the constant fluid segment displays non-Newtonian movement characteristics. In the last two decades, the impact of numerous heat transfer behaviors in the industry and engineering sectors has benefited from and been improved by nanofluid science. The development of a hybrid nanofluid is another recent advancement in nanotechnology. This new product combines at least two substances with various physical and chemical features such as heat flow and thermal conductivity. In essence, the development of a hybrid nanofluid has completely transformed this new product. Numerous researchers have become interested in nanofluids due to their thermal solid conductivity performance. Examples abound in the biomedical, biochemical, and food distribution industries (Bräuer et al., 2021). Zheng et al. (2021) explored how a vortex maker formed affected fluids and the thermal conversion of HNFs in a channel. D'Ippolito et al. (2021) evaluated the systematic scale conflict of channel movement caused by vegetation. Using the CF derivative, Haq et al. (2020) developed MHD's fractional viscid fluid impact in a channel across a permeable surface.

The exceptional perception of nanoscience to increase the amount of heat sources has motivated researchers due to the constantly growing requirement for heat storage. For example, thermal transmission properties are claimed in fields ranging from biomedical to manufacturing industries. Improvements in thermal efficiency provide an advantage for plasma research, electronic equipment like computer chips, nuclear reactors, electricity generation, space cooling, and many others. The macroscopic fluid convection motion phenomenon, which is known as "bioconvection," is caused by the thickness angle formed by the mass of directional swimming microorganisms. Bioconvection was a fundamental principle introduced by Platt in 1961. Bioconvection is used, among other things, in the manufacturing of biological polymers in biotechnology and biosensors and in the testing and lab equipment sectors (Platt, 1961; Asjad et al., 2021). Sisko's three-dimensional radiative bioconvective stream was used by Ge-JiLe et al. (2021) to analyze nanofluids containing moving microorganisms. Ramzan et al. (2021) showed the occurrence of bioconvection in a three-dimensional meandering hyperbolic partially ionized magnetized nanofluid stream with Cattaneo–Christov heat flux and activation vitality. An examination of magneto-bioconvective enhancement and thermal conductivity in a nanofluid stream containing gyrotactic microorganisms was conducted by Alhussain et al. (2021). Farooq et al. (2021) adjusted Cattaneo–Christov equations and exponential space-based heat sources to account for a thermally radioactive Carreau nanofluid bioconvection flow. Yusuf et al. (2021) investigated the role of gyrotactic bacteria and entropy generation in the movement of Williamson nanofluids across an inclined plate. A Brinkman-type fluid (BTF) fractional model utilizing hybrid nanoparticles was examined by Saqib et al. (2020). Danish Ikram et al. considered the heat transfer of an

exponentially moving vertical plate over a viscous fluid containing clay nanoparticles. Using a hybrid fractional operator, Asjad et al. (2020) looked into the thermophysical characteristics of clay nanofluids. Using a constant and proportional Caputo fractional operator, Ikram et al. (2021) established a fractional model of a Brinkman-type fluid transporting hybrid nanoparticles in a confined microchannel.

A specific or isolated nanomaterial might exhibit extraordinary thermophysical or rheologic properties in addition to the excellent and typical requirements for a certain use. HNF is controlled to maintain different properties despite the multiple applications. An advanced NF, which is called a hybrid nanofluid, combines "two or more distributed NPs in the base liquid." The purpose of examining HNFs is to improve various thermal processes, such as heat transfer, highly well-organized heat conductivity, and solidity, by balancing the benefits and drawbacks of remarkable suspensions. Examples of these processes include the refrigeration of generators, cooling systems for machines, electric refrigeration, refrigeration of converters, and atomic structure refrigeration. HNFs' capacities to improve thermal conductivity offers an opportunity to account for them in real-valued energy models. An HNF was tested over a porous surface in motion along with alumina NPs in Waini et al. (2019), and studies of the volume fraction for copper NPs were confirmed. To simulate the HNF, two NPs were included in the composite along with water. To study the mobility of HNF ($\text{Al}_2\text{O}_3\text{-CuO/H}_2\text{O}$), Ashwinkumar et al. (2021) used radiation passing through a vertical plate and cone. Their research focused on contrasting two different forms and the characteristics of HNF flow. Samrat et al. (2022) considered heat transmission when analyzing the movement of NF and HNF due to the stretched surface. Characteristic groundwork investigations completed on HNFs have also been conducted (Raza et al., 2019; Anuar et al., 2020; Sulochana et al., 2020; TÜRKİYİLMAZOĞLU, 2021; Ibraheem et al., 2022; Raza et al., 2022; Turkyilmazoglu, 2022; Zhang et al., 2022; Turkyilmazoglu and Altanji, 2023).

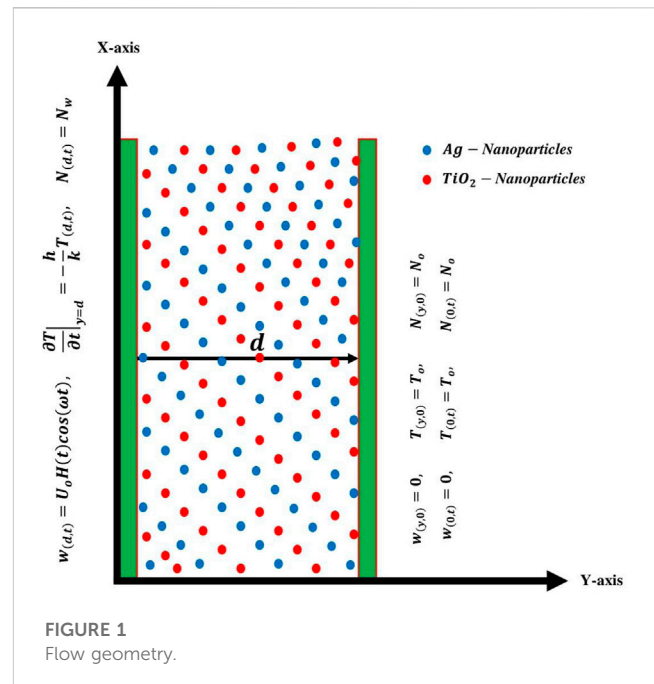
The field of fractional calculus is rapidly expanding due to the wide variety of processes that it can be applied to every day. Numerous definitions of fractional derivatives have been published in the literature due to the curiosity of academics. A fractional-order derivative based on an exponential function was created by Caputo–Fabrizio (CF) to address the challenges with earlier research on the singularity problem of the kernel. However, the fractional model of Caputo and Fabrizio lacks a specific kernel. This idea of fractional order has received significant attention in recent studies in the area of fractional calculus. Understanding the viscoelastic and rheologic properties of HNFs in detail are difficult due to the self-similar properties and memory-taking capacities of fractional operators. They provide a reasonable explanation for the behavior and heat efficiency of nanofluids. These operators have frequently been used to mimic and examine the specifics of various natural formations over the past few years. Fractional derivatives are widely applicable in signal processing, epidemiology, population modeling, economics, dynamic structures, fluid dynamics, electrochemistry, and many other fields. The three most fundamental standard fractional operators in fractional calculus depend on the convolution of regular derivatives and distinctive kernels. The two leading derivatives in this hierarchy are Riemann–Liouville and Caputo's derivatives, where the first operator

complicates a power-law kernel (Podlubny, 1999). Due to its widespread use, the definition of CF has been used by numerous researchers for a variety of scientific inquiries. The kernel's non-locality, which is a difficulty in the definition of CF, was addressed by Atangana and Nieto (2015) in a new formulation. The most current explanation of fractional derivatives without these problems was given by Atangana (2016). AB derivatives are rarely used in research, and this word is brand-new. Arif et al. (2019) used this most recent concept of AB-fractional derivatives to compare these two ideas, and the current issue is also applied to CF-fractional derivatives. In addition, this study solves the well-known pair stress fluid model with an external pressure gradient in a closed-form channel. Even though they employed the Caputo and CF-fractional model, Akhtar (2016) estimated the closed-form solutions (CSF) in channels. To avoid these obstacles, Atangana and Baleanu produced a novel operator whose mathematical expansion encompasses the convolution of the regular derivative and a general kernel, which is included in the Mittag-Leffler function (Atangana and Baleanu, 2016). Currently, in perceiving the worth of fractional-order operators, an extensive range of investigators has explored real-life phenomena in fractional situations rather than in regular contexts. Asjad et al. (2022) investigated the fractional bioconvection nanofluid solution moving through a channel. Investigations on heat transfer and fluid problems were conducted using local and non-local kernel approaches by Ali et al. (2022a) and Ali et al. (2022b). Tarasov explained how a novel rebellion, "memory revolution," occurred in present mathematical economics just because of fractional derivatives and corresponding integrals. The investigation of neurology has also been impacted by the initiation of fractional calculus (Tarasov, 2019; Riaz et al., 2022).

In the absence of fractional bioconvection, those previously mentioned were carried out by or lacking fractional approaches. However, the fundamental purpose is to combine these two fascinating topics: bioconvection and fractional operators. In the previous literature, we did not find any investigation on the focus of fractional bioconvection of an applied magnetic field on a naturally occurring Brinkman-type flow of a hybrid nanofluid over two parallel plates with CF- and AB-fractional derivative approaches. Consequently, we applied the Laplace transform method to solve the thermal transmission and fluid flow problems of bioconvection. In addition, graphical analysis was applied to present a graphical description of the diverse flow parameters.

2 Description of the problem

Suppose an incompressible, unsteady, and free convective Brinkman-type hybrid nanofluid moves along the path of two parallel plates with characteristics of mass diffusion and temperature gradient, as described in Figure 1. Both plates are fixed in the xy-plane at a distance d that is vertical to the y-axis and parallel to the x-axis. The whole system, including the fluid and any relevant limitations, is initially at $t = 0$ in the rest position. One plate starts to move at time $t > 0^+$ as a result of the imposed time-dependent shear force. The hybrid nanofluid made of water and sodium alginate begins to flow between the poured plates as a result of oscillations and the rise in temperature. The flowing fluid is



subjected to a consistent magnetic field with an inclination angle of θ . For this flow model, the following suppositions are used.

- The length of the parallel plates is infinite with width d .
- The poured plates are vertical to the y-axis and oriented in the x-direction.
- At $t \leq 0$, both temperature and bioconvection have constant values as T_d and N_d , respectively.
- Different nanoparticles in the mixed hybrid nanofluid accelerate in the x-direction.
- The constant magnetic field of strength B_o is applied to the flowing fluid.

By utilizing Boussinesq's (Mayeli and Sheard, 2021) and Roseland approximations (Chu et al., 2020), the governed partial differential equations can be formulated as follows (Asjad et al., 2022):

$$\rho_{hmf} \frac{\partial w(y,t)}{\partial t} + \rho_{hmf} \beta_1 w(y,t) = \mu_{hmf} \frac{\partial^2 w(y,t)}{\partial y^2} - \sigma_{hmf} B_o^2 \sin(\theta) w(y,t) - \frac{\mu_{hmf} \phi_{hmf}}{K} w(y,t) + g \left((\rho \beta_T)_{hmf} (T(y,t) - T_o) - \gamma (\rho_m - \rho) (N(y,t) - N_o) \right), \quad (1)$$

$$(\rho C_p)_{hmf} \frac{\partial T(y,t)}{\partial t} = k_{hmf} \frac{\partial^2 T(y,t)}{\partial y^2}, \quad (2)$$

$$\frac{\partial N(y,t)}{\partial t} = D \frac{\partial^2 N(y,t)}{\partial y^2}, \quad (3)$$

where ρ_{hmf} , μ_{hmf} , σ_{hmf} , $(\rho C_p)_{hmf}$, k_{hmf} and D represent the dynamic density viscosity, electrical conductivity, volumetrically thermal expansion, heat capacitance of the nanofluid, thermal conductivity, and thermal diffusion coefficient, respectively. Its corresponding boundary conditions are as follows:

TABLE 1 Quantities of hybrid nanofluids' thermophysical properties.

Thermal feature	Regular nanofluid	Hybrid nanofluid
Density	$\rho_f = \frac{\rho_{nf}}{(1-\varphi)+\varphi\frac{\rho_s}{\rho_f}}$	$\rho_f = \frac{\rho_{hnf}}{((1-\varphi_2)((1-\varphi_1)+\varphi_1\frac{\rho_{s1}}{\rho_f})+\varphi_2\rho_{s2})}$
Dynamic viscosity	$\mu_f = \mu_{nf}(1-\varphi)^{2.5}$	$\mu_f = \mu_{hnf}(1-\varphi_1)^{2.5}(1-\varphi_2)^{2.5}$
Electrical conductivity	$\sigma_f = \frac{\sigma_{nf}}{(1+\frac{(\frac{\sigma_s}{\sigma_f}-1)\varphi}{(\frac{\sigma_s}{\sigma_f}+2)-(\frac{\sigma_s}{\sigma_f}-1)\varphi})}$	$\sigma_{bf} = \frac{\sigma_{hnf}}{(1+\frac{3\varphi(\varphi_1\sigma_1+\varphi_2\sigma_2-\sigma_{bf})(\varphi_1+\varphi_2))}{(\varphi_1\sigma_1+\varphi_2\sigma_2+2\varphi\sigma_{bf}-\varphi\sigma_{bf}(\varphi_1\sigma_1+\varphi_2\sigma_2-\sigma_{bf}(\varphi_1+\varphi_2)))})}$
Thermal conductivity	$k_f = \frac{k_{nf}}{(\frac{k_s+(n-1)k_f-(n-1)(k_f-k_s)\varphi}{k_s+(n-1)k_f+(k_f-k_s)\varphi})}$	$k_{bf} = \frac{k_{hnf}}{(\frac{k_{s2}+(n-1)k_{bf}-(n-1)(k_{bf}-k_{s2})\varphi_2}{k_{s2}+(n-1)k_{bf}+(k_{bf}-k_{s2})\varphi_2})}$ and $k_f = \frac{k_{bf}}{(\frac{k_{s1}+(n-1)k_f-(n-1)(k_f-k_{s1})\varphi_1}{k_{s1}+(n-1)k_f+(k_f-k_{s1})\varphi_1})}$
Heat capacitance	$(\rho C_p)_f = \frac{(\rho C_p)_{nf}}{(1-\varphi)+\varphi\frac{(\rho C_p)_s}{(\rho C_p)_f}}$	$(\rho C_p)_s = \frac{(\rho C_p)_{hnf}}{(1-\varphi_2)((1-\varphi_1)+\varphi_1\frac{(\rho C_p)_{s1}}{(\rho C_p)_f})+\varphi_2(\rho C_p)_{s2}}$
Thermal expansion coefficient	$(\rho\beta)_f = \frac{(\rho\beta)_{nf}}{(1-\varphi)+\varphi\frac{(\rho\beta)_s}{(\rho\beta)_f}}$	$(\rho\beta)_f = \frac{(\rho\beta)_{hnf}}{(1-\varphi_2)((1-\varphi_1)+\varphi_1\frac{(\rho\beta)_{s1}}{(\rho\beta)_f})+\varphi_2(\rho\beta)_{s2}}$

$$w_{(y,0)} = 0, T_{(y,0)} = T_o, N_{(y,0)} = N_o; \forall y \geq 0 \quad (4)$$

$$w_{(0,t)} = 0, T_{(0,t)} = T_o, N_{(0,t)} = N_o; \quad y = 0 \quad (5)$$

$$w_{(d,t)} = U_o H(t) \cos(\omega t), \left. \frac{\partial T}{\partial y} \right|_{y=d} = -\frac{h}{k} T_{(d,t)}, N_{(d,t)} = N_w \quad (6)$$

The initial conditions of the entire system are considered in Eq. 4 at $t = 0$, where in Eq. 5, the boundary conditions are taken at $y = 0$ in which the whole system is in a rest position for $y = 0$, where in the last boundary condition (6) at $y = d$, the rate of shear stress and the Newtonian heating effect are considered with the constant bioconvection parameter. Now that the following dimensionless variables have been included, the linked governed equations may not be analyzed with the dimension of influence of all influencing parameters as follows:

$$\begin{aligned} w^* &= \frac{d}{\nu_f} w, t^* = \frac{\nu_f}{d^2} t, y^* = \frac{y}{d}, T^* = \frac{T_{(y,t)} - T_o}{T_w - T_o}, \\ N^* &= \frac{N_{(y,t)} - N_o}{N_w - N_o}, \lambda_{hnf} = \frac{k_{hnf}}{k_f}, \\ Sc &= \frac{\nu}{D}, M = \frac{\sigma_f d^2 B_o^2}{\mu_f}, Gr = \frac{g \beta_T d^3 (T_w - T_o)}{\nu^2}, \\ Ra &= \frac{\gamma(\rho_m - \rho)(N_w - N_o)}{\rho_f (\beta_T)_f (T_w - T_o)}, N = \frac{Gm}{Gr}, \\ K_{eff} &= \frac{\nu \varphi}{K^* U_o^2}, Pr = \frac{\mu_f C_p}{k_f}, Gm = \frac{g \beta_C (N_w - N_o) d^3}{\nu^2}, \\ \phi_o &= (1 - \varphi) + \varphi \frac{\rho_s}{\rho_f}, \\ \phi_1 &= \frac{1}{(1 - \varphi)^{2.5}}, \phi_2 = 1 + \frac{3\left(\frac{\sigma_s}{\sigma_f} - 1\right)\varphi}{\left(\frac{\sigma_s}{\sigma_f} + 2\right) - \left(\frac{\sigma_s}{\sigma_f} - 1\right)\varphi}, \\ \phi_3 &= (1 - \varphi) + \varphi \frac{(\rho\beta_T)_s}{(\rho\beta_T)_f}, \\ \Lambda_o &= (1 - \varphi) + \varphi \frac{(\rho\beta_C)_s}{(\rho\beta_T)_f}, \Lambda_1 = \frac{\nu_f}{D_{hnf}}, \end{aligned}$$

and utilizing the aforementioned none-dimensional constraints in the governed equations and conditions (1)–(6), one can obtain the

following results by adjusting the abovementioned dimensionless variables while ignoring the “*” symbols:

$$\begin{aligned} \phi_o \frac{\partial w_{(y,t)}}{\partial t} &= \phi_1 \frac{\partial^2 w_{(y,t)}}{\partial y^2} - \beta_1 w_{(y,t)} - (\phi_2 M \sin(\theta) + K_{eff}) w_{(y,t)} \\ &+ Gr(\phi_3 T_{(y,t)} - Ra N_{(y,t)}), \end{aligned} \quad (7)$$

$$\Lambda_o \frac{\partial T_{(y,t)}}{\partial t} = \frac{\partial^2 T_{(y,t)}}{\partial y^2}, \quad (8)$$

$$\Lambda_1 \frac{\partial N_{(y,t)}}{\partial t} = \frac{\partial^2 N_{(y,t)}}{\partial y^2}, \quad (9)$$

with consistent dimensionless circumstances

$$w_{(y,0)} = 0, T_{(y,0)} = 0, N_{(y,0)} = 0, \quad (10)$$

$$w_{(0,t)} = 0, T_{(0,t)} = 0, N_{(0,t)} = 0, \quad (11)$$

$$w_{(d,t)} = H(t) \cos(\omega t), \left. \frac{\partial T}{\partial t} \right|_{y=d} = -(1 + T_{(d,t)}), N_{(d,t)} = 1, \quad (12)$$

where $M, Gr, \beta_1, K_{eff}, Gm, Ra$ stand for the applied magnetic field constraint, heat Grashof number, Brinkman fluid parameter, porosity, mass Grashof number, and the dimensionless bioconvection Rayleigh number, respectively. The hybrid nanofluid model, base material, and solid nanoparticles' thermal characteristics are listed in Tables 1 and 2.

3 Basic preliminaries

In the fractional modeling of the set, as mentioned previously for the governing equations, the ABC (Atangana and Baleanu, 2016) and CF (Caputo and Fabrizio, 2015) formulations are employed, and these temporal derivatives are specified as follows:

$${}^{ABC} \mathfrak{D}_t^\beta f(y, t) = \frac{1}{1 - \beta} \int_0^t E_\beta \left(\frac{\beta(t - \tau)^\beta}{1 - \beta} \right) \frac{\partial f(y, \tau)}{\partial \tau} d\tau,$$

with its LT

TABLE 2 Thermal features of nanoparticles and regular fluids.

Material	$NaC_6H_7O_6$	H_2O	TiO_2	Ag
$\rho(kg/m^3)$	989	997.1	425	10,500
$C_p(J/kgK)$	4,175	4,179	6,862	235
$k(W/mK)$	0.6376	0.613	8.9538	429
$\beta_T \times 10^{-5}(K^{-1})$	18	21	0.9	1.89

$$\mathcal{L}\{\Lambda_o^{ABC} \mathfrak{D}_t^\beta f(y, t)\} = \frac{q^\beta \mathcal{L}\{f(y, t)\} - q^{\beta-1} f(y, 0)}{(1-\beta)q^\beta + \beta}. \quad (13)$$

The mathematical form of the CF-fractional derivative is (Caputo and Fabrizio, 2015)

$${}^{CF}\mathfrak{D}_t^\alpha g(y, t) = \frac{1}{1-\alpha} \int_0^t \exp\left(\frac{\alpha(1-\tau)}{1-\alpha}\right) g'(\tau) d\tau,$$

and the LT of the CF-fractional derivative is

$$\mathcal{L}\{{}^{CF}\mathfrak{D}_t^\alpha g(y, t)\} = \frac{s\mathcal{L}\{g(y, t)\} - g(y, 0)}{(1-\alpha)s + \alpha}. \quad (14)$$

4 Solution with the AB-fractional derivative

4.1 Solution of the temperature profile

The solution of the non-dimensional equation of the temperature field can be represented as follows in the sense of the AB-time fractional derivative:

$$\Lambda_o^{ABC} \mathfrak{D}_t^\beta T(y, t) = \frac{\partial^2 T(y, t)}{\partial y^2},$$

with

$$\left. \frac{\partial T}{\partial y} \right|_{y=d} = -(1 + T_{(1,t)}), T_{(0,t)} = 0.$$

The result of the temperature field can be found by applying the Laplace transformation to the abovementioned equation and utilizing the relevant conditions as follows:

$$\bar{T}_{(y,q)} = \frac{1}{q \left(\sqrt{\frac{\Lambda_o q^\beta}{(1-\beta)q^\beta + \beta}} - 1 \right)} \frac{\text{Sinh} \left[y \sqrt{\frac{\Lambda_o q^\beta}{(1-\beta)q^\beta + \beta}} \right]}{\text{Sinh} \left[\sqrt{\frac{\Lambda_o q^\beta}{(1-\beta)q^\beta + \beta}} \right]}. \quad (15)$$

The Laplace inverse of the solution, as described previously, will be numerically evaluated using Stehfest and Tzou's methods in Tables 3–5.

4.2 Solution of the bioconvection profile

In terms of the AB-time fractional derivative, the solution of a non-dimensional equation of the bioconvection profile may be attained by employing the Laplace transformation on the governed equations in terms of the AB-time fractional derivative, and we get

$$\Lambda_1 \left(\frac{q^\beta}{(1-\beta)q^\beta + \beta} \right) \bar{N}_{(y,q)} = \frac{\partial^2 \bar{N}_{(y,q)}}{\partial y^2}, \quad (16)$$

with the corresponding conditions

$$\bar{N}_{(1,q)} = \frac{1}{q}, \bar{N}_{(0,q)} = 0.$$

By using the aforementioned conditions and Eq. 16, the solution of the bioconvection profile can be derived as

$$\bar{N}_{(y,q)} = \frac{1}{q} \frac{\text{Sinh} y \left[\sqrt{\frac{\Lambda_1 q^\beta}{(1-\beta)q^\beta + \beta}} \right]}{\text{Sinh} \left[\sqrt{\frac{\Lambda_1 q^\beta}{(1-\beta)q^\beta + \beta}} \right]}. \quad (17)$$

TABLE 3 Numerical analysis of numerical algorithms at different times.

y	$T_{(y,t)}$ by Stehfest	$T_{(y,t)}$ by Tzou's	$N_{(y,t)}$ by Stehfest	$N_{(y,t)}$ by Tzou's	$W_{(y,t)}$ by Stehfest	$W_{(y,t)}$ by Tzou's
0.1	0.0280	0.0294	0.0617	0.0630	0.1603	0.1643
0.2	0.0566	0.0595	0.1254	0.1279	0.3151	0.3229
0.3	0.0866	0.0908	0.1933	0.1969	0.4584	0.4689
0.4	0.1158	0.1240	0.2674	0.2719	0.5839	0.5986
0.5	0.1531	0.1599	0.3502	0.3554	0.6845	0.7021
0.6	0.1913	0.1991	0.4442	0.4498	0.7520	0.7720
0.7	0.2332	0.2426	0.5526	0.5580	0.7770	0.7990
0.8	0.2817	0.2911	0.6786	0.6832	0.7481	0.7724
0.9	0.3361	0.3451	0.8267	0.8236	0.6545	0.6795

TABLE 4 Numerical analysis of governed solutions with the AB- and CF-fractional derivatives at $t = 0.5$

y	$T_{(y,t)}$ by AB	$T_{(y,t)}$ by CF	$N_{(y,t)}$ by AB	$N_{(y,t)}$ by CF	$W_{(y,t)}$ by AB	$W_{(y,t)}$ by CF
0.1	0.0333	0.0360	0.0650	0.0659	1.1174	1.0972
0.2	0.0672	0.0726	0.1320	0.1337	1.0630	1.0432
0.3	0.1023	0.1103	0.2028	0.2053	0.9906	0.9711
0.4	0.1390	0.1495	0.2793	0.2825	0.9018	0.8829
0.5	0.1782	0.1910	0.3639	0.3675	0.7966	0.7782
0.6	0.2204	0.2352	0.4588	0.4626	0.6695	0.6517
0.7	0.2663	0.2828	0.5667	0.5704	0.5092	0.4922
0.8	0.3166	0.3345	0.6901	0.6937	0.2926	0.2764
0.9	0.3724	0.3910	0.8337	0.8356	0.0324	0.0463

TABLE 5 Numerical analysis of the Nusselt number and skin friction coefficient at different times.

α, β	Nu at $t = 0.5$	Nu at $t = 1.0$	C_f at $t = 0.5$	C_f at $t = 1.0$
0.1	0.8830	0.8839	1.8983	0.8842
0.2	0.8821	0.8861	1.8353	0.8332
0.3	0.8807	0.8906	1.7467	0.7590
0.4	0.8791	0.8982	1.6349	0.6644
0.5	0.8771	0.9105	1.4992	0.5483
0.6	0.8768	0.9287	1.3348	0.4067
0.7	0.8762	0.9544	1.1312	0.2318
0.8	0.8717	0.9876	0.8687	0.0892
0.9	0.8294	1.0239	0.5108	0.0285

TABLE 6 Numerical analysis of attained results with the ordinary derivative and Asjad et al. (2022).

α, β	Velocity by AB	Velocity by CF	Velocity by ordinary derivative $\alpha, \beta \rightarrow 1$	Velocity by Asjad et al. (2022)
0.1	0.2151	0.2182	0.2347	0.2264
0.2	0.4236	0.4297	0.4623	0.4460
0.3	0.6186	0.6277	0.6753	0.6516
0.4	0.7928	0.8047	0.8661	0.8357
0.5	0.9385	0.9529	1.0261	0.9903
0.6	1.0483	1.0633	1.1464	1.1064
0.7	1.1082	1.1269	1.2164	1.1742
0.8	1.1118	1.1319	1.2245	1.1822
0.9	1.0445	1.0657	1.1569	1.1172

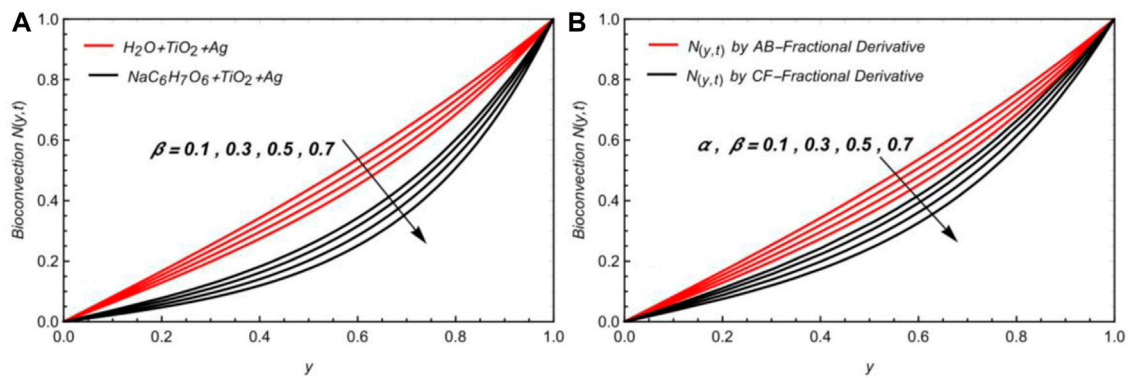


FIGURE 2

$N(y,t)$ due to variation in fractional parameters with $\varphi = 0.02$ and $t = 0.8$.

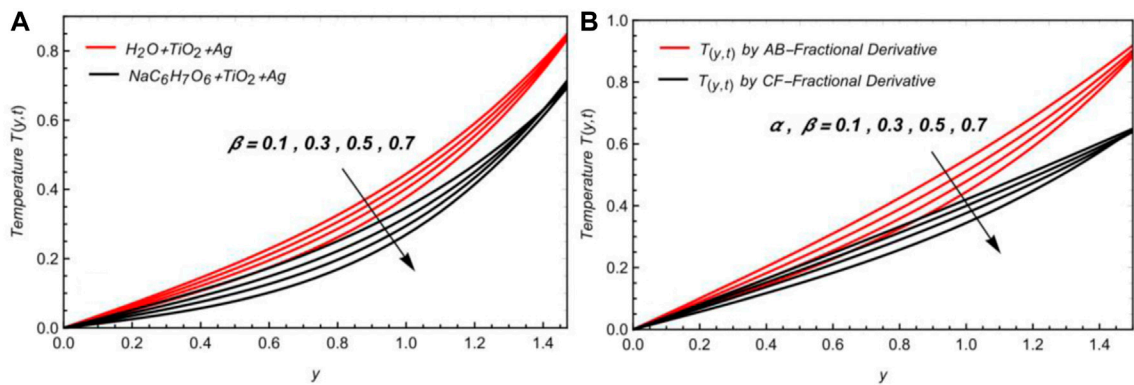


FIGURE 3

$T(y,t)$ due to variation in fractional parameters with $\varphi = 0.02$ and $t = 0.8$.

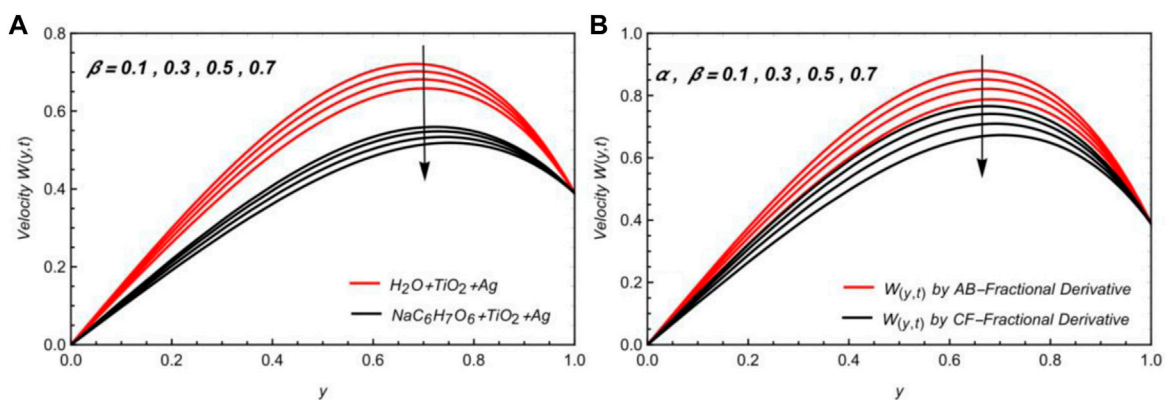


FIGURE 4

$W(y,t)$ due to variation in α, β with $\varphi = 0.02, M = 1.65, Ra = 1.2, K_{eff} = 0.7, Gr = 8.0, Gm = 6.3, \beta_1 = 1.5, \theta = \pi/4$, and $t = 0.8$.

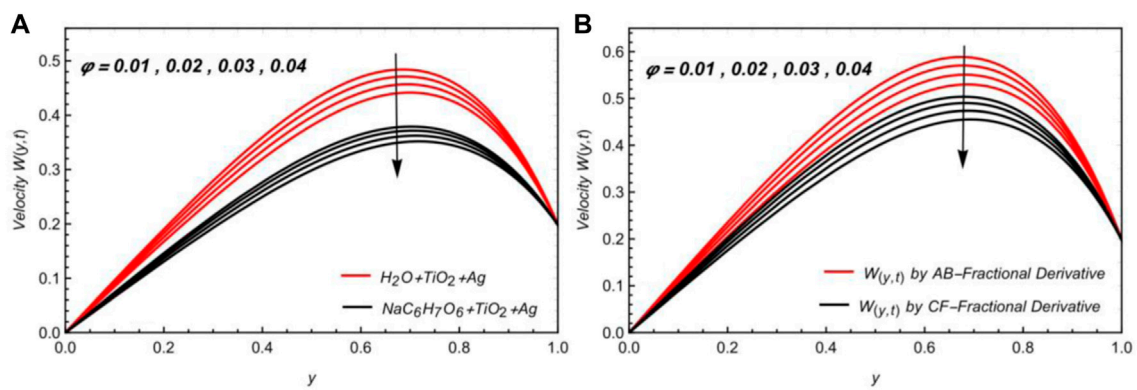


FIGURE 5

$W(y,t)$ due to variation in ϕ with $\alpha, \beta = 0.5, M = 1.65, Ra = 1.2, K_{eff} = 0.7, Gr = 8.0, Gm = 6.3, \beta_1 = 1.5, \theta = \pi/4$, and $t = 0.8$.

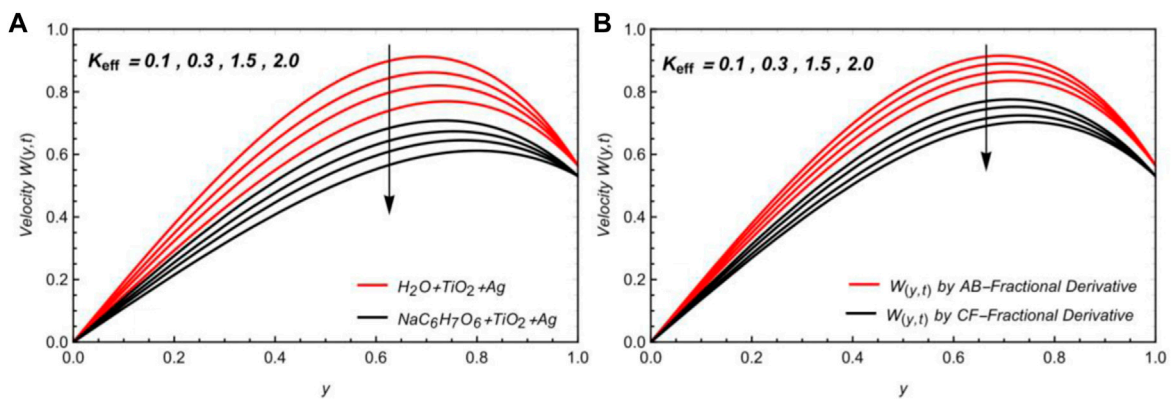


FIGURE 6

$W(y,t)$ due to variation in K_{eff} with $\alpha, \beta = 0.5, \phi = 0.02, M = 1.65, Ra = 1.2, Gr = 8.0, Gm = 6.3, \beta_1 = 1.5, \theta = \pi/4$, and $t = 0.8$.

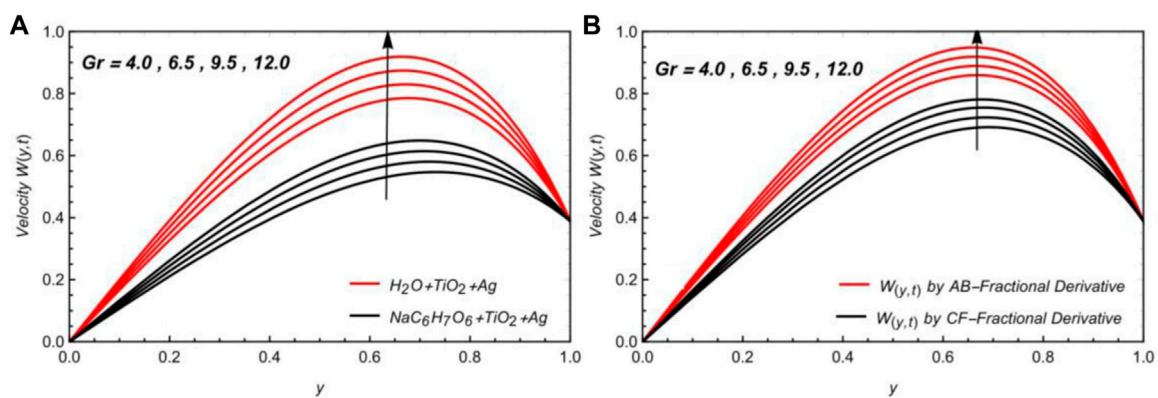


FIGURE 7

$W(y,t)$ due to variation in Gr with $\alpha, \beta = 0.5, \phi = 0.02, M = 1.65, Ra = 1.2, K_{eff} = 0.7, Gm = 6.3, \beta_1 = 1.5, \theta = \pi/4$, and $t = 0.8$.

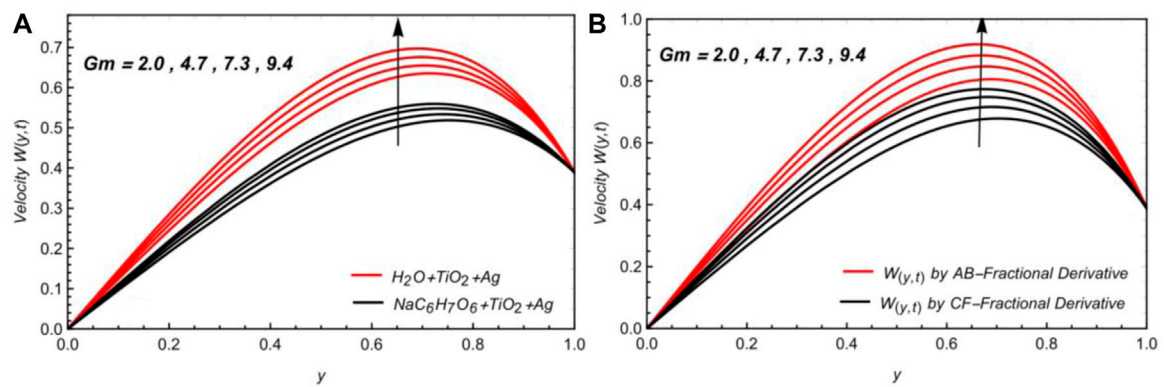


FIGURE 8

$W(y,t)$ due to variation in Gr with $\alpha, \beta = 0.5, \varphi = 0.02, M = 1.65, Ra = 1.2, K_{eff} = 0.7, Gr = 8.0, \beta_1 = 1.5, \theta = \pi/4$, and $t = 0.8$.

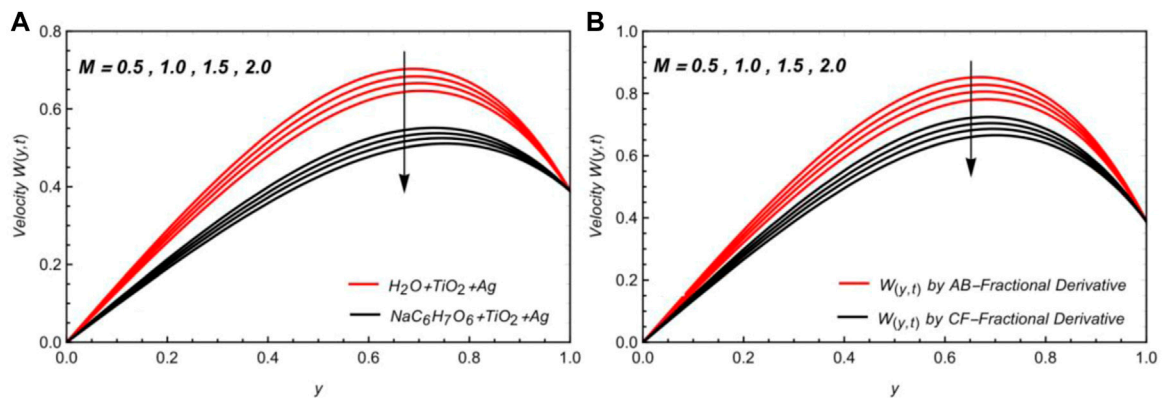


FIGURE 9

$W(y,t)$ due to variation in M with $\alpha, \beta = 0.5, \varphi = 0.02, Ra = 1.2, K_{eff} = 0.7, Gr = 8.0, Gm = 6.3, \beta_1 = 1.5, \theta = \pi/4$, and $t = 0.8$.

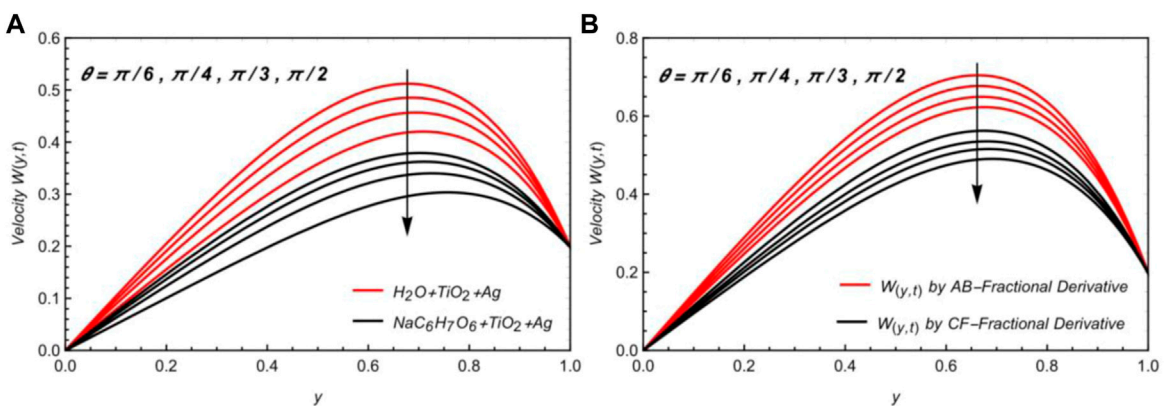


FIGURE 10

$W(y,t)$ due to variation in θ with $\alpha, \beta = 0.5, \varphi = 0.02, M = 1.65, Ra = 1.2, K_{eff} = 0.7, Gr = 8.0, Gm = 6.3, \beta_1 = 1.5$, and $t = 0.8$.

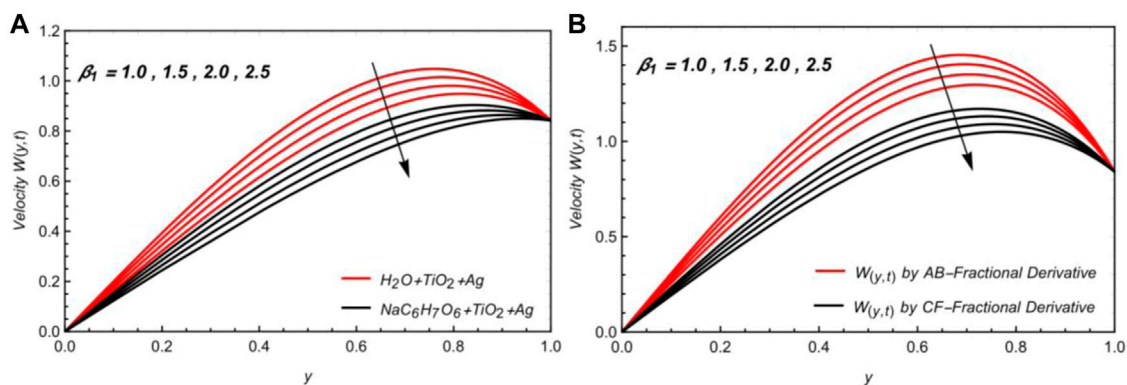


FIGURE 11

$W_{(y,t)}$ due to variation in β_1 with $\alpha, \beta = 0.5, \varphi = 0.02, M = 1.65, Ra = 1.2, K_{eff} = 0.7, Gr = 8.0, Gm = 6.3, \theta = \pi/4$, and $t = 0.8$.

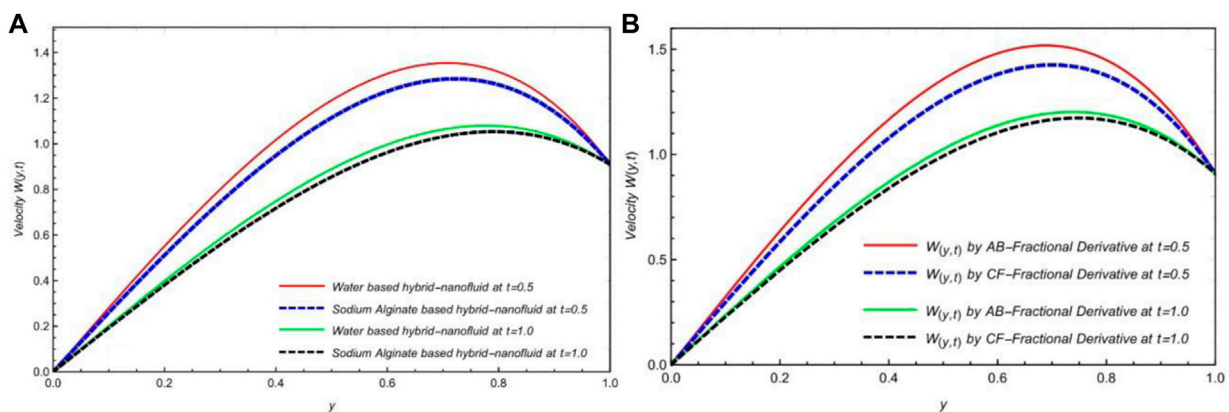


FIGURE 12

Comparison of $W_{(y,t)}$ for AB- and CF-fractional derivatives at (A) $t = 0.5$ and (B) $t = 1.0$.

The Laplace inverse of the aforementioned Eq. 17 will be analyzed numerically in Tables 3–5 with numerical algorithms.

4.3 Solution of the velocity profile

For the solution of the velocity profile by employing the LT on the non-dimensional governed equation of the velocity field in Eq. 7,

$$\frac{\partial^2 \bar{w}_{(y,q)}}{\partial y^2} - \frac{1}{\phi_1} (\phi_2 M \sin(\theta) + K_{eff} + \beta_1 + \phi_o q) \bar{w}_{(y,q)} = -\frac{Gr}{\phi_1} \left(\phi_3 \bar{T}_{(y,q)} - Ra \bar{N}_{(y,q)} \right), \quad (18)$$

with

$\bar{w}_{(d,q)} = \frac{q}{q^2 + \omega^2}$ and $\bar{w}_{(0,q)} = 0$. With the help of the aforementioned conditions, the solution of the momentum profile is as follows:

$$\bar{w}_{(y,q)} = \frac{\text{Sinh} \left(y \sqrt{\frac{1}{\phi_1} (\phi_2 M \sin(\theta) + K_{eff} + \beta_1 + \phi_o q)} \right)}{\text{Sinh} \left(\sqrt{\frac{1}{\phi_1} (\phi_2 M \sin(\theta) + K_{eff} + \beta_1 + \phi_o q)} \right)} \left(\frac{\phi_3 Gr}{q \phi_1 \left(\sqrt{\Lambda_o q^\beta} - \sqrt{(1-\beta)q^\beta + \beta} \right)} \right. \\ \left. \frac{\frac{\Lambda_o q^\beta}{(1-\beta)q^\beta + \beta} - \frac{1}{\phi_1} (\phi_2 M \sin(\theta) + K_{eff} + \beta_1 + \phi_o q)}{+ \frac{Gm}{q \phi_1} \frac{\frac{\Lambda_1 q^\beta}{(1-\beta)q^\beta + \beta} - \frac{1}{\phi_1} (\phi_2 M \sin(\theta) + K_{eff} + \beta_1 + \phi_o q)}{+ \frac{q}{q^2 + \omega^2} - \frac{\phi_3 Gr}{q \phi_1 \left(\sqrt{\Lambda_o q^\beta} - \sqrt{(1-\beta)q^\beta + \beta} \right)}} \right. \\ \left. \frac{\frac{\Lambda_o q^\beta}{(1-\beta)q^\beta + \beta} - \frac{1}{\phi_1} (\phi_2 M \sin(\theta) + K_{eff} + \beta_1 + \phi_o q)}{\text{Sinh} \left(y \sqrt{\frac{\Lambda_o q^\beta}{(1-\beta)q^\beta + \beta}} \right) + \frac{Gm}{q \phi_1} \frac{\frac{\Lambda_o q^\beta}{(1-\beta)q^\beta + \beta}}{\text{Sinh} \left(\sqrt{\frac{\Lambda_o q^\beta}{(1-\beta)q^\beta + \beta}} \right)}} \right. \\ \left. \frac{1}{\frac{\Lambda_1 q^\beta}{(1-\beta)q^\beta + \beta} - \frac{1}{\phi_1} (\phi_2 M \sin(\theta) + K_{eff} + \beta_1 + \phi_o q)} \frac{\text{Sinh} \left(y \sqrt{\frac{\Lambda_1 q^\beta}{(1-\beta)q^\beta + \beta}} \right)}{\text{Sinh} \left(\sqrt{\frac{\Lambda_1 q^\beta}{(1-\beta)q^\beta + \beta}} \right)} \right). \quad (19)$$

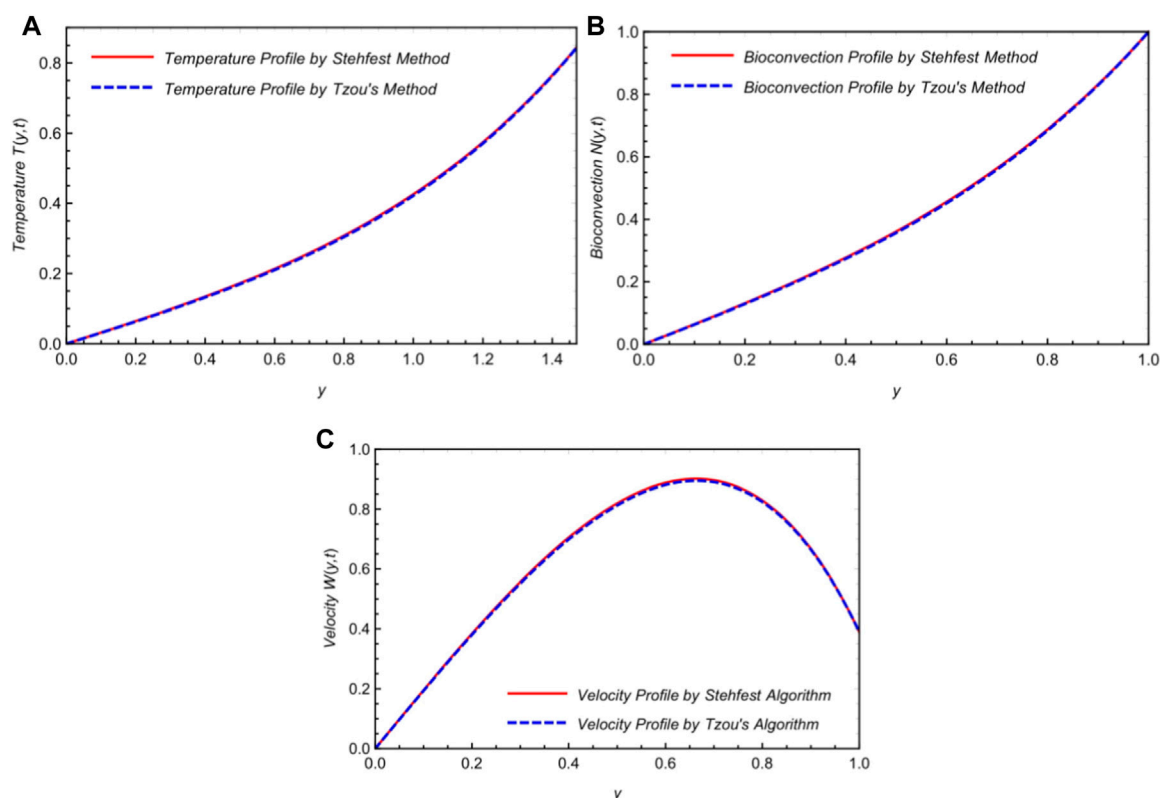


FIGURE 13
Comparison of governed equations for different numerical schemes.

5 Solution with the CF-fractional derivative

5.1 Solution of the temperature field

The following representation shows the evaluation of the non-dimensional temperature field solution using the CF-time fractional derivative

$$\Lambda_{oCF} \mathfrak{D}_t^\alpha T(y,t) = \frac{\partial^2 T(y,t)}{\partial y^2}$$

with

$$\left. \frac{\partial T}{\partial y} \right|_{y=d} = -(1 + T_{(1,t)}), \quad T_{(0,t)} = 0.$$

The solution of the temperature field will be obtained by applying Laplace to the preceding equation and employing the appropriate conditions as follows:

$$\bar{T}_{(y,s)} = \frac{\sqrt{(1-\alpha)s + \alpha}}{s(\sqrt{\Lambda_0 s} - \sqrt{(1-\alpha)s + \alpha})} \frac{\text{Sinh}\left[y\sqrt{\frac{\Lambda_0 b_1 s}{1+(b_1-1)s}}\right]}{\text{Sinh}\left[\sqrt{\frac{\Lambda_0 b_1 s}{1+(b_1-1)s}}\right]}. \quad (20)$$

Using Stehfest and Tzou's techniques in Tables 3–5, the Laplace inverse of the aforementioned solution will be numerically examined.

5.2 Solution of the bioconvection field

By using the Laplace transformation on the guided equations in terms of the CF-time fractional derivative, we gain the solution of a non-dimensional equation of the bioconvection profile as follows:

$$\Lambda_1 \left(\frac{s}{(1-\alpha)s + \alpha} \right) \bar{N}_{(y,s)} = \frac{\partial^2 \bar{N}_{(y,s)}}{\partial y^2},$$

with the following conditions

$$\bar{N}_{(1,s)} = \frac{1}{s}, \quad \bar{N}_{(0,s)} = 0.$$

By using the aforementioned conditions, the solution of the bioconvection profile in terms of the CF-fractional derivative can be derived as follows:

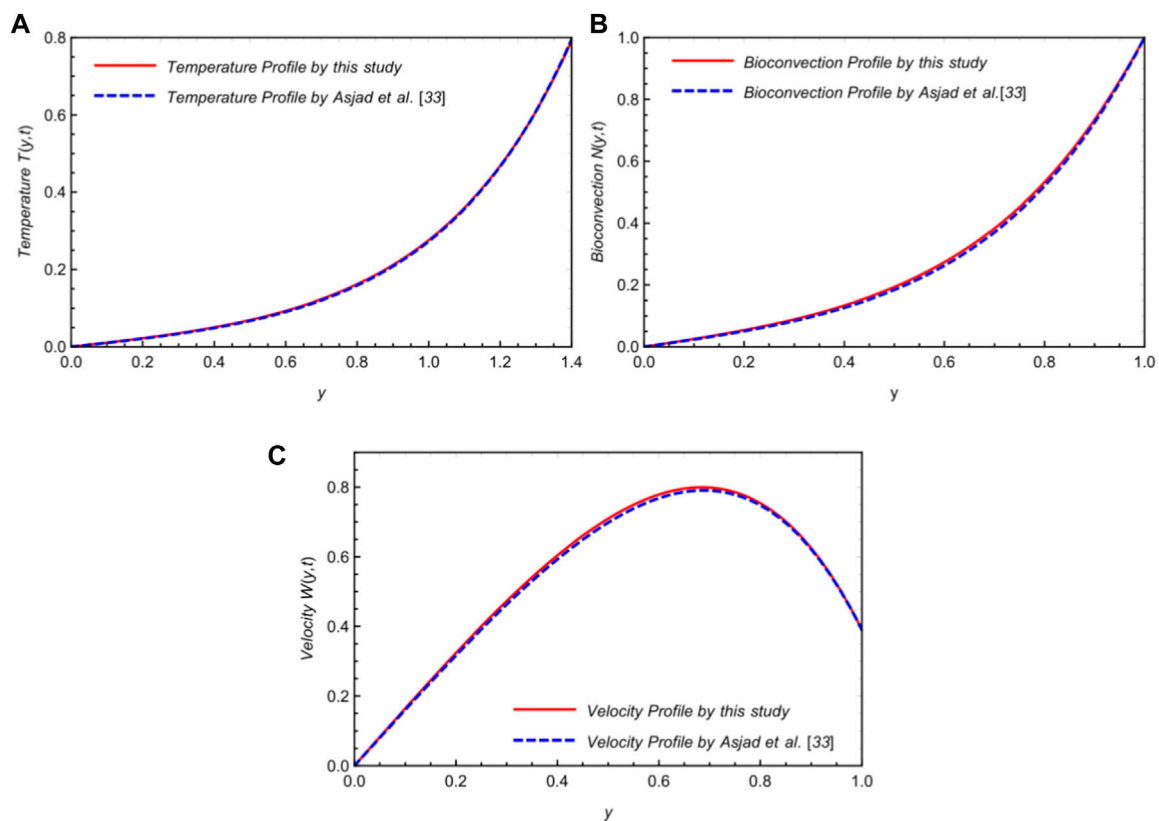


FIGURE 14

Comparison of the validity of governed equations with the attained results of Asjad et al. (2022).

$$\bar{N}_{(y,s)} = \frac{1}{s} \frac{\text{Sinh} y \left[\sqrt{\frac{\Lambda_1 b_1 s}{1+(b_1-1)s}} \right]}{\text{Sinh} \left[\sqrt{\frac{\Lambda_1 b_1 s}{1+(b_1-1)s}} \right]}. \quad (21)$$

The Laplace inverse of Eq. 21 will be numerically analyzed using the techniques in Tables 3–5.

5.3 Solution of the velocity profile

The solution of the velocity profile is obtained by employing the LT on the non-dimensional governed equation of the velocity field (Eq. 7):

$$\phi_1 \frac{\partial^2 \bar{w}_{(y,s)}}{\partial y^2} - (\beta_1 + \phi_0 s) \bar{w}_{(y,s)} - (\phi_2 M \sin(\theta) + K_{eff}) \bar{w}_{(y,s)} + Gr(\phi_3 \bar{T}_{(y,s)} - Ra \bar{N}_{(y,s)}) = 0, \quad (22)$$

with

$$\bar{w}_{(d,s)} = \frac{s}{s^2 + \omega^2} \text{ and } \bar{w}_{(0,s)} = 0$$

$$\begin{aligned} \bar{w}_{(y,s)} = & \frac{\text{Sinh} \left(y \sqrt{\frac{1}{\phi_1} (\phi_2 M \sin(\theta) + K_{eff} + \Theta_1 s)} \right)}{\text{Sinh} \left(\sqrt{\frac{1}{\phi_1} (\phi_2 M \sin(\theta) + K_{eff} + \Theta_1 s)} \right)} \\ & \left(\frac{\phi_3 Gr}{s \phi_1 \left(\sqrt{\frac{\Lambda_0 s}{(1-\alpha)s + \alpha}} - 1 \right)} \frac{1}{(1-\alpha)s + \alpha} - \frac{1}{\phi_1} (\phi_2 M \sin(\theta) + K_{eff} + \Theta_1 s) \right. \\ & \left. + \frac{Gm}{s \phi_1} \frac{\Lambda_1 s}{(1-\alpha)s + \alpha} - \frac{1}{\phi_1} (\phi_2 M \sin(\theta) + K_{eff} + \Theta_1 s) + \frac{s}{s^2 + \omega^2} \right) \\ & - \frac{\phi_3 Gr}{s \phi_1 \left(\sqrt{\frac{\Lambda_0 s}{(1-\alpha)s + \alpha}} - 1 \right)} \frac{1}{(1-\alpha)s + \alpha} - \frac{1}{\phi_1} (\phi_2 M \sin(\theta) + K_{eff} + \Theta_1 s) \\ & \frac{\text{Sinh} \left(y \sqrt{\frac{\Lambda_0 s}{(1-\alpha)s + \alpha}} \right)}{\text{Sinh} \left(\sqrt{\frac{\Lambda_0 s}{(1-\alpha)s + \alpha}} \right)} + \frac{Gm}{s \phi_1} \frac{\Lambda_1 s}{(1-\alpha)s + \alpha} - \frac{1}{\phi_1} (\phi_2 M \sin(\theta) + K_{eff} + \Theta_1 s) \\ & \frac{\text{Sinh} \left(y \sqrt{\frac{\Lambda_1 s}{(1-\alpha)s + \alpha}} \right)}{\text{Sinh} \left(\sqrt{\frac{\Lambda_1 s}{(1-\alpha)s + \alpha}} \right)}. \end{aligned} \quad (23)$$

Analyzing the results of the momentum, concentration, and temperature profiles is difficult. We also employed numerical approaches for the Laplace inverse, specifically Stehfest and Tzou's numerical schemes, as numerous authors have previously performed. The mathematical formulations of these algorithms (Raza et al., 2021a; Raza et al., 2021b; Guo et al., 2021) can be characterized as

$$U(y, t) = \frac{\ln(2)}{t} \sum_{n=1}^N v_n \bar{U}\left(y, n \frac{\ln(2)}{t}\right),$$

$$v_n = (-1)^{n+\frac{N}{2}} \sum_{r=\lfloor \frac{q+1}{2} \rfloor}^{\min(q, \frac{N}{2})} \frac{r^{\frac{N}{2}} (2r)!}{(\frac{N}{2}-r)! (r-1)! (q-r)! (2r-q)!},$$

and

$$U(y, t) = \frac{e^{4.7}}{t} \left[\frac{1}{2} \bar{U}\left(r, \frac{4.7}{t}\right) + \operatorname{Re} \left\{ \sum_{j=1}^N (-1)^j \bar{U}\left(r, \frac{4.7 + k\pi i}{t}\right) \right\} \right].$$

6 Discussion of the results

Bioconvection is investigated by employing the combined effects of porosity and the applied magnetic field on a naturally occurring Brinkman-type flow of a viscous and incompressible HNF (Ag-TiO₂-H₂O and Ag-TiO₂-C₆H₉NaO₇) over two parallel plates. The thermal transmission and fluid flow model is fractionalized with two fractional techniques (AB- and CF-fractional derivatives). The Laplace transformation approach is utilized to solve the governing equations. The impact of different constraints has been analyzed graphically with their ranges as follows:

$0.1 < \alpha, \beta < 0.9$; $0.01 < \varphi < 0.04$; $0.1 < K_{eff} < 2.0$; $4.0 < Gr < 12.0$; $2.0 < Gm < 10$; $0.5 < M < 2.0$; $0 < \theta < \frac{\pi}{2}$; and $0.5 < \beta_1 < 2.5$. Finally, graphical representations are applied to clarify the physical impacts of flow parameters in Figures 2–14.

Figure 2A illustrates the influence of the fractional parameter β on bioconvection. The growing value of β causes a decline in bioconvection. This results in a decrease in bioconvection as the boundary layer enlarges. Figure 2B shows the effects of α, β and both AB and CF-fractional operators on bioconvection, and we noted that bioconvection is also reduced by increasing the fractional parameters α and β . Moreover, the effect of the AB derivative approach is higher than the CF derivative approach, which is due to the different kernels (Mittage–Leffler and exponential-based kernels) of both fractional operators. In fluid mechanics, we usually see that a fractional method is better for controlling the boundary layer viscosity of fluid characteristics. In addition, we found that compared to a silver–titanium dioxide sodium alginate HNF, the bioconvection profile for HNF based on water and silver titanium dioxide has a comparatively larger impact.

Figure 3A shows that the temperature field declined by increasing β . As the boundary layer becomes extensive, the temperature reduces, which is expected. Figure 3B shows the effects of α, β and both AB and CF-fractional operators on the temperature field and notes that the thermal profile is also reduced by increasing fractional parameters α and β . Furthermore, the AB derivative approach has a more substantial impact than the CF approach, which is also a result of the different kernels used by the relevant fractional operators (Mittage–Leffler and exponential-based kernels). Additionally, we discovered that the heat profile for silver–titanium dioxide sodium alginate HNF has a substantially less significant impact than the temperature profile for water–silver–titanium dioxide-based HNF.

Figure 4A shows that the velocity profile is reduced by increasing β , which is due to the effect of the Mittage–Leffler kernel. Figure 4B shows

the effects of α, β and both AB and CF-fractional operators on the velocity profile, and the velocity profile is also reduced by increasing the fractional parameters α and β . This is because as the boundary layer widens, bioconvection and thermal and momentum fields decrease. Typically, a fractional method is preferable in fluid dynamics for adjusting the boundary layer thickness of the fluid characteristics. Furthermore, the effect of the AB approach is higher than the CF approach, which is also due to the different kernels of involved fractional operators. Additionally, we detected that the velocity profile for water–silver–titanium dioxide-based HNF has a relatively more substantial effect than silver–titanium dioxide sodium alginate HNF. The consequence of HNF is represented in Figures 5A, B. The velocity is reduced for a more considerable value of φ . Actually, for greater φ , the velocity is lessened due to the dominance of viscous effects. It was found that the temperature might rise with larger φ values and velocity-indicated drops. In the velocity field, the nanofluid density is significant. When the base fluid and nanoparticles are combined, the resulting hybrid nanofluids become thicker, which reduces the velocity and increases the temperature.

Figures 6A, B represent the velocity diagrams to understand the influence of K_{eff} . The velocity displays a lessening trend for larger values of K_{eff} . When the holes in a porous media are incredibly sufficient, the porous medium's resistance can be disregarded. Consequently, the velocity increases as the porous surface develops resistance to the liquid. The impact of Gr is shown in Figures 7A, B, and it was revealed that growing Gr (more bouncy influence) boots the fluid speed. Since the buoyancy forces increase as Gr rises, the fluid velocity also rises. The velocity is also increased with Gm , as observed in 8a and b. A higher Gm improves the concentration gradient, which raises the buoyant forces, and therefore, the fluid flow rises. Figures 9A, B indicate that the velocity is decreased as we increase the values of M . Physically, it responds to the drag force, which affects the velocity that faces the fluid speed. This is true for large values of M because M strengthens the Lorentz forces, which tend to slow down the velocity. The Lorentz forces are closest to the channel walls and weakest in the center. As a result, the velocity is zero at the channel's edges and maximal in the middle, and therefore, the velocity declines. Figures 10A, B show that the momentum profile is inversely proportional to the inclination angle θ .

The Brinkman parameter β_1 impacts the momentum, and the field is presented in Figures 11A, B. The velocity decreases as the value of β_1 is enlarged. This occurs by growing the estimations of β_1 , and the drag forces are stronger so that the velocity decreases. Figures 12A, B indicate the comparison of the momentum profiles for diverse HNFs (Ag-TiO₂-H₂O and Ag-TiO₂-C₆H₉NaO₇) at different times. We see that Ag-TiO₂-H₂O-based HNF has a significant effect on the velocity profile compared to Ag-TiO₂-C₆H₉NaO₇-based HNF. By adding different NPs in the base fluid, the consequent HNF develops significantly thicker and reduces the velocity. Moreover, it is prominent that the bioconvection, temperature, and momentum profiles for water-based HNF have a relatively progressive value compared to the sodium alginate-based HNF. Furthermore, the effect of the AB approach is higher than the CF approach on the bioconvection, temperature, and velocity fields, which is also due to the different kernels of both fractional operators. To find the numerical inverse Laplace for the temperature, bioconvection,

and velocity fields, Figures 13A–C represent a comparison of Tzou and Stehfest approaches and an overall decent agreement was initiated. Furthermore, to check the reliability of our results, Asjad et al. (2022) examined the consequences for the temperature and bioconvection profiles, as compared in Figures 14A, B. The diagrams indicate that the consequences we accomplished overlap with those obtained by Asjad et al. (2022). Table 3 shows the numerical assessment of the bioconvection, temperature, and momentum fields using various computational techniques. Table 4 provides a numerical analysis of the attained solutions with AB- and CF-fractional derivatives. The numerical possessions of the Nusselt number and skin friction coefficient are shown in Table 5. Table 6 shows the numerical analysis of obtained results with ordinary and published work (Asjad et al., 2022).

7 Conclusion

The free convective flow of an unsteady and incompressible Brinkman-type flow mixed with (Ag, TiO_2) hybrid nanofluid was studied flowing through two parallel poured plates. A fractional model was developed with the recent definitions of fractional derivative, i.e., AB and CF-fractional derivatives, and solved with the help of the Laplace transformation. The impact of different constraints on the attained results of temperature, bioconvection, and the momentum profile was analyzed graphically and numerically. Some remarkable conclusions of this work can be summarized as follows:

- This approach may be broadened to include more varied physical science categories with intricate geometries.
- The enhancing value of Pr_{eff} decelerates both the momentum and thermal profiles.
- The bioconvection profile also decelerates by enhancing the value of fractional constraints.
- The momentum field is enhanced by the parameter Gr, Gm , while declarations are due to M and β_1 .
- The fractional parameter can control the momentum and thermal boundary layer thickness.
- The discovered solutions can aid in accurately interpreting actual data and serve as a tool for testing potential approximations of solutions as necessary.
- The results of Asjad et al. (2022) and the overlap of both curves from the numerical scheme verify the conclusions of this investigation.

The subsequent recommendations are based on methods, expansions, geometries, and analyses and are intended to indicate a future extension of the issue that this study examines. For example, a horizontal plate of constant length and linear velocity may be used to assess the current issue. A Keller Box scheme analysis of the same issue is also possible.

Data availability statement

The raw data supporting the conclusion of this article will be made available by the authors, without undue reservation.

Author contributions

Conceptualization, SME, SE, AR, and UK; methodology, SE, AR, and UK; software, NN, SE, AA, and UK; validation, NN, SE, AR, and UK; formal analysis, AR, SE, and AA; investigation, UK and AA; resources, AR; data curation, AR; writing—original draft preparation, NN, SME, UK, and SE; writing—review and editing, NN, SME, and AA; visualization, SME; supervision, UK; project administration, AA and SE; funding acquisition, SE and AA. All authors have read and agreed to the published version of the manuscript.

Funding

This work received support from Princess Nourah bint Abdulrahman University Researchers Supporting Project number (PNURSP2023R163), Princess Nourah bint Abdulrahman University, Riyadh, Saudi Arabia. In addition, this study is also funded by Prince Sattam bin Abdulaziz University project number (PSAU/2023/R/1444).

Acknowledgments

The authors are thankful for the support of Princess Nourah bint Abdulrahman University Researchers Supporting Project number (PNURSP2023R163), Princess Nourah bint Abdulrahman University, Riyadh, Saudi Arabia. Also, this work is supported via funding from Prince Sattam bin Abdulaziz University project number (PSAU/2023/R/1444).

Conflict of interest

The authors declare that the research was conducted in the absence of any commercial or financial relationships that could be construed as a potential conflict of interest.

Publisher's note

All claims expressed in this article are solely those of the authors and do not necessarily represent those of their affiliated organizations, or those of the publisher, the editors, and the reviewers. Any product that may be evaluated in this article, or claim that may be made by its manufacturer, is not guaranteed or endorsed by the publisher.

References

- Akhtar, S. (2016). Flows between two parallel plates of couple stress fluids with time-fractional Caputo and Caputo-Fabrizio derivatives. *Eur. Phys. J. Plus* 131 (11), 401–413. doi:10.1140/epjp/i2016-16401-3
- Alhussain, Z. A., Renuka, A., and Muthtamilselvan, M. (2021). A magneto-bioconvective and thermal conductivity enhancement in nanofluid flow containing gyrotactic microorganism. *Case Stud. Therm. Eng.* 23, 100809. doi:10.1016/j.csite.2020.100809
- Ali, Q., Al-Khaled, K., Khan, M. I., Khan, S. U., Raza, A., Oreijah, M., et al. (2022). Diffusion phenomenon for natural convection flow of classical hartmann problem due to a cylindrical tube by generalized fourier's theories: A fractional analysis. *Int. J. Mod. Phys. B*, 2350104. doi:10.1142/s0217979223501047
- Ali, Q., Al-Khaled, K., Omar, J., Raza, A., Khan, S. U., Khan, M. I., et al. (2022). Analysis for advection–diffusion problem subject to memory effects and local and nonlocal kernels: A fractional operators approach. *Int. J. Mod. Phys. B*, 2350099. doi:10.1142/s0217979223500996
- Anuar, N. S., Bachok, N., Turkyilmazoglu, M., Arifin, N. M., and Rosali, H. (2020). Analytical and stability analysis of MHD flow past a nonlinearly deforming vertical surface in Carbon Nanotubes. *Alexandria Eng. J.* 59 (1), 497–507. doi:10.1016/j.aej.2020.01.024
- Arif, M., Ali, F., Sheikh, N. A., Khan, I., and Nisar, K. S. (2019). Fractional model of couple stress fluid for generalized Couette flow: A comparative analysis of atangana–baleanu and caputo–fabrizio fractional derivatives. *IEEE Access* 7, 88643–88655. doi:10.1109/access.2019.2925699
- Ashwinkumar, G., Samrat, S., and Sandeep, N. (2021). Convective heat transfer in MHD hybrid nanofluid flow over two different geometries. *Int. Commun. Heat Mass Transf.* 127, 105563. doi:10.1016/j.icheatmasstransfer.2021.105563
- Asjad, M. I., Ikram, M. D., Ali, R., Baleanu, D., and Alshomrani, A. S. (2020). New analytical solutions of heat transfer flow of clay-water base nanoparticles with the application of novel hybrid fractional derivative. *Therm. Sci.* 24 (1), 343–350. doi:10.2298/tsci20s1343a
- Asjad, M. I., Ikram, M. D., Sarwar, N., Muhammad, T., Sivasankaran, S., and Subaihi, S. A. A. (2022). Analysis of fractional bioconvection with hybrid nanoparticles in Channel flow. *Math. Problems Eng.* 2022, 1–14. doi:10.1155/2022/8600591
- Asjad, M. I., Sarwar, N., Ali, B., Hussain, S., Sitthiwiratham, T., and Reunsumrit, J. (2021). Impact of bioconvection and chemical reaction on MHD nanofluid flow due to exponential stretching sheet. *Symmetry* 13 (12), 2334. doi:10.3390/sym13122334
- Atangana, A., and Baleanu, D. (2016). *New fractional derivatives with nonlocal and non-singular kernel: Theory and application to heat transfer model*. arXiv preprint arXiv:1602.03408.
- Atangana, A., and Nieto, J. J. (2015). Numerical solution for the model of RLC circuit via the fractional derivative without singular kernel. *Adv. Mech. Eng.* 7 (10), 168781401561375. doi:10.1177/1687814015613758
- Atangana, A. (2016). On the new fractional derivative and application to nonlinear Fisher's reaction–diffusion equation. *Appl. Math. Comput.* 273, 948–956. doi:10.1016/j.amc.2015.10.021
- Bräuer, F., Trautner, E., Hasslberger, J., Cifani, P., and Klein, M. (2021). Turbulent bubble-laden channel flow of power-law fluids: A direct numerical simulation study. *Fluids* 6 (1), 40. doi:10.3390/fluids6010040
- Caputo, M., and Fabrizio, M. (2015). A new definition of fractional derivative without singular kernel. *Prog. Fract. Differ. Appl.* 1 (2), 73–85.
- Chu, Y. M., Bilal, S., and Hajizadeh, M. R. (2020). *Mathematical methods in the applied sciences*. Hybrid ferrofluid along with MWCNT for augmentation of thermal behavior of fluid during natural convection in a cavity
- D'Ippolito, A., Calomino, F., Alfonsi, G., and Lauria, A. (2021). Flow resistance in open channel due to vegetation at reach scale: A review. *Water* 13 (2), 116. doi:10.3390/w13020116
- Farooq, U., Waqas, H., Khan, M. I., Khan, S. U., Chu, Y.-M., and Kadry, S. (2021). Thermally radioactive bioconvection flow of Carreau nanofluid with modified Cattaneo-Christov expressions and exponential space-based heat source. *Alexandria Eng. J.* 60 (3), 3073–3086. doi:10.1016/j.aej.2021.01.050
- Ge-JiLe, H., Waqas, H., Khan, S. U., Khan, M. I., Farooq, S., and Hussain, S. (2021). Three-dimensional radiative bioconvective flow of a sisko nanofluid with motile microorganisms. *Coatings* 11 (3), 335. doi:10.3390/coatings11030335
- Guo, B., Raza, A., Al-Khaled, K., Khan, S. U., Farid, S., Wang, Y., et al. (2021). Fractional-order simulations for heat and mass transfer analysis confined by elliptic inclined plate with slip effects: A comparative fractional analysis. *Case Stud. Therm. Eng.* 28, 101359. doi:10.1016/j.csite.2021.101359
- Haq, S. U., Khan, M. A., Khan, Z. A., and Ali, F. (2020). MHD effects on the channel flow of a fractional viscous fluid through a porous medium: An application of the Caputo-Fabrizio time-fractional derivative. *Chin. J. Phys.* 65, 14–23. doi:10.1016/j.cjph.2020.02.014
- Ibraheem, G. H., Turkyilmazoglu, M., and Al-Jawary, M. (2022). Novel approximate solution for fractional differential equations by the optimal variational iteration method. *J. Comput. Sci.* 64, 101841. doi:10.1016/j.jocs.2022.101841
- Ikram, M. D., Asjad, M. I., Akgül, A., and Baleanu, D. (2021). Effects of hybrid nanofluid on novel fractional model of heat transfer flow between two parallel plates. *Alexandria Eng. J.* 60 (4), 3593–3604. doi:10.1016/j.aej.2021.01.054
- Mayeli, P., and Sheard, G. J. (2021). Buoyancy-driven flows beyond the boussinesq approximation: A brief review. *Int. Commun. Heat Mass Transf.* 125, 105316. doi:10.1016/j.icheatmasstransfer.2021.105316
- Platt, J. R. (1961). Bioconvection patterns" in cultures of free-swimming organisms. *Science* 133 (3466), 1766–1767. doi:10.1126/science.133.3466.1766
- Podlubny, I. (1999). An introduction to fractional derivatives, fractional differential equations, to methods of their solution and some of their applications. *Math. Sci. Eng.* 198, 340.
- Ramzan, M., Gul, H., Kadry, S., and Chu, Y.-M. (2021). Role of bioconvection in a three dimensional tangent hyperbolic partially ionized magnetized nanofluid flow with Cattaneo-Christov heat flux and activation energy. *Int. Commun. Heat Mass Transf.* 120, 104994. doi:10.1016/j.icheatmasstransfer.2020.104994
- Raza, A., Almusawa, M. Y., Ali, Q., Haq, A. U., Al-Khaled, K., and Sarris, I. E. (2022). Solution of water and sodium alginate-based casson type hybrid nanofluid with slip and sinusoidal heat conditions: A prabhakar fractional derivative approach. *Symmetry* 14 (12), 2658. doi:10.3390/sym14122658
- Raza, A., Khan, I., Farid, S., My, C. A., Khan, A., and Alotaibi, H. (2021). Non-singular fractional approach for natural convection nanofluid with Damped thermal analysis and radiation. *Case Stud. Therm. Eng.* 28, 101373. doi:10.1016/j.csite.2021.101373
- Raza, A., Khan, S. U., Khan, M. I., Farid, S., Muhammad, T., Khan, M. I., et al. (2021). Fractional order simulations for the thermal determination of graphene oxide(GO)and molybdenum disulphide(MoS2)nanoparticles with slip effects. *Case Stud. Therm. Eng.* 28, 101453. doi:10.1016/j.csite.2021.101453
- Raza, A., Khan, U., Eldin, S. M., Alotaibi, A. M., Elattar, S., Prasannakumara, B. C., et al. (2019). Significance of free convection flow over an oscillating inclined plate induced by nanofluid with porous medium: The case of the prabhakar fractional approach. *Micromachines* 13 (11), 2019. doi:10.3390/mi13112019
- Riaz, S., Amir, M., Memon, I. Q., Ali, Q., and Abro, K. A. (2022). A comparative study for solidification of nanoparticles suspended in nanofluids through non-local kernel approach. *Arabian J. Sci. Eng.*, 1–19. doi:10.1007/s13369-022-07493-y
- Samrat, S., Ashwinkumar, G., and Sandeep, N. (2022). Simultaneous solutions for convective heat transfer in dusty-nano and dusty-hybrid nanofluids. *Proc. Institution Mech. Eng. Part E J. Process Mech. Eng.* 236 (2), 473–479.
- Saqib, M., Shafie, S., Khan, I., Chu, Y.-M., and Nisar, K. S. (2020). Symmetric MHD channel flow of nonlocal fractional model of BTF containing hybrid nanoparticles. *Symmetry* 12 (4), 663. doi:10.3390/sym12040663
- Sulochana, C., Aparna, S., and Sandeep, N. (2020). Magnetohydrodynamic MgO/CuO-water hybrid nanofluid flow driven by two distinct geometries. *Heat. Transf.* 49 (6), 3663–3682. doi:10.1002/htj.21794
- Tarasov, V. E. (2019). On history of mathematical economics: Application of fractional calculus. *Mathematics* 7 (6), 509. doi:10.3390/math7060509
- Turkyilmazoglu, M., and Altanji, M. (2023). Fractional models of falling object with linear and quadratic frictional forces considering Caputo derivative. *Chaos, Solit. Fractals* 166, 112980. doi:10.1016/j.chaos.2022.112980
- Turkyilmazoglu, M. (2021). Magnetohydrodynamic moving liquid plug within a microchannel: Analytical solutions. *J. BIOMECHANICAL ENGINEERING-TRANSACTIONS ASME* 143 (1), 011012. doi:10.1115/1.4048713
- Turkyilmazoglu, M. (2022). Transient and passage to steady state in fluid flow and heat transfer within fractional models. *Int. J. Numer. Methods Heat Fluid Flow* 33, 728–750. no. ahead-of-print. doi:10.1108/hff-04-2019-0277
- Waini, I., Ishak, A., and Pop, I. (2019). Hybrid nanofluid flow and heat transfer past a vertical thin needle with prescribed surface heat flux. *Int. J. Numer. Methods Heat Fluid Flow* 29 (12), 4875–4894. doi:10.1108/hff-04-2019-0277
- Yusuf, T. A., Mabood, F., Prasannakumara, B., and Sarris, I. E. (2021). Magneto-bioconvection flow of Williamson nanofluid over an inclined plate with gyrotactic microorganisms and entropy generation. *Fluids* 6 (3), 109. doi:10.3390/fluids6030109
- Zhang, J., Raza, A., Khan, U., Ali, Q., Zaib, A., Weera, W., et al. (2022). Thermophysical study of oldroyd-B hybrid nanofluid with sinusoidal conditions and permeability: A prabhakar fractional approach. *Fractal Fract.* 6 (7), 357. doi:10.3390/fractalfract6070357
- Zheng, Y., Yang, H., Mazaheri, H., Aghaei, A., Mokhtari, N., and Afrand, M. (2021). An investigation on the influence of the shape of the vortex generator on fluid flow and turbulent heat transfer of hybrid nanofluid in a channel. *J. Therm. Analysis Calorim.* 143 (2), 1425–1438. doi:10.1007/s10973-020-09415-2



OPEN ACCESS

EDITED BY

Safia Akram,
National University of Sciences and
Technology, Pakistan

REVIEWED BY

Mustafa Turkyilmazoglu,
Hacettepe University, Türkiye
Animasaun I. L.,
Federal University of Technology, Nigeria

*CORRESPONDENCE

Muhammad Imran Asjad,
✉ Imran.asjad@umt.edu.pk

SPECIALTY SECTION

This article was submitted to Colloidal
Materials and Interfaces,
a section of the journal
Frontiers in Materials

RECEIVED 05 January 2023

ACCEPTED 08 February 2023

PUBLISHED 14 March 2023

CITATION

Bilal S, Ullah A, Shah IA, Asjad MI,
Almusawa MY and Eldin SM (2023),
Analysis of free and forced convections in
the flow of radiative viscous fluid with
oxytactic microorganisms.
Front. Mater. 10:1138313.
doi: 10.3389/fmats.2023.1138313

COPYRIGHT

© 2023 Bilal, Ullah, Shah, Asjad,
Almusawa and Eldin. This is an open-
access article distributed under the terms
of the [Creative Commons Attribution
License \(CC BY\)](#). The use, distribution or
reproduction in other forums is
permitted, provided the original author(s)
and the copyright owner(s) are credited
and that the original publication in this
journal is cited, in accordance with
accepted academic practice. No use,
distribution or reproduction is permitted
which does not comply with these terms.

Analysis of free and forced convections in the flow of radiative viscous fluid with oxytactic microorganisms

S. Bilal¹, Asad Ullah¹, Imtiaz Ali Shah¹, Muhammad Imran Asjad^{2*},
Musawa Yahya Almusawa³ and Sayed M. Eldin⁴

¹Department of Mathematics, AIR University, Islamabad, Pakistan, ²Department of Mathematics, University of Management and Technology Lahore, Lahore, Pakistan, ³Department of Mathematics, Faculty of Science, Jazan University, Jazan, Saudi Arabia, ⁴Center of research, Faculty of Engineering and Technology, Future University in Egypt, New Cairo, Egypt

The prime intend behind the current effort is to explicate flow attributes of magnetically influenced Newtonian fluids toward a stretchable sheet under the novel physical impact of oxytactic microorganisms in a comparative manner for free and forced convections. In addition, modified Fourier and Fick's laws are implemented to examine the change in temperature and concentration distributions in a more realistic manner by accounting thermal and mass relaxation parameters in the flow. The obtained PDEs are reduced into the non-linear ODEs by employing similarity variables. Due to the complexity of parametrically based differential equations, a numerical scheme based on a finite-difference approach is implemented via the MATLAB built-in routine known as BVP4C. Flow-controlling parameter effects on associated distributions are evaluated through graphs and tables. Subsequently, the influence of flow-controlling parameters on associated distributions is revealed through pictures in a comparative manner for different convection regimes. Additionally, the quantities such as heat and mass fluxes along with the density of motile microorganisms are also illustrated. From the thorough analysis of the current investigation, it is inferred that velocity distribution enhances for free and forced convections, whereas the temperature of the fluid diminishes against the mentioned convective regimes. It is manifested that the Nusselt number is more in the situation of free convection instead of the forced convection situation. The magnitude of the skin friction factor is more in case of free convection as compared to the forced convection regime. It is also reported that by uplifting the magnitudes of concentration and thermal relaxation parameters, depreciation in associated heat and mass transfer rate arises. In addition, it is also reported that with the increment in the magnetic field, buoyancy ratio, bioconvection

Abbreviations: A , velocities ratio parameter; Nu_x , Nusselt number; M , magnetic parameter; q_m , mass flux; Λ , buoyancy ratio parameter; Sh_x , Sherwood number; Nr , buoyancy ratio parameter; Nn_x , motile microorganism density number; Rb , bioconvection Rayleigh number; σ^* , Stefan–Boltzmann constant; Pr , Prandtl number; u_w , stretching velocity; Rd , radiation parameter; T_w , temperature at the surface; C_w , concentration at the surface; Sc , Schmidt number; N_w , density of the motile microorganism; Pe , Peclet number of the microorganism at the surface; Lb , bioconvection Lewis number; T_∞ , temperature far away from; σ , microorganism concentration parameter at the surface; q_w , surface heat flux; C_∞ , concentration far away from the surface; k^* , mean absorption coefficient; N_∞ , density of the motile microorganism far away from the surface; δ_1, δ_2 , thermal and concentration relaxation time parameter; q_r , radiative heat flux; U_∞ , free stream velocity; ν , kinematic viscosity; Ψ , stream function; α , thermal diffusivity.

parameters, and Rayleigh number skin friction accelerate, while the behavior is quite opposite in case of stretching the ratio parameter.

KEYWORDS

MHD flow, Newtonian fluid, variable molecular diffusivity, thermal radiation, motile gyrotactic microorganisms

1 Introduction

The region in the flow domain where the local velocity of the fluid tends to zero while the pressure is at its maximum is defined as the stagnation point. The existence of the stagnation region in the flow process over the stretchable surface has received valuable utilization in multiple engineering processes such as cooling of a nuclear reactor, coating dynamics, and vapor deposition. In addition, it is worthwhile to mention that two diversified situations of velocity distribution occur in the neighborhood of the stagnation point due to the relation of the free stream and stretching velocity ratio. In view of the extensive utilization of fluid flow in the stagnant region, several enthusiastic researchers have conducted studies in this direction. We initialize from the work done by Hiemenz (1911) in which he analyzed 2D stagnant flow toward a static semi-infinite wall by heeding an analytical solution. The axisymmetric stagnant flow over a static semi-infinite wall was discussed by Homann (1936). The stagnant flow of the viscous fluid past a deformable stretched sheet was discussed by Mahapatra and Gupta (Ibrahim et al., 2013). They reported that if the stretching

velocity dominates the free stream velocity, the boundary layer thickness exceeds. In addition, they observed that by uplifting the magnitude of the stagnant point parameter, the velocity of the fluid increases. A similarity solution for Navier–Stokes equations was obtained by Mahapatra and Gupta (2003). The formulation of the Navier–Stokes equation for the stagnant flow in the form of partial differential equations was manifested by Wang (2008). Later on, Wang constructed a set of similar variables to transform PDEs into ODEs. A two-dimensional stagnant flow over a stretchable surface was explored by Lok et al. (2011) by accounting the quadratic velocity distribution. The non-orthogonal stagnant flow of the viscous incompressible fluid toward a stretchable sheet was demonstrated by Ishak et al. (2010) and measured for the formation of streamline patterns in the flow distribution. In addition, they also reported that the inclination angle affects the shiftiness of the stagnation point. The stagnation point flow of the non-Newtonian fluid also possesses promising utilization in numerous procedures. In view of its extensive effectiveness, researchers have presented theoretical and experimental studies in recent years. For example, the stagnant flow of the shear

TABLE 1 Comparison of the magnitude of the skin friction coefficient with the existing literature.

A	$f''(0)$			
	Present results	Mustafa et al. (2011)	Mahapatra and Gupta (2002)	Ibrahim et al. (2013)
0.01	0.9980	0.9982	0.9980	0.9980
0.1	0.9694	0.9695	0.9694	0.9694
0.2	0.9181	0.9181	0.9181	0.9181
0.5	0.6673	0.6673	0.6673	0.6673
2.0	2.0175	2.0176	2.0175	2.0175

TABLE 2 Comparison of the magnitude of the Nusselt number with existing studies.

Pr	A	$-\theta'(0)$			
		Present results	Mustafa et al. (2011)	Mahapatra and Gupta (2002)	Ibrahim et al. (2013)
1.0	0.1	0.6022	0.6021	0.603	0.6022
	0.3	0.6255	0.6244	0.625	0.6255
	0.5	0.6924	0.6924	0.692	0.6924
1.5	0.1	0.7768	0.7768	0.777	0.7768
	0.3	0.7971	0.7971	0.797	0.7971
	0.5	0.8648	0.8647	0.863	0.8648

TABLE 3 Variations in skin friction against the buoyancy ratio parameter for forced ($\Lambda < 1$) and free ($\Lambda > 1$) convections.

Nr	$f''(0) (\Lambda > 1)$
0.1	0.1571
0.2	0.2099
0.3	0.2630
0.4	0.3166
0.5	0.3707
Nr	$f''(0) (\Lambda < 1)$
0.1	0.5463
0.2	0.5651
0.3	0.5839
0.4	0.6028
0.5	0.6218

TABLE 4 Variations in the Nusselt number against the radiation parameter Rd for forced ($\Lambda < 1$) and free ($\Lambda > 1$) convections.

Rd	$-\theta'(0) (\Lambda < 1)$
0.5	1.1307
0.6	1.1654
0.7	1.1990
0.8	1.2315
0.9	1.2631
Rd	$-\theta'(0) (\Lambda > 1)$
0.5	1.1783
0.6	1.2164
0.7	1.2534
0.8	1.2893
0.9	1.3243

thinning fluid flowing toward a stretchable sheet under the action of the magnetic field was demonstrated by Hashim et al. (2019). They reported that the thickness of the thermal boundary layer accelerates for uplifting both the magnetic field and non-Newtonian fluid parameters. Multiple solutions for the velocity profile within the critical range of the stagnation point parameter over the stretching/shrinking surface in the rotating frame were heeded by Khan et al. (2022). The evaluation of homogeneous and heterogeneous reactions in the stagnant flow of the viscous fluid over a stretching surface was carried out by Abbas et al. (2015). It was reported by them that solutions for velocity and concentration profiles exist only for specific values of the velocity ratio parameter. The 2D boundary layer flow of the viscous incompressible fluid toward a stretchable sheet was explored by

TABLE 5 Variations in skin friction against different parameters.

A	M	Nr	Rb	Λ	$-f''(0)$
0.1	0.0	0.1	0.1	0.1	0.9382
0.2					0.8873
0.3					0.8193
0.4					0.7359
	1.0				1.2902
	2.0				1.5690
	3.0				1.8066
		0.4			0.9558
		0.7			0.9736
		1.0			0.9917
			0.4		0.9683
			0.7		1.0006
			1.0		1.0373
				0.2	0.9073
				0.3	0.8769
				0.4	0.8467

Chamkha (2015). The results for the impacts of both variable thickness and radiation parameters on the fluid flow were obtained by them. The stagnation point flow of the viscous fluid in a stratified medium along with permeability aspects was evaluated by Khashi'ie et al. (2020).

The process in which molecules diffuse from the region of higher to lower thermal convective potential is called heat convection. Mesmerizing applications of the thermal exchange procedure are revealed in electronic device cooling, nuclear reactor cooling, generation of power, production of energy, and so forth as referred (Mirzaei and Mehdi, 2012; Hosseinzadeh et al., 2013; Dehghan and Abbaszadeh, 2016; Shirvan et al., 2017a; Shirvan et al., 2017b; Dehghan and Abbaszadeh, 2017; Ellahi et al., 2017; Esfahani et al., 2017; Kamranian et al., 2017; Rashidi et al., 2017). In the past, the propagation of heat was considered with infinite speed in accordance with the Fourier law of heat conduction principle (Fourier JBJ., 1822). However, due to the formation of thermal singularities and more passive use of controlled heat in different phenomena, Cattaneo–Christov (Cattaneo and Calore, 1948) modified the existing law by adding the thermal relaxation term (Christov, 2009). This new development has opened new arenas for researchers to work, and nowadays, researchers are incorporating modified laws instead of using old version of laws. Bilal et al. (2021) scrutinized heat and mass transfer characteristics in the Maxwell fluid by obliging modified Fourier and Fick's laws. The effectiveness of heat and mass transfer control via implementing modified laws in cooling procedures was evaluated by Lyu et al. (2022). Heat transfer in an annulus by varying the shape and number of fins was explored by Madhavadas et al. (2021). They deduced that the efficiency of the heat exchanger is conclusively dependent on the orientation of fins.

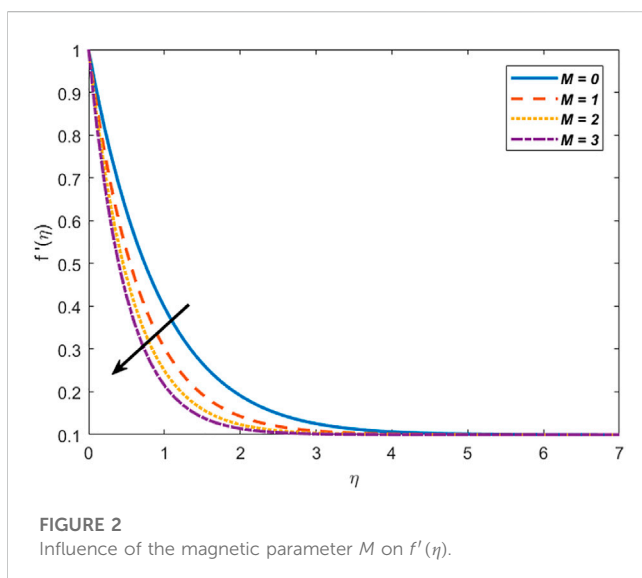
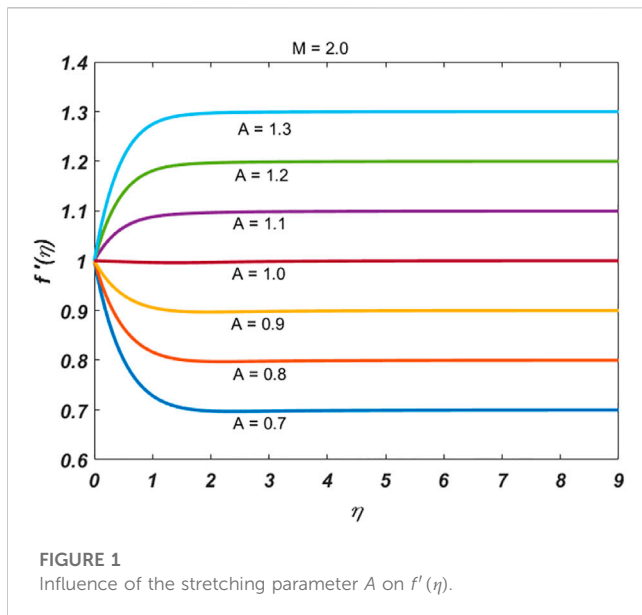
TABLE 6 Variations in the Nusselt, Sherwood, and motile microorganism density numbers against various parameters.

δ_1	δ_2	Rd	Sc	Pe	Lb	σ	$Nu_x Re_x^{-1/2}$	$Sh_x Re_x^{-1/2}$	$Nn_x Re_x^{-1/2}$
0.01	0.02	0.1	1.0	0.1	0.1	0.1	0.8376	0.3344	0.1821
0.02							0.8389	0.3343	0.1820
0.03							0.8403	0.3342	0.1813
0.04							0.8416	0.3341	0.1754
	0.04						0.8377	0.3372	0.1825
	0.06						0.8378	0.3360	0.1823
	0.09						0.8379	0.3352	0.1822
		0.3					0.8883	0.3353	0.1825
		0.5					0.9330	0.3362	0.1828
		0.7					0.9732	0.3371	0.1831
			1.3				0.8316	0.4052	0.1898
			1.5				0.8404	0.4484	0.1945
			1.7				0.8411	0.4889	0.1988
				0.3			0.8429	0.3394	0.2430
				0.5			0.8471	0.3431	0.3068
				0.7			0.8505	0.3462	0.3730
					0.3		0.8491	0.3452	0.2910
					0.5		0.8555	0.3508	0.3994
					0.7		0.8591	0.3537	0.4959
						0.3	0.8383	0.3351	0.1871
						0.5	0.8389	0.3357	0.1921
						0.7	0.8396	0.3363	0.1971

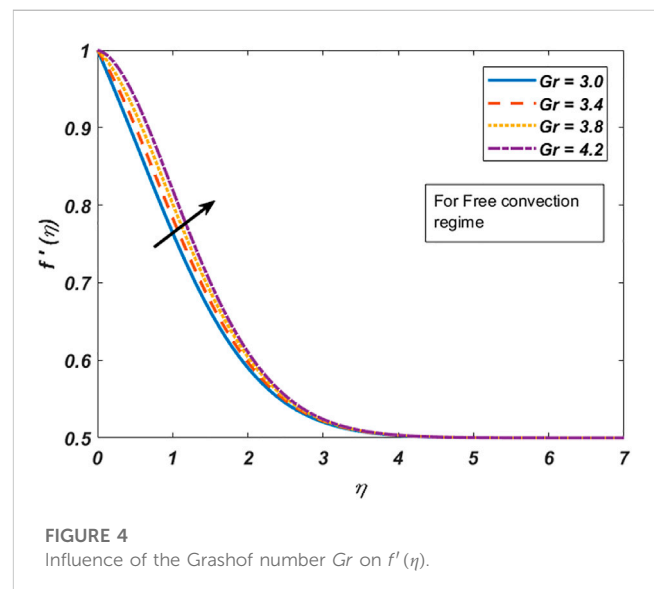
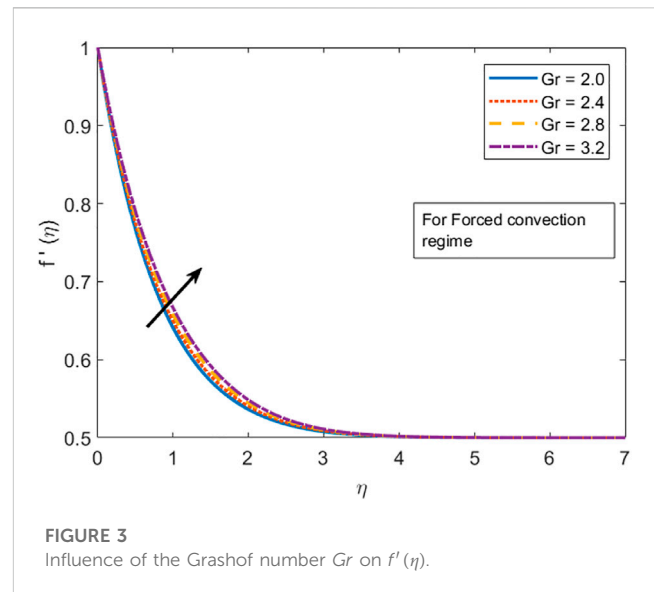
Formation of thermal boundary layer thickness in hydrothermal flow of viscous fluid over a vertical surface along with advection phenomenon was investigated by (Zhao et al., 2022).

Density differences generated due to the diffusion of microorganisms is known as bioconvection. Hydrothermal characteristics of poorly conducting liquids are improved by the swimming of microorganisms. The inclusion of microorganisms in the flow field increased their utility in the biotechnological field such as in biofuel production and fertilizer production. The phenomenon discussing the motion of microorganisms is known as gyrotaxis. Since most microorganisms are sensitive to oxygen and light, they are characterized into gyrotactic and oxytactic. Tremendous effort has been taken in the direction of bioconvective flow in recent years due to overwhelming utilizations. The influence of the radiative heat flux and gyrotactic microorganism on the fluid flow toward a stretchable sheet was explored by Chamkha et al. (2017). Khan (2018) highlighted the effects of gyrotactic microorganisms on the second-grade stratified nanofluid. The influence of gyrotactic microorganisms on the Powell–Eyring nanofluid was illustrated by Pal et al. (2019). The behavior of the magneto Jeffery fluid toward a vertical cone accompanied with nanoparticles and gyrotactic microorganisms

was explored by Saleem et al. (2019). The influence of gyrotactic microorganisms on the power law fluid over a stretchable sheet was explored by Ferdows et al. (2019). Numerical solutions for a water-based nanofluid over a stretchable surface along with the effects of motile gyrotactic microorganisms were explored by De (2019). Later on, Kuznetsov (2011) explored biothermal characteristics on the suspension of nanoparticles along with gyrotactic microorganisms. The impact of velocity slip and thermal radiation on the MHD hybrid nanofluid flow over a permeable sheet was investigated by Wahid et al (2020). Mustafa (2021a) investigated the stagnant flow toward a stretchable sheet or a circular cylinder. The prime intend behind this investigation was to target the exact solution for both momentum and thermal fields. It was also reported that the axial velocity and thermal distributions got suppressed under the stretching impacts. The influence of the MHD steady 2D mixed convective flow due to the non-linear surface in carbon nanotubes was investigated by Mustafa et al. (Syazana et al., 2020). A mathematical demonstration about enhancement in the rate of heat transfer by considering the stretching surface was explored by Mustafa (2021b). Some latest studies on the bioconvective flow are those of Khan et al. (2014), Cao et al. (2022), Sajid et al. (2022), and Prasad et al. (2023).



From the aforementioned literature, the current work comprises the novel influence of the oxytactic microorganism species, variable molecular diffusivity, and Cattaneo–Christov diffusion on the stagnant flow of the viscous fluid flowing toward a stretchable sheet. Oxytactic microorganisms such as bacteria are used for water purification in the drinking water treatment system. Removal of contaminants from water through bioconvection and biodegradation is a life savior. In addition, consideration of the Cattaneo–Christov heat flux model is helpful in controlling heat and mass transfer in the HVAC industry, fire alarms and extinguishers, fuel production, food preservation, and so many other areas. This model makes the study of different systems' working in daily life more realistic. Lastly, the disclosure of variable molecular diffusivity instead of assuming it linear is more appropriate because in thermosolutal diffusion, the particles move randomly instead of moving on a linear path.



So, it is highly important to assume it variable. In view of the aforementioned originality and significance, the present study is conducted.

2 Mathematical modeling

Let us consider the 2D incompressible mixed convective steady and stagnant flow of the viscous fluid over a stretching sheet. The sheet is stretched along the x -axis. The process of mixed convection is taken into account due to the transfer of heat. The effects of oxytactic microorganisms and modified Fourier and Fick's law are encompassed, respectively.

The mass flux equation for the considered problem is represented as follows:

$$\frac{\partial u}{\partial x} + \frac{\partial v}{\partial y} = 0. \quad (1)$$

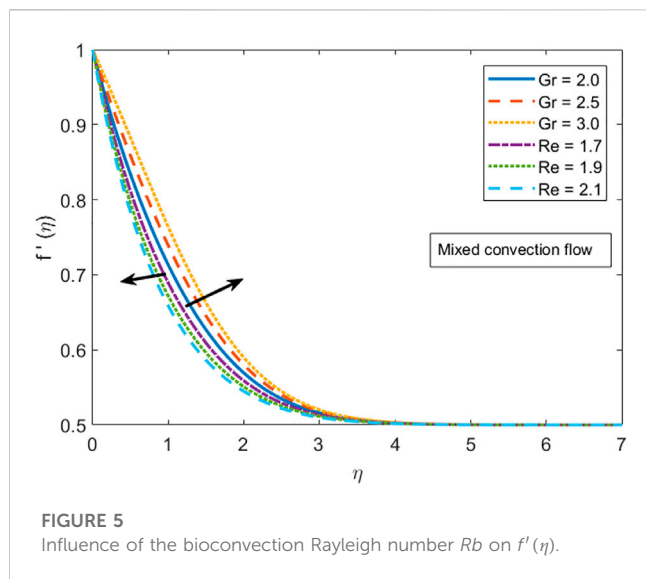


FIGURE 5
Influence of the bioconvection Rayleigh number Rb on $f'(\eta)$.

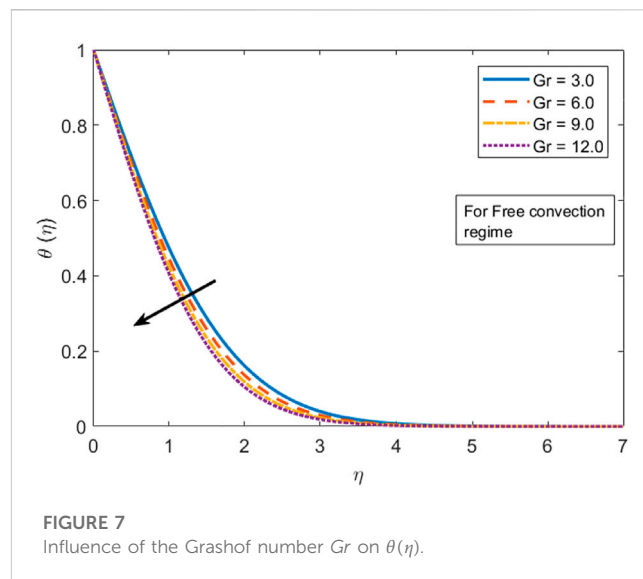


FIGURE 7
Influence of the Grashof number Gr on $\theta(\eta)$.

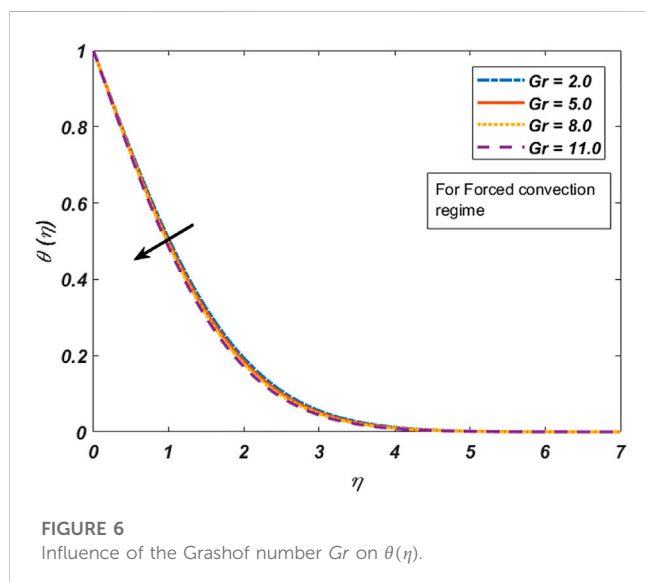


FIGURE 6
Influence of the Grashof number Gr on $\theta(\eta)$.

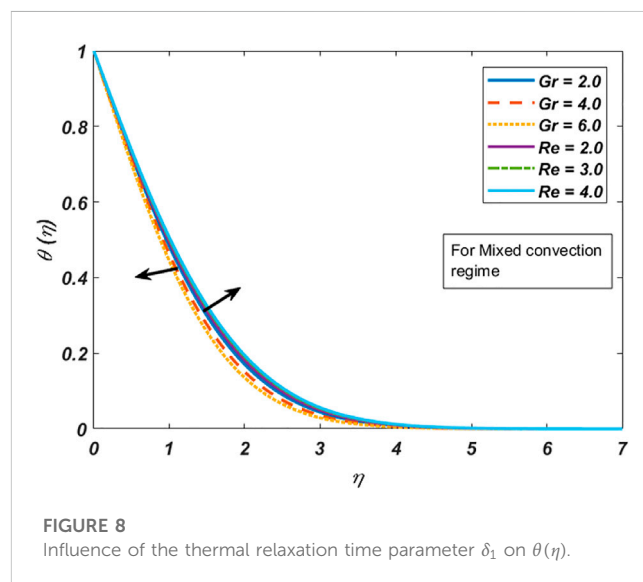


FIGURE 8
Influence of the thermal relaxation time parameter δ_1 on $\theta(\eta)$.

Governing momentum equations by employing the boundary layer approach are shown as follows, as in Cao et al. (2022) and Prasad et al. (2023):

$$u \frac{\partial u}{\partial x} + v \frac{\partial u}{\partial y} = U_{\infty} \frac{\partial U_{\infty}}{\partial x} + \nu \frac{\partial^2 u}{\partial y^2} + \frac{\sigma B_0^2}{\rho_f} (U_{\infty} - u) + \frac{g}{\rho_f} [\beta \rho_f (1 - C_{\infty}) (T - T_{\infty}) - (\rho_p - \rho_f) (C - C_{\infty}) - (\rho_m - \rho_f) (N - N_{\infty})]. \quad (2)$$

Modeled energy, concentration, and motile microorganism mass density equations are expressed as follows, referring to Prasad et al. (2023):

$$u \frac{\partial T}{\partial x} + v \frac{\partial T}{\partial y} + \lambda_E \phi_E = \alpha \frac{\partial^2 T}{\partial y^2} - \frac{1}{\rho c_p} \frac{\partial q_r}{\partial y}, \quad (3)$$

$$u \frac{\partial C}{\partial x} + v \frac{\partial C}{\partial y} + \lambda_C \phi_C = D \frac{\partial^2 C}{\partial y^2}, \quad (4)$$

$$u \frac{\partial N}{\partial x} + v \frac{\partial N}{\partial y} = D_m \frac{\partial^2 N}{\partial y^2} - \frac{bW_c}{C_w - C_{\infty}} \frac{\partial}{\partial y} \left(N \frac{\partial C}{\partial y} \right), \quad (5)$$

where λ_E and λ_C are the dimensional thermal and concentration relaxation parameters derived from Cattaneo–Christov heat and mass flux relations.

Associated boundary conditions are as follows:

$$u = u_w = ax, v = 0, T = T_w, C = C_w, N = N_w \quad \text{at } y = 0 \quad \text{and} \\ u \rightarrow U_{\infty} = bx, T \rightarrow T_{\infty}, C \rightarrow C_{\infty}, N \rightarrow N_{\infty} \quad \text{as } y \rightarrow \infty. \quad (6)$$

Here, $u_w = ax$ is the stretching sheet velocity. The sheet is stretched along the horizontal axis, and the velocity away from the sheet is $u_{\infty} = bx$. The temperature at the sheet surface is T_w , concentration at

the wall is described by C_w , and density for motile microorganisms is signified by N_w , while the temperature, concentration, and motile microorganisms at infinity are represented by T_∞ , C_∞ , and N_∞ , respectively.

Here,

$$\phi_E = \left(u^2 \frac{\partial^2 T}{\partial x^2} + v^2 \frac{\partial^2 T}{\partial y^2} + 2uv \frac{\partial^2 T}{\partial x \partial y} \right) + \left[\left(u \frac{\partial u}{\partial x} + v \frac{\partial u}{\partial y} \right) \frac{\partial T}{\partial x} + \left(u \frac{\partial v}{\partial x} + v \frac{\partial v}{\partial y} \right) \frac{\partial T}{\partial y} \right], \quad (7)$$

and

$$\phi_C = \left(u^2 \frac{\partial^2 C}{\partial x^2} + v^2 \frac{\partial^2 C}{\partial y^2} + 2uv \frac{\partial^2 C}{\partial x \partial y} \right) + \left[\left(u \frac{\partial u}{\partial x} + v \frac{\partial u}{\partial y} \right) \frac{\partial C}{\partial x} + \left(u \frac{\partial v}{\partial x} + v \frac{\partial v}{\partial y} \right) \frac{\partial C}{\partial y} \right]. \quad (8)$$

The mathematical expression for the radiative heat flux is given as

$$q_r = -\frac{4\sigma^* \partial T^4}{3k^* \partial y}, \quad (9)$$

where

$$T^4 = 4T_\infty^3 T - 3T_\infty^4, \quad (10)$$

where k^* represents the mean absorption coefficient and σ^* highlights the Stefan–Boltzmann constant.

Similarity transformations are used to convert PDEs into ODEs.

$$\Psi = \sqrt{av}xf(\eta), \eta = \sqrt{\frac{a}{v}}y, \theta(\eta) = \frac{T - T_\infty}{T_w - T_\infty}, \phi(\eta) = \frac{C - C_\infty}{C_w - C_\infty}, \quad (11)$$

$$\chi(\eta) = \frac{N - N_\infty}{N_w - N_\infty},$$

where the stream function is represented by Ψ and is defined as $u = \frac{\partial \Psi}{\partial y}$ and $v = -\frac{\partial \Psi}{\partial x}$.

After applying the similarity transformation, the following system of ODEs is obtained:

$$f''' + ff' - f'^2 + M(A - f') + A^2 + \Lambda[\theta - Nr\phi - Rb\chi] = 0, \quad (12)$$

$$(1 + Rd)\theta'' - Pr\delta_1[f^2\theta'' + ff'\theta'] + Prf\theta' = 0, \quad (13)$$

$$\phi'' + Scf\phi' - Sc\delta_2[f^2\phi'' + ff'\phi'] = 0, \quad (14)$$

$$\chi'' + Lbf\chi' - Pe[(\sigma + \chi)\phi'' + \chi'\phi'] = 0. \quad (15)$$

After using similarity transformation, boundary conditions are reduced as follows:

$$\begin{aligned} \eta = 0: f(\eta) = 0, f'(\eta) = 1, \theta(\eta) = 1, \phi(\eta) = 1, \\ \chi(\eta) = 1, \eta \rightarrow \infty: f'(\eta) \rightarrow A, \theta(\eta) \rightarrow 0, \phi(\eta) \rightarrow 0, \chi(\eta) \rightarrow 0. \end{aligned} \quad (16)$$

Dimensionless parameters that appear in ODEs are of great importance for the results and discussion section. These parameters are mathematically highlighted by the following expressions:

$$\begin{aligned} Pr = \frac{\nu}{\alpha}, Sc = \frac{\nu}{D}, Rd = \frac{16\sigma^*T_\infty^3}{3k^*k}, \sigma = \frac{N_\infty}{N_w - N_\infty}, Lb = \frac{\nu}{D_m}, \\ Pe = \frac{bW_c}{D_m}, \delta_1 = a\lambda_E, \delta_2 = a\lambda_C, \Lambda = \frac{Gr}{Re_x^2}, \\ Nr = \frac{(\rho_p - \rho_f)(C_w - C_\infty)}{(1 - C_\infty)\rho_f\beta(T_w - T_\infty)}, Rb = \frac{(\rho_m - \rho_f)(N_w - N_\infty)}{(1 - C_\infty)\rho_f\beta(T_w - T_\infty)}, \\ M = \frac{\sigma B_0^2}{\rho_f a}, A = \frac{b}{a}, \end{aligned} \quad (17)$$

where $\Lambda = \frac{Gr}{Re_x^2}$ highlights the mixed convection parameter. The Grashof number is represented by Gr , which is the ratio of buoyancy to the viscous forces.

The mathematical expression for skin frictions is defined as follows:

$$Cf_x = \frac{\tau}{\frac{U_w^2}{2}}. \quad (18)$$

The dimensionless form is given as

$$\frac{1}{2}Cf_x Re_x^{\frac{1}{2}} = -f''(0). \quad (19)$$

The expression for the Nusselt number is given as follows:

$$Nu_x = \frac{xq_w}{k_f(T_w - T_\infty)}, \quad (20)$$

where q_w denotes the heat flux, and the mathematical expression for the heat flux is given by the relation

$$q_w = -k \frac{\partial T}{\partial y} - \frac{4\sigma^* \partial T^4}{3k^* \partial y}. \quad (21)$$

The dimensionless form of the heat transfer rate is represented by the following expression:

$$Nu_x Re_x^{-\frac{1}{2}} = -(1 + Rd)\theta'(0). \quad (22)$$

The mathematical expression for the mass transfer rate is represented as

$$Sh_x = \frac{xq_m}{D_B(C_w - C_\infty)}, \quad (23)$$

where q_m denotes the mass flux, which is represented by

$$q_m = -D_B \frac{\partial C}{\partial y}. \quad (24)$$

The dimensionless form of the mass transfer is represented by the expression

$$Sh_x Re_x^{-\frac{1}{2}} = -\phi'(0). \quad (25)$$

Here, the Reynolds number is highlighted by Re , that is, the ratio of inertial to the viscous forces. The density of the motile microorganism profile is highlighted by

$$Nn_x = \frac{xq_n}{D_m(N_w - N_\infty)}, \quad (26)$$

where

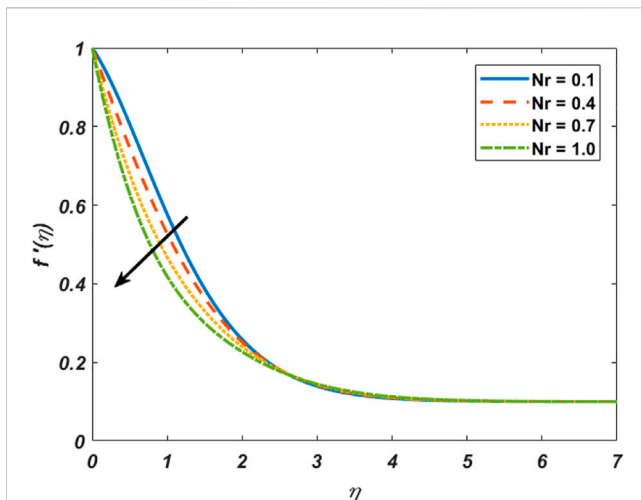


FIGURE 9
Influence of the buoyancy ratio parameter Nr on $f'(\eta)$.

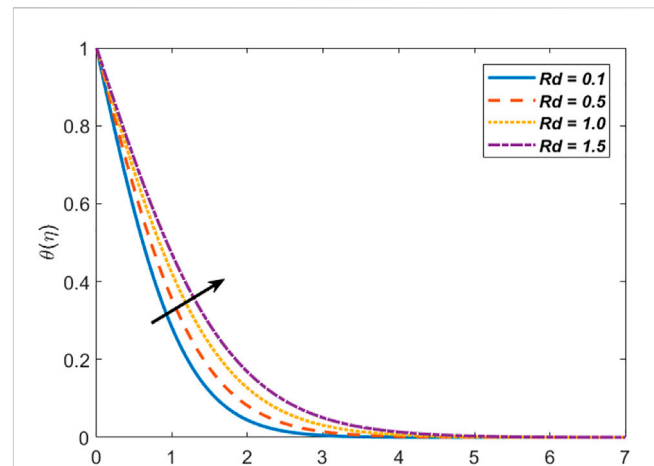


FIGURE 11
Influence of the radiation parameter Rd on $\theta(\eta)$.

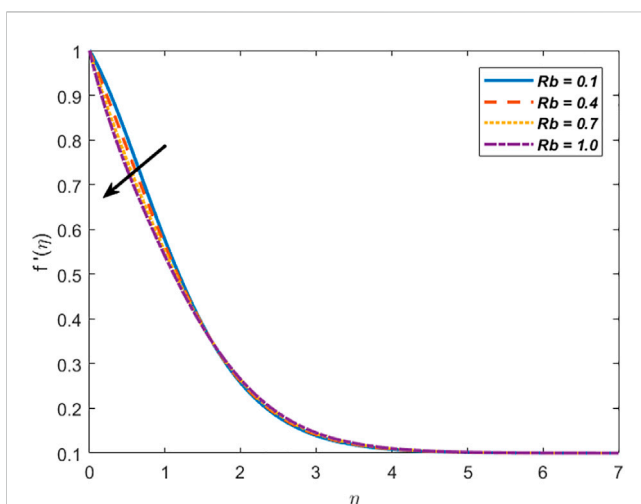


FIGURE 10
Influence of the bioconvection Rayleigh number Rb on $f'(\eta)$.

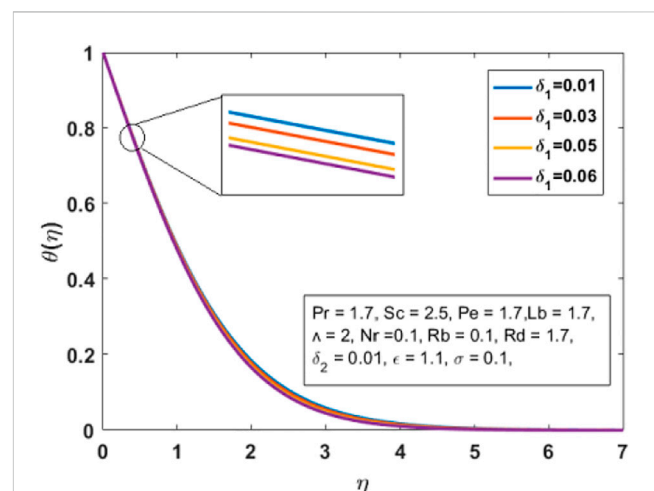


FIGURE 12
Influence of the thermal relaxation time parameter δ_1 on $\theta(\eta)$.

$$q_n = -D_m \frac{\partial \chi}{\partial y}, \quad (27)$$

and the dimensionless form is given by

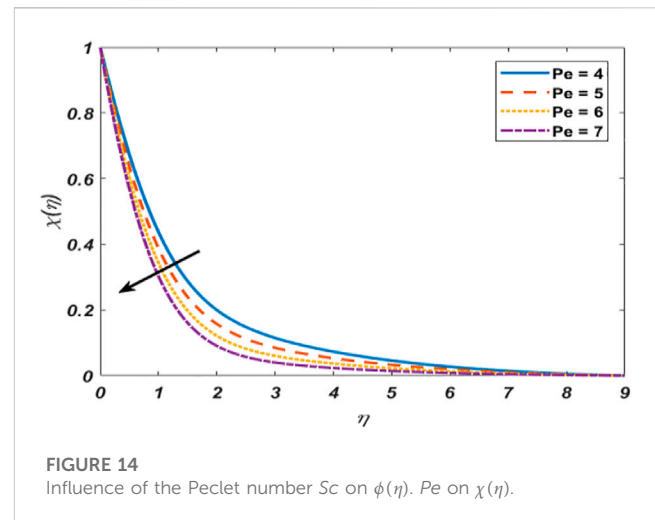
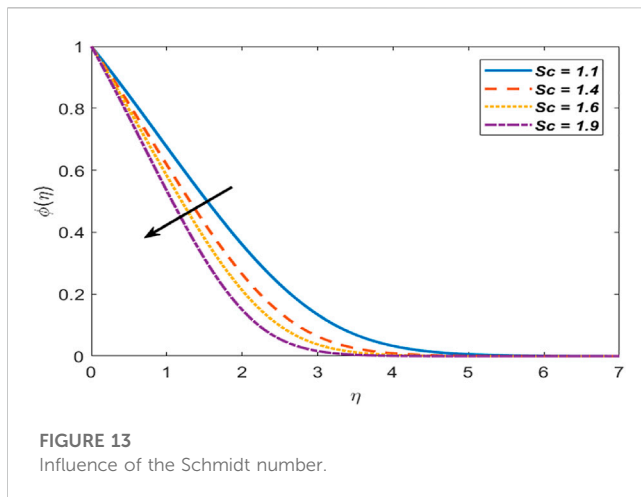
$$Nn_x Re_x^{-1/2} = -\chi'(0). \quad (28)$$

3 Solution methodology

The translated coupled non-linear ODEs are not easy to solve. It is impossible to solve these equations analytically. Therefore, the approximate solution of these equations along with the associated boundary conditions is attained by using the BVP4C built-in technique. To use the BVP4C technique, higher-order ODEs are reduced into ODEs of the first order by considering new variables $f = y_1, f' = y_2, f'' = y_3, f''' = y_4, \theta = y_5, \theta' = y_6, \theta'' = y_7, \theta''' = y_8, \chi = y_9, \chi' = y_{10}, \chi'' = y_{11}$.

$\phi' = y_7, \phi'' = y_8, \chi' = y_9, \chi'' = y_{10}$. So, the translated first-order ODEs are

$$\begin{aligned} y_1' &= y_2, \\ y_2' &= y_3, \\ y_3' &= -y_1 y_3 + y_2^2 - M(A - y_2) - A^2 - \Lambda[y_4 - Nry_6 - Rby_8], \\ y_4' &= y_5, \\ y_5' &= \frac{Pr \delta_1 y_1 y_2 y_5 - Pr y_1 y_5}{(1 + Rd) - Pr \delta_1 y_1^2}, \\ y_6' &= y_7, \\ y_7' &= \frac{Sc \delta_2 y_1 y_2 y_7 - Sc y_1 y_7}{1 - Sc \delta_2 y_1^2}, \\ y_8' &= y_9, \\ y_9' &= Pe[(\sigma + y_8)y_7 + y_7 y_9] - Lby_1 y_9, \end{aligned}$$



where boundary conditions are

$$\eta=0: y_1(\eta)=0, y_2(\eta)=1, y_4(\eta)=1, y_6(\eta)=1, \\ y_8(\eta)=1, \eta \rightarrow \infty: y_2(\infty) \rightarrow A, y_4(\infty) \rightarrow 0, y_6(\infty) \rightarrow 0, y_8(\infty) \rightarrow 0.$$

4 Results and discussion

This section comprises the graphical representation of impacts of different rheological parameters on the velocity, temperature, concentration, and motile microorganism profile. The results for the skin friction, Nusselt number, Sherwood, and motile density of microorganism numbers are also tabulated. Validation of the implemented numerical scheme and computed results is given in Table 1 by constructing a comparison with the results published by authors Mahapatra and Gupta (2002), Mustafa et al. (2011), and Ibrahim et al. (2013). From the attained data mentioned in Table 1, variation in the skin friction coefficient is noticed against the stagnation parameter (A) by fixing $M = \Lambda = Nr = Rb = Rd = Pr = \delta_1 = Sc = Lb = Pe = \sigma = 0$. Here, a complete agreement in derived and available values is found, which shows a complete agreement of results. Subsequently, in Table 2, variations are found in the Nusselt number against the stagnation point parameter (A) for $Pr = 1$ and 1.5 along with restriction on other parameters like $M = \Lambda = Nr = Rb = Rd = Pr = \delta_1 = Sc = Lb = Pe = \sigma = 0$. Again, a good match between the presently computed and existing studies has been delineated. Deviation in the skin friction coefficient ($f''(0)$) for free and forced convections is enumerated in Table 3. The impact of the buoyancy ratio parameter Nr on the shear stress at the wall for mentioned regimes is manipulated in this table. It is observed that skin friction is more in the case of free convection ($\Lambda > 1$) in comparison to forced convection ($\Lambda < 1$). It is because of the fact that in the case of $\Lambda > 1$, the magnitude of buoyancy forces dominates over inertial forces. Due to this reason, less movement is generated, and the force exerted by the wall on fluid particles is more than in other cases. The change in the heat flux coefficient against the radiation parameter (Rd) for free convection ($\Lambda > 1$) and forced convection ($\Lambda < 1$) in a comparative manner is evaluated in Table 4. It is seen that the heat

flux is more in case of free convection compared to forced convection. It is due to the fact that for $\Lambda > 1$, the magnitude of $Gr > Re$, which shows that the temperature difference between hot and cold regions rises and, thus, as a consequence, heat flux generates in the domain. The influence of various dimensionless parameters on the skin friction coefficient is illustrated in Table 5. It is shown that the skin friction coefficient amplifies for the uplifting magnetic parameter M , buoyancy ratio parameter Nr , and bioconvection Rayleigh number Rb , while the behavior of the skin friction coefficient is quite opposite for the remaining parameters. Table 6 is formulated by examining the impacts of various dimensionless parameters on the Nusselt number, Sherwood number, and motile microorganism density number by keeping $A = 0.1$, $M = 0$, $Nr = 0.5$, $Rb = 1.5$, and $\Lambda = 0.05$. It is reported that the Nusselt number amplifies for surging the values of the thermal and concentration relaxation time parameters δ_1, δ_2 , the radiation parameter Rd , the Schmidt number Sc , the bioconvection Lewis number Lb , the Peclet number Pe , and microorganism concentration diffusion parameter σ . The Sherwood number amplifies for higher values of the radiation parameter Rd , Schmidt number Sc , bioconvection Lewis number Lb , Peclet number Pe , and microorganism concentration diffusion parameter σ but decreases for higher values of thermal and concentration relaxation time parameters δ_1 and δ_2 . The motile microorganism density enhances for the uplifting radiation parameter Rd , Schmidt number Sc , bioconvection Lewis number Lb , Peclet number Pe , and microorganism concentration diffusion parameter σ but depreciates for higher values of thermal and concentration relaxation time parameters δ_1 and δ_2 .

Figure 1 depicts the effect of the stretching ratio parameter A on $f'(\eta)$. It is reported that when the stretching velocity is more than the free stream velocity ($A < 1$), the velocity of the fluid as well as the boundary layer thickness depreciates. However, in the case when the stretching sheet velocity is less than the free stream velocity ($A > 1$), the fluid velocity accelerates while the thickness of the boundary layer depreciates. The influence of the magnetic parameter M on the velocity field $f'(\eta)$ is represented in Figure 2. It is reported that for surging M , fluid velocity depreciates. This

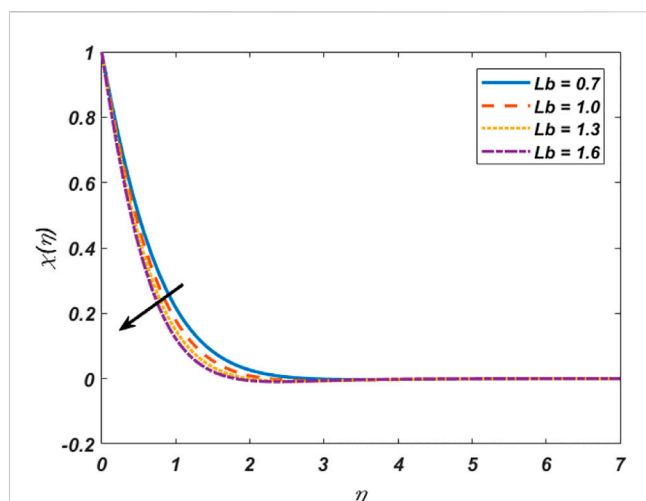


FIGURE 15
Influence of bioconvection Lewis number Lb on $\chi(\eta)$.

whole phenomenon arises due to the opposing behavior of the Lorentz force. The impact of the Grashof number (Gr) on the momentum distribution for the forced convective regime is illustrated in Figure 3. Since, in the present study, the effects of convection are considered, to exemplify the influence of forced convection on the velocity profile, the Reynolds number (Re) is fixed at 2.5 and the Grashof number (Gr) is varied from 2.0 to 3.2. Here, the buoyancy ratio parameter will take the form ($\Lambda < 1$) for forced convection. It is found that by increasing the Grashof number (Gr), the velocity field enhances. It is because of the fact that for ($\Lambda < 1$), the impact of inertial forces is dominant over that of buoyancy forces; thus, as an outcome momentum of fluid accelerates. The influence of the Grashof number (Gr) on the velocity distribution for the free convective regime is addressed in Figure 4. For interpretation about the change in the velocity distribution in the free convection situation, the Reynolds number (Re) is fixed at 1.5 and the Grashof number (Gr) varies from 3 to 4.2. So, the buoyancy ratio parameter will take the form ($\Lambda > 1$) for free convection. It is reported that by upsurging the Grashof number (Gr), the momentum field accelerates. Physically, buoyancy forces dominate inertial by uplifting the Grashof number (Gr). As a result, the velocity of the fluid accelerates. Figure 5 shows the behavior of the momentum profile for the mixed convective regime including the aspects of forced ($\Lambda < 1$) and free ($\Lambda > 1$) convection. It is noted that for higher values of the Grashof number (Gr), the velocity profile accelerates, whereas for higher magnitude of the Reynolds number (Re), momentum distributions depreciate. Figure 6 depicts the impact of the Grashof number (Gr) on the temperature profile for the forced convective regime. It is found that intensification in the Grashof number (Gr) caused decrement in the temperature field. To depict the concerned behavior, the Reynolds number (Re) is fixed at 3.5 and the Grashof number (Gr) varies from 2 to 11, which shows the dominance of the Reynolds number (Re), i. e., ($\Lambda < 1$). The effect of the Grashof number (Gr) on the temperature profile for the free convection regime is illustrated in Figure 7. Here, the Reynolds number (Re) is fixed

with a value of 1.5, and the Grashof number (Gr) is varied from 3 to 12, i. e., ($\Lambda > 1$). It is reported that by uplifting the magnitude of the Grashof number (Gr), temperature distributions depreciate. Figure 8 illustrates the behavior of temperature distributions for the mixed convective regime for forced ($\Lambda < 1$) and free ($\Lambda > 1$) convection. It is noted that for higher values of the Grashof number (Gr), the temperature profile depreciates, while the opposite behavior is reported in the case of the Reynolds number (Re). The influence of the buoyancy ratio parameter Nr on $f'(\eta)$ is highlighted in Figure 9. A boosting behavior of Nr depreciates the fluid velocity. Figure 10 shows the influence of the bioconvection Rayleigh number Rb on $f'(\eta)$. In the process of bioconvection, the microorganism, whose density is smaller than fluid density, escapes toward the upper layer due to which the viscosity of the upper layer increases, and as a result, the fluid velocity depreciates. The influence of the radiation parameter Rd on the profile of temperature is highlighted in Figure 11. When high temperature is required, thermal radiation is used in devices such as nuclear reactors and combustion reactors. Physically, the fluid absorbed these radiations to kill harmful microorganisms due to which the heat transfer rate increases. Radiation also carried energy due to which temperature increased. The influence of the thermal relaxation time parameter δ_1 on the temperature profile is depicted in Figure 12. For uplifting δ_1 , the temperature profile depreciates. Physically, the time taken by the fluid to regain its original shape after removing shear stress is the relaxation time. The energy of the fluid depreciates with the passage of time, due to which the temperature field decelerates. The effect of the Schmidt number Sc on the mass transfer is depicted in Figure 13. Sc is the ratio of the momentum to the mass diffusivity. Diffusion is the process of transfer of molecules from a higher-concentration to lower-concentration region. The transfer of mass from the higher-concentration region to the lower one is termed as mass diffusion, where Sc is inversely proportional to the mass diffusion phenomenon. Therefore, for higher values of Sc , the rate of mass transfer and concentration of fluid depreciates. The behavior of the motile microorganism profile $\chi(\eta)$ against the Peclet number Pe is highlighted in Figure 14. It is reported that microorganism motion in the fluid is controlled by Pe . Pe is the ratio of the convection rate to the diffusion rate caused by the transfer of heat. For higher values of Pe , the convection phenomenon dominates the diffusion phenomenon. For higher values of Pe , the motion of microorganisms present in the fluid decreases, due to which the motile microorganism profile decreases. The impact of the bioconvection Lewis number Lb on $\chi(\eta)$ is depicted in Figure 15. It is noted that with the increase in the values of Lb , $\chi(\eta)$ decreases. Physically, the bioconvection phenomenon occurs in the fluid due to the collection of microorganisms. As a result, for higher values of Lb density, the boundary layer thickness depreciates.

5 Conclusion

The effect of mixed convection, thermal radiation, and motile microorganism on the stagnant flow of the viscous fluid toward a stretchable sheet is examined. The governing PDEs are translated into ODEs by employing suitable similarity transformations. For the

solution of the problem, the BVP4C technique is used. The central findings are as follows:

- i) By uplifting the Grashof number, the velocity field accelerates, whereas the temperature profile depreciates in both forced and free convection cases
- ii) The skin friction coefficient is higher in forced convection ($\Lambda < 1$) than in free convection ($\Lambda > 1$) due to the effective role of inertial forces
- iii) Heat flux is higher in the situation of free convection ($\Lambda > 1$) than in forced convection ($\Lambda < 1$) due to the production of temperature gradients
- iv) The velocity decelerates for uplifting magnetic and bioconvection parameters
- v) The temperature profile amplifies for uplifting the radiation parameter Rd and depreciates for uplifting the thermal relaxation parameter δ_1
- vi) It is delineated that Pe (Peclet number) controls bioconvection in the motile microorganism $\chi(\eta)$

Data availability statement

The original contributions presented in the study are included in the article/Supplementary Material; further inquiries can be directed to the corresponding author.

References

- Abbas, Z., Sheikh, M., and Pop, I. (2015). Stagnation-point flow of a hydromagnetic viscous fluid over stretching/shrinking sheet with generalized slip condition in the presence of homogeneous-heterogeneous reactions. *J. Taiwan Inst. Chem. Eng.* 55, 69–75. doi:10.1016/j.jtice.2015.04.001
- Bilal, M., Mazhar, S. Z., Ramzan, M., and Mehmood, Y. (2021). Time-dependent hydromagnetic stagnation point flow of a Maxwell nanofluid with melting heat effect and amended Fourier and Fick's laws. *Heat. Transf.* 50 (5), 4417–4434. doi:10.1002/htj.22081
- Cao, W., Animasaun, I. L., Yook, S. J., Oladipupo, V. A., and Xianjun, J. (2022). Simulation of the dynamics of colloidal mixture of water with various nanoparticles at different levels of partial slip: Ternary-hybrid nanofluid. *Int. Commun. Heat Mass Transf.* 135, 106069. doi:10.1016/j.icheatmasstransfer.2022.106069
- Cattaneo, C., and Calore, S. C. (1948). Sulla condizione del Calore. *Atti Semin. Mat. Fis. Univ. Modena Reggio Emilia* 3, 83–101. doi:10.1007/978-3-642-11051-1_5
- Chamkha, A. J., Rashad, A. M., Kameswaran, P. K., and Abdou, M. M. M. (2017). Radiation effects on natural bioconvection flow of a nanofluid containing gyrotactic microorganisms past a vertical plate with streamwise temperature variation. *J. Nanofluids* 3, 587–595. doi:10.1166/jon.2017.1351
- Chamkha, Ali. (2015). Stagnation-point flow of a viscous fluid towards a stretching surface with variable thickness and thermal radiation. *Int. J. Ind. Math.* 7, 77–85.
- Christov, C. I. (2009). On frame indifferent formulation of the Maxwell–Cattaneo model of finite-speed heat conduction. *Mech. Res. Commun.* 36 (4), 481–486. doi:10.1016/j.mechrescom.2008.11.003
- De, P. (2019). Impact of dual solutions on nanofluid containing motile gyrotactic micro-organisms with thermal radiation. *Bio Nano Sci.* 1, 13–20. doi:10.1007/s12668-018-0584-6
- Dehghan, M., and Abbaszadeh, M. (2017). A finite element method for the numerical solution of Rayleigh–Stokes problem for a heated generalized second grade fluid with fractional derivatives. *Eng. Comput.* 33 (3), 587–605. doi:10.1007/s00366-016-0491-9
- Dehghan, M., and Abbaszadeh, M. (2016). Proper orthogonal decomposition variational multiscale element free Galerkin (POD-VMEFG) meshless method for solving incompressible Navier–Stokes equation. *Comput. Methods Appl. Mech. Eng.* 311, 856–888. doi:10.1016/j.cma.2016.09.008
- Ellahi, R., Muzammal, H. T., Mohsan, H., and Vafai, K. (2017). On boundary layer nano-ferrofluid flow under the influence of low oscillating stretchable rotating disk. *J. Mol. Liq.* 229, 339–345. doi:10.1016/j.molliq.2016.12.073
- Esfahani, J. A., Akbarzadeh, M., Rashidi, S., Rosen, M. A., and Ellahi, R. (2017). Influences of wavy wall and nanoparticles on entropy generation over heat exchanger plate. *Int. J. Heat Mass Transf.* 109, 1162–1171. doi:10.1016/j.ijheatmasstransfer.2017.03.006
- Ferdows, M., Reddy, M. G., Sun, S., and Alzahrani, F. (2019). Two-dimensional gyrotactic microorganisms flow of hydromagnetic power law nanofluid past an elongated sheet. *Adv. Mech. Eng.* 11, 168781401988125. doi:10.1177/1687814019881252
- Fourier Jbj., T. A. (1822). *Theorie analytique de la chaleur*. Paris: Cambridge University Press.
- Hashim, H., Mohamed, M. K. A., Ishak, N., Sarif, N. M., and Salleh, M. Z. (2019). Thermal radiation effect on MHD stagnation point flow of Williamson fluid over a stretching surface. *J. Phys. Conf. Ser.* 1366, 012011. doi:10.1088/1742-6596/1366/1/012011
- Hiemenz, K. (1911). Die Grenzschicht an einem in den gleichförmigen Flüssigkeitsstrom eingetauchten geraden Kreiszylinder. *Dingler's Polytech. J.* 326, 321–324.
- Homann, F. (1936). Der Einfluss grosser Zähigkeit bei der Strömung um den Zylinder und um die Kugel. *Z. Angew. Math. Mech.* 16, 153–164. doi:10.1002/zamm.19360160304
- Hosseinzadeh, H., Mehdi, D., and Mirzaei, D. (2013). The boundary elements method for magneto-hydrodynamic (MHD) channel flows at high Hartmann numbers. *Appl. Math. Model.* 37 (4), 2337–2351. doi:10.1016/j.apm.2012.05.020
- Ibrahim, W., Shankar, B., and Nandeppanavar, M. M. (2013). MHD stagnation point flow and heat transfer due to nanofluid towards a stretching sheet. *Int. J. heat mass Transf.* 1–2, 1–9. doi:10.1016/j.ijheatmasstransfer.2012.08.034
- Ishak, A., Lok, Y. Y., and Pop, I. (2010). Stagnation-point flow over a shrinking sheet in a micropolar fluid. *Chem. Eng. Comm.* 197, 1417–1427. doi:10.1080/00986441003626169
- Kamranian, M., Mehdi, D., and Mehdi, T. (2017). An adaptive meshless local Petrov–Galerkin method based on a posteriori error estimation for the boundary layer problems. *Appl. Numer. Math.* 111, 181–196. doi:10.1016/j.apnum.2016.09.007
- Khan, N. S. (2018). Bioconvection in second grade nanofluid flow containing nanoparticles and gyrotactic microorganisms. *Braz. J. Phys.* 3, 227–241. doi:10.1007/s13538-018-0567-7
- Khan, U., Naveed, A., Ullah Khan, S. I., and Tauseef, S. M. D. (2014). Thermo-diffusion effects on MHD stagnation point flow towards a stretching sheet in a nanofluid. *Propuls. Power Res.* 3, 151–158. doi:10.1016/j.jprr.2014.07.006

Author contributions

SB (Conceptualization, extraction of results and discussion, write up). AU (Results validation, discussion of results) MIA (Write up, results discussion, code validation). MYA (Discussion of results, conclusions, results extraction). SE (Write up of results, discussion of results, funds acquisition). IS (New results findings, discussion of new results, addition of review comments response).

Conflict of interest

The authors declare that the research was conducted in the absence of any commercial or financial relationships that could be construed as a potential conflict of interest.

Publisher's note

All claims expressed in this article are solely those of the authors and do not necessarily represent those of their affiliated organizations, or those of the publisher, the editors, and the reviewers. Any product that may be evaluated in this article, or claim that may be made by its manufacturer, is not guaranteed or endorsed by the publisher.

- Khan, U., Zaib, A., Abu Bakar, S., Ishak, A., Baleanu, D., Sherif, E. S. M., et al. (2022). Computational simulation of cross-flow of Williamson fluid over a porous shrinking/stretching surface comprising hybrid nanofluid and thermal radiation. *AIMS Math.* 7 (4), 6489–6515. doi:10.3934/math.2022362
- Khashi'ie, N. S., Arifin, N. M., Rashidi, M. M., Hafidzuddin, E. H., and Wahi, N. (2020). Magneto hydrodynamics (MHD) stagnation point flow past a shrinking/stretching surface with double stratification effect in a porous medium. *J. Therm. Analysis Calorim.* 139 (6), 3635–3648. doi:10.1007/s10973-019-08713-8
- Kuznetsov, A. V. (2011). Non-oscillatory and oscillatory nanofluid bio-thermal convection in a horizontal layer of finite depth. *Eur. J. Mechanics-B/Fluids* 302, 156–165. doi:10.1016/j.euromechflu.2010.10.007
- Lok, Y. Y., Ishak, A., and Pop, I. (2011). MHD stagnation-point flow towards a shrinking sheet. *Int. J. Numer. Meth. Heat. Fluid Flow.* 21, 61–72. doi:10.1108/0961553111095076
- Lyu, J., Chang, S., Gao, L., Xing, Z., and Bai, M. (2022). Experimental investigation on the heat transfer enhancement of wall modification inside a piston cooling gallery. *Exp. Heat. Transf.* 2022, 1–22. doi:10.1080/08916152.2022.2151056
- Madhavadas, V., Das, D., Mohta, K. A., and Prabu, S. S. (2021). Comparative analysis on heat transfer of various fin profile using solid works: A systematic review. *IOP Conf. Ser. Earth Environ. Sci.* 850, 012029. doi:10.1088/1755-1315/850/1/012029
- Mahapatra, T. R., and Gupta, A. S. (2002). Heat transfer in stagnation-point flow towards a stretching sheet. *Heat Mass Transf.* 6, 517–521. doi:10.1007/s002310100215
- Mahapatra, T. R., and Gupta, A. S. (2003). Stagnation-point flow towards a stretching surface. *Can. J. Chem. Eng.* 81, 258–263. doi:10.1002/cjce.5450810210
- Mirzaei, D., and Mehdi, D. (2012). New implementation of MLBIE method for heat conduction analysis in functionally graded materials. *Eng. analysis Bound. Elem.* 36 (4), 511–519. doi:10.1016/j.enganabound.2011.11.007
- Mustafa, M., Hayat, T., Pop, I., Asghar, S., and Obaidat, S. (2011). Stagnation-point flow of a nanofluid towards a stretching sheet. *Int. J. Heat Mass Transf.* 54, 5588–5594. doi:10.1016/j.ijheatmasstransfer.2011.07.021
- Mustafa, T. (2021). Heat transfer enhancement feature of the Non-Fourier Cattaneo–Christov heat flux model. *J. Heat Transf.* 9, 4051671. doi:10.1115/1.4051671
- Mustafa, T. (2021). Stagnation-point flow and heat transfer over stretchable plates and cylinders with an oncoming flow: Exact solutions. *Chem. Eng. Sci.* 238, 116596. doi:10.1016/j.ces.2021.116596
- Pal, D., Mondal, S. K., and Mondal, H. (2019). Entropy generation on MHD Jeffrey nanofluid over a stretching sheet with nonlinear thermal radiation using spectral quasilinearisation method. *Int. J. Ambient Energy* 42, 1712–1726. doi:10.1080/01430750.2019.1614984
- Prasad, K. V., Rajashekhar, C., Hanumesh, V., Ashwini, B., and Animasaun, I. L. (2023). Analysis of couple stress nanofluid flow under convective condition in the temperature-dependent fluid properties and Lorentz forces. *Heat. Transf.* 1, 216–235. doi:10.1002/htj.22692
- Rashidi, S., Esfahani, J. A., and Ellahi, R. (2017). Convective heat transfer and particle motion in an obstructed duct with two side by side obstacles by means of DPM model. *Appl. Sci.* 7, 431. doi:10.3390/app7040431
- Sajid, T., Jamsheed, W., Shahzad, F., Mohamed, R. E., Sohail, M., and Ullah, I. (2022). Influences of Fourier and Fick's relations in stagnation point flow of Reiner-Philippoff fluid containing oxytactic-microorganisms with variable molecular diffusivity. *Waves Random Complex Media* 2022, 1–22. doi:10.1080/17455030.2022.2148013
- Saleem, S., Rafiq, H., Al-Qahtani, A., El-Aziz, M. A., Malik, M. Y., and Animasaun, I. L. (2019). Magneto Jeffery nanofluid biconvection over a rotating verticle cone due to gyrotactic microorganism. *Math. Problem Eng.* 2019, 1–11. doi:10.1155/2019/3478037
- Shirvan, K. M., Ellahi, R., Mamourian, M., and Moghiman, M. (2017). Effects of wavy surface characteristics on natural convection heat transfer in a cosine corrugated square cavity filled with nanofluid. *Int. J. Heat Mass Transf.* 107, 1110–1118. doi:10.1016/j.ijheatmasstransfer.2016.11.022
- Shirvan, K. M., Mamourian, M., Mirzakhani, S., and Ellahi, R. (2017). Numerical investigation of heat exchanger effectiveness in a double pipe heat exchanger filled with nanofluid: A sensitivity analysis by response surface methodology. *Powder Technol.* 313, 99–111. doi:10.1016/j.powtec.2017.02.065
- Syazana, A. N., Norfifah, B., Mustafa, T., Arifin, N. M., and Haliza, R. (2020). Analytical and stability analysis of MHD flow past a nonlinearly deforming vertical surface in Carbon Nanotubes. *Alexandria Eng. J.* 59, 497–507. doi:10.1016/j.aej.2020.01.024
- Wahid, N. S., Arifin, N. M., Mustafa, T., Mohd, E. H. H., and Rahmin, N. A. A. (2020). MHD hybrid Cu-Al₂O₃/water nanofluid flow with thermal radiation and partial slip past a permeable stretching surface: Analytical solution. *J. Nano Res.* 64, 75–91. doi:10.4028/www.scientific.net/jnanor.64.75
- Wang, C. Y. (2008). Stagnation flow towards a shrinking sheet. *Int. J. Non Linear Mech.* 43, 377–382. doi:10.1016/j.ijnonlinmec.2007.12.021
- Zhao, Y., Zhuotong, N., Hailong, J., and Zhao, L. (2022). Convective heat transfer of spring meltwater accelerates active layer phase change in Tibet permafrost areas. *Cryosphere* 16 (3), 825–849. doi:10.5194/tc-16-825-2022

Frontiers in Materials

Investigates the discovery and design of materials
for future application

A multidisciplinary journal that explores the
breadth of materials science, engineering and
mechanics - from carbon-based materials to
smart materials.

Discover the latest Research Topics

[See more →](#)

Frontiers

Avenue du Tribunal-Fédéral 34
1005 Lausanne, Switzerland
frontiersin.org

Contact us

+41 (0)21 510 17 00
frontiersin.org/about/contact

